Physics of the Solid State, Vol. 46, No. 3, 2004, pp. 395–410. Translated from Fizika Tverdogo Tela, Vol. 46, No. 3, 2004, pp. 385–400.

REVIEWS

New Type of Domain Walls: Domain Walls Caused by Frustrations in Multilayer Magnetic Nanostructures

A. I. Morosov and A. S. Sigov

Moscow State Institute of Radioengineering, Electronics, and Automation (Technical University), pr. Vernadskogo 78, Moscow, 119454 Russia

e-mail: mor-alexandr@yandex.ru

Received May 26, 2003

Abstract—Roughness of the interfaces between layers in a multilayer magnetic structure causes frustration of the exchange interaction between spins. Under certain conditions, frustration brings about the formation of domain walls (DWs) of a new type, whose parameters are determined by the competition between different exchange interactions rather than between the exchange and anisotropy energies as is the case with conventional DWs. Such DWs are much sharper than conventional DWs. The conditions under which micro- (nano-) domains arise are considered, and magnetic phase diagrams for ferromagnet–nonmagnetic metal–ferromagnet and ferromagnet–antiferromagnet nanostructures are discussed. © *2004 MAIK "Nauka/Interperiodica".*

1. INTRODUCTION

Multilayer magnetic structures several nanometers thick have been attracting considerable research attention since the discovery of giant magnetoresistance (GMR) [1], which immediately found wide practical application. This effect is used, in particular, in reading heads for gigabyte hard disks in personal computers. Such heads made it possible to increase the recording density and, hence, the memory capacity of hard disks. Multilayer magnetic structures are widely used as magnetic-field sensors and are still finding new areas of application. They offer promise as a basis for nonvolatile magnetic random-access memory (MRAM), which could be expected to take the place of both hard disks and semiconductor-based RAM.

Multilayer magnetic nanostructures are also of considerable interest from the fundamental point of view. In the case of such thin layers (ranging in thickness from several nanometers to several tens of nanometers), the effect of interfaces is very significant and the properties of thin layers can differ radically from those of the corresponding bulk materials. Furthermore, the condition of the interfaces has been found to dictate the physical and, in particular, magnetic properties of the layers. The present review is devoted to this topic.

The review is organized as follows. In Section 2, we discuss frustration in multilayer magnetic structures. Section 3 deals with domain walls (DWs) due to frustration and with a phase diagram for the ferromagnet–nonmagnetic metal–ferromagnet three-layered structure. The ferromagnet–antiferromagnet two-layer system is considered in Section 4, and the ferromagnet–antiferromagnet–ferromagnet three-layered system is treated in Section 5. Finally, in Section 6, the main conclusions are drawn and lines of further investigations are proposed.

2. FRUSTRATION IN MULTILAYER MAGNETIC STRUCTURES

2.1. Giant Magnetoresistance

Let us briefly consider giant magnetoresistance on the example of a ferromagnet–nonmagnetic metal–ferromagnet three-layer metallic system with ideally smooth interfaces (Fig. 1). The exchange coupling between the ferromagnetic (FM) layers is effected through a paramagnetic spacer layer of thickness d via the Ruderman–Kittel–Kasuya–Yosida (RKKY) interaction. The exchange integral $J_\perp(d)$ in the case of free electrons has the form [2]

$$J_\perp(d) = J_0\frac{\sin(2k_F d)}{(2k_F d)^2}, \quad (1)$$

where J_0 is a constant and k_F is the Fermi wave vector of conduction electrons.

Expression (1) takes no account of the specific shape of the Fermi surface of the nonmagnetic spacer

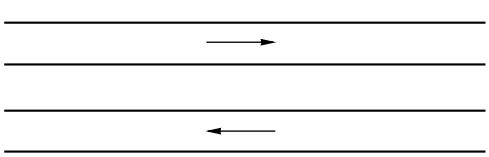

Fig. 1. Ferromagnet–nonmagnetic metal–ferromagnet three-layered system (schematic).

1063-7834/04/4603-0395$26.00 © 2004 MAIK "Nauka/Interperiodica"

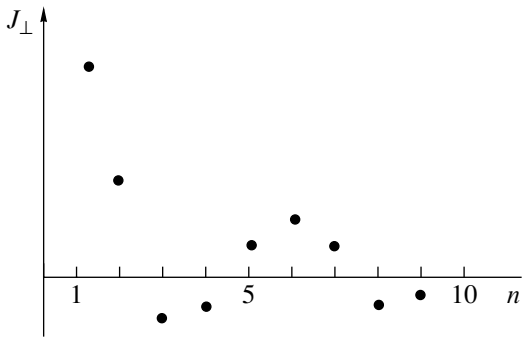

Fig. 2. Exchange integral of interlayer interaction as a function of the number of atomic planes in the nonmagnetic spacer layer.

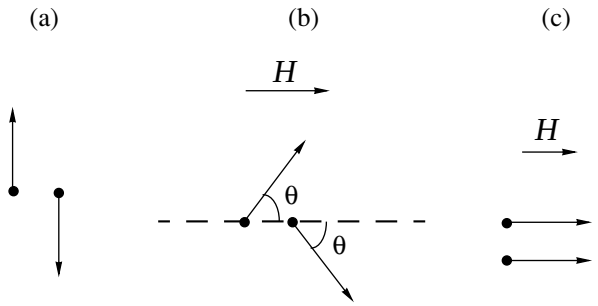

Fig. 3. Orientation of the magnetization vectors of FM layers corresponding to different ranges of values of the external magnetic field in the exchange approximation. (a) $H = 0$, (b) $H < H_{sat}$, and (c) $H > H_{sat}$.

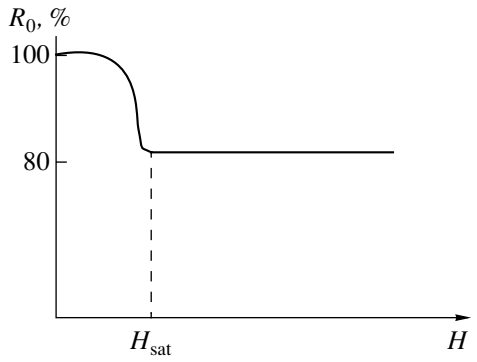

Fig. 4. Resistance of a magnetic multilayer structure as a function of external magnetic field.

and the size effects due to finite transverse dimensions of the layers. These effects have been considered in a large number of papers (see, e.g., [3–7]). The $J_\perp(d)$ dependence can also be strongly affected by the presence of several extremal cross-sectional dimensions of the complicated Fermi surface resulting in a superposition of spatial oscillations with different periods. However, the factors indicated above do not change the oscillatory character of the exchange coupling between the FM layers.

It should also be noted that the thickness d takes on discrete values, changing by one atomic layer. The dependence of $J_\perp$ on the number n of atomic layers is shown in Fig. 2.

It can be seen from Fig. 2 that $J_\perp$ is negative at certain values of n. Therefore, the interaction energy E_{int} between the FM layers

$$E_{int} = -J_\perp(\mathbf{M}_1, \mathbf{M}_2) \quad (2)$$

is minimal when the magnetizations $\mathbf{M}_1$ and $\mathbf{M}_2$ of the layers are antiparallel. It is this magnetization orientation that is realized in the absence of an external magnetic field. When a magnetic field is applied, the magnetization of each layer tends to be oriented along the magnetic field. Therefore, as the magnetic field is increased, the mutual orientation of the magnetizations changes from antiparallel to canted (Fig. 3) and then, as the saturation field H_{sat} is reached, the magnetizations become parallel. In the case where the two FM layers are identical, the magnetizations behave in the same way as the magnetizations of a mirror-symmetric antiferromagnet in an external magnetic field.

When the mutual orientation of adjacent FM layers of a three-layer structure (or of a multilayer structure consisting of alternating FM and nonmagnetic layers) changes from antiparallel to parallel, the resistance of the structure decreases by several percent or several tens of percent; that is, GMR takes place. The typical dependence of the resistance $R_0(H)$ on magnetic field is shown in Fig. 4.

Naturally, for the values of n at which $J_\perp > 0$, the magnetizations of layers are parallel to each other even in the absence of a magnetic field and GMR does not occur.

Here, we do not discuss the mechanisms of GMR and refer the reader to the recent review dedicated to this subject [8]. It should be noted that many simple explanations of GMR involve (explicitly or implicitly) the assumption that the mean free path of charge carriers is less than the layer thicknesses, which is not the case even at room temperature in the range of layer thicknesses in question in this review.

2.2. Frustration in a Three-Layered System with a Nonmagnetic Spacer Layer

The simple pattern of magnetic ordering considered above occurs in the case with ideally smooth interfaces between layers. In actuality, the layer interfaces are rough; i.e., the spacer is not uniform in thickness. In the case of crystalline layers (to which we will restrict our consideration), the roughness is due to atomic steps that arise on the interfaces and change the layer thickness by one monatomic layer (Fig. 5).

Let us consider how atomic steps affect the coupling between FM layers, which is the sum of pairwise RKKY interactions between atomic spins belonging to different layers. For this purpose, we should determine the region that contributes to the molecular field exerted by one layer on the atomic spin of the other layer.

A simple analysis shows that this region lies opposite the atom and that its size is typically of the order of the thickness of the nonmagnetic spacer d (Fig. 5). In other words, the thickness d characterizes nonlocality of interaction between the layers. Thus, the exchange interaction between the layers at a given point of the layer plane is determined not by the local thickness of the spacer but rather by its thickness in a region whose dimensions in the spacer layer plane are of the order of d.

We assume that d is much smaller than the other length scales characterizing the magnetic ordering in the structure in question. In other words, we neglect nonlocality and assume that $J_\perp(x, y) \equiv J_\perp(d(x, y))$, where the x and y axes of the Cartesian coordinate system lie in the layer plane and the z axis is normal to it. The edge of a step is taken to be parallel to the y axis.

On one side of the step, we have $J_\perp = J_\perp(n)$, and on the other side, $J_\perp = J_\perp(n-1)$. If $J_\perp(n)J_\perp(n-1) < 0$, frustration occurs in the system. This term is widely used in describing the properties of spin glasses. In the presence of frustration, there is no orientation of spins for which all their pairwise exchange interaction energies are simultaneously minimal. As the simplest example of a frustrated system, we can cite three spins situated at the vertices of a triangle, with all their pairwise interactions being antiferromagnetic (AFM).

In the case considered above, we have a similar situation. A uniform distribution of order parameters (magnetizations in our case) over the layers, which minimizes the exchange energy in each layer, does not minimize the interaction energy between the layers.

The state that arises in this frustrated system will be considered in Section 3.

2.3. Frustration in the Ferromagnet–Antiferromagnet System

In this system, the short-range Heisenberg exchange interaction between spins is dominant. In a ferromagnet–antiferromagnet–ferromagnet three-layered structure, the FM layers interact via the spins of the antiferromagnet; this interaction is much stronger than the RKKY interaction. Therefore, in treating such systems, it will suffice to take into account the nearest neighbor interaction alone. Let us consider the frustration occurring at the interface between an FM and an AFM layer.

The magnetic moment of an antiferromagnet atomic plane parallel to the interface can be either nonzero or zero. In the former case, the antiferromagnet surface is called uncompensated, and in the latter, compensated. For example, for a cubic mirror-symmetric antiferromagnet, the (111) surface is uncompensated, while the (100) and (110) surfaces are compensated. In this review, we consider only the case of an uncompensated antiferromagnet surface, whose roughness causes frustration, as will be shown below. The system consisting of an antiferromagnet with a compensated surface and a ferromagnet is frustrated even if the interface between them is ideally smooth; therefore, the roughness of this interface is of no importance in this respect.

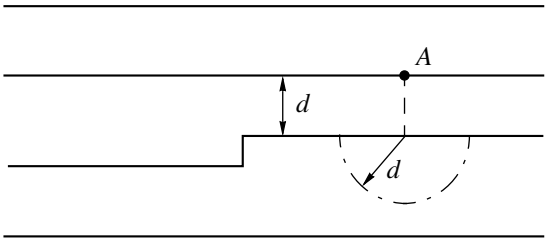

Fig. 5. Atomic step on the interface between layers. The dot-and-dash curve is the boundary of the region making the main contribution to the molecular field at point *A*.

Let us consider the perfectly smooth planar interface between a ferromagnet and an uncompensated antiferromagnet (Fig. 6a). In the ground state and in the absence of an external magnetic field, the spins in the ferromagnet are parallel or antiparallel to the spins located on the top atomic plane of the antiferromagnet depending on the sign of the exchange integral $J_{f,af}$ between neighboring spins belonging to different layers ($J_{f,af} > 0$ corresponds to the parallel orientation).

Now, we consider an atomic step on the interface between a ferromagnet and an uncompensated antiferromagnet (Fig. 6b). The spins of the ferromagnet located on different sides of the step are in contact with antiferromagnet spins belonging to different atomic planes. If the collinear orientation of the FM and AFM order parameters on one side of the step corresponds to a minimum of the interface energy, then this energy on the other side of the step is maximal; therefore, a frustration occurs that is caused by the step.

3. DOMAIN WALLS AND A PHASE DIAGRAM OF A FERROMAGNET–NONMAGNETIC METAL–FERROMAGNET THREE-LAYERED SYSTEM

3.1. A Domain Wall due to Frustration

Let us consider an isolated straight step on one of the interfaces of the three-layered system (Fig. 5). For the sake of definiteness, we assume that

$$J_\perp(x) = \begin{cases} J_1 > 0, & x < 0 \\ J_2 < 0, & x > 0. \end{cases} \quad (3)$$

It is clear that far from the step the mutual orientation of the layer magnetizations must be such that their

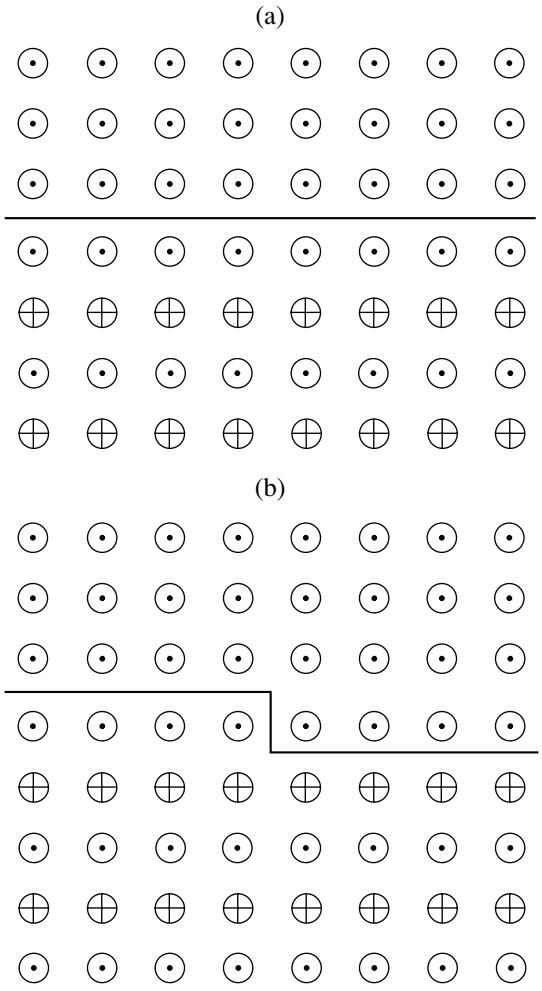

Fig. 6. Interfaces between a ferromagnet and an uncompensated antiferromagnet. (a) Perfectly smooth planar interface and (b) an interface containing an atomic step.

interaction energy is minimal; that is, the magnetizations are parallel to each other for $x \longrightarrow -\infty$ and are antiparallel for $x \longrightarrow +\infty$.

In other words, near the edge of the step a DW arises that runs through all layers and separates the half-space where the layer magnetizations are parallel ($x < 0$) from the half-space of the antiparallel mutual orientation of the magnetizations ($x > 0$).

In this review, we assume that the atomic spins lie in the layer plane; therefore, no stray demagnetizing fields arise in the case of perfectly smooth interfaces. The position of the ith spin is defined by the angle θ_i between the spin and the x axis. The order parameter is assumed not to change in magnitude.

Furthermore, we restrict our consideration to the exchange approximation neglecting anisotropy in the layer plane. This approximation is valid if the exchange energy causing the formation of the DW is much higher than the anisotropy energy and the DW is much thinner than the conventional DW, whose thickness is dictated by the balance between the exchange and anisotropy energies.

The thickness of such a DW of a new type was estimated in [9], and its characteristics were calculated analytically in [10].

The analytical calculation was performed within a continuum approximation. As shown below, the characteristic DW thickness is much larger than the thicknesses of the layers of the nanostructure at hand. Therefore, we can assume that the DW thickness does not vary along the z axis (which is perpendicular to the layer plane). Thus, the problem becomes one-dimensional in the case of a step with a straight edge.

According to [11], the addition to the exchange energy between spins in the layers due to nonuniformity of the order parameter (magnetization) is

$$W_1 = \int\left[\frac{\alpha_1}{2}(\theta_1')^2 + \frac{\alpha_2}{2}(\theta_2')^2\right]d^2\boldsymbol{\rho}, \qquad (4)$$

where θ_i is the tilt angle of the order parameter in the ith FM layer ($i = 1, 2$), the prime denotes differentiation with respect to x, and integration is performed over the surface of the multilayer structure. In order of magnitude, the exchange stiffnesses of the layers α_i are

$$\alpha_i \sim J_i S_i^2 l_i / b, \qquad (5)$$

where J_i is the exchange integral between neighboring spins in the ith layer; S_i is the average value of the atomic spin in this layer; l_i is the thickness of the ith layer; and b is the interatomic distance, which we assume to be the same for all layers.

The interaction energy between the layers in the mean-field approximation is

$$W_2 = -\int\beta(x)\cos(\theta_1 - \theta_2)d^2\boldsymbol{\rho}, \qquad (6)$$

where

$$\beta(x) = \begin{cases}\beta_1 > 0, & x < 0\\ -\beta_2 < 0, & x > 0,\end{cases} \quad \sim J_\perp(x)S_1S_2b^{-2}. \qquad (7)$$

By varying the sum $W_1 + W_2$ with respect to θ_1 and θ_2, we obtain a set of equations

$$\begin{aligned}\alpha_1\theta_1'' - \beta\sin(\theta_1 - \theta_2) &= 0,\\ \alpha_2\theta_2'' + \beta\sin(\theta_1 - \theta_2) &= 0\end{aligned} \qquad (8)$$

with the boundary conditions $\theta_i' \longrightarrow 0$ as $x \longrightarrow \pm\infty$, $\theta_i \longrightarrow 0$ as $x \longrightarrow -\infty$, and $|\theta_1 - \theta_2| \longrightarrow \pi$ as $x \longrightarrow +\infty$. The solution to this set of equations is $\theta_2 = -\alpha_1\theta/(\alpha_1 +$

α_2) and $\theta_1 = \alpha_2\theta/(\alpha_1 + \alpha_2)$, where $\theta(x)$ can be found from the equations

$$\cos\frac{\theta}{2} = -\tanh\left[\left(\frac{\beta_1}{\alpha^*}\right)^{1/2}(x + x_1)\right], \quad x < 0,$$
$$\sin\frac{\theta}{2} = \tanh\left[\left(\frac{\beta_2}{\alpha^*}\right)^{1/2}(x + x_2)\right], \quad x > 0. \tag{9}$$

Here, $\alpha^* = \alpha_1\alpha_2/(\alpha_1 + \alpha_2)$ and the constants x_1 and x_2 can be found from the conditions of continuity of $\theta(x)$ and its derivative $\theta'(x)$ at $x = 0$, which reduces to the equation

$$\tan\frac{\theta}{2}\bigg|_{x=0} = \left(\frac{\beta_2}{\beta_1}\right)^{1/2}. \tag{10}$$

It is easy to see that, for $\beta_1 \gg \beta_2$, the DW is almost entirely located in the region $x > 0$ and, for $\beta_1 \ll \beta_2$, the DW is in the region $x < 0$. In the case of $\alpha_1 = \alpha_2$, the spins of different layers rotate in opposite directions through an angle of 90°. If one of the values of α is much larger than the other (which corresponds to the case where one of the FM layers is much thicker than the other), then the rotation of spins occurs virtually entirely in the thinner layer, whereas in the thicker layer the spins deviate only slightly.

The characteristic DW thickness δ is

$$\delta = \pi\left(\frac{\alpha^*}{\min(\beta_1, \beta_2)}\right)^{1/2}$$
$$\sim \pi b\left(\frac{J_i l_{\min}}{J_\perp b}\right)^{1/2} \sim \pi d\left(\frac{J_i l_{\min}}{J_0 b}\right)^{1/2} \gg d, \tag{11}$$

where $l_{\min}$ is the thickness of the thinner FM layer. For $l/b \sim 3$–5, $J_i/J_0 \sim 1$–10, and $d \sim 10$ Å, we have $\delta \sim 100$ Å, which is much smaller than the DW thickness in iron (800 Å).

If the thickness of this unusual DW is comparable to or larger than the thickness of the conventional DW, then we should include the anisotropy energy $E_a^i = -l_i K_i \cos 2\theta_i$ (for the easy magnetization axis lying in the layer plane) or $E_a^i = -l_i K_i \cos 4\theta_i$ (for the case of a fourfold axis perpendicular to the layer plane). In this case, an order-of-magnitude estimation of the DW thickness gives

$$\delta \sim \pi b^{-1/2}\left(\frac{J_i}{K + J_0/d^2 l_{\min}}\right)^{1/2}. \tag{12}$$

Substituting solution (8) into the functional $W_1 + W_2$, we can find the DW energy integrated over the layer thicknesses, i.e., the energy per unit length of the DW line on the layer surfaces. This energy is equal to the difference between the above-mentioned functional and the sum of the energies of the uniform states with $\theta = 0$ for $x < 0$ and $\theta = \pi$ for $x > 0$ and is found to be

$$\sigma = 4(\alpha^*)^{1/2}[\beta_1^{1/2} + \beta_2^{1/2} - (\beta_1 + \beta_2)^{1/2}]$$
$$\sim d^{-1}S^2[J_i J_0 l_{\min}/b]^{1/2} \sim b^{-1}S^2[J_i J_\perp l_{\min}/b]^{1/2}. \tag{13}$$

Thus, we have calculated the characteristics of an isolated DW in the ferromagnet–nonmagnetic metal–ferromagnet structure.

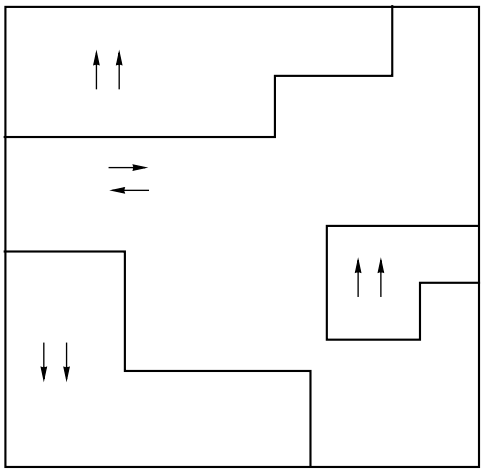

Fig. 7. Domains with parallel and the antiparallel mutual orientation of the magnetizations of FM layers in a three-layered structure.

3.2. Phase Diagram

Now, we investigate the phase diagram for variable interface roughness [12]. If the characteristic distance R between atomic steps on the interface between the layers (giving rise to frustration) is much larger than the DW thickness δ ($R \gg \delta$), then it is energetically favored for the magnetic layers to break up into domains. The domains with parallel and antiparallel mutual orientation of the magnetizations of the FM layers are separated by DWs. The structure pattern of the domain is shown in Fig. 7.

In the opposite extreme case where the characteristic roughness scale is such that $R \ll \delta$, domains cannot form. We restrict our consideration to the case of $R \gg d$, which allows us to use, as before, the local approximation to $J_\perp(\boldsymbol{\rho})$. If $R \ll d$, then $J_\perp(\boldsymbol{\rho})$ is effectively averaged over the region of nonlocality to give $J_\perp(\boldsymbol{\rho}) \approx$ const.

The transition from the state with $R \gg \delta$ to the state with $R \ll \delta$ can occur as the thickness of the spacer layer increases, because $\delta \propto d$. In the case of $R \ll \delta$, the deviations $\psi_i(\boldsymbol{\rho}) = \theta_i(\boldsymbol{\rho}) - \langle\theta_i\rangle$ of the angles θ_i from their average values $\langle\theta_i\rangle$ are small, $|\psi_i| \ll 1$ ($i = 1, 2$).

Now, we show that these deviations are energetically unfavorable in the case of $\langle\theta_1\rangle = \langle\theta_2\rangle$. Indeed, by

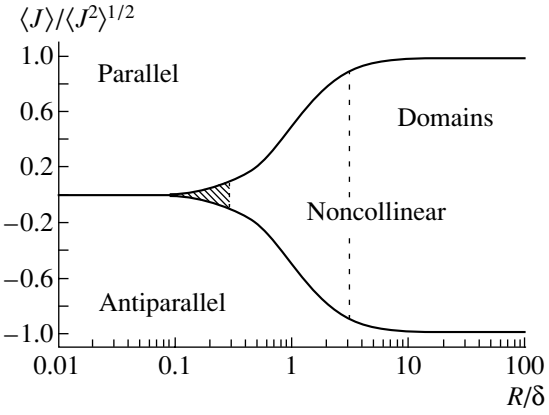

Fig. 8. Exchange–roughness phase diagram for a three-layered system with a nonmagnetic spacer. The region of existence of the noncollinear state is shown by hatching. The dotted line is the boundary of the region of existence of domains.

varying the total energy $W_1 + W_2$ with respect to ψ_i, it is easy to show (following [10]) that ψ_1 and ψ_2 are expressed in terms of the variable $\psi = \psi_1 - \psi_2$ as

$$\psi_1 = \frac{\alpha^*}{\alpha_1}\psi, \quad \psi_2 = -\frac{\alpha^*}{\alpha_2}\psi, \tag{14}$$

$$W_1 = \frac{\alpha^*}{2}\int(\nabla\psi)^2 d^2\boldsymbol{\rho}. \tag{15}$$

When an inhomogeneity occurs with a characteristic maximal magnetization deviation through an angle ψ_0, the specific energy $w_1 = W_1/\sigma$ (σ is the area of the layers) increases by

$$\Delta w_1 \approx \alpha^*\left(\frac{\psi_0}{R}\right)^2, \tag{16}$$

because $|\nabla\psi| \approx \psi_0/R$.

The specific exchange energy between the layers $w_2 = W_2/\sigma$ changes by

$$\begin{aligned}\Delta w_2 &\approx -|J_\perp|S_1S_2b^{-2}(1-\cos\psi_0)\\ &\approx -|J_\perp|S_1S_2b^{-2}\psi_0^2 \approx -\alpha^*\frac{\psi_0^2}{\delta^2}.\end{aligned} \tag{17}$$

If $R \ll \delta$, this gain in energy W_2 is lower than the cost in energy W_1; therefore, in the case of $\langle\theta_1\rangle = \langle\theta_2\rangle$, we have $\psi_1(\boldsymbol{\rho}) = \psi_2(\boldsymbol{\rho}) = 0$.

If $\langle\theta_1\rangle \neq \langle\theta_2\rangle$, then the decrease in W_2 is linear in ψ_0 and is equal to

$$\begin{aligned}\delta w_2 &\approx -J_\perp S_1S_2b^{-2}[\cos(\langle\theta_1\rangle - \langle\theta_2\rangle)\\ &\quad - \cos(\langle\theta_1\rangle - \langle\theta_2\rangle + \psi_0)]\\ &\approx -J_\perp S_1S_2b^{-2}\sin\theta\sin\psi_0 \approx -\alpha^*\frac{\sin\theta}{\delta^2}\psi_0,\end{aligned} \tag{18}$$

where $\theta = \langle\theta_1\rangle - \langle\theta_2\rangle$.

By minimizing the total energy, we find the characteristic value ψ_0 to be

$$\psi_0 \approx \frac{R^2}{\delta^2}\sin\theta, \tag{19}$$

and the decrease in the total energy to be

$$\Delta w_1 + \Delta w_2 \approx -\frac{\langle J_\perp^2\rangle S_1^2S_2^2R^2\sin^2\theta}{\alpha^* b^4} \approx -\frac{\langle J_\perp^2\rangle R^2\sin^2\theta}{J_0 l_{\min} b^3}, \tag{20}$$

where $l_{\min}$ is the smallest of the thicknesses l_1 and l_2 of the FM layers.

Thus, weak nonuniformities of the magnetization distributions over the FM layers become energetically favored in a noncollinear state with $\theta \neq 0$. However, the formation of such a state occurs at a cost in energy of the uniform state because of the term

$$w_2^{(0)} = -\langle J_\perp\rangle S_1S_2b^{-2}\cos\theta. \tag{21}$$

Phenomenologically, this term is interpreted as bilinear exchange. Replacing $\sin^2\theta$ in Eq. (20) by $1 - \cos^2\theta$, we obtain a term proportional to $\cos^2\theta$, which is interpreted as the specific biquadratic-exchange energy

$$w_{BQ} = -J_{BQ}S_1^2S_2^2b^{-2}\cos^2\theta. \tag{22}$$

For the case of periodically arranged steps, the form of the exchange integral J_{BQ} was found in [13]. Note that the exchange integral J_{BQ} is always negative; that is, biquadratic exchange favors the occurrence of a noncollinear state. An order-of-magnitude estimation gives

$$J_{BQ} \approx -\frac{\langle J_\perp^2\rangle R^2}{J_i S^2 l_{\min} b}. \tag{23}$$

A necessary condition for a noncollinear ordered state with $\theta \neq 0$ to arise is

$$|\langle J_\perp\rangle| < 2|J_{BQ}|S_1S_2. \tag{24}$$

Since $|J_1| \approx |J_2| \approx \langle J_\perp^2\rangle^{1/2}$, we can conclude that, to within numerical factors of order unity, inequality (24) is equivalent to the condition

$$\frac{\langle J_\perp\rangle}{\langle J_\perp^2\rangle^{1/2}} < \frac{R^2}{\delta^2}. \tag{25}$$

It is unlikely that the values of J_1 and J_2 and the total area occupied by regions corresponding to spacer thicknesses d_1 and d_2, respectively, satisfy the inequality

$$\frac{\langle J_\perp\rangle}{\langle J_\perp^2\rangle^{1/2}} < 10^{-2}.$$

Therefore, only collinear ordering must occur in multilayer structures with $R \ll \delta$.

The corresponding exchange–roughness phase diagram is shown in Fig. 8. The crosshatched region corresponds to a noncollinear phase in which the layer magnetizations are practically uniform. It is easy to see that the region of parameter values for which this approximation (frequently used in the literature) is adequate is very narrow. As the size R increases (i.e., roughness decreases), the angle ψ_0 of deviation of the magnetization vector from its average direction increases and a continuous transition occurs to a microdomain state.

3.3. The Behavior in a Magnetic Field

Let us consider the behavior of the different phases in a magnetic field applied parallel to the layer plane. The anisotropy in the layer plane is assumed to be negligible.

For the phase in which the magnetizations of the FM layers are parallel to each other, narrow square hysteresis loops will be observed (Fig. 9a).

In the phase with antiparallel mutual orientation of the magnetizations of the two identical FM layers, the total magnetization will increase smoothly with the magnetic field (Fig. 9b). This behavior is identical to that of a mirror-symmetric two-sublattice antiferromagnet with intersublattice exchange energy β. The angle between the magnetization vectors of the FM layers can be found by minimizing the energy:

$$\tilde{W} = -2M_0 lB\cos\theta - \beta\cos 2\theta, \qquad (26)$$

where M_0 is the magnetization of the FM layers, l is their thickness, $\beta < 0$, and θ is the angle between the magnetic induction and the magnetic moment of an FM layer (Fig. 3b).

It is easy to see that saturation occurs in a magnetic field

$$B_{\text{sat}} = \frac{2|\beta|}{M_0 l}. \qquad (27)$$

In the region where a microdomain state exists, the magnetization curve, in a first approximation, will be a superposition of the curves described above with the weights corresponding to the volume fractions of the domains with parallel and antiparallel mutual orientations of the layer magnetizations (Fig. 9c).

If the structure under study exhibits a magnetization curve of this type, there is a good probability that this structure is in a microdomain state. The small crosshatched region in Fig. 8 corresponds to another possible state.

3.4. Experimental Observations

Hysteresis loops similar to that shown in Fig. 9c have been observed in many studies (see, e.g., [14, 15]). However, such curves were interpreted in terms of biquadratic exchange and the magnetic microstructure, as a rule, was not examined. Microdomains with parallel and antiparallel mutual magnetization orientations were observed using spin-polarized low-energy electron microscopy (SPLEEM) [16]. It was found that the boundaries between microdomains coincide with the boundaries of atomic terraces on interfaces. Microdomains can also be observed using transmission electron microscopy [17], spin-polarizing scanning tunneling microscopy [18], and magnetic-force microscopy.

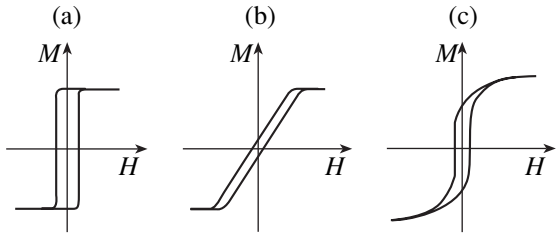

Fig. 9. Hysteresis loops in the regions of the phase diagram corresponding (a) to the parallel and (b) antiparallel mutual orientation of the magnetizations of the FM layers and (c) to the microdomain state.

It is of considerable interest to make *in situ* measurements of the relief of the layer surface before sputtering the next layer and then to investigate the magnetic microstructure, magnetization curves, and magnetoresistance.

4. FERROMAGNET–ANTIFERROMAGNET TWO-LAYER SYSTEM

In contrast to the case considered above, the spins of the AFM layer in this system are ordered and are characterized by their own exchange stiffness. The type of DWs caused by frustration essentially depends on the relationship between the exchange stiffnesses of the ferromagnet and antiferromagnet (see below).

4.1. Model

We assume that the AFM order parameter **L**, which is the difference between the magnetizations of the sublattices, lies in the layer plane and, as before, is specified by the angle that the vector **L** makes with the x axis ($|\mathbf{L}| = \text{const}$).

In this case, the contribution to the exchange energy of each layer coming from nonuniformities in the distribution of the order parameter over the layer can be represented in the form [11]

$$W_i = \frac{J_i S_i^2}{2b}\int(\nabla\theta_i)^2 dV, \qquad (28)$$

where integration is performed over the volume of the layer.

Here, in contrast to the preceding section, the problem is not one-dimensional. Indeed, the DW thick-

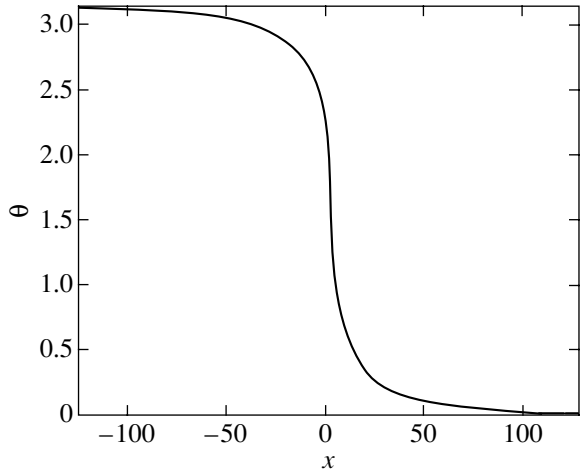

Fig. 10. Typical variation in the tilt angle of the order parameter through the DW thickness.

nesses, as shown below, are comparable to atomic-scale lengths in this case and significantly vary with the distance from the interface. Therefore, even in the case of an atomic step with an infinite edge, the problem is two-dimensional.

By varying expression (28) with respect to the parameter θ_i, we obtain an equation for the order parameter in the interior of the *i*th layer [19],

$$\Delta\theta_i = 0. \tag{29}$$

In order to find the boundary conditions, one should write the interaction energy between spins situated near the interface in the discrete representation and differentiate this energy with respect to the rotation angle of the particular spin. After passing to the continuum representation, we thus obtain

$$\tilde{\Delta}\theta_i - \frac{\partial\theta_i}{\partial n} = \pm\frac{J_{f,af}S_{i+1}}{J_iS_i}\sin(\theta_i - \theta_{i+1}), \tag{30}$$

where $\tilde{\Delta}$ is the two-dimensional Laplacian in the layer plane, $\frac{\partial}{\partial n}$ is the derivative along the outward normal to the layer, and $J_{f,af}$ is the exchange constant characterizing the interaction between spins belonging to different layers; all distances are measured in units of the interatomic distance *b*. The plus and minus signs on the right-hand side of Eq. (30) correspond to spins lying on different sides of the atomic step at the interface, respectively. For the free surface, the right-hand side of Eq. (30) vanishes.

If we vary the interaction energy between the layers with respect to θ_i in the continuum representation, we will arrive at an equation that does not contain the first term on the left-hand side of Eq. (30) and, therefore, does not reduce to Eq. (29) in the case where the adjacent layers are identical.

The exchange interaction energy between the adjacent layers is

$$W_{i,i+1} = \pm\frac{J_{f,af}S_iS_{i+1}}{b^2}\int\cos(\theta_i - \theta_{i+1})d^2\boldsymbol{\rho}, \tag{31}$$

where integration is performed over the interface between the layers. The plus and minus signs on the right-hand side of Eq. (31) correspond to those in Eq. (30).

4.2. Domain Wall in a Ferromagnetic Film on an Antiferromagnetic Substrate

Let us consider a thin FM film deposited on a much thicker AFM substrate (or a thin AFM film deposited on a thick FM substrate). In the exchange approximation, the latter problem will reduce to the former, in which we replace the indices $f \rightleftharpoons af$. A DW that arises in this case is described by the following three dimensionless parameters: the film thickness $a = l_f/b$; the quantity

$$\alpha_f = \frac{J_{f,af}S_{af}}{J_fS_f}, \tag{32}$$

which characterizes the ratio of the exchange interaction energy between neighboring spins belonging to different layers to the exchange interaction energy between adjacent spins belonging to the FM layer; and the quantity

$$\gamma = \frac{J_fS_f^2}{J_{af}S_{af}^2}, \tag{33}$$

which is the ratio between the exchange energies in the film and in the substrate.

Equations (29) and (30) form a set of Laplace equations with nonlinear boundary conditions. These equations were solved numerically in [20, 21] using a method similar to integral transformation.

The orientation of the coordinate system is similar to that chosen in Subsection 2.2; namely, the *y* axis coincides with the edge of a step and the *z* axis is perpendicular to the film plane. The plane $z = 0$ coincides with the film–substrate interface, and the plane $z = a$ is the free surface of the film. In the region $x \ll -\delta_f$ (δ_f is the DW thickness), we have $\theta_{af} = \theta_f = 0$, and in the region $x \gg \delta_f$, we have $\theta_{af} = 0$ and $\theta_f = \pi$. From the symmetry of the problem, it follows that $\theta_{af} = 0$ and $\theta_f = \pi/2$ at $x = 0$.

First, let us consider the case where $\gamma \ll 1$ and, therefore, the exchange stiffness of the substrate is much higher than that of the film [20]. In this case, the distribution of the order parameter over the substrate is virtually uniform. The typical $\theta(x)$ dependence in the region $0 < z < a$ is shown in Fig. 10. Note that at $x = z = 0$ the derivative θ''_{xx} is discontinuous, while θ'_z remains continuous. The DW thickness $\delta_f(z)$ is defined as the

distance between the points with coordinates (x_1, z) and (x_2, z) corresponding to the values $\theta_1 = \pi/4$ and $\theta_2 = 3\pi/4$, respectively.

The main feature of the DWs under study is that their thickness increases with distance from the interface. The $\delta_f(z)$ dependence for $\alpha_f a \gg 1$ is shown in Fig. 11. It can be seen that this dependence is linear near the substrate, whereas near the free surface the DW thickness δ_f virtually does not vary. In the opposite case of $\alpha_f a \ll 1$, the variation of the DW in thickness is insignificant.

The dimensionless DW thickness $\delta_0^f = \delta_f(z = 0)$ and the thickness-averaged value of $(\delta_f)_z'$, which we denote as $\tilde{\beta}$ in what follows, can be estimated using simple energy arguments. Indeed, let us approximate $\theta(x, z)$ by the function

$$\theta(x, z) = \begin{cases} \pi, & x \geq \delta_f(z), \\ \frac{\pi}{2}(1 + x/\delta_f(z)), & -\delta_f(z) < x < \delta_f(z) \\ 0, & x \leq -\delta_f(z), \end{cases} \quad (34)$$

where

$$\delta_f(z) = \delta_0^f + \tilde{\beta} z, \quad 0 \leq z \leq a. \quad (35)$$

The contribution to the energy (per unit length of the DW along the y axis) from nonuniformities of the order parameter in the DW is

$$w_1 = \frac{J_f S_f^2}{2b} \int_0^a dz \int_{-\infty}^{\infty} dx [(\theta_x')^2 + (\theta_z')^2] \approx \frac{\pi^2 J_f S_f^2}{4b} \left(\frac{1}{\tilde{\beta}} + \frac{\tilde{\beta}}{3} \right) \ln \frac{\tilde{\beta} a + \delta_0^f}{\delta_0^f}. \quad (36)$$

Due to the step, the interaction energy between the film and substrate increases by the quantity

$$w_2 = \frac{2 J_{f,af} S_f S_{af}}{b} \int_0^{\infty} dx [1 - \cos\theta(x, 0)] \approx \frac{2 J_{f,af} S_f S_{af}}{b} \delta_0^f. \quad (37)$$

Minimizing the energy w_1 with respect to the parameter $\tilde{\beta}$ and then minimizing the total DW energy $\tilde{w} = w_1 + w_2$ with respect to the parameter δ_0^f, we can find these parameters. The result is

$$\tilde{\beta} \sim \sqrt{\alpha_f a}, \quad (38)$$

$$\delta_0^f \sim \sqrt{a/\alpha_f} \quad (39)$$

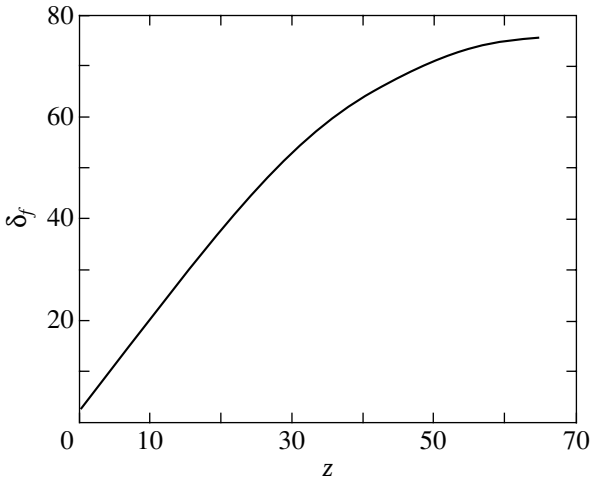

Fig. 11. Typical variation in the DW thickness with distance from the interface for $\alpha_f a \gg 1$ ($\alpha_f = 1$, $a = 64$).

in the case of $\alpha_f a \ll 1$ and

$$\tilde{\beta} \sim 1, \quad (40)$$

$$\delta_0^f \sim 1/\min(1, \alpha_f) \quad (41)$$

for $\alpha_f a \gg 1$. The continuum approximation is valid if $\delta_0^f \gg 1$.

The characteristic DW thickness $\delta_f(a/2)$ is found to be

$$\delta_f\left(\frac{a}{2}\right) \sim \begin{cases} \delta_0^f \sim \sqrt{a/\alpha_f}, & \alpha_f a \ll 1 \\ a, & a\alpha_f \gg 1. \end{cases} \quad (42)$$

It is significant that for $a \sim 10$–100 Å the DW thickness δ_f is much smaller than the thickness of a conventional DW, because the value of δ_f is determined by the balance between the exchange energies rather than between the exchange and anisotropy energies.

The DW energy per unit length is estimated to be

$$\tilde{w} \sim \begin{cases} \frac{J_f S_f^2}{b} \sqrt{\alpha_f a}, & \alpha_f a \ll 1 \\ \frac{J_f S_f^2}{b} \ln(\alpha_f a), & \alpha_f a \gg 1. \end{cases} \quad (43)$$

Due to the DW broadening, the DW energy increases with the thickness of the film only logarithmically for $\alpha_f a \gg 1$.

Now, we consider the case where $\gamma \gg 1$ and, therefore, the exchange stiffness of the film is much higher than that of the substrate. If $\gamma^2 a \alpha_f \ll 1$, then the order parameter of the substrate is affected only slightly and the DW parameters are similar to those found in the case of $\alpha_f a \ll 1$.

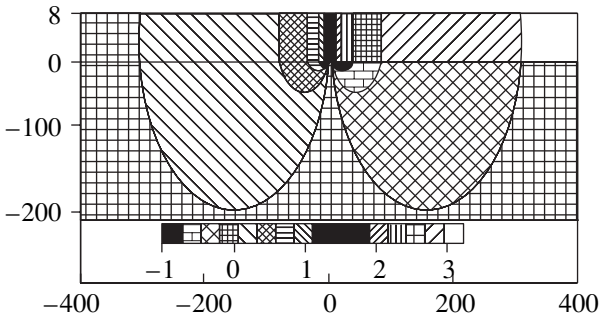

Fig. 12. Distribution of the order parameters over a DW. The ordinate is equal to zero at the film–substrate interface. All distances are reduced to the lattice parameter. The correspondence between the hatching and the value of θ_i (measured in radians) is shown in the inset.

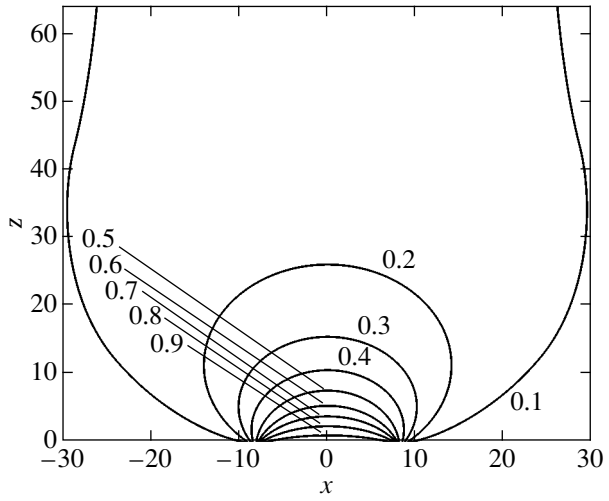

Fig. 13. Static spin vortex in the film near the film–substrate interface in the case of $a \gg R$. The lines of constant values of θ_f are labeled by the values of θ_f measured in units of π.

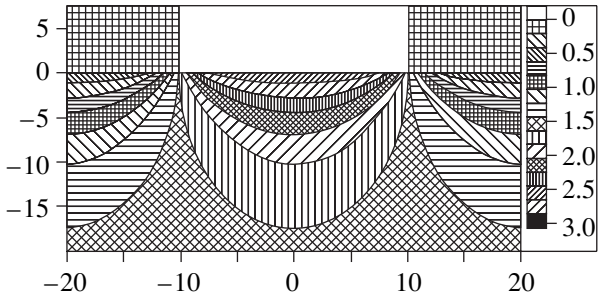

Fig. 14. Distribution of the order parameters in the vortex phase. The ordinate is equal to zero at the film–substrate interface. All distances are reduced to the lattice parameter. The correspondence between the hatching and the value of θ_i (measured in radians) is shown in the inset.

In the opposite case of $\gamma^2 a\alpha_f \gg 1$, the order parameter of the substrate is distorted and two characteristic lengths arise. One of them is the DW thickness in the FM layer

$$\delta_f \approx \gamma a. \tag{44}$$

Since $\delta_f \gg a$, the DW broadening in the ferromagnet can be neglected. The other characteristic length is the thickness δ_0^{af} of the region near the film–substrate interface in which the quantity $\theta_f - \theta_{af}$ differs from its optimum value (0 for $x < 0$ and π for $x > 0$):

$$\delta_0^{af} \approx (1 + \gamma\alpha_f)/\gamma\alpha_f, \quad \delta_f \gg \delta_0^{af}. \tag{45}$$

In the region $|x| < \delta_f$ and $|z| < \delta_f$, vortical distortions of the AFM order parameter arise in the substrate (Fig. 12). The DW energy per unit length in this case is

$$w \approx \frac{J_{af} S_{af}^2}{b} \ln \frac{\delta_f}{\delta_0^{af}}, \tag{46}$$

with the dominant contribution to it coming from the order parameter distortions in the substrate.

If the substrate thickness $d_{af} < \gamma a$, then the DW runs through it; therefore, the AFM layer breaks up into domains, while the FM layer remains virtually uniform. In other words, the pattern is the same as that in the case of $\gamma \ll 1$ but the layers exchange places.

Thus, we have found the critical thickness above which the substrate can be considered thick. If the distance between the steps is large, we have $d_{af}^* = \gamma a$.

4.3. Phase Diagram

Atomic steps break up the film–substrate interface into regions of two types. In the first type of region, the interface energy is minimal when the FM and AFM order parameters are parallel to each other, and in the second type, the interface energy is minimal when these order parameters are antiparallel.

If the characteristic spacing between the steps is much larger than its critical value, $R \gg \delta_f(a/2)$, then the film breaks up into microdomains, with their boundaries coinciding with the edges of the atomic steps [22, 23]. The magnetizations in adjacent domains are oppositely directed, and their direction corresponds to a minimum value of the interface energy.

In the case of $R \ll \delta_f(a/2)$, DWs overlap; therefore, domains cannot form and the film passes into a single-domain state. For $\gamma \ll 1$ and $a\alpha_f \ll 1$ or for $\gamma \gg 1$ and $\gamma^2 a\alpha_f \ll 1$, order-parameter distortions are small in both the film and the substrate.

If $\gamma \ll 1$, $a\alpha_f \gg 1$, and $\delta_0^f \ll R \ll a$, then specific static spin vortices arise near the substrate (Fig. 13). These vortices penetrate a distance of the order of R into the film, while in the other part of the film the uni-

form distribution of the order parameter remains unperturbed. In the case of $\gamma \gg 1$, $\gamma^2 a\alpha_f \gg 1$, and $\delta_0^{af} \ll R \ll \delta_f$, the film remains uniform and analogous spin vortices arise in the substrate near the interface (Fig. 14). Each vortex is confined by the edges of steps and becomes progressively wider as the distance from the steps increases. The vortex size in the direction perpendicular to the interface is of the order of R.

For smaller values of R, the state of the system corresponds to the region of weak distortions in the phase diagram.

Let us consider the mutual orientation of the FM and AFM order parameters in the vortex phase. As mentioned above, steps break up the entire interface into regions of two types. We denote their total areas by σ_1 and σ_2, respectively. Let ψ be the angle between the average magnetization of the FM film and the AFM order parameter in the substrate bulk. The difference $\theta_f - \theta_{af}$ varies from zero to ψ in a vortex occupying a region of the first type and from ψ to π in a vortex occupying a region of the second type.

By analogy with the "magnetic proximity" model proposed by Slonczewski [24], we represent the energy of the system in the form

$$W = C_1\psi^2 + C_2(\pi - \psi)^2, \tag{47}$$

where, according to [19, 25, 26],

$$C_j \equiv C\sigma_j \approx \frac{\min(J_f S_f^2, J_{af} S_{af}^2)\sigma_j}{Rb}. \tag{48}$$

In the case of $\sigma_1 = \sigma_2$, the equilibrium film magnetization must be perpendicular to the AFM order parameter in both the vortex phase and the weak-distortion region if the external magnetic field is zero and the anisotropy energy due to steps is ignored.

The thickness–roughness phase diagram for the film–substrate system is shown in Fig. 15. It should be noted that the transition from the multidomain to the single-domain state that occurs in the film as the parameter R decreases is continuous and, strictly speaking, is not a phase transition. If $\gamma \gg 1$ and, therefore, the Curie temperature of the ferromagnet is higher than the Néel temperature of the antiferromagnet, this transition can be initiated by heating the sample. As the Néel temperature is approached, the DW thickness $\delta_f \propto \gamma \propto T_N/(T_N - T)$ increases indefinitely and the transition to the single-domain state occurs.

4.4. The Behavior in a Magnetic Field

Now, we consider the behavior of the phases in an external magnetic field.

When the FM film is in the single-domain state, the application of an external magnetic field directed at an angle to the spontaneous magnetization causes the magnetization vector to rotate everywhere in the film plane. We restrict ourselves to the case where the film thickness is fairly small and, therefore, the magnetization rotation is accompanied by the formation of a conventional DW, which is parallel to the film–substrate interface and positioned in the AFM substrate near the interface. In the case of a thick film, a conventional DW can initially arise, for certain relationships between the model parameters, in the film itself near the interface with the substrate. The situation is fully analyzed in our papers [25, 26].

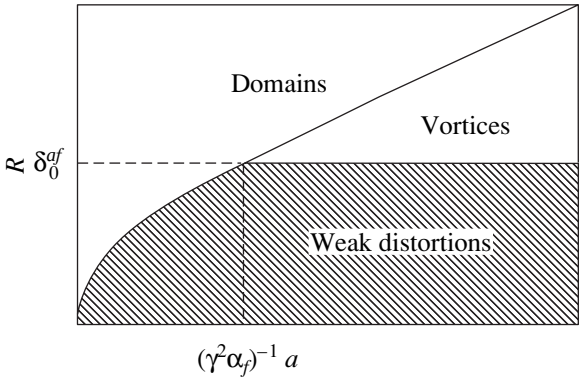

Fig. 15. Thickness–roughness phase diagram for the film–substrate system.

Since the gain in the Zeeman energy of the film in an external magnetic field must compensate for the cost of producing a DW, the magnetization rotation will begin in a magnetic field that is equal, in order of magnitude, to [27, 28]

$$B_{af}^0 \sim \frac{\sigma_{af}}{Ma}, \tag{49}$$

where σ_{af} is the surface energy density of a conventional DW in the antiferromagnet and M is the magnetization of the film. Therefore, the magnetization curve is biased to the range of negative fields (with respect to the magnetization direction in the absence of a magnetic field) by the quantity B_{af}^0. This effect of an AFM substrate is called unidirectional anisotropy. A great number of papers have been dedicated to this phenomenon (see, e.g., review [29]). However, it is beyond the scope of the present review to discuss this effect. The width of the field range within which the magnetization reversal occurs is also of the order of B_{af}^0.

The unidirectional anisotropy does not arise in the multidomain phase. In an external magnetic field aligned with or opposed to the magnetization of domains (we call them domains of the first and second types, respectively), the magnetization in domains of the first type remains unchanged, while the magnetization of the second-type domains rotates through an angle of 180°. If the domain size R is larger than the thickness Δ_{af} of a conventional DW in the antiferromag-

net, then this rotation is accompanied by the formation of such a DW in the substrate near the interface with the film; the characteristic field of the magnetization reversal is of the order of B_{af}^0.

In the case of $R \ll \Delta_{af}$, the magnetization rotation in a domain is accompanied by the formation of a static spin vortex in the AFM substrate; the characteristic magnetization reversal field is of the order of $B_{af}^0 \Delta_{af}/R$. In addition to the vortex, a 90° DW arises in the substrate. The reason for its formation is analogous to that for the film magnetization in the single-domain state being perpendicular to the order parameter in the substrate bulk in the absence of an external magnetic field; namely, the formation of a DW reduces the energy of the vortex system.

Indeed, in the absence of a DW, no vortices arise in domains in which the magnetization is parallel to the external magnetic field, whereas in domains with the initial antiparallel orientation of the magnetization with respect to the magnetic field a 180° vortex forms when the field becomes equal to $B_{af}^0 \Delta_{af}/R$. In the presence of a 90° DW, vortices arise in both types of domain, with the AFM order parameter twisting in opposite directions in domains of different types. Since the energy of a vortex is proportional to the twist angle, the formation of a DW decreases the vortex energy, and this decrease in energy due to the DW is larger than the energy required for the DW formation [26].

If a magnetic field is applied in the film plane at right angles to the magnetization of domains, the characteristic magnetization reversal field is of the same order of magnitude as in the case of a magnetic field applied along the domain magnetizations; however, in the former case, a 90° DW does not form, because static 90° vortices with the AFM order parameter twisting in opposite directions arise in both types of domains.

4.5. Experimental Data

The magnetization pattern discussed in Subsection 4.3 agrees with the data from [30], where the thickness–vicinal angle β' phase diagram was investigated for an iron film deposited on Cr(001). For β' close to zero, the multidomain phase was observed at film thicknesses $a < a_c = 3.5$ nm. In a film with critical thickness a_c, the characteristic distance R between the edges of randomly arranged steps is equal to γa. For large values of a, a single-domain phase was observed in which the magnetization was perpendicular to the edges of steps. According to the theory described above, the antiferromagnetism vector must be parallel to steps. It is of interest to determine its orientation experimentally.

If $\beta' \neq 0$, there are not only randomly arranged atomic steps but also regularly arranged parallel steps. When the concentration of the latter steps becomes dominant (at $\beta' \geq 1°$), the value of a_c begins to decrease. According to the theory described above, $a_c \approx R/\gamma \propto \tan^{-1}\beta' \propto (\beta')^{-1}$.

At large values of β', an orientational phase transition to a phase in which the magnetization was parallel to steps was observed [30]. This transition was due to the anisotropy induced by steps through relativistic effects, e.g., through dipole–dipole interaction [31].

5. FERROMAGNET–ANTIFERROMAGNET–FERROMAGNET THREE-LAYERED SYSTEM

In this section, we restrict ourselves to the case of $\gamma \gg 1$, where the exchange stiffness of the AFM spacer layer is lower than that of the FM layers. In the opposite extreme case (for approximately equal layer thicknesses), the problem for each interface between the layers reduces to that for a two-layer system. To reduce the number of model parameters, we assume the thicknesses of all layers to be equal.

5.1. Domain Walls

DWs run through each of the three layers, and their coordinates in the layer plane coincide with those of the edges of atomic steps at any of the two interfaces. The magnetization vector in a DW rotates in opposite directions in different FM layers. The AFM order parameter rotates together with the magnetization of that FM layer at whose interface with the AFM spacer there is no step at the given site.

The structure and energy of a DW depend on the parameter $\gamma\alpha_f a$ [21]. In the case of $\gamma\alpha_f a \ll 1$, the $\theta_{f(af)}(z)$ dependence (i.e., the DW broadening) can be neglected and the problem becomes one-dimensional.

The quantity $|\nabla\theta_f|$ in a DW is of the order of δ_f^{-1}. Using Eq. (28), the energy per unit DW length w_1 can be found to be

$$w_1 = \frac{J_f S_f^2 a}{b\delta_f}. \tag{50}$$

The angle between spins belonging to different layers differs significantly from its value corresponding to the minimum interaction energy between the layers in the region $|x| < \delta_f$. The increase in the interaction energy between the layers (per unit DW length) is equal to

$$w_2 = \frac{J_{f,af} S_f S_{af} \delta_f}{b}. \tag{51}$$

Minimizing the sum $w_1 + w_2$, we find

$$\delta_f \approx \sqrt{a/\alpha_f}. \tag{52}$$

In the AFM spacer layer, the DW thickness is $\delta_{af} \approx \sqrt{a/\gamma\alpha_f} = \delta_f/\sqrt{\gamma} \ll \delta_f$. The distribution of the order

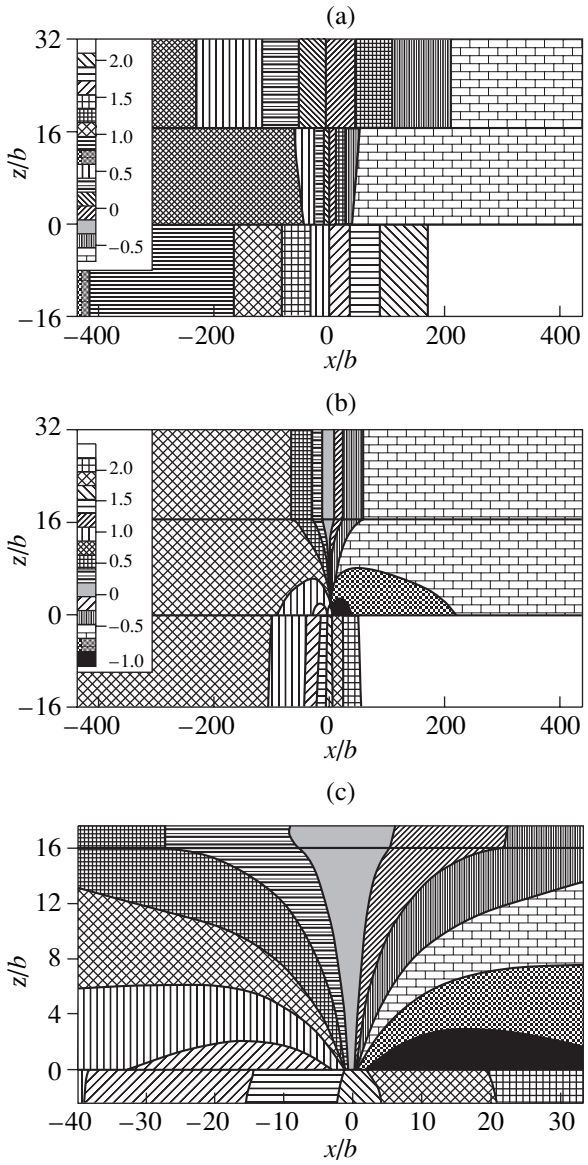

Fig. 16. Domain wall in the ferromagnet–antiferromagnet–ferromagnet three-layered system in the case of (a) $\gamma\alpha_f a \ll 1$ and (b) $\gamma\alpha_f a \gg 1$. The correspondence between the hatching and the value of θ_i (measured in radians) is shown in the inset. Panel (c) shows the central fragment of panel (b). Coordinates $z = 0$ and 16 correspond to the interfaces between the layers. The step is located at the point $x = 0$ and $z = 0$.

parameters over the DW is shown in Fig. 16a. The DW energy per unit length is

$$w \approx \frac{J_f S_f^2}{b}\sqrt{a\alpha_f} \sim \frac{S_f}{b}\sqrt{aJ_f J_{f,af} S_f S_{af}}. \qquad (53)$$

Exact numerical calculations of δ_f and w performed in a wide range of values of α_f and a lend support to the validity of the estimates presented above (and of the results discussed below).

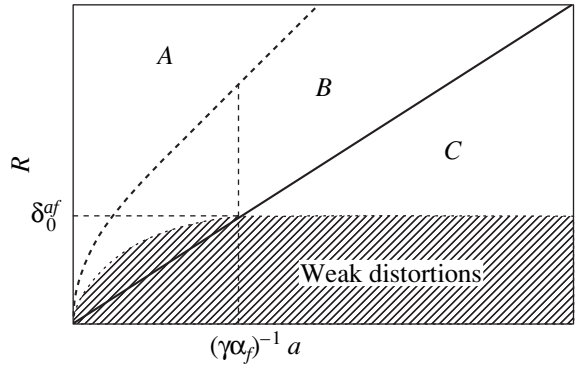

Fig. 17. Phase diagram of the ferromagnet–antiferromagnet–ferromagnet three-layered system. The solid and dashed lines correspond to $R = a$ and $R = \delta_f'$, respectively. The hatched region corresponds to weak order parameter distortions.

In the opposite extreme case of $\gamma\alpha_f a \gg 1$, the DW thickness in the AFM spacer increases significantly with distance from the interface containing an atomic step. The distribution of the order parameters over the DW in this case is shown in Fig. 16b. The characteristic parameters of this distribution can be estimated in the same way as in the case of $\gamma\alpha_f a \ll 1$. The dominant contribution to the DW energy comes from order parameter distortions in the antiferromagnet. In the region $|x| \le a$, the quantity $|\nabla\theta_{af}|$ varies inversely with the distance from the step, whereas in the region $a \ll |x| \ll \delta_f'$ (δ_f' is the DW thickness in the FM layers) the lines of constant values of θ_{af} are almost parallel to the interfaces (Fig. 16c). In this region, we have $|\nabla\theta_{af}| \approx a^{-1}$.

The minimum value of the DW thickness in the antiferromagnet is $\delta_0^{af} = (1 + \gamma\alpha_f)/\gamma\alpha_f$, the derivative is $\partial\delta_{af}/\partial z \approx 1$ near the step, and the quantity δ_f' is given by

$$\delta_f' \approx a\sqrt{\gamma} \gg a. \qquad (54)$$

The DW energy per unit length is

$$w \approx \frac{J_{af} S_{af}^2}{b}\left(\sqrt{\gamma} + \frac{\pi}{2}\ln\frac{a}{\delta_0^{af}}\right). \qquad (55)$$

It is easy to see that δ_0^{af} is of the order of the interatomic distance and that the average DW thickness is of the order of tens of angstroms; therefore, the DWs due to frustration are much thinner than conventional DWs in a ferromagnet, where the DW thickness is dictated by the balance between the exchange and anisotropy energies.

5.2. Phase Diagram

The three-layered system can be in the following three different phases (Fig. 17).

5.2.1. Phase A. At large values of the parameter $R > \delta_f$ (δ_f'), all layers break up into domains with parallel and antiparallel mutual orientations of the magnetizations of the FM layers. Note that, in the case of an AFM spacer, the domains can be much smaller in size than in the case of a nonmagnetic spacer, where the domain size is of the order of tenths of a micrometer.

For $a \sim 10$ Å and $\gamma \sim 3$, the condition $R > \delta_f(\delta_f')$ is satisfied even for domain sizes as small as several hundreds of angstroms. Therefore, the system is in a nanodomain rather than microdomain state in this case; significantly subtler techniques are required to examine such states. This fact can be the reason why such domain structures have not been observed in three-layered systems with an AFM spacer layer.

5.2.2. Phase B. As the parameter R decreases, DWs begin to overlap and, at the critical value $R_c = \delta_f(\delta_f')$, a continuous transition occurs to a state in which the FM layers are almost uniformly magnetized. In this state (we refer to it as phase *B*), the additional energy relative to the energy of the state without frustration is associated either with order parameter distortions in the AFM spacer or with the interaction energy between the layers. Near the Néel temperature of the spacer T_N (which is lower than the Curie temperature of the ferromagnet), we have $\gamma \propto T_N/(T_N - T)$; therefore, the $A \longrightarrow B$ transition can be initiated by heating the system from a temperature $T_0 < T_N$.

Note that the Slonczewski magnetic-proximity model is applicable in the range of values of R where phase *B* exists [24].

In the range $\max(a, \delta_0^{af}) \ll R \ll R_c$, the dependence of the energy of the system on the angle ψ between the magnetization vectors of the FM layers is described by Eq. (47) in the case of $\gamma\alpha_f a \gg 1$. The constants C_1 and C_2 can be estimated to be [32]

$$C_{1,2} = \frac{J_{af}S_{af}^2}{2a}\frac{\sigma_{1,2}}{b^2}, \quad (56)$$

where σ_1 and σ_2 are the total areas of the regions of the first and second types, respectively, on the surface of the spacer layer.

In the opposite extreme case of $\gamma\alpha_f a \ll 1$, the interaction energy between the layers is

$$W = -\frac{2J_{f,af}S_fS_{af}}{b^2}\left(\sigma_1\cos\frac{\psi}{2} + \sigma_2\cos\frac{\pi-\psi}{2}\right). \quad (57)$$

If $\sigma_1 = \sigma_2$, the energy reaches its minimum at $\psi = \pi/2$; therefore, in the absence of an external magnetic field, the magnetizations of the FM layers are perpendicular to each other.

In contrast to phase *A*, where the energy of the system is independent of the direction of order parameter rotation in a DW, the situation is quite different in phase *B*. Indeed, as DWs begin to overlap, the degeneracy with respect to the direction of rotation is lifted and a large number of metastable states arise that differ in the direction and angle of rotation of the AFM order parameter in certain regions confined by atomic steps.

As the parameter R is decreased further in the case of $\gamma\alpha_f a \ll 1$, the system transforms into a state with weak distortions in the range $a \ll R \ll \delta_{af}$. In this state, the order parameters are almost uniform, the magnetizations of the FM layers remain perpendicular to each other, and the energy W decreases by a factor of $(R/\delta_{af})^2$ with respect to its value given by Eq. (57).

5.2.3. Phase C. Now, we consider the range $R \ll a$. In this case, all distortions are concentrated near the interfaces, the interaction between the FM layers becomes weak, and the interaction energy between adjacent layers is of primary importance. This energy is considered in [15] for a two-layer system.

If $\sigma_1 = \sigma_2$, the AFM order parameter is directed at right angles to the (collinear) magnetizations of the FM layers (phase *C*).

In the case of $\gamma\alpha_f a \gg 1$, static vortices form in the AFM spacer layer near the interfaces if $\delta_0^{af} \ll R \ll a$ (Fig. 14). For smaller values of R, the system transforms into a state with weak distortions.

In the case of $\gamma\alpha_f a \ll 1$, the transition from phase *B* to phase *C* occurs when the system is in a state with weak distortions. Both phases *B* and *C* are characterized by a large number of metastable states. The computer simulation performed in [21] showed that the transition from phase *B* to phase *C* is a first-order phase transformation. These phases coexist in a certain range of values of R, and their energies become equal at a certain value $R^* \sim a$. This value is independent of temperature; therefore, the $B \longrightarrow C$ phase transition cannot be initiated by varying the temperature of the system.

5.3. The Behavior in a Magnetic Field

The magnetization reversal occurs almost independently in the FM layers in phase *C*. Therefore, the hysteresis loop must coincide with that for a two-layer system consisting of an FM and an AFM layer. Here and henceforth, we assume that the maximum magnetic field is much lower than the exchange field in an antiferromagnet. Therefore, the magnetization of AFM layers can be ignored.

If the applied magnetic field is weak but higher than the anisotropy field in the plane of the FM layers, then the magnetization vectors of the FM layers in phase *B* make an angle of 45° with the external field and remain

virtually perpendicular to each other. The magnetization of the system is equal to $M_{\max}/\sqrt{2}$, where $M_{\max}$ is the maximum magnetization of the FM layers. The further evolution of the system can be studied by minimizing the sum of the interaction energies of the FM layers with each other [Eq. (47) or (57)] and with the external magnetic field. The energy of the FM layers in an external magnetic field B is

$$W_f = -2MaBb(\sigma_1 + \sigma_2)\cos\frac{\psi}{2}. \quad (58)$$

In the case of $\sigma_1 = \sigma_2$, $R \gg \delta_0^{af}$, and $\gamma a\alpha_f \gg 1$, the angle ψ between the magnetizations of the FM layers can be found from the transcendent equation

$$\frac{J_{af}S_{af}^2}{ab^2}\left(\frac{\pi}{2} - \psi\right) = MaBb\sin\frac{\psi}{2}. \quad (59)$$

The characteristic field B^*, in which the magnetization changes significantly, is

$$B^* \sim \frac{J_{af}S_{af}^2}{Ma^2b^3}. \quad (60)$$

This field is much lower than the exchange field of the antiferromagnet if the temperature is not in the immediate vicinity of T_N.

If $\gamma a\alpha_f \ll 1$, then we have

$$\tan\frac{\psi}{2} = \frac{J_{f,af}S_{af}S_f}{J_{f,af}S_fS_{af} + 2Mab^3B}, \quad (61)$$

and the characteristic field B^* is given by

$$B^* \sim \frac{J_{f,af}S_{af}S_f}{Mab^3}. \quad (62)$$

In phase A, in a weak magnetic field, domains of the first type (with their magnetizations parallel to each other) are aligned with the field and the magnetization of the system is $M_{\max}/2$. The magnetizations of the FM layers in second-type domains (with their magnetizations antiparallel to each other in a zero magnetic field) behave in the same way as sublattice magnetizations in a bulk antiferromagnet; namely, they are directed almost at right angles to the external field.

As the field B increases, the angle ψ between the magnetizations decreases. The characteristic value B^* of the external magnetic field for which the angle ψ changes significantly can be found in the case of $R > R_c$ in the same way as that for phase B, and its order-of-magnitude estimate can be made using Eqs. (60) and (62). Therefore, the hysteresis loops for phases A and B differ only in the value of the magnetization in weak fields.

5.4. Experimental Data

There are many papers devoted to studying the relation between the interface roughness and the value of magnetoresistance. However, their discussion is beyond the scope of this review. We consider only the experimental data on the mutual orientation of the order parameters and on the domain structure. Such data have been obtained for the most part for Fe/Cr multilayer structures.

According to experimental neutron diffraction data [33, 34], Fe/Cr multilayers are ferromagnet–uncompensated-antiferromagnet structures. For thickness $a <$ 45 Å, chromium layers consist of ferromagnetic atomic planes with antiparallel orientation of spins in adjacent planes. The spins of chromium atoms lie in these planes, which, in turn, are parallel (on the average) to the interfaces between the layers. An analogous magnetic structure has also been observed in manganese layers in Fe/Mn multilayers [35, 36]. Therefore, the theory described above is applicable to Fe/Cr and Fe/Mn structures, and experiments on these structures can be performed to verify this theory.

In [37], domain structures in Fe/Cr multilayers were reported to be detected using polarized neutrons. However, the experimental data were not interpreted in [37] as those corresponding to the partition of a multilayer into regions with parallel and antiparallel mutual orientations of the magnetizations of adjacent FM layers. Instead, it was concluded that the magnetizations of adjacent layers are antiparallel to each other and that a multilayer breaks up into 180° domains running through the structure. The reason for the occurrence of this state, which is not favored energetically (because there is no gain in energy compensating for the energy that is required for the formation of a DW), was not discussed in [37].

In [38], an Fe/Cr multilayer was investigated in which the average thickness of AFM layers corresponded to the antiparallel mutual orientation of the magnetizations of adjacent FM layers. It was found that, as the roughness of the interfaces increases, the volume fraction of regions with parallel mutual orientation of the magnetizations of adjacent FM layers increases and can be as high as 50%.

6. CONCLUSIONS

(1) Due to the frustration caused by the roughness of the interfaces, DWs of a new type arise in magnetic multilayer structures.

(2) The thickness of these DWs is dictated by the balance of the exchange interactions in the interior of the layers and between them. The DW thickness in multilayers with a nonmagnetic spacer and in multilayers with an AFM spacer is smaller and much smaller, respectively, than the thickness of a conventional DW.

(3) The magnetic phase diagram and, therefore, the magnetic and galvanomagnetic characteristics of a

magnetic multilayer structure depend critically on the roughness of the interfaces between the layers.

It is desirable to perform complex studies, including the determination of the characteristics of the surface of layers during their deposition in a wide range of technological parameters, and to study the micromagnetic state of layers, magnetization curves, the dynamics of magnetization reversal, ferromagnetic resonance, and galvanomagnetic characteristics.

The determination of the relationship between the structure and properties of multilayers will make it possible to vary the technological parameters in such a way as to optimize the characteristics of magnetic multilayer structures for various practical applications.

ACKNOWLEDGMENTS

The authors are grateful to Ecole Centrale de Lille for providing conditions conducive to fruitful work.

This study was supported by CRDF and the Ministry of Education of the Russian Federation (grant no. VZ-010-0) and by PICS/RFBR (grant no. 1573/02-02-22002).

REFERENCES

1. M. N. Baibich, J. M. Broto, A. Fert, *et al.*, Phys. Rev. Lett. **61** (21), 2472 (1988).
2. Y. Yafet, Phys. Rev. B **36** (7), 3948 (1987).
3. P. Bruno and C. Chappert, Phys. Rev. B **46** (1), 261 (1992).
4. P. Bruno, Phys. Rev. B **52** (1), 411 (1995).
5. M. D. Stiles, Phys. Rev. B **48** (10), 7238 (1993).
6. L. Nordstrom, P. Lang, R. Zeller, and P. H. Dederichs, Phys. Rev. B **50** (17), 13058 (1994).
7. P. Bruno, J. Phys.: Condens. Matter **11** (48), 9403 (1999).
8. P. M. Levy and S. Zhang, J. Magn. Magn. Mater. **151** (3), 315 (1995).
9. R. Ribas and B. Dieny, Phys. Lett. A **167** (1), 103 (1992).
10. A. I. Morosov and A. S. Sigov, Pis'ma Zh. Éksp. Teor. Fiz. **61** (11), 893 (1995) [JETP Lett. **61**, 911 (1995)].
11. L. D. Landau and E. M. Lifshitz, *Course of Theoretical Physics*, Vol. 8: *Electrodynamics of Continuous Media*, 2nd ed. (Nauka, Moscow, 1982; Pergamon, Oxford, 1984).
12. A. I. Morosov and A. S. Sigov, Fiz. Tverd. Tela (St. Petersburg) **39** (7), 1244 (1997) [Phys. Solid State **39**, 1104 (1997)].
13. J. C. Slonczewski, Phys. Rev. Lett. **67** (22), 3172 (1991).
14. A. Dinia, S. Zoll, M. Gester, *et al.*, Eur. Phys. J. B **5** (1), 203 (1998).
15. C. H. Marrows, J. Hickey, M. Herrman, *et al.*, Phys. Rev. B **61** (6), 4131 (2000).
16. E. Bauer, T. Duden, H. Pinkvos, *et al.*, J. Magn. Magn. Mater. **156** (1), 1 (1996).
17. T. Zimmermann, J. Zweck, and H. Hoffmann, J. Magn. Magn. Mater. **149** (3), 409 (1995).
18. A. Kubetzka, M. Bode, O. Piezsch, and R. Wiesendanger, Phys. Rev. Lett. **88**, 057201 (2002).
19. V. D. Levchenko, A. I. Morosov, and A. S. Sigov, Pis'ma Zh. Éksp. Teor. Fiz. **71** (9), 544 (2000) [JETP Lett. **71**, 373 (2000)].
20. V. D. Levchenko, A. I. Morosov, A. S. Sigov, and Yu. S. Sigov, Zh. Éksp. Teor. Fiz. **114** (5), 1817 (1998) [JETP **87**, 985 (1998)].
21. V. D. Levchenko, A. I. Morosov, and A. S. Sigov, Zh. Éksp. Teor. Fiz. **121** (5), 1149 (2002) [JETP **94**, 985 (2002)].
22. A. Berger and H. Hopster, Phys. Rev. Lett. **73** (1), 193 (1994).
23. E. J. Escorcia-Aparicio, H. J. Choi, W. L. Ling, *et al.*, Phys. Rev. Lett. **81** (10), 2144 (1998).
24. J. C. Slonczewski, J. Magn. Magn. Mater. **150** (1), 13 (1995).
25. V. D. Levchenko, A. I. Morosov, and A. S. Sigov, Fiz. Tverd. Tela (St. Petersburg) **44** (1), 128 (2002) [Phys. Solid State **44**, 133 (2002)].
26. A. I. Morosov and A. S. Sigov, Fiz. Tverd. Tela (St. Petersburg) **44** (11), 2004 (2002) [Phys. Solid State **44**, 2098 (2002)].
27. A. P. Malozemoff, Phys. Rev. B **35** (7), 3679 (1987).
28. D. Mauri, H. C. Siegmann, P. S. Bagus, and E. Kag, J. Appl. Phys. **62** (7), 3047 (1987).
29. J. Nogues and I. K. Schuller, J. Magn. Magn. Mater. **192** (2), 203 (1999).
30. E. J. Escorcia-Aparicio, J. H. Wolfe, H. J. Choi, *et al.*, Phys. Rev. B **59** (18), 11892 (1999).
31. R. Arias and D. L. Mills, Phys. Rev. B **59** (18), 11871 (1999).
32. A. I. Morosov and A. S. Sigov, Fiz. Tverd. Tela (St. Petersburg) **41** (7), 1240 (1999) [Phys. Solid State **41**, 1130 (1999)].
33. A. Schreyer, C. F. Majkrzak, Th. Zeidler, *et al.*, Phys. Rev. Lett. **79** (24), 4914 (1997).
34. P. Bodeker, A. Schreyer, and H. Zabel, Phys. Rev. B **59** (14), 9408 (1999).
35. M. Chirita, G. Robins, R. L. Stamp, *et al.*, Phys. Rev. B **58** (2), 869 (1998).
36. S. Yan, R. Schreiber, F. Voges, *et al.*, Phys. Rev. B **59** (18), R11641 (1999).
37. D. L. Nagy, L. Bottyan, B. Croonenborghs, *et al.*, Phys. Rev. Lett. **88**, 157202 (2002).
38. A. Paul, J. Magn. Magn. Mater. **240** (1–3), 497 (2002).

Translated by Yu. Epifanov

Physics of the Solid State, Vol. 46, No. 3, 2004, pp. 411–419. Translated from Fizika Tverdogo Tela, Vol. 46, No. 3, 2004, pp. 401–409.

METALS AND SUPERCONDUCTORS

The Discrete Evolution of the Structure of Hydrogenated Palladium-Based Alloys

V. M. Avdyukhina, A. A. Anishchenko, A. A. Katsnel'son, A. I. Olemskoĭ, and G. P. Revkevich

Moscow State University, Vorob'evy gory, Moscow, 119992 Russia

e-mail: albert@solst.phys.msu.ru

Received July 17, 2003

Abstract—The discrete character of the diffraction-angle dependence of displacements in the position of the components of diffraction peaks of hydrogenated Pd–Mo and Pd–Ta alloys is established using precise x-ray diffractometry. Such behavior is interpreted in terms of discontinuous transitions between long-lived metastable states under the assumption of a multivalley structure of the thermodynamic potential in **k** space. This assumption makes it possible to explain the fact that the components of diffraction reflections were narrow over the storage time (which was as long as several thousand hours). © *2004 MAIK "Nauka/Interperiodica".*

1. INTRODUCTION

The time evolution of the structure of palladium alloys exhibits unexpected features after their saturation with hydrogen. For example, it was found in [1–4] that after hydrogenation the evolution of Pd–Er–H, Pd–Ta–H, and Pd–Mo–H alloys is nonmonotonic in character and that this behavior persists over tens of thousands of hours. It was also established in [3] that, during certain time periods of the evolution of a Pd–Mo–H alloy, structural transitions occur between several phases. The diffraction peaks or their components were observed to remain fairly narrow over the entire storage time. All these data make it possible to conclude that the energy relief of the alloys under study has a multivalley structure, with the thermodynamic-potential minima (valleys) separated by macroscopic barriers. Therefore, the positions of the components of diffraction peaks must change discretely, in accordance with the spectrum of metastable structural states. In this case, structural transformations will be discontinuous in character, because the probabilities of the system being in the states corresponding to the potential barriers are negligibly small.

However, it is very difficult to directly establish the existence of a discrete set of positions of diffraction peak components for Pd–Mo–H alloys, because the atomic radii of Pd and Mo are almost equal. In order to reveal this effect, alloys consisting of components with significantly different atomic radii need to be studied. Such a study is the aim of this work. We thoroughly investigated a Pd–Ta–H alloy (the Pd and Ta atomic radii differ by 6%) and not only established the existence of a discrete set of the diffraction peak components mentioned above but also refined the model of the nonmonotonic evolution of the structure of a condensed medium that is far -from equilibrium.

2. SAMPLES, EXPERIMENTAL TECHNIQUE, AND PROCESSING OF THE DATA

We performed an x-ray diffraction study [1–4] of Pd–5 at. % Mo and Pd–7 at. % Ta–H alloys using a computerized DRON-UM2 diffractometer (monochromatized Cu$K_{\alpha 1}$ radiation). After cutting on a machine, the surface of the samples was ground and polished. The Pd–Mo alloy was saturated with hydrogen electrolytically at a current density of 80 mA/cm^2 for one hour. The Pd–Ta alloy was studied after the fifth and sixth saturations, which were performed at a current density of 160 mA/cm^2 for 0.5 h; between the saturations, the alloy was stored in air over 3500 h.

The diffraction peak profiles were analyzed with the Origin software package. Their deconvolution was performed with allowance for their actual shape.

According to [1–4], grinding and polishing produces defect complexes in palladium alloy samples. Due to image forces, these defects induce elastic stresses, which cause anisotropic tensile strains [5, 6]. After hydrogenation, these strains transform into compression strains, because the defect complexes are saturated with hydrogen and vacancies [7].

3. EXPERIMENTAL RESULTS

The data on the structural evolution of the Pd–Ta–H alloy after the fifth and sixth saturations with hydrogen [the (220) and (311) diffraction peaks, respectively] are of chief interest, because the measurements proved to be the most complete in these cases. These data are represented in Figs. 1–6 and Tables 1 and 2. The data in the tables are the angular positions 2ϑ (measured in degrees) and relative intensities (indicated by superscripts) of the components of the diffraction peaks decomposed on-line with the Origin program package.

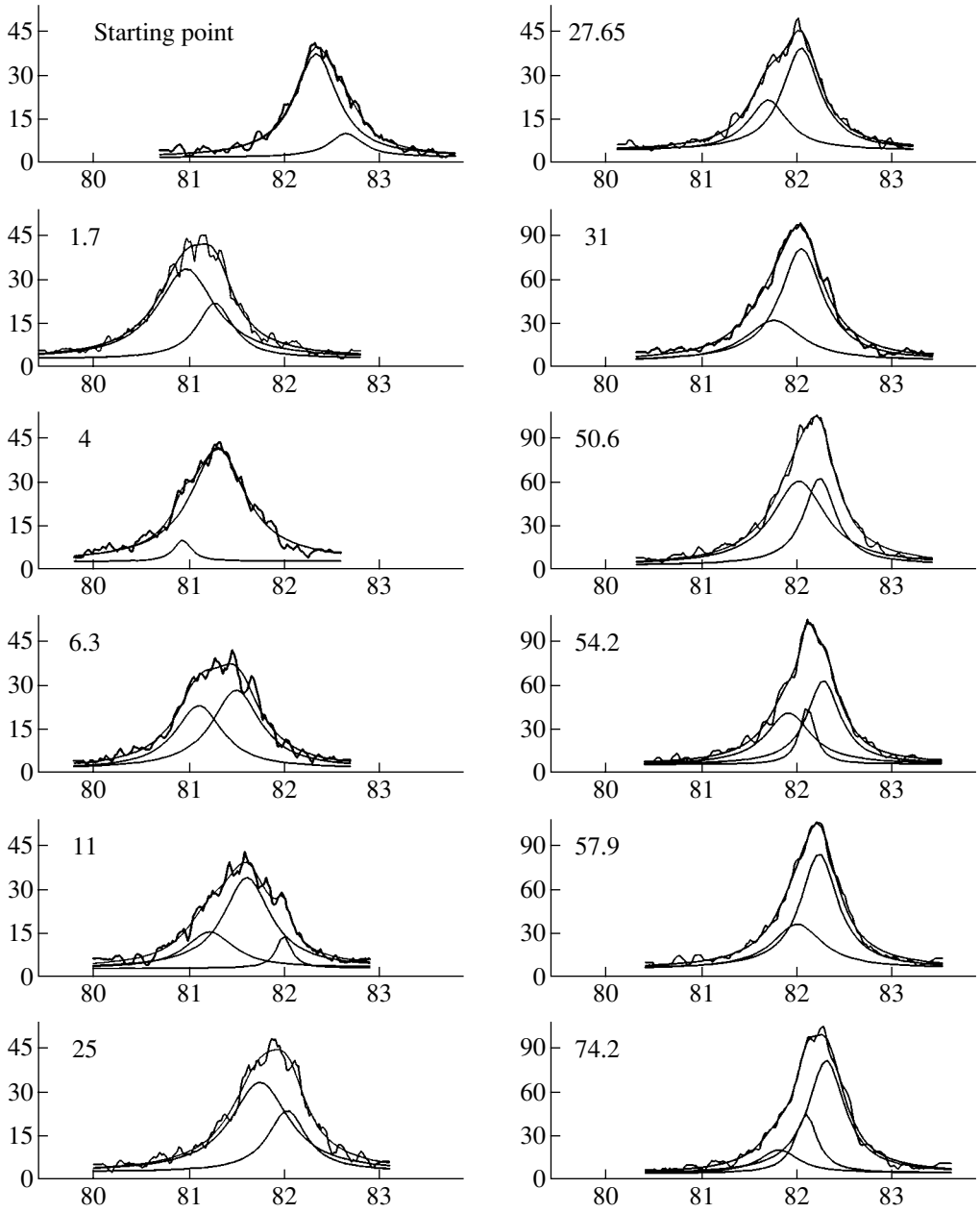

Fig. 1. Time evolution of the (311) diffraction peak after the sixth saturation of the alloy with hydrogen. The numerals near the curves indicate the time measured in hours.

The data obtained after the other saturations and for the other diffraction peaks are similar in character to those described below.

First, let us consider the structural evolution of the (311) diffraction peak after the sixth saturation with hydrogen. It can be seen from Fig. 1 that, as a result of the sixth saturation and subsequent 1.7-h relaxation, the diffraction peak shifts to smaller diffraction angles and the relative intensity of the component observed at smaller angles (the corresponding coherent-scattering domains (CSDs) are enriched in tantalum) decreases. These features indicate that, according to [8], the amount of hydrogen becomes larger in the Pd-rich phase due to hydrogenation. Thereafter, the hydrogen begins to leave the system and the diffraction peak shifts to larger diffraction angles. Simultaneously, nonmonotonic structural transformations occur that are very complex in character. During these transformations, the system transfers to a two- or three-phase state and the relative intensities of the diffraction peak components (and, therefore, the volume fractions of the phases) change radically. The peak shifting to larger diffraction angles terminates, for the most part, by time $t = 54$ h; thereafter, only stochastic variations occur in

Table 1. Structural evolution of the (311) diffraction peak after the sixth saturation

Time, h	–5	–4	–3	–2	–1	0	1	2	3	4	5	6	⟨2ϑ⟩
3500									82.34_{86}			82.65_{14}	82.56
34			81.91_{63}			82.17_{37}							82.01
51				82.01_{62}			82.22_{38}						82.09
54			81.90_{39}		82.10_{15}			82.27_{46}					82.21
58				81.99_{34}			82.22_{66}						82.14
74	81.80_{15}				82.08_{21}			82.29_{64}					82.17
78		81.86_{02}				82.18_{90}					82.43_{08}		82.17
82						82.15_{82}			82.35_{18}				82.19
98				81.98_{23}				82.28_{77}					82.21
102				81.98_{18}				82.25_{82}					82.20
128						82.17_{80}				82.39_{20}			82.21
170						82.18_{96}				82.38_{04}			82.19
176						82.19_{99}					82.45_{01}		82.19
199						82.17_{83}			82.32_{17}				82.20
221			81.92_{22}			82.18_{33}			82.34_{45}				82.19
246				82.01_{31}				82.25_{69}					82.18
268					82.09_{46}			82.27_{54}					82.19
296						82.16_{82}			82.34_{18}				82.19
341				82.00_{17}				82.25_{83}					82.21

Table 2. Structural evolution of the (220) diffraction peak after the fifth saturation

Time, h	–5	–4	–3	–2	–1	0	1	2	3	4	⟨2ϑ⟩
35			67.74_{100}								67.74
48	67.51_{27}		67.75_{23}		67.92_{50}						67.77
51			67.72_{68}			67.97_{32}					67.80
53			67.78_{72}		67.95_{24}			68.14_{04}			67.83
58		67.57_{08}		67.86_{84}				68.10_{08}			67.86
73			67.76_{50}			67.98_{50}					67.87
76			67.78_{48}			67.99_{52}					67.89
98	67.51_{05}			67.87_{59}			68.06_{36}				67.92
123				67.85_{61}		68.00_{04}	68.06_{35}				67.93
147				67.86_{60}			68.04_{28}		68.21_{12}		67.95
171		67.54_{04}	67.74_{04}		67.95_{75}			68.15_{17}			67.94
196				67.84_{52}		67.99_{32}			68.18_{16}		67.94
219			67.73_{64}				68.03_{36}				67.96
246			67.72_{28}			67.98_{64}			68.22_{08}		67.93
3500									68.20_{80}	68.38_{20}	68.24

the topmost part of the peak (as we indicated earlier in [2]). Note that the shift in the peak position to larger angles is not entirely due to a decrease in the lattice parameter of the crystal; a certain part of this shift is caused by elastic compressive stresses directed along the normal to the sample surface [1–4].

The data presented in Table 1 and Fig. 2 clearly show that the shifts in angle 2ϑ of the components of the (311) diffraction peak are discrete in character. Restricting our consideration to the peak components (states) observed over the period of evolution from t = 34 to 341 h, we see that the angular positions of the

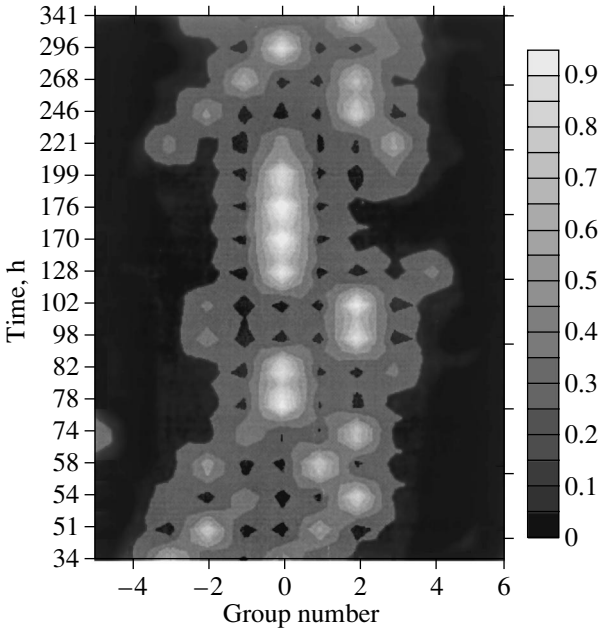

Fig. 2. Positions and intensities of the maxima of the (311) diffraction peak components.

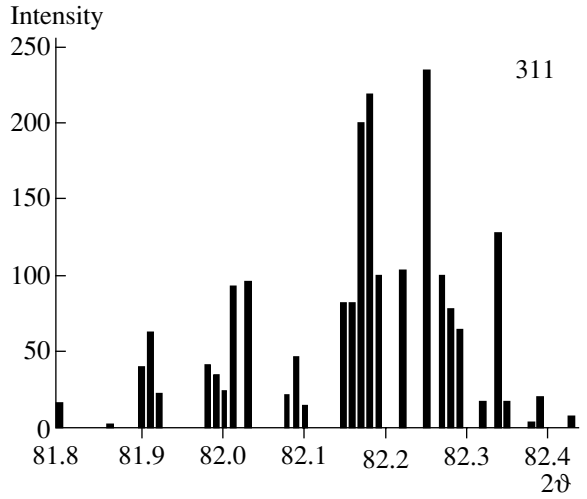

Fig. 3. Diffraction angle dependence of the integrated intensity of the maxima of the (311) diffraction peak components.

maxima of these components are arranged near values differing by approximately $2\vartheta = 3.5'–6'$. As a result, all components differing in position (we observed more than forty components) can be divided into groups in which the number of components varies from one to nine. The most numerous group (located in the middle of Table 1) is labeled by the index 0. Note that the main component of the diffraction peak observed after 3500 h following the fifth saturation is one of these groups (Table 1).

The distribution in the position of the diffraction peak components remains discrete if we characterize their positions only by the values of the diffraction angle 2ϑ at different instants of time. These values can be obtained by projecting the peak components shown in Fig. 2 onto the axis of diffraction angle 2ϑ. The result is shown in Fig. 3. The integrated distribution thus obtained is clearly seen to consist of individual peaks.

An analysis of the structural characteristics of the (311) diffraction peak (including the time variation in the average angle $\langle 2\vartheta \rangle$ shown in the last column of Table 1) revealed the following important features.

First, an increase in angle $\langle 2\vartheta \rangle$ with time due to a decrease in the lattice parameter and to an increase in the elastic compression is followed by a small oscillation in $\langle 2\vartheta \rangle$. Since the lattice parameter of the matrix depends on the impurity concentration, this oscillation can be associated only with the migration of hydrogen and vacancies between the matrix and defect complexes acting as dynamic traps, which were first detected in [2–4, 7].

Second, from analysis of the time dependence of the positions of the maxima of the peak components (angles $2\vartheta_{mc}$ listed in Table 1), it follows that their positions change in a jump with time. For example, as the time t elapsing from the saturation increases from 34 to 51 h, the peak components belonging to groups (–3, 0) transform into peak components of groups (–2, 1). After 3 h, this doublet transforms into a triplet (–3, –1, 2), and then, after 4 h, components (–3, –1) coalesce into one component (–2). However, 16 h later, this component splits into two (–5, –1). Over certain periods of time, e.g., from $t = 98$ to 102 h, the positions of the peak components remain unchanged but their relative intensities vary. After $t = 170–176$ h, the system becomes virtually single-phase; however, 23 h later, the system again separates into two phases and then, after the next 22 h, into three phases. The intensity of the peak component with index 0 decreases with time in this case. Nevertheless, at $t = 246$ h, the system transfers to state (–2, 2) and so on. Therefore, we can conclude that the system undergoes stochastic transitions between various states differing in the peak components present and in their relative intensities.

Based on these experimental data, we can also conclude that, in the course of evolution of the system, the hydrogen leaves the system and, in addition, the following processes occur: (i) hydrogen and vacancies migrate between dynamic traps and the matrix, which brings about stochastic changes (oscillation) in angle $\langle 2\vartheta \rangle$, and (ii) jumps occur between various states of the matrix.

The experimental data on the structural evolution of the (220) diffraction peak after the fifth saturation are shown in Table 2 and Figs. 4 and 5. The observed pattern is more complicated than that for the (311) peak. For example, one hour after the fifth saturation, the

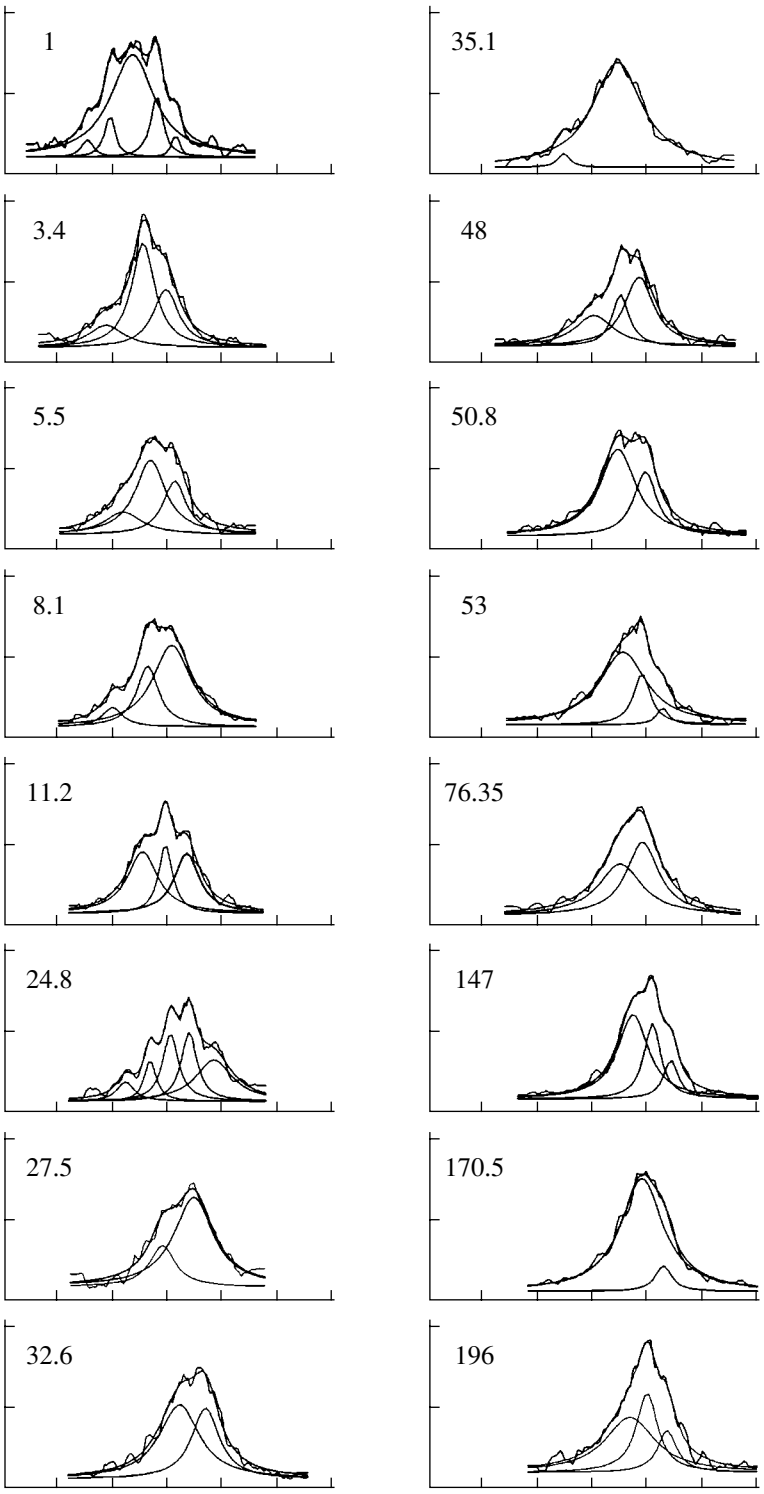

Fig. 4. Time evolution of the (220) diffraction peak after the fifth saturation of the alloy with hydrogen. The numerals near the curves indicate the time measured in hours.

(220) diffraction peak becomes a quintuplet (Fig. 4). Over the period from $t = 3.4$ to 11.2 h, this peak is a triplet, but 15.6 h later it again transforms into a quintuplet. Then, with the passage of time, the diffraction peak becomes simpler and consists of no more than three components. However, while the evolution of this peak differs from that of the (311) diffraction peak, the experimental data represented in Fig. 5 and Table 2

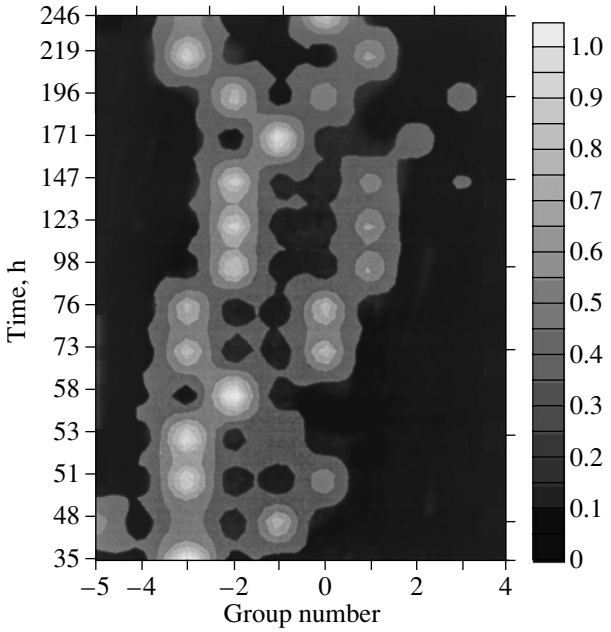

Fig. 5. Positions and intensities of the maxima of the (220) diffraction peak components.

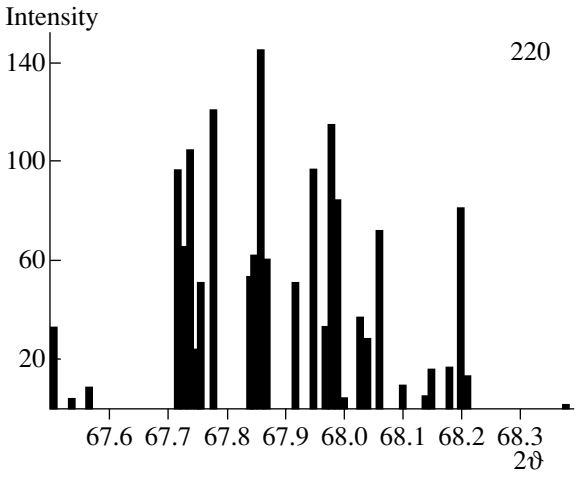

Fig. 6. Diffraction angle dependence of the integrated intensity of the maxima of the (220) diffraction peak components.

show that the values of angle 2ϑ corresponding to the maxima of the peak components form groups, with the number of components in them varying from two to nine. The most numerous group is not located in the middle of Table 2; however, it is not clear what this shift means. The positions of the central components of the groups differ by $2\vartheta = 3'–6'$. The fact that the above-described transitions between the matrix and traps are observed not only for (311) but also for the (220) diffraction peak (Table 2, Fig. 5) is of fundamental importance, because it indicates that discrete evolution is a common property of hydrogenated systems. For the (220) peak, we also constructed the dependence of the integrated intensity of the maxima of the peak components on the diffraction angle (Fig. 6). The results are similar to those shown in Fig. 3.

The effect under study was first observed for the (200) diffraction peak from a Pd–Mo–H alloy during the time interval from $t = 23.6$ to 121 h after saturation of the alloy with hydrogen [3]. For example, two diffraction lines of two phases differing markedly in intensity were observed after 23.6-h relaxation. Then, 3.5 h later, the intensities of the lines become almost equal, although their positions vary only slightly. After the next 3.5 h, a clearly visible weak peak of a new phase appears between the peaks of the observed phases and becomes dominant after a day. The peak on the larger angle 2ϑ side remains virtually unchanged, while the peak on the smaller angle 2ϑ side almost vanishes. However, after approximately two days, all of the three peaks that appeared three days before become clearly visible. A day later, these peaks coalesce into one wide peak, which then again becomes a double peak.

4. DISCUSSION

Thus, the distribution in the angle 2ϑ of the maxima of the diffraction peak components is quasi-discrete for Pd–Mo–H and Pd–Ta–H alloys. According to [9–11], this suggests that the initial crystalline structure transforms into the final structure by passing through a number of intermediate metastable states. One of the most typical transformations of this kind is the formation of one-dimensional long-period structures [11, 12]. Such structures are usually in a strongly nonequilibrium state; therefore, conventional thermodynamic methods are completely inapplicable in this case. This type of structure can be associated with specific features of the electronic energy spectrum [12] that arise as the Fermi surface approaches the boundary of the Brillouin zone. It is significant that the evolution of such a structure is manifested differently in the diffraction peaks depending on their type.

Following [13, 14], we assume that the nonmonotonic variations in the phase composition of a Pd–Ta–H alloy, including the formation of several phases, are associated with the complex profile of the thermodynamic potential as a function of the state of the alloy; in particular, we assume that the potential has a variety of minima differing in depth (as exemplified in Fig. 7). Since the probability of the system being in the potential minima is much higher than that in the maxima, only the configurations corresponding to the minima are observed experimentally. For this reason, the positions of the maxima of the diffraction peak components exhibit a discrete dependence on the diffraction angle 2ϑ. According to the analysis performed in the Appendix, the data listed in Tables 1 and 2 can be explained in terms of the fractal pattern of the hierarchy of states corresponding to the dependence of the thermodynamic

potential on the wave vector **k** [15]. It is of fundamental importance that the single-phase states that are observed in the (311) diffraction peak at time $t = 170$ and 176 h after the sixth saturation and in the (220) peak at time $t = 35$ h after the fifth saturation correspond to the groups with the maximum number of components in Tables 1 and 2. This fact lends further support to the validity of the assumption that the minima of the thermodynamic potential are related to metastable CSDs. The decomposition of the single-phase states into two or more phases with the elapse of time is due to the system being in a nonequilibrium state, in which Pd–Mo–H alloys can persist as long as 2×10^4 h [7].

In terms of structure, the observed processes are associated with the formation of the various complexes making up a hierarchical structure. The evolution of such a structure is determined by transitions between nearest neighbor minima of the thermodynamic potential corresponding to the phases that are most clearly pronounced after saturation with hydrogen. Further evolution is associated with redistribution of the hydrogen and vacancies between the matrix and traps, which arise in the initial stage. The traps capture vacancies and hydrogen atoms even after the greater part of the hydrogen has left the system and are favorable for palladium and tantalum atoms migrating in the matrix. In macroscopic terms, the evolution of the system is determined by transitions between the thermodynamic-potential minima corresponding to different phases. Therefore, the evolution is discrete in character and is associated with jumps between metastable, long-lived states of the system. In this case, fluctuations are of fundamental importance, because they induce such jumps [16].

In [14], we established that the evolution of the structure of Pd–H based multiphase alloys is nonmonotonic and can be described using the Edwards representation and the Lorenz model, in which the structure of the system is characterized by the volume fraction of the ordered phase. The consideration performed in this paper shows that, in the Pd–Ta–H alloys under study, not only the time dependence but also the discrete structural changes are stochastic in character. It is worth noting that these stochastic structural transformations are similar in nature to the transient processes that occur in a chemical clock and in the Benard instability [17] and are followed by regular variations in the state of the system. In our case, the processes in question occur in a solid, where they are caused by relatively rapid transport processes due to excess hydrogen and vacancies.

The model proposed above also explains the fact that the diffraction peaks (or their components) of the alloys under study remain narrow, as a rule, at all stages of their evolution (see also [1–4]). Indeed, since the possible metastable states of the system are limited in number, its evolution is associated with hopping between these states, which gives rise to variations in the number of components in the diffraction peaks rather than to their broadening. In the final analysis, this behavior is due to the stability of the multivalley structure of the energy profile in the space of states of the system; this structure is caused by the combined effect of interactions between atoms, defects, and their complexes. Therefore, all changes produced by the migration of hydrogen atoms and vacancies between defect clusters and the matrix and between CSDs of different phases reduce to jumps of the system between the valleys. Due to these jumps, the diffraction peaks consist of several components whose width is dictated by the sizes of the CSDs of the corresponding phases, which vary with time only slightly.

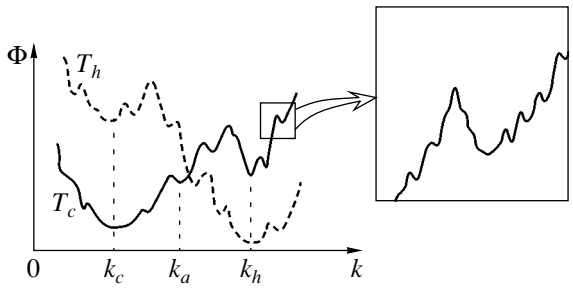

Fig. 7. Thermodynamic potential of a multilevel system as a function of k.

APPENDIX

HIERARCHICAL PARAMETRIZATION OF RECIPROCAL SPACE

It is well known that diffraction theory is based on the Fourier transforms of spatial atomic distributions [18]. For perfect crystals, possessing a periodic structure, the Fourier transform exhibits a set of peaks arranged periodically in k space with period $2\pi/d$, where d is a characteristic distance. Thermodynamically, this means that the internal energy of the system $U(k)$ possesses regularly arranged minima at the wave vectors corresponding to these peaks. The quasi-discrete values of the diffraction angle observed in the alloys under study are indicative of the $U(k)$ dependence being fractal in character and, therefore, of a hierarchical structure of the space of states (see [15, Fig. 7]).

To illustrate this structure, we consider the simplest case of the polymorphic transformation of an hcp lattice characterized by a wave number k_h into an fcc lattice with wave number k_c [9, 10]. The fundamental feature of the fractal $U(k)$ dependence is the existence of a variety of local minima between the states with k_h and k_c. These minima correspond to long-period structures with wave vectors k_a ($a = 1, 2, \ldots$). During isothermal annealing in the temperature range of existence of the fcc structure, the system transfers from the initial state

k_h to the energetically more favored state k_c via a number of intermediate structures with k_a. The deepest minima in the $U(k)$ dependence are characterized by "good" rational numbers corresponding to long-period structures (we call a rational number $m/n < 1$ good if the integers m and n are small). However, for two such structures corresponding to nearest neighbor minima with wave vectors $k_1 = (\pi/d)n_1$ and $k_2 = (\pi/d)n_2$ (where n_1, n_2 are good rational numbers), there is always a countable set of other rational numbers n_a corresponding to intermediate structures via which the system can pass in transferring from the k_1 to the k_2 state. Since the difference between k_1 and k_2 is less than that between k_h and k_c ($|k_1 - k_2| \ll |k_c - k_h|$) one might expect that the minima corresponding to them in the $U(k)$ dependence will be less deep than those corresponding to k_h and k_c (see inset to Fig. 7). In turn, each of the minima that can be resolved on the given scale exhibits a finer structure of minima when drawn on an enlarged scale; these minima are less deep and correspond to structures that differ from each other to a smaller extent. For a macroscopic system consisting of an infinite number of building blocks, the $U(k)$ dependence can be detailed to a progressively greater extent until the change in the thermodynamic potential caused by the formation of a minimal correlation cluster becomes resolved.

Thus, when a sudden transformation of the k_h structure into the k_c c structure takes place, correlated shifts of individual closely packed layers in minimal clusters occur first, which corresponds to filling of the shallowest minima in the $U(k)$ dependence. Then, due to correlation, the minimal clusters are combined, which corresponds to filling of deeper minima. In turn, new clusters coalesce into larger clusters and progressively deeper minima in the $U(k)$ dependence are filled. This step-by-step extension of correlation proceeds until the k_c structure arises in the entire crystal. A key feature of this process is that it has a hierarchical structure; namely, minimal clusters form only after individual close-packed layers are displaced, larger clusters are formed from small clusters rather than from closely packed layers, etc. In terms of the $U(k)$ dependence, this hierarchy is manifested in the successive filling of minima differing in depth; namely, deeper minima are filled only after filling of shallower minima (Fig. 7).

The process under study can be described in terms of ultrametric space, which can be represented by a hierarchical Cayley tree [15]. This tree reflects the changes occurring in the topology of surfaces of constant potential, $U(k) = \text{const}$, and clearly illustrates the step-by-step rearrangement of the structure, as can be seen from Fig. 7. For example, if clusters characterized by wave vectors k_{ab} (a, b = 1, 2, …) form at the instant of time corresponding to level $n - 1$, then, as one goes to the nth level, the k_{a1} states unite into supercluster k_1, the k_{a2} states unite into supercluster k_2, etc. At the $(n + 1)$th level, superclusters k_a unite into the resultant structure k_c. Thus, the structural transformation involving the formation of long-period structures proceeds as step-by-step coalescence of clusters of closely packed layers, which does not reduce to displacements of individual layers. Therefore, in order to describe the evolution of the system, it is convenient to pass over from the usual space (and spatial displacement waves) to ultrametric space. The topology of the latter space adequately represents the hierarchical structure of the system.

In order to describe this structure quantitatively, we introduce the occupation numbers n_i (i = 1, 2, …, N); we have $n_i = 1$ if the ith layer occupies the c position and $n_i = 0$ if this layer is in the h position (N is the total number of closely packed layers). The average value $\bar{n}$ determines the number of c layers $N_c = \bar{n}N$ for given external factors (temperature and composition). Since spatial fluctuations $\delta n_i \equiv n_i - \bar{n}$ are periodic, we consider the lattice Fourier transform

$$\delta n(k) = \frac{1}{N}\sum_i \delta n_i \exp(-ikR_i), \qquad (1)$$

where k is the wave vector and R_i is the coordinate of the ith layer. In order to take into account the step-by-step rearrangement of the structure, we divide the entire volume V of the sample into a hierarchical system of volumes differing in value and embedded in one another. Each of these volumes corresponds to a cluster with correlated layer shifts. For example, the entire volume V is composed of volumes $V_{a1} \ll V$ specified by coordinates r_{a1} (where a_1 = 1, 2, …, N_1 is the index numbering these volumes). In turn, each of the clusters V_{a1} is composed of smaller volumes V_{a1a2} specified by coordinates r_{a1a2} (a_2 = 1, 2, …, N_2). This step-by-step partition of volumes can be carried out indefinitely by separating the volumes $V_{a1a2\ldots an}$ specified by coordinates $r_{a1a2\ldots an}$, where a set of indices a_l = 1, 2, …, N_l (l = 1, 2, …, $n \longrightarrow \infty$) determines each given cluster. We assume that $V_{a1\ldots a(l-1)} \gg V_{a1\ldots al}$ and, therefore, $N_l \gg 1$.

Upon carrying out the partition, we take the lattice Fourier transform over a minimum cluster $V^{(n)} = V_{a1\ldots an}$:

$$\delta n(r_{a1a2\ldots a(n-1)}) = \frac{1}{N_n}\sum_{R_i \in V^{(n)}} \delta n(R_i)\exp[-ik(R_i - r_{a1a2\ldots a(n-1)})]. \qquad (2)$$

As a result, we obtain the spatial-wave amplitude $\delta n_k(r_{a1a2\ldots a(n-1)}) \equiv \delta n_k^{n-1}$ depending on the coordinate $r_{a1a2\ldots a(n-1)}$. This dependence can be allowed for by taking the Fourier transform with respect to the coordinate $r_{a1a2\ldots a(n-1)} \in V^{(n-1)}$ with phase factor $N_{n-1}^{-1}\exp[-ik(r_{a1\ldots a(n-1)} - r_{a1\ldots a(n-2)})]$. By performing this procedure further up to volume V, we arrive at the

following generalization of the Fourier series to hierarchical structures:

$$\delta n_k = \sum_{r_{a1} \in V^{(1)}} \frac{1}{N_1} \exp(-ikr_{a1}) \times \sum_{r_{a1a2} \in V^{(2)}} \frac{1}{N_2} \exp[-ik(r_{a1a2} - r_{a1})] \ldots, \sum_{R_i \in V^{(n)}} \frac{1}{N_n} \exp[-ik(R_i - r_{a1a2\ldots a(n-1)})] \delta n(R_i) = \sum_{r_{a1}} \ldots \sum_{r_{a(n-1)}} \sum_{R_i \in V^{(n)}} \exp(-ikR_i) \delta n(R_i), \quad (3)$$

where we took into account that $N = \prod_i N_i$.

The partition of the direct space leads to clusterization of the conjugate k space near a wave vector of a reciprocal lattice of the hcp structure. It is easy to see that, as a rough approximation to the dependence on the coordinates r_{a1}, we can specify the corresponding function at N_1 points k_{a1} in the minimum zone of k space $W^{(1)}$ of size $K_1 = (N_1/N)(2\pi/d)$. In turn, the dependence on the coordinates r_{a1a2} is associated with points k_{a1a2} separated by distance K_1 in a zone W^2 of size $K_2 = N_2K_1 = (N_1N_2/N)(2\pi/d)$. Finally, atomic-scale variations in the coordinate R_i correspond to points $k_{a1\ldots an} \in W^{(n)}$ located far from one another in the Brillouin zone (with spacing $K_n = (2\pi/N_n)d$ between them). Taking the inverse Fourier transform of Eq. (3), we obtain

$$\delta n_i = \sum_{k_{a1\ldots an} \in W^{(n)}} \exp(ik_{a1\ldots an}R_i) \ldots \times \sum_{k_{a1} \in W^{(1)}} \exp(ik_{a1}R_i) \delta n(k_{a1, \ldots, k_{a1\ldots an}}) = \sum_{k \in W^{(n)}} \ldots \sum_{k \in W^{(1)}} \exp(ikR_i) \delta n(k). \quad (4)$$

Since the consecutive sets of wave numbers k_{a1}, …, $k_{a1\ldots an}$ correspond to progressively larger scales, one might expect that they will also correspond to progressively deeper minima in the $U(k)$ dependence. Thus, the partition of the direct space into volumes $V^{(n)}$ and the corresponding partition of k space into zones $W^{(n)}$ reveal a hierarchy of conjugate sets $V^{(n)}$ and $W^{(n)}$ at different levels n. This hierarchy can be discovered most simply by representing the sets $V^{(n)}$ and $W^{(n)}$ in ultrametric space, in which the distance between points is determined by the number of steps along the hierarchical tree leading to the common ancestor [15].

ACKNOWLEDGMENTS

This study was supported by the Russian Foundation for Basic Research, project nos. 02-02-16537 and 03-02-06690.

REFERENCES

1. V. M. Avdyukhina, A. A. Katsnel'son, and G. P. Revkevich, Kristallografiya **44** (1), 49 (1999) [Crystallogr. Rep. **44**, 44 (1999)].
2. V. M. Avdyukhina, A. A. Katsnel'son, G. P. Revkevich, *et al.*, Altern. Énerg. Ékol. **1** (1), 11 (2000).
3. V. M. Avdyukhina, A. A. Anishchenko, A. A. Katsnel'son, and G. P. Revkevich, Perspekt. Mater., No. 6, 12 (2001).
4. V. M. Avdyukhina, A. A. Katsnelson, and G. P. Revkevich, Platinum Met. Rev. **46** (4), 169 (2002).
5. Ya. S. Umanskiĭ, *X-ray Diffractometry of Metals and Semiconductors* (Metallurgiya, Moscow, 1969).
6. A. Reuss, Z. Angew. Met. **9** (1), 49 (1929).
7. V. M. Avdyukhina, A. A. Anishchenko, A. A. Katsnel'son, and G. P. Revkevich, Perspekt. Mater., No. 4, 5 (2002).
8. J. Sakamoto, K. Kajinara, K. Kikumura, and T. B. Flanagan, J. Chem. Soc., Faraday Trans. **86** (2), 377 (1990).
9. A. I. Olemskoĭ and A. A. Katsnel'son, Usp. Fiz. Met. **3** (1), 1 (2002).
10. A. I. Olemskoĭ and A. A. Katsnel'son, *Synergetics of Condensed Media* (URSS, Moscow, 2003).
11. V. I. Nikolin, *Multilayered Structures and Polytypism in Metal Alloys* (Naukova Dumka, Kiev, 1984).
12. D. A. Vul' and M. A. Krivoglaz, Fiz. Met. Metalloved. **51**, 231 (1981).
13. V. M. Avdyukhina, A. A. Katsnel'son, A. I. Olemskoĭ, and G. P. Revkevich, Perspekt. Mater., No. 3, 5 (2001).
14. V. M. Avdyukhina, A. A. Katsnel'son, A. I. Olemskoĭ, *et al.*, Fiz. Tverd. Tela (St. Petersburg) **44** (6), 979 (2002) [Phys. Solid State **44**, 1022 (2002)].
15. A. I. Olemskoĭ and A. Ya. Flat, Usp. Fiz. Nauk **163** (12), 1 (1993) [Phys. Usp. **36**, 1087 (1993)].
16. W. Horsthemke and R. Lefever, *Noise Induced Transitions. Theory and Applications in Physics, Chemistry and Biology* (Springer, Heidelberg, 1984; Mir, Moscow, 1987).
17. H. Haken, *Mysteries of Nature (Synergetics: Study of Interaction)* (Inst. Komp'yut. Issled., Moscow, 2003).
18. M. A. Krivoglaz, *Theory of X-ray and Thermal Neutron Scattering by Real Crystals*, 2nd ed. (Naukova Dumka, Kiev, 1983; Plenum, New York, 1969).

Translated by Yu. Epifanov

Physics of the Solid State, Vol. 46, No. 3, 2004, pp. 420–423. Translated from Fizika Tverdogo Tela, Vol. 46, No. 3, 2004, pp. 410–413.

METALS AND SUPERCONDUCTORS

Distribution of a Local Magnetic Field in Superconductors with an Uncorrelated Random Lattice of Abrikosov Vortices

A. V. Minkin and S. L. Tsarevskiĭ

Kazan State University, Kremlevskaya ul. 18, Kazan, 420008 Tatarstan, Russia

e-mail: Sergey.Tsarevskii@ksu.ru

Received March 3, 2003; in final form, May 15, 2003

Abstract—The distribution of a local magnetic field near the surface of a uniaxial anisotropic type-II superconductor is determined in the framework of the London model in the case when the Abrikosov vortices are randomly distributed in the superconductor. The distribution of a local magnetic field is obtained as a function of the distance from the surface of the superconductor. It is demonstrated that the shape of the distribution of the local magnetic field near the surface differs substantially from that in the bulk of the superconductor. This difference should be taken into account in interpreting experimental data on the local magnetic field in the surface region of the superconductor and in thin superconducting films (with a thickness of less than or equal to λ, where λ is the depth of penetration of the magnetic field into the superconductor). It is shown that, as in the case of a regular lattice of vortices, the value of λ can be determined from observations of the distribution of the local magnetic field in type-II superconductors with an uncorrelated random lattice of vortices. © *2004 MAIK "Nauka/Interperiodica".*

1. It is known that, under certain conditions, the lattice of Abrikosov vortices in thin high-temperature superconductor films in an external magnetic field **H** becomes unstable [1–3]. In this case, the vortices are distributed chaotically and the distribution of the magnetic field is randomly inhomogeneous. The randomly inhomogeneous state of a high-temperature superconductor is characterized by a number of specific features, for example, the nonmonotonic dependence of the critical current $J_c(H)$, the "fishtail" effect [4], the electrical bistability [5], changes in the character of absorption of the microwave energy [6], etc. When processing experimental data on the μ^+SR rotation of muons in uncorrelated lattices [7], accurate approximation of the distribution function of the local magnetic field is particularly important for determining the pinning parameters of the superconductor. Knowledge of the distribution of the local magnetic field is also very important in the case when thin superconducting films are studied using magnetic resonance (inhomogeneous line width) and microwave absorption spectroscopy. In this connection, it is of interest to determine the distribution function of the local magnetic field of randomly distributed Abrikosov vortices. Earlier, this problem was solved for a massive superconductor (see, for example, [7]). However, it is known that, as the surface is approached, the local magnetic field of the superconductor changes significantly [8, 9]. For regular vortex lattices, making allowance for this circumstance leads to a drastic change in the magnetic resonance line [10]. The purpose of the present work was to calculate the distribution function $W(h, z)$ of a local magnetic field **h** in a half-space occupied by a superconductor as a function of the depth z from the surface of the superconductor. It was demonstrated that, as the surface of the superconductor is approached, the shape of the distribution changes appreciably and the width of the line becomes substantially narrower. Note that these changes manifest themselves at distances of less than or equal to λ from the surface of the superconductor (λ is the London penetration depth of the magnetic field in the superconductor).

2. Let us consider a type-II superconductor with $\kappa \gg 1$ (where κ is the Ginzburg–Landau parameter) in an external magnetic field H. It is assumed that the superconductor occupies a half-space $z < 0$ and the magnetic field **H** is directed along the **z** axis. The **z** axis is aligned parallel to the **c** axis of the superconductor. We consider the situation where the external magnetic field satisfies the condition $H_{c1} < H < H_{c2}$ (where H_{c1} and H_{c2} are the first and the second critical fields, respectively); i.e., the local magnetic field penetrates into the superconductor in the form of quantum Abrikosov vortices and can be described by Londons' equations. It is also assumed that the system of vortices is a two-dimensional structure of randomly (uncorrelatedly) arranged vortices. The assumption of the uncorrelatedness of the vertex structure implies smallness of the "eliminated volume" in which the vertex–vertex repulsion is significant. For $\kappa \gg 1$, this holds true over a wide range of intermediate fields as long as the density of vortices ρ_0 does not greatly exceed λ^{-2}.

1063-7834/04/4603-0420$26.00 © 2004 MAIK "Nauka/Interperiodica"

In the London limit, the local magnetic field is a superposition of magnetic fields of single vortices [7]:

$$\mathbf{h}(\boldsymbol{\rho}, z) = \sum_i \mathbf{h}_s(|\boldsymbol{\rho} - \boldsymbol{\rho}_i|, z), \quad (1)$$

where $\mathbf{h}_s(\boldsymbol{\rho}, z)$ is the local magnetic field of a single vortex, $\boldsymbol{\rho}$ is the radius vector in the xy plane, $\boldsymbol{\rho}_i$ is the radius vector of the core of the ith filament, and z is the distance from the surface of the superconductor. It what follows, the length will be measured in units of λ.

In order to determine the probability density of the distribution of an internal magnetic field $W(h, z)$ for a stochastic lattice of uncorrelated vortices, we use the Holtsmark method [11]. The function $W(h, z)$ can be represented by the standard relationship

$$W(h, z) = \int\int\ldots\int\delta\left(h - \sum_{i=1}^{n} h_i\right) W_i(h_i, z)\, dh_1 dh_2 \ldots dh_n, \quad (2)$$

where $W_i(h_i, z)$ is the probability that the ith vortex takes on a value of the magnetic field in the range between h_i and $h_i + dh_i$.

Hence, for the Fourier transform

$$W(\nu_h, z) = \frac{1}{2\pi}\int W(h, z)\exp(i\nu_h h)\, dh \quad (3)$$

we obtain the convenient formula

$$W(\nu_h, z) = \prod_{i=1}^{n} W_i(\nu_h, z), \quad (4)$$

where

$$W_i(\nu_h, z) = \frac{1}{2\pi}\int W_i(h, z)\exp(i\nu_h h)\, dh. \quad (5)$$

For a region of sufficiently large radius R_n, the number of vortices inside the region can be determined from the formula $N = \pi\rho_0 R_n^2$, where $\rho_0 = H/\Phi_0$ is the density of vortices and $\Phi_0 = 2 \times 10^{-7}$ G cm^2 is the magnetic flux quantum.

It is simple to obtain the distribution function of the magnetic field $W_i(\nu_h)$ for a single vortex:

$$W_i(\nu_{h,z}) = \frac{1}{\pi R_n^2}\int_0^{R_n}\int_0^{2\pi} \exp(i\nu_h h_s(\rho, z))\rho\, d\rho\, d\varphi. \quad (6)$$

Taking into account that the integrand does not depend on φ and replacing the upper limit of integration with respect to ρ by ∞, we have

$$W_i(\nu_h, z) = 1 - \frac{2}{R_n^2}\int_0^{\infty}[1 - \exp(i\nu_h h_s(\rho, z))]\rho\, d\rho. \quad (7)$$

Substituting expression (7) into formula (5) and passing to the limit $N \longrightarrow \infty$, we obtain the relationship [7]

$$W(\nu_h, z) = \exp\left[-2\pi\rho_0\int_0^{\infty}[1 - \exp(i\nu_h h_s(\rho, z))]\rho\, d\rho\right]. \quad (8)$$

The distribution of internal magnetic fields can be represented by the inverse Fourier transform

$$W(h, z) = \int W(\nu_h, z)\exp(-ih\nu_h)\, d\nu_h. \quad (9)$$

Thus, in order to determine the distribution function $W(h, z)$, it is necessary to know the local magnetic field of a single vortex with allowance made for the changes in the boundary region of the superconductor. In our case, the magnetic field inside the superconductor is described by the Londons' generalized equation and the magnetic field outside the superconductor (in vacuum) is represented by the Maxwell equations. The solution to these equations must satisfy the boundary conditions at the superconductor–vacuum interface ($z = 0$) [8]. The desired solution can be represented in the form of a Fourier integral; hence, it is possible to obtain an analytical solution for the Fourier components. However, the local magnetic field cannot be represented in analytical form. Therefore, the local magnetic field should be reconstructed numerically with the inverse Fourier transform [9]. The computer calculation of the inverse Fourier transform for a single vortex is reduced to the calculation of a two-dimensional integral sum at points with a definite step; i.e., the integral is replaced by a Fourier series. This means that the single vortex is replaced by a periodic two-dimensional structure with a spatial period a. Since the magnetic field of a single vortex varies at distances of less than or equal to λ from the center of the vortex, the overlap of the vortices at a spatial period $a > \lambda$ can be disregarded and the values of the magnetic field (from the maximum to the minimum) in a cell of the regular vortex lattice along a particular direction can be taken as a local magnetic field of the single vortex. The accuracy of the calculations is determined by the spatial period and the number of points where the magnetic field is calculated: the larger the spatial period a (with the corresponding increase in the number of points), the higher the accuracy in calculating the magnetic field of a single vortex. In this case, the local magnetic field is sought in the form of a Fourier series in the reciprocal vectors $\mathbf{G}$ of the vortex lattice and the reconstruction of the magnetic field can be accomplished using the fast Fourier transformation. In our case, we numerically calculated the probability $W(h, z)$ with the Fourier coefficients of the local magnetic field $h(\mathbf{G}, z)$ obtained earlier in [12] for a regular vortex lattice.

3. The distribution functions $W(h, z)$ calculated for different values of λ, ξ, and H (where ξ is the coherence length) are presented in Figs. 1–3. All the distribution

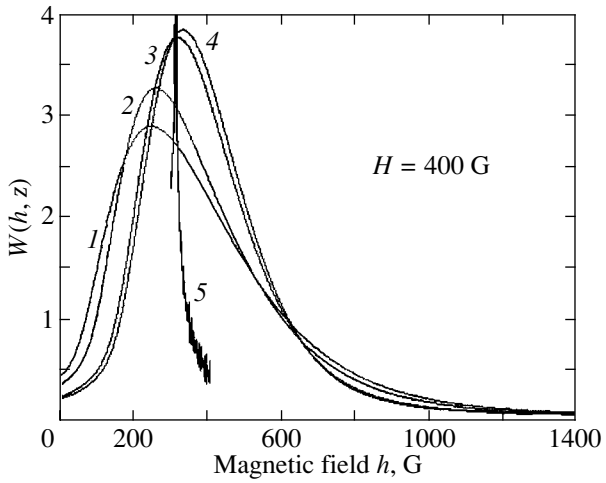

Fig. 1. Distribution function of a local magnetic field $W(h, z)$ at different depths z in a superconductor with parameters $\lambda = 1400$ Å and $\xi = 20$ Å for (*1*–*4*) stochastic and (*5*) triangular vortex lattices in an external magnetic field $H = 400$ G. z = (*1*, *5*) –5, (*2*) –0.5, (*3*) –0.05, and (*4*) 0.

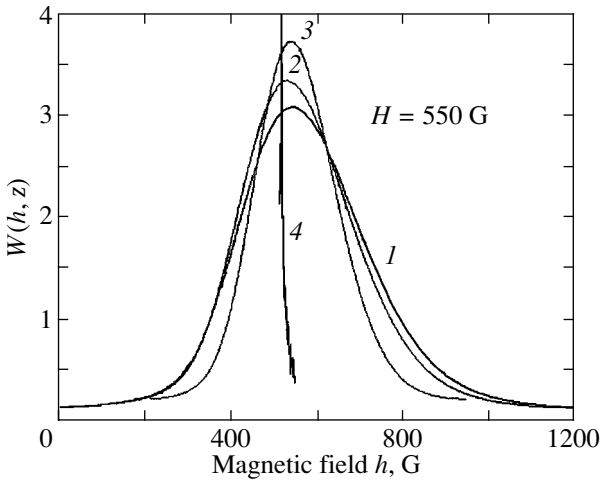

Fig. 2. Distribution function of a local magnetic field $W(h, z)$ at different depths z in a superconductor with parameters $\lambda = 2700$ Å and $\xi = 5$ Å for (*1*–*3*) stochastic and (*4*) triangular vortex lattices in an external magnetic field $H = 550$ G. z = (*1*, *4*) –5, (*2*) –0.5, and (*3*) 0.

curves $W(h, z)$ depicted in these figures are normalized to unity. The calculations were performed according to the procedure described by Kochelaev *et al.* [10]. The accuracy of the calculations was verified by increasing the spatial period a with a constant step in the calculated sums. The local magnetic field of a single vortex was calculated using the appropriate summation of the reciprocal vectors of an imaginary lattice with a period equal to 10λ. Figure 1 presents the results of our calculations of the distribution function $W(h, z)$ of the local magnetic field at depths $z = 0$, –0.05, –0.5, and –5 for a superconductor with parameters $\lambda = 1440$ Å and $\xi = 20$ Å in an external magnetic field $H = 400$ G. In this case, we obtain $\lambda^{-2} \geq \rho_0$ and our calculations are valid. The distribution function $W(h)$ for a massive superconductor with these parameters was calculated earlier in [7]. It can be seen from the figure that, at $z = -0.5$ (recall that the length is measured in λ), the curve $W(h, z)$ approaches the distribution $W(h)$ for a massive superconductor and, at $z = -5$, the results of our calculations coincide with the calculated data on the distribution $W(h)$ taken from [7] (the bulk mode). This confirms the validity of the representation of the local magnetic field of a single vortex in the form of a Fourier series in the reciprocal vectors of the regular lattice. The narrow distribution (Fig. 1, curve *5*) corresponds to the local magnetic field for a regular triangular lattice. As can be seen from Fig. 1, the distortion of the regular vortex lattice leads to a substantial broadening of the distribution of the magnetic field. As the boundary of the superconductor is approached, the shape of the distribution of the local magnetic field changes significantly. This is associated with the fact that the lines of force of the magnetic field of the vortex diverge as the surface of the superconductor is approached and, hence, the inhomogeneity of the local magnetic field decreases. Figure 2 presents the results of the calculation for YBaCuO high-temperature superconductors with critical temperature $T_c = 90$ K ($\lambda = 2700$ Å, $\xi = 5$ Å) in an external magnetic field $H = 550$ G (in this case, the penetration depth of the magnetic field also satisfies the relationship $\lambda^{-2} \approx \rho_0$). The distribution function $W(h, z)$ for a regular triangular vortex lattice of this superconductor was calculated earlier in [12] (Fig. 2, curve *4*). It is evident from Fig. 2 that the width of the distribution $W(h, z)$ for this superconductor decreases still further as the surface is approached. Figure 3 presents the results of calculating the distribution function $W(h, z)$ at the surface of a superconductor ($z = 0$) for different values of λ in an external magnetic field $H = 550$ G. It is seen

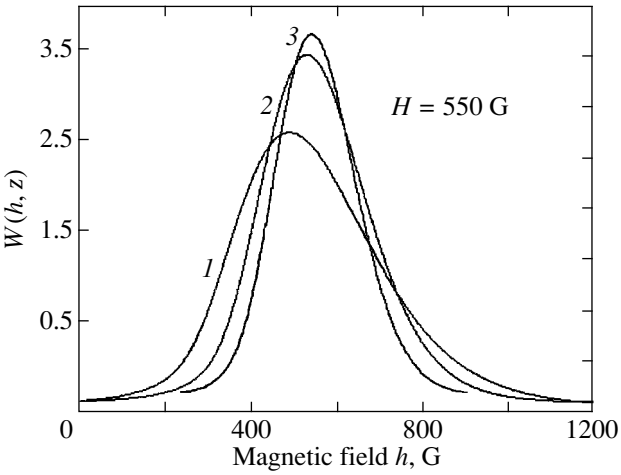

Fig. 3. Distribution function of a local magnetic field $W(h, z)$ at the surface of a superconductor ($z = 0$) with $\xi = 5$ Å in an external magnetic field $H = 550$ G with different values of λ. λ = (*1*) 1400, (*2*) 2000, and (*3*) 2700 Å.

from this figure that the distribution function $W(h, z)$ at the surface of the superconductor in a magnetic field essentially depends on the parameter λ.

4. In conclusion, it should be noted that, since the changes in the distribution of the local magnetic field take place at distances of less than or equal to λ, the width of the distribution of the local magnetic field in a random vortex lattice of thin superconducting films with a thickness of $\leq\lambda$ can be 1.5 times less than that in a massive superconductor with the same parameters (λ, ξ). This circumstance must be taken into account when interpreting the experimental data on the μ^+SR rotation of muons in thin superconducting films (particularly when approximating the distribution function of the local magnetic field) [7]. Since magnetic resonance methods deal with the surface region of a superconductor ($\sim\lambda$), these experiments must also account for the changes in the scatter of local magnetic fields as the surface of the superconductor is approached. Our calculations demonstrated that, for a random uncorrelated lattice of vortices, the calculation technique described above makes it possible to determine the parameter λ of a superconductor from the experimental data.

ACKNOWLEDGMENTS

This work was supported in part by the US Civilian Research and Development Foundation for the Independent States of the Former Soviet Union (CRDF) (project no. REC-007).

REFERENCES

1. G. Blatter, M. V. Feigelman, V. B. Geshkenbein, *et al.*, Rev. Mod. Phys. **66**, 1125 (1994).
2. E. H. Brandt, Rep. Prog. Phys. **58**, 1465 (1995).
3. L. F. Colun and H. J. Jensen, Rep. Prog. Phys. **60**, 1465 (1997).
4. H. Küpfer, Th. Wolf, C. Lessing, *et al.*, Phys. Rev. B **58**, 2886 (1998).
5. A. Gurevich and V. M. Vinokur, Phys. Rev. Lett. **83**, 3037 (1999).
6. T. Shaposhnikova, Yu. Talanov, and Yu. Vashakidze, Physica C (Amsterdam) **385**, 383 (2003).
7. Yu. M. Belousov, V. N. Gorbunov, V. P. Smilga, and V. I. Fesenko, Usp. Fiz. Nauk **160** (11), 55 (1990) [Sov. Phys. Usp. **33**, 911 (1990)].
8. B. I. Kochelaev and E. P. Sharin, Sverkhprovodimost: Fiz., Khim., Tekh. **5** (10), 1931 (1992).
9. V. G. Kogan, A. Yu. Simonov, and M. Ledvij, Phys. Rev. B **48**, 392 (1993).
10. B. I. Kochelaev, Yu. N. Proshin, and S. L. Tsarevskiĭ, Fiz. Tverd. Tela (St. Petersburg) **38** (11), 3220 (1996) [Phys. Solid State **38**, 1758 (1996)].
11. A. Isihara, *Statistical Physics* (Academic, New York, 1971; Mir, Moscow, 1973).
12. S. A. Efremova and S. L. Tsarevskiĭ, Fiz. Tverd. Tela (Leningrad) **39** (11), 1935 (1997) [Phys. Solid State **39**, 1729 (1997)].

Translated by O. Moskalev

Physics of the Solid State, Vol. 46, No. 3, 2004, pp. 424–429. Translated from Fizika Tverdogo Tela, Vol. 46, No. 3, 2004, pp. 414–418.

METALS AND SUPERCONDUCTORS

Correlation between the Dynamics of Oxygen Atoms and Oxidation Kinetics of Solid Solutions Based on $Bi_2Sr_2CaCu_2O_8$

A. V. Knotko*, A. V. Garshev*, M. N. Pulkin*, V. I. Putlyaev*, and S. I. Morozov**

** Moscow State University, Vorob'evy gory, Moscow, 119992 Russia*

e-mail: knotko@inorg.chem.msu.ru

*** Institute of Physics and Power Engineering, Russian Federal Research Center, pl. Bondarenko 1, Obninsk, Kaluzhskaya oblast, 249033 Russia*

Received July 24, 2003

Abstract—The oxidation kinetics of $Bi_{1.3}Pb_{0.8}Sr_2Ca_{0.8}Y_{0.2}Cu_2O_{8+\delta}$ solid solutions at different temperatures and p_{O_2} = 0.21 atm is investigated by thermogravimetry. The results obtained are compared with the previously studied oxidation kinetics of $Bi_{1.5}Pb_{0.6}Sr_2CaCu_2O_{8+\delta}$ solid solutions. It is found that the substitution of yttrium for calcium leads to an appreciable retardation of the initial oxidation stage associated with the oxygen diffusion. The phonon spectra of the solid solutions are examined using inelastic neutron scattering on a DIN-2PI direct-geometry spectrometer. The high-frequency (>50 meV) phonon densities of states for yttrium-containing and yttrium-free solid solutions are analyzed. The possible model is proposed for a correlation between the differences observed in the high-frequency phonon densities of states attributed to the vibrations of oxygen atoms and the differences in the oxidation kinetics of the solid solutions under consideration. © *2004 MAIK "Nauka/Interperiodica".*

1. INTRODUCTION

Phase transformations occurring in superconductor materials with the formation of a "superconductor matrix–nonsuperconducting inclusion" composite are considered a promising tool for producing efficient centers of magnetic flux pinning. For example, in the $Bi_2Sr_2CaCu_2O_8$ (Bi-2212) compound, which holds the greatest promise as a superconductor for use in practice, precipitates formed at the initial stage of decomposing solid solutions based on this phase can serve as efficient centers of magnetic flux pinning. The efficiency of these centers depends on the uniformity of their distribution and the closeness of the sizes to the coherence length of the superconductor. However, the low rate of cation redistribution considerably complicates the practical use of phase decomposition for this purpose in the case of substituents with a constant oxidation number [1]. Therefore, it is of particular interest to use redox reactions for producing inhomogeneities in a Bi-2212 matrix, because these processes can provide a considerable acceleration of the phase decomposition owing to the appreciably higher rate of oxygen diffusion as compared to the rate of cation diffusion (at temperatures of approximately 650°C, the diffusion coefficients D are of the order of 10^{-8} and 10^{-10} cm^2/s, respectively [2]).

It should be noted that the oxidation of copper entering into the composition of the Bi-2212 cuprate results in a substantial decrease in the superconducting transition temperature (see, for example, review [3]). In this respect, of special interest are phase transformations in solid solutions prepared either through substitution of lead (or antimony) for bismuth or through simultaneous substitution in several crystallographic positions [for example, the substitution of lead and calcium for bismuth and (or) rare-earth elements for strontium]. The former solid solutions are of interest due to the specific features of the bismuth crystallographic position with respect to the electronic structure of the cation (Bi^{3+} in the Bi-2212 matrix can be replaced by Pb^{2+}, whose oxidation to Pb^{4+} leads to the precipitation of the second phases ($(Pb,Bi)_3(Sr,Ca)_5CuO_2$ [4]). Solid solutions synthesized through the replacement of calcium and strontium by rare-earth elements with a variable oxidation number (Pr, Tb, Ce) seem to be of lesser interest.

Earlier [5], we studied $Bi_{2-x}Pb_xSr_2CaCu_2O_8$ solid solutions and showed that, at high lead contents, the oxidation proceeds in two stages. The first stage can be associated with the oxygen redistribution in the initially homogeneous solid solution, and the second stage involves a slower cation redistribution accompanied by the precipitation of the second phases. The first stage of oxidative decomposition of the solid solution occurs through the spinodal mechanism followed by coarsening of the microstructure.

The double heterovalent substitution in the structure of the Bi-2212 cuprate makes it possible to control the oxidation kinetics of solid solutions and the resultant

microstructures by varying the effective electric charges of the crystal chemical layers. In order to gain better insight into the mechanism of oxidation of solid solutions based on the Bi-2212 compound and the effect of heterovalent substitution, it is expedient to perform a comparative analysis of the rate of absorption of oxygen by a sample and the vibrational states of oxygen atoms with the use of the same samples.

2. EXPERIMENTAL TECHNIQUE AND DATA PROCESSING

Samples of $Bi_{2.1-x}Pb_xSr_2Ca_{1-y}Y_yCu_2O_{8+\delta}$ solid solutions ($x = 0.6$, $y = 0$; $x = 0.8$, $y = 0.2$) were synthesized from nitrate–oxynitrate mixtures prepared by dissolving Bi_2O_3, $SrCO_3$, CuO, $Pb(NO_3)_2$ (analytical grade), $CaCO_3$, and Y_2O_3 (special-purity grade) in 20% nitric acid, followed by evaporation of the resultant solution. For the chosen compositions of the solid solutions, copper had the same mean oxidation number due to the heterovalent substitution of Pb^{2+} for Bi^{3+} and Y^{3+} for Ca^{2+}. The synthesis of the samples involved decomposition of the salt mixture at 750°C in air and several annealings in a nitrogen flow (at the residual pressure $p_{O_2} = 10^{-3}$ atm) at a temperature of 760°C for 24 h with intermediate grinding.

X-ray powder diffraction analysis of the synthesized samples was performed on a DRON-3M diffractometer (Cu-$K_{\alpha, cp}$ radiation). The unit cell parameters were determined with the use of silicon as an internal standard. According to the x-ray diffraction data, the prepared samples correspond in composition to $Bi_2Sr_2CaCu_2O_8$-based solid solutions. The unit cell parameters refined by the least-squares technique for the synthesized samples and the corresponding parameters obtained in our earlier work [6] for similar solid solutions are presented in Fig. 1.

The microstructure of the synthesized samples was examined on a Jeol JEM-2000FXII transmission electron microscope (Japan) with an LaB_6 cathode at an accelerating voltage of 200 kV.

The oxidation kinetics of the solid solutions was investigated by thermogravimetry on a MOM Q-1500D derivatograph (Hungary). The studied sample was heated in air to a temperature of 650–750°C at a rate of 20°C/min, followed by isothermal treatment. The base line of the derivatograph was determined by measuring a Bi_2O_3 reference sample under the same conditions.

The experiments on inelastic neutron scattering were carried out on a DIN-2PI direct-geometry spectrometer installed on an IBR-2 reactor (Joint Institute for Nuclear Research, Dubna) [7]. The time-of-flight spectra were recorded in the energy gain (E) mode with the initial neutron energy $E_0 = 7.90$ meV at room temperature in the scattering angle range 42°–134°. Detectors located at smaller scattering angles recorded neutron fluxes with energies >100 meV, which corresponded to the thermal background. The spectrometer resolution was $\Delta E/E \approx 5$–8% in the energy transfer range $\varepsilon = E - E_0 = 0$–100 meV. In this case, the momentum transferred to a neutron fell in the range $Q = 1.8$–4.2 Å^{-1} at $\varepsilon = 6$ meV and $Q = 5.9$–8.7 Å^{-1} at $\varepsilon = 100$ meV. The spectra were normalized with respect to the elastic peak of vanadium.

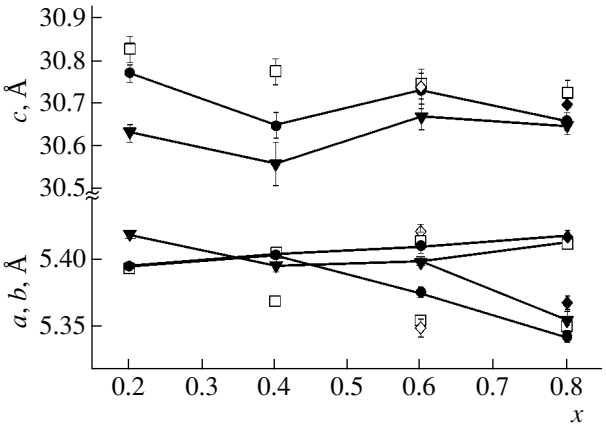

Fig. 1. Unit cell parameters of the solid solutions $Pb_{0.6}Bi_{1.5}Sr_2CaCu_2O_z$ (open rhombuses) and $Pb_{0.8}Bi_{1.3}Sr_2Ca_{0.8}Y_{0.2}Cu_2O_z$ (closed rhombuses) in comparison with the unit cell parameters of the solid solutions $Pb_xBi_{2.1-x}Sr_2Ca_{1-y}Y_yCu_2O_z$ synthesized in [6]: $Pb_xBi_{2.1-x}Sr_2Ca_{0.6}Y_{0.4}Cu_2O_z$ (closed triangles), $Pb_xBi_{2.1-x}Sr_2Ca_{0.8}Y_{0.2}Cu_2O_z$ (closed circles), and $Pb_xBi_{2.1-x}Sr_2CaCu_2O_z$ (open squares).

The spectra were processed in the incoherent approximation with due regard for multiphonon scattering [8]. After introducing standard corrections for detector efficiency and neutron-flux attenuation in the sample, the inelastic neutron scattering spectra recorded in the scattering angle range 42°–134° were processed to derive the function $G(\varepsilon)$. This function describes the weighted frequency spectrum of the crystal lattice (the so-called neutron-weighted vibrational density of states) with the weighting factor $\sum \exp(-2W_i)c_i\sigma_i\langle|\xi_i(\varepsilon)|^2\rangle/m_i$, where c_i, σ_i, m_i, and $\langle|\xi_i(\varepsilon)|^2\rangle$ are the concentration, the scattering cross section, the mass, and the mean-square polarization vector of the ith atom, respectively, and $\exp(-2W_i)$ is the Debye–Waller factor.

The neutron-weighted frequency spectra of the solid solutions studied are shown in Fig. 2. These spectra were obtained by averaging over the results of measurements on all detectors in the scattering angle range 42°–134°. In order to estimate numerically the differences in the phonon densities of states for the samples of different cationic compositions, the low-frequency ($\varepsilon <$ 50 meV) portions of the spectra were approximated by the superposition of the Gaussian functions

$$I = A/(w(\pi/2)^{1/2})\exp(-2(\varepsilon - \varepsilon_c)/w)^2, \qquad (1)$$

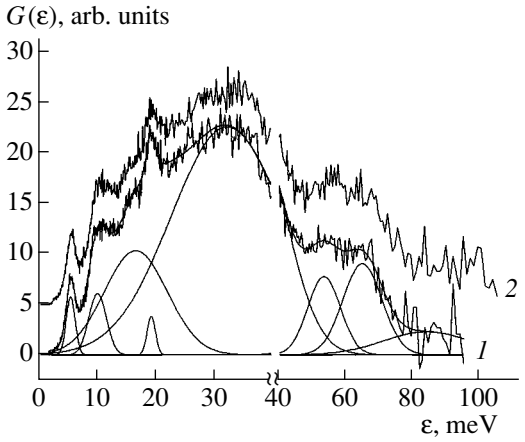

Fig. 2. Generalized frequency spectra $G(\varepsilon)$ of $Bi_{2.1-x}Pb_xSr_2Ca_{1-y}Y_yCu_2O_z$ solid solutions: (*1*) $x = 0.6$, $y = 0$ and (*2*) $x = 0.8$, $y = 0.2$. The approximation of spectrum *1* by functions (1) is shown under this spectrum.

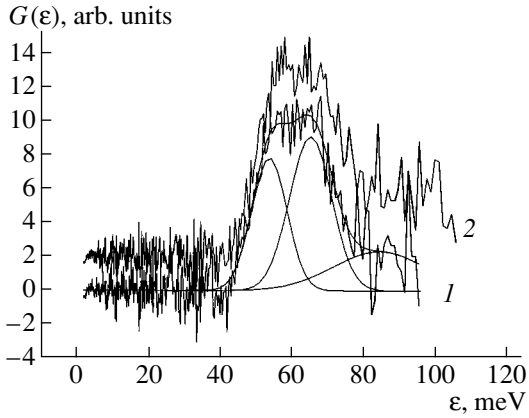

Fig. 3. High-frequency portions of the spectra $G(\varepsilon)$ of $Bi_{2.1-x}Pb_xSr_2Ca_{1-y}Y_yCu_2O_z$ solid solutions [after subtracting the sum of functions (1) describing peaks *1–5*]: (*1*) $x = 0.6$, $y = 0$ and (*2*) $x = 0.8$, $y = 0.2$. The approximation of spectrum *1* by functions (1) is shown under this spectrum.

where I is the intensity; ε is the energy; and A, w, and ε_c are parameters. By subtracting the sum of the functions describing the low-frequency portion from the spectrum $G(\varepsilon)$, we separated the spectral portions that, according to the data available in the literature, correspond to vibrations of oxygen atoms in CuO_2 and SrO layers (Fig. 3). These portions were also approximated by functions (1). The parameters of the Gaussian functions for all the samples are listed in the table. The graphs of the functions describing the spectrum $G(\varepsilon)$ of the $Bi_{1.5}Pb_{0.6}Sr_2CaCu_2O_8$ solid solution are depicted in Figs. 2 and 3.

3. RESULTS AND DISCUSSION

The kinetic curves for oxidation of the solid solutions in air at 650 and 700°C are shown in Fig. 4. The presented data on the oxidation of the $Bi_{1.5}Pb_{0.6}Sr_2CaCu_2O_{8+\delta}$ solid solution are taken from our previous work [5]. It can be seen that the oxidation of the $Bi_{1.3}Pb_{0.8}Sr_2Ca_{0.8}Y_{0.2}Cu_2O_{8+\delta}$ solid solution is characterized by an appreciable retardation of the initial oxidation stage (as compared to the yttrium-free samples) at a virtually unchanged rate of the second stage. As was noted above, the initial oxidation stage of the lead-substituted Bi-2212 compound is associated primarily with the oxygen redistribution in the solid solution, whereas the second stage involves the cation redistribution. Therefore, we can draw the inference that the oxygen diffusion is considerably retarded in all the yttrium-containing samples in which copper has the same mean oxidation number due to the heterovalent substitution. Electron microscopic examinations of the samples prior to and after oxidation (performed earlier in [5] for yttrium-free solid solutions) revealed that the early stage of the process involves both the oxygen and, most likely, cation separation of the solid solution into layers with the formation of a lamellar micromorphology, which is characteristic of spinodal decomposition and favors efficient pinning of the magnetic flux. Further oxidation of yttrium-free samples is accompanied by coarsening of the microstructure [5]. For the $Bi_{1.3}Pb_{0.8}Sr_2Ca_{0.8}Y_{0.2}Cu_2O_{8+\delta}$ solid solution, it was found that the lamellar structure has a considerably smaller period (approximately 3 nm, as compared to 10 nm in the yttrium-free solid solution [5]); moreover, the coarsening of this structure decreases significantly. Thus, the double heterovalent substitution provides a

Parameters of Gaussian functions (1) describing (upon superposition) the generalized frequency spectra of $Bi_{2.1-x}Pb_xSr_2Ca_{1-y}Y_yCu_2O_z$ solid solutions

x, y		1	2	3	4	5	6	7	8
$x = 0.6$, $y = 0$	ε_c, meV	5.28	9.9	16.5	19.2	32.3	53.5	65.1	84
	w, meV	1.53	3.02	10.9	1.44	19.4	9.84	11.8	26
	A, au	11.1	23.2	141	6.92	554	96.4	133	74
$x = 0.8$, $y = 0.2$	ε_c, meV	5.37	10.1	16.6	19.3	32.9	54.0	65.7	93
	w, meV	1.55	2.81	11.3	1.63	19.9	9.69	16.0	23
	A, au	9.85	19.8	132	6.10	535	81.0	206	119

means for controlling the microstructure formed upon oxidative decomposition of the solid solution based on the Bi-2212 compound.

The vibrational spectra of the solid solutions under investigation were analyzed with the aim of elucidating the mechanism of retardation of oxygen diffusion in the lead-containing Bi-2212 compound upon substitution of yttrium for calcium. As was done in [10, 11], the specific features revealed in the spectra $G(\varepsilon)$ were assigned to vibrations of particular atoms in crystal chemical layers of the Bi-2212 structure by comparing the experimental data with the results obtained in [12–15] for $Bi_2Sr_2Ca_{1-x}Y_xCu_2O_{8+\delta}$ solid solutions and the unsubstituted $Bi_2Sr_2CaCu_2O_8$ compound. The results of our assignment are also similar to those obtained in [10, 11] and can be summarized as follows: peak *1* is attributed to the vibrations of bismuth atoms, peak *2* corresponds to the vibrations of strontium atoms, peaks *3* and *4* are assigned to the vibrations of copper atoms and cations in the calcium layer, peak *5* arises from the superposition of the vibrations of copper atoms and several vibrational modes of oxygen atoms (primarily, in the Bi_2O_2 layer), peaks *6* and *7* correspond to the vibrations of oxygen atoms in the SrO layer, and peak *8* is due to the vibrations of oxygen atoms in the CuO_2 layer. The alternative assignment of peaks *6*, *7*, and *8* to the vibrations of oxygen atoms in the SrO and CuO_2 layers seems improbable because of the strong covalent bonding of oxygen and copper in the CuO_2 layer. There are many works devoted to the investigation of the phonon spectrum of the Bi-2212 compound by Raman spectroscopy. According to these data, the peak at the maximum frequency, as a rule, is attributed to the vibrations of oxygen atoms in the SrO layer [16]. However, the model calculations performed by Shannon and Prewitt [17] demonstrated that the higher frequency peaks associated with the vibrations of oxygen atoms in the CuO_2 layer cannot be observed in Raman spectra (the A_{2u} and E_u vibration modes are active in the absorption or reflection spectra). Therefore, the vibrations at frequencies of 627 and 656 cm^{-1} (phonon energies of 75.2 and 78.7 meV, respectively) [16] most likely correspond to peaks *6* and *7* in our spectra. In this respect, comparison of peaks *6*, *7*, and *8* in the spectra $G(\varepsilon)$ of the solid solutions studied is of primary interest for the analysis of the influence of heterovalent substitution on the mobility of oxygen atoms in the structure of the Bi-2212 compound.

The crystal structure of the Bi-2212 compound (with equidistantly arranged crystal chemical layers and without regard for the incommensurate modulation in the Bi_2O_2 and SrO layers) and layers in which different processes proceed in the course of oxidation (see, for example, [3]) are schematically shown in Fig. 5. The oxygen nonstoichiometry is associated with the Bi_2O_2 crystal chemical layer. In the Bi-2212 structure, oxygen diffusion also occurs along the Bi_2O_2 layers. This process is due to the incommensurate modulation

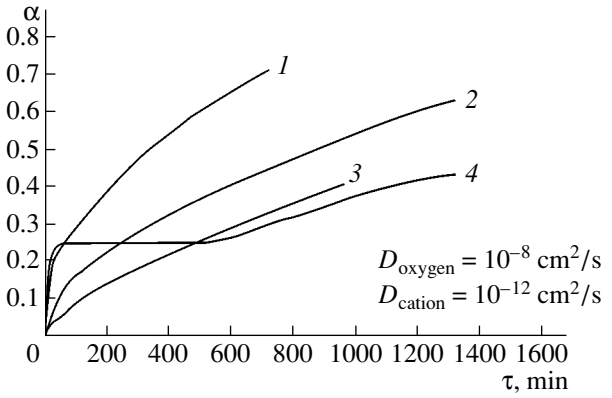

Fig. 4. Kinetic curves (in the coordinates of the degree of conversion with respect to complete oxidation of lead to Pb^{4+} versus time) for oxidation of $Pb_xBi_{2.1-x}Sr_2Ca_{1-y}Y_yCu_2O_z$ solid solutions at temperatures of (*1*, *2*) 700 and (*3*, *4*) 650°C: (*1*, *4*) $Pb_{0.6}Bi_{1.5}Sr_2CaCu_2O_z$ and (*2*, *3*) $Pb_{0.8}Bi_{1.3}Sr_2Ca_{0.8}Y_{0.2}Cu_2O_z$.

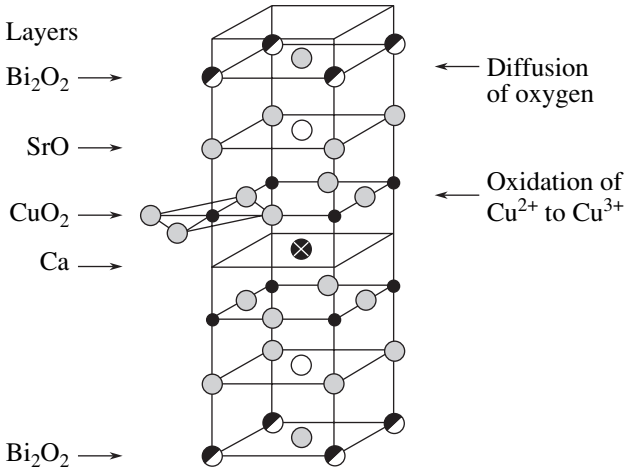

Fig. 5. Schematic drawing of the $Bi_2Sr_2CaCu_2O_8$ structure (one-half the unit cell in the tetragonal setting).

of atomic positions in the Bi_2O_2 layer, which, in turn, is responsible for the formation of additional sites occupied by oxygen atoms. Moreover, the Bi_2O_2 layer is characterized by the heterovalent substitution of lead for bismuth. As regards the substitution of yttrium for calcium, since the ionic radius of Y^{3+} (1.22 Å) is smaller than the ionic radius of Sr^{2+} (1.45 Å) at a coordination number of 9 (for cations in the SrO layer) [18], it can be expected that yttrium atoms will be located in the calcium crystal chemical layer. Furthermore, calcium, strontium, and yttrium cations can be redistributed over the Ca and SrO layers, as was observed for Bi-2212-based solid solutions containing Nd, La [1], or Pr [19]. In the lead-containing solid solutions based of

the Bi-2212 compound, the oxidation number can change for copper, lead, and bismuth. However, according to x-ray photoelectron spectroscopy, bismuth in these solid solutions has an oxidation number of 3+. In our opinion, it is highly improbable that bismuth can have an oxidation number of 5+, because ions containing a lone ($6s^2$) electron pair reside in a very specific coordination environment. It was shown earlier in [4, 5] that, upon the oxidation $Pb^{2+} \longrightarrow Pb^{4+}$, lead precipitates from the Bi-2212 matrix in the form of the second phase $(Pb,Bi)_3(Sr,Ca)_5CuO_z$ after preliminary separation of the solid solution. Therefore, it can be assumed that the change in the oxidation number of elements during the oxidation of the solid solution should occur primarily in the CuO_2 crystal chemical layer (since this layer exhibits metallic properties, we can say only on a change in the position of the Fermi level). The lower rate of oxygen diffusion in the $Bi_{1.3}Pb_{0.8}Sr_2Ca_{0.8}Y_{0.2}Cu_2O_{8+\delta}$ solid solution as compared to that in the $Bi_{1.5}Pb_{0.6}Sr_2CaCu_2O_{8+\delta}$ solid solution cannot be explained by the change in the cationic composition of the Bi_2O_2 crystal chemical layer of the Bi-2212 structure, because the replacement of the Bi^{3+} ion by the isoelectron ion Pb^{2+} with a smaller charge should lead to a decrease in the strength of bonds between the oxygen atoms and the cation environment. An enhancement of the oxygen bonding in the Bi_2O_2 layer could occur if a considerable part of the yttrium atoms were to be located in the SrO crystal chemical layer (with simultaneous redistribution of calcium and strontium atoms over positions in the crystal structure). However, this should be attended by an enhancement of the oxygen bonding in the SrO layer and, as a consequence, by a shift of peaks *6* and *7* in the spectrum $G(\varepsilon)$ toward the high-energy range, which is not observed in our case. Moreover, as was noted above, the presence of a large amount of yttrium in the SrO layer of the Bi-2212 structure seems to be unlikely due to the large difference in the ionic radii of strontium and yttrium.

In our opinion, the available experimental data are in better agreement with the mechanism of retardation of oxygen diffusion upon substitution of yttrium for calcium in the lead-containing Bi-2212 compound in the case when yttrium is located in the calcium layer of the Bi-2212 structure. It is evident that the positive electrostatic charge increases in the calcium layer. On the other hand, the oxidation of the Bi-2212-based solid solution leads to the $Cu^{2+} \longrightarrow Cu^{3+}$ transition in the CuO_2 layer. Although the net charge of this layer remains negative, the localization of holes on copper atoms (the formation of Cu^{3+} ions) turns out to be less favorable for the yttrium-substituted solid solution due to the electrostatic repulsion from the calcium layer. This circumstance can be responsible for the retardation of oxygen diffusion. Furthermore, when yttrium is located in the calcium layer of the Bi-2212 structure, the bonds between oxygen atoms in the CuO_2 layer and cations of the coordination environment become stronger, which leads to the experimentally observed shift of peak *8* in the spectrum $G(\varepsilon)$ toward the high-energy range.

4. CONCLUSIONS

Thus, it was demonstrated that the substitution of yttrium for calcium in lead-containing solid solutions based on the $Bi_2Sr_2CaCu_2O_8$ compound results in an appreciable retardation of oxygen diffusion. This considerably facilitates the nanostructured modification of the aforementioned solid solutions with the use of internal oxidation.

From analyzing the high-frequency portion of the vibrational spectrum (associated with the vibrations of oxygen atoms in the SrO and CuO_2 crystal chemical layers of the $Bi_2Sr_2CaCu_2O_8$ structure), it was concluded that the change in the electrostatic interaction of the Ca and CuO_2 layers is responsible for the retardation of oxygen diffusion.

ACKNOWLEDGMENTS

This work was supported by the Russian State Scientific and Technical program “Topical Directions in the Physics of Condensed Matter: Neutron Investigations of Condensed Matter” and the Russian Foundation for Basic Research (project no. 02-03-33270a).

REFERENCES

1. A. V. Knot’ko, A. V. Garshev, A. G. Veresov, *et al.*, Materialovedenie, No. 1, 42 (2000).
2. A. A. Fotiev, B. V. Slobodin, and V. A. Fotiev, *Chemistry and Technology of High-Temperature Superconductors* (Inst. Khim. Tverd. Tela Ural. Otd. Ross. Akad. Nauk, Yekaterinburg, 1994), p. 250.
3. P. Majewski, Adv. Mater. **6** (6), 460 (1994).
4. H.-L. Su, P. Majewski, and F. Aldinger, Physica C (Amsterdam) **249** (3–4), 241 (1995).
5. A. Veresov, M. Pulkin, A. Knotko, *et al.*, Mater. Res. Soc. Symp. Proc. **659**, II9.6.1 (2001).
6. A. Veresov, A. Knotko, M. Pulkin, *et al.*, in *Abstracts of the Conference on Solid State Chemistry* (Oslo, 2001), p. 108.
7. V. A. Parfenov, P. S. Klemyshev, I. G. Morozov, and A. F. Pavlov, in *Neutron Inelastic Scattering* (IAEA, Vienna, 1978), Vol. 1, p. 81.
8. V. F. Turchin, *Slow Neutrons* (Atomizdat, Moscow, 1963; Israel Program for Scientific Translations, Jerusalem, 1965).
9. A. V. Knot’ko, A. V. Garshev, V. I. Putlyaev, and S. I. Morozov, Fiz. Tverd. Tela (St. Petersburg) **42** (9), 1537 (2000) [Phys. Solid State **42**, 1579 (2000)].
10. A. V. Knot’ko, V. I. Putlyaev, and S. I. Morozov, Fiz. Tverd. Tela (St. Petersburg) **44** (7), 1174 (2002) [Phys. Solid State **44**, 1224 (2002)].
11. B. Renker, F. Gompf, D. Ewert, *et al.*, Z. Phys. B **77** (1), 65 (1989).

12. D. Shimada, N. Tsuda, U. Paltzer, and F. W. de Wette, Physica C (Amsterdam) **298** (3–4), 195 (1998).
13. P. P. Parshin, M. G. Zemlyanov, and A. V. Irodova, Fiz. Nizk. Temp. **22** (5), 564 (1996) [Low Temp. Phys. **22**, 435 (1996)].
14. P. P. Parshin, M. G. Zemlyanov, A. V. Irodova, *et al.*, Fiz. Tverd. Tela (St. Petersburg) **38** (6), 1665 (1996) [Phys. Solid State **38**, 919 (1996)].
15. M. Kakihana, M. Osada, M. Kall, *et al.*, Phys. Rev. B **53** (17), 11796 (1996).
16. *Physical Properties of High-Temperature Superconductors*, Ed. by D. M. Ginzberg (Mir, Moscow, 1990; World Sci., Singapore, 1992), p. 411.
17. R. D. Shannon and C. T. Prewitt, Acta Crystallogr. B **25** (5), 935 (1969).
18. A. V. Knot'ko, A. V. Garshev, and V. I. Putlyaev, in *Abstracts of the Conference on Inorganic Chemistry and Radiochemistry Dedicated to the 100th Anniversary of V.I. Spitsyn* (Moscow, 2002), p. 52.
19. C. Hinnen, C. Nguyen van Huong, and P. Marcus, J. Electron Spectrosc. Relat. Phenom. **73** (3), 293 (1995).

Translated by O. Borovik-Romanova

Physics of the Solid State, Vol. 46, No. 3, 2004, pp. 430–434. Translated from Fizika Tverdogo Tela, Vol. 46, No. 3, 2004, pp. 419–423.

METALS AND SUPERCONDUCTORS

Thermal Effects and Diamagnetic Response of a Current-Carrying YBCO Film

A. N. Artemov, Yu. V. Medvedev, A. I. Kosse, A. Yu. Prokhorov, V. A. Khokhlov, G. G. Levchenko, and V. F. Drobot'ko

Donetsk Physicotechnical Institute, National Academy of Sciences, ul. R. Luxemburg 72, Donetsk, 83114 Ukraine

Received August 26, 2003

Abstract—The temperature dependence of the dissipative part of the response to an ac magnetic field has been studied for an YBCO high-temperature superconductor film carrying a transport current. The response is found to exhibit a thermal hysteresis, whose magnitude depends on the transport current. The hysteresis is assigned to the current-carrying superconductor having two stable equilibrium states within a certain thermostat temperature interval. The existence of these states governed by specific features of the release and removal of heat.

1. INTRODUCTION

The response of a superconductor to a weak magnetic field is determined by the characteristics of the state in which the sample resides. The superconductor state depends, in turn, on a number of external parameters, such as the temperature, pressure, external magnetic field, and transport current. For instance, a current-carrying superconductor can be in a superconducting nondissipative, superconducting resistive, or normal uniform equilibrium state. The possible superconductor states and their stability can be studied theoretically in terms of simple phenomenological models describing the balance between the liberation and removal of heat in the superconductor–thermostat system [1, 2]. These models make it possible to formulate the main relations governing the onset of instabilities of the superconducting state in bulk [1–4], thin-film [5–8], composite [1, 2, 9, 10], and layered [11, 12] current-carrying superconductors.

The combined action of a transport current and an external ac magnetic field on a superconductor was studied in [13–22]. In particular, current damping in a superconducting coil placed in an ac magnetic field [13–15] and the response of a superconducting current-carrying plate to an ac magnetic field [16–22] directed parallel to the plate plane and perpendicular to the transport current were considered. The analysis of the experimental data obtained was based on the electrodynamics of superconductors in terms of Bean's model of the critical state [23], neglecting thermal processes in the system. This approach is valid provided the sample is in good thermal contact with the thermostat and resides in a nondissipative superconducting equilibrium state or is close to this state. In this case, the temperature of the sample differs very little from that of the thermostat; it is the latter temperature that is actually measured in an experiment.

We note in this connection that a gas at a low pressure (a few pascals) is usually employed as a thermostat in induction experiments, with the heat exchange with the sample being mediated by radiation. The rate of heat transport in this case is very low, so the temperature of a current-carrying sample may differ substantially from that of the thermostat. Furthermore, because of the low rate of heat exchange, thermal transient processes in the sample may be far from completion; this would exert an additional influence on the susceptibility.

We carried out an experiment in which the thermal processes in the sample–thermostat system cause a hysteresis in the temperature dependence of the response of a current-carrying superconductor to a weak external magnetic field. The observed phenomena can be easily explained by the fact that there is a region of bistability within which a current-carrying superconductor may reside in one of two stationary states with temperatures T_1 or T_2 ($T_1 < T_2$). We note in this connection that measurements of the temperature dependence of susceptibility may prove useful for studying the state diagram of superconducting films carrying a transport current.

2. EXPERIMENTAL SETUP AND RESULTS

In the experiment, we measured the response of a sample of the high-temperature YBCO superconductor to an external ac magnetic field. The sample was a 2000-Å-thick YBCO film 10×10 mm in area, grown by laser ablation on a Nd-doped $LaCaO_3$ substrate. The film was grown by A. Klimov at the Institute of Physics, PAS, Warsaw. Silver contacts 1 mm in width were deposited on opposite sides of the sample and had a total resistance of 0.7 Ω. The complex susceptibility $\chi_1 = \chi_1' + i\chi_1''$ was measured at the main frequency on a setup described in [22]. The sample pasted to a texto-

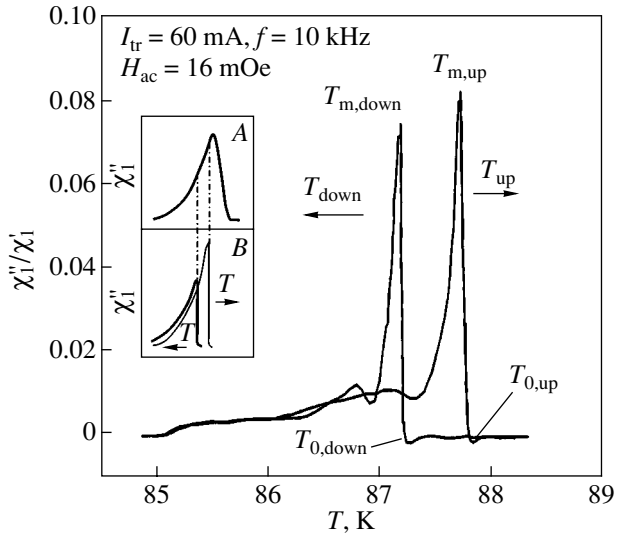

Fig. 1. Temperature dependences of the imaginary part of the susceptibility of an YBCO film carrying a transport current I_{tr} = 60 mA (normalized against χ_1') measured under increasing and decreasing thermostat temperature ($T_{m,up}$ and $T_{m,down}$, respectively). The inset shows a scheme illustrating the reason for the difference in the χ_1''/χ_1' amplitudes between the heating and cooling runs.

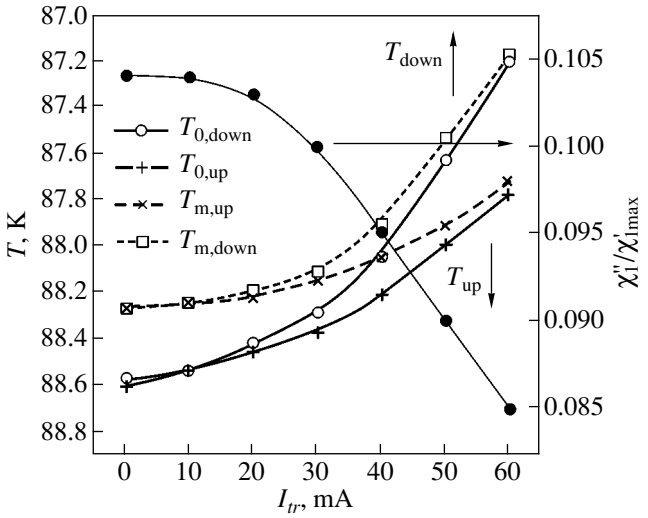

Fig. 2. Transport-current dependences of the temperatures at which the diamagnetic response appears for the cases of heating ($T_{0,up}$) and cooling ($T_{0,down}$), as well as of the temperatures of the maximum in χ_1'' ($T_{m,up}$, $T_{m,down}$) under the same conditions. Filled circles represent the dependence of the maximum of the reduced susceptibility χ_1''/χ_1' on I_{tr} obtained under sample heating.

lite insert was clamped to a flat receiving coil and placed in a tubular furnace. The receiver and the furnace were arranged in a vacuum chamber in which a base air pressure on the order of a few pascals was maintained. The temperature was measured with a thermocouple located in the immediate vicinity of the film. The rate of the variation in temperature during measurement of the signal was ≈0.3 K/min under both increasing and decreasing temperature. This rate was chosen so as to exclude temperature hysteresis at $I_{tr} = 0$. The measurements were performed at ac field amplitude H_{ac} = 16 and 200 mOe at a frequency f = 10 kHz.

Figure 1 displays the $\chi_1''(T)$ dependences obtained under increasing and decreasing thermostat temperature (T_{up} and T_{down}, respectively) with a transport current I = 60 mA and H_{ac} = 16 mOe. Figure 2 plots the temperatures $T_{0,up}$, $T_{0,down}$, $T_{m,up}$, and $T_{m,down}$ vs. transport current and the χ_1''/χ_1' amplitudes measured under increasing sample temperature (here, $T_{0,up}$ and $T_{0,down}$ are the temperatures of the appearance of a diamagnetic response under heating and cooling, respectively, and $T_{m,up}$ and $T_{m,down}$ are the temperatures of the maximum in the imaginary part of the susceptibility χ_1'' recorded under heating and cooling, respectively). The $\chi_1''(T)$ curves follow a pattern characteristic of such relations. They reveal a clearly pronounced maximum at a temperature T_m and low- and high-temperature tails. The maximum (which is usually assigned to the size effect) is reached as soon as the magnetic field penetration depth becomes equal to the characteristic dimension of the sample.

The most remarkable feature of these relations is the hysteresis observed when the direction of temperature variation is changed during the course of measurement (Figs. 1, 2). The magnitude of the hysteresis grows with increasing transport current, and the high-temperature slope of the $\chi_1''(T)$ plot becomes steeper than in the case of susceptibility measurements performed in the absence of a transport current in the sample. Furthermore, the increase in the transport current is accompanied by a displacement of the temperature T_0 (at which the diamagnetic response appears) toward low temperatures and by a decrease in the amplitude of the maximum of the quantity χ_1'' responsible for the hysteresis losses.

These features are intimately related to the processes of heat exchange between the sample and the thermostat. In the next section, we discuss the role played by these processes in the formation of the superconductor response to an external ac magnetic field.

3. HEAT TRANSPORT AND ITS EFFECT ON SUSCEPTIBILITY

If a superconductor is in the normal or superconducting resistive state, the transport current flowing through it generates heat. Therefore, the equilibrium temperature of a current-carrying superconductor differs from that of the thermostat.

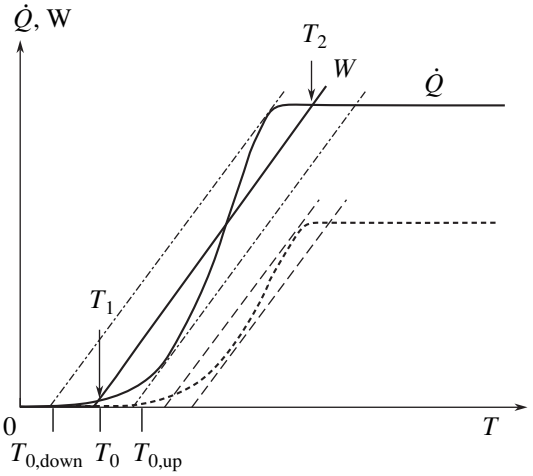

Fig. 3. Model temperature dependences of the heat release rate $\dot{Q}(T)$ and heat removal rate $W(T)$ in a layered current-carrying superconductor.

As already mentioned, the response of a superconductor to an external field depends on its state. Consider the equilibrium states in which a superconductor with current can reside and how the transition from one state to another takes place. The analysis will be performed in terms of the nonlinear heat generation model proposed in [11].

The equilibrium states of a current-carrying superconductor are determined by the balance between the rates of generation and removal of heat [1, 2]. In the case of interest to us here, a qualitative analysis of the states can be carried out using the one-dimensional thermal conductivity equation

$$D_s C_s \frac{\partial T}{\partial t} = D_s \frac{\partial}{\partial x} k_s \frac{\partial T}{\partial x} + d_f \dot{Q}(T) - W(T), \qquad (1)$$

where D_s is the substrate thickness; C_s and k_s are the heat capacity and thermal conductivity of the substrate material, respectively; d_f is the thickness of the superconducting film; $\dot{Q}(T)$ is the heat power generated by the transport current; and $W(T)$ is the rate of heat removal. We readily see that the equation has trivial stationary solutions of the kind $T = T_i$, where the temperature T_i is independent of the coordinate and satisfies the condition

$$d_f \dot{Q}(T_i) - W(T_i) = 0. \qquad (2)$$

Figure 3 gives a schematic representation of the temperature dependences of the rate of heat release $\dot{Q}(T)$ for various transport currents and of the rate of heat removal $W(T) = h(T - T_0)$ for various thermostat temperatures T_0. The effective heat transfer coefficient h depends on the actual mechanism of heat removal [11]. The solid lines plot the $\dot{Q}(T)$ function for a fixed value of the transport current I and the function $W(T)$ for a certain value of the thermostat temperature T_0.

The equilibrium states of the system are determined by condition (2) of the balance between the rates of generation and removal of heat. In the case illustrated in Fig. 3, there are three such states. Two of them, T_1 and T_2, are points of stable equilibrium, and the third state is unstable. Here, the low-temperature state can be either superconducting nondissipative or superconducting resistive and the high-temperature state can be either superconducting resistive or normal. For the sake of brevity, we refer to the low-temperature state as superconducting and to the high-temperature state as normal. The dash-dotted lines correspond to the rate of heat removal at the thermostat temperatures $T_{0,\mathrm{down}}$ and $T_{0,\mathrm{up}}$ bounding the region within which the two stable states can exist. Outside this region, a superconductor can reside either in the superconducting state alone (for $T_0 < T_{0,\mathrm{down}}$) or in the normal state alone (for $T_0 > T_{0,\mathrm{up}}$). The dashed lines in Fig. 3 plot the rate of heat generation and the region of bistability for a lower value of the transport current. It can be seen that, in this case, the interval of thermostat temperatures over which the system has two stable states becomes narrower and the temperatures themselves increase.

Let us follow the variation of the superconductor state as the thermostat temperature is lowered starting from a value of $T_0 > T_{0,\mathrm{up}}$. Here, there is only one normal equilibrium state of the superconductor. The heat release rate in this state is high, and, as a consequence, the temperature of the sample considerably exceeds that of the thermostat, $T_2 > T_0$. On the other hand, the dissipation of the ac magnetic field energy associated with the damping of induced normal currents is low, because the skin depth is far in excess of the sample size at the ac field frequency used in the experiment. This situation persists even in the bistability interval (because the normal state is separated from the superconducting state by a potential barrier), i.e., until the thermostat temperature reaches $T_{0,\mathrm{down}}$.

At the thermostat temperature $T_0 = T_{0,\mathrm{down}}$, the normal state is no longer stable. The system switches to the superconducting state with a temperature close to that of the thermostat, $T_1 \approx T_0$. In this state, the rate of heat generation associated with the flow of transport current is considerably lower than that in the normal state, whereas the dissipation of the external ac magnetic field energy is substantially larger than that in the normal state, because this energy dissipation is due to the pinning of the magnetic flux penetrating into the sample. Therefore, the response undergoes a jump at this point. As the temperature is lowered still further, the response behaves qualitatively in the same way as it does in a current-free sample.

As the thermostat temperature is increased from the level $T_0 < T_{0,\mathrm{down}}$, the sample remains in the supercon-

ducting state up to the temperature $T_0 = T_{0,up}$. At this temperature, the sample switches to the normal state.

Thus, due to the existence of the temperature interval ($T_{0,down}$, $T_{0,up}$) within which a superconductor has two stable states (Fig. 3), a temperature hysteresis occurs in the response to an ac external magnetic field (Fig. 1).

However, this factor does not fully explain the specific features of the temperature dependence of the susceptibility of a sample in our experiment. If the superconductor is in equilibrium at any temperature, the low-temperature tails ($T_0 < T_{0,down}$) in the $\chi_1''(T)$ dependence obtained under heating and cooling of the sample should coincide. As seen, however, from Fig. 1, these sections likewise undergo hysteresis. This feature in the response can be explained by assuming that a sample has no time to reach thermal equilibrium with the thermostat during the experiment.

The lack of equilibrium should be particularly revealing in the case when the thermostat temperature is decreased if the sample is originally in the normal state, because in this state the sample temperature T_2 is appreciably higher than that of the thermostat T_0 (Fig. 3). Therefore, when the normal state becomes no longer stable at the point $T_0 = T_{0,down}$, the sample temperature should change by a fairly large amount $\Delta T = T_2(T_{0,down}) - T_1(T_{0,down})$. Because the heat withdrawal rate in the experiment is not high, a fairly long time (on the scale of the duration of the experiment) is needed for the sample to cool down to the equilibrium state.

It is easy to estimate this time from the experimental data. For instance, for a current $I_{tr} = 60$ mA, as seen from Fig. 1, the curves begin to coincide approximately 1.5 K below the temperature $T_{0,down}$. Recalling that the rate of temperature variation in the experiment was about 0.3 K/min, this yields approximately 5 min for the relaxation time.

As seen from Fig. 1, the maximum in the dissipative part of the response χ_1'' measured under increasing temperature is larger than that obtained in the cooling run. This observation can be easily understood by looking at the inset to Fig. 1, where the $\chi_1''(T)$ dependence is plotted schematically for the hypothetical case of no instability occurring in the superconducting state of the current-carrying sample (inset *A* in Fig. 1). The inset also shows possible temperature dependences of the susceptibility of a current-carrying superconductor in an equilibrium state (for cases of both increasing and decreasing temperature) that take into account the thermal instabilities of the superconducting and normal states (inset *B* in Fig. 1). If the transport current is small enough, both temperatures at which the instabilities occur, $T_{0,down}$ and $T_{0,up}$, lie above the temperature T_m at which the dissipative part of the susceptibility reaches a maximum. In this case, the maximum lies at the point of an extremum and, therefore, does not depend on the direction of temperature variation. As the current increases, however, first the temperature $T_{0,down}$ and then $T_{0,up}$ become lower than T_m. Now, the maximum susceptibility is reached not at the extremum but rather at the boundary of the temperature interval over which the superconducting state is stable. This is what accounts for the difference in magnitude between the maxima of susceptibility observed for different directions of temperature variation.

This explanation applies, however, only to a superconductor in an equilibrium state. As already mentioned, in our experiment, the sample has no time to reach thermal equilibrium as the temperature is lowered after the switching to the superconducting state. As a result, the difference in magnitude between the susceptibility maxima in a real case is much less pronounced than that in insets *A* and *B* to Fig. 1.

Heat liberation in an YBCO film is determined not only by the state (normal or resistive) of the film but also by the heat release at the contacts. Heat release at the contacts does not change the above pattern radically. However, a break appears in the linear dependences of $T_{0,up}$ or $T_{0,down}$ on I_{tr}^2 (i.e., on the heat power generated in the film) at a certain value of current I_{tr}. We assign this break to the effect of heat release at the contacts. Such measurements make it possible to determine, for a given sample, the maximum transport current above which the heat release at contacts has to be taken into account in studying the electrophysical properties of HTSC samples.

4. CONCLUSIONS

The main result of this study is the observation of the effect of heat exchange between a superconductor carrying a transport current and a thermostat on the response of the superconductor to an ac magnetic field. The heat exchange gives rise to a temperature hysteresis in the susceptibility. The main cause of the hysteresis is that a superconductor carrying current has two stable states in a certain temperature interval. The existence of these two states is dictated by the character of heat generation associated with the transport current and by the rate of heat removal.

As seen from the results of the experiment (Fig. 2), an increase in the value of the current not only increases the hysteresis width $T_{0,up} - T_{0,down}$ but also reduces both these temperatures. In our opinion, this is evidence of the nonlinear character of the conductivity of the sample under study. This conclusion agrees qualitatively with the pattern in Fig. 3, which was drawn using the model of nonlinear heat generation in layered superconductors proposed in [11].

Another hysteresis mechanism is related to thermal transient processes. The corresponding contribution to the hysteresis becomes manifest in the low-temperature tails in the dissipative part of the response not being

coincident and can be eliminated by properly adjusting the rate of varying the thermostat temperature.

ACKNOWLEDGMENTS

This study was supported in part by the Ministry of Education and Science of Ukraine, project no. 2M.71-2000.

REFERENCES

1. R. G. Mints and A. L. Rakhmanov, *Instabilities in Superconductors* (Nauka, Moscow, 1989).
2. A. V. Gurevich, R. G. Mints, and A. L. Rakhmanov, *Physics of Composite Superconductors* (Nauka, Moscow, 1987).
3. I. L. Maksimov, Yu. N. Mastakov, and N. A. Taĭlanov, Fiz. Tverd. Tela (Leningrad) **28**, 2323 (1986) [Sov. Phys. Solid State **28**, 1300 (1986)].
4. N. A. Taĭlanov and U. G. Yakhshiev, Pis'ma Zh. Tekh. Fiz. **26**, 8 (2000) [Tech. Phys. Lett. **26**, 897 (2000)].
5. V. G. Volotskaya, I. M. Dmitrenko, L. E. Musienko, and A. G. Sivakov, Fiz. Nizk. Temp. **7**, 383 (1981) [Sov. J. Low Temp. Phys. **7**, 188 (1981)].
6. Yu. M. Ivanchenko, P. N. Mikheenko, and V. F. Khirnyĭ, Zh. Éksp. Teor. Fiz. **80**, 171 (1981) [Sov. Phys. JETP **53**, 86 (1981)].
7. Yu. M. Ivanchenko and P. N. Mikheenko, Zh. Éksp. Teor. Fiz. **83**, 684 (1982) [Sov. Phys. JETP **56**, 380 (1982)].
8. I. M. Dmitrenko, Fiz. Nizk. Temp. **22**, 849 (1996) [Low Temp. Phys. **22**, 645 (1996)].
9. V. V. Lysenko, Zh. Tekh. Fiz. **70**, 67 (2000) [Tech. Phys. **45**, 736 (2000)].
10. V. R. Romanovskiĭ, Pis'ma Zh. Tekh. Fiz. **23** (2), 14 (1997) [Tech. Phys. Lett. **23**, 94 (1997)].
11. A. N. Artemov and Yu. V. Medvedev, Fiz. Nizk. Temp. **28**, 349 (2002) [Low Temp. Phys. **28**, 242 (2002)].
12. I. L. Maksimov and D. Yu. Vodolazov, Pis'ma Zh. Tekh. Fiz. **24** (21), 1 (1998) [Tech. Phys. Lett. **24**, 829 (1998)].
13. V. V. Sychov, V. B. Zenkevich, V. V. Andrianov, and V. P. Baev, Pis'ma Zh. Éksp. Teor. Fiz. **9**, 53 (1969) [JETP Lett. **9**, 92 (1969)].
14. V. V. Andrianov, V. B. Zenkevich, V. V. Kurguzov, *et al.*, Zh. Éksp. Teor. Fiz. **58**, 1523 (1970) [Sov. Phys. JETP **31**, 826 (1970)].
15. T. Ogasawara, K. Yasukoshi, S. Nose, and H. Sekizawa, Cryogenics **16**, 33 (1976).
16. T. Ogasawara, Y. Takahashi, K. Kanbara, *et al.*, Cryogenics **19**, 736 (1979).
17. T. Matsushita, Cryogenics **30**, 324 (1990).
18. A. M. Grishin, V. M. Korenivski, K. V. Rao, and A. N. Ulyanov, IEEE Trans. Magn. **28**, 2220 (1992).
19. A. N. Ulyanov, V. N. Korenivskii, K. V. Rao, and A. M. Grishin, Appl. Supercond. **1**, 971 (1993).
20. A. M. Grishin, V. F. Drobot'ko, D. G. Emel'yanenkov, *et al.*, Sverkhprovodimost: Fiz., Khim., Tekh. **5**, 249 (1992).
21. A. N. Ul'yanov and A. M. Grishin, Fiz. Nizk. Temp. **20**, 416 (1994) [Low Temp. Phys. **20**, 329 (1994)].
22. A. M. Grishin, V. F. Drobot'ko, V. D. Stasovskiĭ, and V. A. Khokhlov, Zh. Tekh. Fiz. **63** (8), 190 (1993) [Tech. Phys. **38**, 730 (1993)].
23. C. P. Bean, Phys. Rev. Lett. **8**, 250 (1962).

Translated by G. Skrebtsov

Physics of the Solid State, Vol. 46, No. 3, 2004, pp. 435–441. Translated from Fizika Tverdogo Tela, Vol. 46, No. 3, 2004, pp. 424–429.

SEMICONDUCTORS AND DIELECTRICS

Optical Absorption of Hexagonal Boron Nitride Involving Nitrogen Vacancies and Their Complexes

S. N. Grinyaev, F. V. Konusov, V. V. Lopatin, and L. N. Shiyan

Research Institute of High-Voltage Equipment, Tomsk Polytechnical University, Tomsk, 634050 Russia

e-mail: Konusov@hvd.tpu.ru

Received May 5, 2003; in final form, July 17, 2003

Abstract—The pseudopotential and supercell methods are used to study the optical absorption of graphite-like hexagonal boron nitride involving deep levels of nitrogen vacancies and their clusters. The impurity-induced absorption is shown to be mainly related to electron transitions between the states that are antisymmetric with respect to the horizontal plane. Therefore, this absorption is highly anisotropic and is maximum for light waves polarized normally to the hexagonal axis. The optical absorption and photoconductivity spectra before and after neutron irradiation and thermal treatment are interpreted, and the activation energies for the thermoluminescence and conductivity of nitrogen-depleted boron nitride before and after fast-neutron irradiation and vacuum annealing are found. © *2004 MAIK "Nauka/Interperiodica".*

1. INTRODUCTION

Graphite-like hexagonal boron nitride *h*-BN produced through gas-phase deposition is a highly disperse polycrystalline material with a pronounced axial texture [1, 2]. Due to the small atomic numbers of its constituents and its high radiation resistance, high resistance to thermal shocks, high thermal diffusivity, and good insulating properties, *h*-BN is a unique material that can be applied in various fields. The operating abilities of boron nitride can be revealed when studying its damage and the changes in its optical properties upon radiation and thermal treatment [3–5]. The nature and structure of the energy states of radiation defects localized in the band gap are still poorly understood, and the mechanisms of the effect of defects on the properties of the material remain unclear.

Self-defects existing in BN ceramics prior to irradiation have high thermochemical stability and are predominantly localized at the boundaries between structural fragments [5]. The formation of thermally stable defects is mainly affected by impurity carbon atoms, which are introduced during the synthesis and thermochemical doping of the material [6, 7]. The optical absorption, luminescence, and photoelectric properties of *h*-BN are also strongly affected by nitrogen vacancies V_N and their complexes [6–9], which serve as activation, recombination, absorption, or photosensitivity centers [10]. Electronic transitions involving the levels of nitrogen divacancies and trivacancies manifest themselves in the stages of incomplete annealing of paramagnetic defect complexes in neutron-irradiated BN [11].

In this work, we use the method [10] of calculating the deep levels of point and cluster defects to determine the oscillator strengths for the most intense interband transitions involving nitrogen vacancies and to calculate the optical properties of *h*-BN in the region of impurity absorption. The calculation results are used to interpret the bands observed in the experimental absorption and photoconductivity spectra of pyrolytic *h*-BN.

2. CALCULATION PROCEDURE

The electronic states of an *h*-BN crystal with neutral unrelaxed nitrogen vacancies are calculated using the pseudopotential and supercell ($4 \times 4 \times 2$) methods; these methods were described in detail in [10]. The absorption coefficient $\alpha(E)$ of the defect crystal is determined by calculating the permittivity in the random-phase approximation [12]

$$\varepsilon(E + i\delta) = 1 + \frac{e^2\hbar^2}{\pi^2 m} \times \sum_{v,c} \int \frac{f_{cv}^{(\mathbf{e})}(\mathbf{k})\,d\mathbf{k}}{(E_{c\mathbf{k}} - E_{v\mathbf{k}})^2 - (E + i\delta)^2}, \quad (1)$$

$$f_{cv}^{(\mathbf{e})}(\mathbf{k}) = \frac{2|\mathbf{e} \cdot \mathbf{M}_{cv}(\mathbf{k})|^2}{m(E_{c\mathbf{k}} - E_{v\mathbf{k}})},$$

where $E_{n\mathbf{k}}$ are the electron energies of the defect crystal ($n = v$ and c are the indices of the filled and free states, respectively), $f_{cv}^{(\mathbf{e})}(\mathbf{k})$ are the oscillator strengths, $\mathbf{M}_{cv}(\mathbf{k})$ is the matrix element of the momentum operator, $\mathbf{e}$ is the polarization vector of an electromagnetic wave, and δ is the imaginary addition to the energy associated with the finite electronic-state lifetime. Inte-

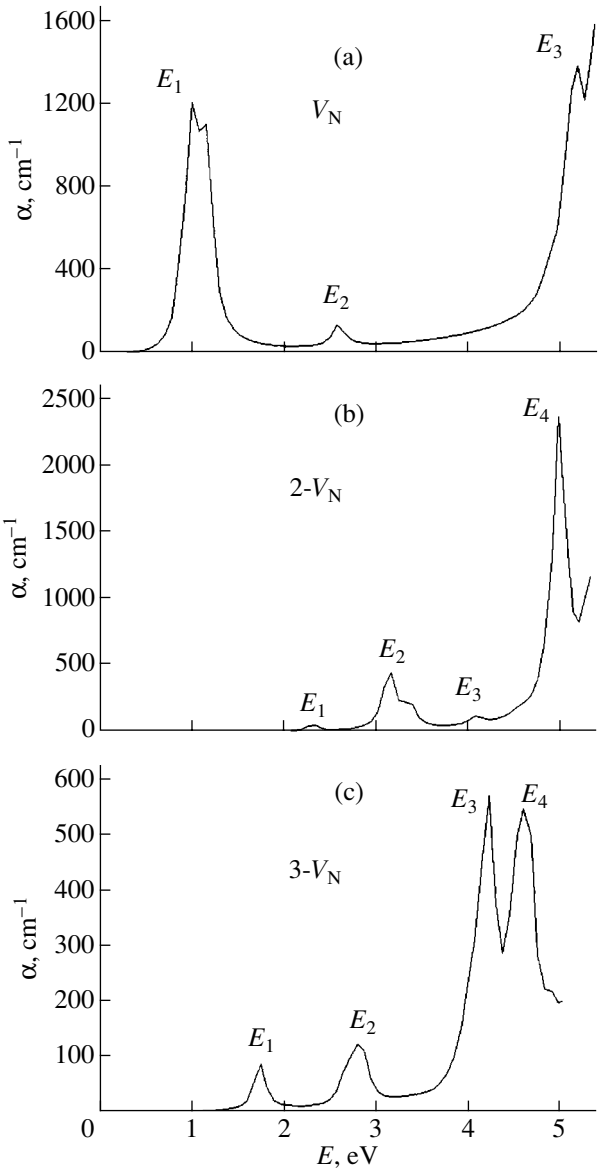

Fig. 1. Absorption coefficient of *h*-BN with (a) single nitrogen vacancies, (b) nitrogen divacancies, and (c) nitrogen trivacancies. The notation for the peaks corresponds to that in the table.

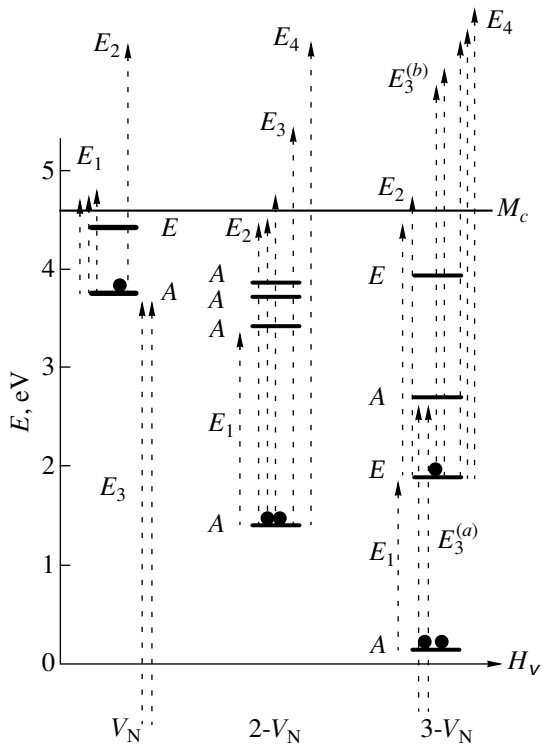

Fig. 2. Schematic diagram of the intense optical transitions involving the deep levels of nitrogen vacancies, divacancies, and trivacancies that cause absorption peaks of a defect crystal in the band-gap region.

gration over the Brillouin zone of the supercell is performed using a mesh of wave vectors **k** of the ideal crystal that are generated in the supercell method and are equivalent to the Γ point of the superlattice. When calculating the absorption coefficient, we took into account the degree of filling of deep levels and put the parameter δ equal to a characteristic value of 0.075 eV. Using linear interpolation in the defect concentration, the coefficient $\alpha(E)$ was calculated for the concentration $N_d = 10^{19}$ cm^{-3} typical of *h*-BN [10]. For complex defects, this value corresponds to the concentration of nitrogen divacancies and trivacancies.

3. OPTICAL ABSORPTION OF IMPERFECT *h*-BN WITH NITROGEN VACANCIES

The calculated absorption coefficients (averaged over the light-vector directions) of *h*-BN with single nitrogen vacancies and with nitrogen divacancies and trivacancies formed from the nearest neighbor defects in the hexagonal plane are shown in Fig. 1. The table gives the oscillator energy ε and the oscillator strength $f_{cv}^{(\mathbf{e})}(\mathbf{k})$ for the interband transitions associated with absorption peaks at photon energies lower than the band gap of the ideal crystal. The direct band gap in *h*-BN corresponds to the H_c–H_v transition with an energy of 5.27 eV, and the minimum indirect band gap corresponds to the M_c–H_v transition with an energy of 4.65 eV. The values of $f_{cv}^{(\mathbf{e})}(\mathbf{k})$ take into account the degeneracy and the degree of filling of the initial and final states, thus including the contribution from charge centers to the absorption. The table also gives the peak values α^{calc} of the absorption coefficient. Figure 2 presents a schematic diagram of the deep levels of nitrogen vacancies, their occupation with electrons, and the most probable optical transitions. Symbol *A* designates a singlet state, and symbol *E*, a doublet state. The nitrogen trivacancy-level occupation and the types of intense transitions are somewhat different from the data in [10], which are incorrect in certain cases.

Characteristics of transitions involving the deep levels of nitrogen vacancies, oscillator strengths, activation energies $\varepsilon_{l,\sigma}$, and the parameters of local absorption bands in pyrolytic *h*-BN before and after (*) neutron irradiation and annealing at (**) T_{ann} = 300–1500 and (***) 1500–2000 K

Defect type	Transition energy ε, eV	*f*	α^{calc}, cm^{-1}	ε_i, eV	α^{exp}, cm^{-1}	γ, eV	$N \times 10^{-19}$, cm^{-3}	ε_l, eV	ε_σ, eV
V_N	0.88 ($A \longrightarrow M_c$)	0.19						0.81	0.83
	0.99 ($A \longrightarrow L_c$)	0.47	1200(E_1)					0.93	0.91
	1.13 ($A \longrightarrow M_c$)	0.29						1.02**	1.12
	2.56 ($A \longrightarrow S_c$, Γ–K)	0.05	150(E_2)	2.52	50–220	0.40	0.2–1.3		
				2.50***	50–70***	0.25***	0.1–0.2		
	4.87 ($M_V \longrightarrow A$)	0.03	1400(E_3)	4.83	1400–1700	0.9	20–27		
	5.04 (L_v, $M_V \longrightarrow A$)	0.07							
2-V_N	2.30 ($A \longrightarrow A$)	0.04	60(E_1)	2.20	50	0.8	0.53		
				2.30**	800–1100**	0.7**	7–10		
	3.10 ($A \longrightarrow L_c$, M_c)	0.09			150	0.30	0.2		
				3.07					
	3.14 ($A \longrightarrow L_c$, M_c)	0.34	410(E_2)	3.13***	100–300***	0.25	0.1		
	3.35 ($A \longrightarrow L_c$, M_c)	0.14		3.33	250–400	0.27	0.3–0.5		
	4.07 ($A \longrightarrow R_c$, Σ_c)	0.06	120(E_3)						
	4.96 ($A \longrightarrow R_c$, Σ_c)	2.20	2400(E_4)	4.83	1400–1700	0.90	0.3–0.5		
				4.93***	1000–1500	0.75***	0.1–0.3		
3-V_N	1.73 ($A \longrightarrow E$)	0.12	90(E_1)	1.75	80	–	–		
				1.85*	1800*	0.5*	3–5		
				1.95***	20–25***	–	–		
				1.55***	30***	0.35	0.05		
	2.68 ($E \longrightarrow L_c$, M_c)	0.09	120(E_2)						
	2.83 ($E \longrightarrow L_c$, M_c)	0.11		2.85***	100–200***	0.30	0.1–0.2		
	3.98 ($E \longrightarrow \Sigma_c$, Γ_c, A_c)	0.10							
	4.13 (L_v, M_v, Γ–$K \longrightarrow A$)	0.09	570(E_3)						
	4.22 (L_v, M_v, $S_V \longrightarrow A$)	0.48							
	4.23 ($E \longrightarrow R_c$, Σ_c)	0.27							
	4.50 ($E \longrightarrow \Gamma_c$, R_c)	0.42							
	4.63 ($E \longrightarrow A_c$, Σ_c, R_c)	0.63	550(E_4)	4.65	1700	0.50	0.8		
	4.89 ($E \longrightarrow \Gamma_c$, A_c)	0.07		4.95	1300–1800	0.43	4–6		

In the absorption coefficient of *h*-BN with single vacancies (Fig. 1a), the first peak E_1 is related to transitions from the lower, half-filled deep level *A* (E = 3.75 eV) to the states originating mainly from the states of the third and fourth conduction bands of the ideal crystal at the *M* and *L* points. The wave functions of these states are antisymmetric with respect to the horizontal-plane reflection; therefore, according to the selection rules [13], this peak corresponds to absorption of electromagnetic waves polarized normally to the hexagonal axis. Similar strong absorption anisotropy was also observed near the fundamental absorption edge of ideal *h*-BN [14]. Comparison of the oscillator strengths indicates that the dominant contribution to the E_1 peak comes from the transition to the degenerate *L*-point state of the conduction band. Another, lower peak (E_2 = 2.56 eV) is caused by transitions to the states of two lower conduction bands at the *S* and Γ–*K* lines. The third peak (E_3) is located near the fundamental absorption edge and is related to transitions from the *L*- and *M*-point states of the upper valence band to the deep level *A*.

For *h*-BN with nitrogen divacancies and trivacancies, all specific features of $\alpha(E)$ also correspond to the absorption of light polarized normally to the hexagonal axis. In the case of nitrogen divacancies, the peaks of the absorption coefficient are caused by transitions from the lower completely filled level *A* (Fig. 1b). The relatively weak peak at E_1 = 2.29 eV corresponds to an intracenter transition to the second empty deep level *A*. The peak at E_2 = 3.1 eV is related to transitions to the *L*- and *M*-point states at the conduction band edge. Peaks E_3 and E_4 are mainly due to transitions to the levels originating from the states of two lower conduction bands at the *R* and Σ lines.

For nitrogen trivacancies, the peak of the absorption coefficient at E_1 = 1.73 eV is also related to the intracenter transition from the lower filled level to the second, partly filled deep level *E* (Fig. 1c). The second peak, at E_2 = 2.7 eV, is due to transitions to the *L*- and *M*-point states at the conduction band edge. The peak at E_3 = 4.2 eV is mainly caused by transitions from the two upper states of the valence band at the *L* and *M* points and from the states at the Γ–*K* and *S* lines to the third deep level *A*, as well as by transitions from the second deep level *E* to the Γ- and *A*-point states of the lowest conduction bands and to the states at the *R* and Σ lines. These partial contributions to the peak E_3 are denoted in Fig. 2 as $E_3^{(a)}$ and $E_3^{(b)}$, respectively.

The optical properties of real materials depend on the position of the Fermi level E_F. For *p*-type crystals, the ionization of the deep level *A* of a single vacancy should decrease its energy by ~0.1–0.2 eV, which results in the disappearance of peaks E_1 and E_2 and in a decrease in the energy of peak E_3 and a possible increase in its intensity. At $E_F < 2$ eV (with respect to the valence band top), the deep level *E* of a nitrogen trivacancy becomes vacant first. As a result, the related E_2 and E_4 peaks and the contribution $E_3^{(b)}$ to the third peak disappear, and the E_1 peak and the contribution $E_3^{(a)}$ undergo a red shift and are likely to increase; then, the deep nitrogen divacancy level *A* becomes ionized and the nitrogen divacancy ceases to be optically active in this energy range.

At $E_F > 2$ eV, a nitrogen trivacancy should acquire negatively charged states, with their levels being higher than those of a neutral trivacancy. This should manifest itself as blue shifts and a decrease in the intensity of the E_1 peak and in the contribution $E_3^{(a)}$ and as red shifts and an increase in the intensity of the E_2 and E_4 peaks and the contribution $E_3^{(b)}$. Moreover, the filling of the upper deep levels *A* and *E* of nitrogen trivacancies can induce additional specific features of the absorption coefficient.

At $E_F > 4$ eV in *n*-type crystals, the E_1 and E_2 peaks of a single vacancy will shift toward lower energies and have higher intensities. In such materials, because of the presence of charged centers formed by nitrogen divacancies and trivacancies, the optical absorption should differ significantly from that due to neutral defects.

4. COMPARISON WITH EXPERIMENTAL OPTICAL SPECTRA

The spectral dependence of the absorption coefficient $\alpha(h\nu)$ (Fig. 3) is calculated from the diffuse reflection spectra with allowance for the transmission spectra [15]. The concentration of centers *N* is calculated using Smakula's formula

$$N = 0.87 \times 10^{17} n f^{-1} \gamma\alpha/(n^2 + 2)^2, \qquad (2)$$

where *n* is the refractive index (n = 1.9–2.0 for $h\nu$ = 1.5–3.5 eV [16] and 2.0–2.3 for $h\nu$ = 3.6–5.3 eV [17]), *f* is the transition oscillator strength (see table), γ is the band half-width, and α is the absorption coefficient at the center of the band ε_i. The activation energies for thermoluminescence ε_l and conduction ε_σ levels are determined using thermal-activation spectroscopy in the fractional-annealing mode [18].

The similarity between the trap population distribution functions $n(\varepsilon_l)$ and $n(\varepsilon_\sigma)$, constructed using thermal-activation spectroscopy for BN with self-vacancies (ε_l = 0.81, 0.93, 1.08 eV and ε_σ = 0.83, 0.91, 1.12 eV) [18–20] and radiation-induced vacancies (ε_l = 0.96, 1.02, 1.10 eV and ε_σ = 0.88, 1.14 eV) [11, 21], and the calculated spectrum $\alpha^{calc}(E)$ (Fig. 1a) for single vacancies, as well as the correlation between the $\varepsilon_l(T)$, $n(\varepsilon_l)$ and $\varepsilon_\sigma(T)$, $n(\varepsilon_\sigma)$ dependences [18], suggests that the transition energies from the level *A* to the conduction

band (peak E_1 in Fig. 1a) are related to the activation energies for luminescence and conductivity σ. If we take into account the identified activation energies for thermoluminescence and conductivity σ ($\varepsilon_{\sigma, l} = 1.0$ eV, (V_N-3 B^{11}) center [9]) and assume that the thermal- and optical-ionization energies of electronic centers in *h*-BN differ by 0.1–0.2 eV [22], then these facts imply that the population depletion of the monoenergetic levels $\varepsilon_{l, \sigma}$ is caused by transitions to the conduction band (see table).

The transitions from A to S_c and Γ–K (peak E_2 in Fig. 1a) can form a band with $\varepsilon_i \cong 2.5$ eV (Fig. 3, curve *1*) having a Gaussian shape and parameters close to those calculated (see table). A band at 2.47 eV appears in the *n*-type photoconductivity spectra [21]. The identification proposed here is an alternative to the assumption that these bands are related to transitions between the levels of interstitial carbon atoms and the conduction band [18, 21]. The vacancy nature of these bands is attested to by the localization and narrowing of the 2.5-eV bands in the material containing radiation-induced vacancies. The narrowing of the bands caused by radiation-induced V_N vacancies (see table) and the localization of electrons participating in absorption [10, 21] can be explained by the location of radiation defects inside crystallites [2] as opposed to self-defects located near crystallite boundaries in the material. This conclusion is confirmed by the difference between the spatial distributions of paramagnetic vacancies in BN before [6, 7, 9, 20, 22, 23] and after neutron irradiation and thermal treatment [11, 24–26].

The $A \longrightarrow A$ transitions ($\varepsilon = 2.29$ eV) in a divacancy (Fig. 2) do not produce a band in the $\alpha^{exp}(h\nu)$ spectra because of a low intensity of the E_1 peak (Fig. 1b) and/or the presence of self-defect-induced bands at similar energies. Radiation divacancies manifest themselves clearly in the localization of the 2.30-eV band (T_{ann} = 900–1500 K) upon incomplete annealing of complex paramagnetic centers [11] (see table).

The intense band at 3.3–3.4 eV (Fig. 3, curve *1*) can be caused by transitions with the participation of the levels of impurity–vacancy complexes V_N-3 B^{11}–C [6, 7, 21, 23], which does not exclude the formation of this band and transitions from the divacancy level A to the conduction band edge (Fig. 1b, peak E_2). The resolution of the band into elementary Gaussian components allowed us to reveal an additional peak at 3.07 eV, which can be related to the $A \longrightarrow$ conduction band transitions ($\varepsilon = 3.10$ eV; Fig. 2 and table). The discrepancy between the values of α^{calc} and α^{exp} at $\varepsilon_i = 3.07$ and 3.33 eV and the scatter of the values of α^{exp} (see table) are caused by the effect of impurity–vacancy complexes producing bands at similar energies [21, 27].

A low intensity of the 3.13-eV band (which is localized after neutron irradiation followed by annealing at 2000 K) indicates suppression of the population of the divacancy levels when electrons are trapped by the deep

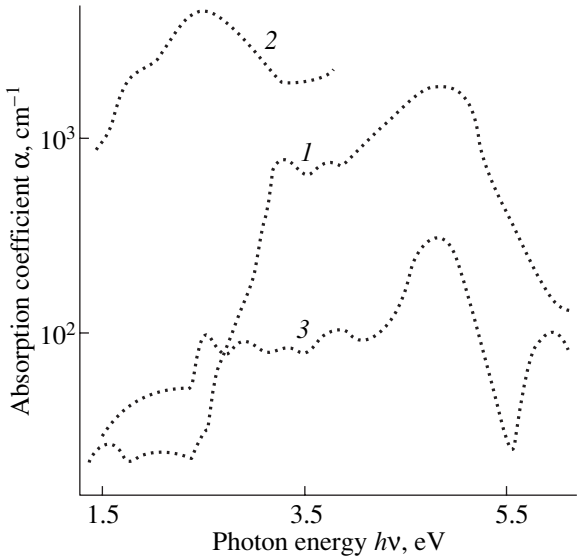

Fig. 3. Spectral dependences of the absorption coefficient of boron nitride at 300 K (*1*) before and (*2*) after fast-neutron irradiation ($\Phi = 9 \times 10^{15}$ cm^{-2}) and (*3*) after neutron irradiation ($\Phi = 2.5 \times 10^{18}$ cm^{-2}) followed by annealing at T_{ann} = 2000 K.

acceptor levels (E = 0.5–1.1 eV) of cation vacancy-based complexes [21]. The changes in the band structure and divacancy concentration (see table and Fig. 3, curves *1, 3*) suggest that radiation-induced 2-V_N vacancies (which are formed through combination of radiation V_N vacancies or dissociation of larger radiation defect complexes [11]) are distributed inside crystallites, in contrast to self-defects.

The fact that the E_3 peak, which is caused by transitions between the divacancy level A and the conduction band (with $\varepsilon = 4.07$ eV; see table), is not detected in the absorption spectra before and/or after radiation and thermal treatments (Fig. 3) is likely due to its relatively low intensity and overlapping with the trivacancy-induced E_3 peak (Figs. 1b, 1c).

A comparison of the parameters of the 4.8-eV band (Fig. 3, curve *1*) and the E_4 peak (Fig. 1b) caused by transitions from the divacancy level A (1.41 eV) to the upper-conduction band levels (Fig. 2) suggests that this band is related to 2-V_N vacancies (see table). The discrepancy between α^{calc} and α^{exp} is due to both the effect of trivacancies and the contribution from transitions involving the V_N levels [10] (see table). The effect of radiation-induced 2-V_N vacancies manifests itself in the shift of the band centers from 4.83 to 4.90–4.95 eV and in a decrease in γ and α (table, Fig. 3).

Electron transitions involving 3-V_N vacancies (Fig. 2) manifest themselves not only upon incomplete annealing of radiation defect complexes [10, 11, 21] but also in BN with a high concentration of self-defects ($N \geq 5 \times 10^{19}$ cm^{-3}). The $A \longrightarrow E$ transitions (ε =

1.73 eV; Fig. 1c) form the 1.55-eV (Fig. 3) and 1.75-eV (table) bands in the absorption spectra. The bands of neutron-induced optical absorption at 1.85 and 1.95 eV (Fig. 3) are likely due to transitions with $\varepsilon = 1.95$ eV from the *A* level (2.70 eV) to the conduction band [10].

A comparison of the E_2 peak parameters (Fig. 1c) with the values of α^{exp}, γ, and *N* for the 2.85-eV band (Fig. 3, curve *3*) suggests that the band is due to transitions with $\varepsilon = 2.68$ and 2.83 eV from the level *E* to the conduction band edge (Fig. 2), which does not exclude its alternative mechanism of formation through the $(\Gamma'_{5v}) \longrightarrow E$ transitions from the valence band [10]. This assumption is confirmed by the localization of the *n*-type photoconductivity excitation band at 2.8–3.0 eV [21, 27].

The E_3 peak, which is due to transitions from the valence band to the trivacancy level *A* and from the level *E* to the conduction band (Fig. 2), is not manifested in the absorption spectra due to the masking effect of the strong divacancy peak E_4 (table) and the peaks at 4.0–4.6 eV ($\alpha^{exp} = 1000$–1500 cm^{-1}), which are likely associated with defect clusters where carbon substitutes for anion vacancies [21]. The intensity of the bands at 4.1–4.3 eV, which appear in the carbon ion–irradiated material with *n*-type conductivity σ and photoconductivity ($\sigma \geq 10^{-9}$ S), is smaller than that in the *p*-type material ($\sigma = 10^{-12}$–10^{-14} S) by a factor of 1.3–2.0 [27]. An analysis of the optical and photoelectrical properties showed that the Fermi level is localized in the upper part of the band gap in the *n*-type material and in the lower part of the band gap in the *p*-type material. The similar behavior of the band at 4.1–4.25 eV [27] and the trivacancy peaks $E_3^{(a, b)}$ as a function of the Fermi level (see Section 3) suggests that the band at 4.1–4.25 eV [27] is induced by transitions involving the trivacancy deep levels (table).

The broad bands at 4.8 and 4.9–4.95 eV (Fig. 3, curves *1*, *3*), which appear before and after radiation–thermal treatment, respectively, result not only from transitions involving V_N and 2-V_N vacancies (table) but also from transitions with energies 4.50, 4.63, and 4.89 eV between the trivacancy level *E* and the conduction band (Fig. 1c, peak E_4; Fig. 2). Electron exchange between the levels of closely spaced divacancies and trivacancies causes band broadening, low resolution between their components, and variations in α^{exp} over wide limits (table), while the values of α^{calc} in peaks E_4 and E_2 (Fig. 1c) are close to the values of α^{exp} in the peaks at 4.8–4.95 and 2.85 eV (Fig. 3). According to the estimation performed in [15, 21], the Fermi level in nonirradiated *h*-BN is located at $\varepsilon = 2.2$–2.8 eV; therefore, the increase in the intensity of the 4.83-eV band (table) corresponds to the theoretical simulation of the behavior of the trivacancy peak E_4. Transitions that involve the trivacancy levels existing before irradiation ($\varepsilon = 4.63$, 4.89 eV) in BN with a defect concentration $N \geq 5 \times 10^{19}$ cm^{-3} manifest themselves in the localization of the 4.65- and 4.95-eV bands (table).

5. CONCLUSIONS

By comparing the calculated optical absorption spectrum (with allowance for the deep levels of nitrogen vacancies and their complexes) with the characteristics detected using thermal-activation and optical spectroscopy in pyrolytic *h*-BN before and after neutron irradiation and thermal treatment, we have revealed the nature of the strong absorption and photoconductivity bands and determined the contributions from vacancy clusters and carbon-containing defects to the absorption spectra. The best agreement between the experimental and calculated data was achieved for vacancies and their complexes in the irradiated material, because radiation defects are distributed within crystallites. In nonstoichiometric BN, nitrogen self-vacancy complexes specify optical properties, which is likely due to small dimensions of the crystallite and to the complex hierarchical structure of the material. The population of the levels of complexes based on anion self-vacancies is suppressed after neutron irradiation and thermal treatment, because these complexes are decomposed and cation vacancy-based complexes become important.

ACKNOWLEDGMENTS

This work was supported in part by the Ministry of Education of the Russian Federation, project no. T02-07.5-140.

REFERENCES

1. S. V. Ordin, B. N. Sharupin, and M. I. Fedorov, Fiz. Tekh. Poluprovodn. (St. Petersburg) **32** (9), 1033 (1998) [Semiconductors **32**, 924 (1998)].
2. V. V. Lopatin, Yu. F. Ivanov, and V. S. Dedkov, Nanostruct. Mater. **4** (6), 669 (1994).
3. O. I. Buzhinskij, I. V. Opimach, A. V. Kabyshev, *et al.*, J. Nucl. Mater. **173**, 179 (1990).
4. V. A. Stepanov and P. A. Stepanov, Opt. Spektrosk. **85** (6), 974 (1998) [Opt. Spectrosc. **85**, 893 (1998)].
5. O. A. Plaksin, V. A. Stepanov, P. A. Stepanov, *et al.*, J. Nucl. Mater. B **233–237**, 1355 (1996).
6. A. W. Moore and L. S. Singer, J. Phys. Chem. Solids **33**, 343 (1972).
7. V. A. Krasnoperov, N. V. Vekshina, M. B. Khusidman, and V. S. Neshpor, Zh. Prikl. Spektrosk. **11** (2), 299 (1969).
8. V. Ageev, S. Klimentov, M. Ugarov, *et al.*, Appl. Surf. Sci. **138–139**, 364 (1999).
9. A. Katzir, J. T. Suss, A. Zunger, and A. Halperin, Phys. Rev. B **11** (6), 2370 (1975).
10. S. N. Grinyaev, F. V. Konusov, and V. V. Lopatin, Fiz. Tverd. Tela (St. Petersburg) **44** (2), 275 (2002) [Phys. Solid State **44**, 286 (2002)].

11. A. V. Kabyshev, V. M. Kezkalo, V. V. Lopatin, *et al.*, Phys. Status Solidi A **126**, K19 (1991).
12. *Semiconductors and Semimetals*, Vol. 3: *Optical Properties of III–V Compounds*, Ed. by R. Willardson and A. Beer (Academic, New York, 1967; Mir, Moscow, 1970).
13. F. Bassani and G. Pastori Parravicini, *Electronic States and Optical Transitions in Solids* (Pergamon, New York, 1975; Nauka, Moscow, 1982).
14. Y.-N. Xu and W. Y. Ching, Phys. Rev. B **44** (15), 7787 (1991).
15. A. V. Kabyshev, F. V. Konusov, and V. V. Lopatin, Fiz. Tverd. Tela (St. Petersburg) **37** (7), 1981 (1995) [Phys. Solid State **37**, 1079 (1995)].
16. M. Schubert, B. Rheinlander, E. Franke, *et al.*, Appl. Phys. Lett. **70** (14), 1819 (1997).
17. O. Stenzel, J. Hahn, M. Roder, *et al.*, Phys. Status Solidi A **158**, 281 (1996).
18. V. V. Lopatin and F. V. Konusov, J. Phys. Chem. Solids **53** (6), 847 (1992).
19. V. A. Ryzhkov, A. V. Kabyshev, and V. V. Lopatin, Zh. Anal. Khim. **46** (6), 1181 (1991).
20. K. P. Arefiev, V. V. Lopatin, and Yu. P. Surov, Phys. Status Solidi A **98**, K27 (1986).
21. A. V. Kabyshev and F. V. Konusov, Poverkhnost, No. 5, 93 (2001).
22. M. B. Khusidman, Fiz. Tverd. Tela (Leningrad) **14** (11), 3287 (1972) [Sov. Phys. Solid State **14**, 2791 (1972)].
23. M. B. Khusidman, Radiokhimiya **16** (6), 916 (1974).
24. V. S. Neshpor, G. V. Samsonov, L. I. Fel'dgun, and M. B. Khusidman, Izv. Akad. Nauk SSSR, Neorg. Mater. **7** (1), 173 (1971).
25. M. B. Khusidman and B. N. Sharupin, Radiokhimiya **9** (2), 279 (1967).
26. V. B. Shipilo, A. E. Rud', A. G. Dutov, *et al.*, Izv. Akad. Nauk SSSR, Neorg. Mater. **27** (8), 1637 (1991).
27. A. V. Kabyshev and F. V. Konusov, Poverkhnost, No. 4, 109 (2003).

Translated by K. Shakhlevich

Physics of the Solid State, Vol. 46, No. 3, 2004, pp. 442–444. Translated from Fizika Tverdogo Tela, Vol. 46, No. 3, 2004, pp. 430–432.

SEMICONDUCTORS AND DIELECTRICS

Galvano-Dipolar Effect

A. I. Grachev

Ioffe Physicotechnical Institute, Russian Academy of Sciences, Politekhnicheskaya ul. 26, St. Petersburg, 194021 Russia

e-mail: grach.shuv@mail.ioffe.ru

Received July 11, 2003

Abstract—The phenomenology of the photogalvanic effect permits prediction of a number of physical phenomena, the most interesting of which is the galvano-dipolar effect. This effect consists in the appearance of an electric dipole moment in a sample through which an electric current is passed. A possible microscopic mechanism of this phenomenon, which can be realized in centrosymmetric media as well, is considered. © *2004 MAIK "Nauka/Interperiodica"*.

A recent communication published by the group led by J. Bednorz reported on the observation of an electric-current-stimulated reversible resistive transition in $SrTiO_3$: Cr crystals [1]. In a lecture read by Bednorz at the St. Petersburg meeting of Nobel Prize laureates *Science and Progress of Mankind* (St. Petersburg, June 16–21, 2003), new results of an investigation into this phenomenon were presented. In particular, it was reported that the resistive transition is accompanied by the appearance of birefringence in $SrTiO_3$ samples with cubic symmetry. The authors assign the appearance of a preferred direction to the sample acquiring volume polarization. However, neither the cause for the appearance of sample polarization nor the nature of the resistive transition itself has been given adequate theoretical explanation.

In the present communication, this experimental observation is treated as a possible manifestation of the physical effect (which, as far as we know, has never been discussed before) consisting in the appearance of (or change in) the polarization of a sample through which an electric current is passed. It is shown that one of possible mechanisms of this effect is the current-induced preferential orientation of dipole impurity centers (or complexes). We call this galvano-dipolar effect (GDE).

The conclusion that the GDE exists follows directly from the theoretical concepts developed earlier for describing the so-called photogalvanic effect (PGE) [2]. The PGE consists in the generation of a dc electric current J^{PG} in uniformly illuminated homogeneous noncentrosymmetric crystals and is described by a phenomenological expression [2],

$$\mathbf{J}_i^{PG} = \beta_{ijk}(E_jE_k^* + E_j^*E_k) + i\gamma_{il}[\mathbf{E}\mathbf{E}^*], \qquad (1)$$

where **E** is the electric field of the light wave. In Eq. (1), the first and second terms relate to the linear and circular photogalvanic effect, respectively, and tensors β_{ijk} and γ_{il} are similar in terms of their transformation properties to piezoelectric and gyration tensors.

The existence of circular PGE was predicted in [3, 4] before its first experimental observation [5]. In addition to the direct effect, i.e., the generation of a current under illumination, the reverse effect was also predicted, consisting in a variation in the optical activity of a gyrotropic crystal through which an electric current is passed [4]. This phenomenon is described by a third-rank tensor θ_{ijk} involved in the expression

$$\delta\varepsilon_{ik}^a = i\theta_{ijk}\mathbf{J}_k \qquad (2)$$

(where $\delta\varepsilon_{ik}^a$ is the variation in the antisymmetric component of the permittivity tensor and **J** is the electric current density) and was indeed found later to exist in tellurium crystals [6].

In contrast to the circular PGE, the experimental observation of various manifestations of the photocurrent in ferroelectric crystals (see the relevant references in [2]) that can be identified with the linear PGE prompted the development of the photogalvanic effect theory. Surprisingly, the practically a priori conclusion that a reverse effect with respect to the linear PGE must also exist has not been made until now. The analogy with the reverse circular PGE suggests that this effect should consist in a corresponding variation of the permittivity tensor of a sample through which an electric current is passed. In the optical range, this should give rise to the appearance of (or variation in) anisotropy in the refraction index, i.e., to induced birefringence (or linear dichroism):

$$\delta\varepsilon_{ik}^s = \nu_{ijk}\mathbf{J}_k, \qquad (3)$$

where $\delta\varepsilon_{ik}^s$ is the variation in the symmetric component of the permittivity tensor. The invariance of Eq. (3) under time inversion implies that the tensor ν_{ijk} should reverse sign, i.e., that this effect is due intrinsically to

dissipative processes. The symmetry of the tensor ν_{ijk} coincides, as that of the linear PGE, with the symmetry of the piezoelectric tensor.

Considered macroscopically, the physical reason for the induced birefringence could be the appearance of mechanical strains in a sample (the elastooptic effect) or of its electrical polarization (the electrooptic effect), both separately or both at the same time, which is determined by the actual experimental conditions (mechanically or electrically clamped samples). In the case of a mechanically free sample, the induced birefringence should be entirely assigned to the appearance of (or variation in) the current-induced sample polarization $\delta\mathbf{P}$:

$$\delta\mathbf{P}_i = \kappa_{ij}\mathbf{J}_j. \quad (4)$$

It is this phenomenon that we call the GDE. The components of tensor κ_{ij} reverse sign under the operation of time inversion (cf. the permittivity tensor), which implies there is a relation between the possible GDE mechanisms and dissipative processes. Tensor κ_{ij} has nonzero components in centrosymmetric crystals as well, although the effect described by Eq. (3) should be absent in these media. This apparent contradiction can be easily removed considering that nonzero components of tensor ν_{ijk} in centrosymmetric crystals appear only if the sample is polarized. Therefore, in a first approximation, we have $\nu_{ijk} \propto |\mathbf{P}| \propto |\mathbf{J}|$, so that Eq. (3) reduces eventually to

$$\delta\varepsilon^a_{ik} = \eta_{ijkl}\mathbf{P}_k\mathbf{P}_l, \quad (5)$$

where η_{ijkl} is a fourth-rank tensor, which can also exist in centrosymmetric crystals. Equation (5) reflects nothing other than the variation of the permittivity tensor in centrosymmetric crystals (for reverse PGE) as a result of the quadratic rather than linear electrooptical effect (or due to electrostriction).

Now, we consider one of the possible microscopic mechanisms of the GDE; his mechanism can also operate in centrosymmetric media, to which the above-mentioned $SrTiO_3$ crystal belongs. Let us consider a sample of a centrosymmetric crystal and assume it to have intrinsic or impurity centers (or complexes) possessing an electric dipole moment **d** (Fig. 1 schematically shows possible orientations of the centers in one of the crystallographic planes). Further, we conjecture that these centers are efficiently involved in radiative recombination of the majority carriers, say, electrons, and assume the magnitude of **d** in the ground (filled) state to be close to zero. The occurrence of a dipole moment on a depleted center gives rise to asymmetry in the electron capture by the center [2]; i.e., the probabilities of electrons with momenta **k** and –**k** being captured will be different. Under conditions of thermodynamic equilibrium, the macroscopic dipole moment of a sample $\langle\mathbf{d}\rangle$, which is the result of averaging the dipole moments of individual centers, should be zero. This is

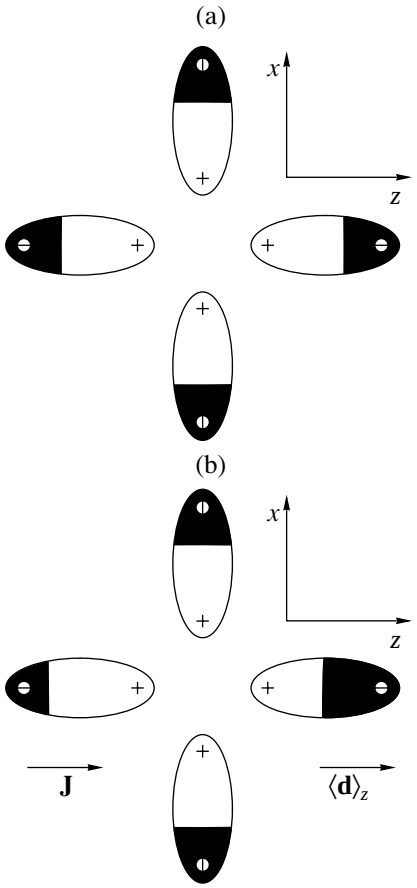

Fig. 1. Schematic distribution of the net dipole moment $\langle\mathbf{d}\rangle$ of centers (a) in the absence and (b) in the presence of an electric current flowing through the sample. The relative magnitude of the white and black areas of the ellipses reflects the extent of occupation of centers with a given dipole moment orientation.

realized, first, due to the centers being oriented isotropically, which means that the number of centers with oppositely directed momenta, for instance, along the *z* axis (Fig. 1a) are, on the average, equal. Second, because the momentum distribution function $\mathbf{f}_0(\mathbf{k})$ of electrons in the conduction band are symmetric, the occupations of oppositely oriented centers will be equal on average (i.e., within time intervals longer than the capture time).

After the electric current flowing, for instance, along the *z* axis (Fig. 1b) is switched on, the distribution function becomes asymmetric, $\mathbf{f}_0(\mathbf{k}_z) \neq \mathbf{f}_0(-\mathbf{k}_z)$; i.e., the average numbers of electrons with momenta $\mathbf{k}_z$ and $-\mathbf{k}_z$ will be different. In these asymmetric conditions, the electron capture will disrupt the balance in the filling of centers with $\mathbf{d} \parallel \mathbf{z}$ and $\mathbf{d} \parallel -\mathbf{z}$ (Fig. 1b) and an unbalanced dipole moment $\langle\mathbf{d}\rangle_z$ will appear along this axis; i.e., the sample will become polarized.

This model of the GDE permits a fairly simple description of the sample polarization kinetics after the electric current is turned on. To do this, we first write

the equation for the population balance of centers with dipole moment **d** ∥ **z** before the current is turned on:

$$dN_z^+(0)/dt = -N_z^+(0)[\gamma_1 n(\mathbf{k}_z) + \gamma_2 n(-\mathbf{k}_z)] + [N_z - N_z^+(0)]\tau_{ex}^{-1}, \quad (6)$$

where N_z is the total number of centers, N_z^+ is the number of unfilled centers, $n(\mathbf{k}_z)$ and $n(-\mathbf{k}_z)$ are the average numbers of electrons with the corresponding momentum directions, $\gamma_1 = v_{th}\sigma_1$, $\gamma_2 = v_{th}\sigma_2$, v_{th} is the electron thermal velocity, σ_1 and σ_2 are the capture cross sections of electrons with opposite momenta, and τ_{ex} is the characteristic time of thermal center excitation. In a steady state, the average center population is constant and, therefore, the right-hand part of Eq. (6) is zero; in addition, we have $n(\mathbf{k}_z) = n(-\mathbf{k}_z) = n_z$.

After the current is switched on, the last condition is no longer met and the corresponding nonequilibrium electron concentrations acquire the form $n^J(\mathbf{k}_z) = n(\mathbf{k}_z) + \delta n(\mathbf{k}_z)$ and $n^J(-\mathbf{k}_z) = n(-\mathbf{k}_z) - \delta n(-\mathbf{k}_z)$, where $\delta n(\mathbf{k}_z) = \delta n(-\mathbf{k}_z) = \delta n_z$. In view of expression (6) being equal to zero, the new balance equation can be cast in the form

$$d\delta N_z^+/dt = -N_z^+(0)\delta n_z(\gamma_1 - \gamma_2) - \delta N_z^+ n_z(\gamma_1 + \gamma_2) - \delta N_z^+\tau_{ex}^{-1}. \quad (7)$$

Here, we represented the varying center population in the form $N_z^+(\mathbf{J}, t) = N_z^+(0) + \delta N_z^+(t)$ and, in addition, dropped terms of higher order of smallness. Equation (7) describes the well-known exponential relaxation of the center population to a new level determined by the magnitude and sign of δN_z^+:

$$\delta N_z^+(t) = -N_z^+(0)\delta n_z(\gamma_1 - \gamma_2)\tau_{rel}(1 - \exp -t/\tau_{rel}). \quad (8)$$

Here, $\tau_{rel} = [n_z(\gamma_1 + \gamma_2) + \tau_{ex}^{-1}]^{-1} = [\tau_f^{-1} + \tau_{ex}^{-1}]^{-1}$ is the relaxation time determined by the relationship between the momentum-averaged rates of filling and depletion of a dipole center.

The expression for the population relaxation of centers with the oppositely directed dipole moment has a similar form (but opposite sign); hence, the polarization kinetics should also be the same. The stationary value of the dipole moment per unit volume of the sample, i.e., of its polarization $\mathbf{P}_z$, can be written as

$$\mathbf{P}_z = 2|\mathbf{d}|\delta n_z N_z^+(0)(\gamma_1 - \gamma_2)\tau_{rel}, \quad (9)$$

which, in turn, can be recast as

$$\mathbf{P}_z = \xi(r/v_{th})(N_z^+(0)/n_z)J_z, \quad (10)$$

where $\xi = 2(\gamma_1 - \gamma_2)/(\gamma_1 + \gamma_2)$ is the degree of capture asymmetry, r is the effective distance between unlike charges of the dipole center, and J_z is the current density. Equation (10) allows us to make an order-of-magnitude estimate of the GDE, more specifically, of the tensor κ_{ij}. We assume the presence of compensating levels in the material providing $N_z^+(0)/n_z \sim 10^3$ and put $\xi \sim 10^{-1}$, $r \sim 3 \times 10^{-8}$ cm, and $v_{th} \sim 3 \times 10^6$ cm s^{-1}. In this case, we obtain $\kappa \sim 10^{-12}$ s. For current pulses with densities ~10^5 A m^{-2}, this estimate gives the polarization $\mathbf{P} \sim 10^{-7}$ C m^{-2} (for comparison, the spontaneous polarization in ferroelectrics is of the order of 10^{-1} to 1 C m^{-2}) or an electric field in the crystal ~10^3 V m^{-1}. These values of the polarization and electric field give grounds to hope that this effect will eventually be experimentally observed by electrical or optical means.

ACKNOWLEDGMENTS

The author is indebted to E.L. Ivchenko for helpful discussions.

REFERENCES

1. Y. Watanabe, J. G. Bednorz, A. Bietsch, *et al.*, Appl. Phys. Lett. **78**, 3738 (2001).
2. V. I. Belinicher and B. I. Sturman, Usp. Fiz. Nauk **130**, 415 (1980) [Sov. Phys. Usp. **23**, 199 (1980)].
3. V. I. Belinicher, Fiz. Tverd. Tela (Leningrad) **20** (10), 2955 (1978) [Sov. Phys. Solid State **20**, 1706 (1978)].
4. E. L. Ivchenko and G. E. Pikus, Pis'ma Zh. Éksp. Teor. Fiz. **27**, 640 (1978) [JETP Lett. **27**, 604 (1978)].
5. V. M. Asnin, A. A. Bakun, A. M. Danishevskiĭ, *et al.*, Pis'ma Zh. Éksp. Teor. Fiz. **28**, 80 (1978) [JETP Lett. **28**, 74 (1978)].
6. L. E. Vorob'ev, E. L. Ivchenko, G. E. Pikus, *et al.*, Pis'ma Zh. Éksp. Teor. Fiz. **29**, 485 (1979) [JETP Lett. **29**, 441 (1979)].

Translated by G. Skrebtsov

Physics of the Solid State, Vol. 46, No. 3, 2004, pp. 445–452. Translated from Fizika Tverdogo Tela, Vol. 46, No. 3, 2004, pp. 433–440.

SEMICONDUCTORS AND DIELECTRICS

Electrical Instability of $LiCu_2O_2$ Crystals

A. A. Bush and K. E. Kamentsev

Moscow State Institute of Radio Engineering, Electronics, and Automation (Technical University), pr. Vernadskogo 78, Moscow, 119464 Russia

e-mail: abush@ranet.ru

Received July 25, 2003

Abstract—The temperature behavior of *I–U* curves and the field and temperature dependences of the electrical resistivity and dielectric permittivity of crystals of the $LiCu_2O_2$ phase have been studied. It was established that the crystals belong to *p*-type semiconductors and that their static resistivity in the range 80–260 K follows the Mott law $\rho = A\exp(T_0/T)^{1/4}$ describing variable-range hopping over localized states. At comparatively low electric fields, the crystals exhibit threshold switching and characteristic *S*-shaped *I–U* curves containing a region of negative differential resistivity. In the critical voltage region, jumps in the conductivity and dielectric permittivity are observed. Possible mechanisms of the disorder and electrical instability in these crystals are discussed.

1. INTRODUCTION

Crystals of the $LiCu_2O_2$ phase attract interest because of their crystallographic and chemical relation to the copper-containing HTSC phases and because of the manifestations of low-dimensional magnetism in them [1–7]. These crystals contain univalent (Cu^+) and divalent (Cu^{2+}) copper cations in equal proportion distributed over their structural positions in an ordered manner [1–3].

The $LiCu_2O_2$ crystal structure has rhombic symmetry (as determined from x-ray diffraction, space group *Pnma* with $a = 5.730(1)$, $b = 2.8606(4)$, $c = 12.417(2)$ Å; $z = 4$; density $\rho_x = 5.42$ g/cm^3) and actually represents an alternation of three layers along the *c* axis: (i) $-Cu^+(1)-$, (ii) $-O(1)Cu^{2+}(2)O(2)Li-$, and (iii) $-LiO(2)Cu^{2+}(2)O(1)-$ [2]. The Cu^+ cations combine with the two nearest oxygen atoms to form O^{2-}–Cu^+–O^{2-} dumbbells. The adjacent $-LiCu^{2+}O_2-$ $LiCu^{2+}O_2-$ layers form a network of CuO_5 and LiO_5 square pyramids sharing base edges [2]. An essential feature of the structure is the presence of Cu–O– chains in it oriented along the **b** axis and making up the so-called two-leg ladder systems.

The closeness of the *a*/*b* ratio to 2 accounts for the twinning of $LiCu_2O_2$ crystals [2], which entails the formation of domains of four different orientations rotated by 90° with respect to one another relative to their common **c** axis. X-ray structural studies of the phase performed in [2, 6] also revealed local strains in its crystal lattice and deviations from the *Pnma* symmetry, which were assigned either to the insertion of additional oxygen atoms into the lattice or to mutual substitutions of the Li and Cu2 atoms in the $-LiCuO_2-$ layers.

The specific features in the magnetic properties of the phase are determined primarily by the above-mentioned Cu–O ladders, in which the Cu^{2+} cations are interacting Heisenberg chains of $S = 1/2$ spins. The nearest neighbor Cu–O ladders are an appreciable distance apart and isolated from one another by Li^+ ions and nonmagnetic univalent Cu^+ copper layers. Therefore, in the case of ideal ladder structures, no long-range magnetic order should arise in them. To account for the long-range antiferromagnetic order observed in the phase below $T_N \approx 23$ K [5–7], it is assumed that there is a partial mixing of copper and lithium ions in the structure, which gives rise to the onset of exchange coupling between isolated ladder pairs via the copper ions incorporated in the lithium chains.

The $Li^+ \rightleftharpoons Cu^{2+}$ substitutions should obviously exert a noticeable influence not only on the magnetic properties of the phase but also on its electrical properties, because these substitutions are accompanied by the insertion of holes into the $-LiCuO_2-$ layers and a change of the band structure. We report here on a study of the electrophysical properties of the phase and of the effect of a dc electric field on its resistive and dielectric characteristics. By the time this study was completed, no information on similar investigations had appeared in the literature.

2. GROWTH OF THE CRYSTALS AND THEIR CHARACTERIZATION

Crystals of the $LiCu_2O_2$ phase were grown under slow cooling of the melt of a $20Li_2CO_3 \cdot 80CuO$ mixture in alundum crucibles in air. The melt was cooled from 1100 to 930°C at a rate of 5.0 K/h, after which the crucible with the crystallized melt was quenched down

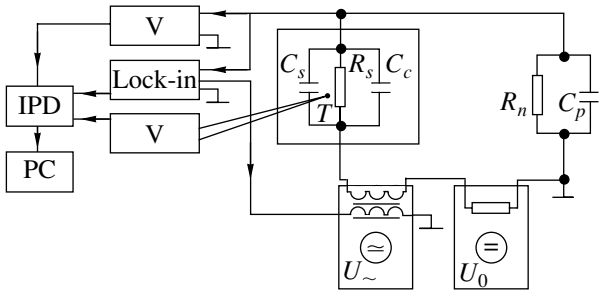

Fig. 1. Electrical circuit used to measure the electrical characteristics of the crystals: V is Shch-300 all-purpose digital voltmeter, Lock-in stands for phase-sensitive PAR-124a nanovoltmeter, $U_\sim$ is ac voltage source, U_0 is B-32 dc voltage source, IPD is physical instrumentation interface, PC is computer, T is thermocouple, R_s and C_s are equivalent resistance and capacitance of the sample, C_c is capacity of the measuring cell without sample (8.0 pF), R_n is load resistance (5.26 kΩ), and C_p is parasitic capacitances (wires, etc.).

to room temperature. The $LiCu_2O_2$ single crystals thus obtained were platelets measuring up to 6 × 10 × 10 mm. The crystals were black and perfectly cleavable along the (001) planes; these faces were the largest and exhibited a high luster. Weakly pronounced {210} growth forms are also observed; typical crystals are shaped as nearly rectangular parallelepipeds with {001} basal planes and {210} side faces. The crystal density, determined by dividing the mass of the parallelepiped by its volume, is 5.2 g/cm^3. X-ray powder diffractograms of the crystals can be indexed in terms of a rhombic unit cell with parameters a = 5.726(2), b = 2.858(1), and c = 12.410(2) Å, which is in agreement with the literature data [1, 2] on the crystal structure of $LiCu_2O_2$.

Thermogravimetric analysis (TGA) performed on a Q-1500D derivatograph showed the region of stable existence of the $LiCu_2O_2$ phase to lie at 890–1050°C; however, when quenched from 900–1050°C to room temperature, this phase does not break down and can persist for an indefinite time under normal conditions. It was established that the increase in sample mass observed under decomposition of the phase, $2LiCu_2O_2 + (1/2)O_2\downarrow \longrightarrow Li_2CuO_2 + 3CuO$, is 16% less than the calculated value. This discrepancy indicates that either inclusions of other phases exist in the crystals or the content of the Cu^+ cations in the phase under study is less than that determined by the stoichiometric formula $LiCu^+Cu^{2+}O_2$. Both microscopic and x-ray diffraction studies suggest the presence of inclusions of other phases (primarily of Li_2CuO_2 and $LiCu_3O_3$) in the crystals, but their total content did not exceed 5%, which makes questionable the explanation that the decrease in mass growth under phase decomposition is due to impurity phases.

Based on data on the ionic radii of lithium and copper [8], as well as on their characteristic coordination in the crystal lattice, the observed deficiency of the Cu^+ cations can be assigned to part of the copper cations in the Cu1 position being in the Cu^{2+} state. Substitution of Li^+ cations for Cu^+ seems very unlikely because of the dumbbell-shaped coordination, which is not characteristic of Li^+. The possibility of substitution of part of the lithium atoms by copper was pointed out earlier in [4, 6] based on x-ray diffraction and magnetic studies. Note also that a partial substitution of Cu^{2+} by Li^+ cations in their positions was established earlier to occur in the phases $LiCu_3O_3 = (Li^+_{0.8}Cu^{2+}_{1.2})Cu^+(Cu^{2+}_{0.8}Li^+_{0.2})O_3$ [1] and $(La,Sr)_2(Cu,Li)O_y$ [9–11]. The enhanced content of the Cu_{Li} and Li_{Cu} antisite defects originates apparently from the quenching of the crystals under preparation from ~900°C to room temperature; the quenching is performed because the phase breaks down when cooled slowly.

From the above discussion, it follows that the refined structural chemical formula of the phase can be written as $(Li^+_{1-u}Cu^{2+}_u)(Cu^+_{1-v}Cu^{2+}_v)(Cu^{2+}_{1-t}Li^+_t)O_{2+\delta}$. The charge neutrality conditions for the crystal define the parameter $\delta = (u + v - t)/2$. The available data are insufficient for an independent evaluation of the parameters u, v, and t characterizing the structure of the phase; these parameters require further refinement.

Measurements of the differential thermopower of $LiCu_2O_2$ crystals showed them to be p-type. Their Seebeck coefficient is positive in the range 130–300 K, and its magnitude grows smoothly with temperature from +0.15 mV/K at 130 K to +0.42 mV/K at 300 K. Therefore, the acceptor substitutions ($Li^+ \longrightarrow Cu^{2+}$, $Cu^+ \longrightarrow Cu^{2+}$) in the phase dominate over the donor substitutions ($Cu^{2+} \longrightarrow Li^+$). Taking into account the measured crystal density, the probable overall phase composition can be written as $Li_{1.15}Cu_{1.85}O_{2+\delta}$.

The variation of crystal mass in the region of the $LiCu_2O_2$ phase stability (890–1050°C) did not exceed ±1 mg. Whence it follows that the possible temperature-induced variations $\Delta\delta$ of the oxygen index in $LiCu_2O_{2+\delta}$ are not in excess of 0.01. Thus, noticeable variations in the oxygen content with temperature, similar to those observed in the HTSC phase $YBa_2Cu_3O_{7-\delta}$ [12], are not observed in the phase under study.

3. ELECTROPHYSICAL STUDIES

3.1. Experimental

The electrical circuit used in measurements of the electrophysical properties contained series-connected sources of dc voltage U_0 and ac voltage $U_\sim$, a load resistance R_n (5.26 kΩ), and the sample under study (Fig. 1). The voltage U_0 was switched over a discrete set of levels ($0 < U_0 < 250$ V), with the ac voltage frequency and

amplitude kept fixed (1.74 kHz, $U_{\sim}$ = 100 mV). The dc voltage across the load resistance and the ac polarization current I_p (phase-shifted by 90°) were measured simultaneously with a Shch-300 digital voltmeter and a PAR-2101 phase-sensitive nanovoltmeter, respectively. The data thus obtained were used to calculate the dc electrical resistivity ρ_{dc} and the dielectric permittivity ε of the samples at various temperatures and bias voltages. Measurements of the ac resistivity $\rho(T, \omega)$ were carried out with a P5083 ac bridge in the range 0.1–100 kHz. The *I–U* curves were measured in the dc mode at 50–300 K.

The temperature dependences of the electrophysical properties in the range 10–300 K were studied in a helium-flow Dewar flask equipped with a cryostat insert, in which the sample was clamped to the cold finger; the temperature was measured with an Au–Au + Fe thermocouple.

The measurements were carried out on a $LiCu_2O_2$ single crystal 4.0 × 2.0 × 1.8 mm in size, with its side surfaces, 4.0 × 2.0 mm and 4.0 × 1.8 mm, coinciding with the (001) and (220) crystallographic planes, respectively; the *c* axis was aligned with the 1.8-mm-long edge. The measuring field was applied along the **c** axis or perpendicular to the (220) plane (and, hence, to the **c** axis). To obtain low-Ohmic electric contacts with the sample, electrodes were deposited on the basal planes of the plate either by rubbing an In–Ga eutectic in or by silver paste firing. The results obtained with the use of these electrodes differed little from one another. It was also established that the results of the resistivity measurements performed using the two- and four-probe techniques practically coincided. Whence it follows that the electrode contact resistance was substantially smaller than the volume resistance of the crystals.

3.2. Temperature Dependences of the Electrical Resistivity

The dc electrical resistivities of the samples measured using the two- or four-probe techniques at room temperature for bias fields not exceeding a few V/cm were found to be approximately 1000 and 100 Ω cm along the **c** axis ($\rho_{\|c}$) and in the plane normal to it ($\rho_{\perp c}$), respectively (Figs. 2, 3). As the temperature was lowered, ρ was observed to grow exponentially, which shows $LiCu_2O_2$ to behave as a semiconducting crystal. The values of $\rho_{\|c}$ at 100 K reached as high as 10^7 and increased sharply to 10^{12} Ω cm near 20 K. The layered character of the $LiCu_2O_2$ crystal structure becomes reflected in the anisotropic conductivity; indeed, the conductivity measured perpendicular to the layers (along the **c** axis) is lower by one to two orders of magnitude than that in the plane parallel to the layers (Fig. 3).

Figure 2 plots the temperature dependences of the dc and ac electrical resistivities of the crystal measured along the **c** axis in the $\log\rho - 1/T$ coordinates most appropriate for semiconductors. The slope of the $d(\log\rho)/d(1/T)$ curve decreases with decreasing tem-

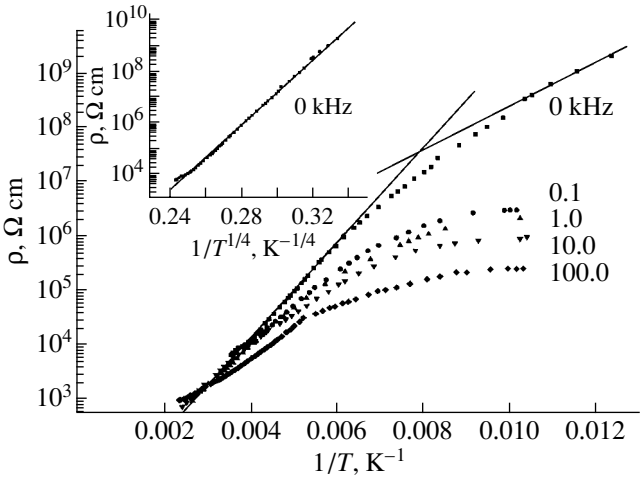

Fig. 2. Temperature dependences of the electrical resistivity ρ of $LiCu_2O_2$ crystals measured along the **c** axis in dc and ac regimes at frequencies of 0.1, 1.0, 10.0, and 100.0 kHz and plotted in logρ vs. $1/T$ coordinates (inset shows the temperature dependence of the resistivity plotted in the Mott coordinates logρ vs. $1/T^{1/4}$).

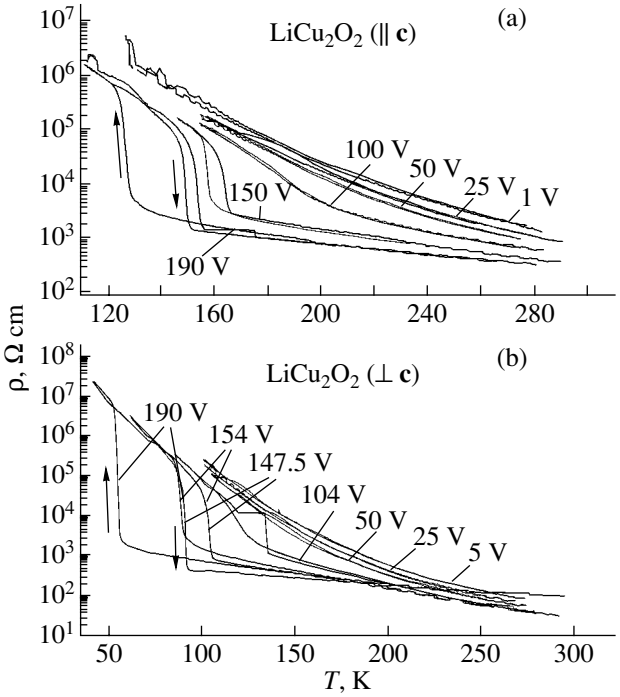

Fig. 3. Temperature dependences of the electrical resistivity ρ_{dc} of $LiCu_2O_2$ crystals measured (a) along and (b) perpendicular to their **c** axis in the dc regime under various bias voltages *U* (specified on the curves).

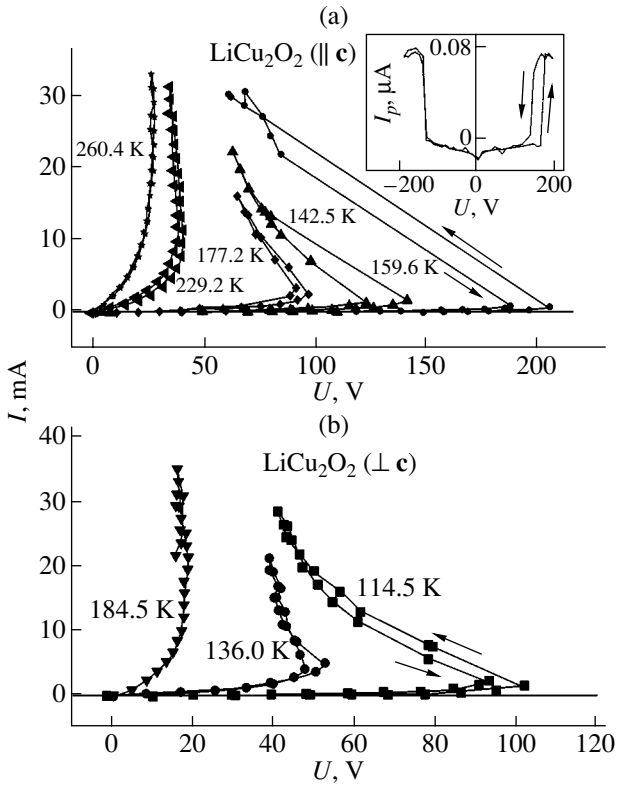

Fig. 4. *I–U* curves measured (a) along and (b) perpendicular to the **c** axis of $LiCu_2O_2$ crystals (the numerals near the curves specify the crystal substrate temperature at which the measurements were performed). The inset presents the dependence of the polarization current on bias voltage applied along the **c** axis at 144 K.

perature, which indicates a gradual decrease in the differential activation energy for charge transport from a value of 0.17 eV in the temperature region 180–290 K to 0.08 eV in the range 80–100 K (for dc resistivity). Increasing the measuring field frequency to 100 kHz brings about a noticeable decrease in resistivity in the range 80–250 K. Below 80 K, the measurements meet with difficulties because of the very strong growth of ρ.

The gradual change in the slope of the ρ(*T*) curve plotted in the $\log\rho - 1/T$ coordinates, as well as the pronounced dependence of the conductivity on measuring field frequency in the low-frequency range, is a characteristic feature of hopping conduction over localized electronic states; this type of conduction is observed in many complex oxides of transition metals, including copper [9, 13–23]. The hopping-conduction model [13] predicts noticeable deviations from linearity of the resistivity in the $\log(\rho_{dc}) - 1/T$ coordinates at temperatures below $T_x \approx \Theta_D/2$, where Θ_D is the Debye temperature, which is 400 K for $LiCu_2O_2$ [7]. This model assumes charge transport above the Debye temperature to occur through thermal carrier activation in multiphonon inelastic collisions. In the low-temperature domain ($T < \Theta_D/2$), the variable-range hopping mechanism (the Mott model) dominates and gives rise to a temperature dependence of the type $\rho = A\exp\{(T_0/T)^{1/(1+d)}\}$, where $d = 3$ for three-dimensional and $d = 2$ for two-dimensional systems.

As seen from Fig. 1, the experimental points in the temperature dependence of the electrical resistivity of $LiCu_2O_2$ plotted in the Mott coordinates $\log\rho_{dc}$ vs. $(1/T)^{1/(1+d)}$ in the range 80–260 K for $d = 3$ fall, within experimental accuracy, on a straight line with slope $T_0^{1/4} = (4.6 \times 10^8\ \mathrm{K})^{1/4}$.

Hopping-conduction models consider the ac conductivity to be a temperature- and frequency-dependent quantity with a power-law dependence on frequency, $\sigma_{ac}(T, \omega) = \sigma(T, \omega) - \sigma_{dc}(T) = A(T)\omega^s$ [13, 16]. The frequency dependences of the conductivity σ_{ac} of $LiCu_2O_2$ crystals measured along the **c** axis in the range 100–167 K and plotted in the $\log\sigma_{ac}$ vs. $\log f$ coordinates are smooth curves with the slope growing with increasing frequency, which corresponds to an increase in *s* with frequency. Estimation of the exponent *s* from these curves at 100 K yields $s \sim 0.2$ in the range 0.1–1.0 kHz and $s \sim 0.6$ in the region 10.0–100.0 kHz. The frequency dependence becomes progressively weaker as the temperature is increased to above 260 K; this feature can be accounted for by the growth of the number of carriers in the band with increasing temperature, with the result that the band conduction (which is frequency-independent in the low-frequency range) becomes dominant.

3.3. I–U Curves

The *I–U* curves were measured in both forward (with increasing dc voltage) and reverse (with decreasing voltage) runs, with a field applied along and perpendicular to the **c** axis, at fixed temperatures in the range 50–300 K (Fig. 4). The *I–U* curves were measured in parallel with the field dependences of the polarization current $I_p(U)$ flowing through the crystal. These characteristics are found to be essentially nonlinear.

As the temperature is lowered, the Ohmic part of the *I–U* characteristic shifts toward lower currents and higher voltages. When the so-called critical voltage U_c is reached (at which the tangent to the *I–U* curve is parallel to the current axis), the curves with saturation become *S*-shaped, exhibiting a negative differential resistivity (NDR). Application of a voltage above U_c gives rise to a sudden increase in the current and a sudden decrease in the voltage along the load curve [$I = (U_0 - U)/R_n$]. Immediately after the jump, the sample overheats sharply by 1.5–2.0 K (because of the liberation of Joule heat) and cools in the reverse transition. By measuring the sample overheating due to the released Joule heat with a differential thermocouple in the course of the *I–U* studies, it was shown that the

increase in the sample temperature with respect to the substrate did not exceed 3 K throughout the fields and temperatures covered here.

S-shaped characteristics are reversible, but the critical voltage measured in the reverse run directly after the forward course is slightly smaller than that observed in the forward run ($U_{c2} < U_{c1}$). It was found that the *I–U* curves obtained in repeated measurements without warming of the crystal do not exhibit a field hysteresis, irrespective of the direction of the electric field applied. After the crystal has been warmed and subsequently cooled, the first measurement again exhibits a hysteresis. If we disregard the field hysteresis in the first measurement, the *I–U* curve is symmetric relative to the polarity of the applied dc voltage at a fixed temperature. The field hysteresis of the polarization current $I_p(U)$ reveals similar features (Fig. 4).

The critical electric field $E_c = U_c/d$ (V/cm) measured with the field applied along the **c** axis obeys an empirical relation $\log(E_c)_{\parallel c} = A - BT$, where $A = 3.97$ and $B = 6.96E - 3$. As seen from Fig. 4, the field $(E_c)_{\parallel c}$ applied along the **c** axis is about fivefold higher than the field $(E_c)_{\perp c}$ applied in the direction perpendicular to the **c** axis at the same temperature.

As the bias voltage is increased, the polarization current increases abruptly near the field E_c, and if the bias field is then reduced, the polarization current decreases reversibly to the original level. The polarization current vs. dc bias field curves (Fig. 4) resemble the ferroelectric hysteresis curve relating the polarization to the applied voltage, provided one takes the total dc voltage at the source for the bias.

3.4. Effect of Electric Field on the Electrical Resistivity

An increase in the dc bias brings about a rise in the conductivity of $LiCu_2O_2$ crystals (Fig. 3). Starting with the voltage $U \approx 50$ V, breaks appear in the $\rho_{\perp c}(T)$ curves. As the voltage is increased further, the breaks transform into abrupt drops in resistance; the temperature at which a jump occurs decreases, and the relative magnitude of a drop becomes as large as $R_{max}/R_{min} \sim 10^4$ (at 200 V and $T \sim 80$ K). As the field decreases, the crystal recovers its original high-Ohmic state. After warming, the jumps in resistance take place at higher temperatures than under cooling. This temperature hysteresis increases with bias and becomes larger than 30 K at $U =$ 190 V (Fig. 3).

The above general features are more pronounced for measurements of resistivity in the direction perpendicular to the **c** axis. In this direction, the jumps in resistivity occur at lower temperatures (Fig. 3b). There is an interesting trend that all curves measured at various bias voltages below the temperatures at which the anomalous jumps occur converge to the resistivity curve obtained at low voltages. The electric-field-induced breaks and jumps in the $\rho(T)$ dependences should apparently be assigned to a manifestation of the *S*-shaped *I–U* curves of these crystals.

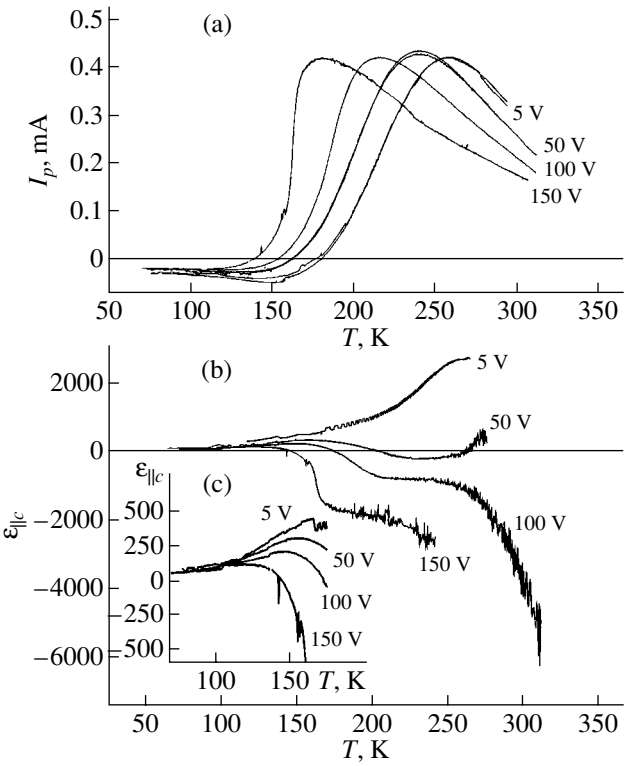

Fig. 5. Temperature dependences of (a) polarization current $I_p(T)$ for various bias voltages (specified at the curves) and (b, c) permittivity $\varepsilon_{\parallel c}(T)$ derived from the $I_p(T)$ relations; the measurements were performed along the **c** axis of $LiCu_2O_2$ crystals at a frequency of 1.74 kHz.

3.5. Effect of Electric Field on the Permittivity

The temperature dependence of permittivity $\varepsilon(T)$ of the crystal for various bias voltages (Fig. 5) was calculated from the temperature dependence of the polarization current $I_p(T)$. The analytical expressions for ε that are based on calculations performed for the electric circuit shown in Fig. 1 were checked and calibrated in a model experiment with $BaTiO_3$ crystals.

Positive values of the polarization current relate to the case where the capacitive resistance of the sample is shorted by its Ohmic resistance; the sample resistance becomes equal to the load resistance of 5.26 kΩ at the maximum in the $I_p(T)$ curve. The I_p current becomes negative at low temperatures, where the capacitive (dielectric) properties of the sample become more pronounced because of the strong increase in its resistivity.

The permittivity exhibits strong temperature and field dependences (Fig. 5). At low bias voltages (<10 V), the $\varepsilon(T)$ dependence exhibits monotonic

growth with temperature. An increase in bias brings about a shift of the high-temperature part of the permittivity toward negative values, thus making the $\varepsilon(T)$ curves nonmonotonic. As the bias voltage increases, bends appear in the $\varepsilon(T)$ curves, with a smooth transition from an increase in ε with temperature to a decrease; the bends transform into abrupt drops in ε to negative values with a further increase in the bias voltage. These bends and drops in the $\varepsilon(T)$ dependence can be identified, in their positions on the temperature scale and in the magnitude of the bias voltages, with bends and jumps in the $\rho(T)$ curves, as well as with the appearance of clearly pronounced nonlinearities in the *I–U* characteristics.

The growth of permittivity with temperature at low bias voltages should probably be assigned to the thermally activated increase in the number of free electrons, which is accompanied by an increase in crystal conductivity. In crystals cooled to 4.2 K, ε tends to ≈ 40 for all bias voltages, which obviously corresponds to the lattice contribution to the permittivity, because at low temperatures the contribution from free electrons is frozen out in these crystals.

The negative values of ε measured in crystals in the region of critical and higher voltages, $U \gtrsim U_c$, are most probably due to the inductive reactance of the crystal with electrodes in this bias region [24–26]. It is well known [26] that a necessary condition for the appearance of NDR is the existence of an internal positive current feedback involving at least two sources of conductivity variation. Because feedback cannot be realized instantaneously, the current in such systems lags behind the voltage in phase by an angle lying in the range $180° > \varphi > 90°$, which accounts for their inductive reactance. The occurrence of internal feedback is associated with the physical phenomena and mechanisms that bring about a change in crystal conductivity.

4. DISCUSSION OF THE RESULTS

From the measurements, it follows that crystals of the $LiCu_2O_2$ phase are *p*-type semiconductors as judged from their electrical resistivity, its temperature behavior, and the sign of the Seebeck coefficient. The dominance of the variable-range hopping mechanism of conduction found to prevail in the crystals in the range 80–260 K suggests a disorder in their structure, which causes localization of electronic states near the Fermi level. Understanding the origin of this disorder would be of considerable importance for proper interpretation of the properties of these crystals.

Based on the structural data available on $LiCu_2O_2$, $LiCu_3O_3$, $(Sr,Ca,La)_{14}Cu_{24}O_{41}$, and La_2CuO_{4+y} crystals (which possess similar crystallochemical properties) [1, 2, 9–11, 24–26], as well as on our TGA measurements, we can suggest the following possible reasons for the disorder in these crystals:

(i) a high concentration of antisite defects originating from mutual partial substitutions of the Li^+, Cu^+, and Cu^{2+} cations in their structural positions;

(ii) the presence of microscopic inclusions of other phases, for instance, of nuclei of $LiCu_3O_3$ and Li_2CuO_2, which form when $LiCu_2O_2$ is decomposed after cooling and passing to a metastable state, or of LiCuO-type impurity phases [7], which are almost regularly distributed in $LiCu_2O_2$ crystals;

(iii) the formation of charge-ordered states of the type of charge density waves (CDWs) in Cu–O chains;

(iv) structural defects due to the formation of microtwins;

(v) copper valence variations accompanied by changes in the oxygen content.

The most probable reason appears to be the redistribution of the Li^+, Cu^+, and Cu^{2+} cations over lattice sites, which gives rise to compositional disorder in accordance with the formula $(Li^+_{1-u}Cu^{2+}_u)(Cu^+_{1-v}Cu^{2+}_v)(Cu^{2+}_{1-t}Li^+_t)O_{2+\delta}$. This conclusion is argued for by the TGA and crystallochemical data, as well as by analysis of the conditions under which the crystals were prepared. The redistribution of the Li^+ and Cu^{2+} cations over the lattice sites is also corroborated by the onset of the phase decomposition with the formation of the $LiCu_3O_3$ phase, in which these cations, according to x-ray diffraction measurements [1], are distributed at random.

However, the other above-mentioned reasons for the onset of disorder in $LiCu_2O_2$ crystals cannot be ruled out. The possible relation between charge localization and the formation of a CDW is suggested by data on the $(Sr,Ca,La)_{14}Cu_{24}O_{21}$ phase with similar crystallochemical properties, in which hopping conduction, localization of electronic states, and nonlinearity are associated with CDWs [27–29].

The characteristic temperature T_0 in Mott's relation for $d = 3$ is given by $2.1^4\alpha^3/k_B N(E_F)$, where $1/\alpha$ is the wave-function localization length, k_B is the Boltzmann constant, and $N(E_F)$ is the density of electronic states per unit volume per unit energy at the Fermi level [13]. For $LiCu_2O_2$, the temperature $T_0 = 4.6 \times 10^8$ K falls into the upper range of the values quoted for disordered semiconductors [9, 13–23], which indicates either a small localization length $1/\alpha$ or a low density of states $N(E_F)$. Quantitative estimation of $1/\alpha$, $N(E_F)$, and other parameters essential for interpreting the charge transport mechanisms is complicated by the uncertain nature of the disorder in these crystals.

Obtaining such data, for instance, by refining the structure by x-ray or neutron diffraction measurements, is an urgent problem. Its solution should favor elucidation of the charge transport mechanisms in the phase under study and indicate how to purposefully modify the properties of the phase by properly varying the con-

ditions of its preparation, introducing various additions, etc. It would hopefully be possible to transfer the crystals to the superconducting state, which, according to the current theoretical concepts [29], is one of possible ground states of spin ladder systems with an even number of chains in the ladder. The possibility of the onset of the superconducting state in spin ladder systems has been recently illustrated with the $Sr_{14-x}Ca_xCu_{24}O_{41}$ phase [29].

Studies of the effect of an electric field on the properties of $LiCu_2O_2$ suggest that these crystals exhibit pronounced nonlinear electric characteristics, which are particularly clearly manifested in their *S*-shaped *I–U* curves with instability in the NDR region.

The electric switching from the low- to a high-Ohmic state in semiconducting substances, which can be realized without purposefully creating inhomogeneities of the type of *p–n* junctions in them, has been attracting special interest since its discovery in glassy chalcogenide semiconductors (CSs) in 1968 [27]. To date, in addition to CSs of the type $Te_{48}As_{30}Ge_{10}Si_{12}$, a similar effect has been revealed in a variety of systems, including low-dimensional semiconductors of the type of charge-transfer organic complexes and $NbSe_3$-type chalcogenides, V_2O_5 single crystals, TlMX_2 (M = In, Ga; X = Se, Te), doped or irradiated Ge and AsGa crystals, and other semiconductors [24–26, 30–35]. Depending on the crystal behavior after removal of the voltage, switching with memory, in which the low-Ohmic state persists after the removal of the field (bistable switching), and threshold switching with recovery of the high-Ohmic state (monostable switching) can be discriminated. The threshold switching is, as a rule, of electronic nature, and the switching with memory is of thermal origin. While extensive research into the properties of the switching effect has been carried out and theoretical concepts have been developed to provide an explanation for the experimental data [24–26, 30–36], no adequate understanding of the mechanisms responsible for the switching effect has thus far been reached. Note that most of the studies of *S*-shaped *I–U* curves relate to the CSs, whereas single crystals have been covered to a much lesser extent.

There are two main groups of processes (differing in origin and character) that account for the *S*-shaped *I–U* curves, namely, (i) purely electronic and (ii) electrothermal processes.

The electronic processes are not directly connected with an increase in sample temperature in the NDR region. In these processes, NDR and the low-Ohmic state appear as a result of an increase in the concentration of nonequilibrium electrons and/or in their mobility. The increase can be initiated by a variety of processes, such as tunneling, charge injection from the electrodes, space-charge-limited currents, etc. For instance, in $NbSe_3$-type chalcogenides, the nonlinearity is assigned to depinning of CDWs and their electric-field-stimulated slip.

Electrothermal processes play a decisive role in the onset of electrical instability in the case of high dissipation power in the sample. It is believed that small local deviations of defects from a uniform distribution give rise to an increase in current density in these regions, which is usually accompanied by the formation of thin channels (filaments) of high-density currents, an increase in Joule energy dissipation, and sample heating. The increase in temperature brings about an increase in the conductivity and, accordingly, in the current, and so on. A steady state in such a conducting channel is reached when the released heat becomes equal to the heat loss. Thus, the occurrence of the NDR caused by electrothermal processes should be accompanied by a noticeable increase in sample temperature in the NDR region. Of the variety of mechanisms responsible for the electrothermal processes, impact ionization is the most significant.

The experimental data available on $LiCu_2O_2$ crystals show that, in measuring *S*-shaped *I–U* curves under conditions of threshold switching, the increase in sample temperature with respect to the substrate does not exceed 3 K. Obviously, the rise in conductivity originating from such a small overheating cannot initiate the formation of the NDR. It also appears important that the switching occurs in the region of hopping conduction, where the carrier mobility is low and, hence, the Joule heating is minimum.

It is appropriate to note here that the *S*-shaped *I–U* curves observed in $LiCu_2O_2$ crystals are similar in terms of their shape and main characteristics to those obtained for the CSs and TlMX_2 and V_2O_5 crystals. The main common structural feature of these substances is the presence of quasi-one-dimensional metallic chains (–*M*–*X*– in TlMX_2 and –Te–Te– in the CSs). In the CSs; the structural rearrangement of chains was established to be related to field-induced switching. Whence one may conclude that quasi-one-dimensional Cu–O ladders play an important role in nonlinearities in the electrical properties of the $LiCu_2O_2$ crystals as well. Local barrier layers that form at the boundaries of microscopic inhomogeneities associated with crystal disorder can also constitute a significant factor in the onset of nonlinearities in *I–U* curves and switching.

5. CONCLUSIONS

Thus, an electrical instability has been revealed in crystals of the $LiCu_2O_2$ phase. This instability manifests itself in *S*-shaped *I–U* curves possessing a region of negative differential resistivity and in abrupt changes in the conductivity and permittivity near the critical voltage. Electrothermal processes do not play a major role in the threshold switching observed to occur in crystals; the switching is stimulated by mechanisms of electronic nature. The specific mechanisms responsible for threshold switching in crystals and their relation to specific features of the crystal structure were not estab-

lished at this stage of study. Further investigations of these crystals are needed to reveal them.

ACKNOWLEDGMENTS

The authors are indebted to É.A. Tishchenko and V.V. Sereneva for assistance in performing the thermopower and electrical resistivity measurements and for helpful discussions.

This study was supported by the Russian Foundation for Basic Research, project no. 02-02-17798.

REFERENCES

1. S. J. Hibble, J. Kohler, A. Simon, and S. Paider, J. Solid State Chem. **88**, 534 (1990).
2. R. Berger, A. Meetsma, S. Smaalen, and M. Sunddberg, J. Less-Common Met. **175**, 119 (1991).
3. D. A. Zatsepin, V. R. Galakhov, M. A. Korotin, *et al.*, Phys. Rev. B **57**, 4377 (1998).
4. F. C. Fritschij, H. B. Brom, and R. Berger, Solid State Commun. **107**, 719 (1998).
5. A. M. Vorotynov, A. I. Ponkrats, G. A. Petrakovskiĭ, and K. A. Sablina, Zh. Éksp. Teor. Fiz. **113**, 1866 (1998) [JETP **86**, 1020 (1998)].
6. B. Roessli, U. Staub, A. Amato, *et al.*, Physica B (Amsterdam) **296**, 306 (2001).
7. S. Zvyagin, G. Gao, Y. Xin, *et al.*, Phys. Rev. B **66**, 064424 (2002).
8. R. G. Shannon, Acta Crystallogr. A **32**, 751 (1976).
9. M. A. Kastner, R. J. Birgeneau, C. J. Chen, *et al.*, Phys. Rev. B **37**, 111 (1988).
10. A. I. Rykov, H. Yasuoka, and Y. Ueda, Physica C (Amsterdam) **247**, 327 (1995).
11. Y. Yoshinari, P. C. Hammel, J. A. Martindale, *et al.*, Phys. Rev. Lett. **77**, 2069 (1996).
12. N. M. Plakida, *High-Temperature Superconductivity* (Mezhdun. Programma Obraz., Moscow, 1996; Springer, Berlin, 1995).
13. N. F. Mott and E. A. Davis, *Electronic Processes in Non-Crystalline Materials* (Clarendon, Oxford, 1971; Mir, Moscow, 1974).
14. G. E. Pike, Phys. Rev. B **6**, 1572 (1972).
15. M. L. Knotek and M. Pollak, Phys. Rev. B **9**, 664 (1974).
16. A. R. Long, Adv. Phys. **31**, 553 (1982).
17. M. Oda, Y. Hidaka, M. Suzuki, *et al.*, Solid State Commun. **67**, 257 (1988).
18. M. Aubin and R. Gagnon, Solid State Commun. **68**, 271 (1988).
19. B. Jayaram, P. C. Lanchester, and M. T. Weller, Physica C (Amsterdam) **160**, 17 (1989).
20. A. Ghosh and D. Chakravorty, J. Phys.: Condens. Matter **2**, 649 (1990).
21. K. K. Som and B. K. Chaudhuri, Phys. Rev. B **41**, 1581 (1990).
22. G. A. Samara, W. F. Hammetter, and E. L. Venturini, Phys. Rev. B **41**, 8974 (1990).
23. S. Mollah, K. K. Som, K. Bose, *et al.*, Phys. Rev. B **46**, 11075 (1992).
24. Kh. S. Valeev and V. B. Kvaskov, *Nonlinear Metal-Oxide Semiconductors* (Énergoizdat, Moscow, 1983).
25. V. B. Kvaskov, *Semiconductor Devices with Bipolar Conductivity* (Énergoatomizdat, Moscow, 1988).
26. C. A. Goryainov and Yu. S. Tikhodeev, *Physical Models of Semiconductor Devices with Negative Resistance* (Radio i Svyaz', Moscow, 1997).
27. B. Gosrshunov, P. Haas, T. Room, *et al.*, Phys. Rev. B **66**, 060508(R) (2002).
28. A. Maeda, R. Inoue, H. Kitano, *et al.*, Phys. Rev. B **67**, 115115 (2003).
29. E. Dagotto, Rep. Prog. Phys. **62**, 1525 (1999).
30. S. R. Ovshinsky, Phys. Rev. Lett. **21**, 1450 (1968).
31. D. Adler, H. K. Henisch, and N. Mott, Rev. Mod. Phys. **50**, 209 (1978).
32. S. V. Subramanian and H. Naik, Proc.–Ind. Acad. Sci. **96**, 499 (1986).
33. M. P. Hanias, A. N. Anagnostopoulos, K. Kambas, and J. Spyridelis, Phys. Rev. B **43**, 4135 (1991).
34. Ch. Rarakotsou, J. A. Kalomiros, M. P. Hanias, *et al.*, Phys. Rev. B **45**, 11627 (1992).
35. M. P. Hanias and A. N. Anagnostopoulos, Phys. Rev. B **47**, 4261 (1993).
36. A. F. Volkov and Sh. M. Kogan, Usp. Fiz. Nauk **96**, 633 (1968) [Sov. Phys. Usp. **11**, 881 (1968)].

Translated by G. Skrebtsov

Physics of the Solid State, Vol. 46, No. 3, 2004, pp. 453–457. Translated from Fizika Tverdogo Tela, Vol. 46, No. 3, 2004, pp. 441–445.

SEMICONDUCTORS AND DIELECTRICS

The Mechanism of Ionic Conductivity in Stabilized Cubic Zirconia

V. G. Zavodinsky

Institute of Materials Science, Far East Division, Russian Academy of Sciences, Khabarovsk, 680042 Russia

e-mail: vzavod@mail.ru

Received July 18, 2003

Abstract—The electron-density functional method (in the gradient approximation) and the pseudopotential method are used to study the mechanism of ionic conductivity in the cubic phase of zirconia stabilized with magnesium or yttrium. The oxygen-ion migration in the stabilized zirconia is shown to be a two-stage process, which consists in the formation of active oxygen vacancies and in oxygen-ion jumps from one active vacancy to another. The total activation energy of these processes is calculated to be 1.0–1.5 eV, which agrees with experimental data. © *2004 MAIK "Nauka/Interperiodica".*

1. INTRODUCTION

Zirconium dioxide (ZrO_2) is of interest as a ceramic material with useful optical, electrical, thermal, strength, and other properties. Phase transitions in it and impurity-induced stabilization have been the subject of many experimental and theoretical studies. At temperatures below 1170°C, the monoclinic phase (*m*) of undoped ZrO_2 is thermodynamically stable. Undoped ZrO_2 is tetragonal (*t* phase) from 1170 to 2370°C and cubic (*c* phase) from 2370°C to the melting point (2706°C) [1, 2]. The cubic phase can be stabilized (i.e., the $c \longrightarrow t$ phase transition temperature can be reduced) by introducing additions such as MgO, CaO, Y_2O_3, etc. Zirconium dioxide is dielectric; its band-gap width was experimentally determined to be 6 eV and is virtually independent of phase type [3].

Pure zirconium dioxide is a good insulator; there is virtually no ionic conductivity in it, since the formation of oxygen vacancies requires a high energy. The stabilization of ZrO_2 with impurities whose degree of ionization is lower than that of Zr results in a certain amount of oxygen vacancies, and stabilized zirconium dioxide conducts an electric current at temperatures above 1000°C [4]. The temperature dependence of the conductivity has a complex two-exponential character, and the conductivity is not a linear function of the number of oxygen vacancies [5–7].

Solier *et al.* [8] proposed a model to explain the conductivity of stabilized zirconium dioxide. According to this model, oxygen vacancies form immobile associates (clusters) at low temperatures and their decomposition requires a certain energy. Thus, the ionic-conductivity activation energy is the sum of two components, the energy E_a of vacancy removal from a cluster and the vacancy migration energy E_m. Analysis of the temperature dependence of the Gibbs energy and the entropy [9] showed that, for stabilized zirconium dioxide with 12 mol % Y_2O_3, $E_a = 0.52$ eV and $E_m = 0.73$ eV. Another approach taking into account relaxation effects [10] gives $E_a = 0.5$ eV and $E_m = 0.66$ eV.

Recently, Bogicevic *et al.* [11] attempted to theoretically study (from first principles) the mechanism of ionic conductivity in stabilized zirconium dioxide. The authors used the electron-density functional to study the binding of individual oxygen vacancies with impurity atoms and proposed that this binding (rather than clusterization) could be the cause of the complex ionic conductivity. However, they used small cells (from 11 to 23 atoms) for simulation; therefore, the results obtained in [11] have to be refined.

In [12], the electronic structure of zirconium dioxide stabilized with CaO and Y_2O additions was studied using nonempirical calculations. It was shown (by studying the Zr_8O_{16} cell without taking relaxation into account) that the additions change the electronic spectrum only insignificantly. By analyzing the interaction between impurity atoms and oxygen vacancies, it was qualitatively concluded in [12] that this interaction is responsible for a decrease in the ionic conductivity at high concentrations of the additions.

The goal of this work is to study the energy characteristics of individual oxygen vacancies near impurity and Zr ions (by using supercells consisting of up to 96 atoms) and to attempt to describe the ionic conductivity of ZrO_2 without the vacancy-clusterization hypothesis. Moreover, we present the results of calculating the electronic structure of stabilized zirconium dioxide (with allowance for lattice relaxation) and consider the effect of oxygen-ion diffusion on the density of states.

1063-7834/04/4603-0453$26.00

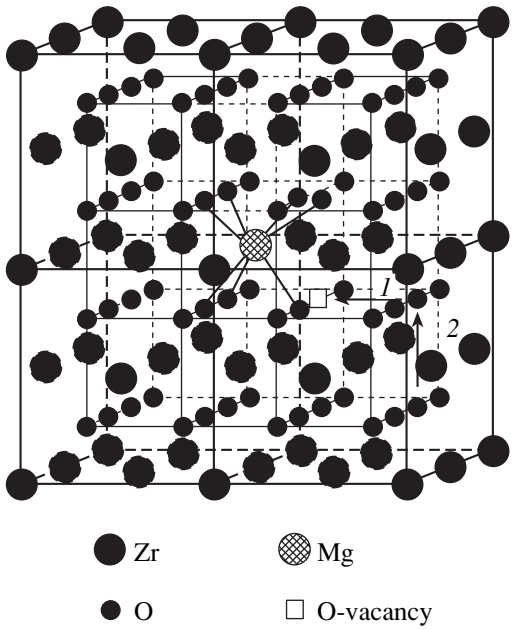

Fig. 1. Schematic atomic arrangement in cubic zirconium dioxide stabilized with 3.125 mol % MgO. Arrows show the motion of oxygen ions during (*1*) the formation of an active vacancy and (*2*) the migration responsible for the electric conduction.

2. CALCULATION PROCEDURE

Calculations were performed using the FHI96MD program [13] based on the electron-density functional theory [14, 15], the pseudopotential method, and a plane-wave basis. To calculate the exchange and correlation energies, we applied the gradient approximation proposed in [16]. Pseudopotentials were constructed using the technique developed in [17] and the FHI98PP program [18] and were checked for the absence of ghost states and the ability to represent the basic lattice characteristics of bulk materials (lattice parameter, modulus of elasticity).

The cut-off energy for a set of plane waves was taken to be 44 Ry, and the main cell of cubic zirconium dioxide was taken to be a $Zr_{32}O_{64}$ supercell. This supercell is shown schematically in Fig. 1 for the case of addition of 3.125 mol % MgO. Because of such a large supercell and the high cut-off energy, we had to consider only one *k* point in the Brillouin zone when calculating the total energy, namely, the Γ point. To construct the density of states, the calculated energy levels were broadened using 0.2-eV-wide Gaussian curves.

Using the equation of state from [19], we found the equilibrium lattice parameter *a* and bulk modulus of elasticity *B* for the cubic phases ZrO_2, MgO, and Y_2O_3. The results and the corresponding experimental data from [20–25] are listed in Table 1. It is seen from the table that the calculated values agree satisfactorily with the experimental values; that is, the constructed pseudopotentials adequately describe the energetics of interaction between Zr, Mg, and Y atoms and oxygen atoms and can be applied for studying the ZrO_2–MgO and ZrO_2–Y_2O_3 systems.

3. RESULTS AND DISCUSSION

Before studying the mechanism of oxygen-ion migration in the stabilized zirconium dioxide, let us consider the behavior of oxygen vacancies in the pure material. The oxygen vacancy migration energy in pure (undoped) *c*-ZrO_2 was calculated to be 1.5 eV. However, the formation of an oxygen vacancy requires a higher energy (according to our calculation, the energy required to remove an oxygen atom from the crystal is about 7 eV, which is an extremely high value for thermally activated processes). That is why pure zirconium dioxide is not a conductor.

To study the behavior of oxygen vacancies in stabilized zirconium dioxide, we chose the ZrO_2–MgO system, and, to compare the calculated activation energies with the experimental data, we performed additional calculations for the ZrO_2–Y_2O_3 system. This approach simplifies the simulation, since one oxygen vacancy is associated with one Mg^{+2} ion, whereas in the case of yttrium oxide one oxygen vacancy corresponds to two Y^{+3} ions. Therefore, to describe the ZrO_2–Y_2O_3 system having the same concentration of oxygen vacancies as the ZrO_2–MgO system, we would have to use the double supercell. Moreover, detailed analysis of the ZrO_2–Y_2O_3 system requires study of the effect of the mutual arrangement of an oxygen vacancy and impurity ions, which is beyond the scope of the task set in this work.

To study the effect of the concentration of a stabilizing impurity on the behavior of oxygen vacancies, we considered the $Zr_{31}Mg_1O_{63}$, $Zr_{30}Mg_2O_{62}$, and $Zr_{28}Mg_4O_{60}$ configurations, which correspond to 3.125, 6.25, and 12.5 mol % MgO, respectively. Mg atoms were distributed almost uniformly and randomly in the

Table 1. Calculated and experimental values of the lattice parameter and modulus of elasticity for Zr, Mg, and Y oxides

Parameter	ZrO_2		MgO		Y_2O_3	
	calculation	experiment	calculation	experiment	calculation	experiment
a, nm	0.522	0.513 [20]	0.424	0.421 [21]	1.11	1.06 [24]
B, GPa	215	194 [22]	160	162 [23]	150	137 [25]

superlattice; one oxygen atom was removed from the nearest environment of each Mg atom so that the neighboring impurity atoms had no common bonding oxygen atoms. Moreover, an impurity atom could not substitute for a zirconium atom located at the supercell boundary, since boundary atoms were fixed while optimizing the geometry (the fixation of impurity atoms during simulation was not warranted physically). Such a distribution of impurity atoms and oxygen vacancies cannot be realized unambiguously, since there are several tens of almost equivalent configurations. The long time required for the calculation did not allow us to study all configurations; therefore, we analyzed only three variants of each configuration and found that the scatter of the energy parameters did not exceed 0.1 eV. We give their average values below.

The calculations showed that an oxygen vacancy located near an impurity atom can move around this atom by overcoming a certain migration barrier E_{bar}, whose height depends on the impurity concentration and varies in the range 0.5–0.7 eV (Table 2).

The total energy for a vacancy in any equilibrium position is, of course, the same. However, this type of motion of oxygen vacancies cannot be responsible for through ionic conduction, since oxygen ions do not move from one part of the crystal to another. This motion can only contribute to displacement currents, which are characteristic of high-frequency electric circuits. To provide through conduction, oxygen vacancies must be located near zirconium atoms. Such vacancies can be called active, since they are responsible for a directed transfer of oxygen ions. For an oxygen vacancy to form near a zirconium atom, one oxygen atom must be transferred from the zirconium surrounding to the magnesium surrounding (process *1* in Figs. 1, 2). In this case, the total energy is calculated to be 0.5–0.8 eV higher (Table 3). This increment is the formation energy of active oxygen vacancies E_a. It is an order of magnitude smaller than the oxygen vacancy formation energy in the pure material. The vacancy migration energy E_m, i.e., the barrier between two equivalent positions of an oxygen atom near neighboring zirconium atoms (Fig. 2, process *2*), is equal to 0.5–1.0 eV. Hence, the total activation energy for ionic conductivity E_{tot} is 1.0–1.5 eV. Note that the height E_b of the energy barrier that an oxygen atom must overcome to form an active vacancy is also small. Its value is almost independent of the impurity concentration and is about 1.0 eV; that is, active vacancies can form at the temperatures of ionic conductivity.

Unfortunately, we failed to find experimental data for the conductivity activation energy of magnesium-stabilized zirconium dioxide. Therefore, to check the results obtained in this work, we performed analogous calculations for zirconium dioxide stabilized with 12.5 mol % yttrium. The formation energy E_a of an active vacancy is calculated to be 0.6 eV, and the vacancy migration energy E_m was found to be 0.7 eV; these energies agree well with the experimental data [4, 26]. A comparison of these values with the corresponding values obtained for the ZrO_2–MgO system indicates that the energetics of the oxygen-ion migration in stabilized zirconium dioxide depends only weakly on the type of stabilizing impurity.

Table 2. Height of an energy barrier for an oxygen atom moving around a magnesium atom

Concentration MgO, mol %	E_{bar}, eV
3.125	0.73
6.25	0.60
12.5	0.46

Table 3. Energy parameters describing the ionic conduction of stabilized zirconium dioxide

Impurity concentration	E_a, eV	E_m, eV	$E_{tot} = E_a + E_m$, eV
ZrO_2–MgO system			
3.125	0.6	1.0	1.6
6.25	0.5	0.5	1.0
12.5	0.8	0.5	1.3
ZrO_2–Y_2O_3 system			
12.5	0.6	0.7	1.2

Note: E_a is the formation energy of an active oxygen vacancy, E_m is the migration energy of an active vacancy, and E_{tot} is the total activation energy for ionic conductivity.

4. ELECTRONIC STRUCTURE OF STABILIZED ZIRCONIUM DIOXIDE

Magnesium-stabilized zirconium dioxide is known to be a dielectric; however, its electronic structure is poorly understood. There is not even any information on the band-gap width of this material. It is of special interest to study the contribution from oxygen vacan-

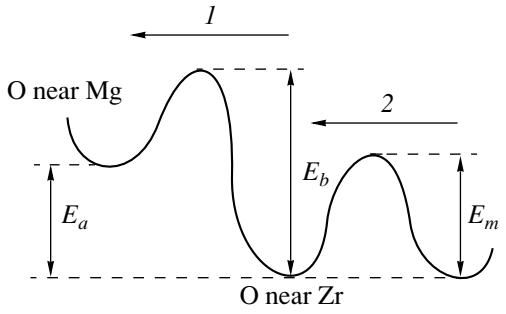

Fig. 2. Schematic diagram for the formation of an active oxygen vacancy (process *1*) and an oxygen-ion jump from one active vacancy to another (process *2*).

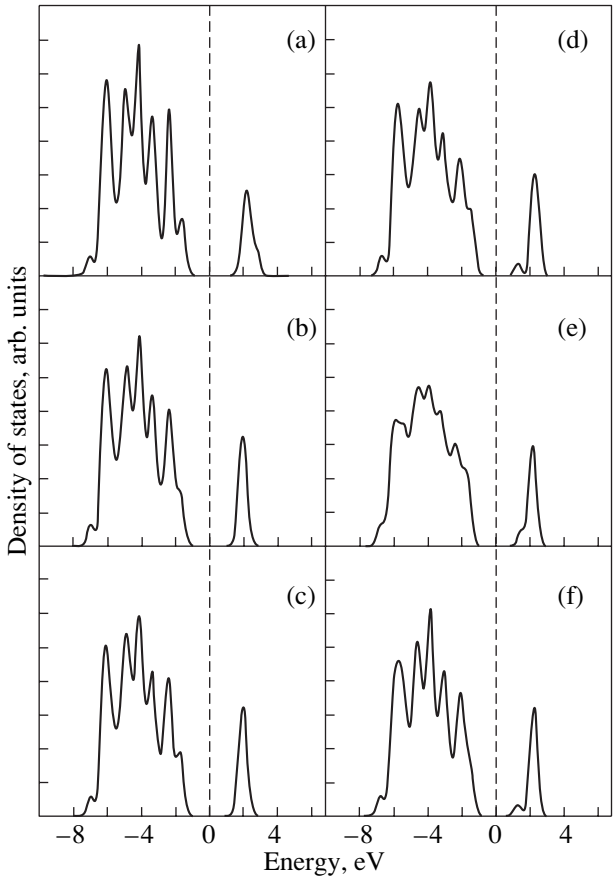

Fig. 3. Density of states for pure and stabilized zirconium dioxide: (a) pure ideal ZrO_2; (b) the same but with an addition of 3.125 mol % MgO, equilibrium configuration; (c) the MgO content is 3.125 mol % and an oxygen ion is located between two active vacancies; (d, e) the MgO contents are 6.25 and 12.5 mol %, respectively; and (f) ZrO_2 with an addition of 12.5 mol % Y_2O_3. Vertical dashed lines show the Fermi level.

cies (especially during their migration) to the electronic structure.

Figure 3a shows the density of states of pure cubic zirconium dioxide, and Figs. 3b–3f shows the density of states for stabilized *c*-ZrO_2.

The band-gap width for pure cubic zirconium dioxide is calculated to be 3.5 eV, which is significantly lower than the experimental value (6 eV) but agrees well with the values (3.3–4.1 eV) obtained by other authors [27–31] in the context of the electron-density functional theory, which always gives underestimated values of the band-gap width. The density-of-states curve in Fig. 3a is similar to the corresponding curve constructed in [31], where a 96-atom supercell with one point (Γ) in the Brillouin zone was also studied.

An addition of 3.125 mol % MgO (Fig. 3b) changes neither the shape of the density of states nor the band-gap width. As the MgO concentration increases to 6.25 mol % (Fig. 3d), the valence-state distribution changes slightly and a peak related mainly to oxygen vacancies appears near the conduction-band bottom (1 eV below). A similar peak was detected in [12] for the 0.875 ZrO_2–0.125 CaO system. A further increase in the MgO content to 12.5 mol % (Fig. 3e) leads to broadening of this peak and its mergence with the conduction-band bottom. The valence-state band becomes smoother, and its maxima and minima level off. The density of states of the zirconium dioxide stabilized with 12.5 mol % Y_2O_3 (Fig. 3f) is virtually identical to the density of states corresponding to an addition of 6.25 mol % MgO, which suggests that the electronic structure is mainly affected by oxygen vacancies, which are in the same amount in the ZrO_2–12.5 mol % Y_2O_3 and ZrO_2–6.25 mol % MgO systems.

We also calculated the density of states corresponding to a migrating oxygen ion (when it is directly between two active oxygen vacancies). Figure 3c shows the calculation result for zirconium dioxide stabilized with 3.125 mol % MgO. Comparison with Fig. 3b indicates that, in this case, the electronic structure is identical to that at equilibrium. In particular, it remains a dielectric with the same band-gap width, although the ionic motion is a through charge transfer, i.e., an electric current.

5. CONCLUSIONS

First-principles calculations have shown that oxygen vacancies forming near impurity ions during doping of cubic zirconium dioxide are inactive for oxygen diffusion, since the transfer of oxygen ions bound to neighboring zirconium ions to the vacancies is accompanied by an increase in the total energy of the crystal. However, this transfer generates active oxygen vacancies surrounded by zirconium ions. The migration of these active vacancies does specify the ionic conductivity. Thus, oxygen-ion diffusion in stabilized zirconium dioxide is a two-stage process with a total activation energy of 1.0–1.5 eV.

The band-gap width of cubic zirconium dioxide stabilized with magnesium or yttrium is calculated to be 3.3 eV. The electronic structure of the stabilized ZrO_2 remains virtually unchanged during the motion of oxygen ions from one active vacancy to another.

ACKNOWLEDGMENTS

The author is grateful to the administration of the Institute of Automatics and Process Control (Far East Division, Russian Academy of Sciences, Vladivostok) for permission to use an Alef computer cluster and an MVS-1000 supercomputer.

REFERENCES

1. R. Aldebert and J. P. Traverse, J. Am. Ceram. Soc. **68**, 34 (1985).

2. R. J. Ackermann, S. P. Garg, and E. G. Rauth, J. Am. Ceram. Soc. **60**, 341 (1977).
3. R. H. French, S. J. Glass, F. S. Ohuchi, *et al.*, Phys. Rev. B **49**, 5133 (1994).
4. T. H. Etsel and S. N. Flengas, Chem. Rev. **70**, 339 (1970).
5. Y. Suzuki, T. Takahashi, and N. Nagae, Solid State Ionics **3–4**, 483 (1981).
6. P. Aberland and J. F. Baumard, Phys. Rev. B **26**, 1005 (1982).
7. J. Bauerle and J. Hrizo, J. Phys. Chem. Solids **30**, 565 (1969).
8. J. D. Solier, I. Cachadiña, and A. Dominquez-Rodriguez, Phys. Rev. B **48**, 3704 (1993).
9. I. Cachadiña, J. D. Solier, and A. Dominquez-Rodriguez, Phys. Rev. B **52**, 10872 (1995).
10. C. León, M. L. Licia, and J. Santamaria, Phys. Rev. B **55**, 882 (1997).
11. A. Bogicevic, C. Wolverton, G. M. Crosbie, and E. B. Stechel, Phys. Rev. B **64**, 014106 (2001).
12. V. M. Zaĭnullina and V. P. Zhukov, Fiz. Tverd. Tela (St. Petersburg) **43** (9), 1619 (2001) [Phys. Solid State **43**, 1686 (2001)].
13. M. Bockstedte, A. Kley, J. Neugebauer, and M. Scheffler, Comput. Phys. Commun. **107**, 187 (1997).
14. P. Hohenberg and W. Kohn, Phys. Rev. **136**, B864 (1964).
15. W. Kohn and L. J. Sham, Phys. Rev. **140**, A1133 (1965).
16. J. P. Perdew and Y. Wang, Phys. Rev. B **33**, 8800 (1986).
17. N. Troullier and J. L. Martins, Phys. Rev. B **43**, 1993 (1991).
18. M. Fuchs and M. Scheffler, Comput. Phys. Commun. **119**, 67 (1999).
19. F. D. Murnagham, Proc. Natl. Acad. Sci. USA **30**, 244 (1944).
20. C. J. Howard, R. J. Hill, and B. E. Reichert, Acta Crystallogr. B **44**, 116 (1988).
21. K. J. Chang and M. L. Cohen, Phys. Rev. B **30**, 4774 (1984).
22. J. Haines, J. M. Leger, S. Hull, *et al.*, J. Am. Ceram. Soc. **80**, 1910 (1997).
23. O. L. Anderson and P. Andreatch, J. Am. Ceram. Soc. **49**, 404 (1966).
24. C. Proust, Y. Vaills, Y. Luspin, and E. Husson, Solid State Commun. **93**, 729 (1995).
25. W. R. Manning, O. Hunter, Jr., and B. R. Powell, Jr., J. Am. Ceram. Soc. **52**, 436 (1969).
26. V. V. Kharton, E. N. Namovich, and A. A. Vecher, J. Solid Electrochem. **3**, 61 (1999).
27. S. E. Kul'kova and O. N. Muryzhnikova, Physica B (Amsterdam) **192**, 284 (1993).
28. H. Jansen, Phys. Rev. B **43**, 7267 (1991).
29. F. Zandiehnadem, R. A. Murray, and W. Y. Ching, Physica B (Amsterdam) **150**, 19 (1988).
30. L. Soriano, M. Abbate, J. Faber, *et al.*, Solid State Commun. **93**, 659 (1995).
31. G. Stapper, B. Bernasconi, N. Nicoloso, and M. Parinello, Phys. Rev. B **59**, 797 (1999).

Translated by K. Shakhlevich

Physics of the Solid State, Vol. 46, No. 3, 2004, pp. 458–461. Translated from Fizika Tverdogo Tela, Vol. 46, No. 3, 2004, pp. 446–448.

SEMICONDUCTORS AND DIELECTRICS

Electromechanical Properties of $Pb_3Ga_2Ge_4O_{14}$ Piezoelectric Crystals Grown from Solution in a Melt

B. P. Sorokin*, D. A. Glushkov*, L. N. Bezmaternykh, V. L. Temerov**, I. A. Gudim**, and K. S. Aleksandrov****

** Krasnoyarsk State University, Svobodnyĭ pr. 79, Krasnoyarsk, 660041 Russia*
e-mail: bsorokin@lan.krasu.ru
*** Kirensky Institute of Physics, Siberian Division, Russian Academy of Sciences, Akademgorodok, Krasnoyarsk, 660036 Russia*

Received July 18, 2003

Abstract—Single crystals of lead gallium germanate $Pb_3Ga_2Ge_4O_{14}$ are grown from their own solution melts. The propagation of bulk acoustic waves is investigated, and the elastic, piezoelectric, and dielectric constants are calculated. The temperature dependences of the dielectric constants of this compound are analyzed. © *2004 MAIK "Nauka/Interperiodica".*

1. Quartz, lithium niobate, germanosillenite, and silicosillenite are the crystals used in piezoelectric engineering and acoustoelectronics. Among these materials, only quartz crystals have found wide application owing to their thermally stable cuts suitable for propagating bulk and surface acoustic waves, even though quartz exhibits relatively small coefficients of piezoelectric coupling for both bulk and surface acoustic waves. One of the most important problems is the search for new crystalline materials that are characterized by large piezoelectric-coupling coefficients and slow attenuation of acoustic waves and that involve cuts providing thermal stability in devices based on these materials. Moreover, the cost of producing these crystals on a mass scale should be relatively low.

In recent years, considerable interest has been expressed by researchers in crystals that are isomorphic to calcium gallium germanate $Ca_3Ga_2Ge_4O_{14}$ and belong to the symmetry class 32. To date, over one hundred compounds of this family (including single crystals) have been synthesized [1]. In particular, this includes the langasite $La_3Ga_5SiO_{14}$, which substantially excels quartz in piezoelectric coupling and, consequently, has already successfully been used in acoustoelectronics and piezoelectric engineering. Although langasite and some other materials have been synthesized using the melting (Czochralski) technique, which was specially devised for growing large-sized single crystals, many problems concerning the crystal chemistry and technology of these materials, particularly those regarding the quality of single crystals, remain unsolved. As a result, the losses due to the propagation of high-frequency elastic waves occurring in these crystals are greater than those in piezoelectric quartz. This can be explained by the fact that virtually all single crystals with a langasite-like structure are considered to be structurally disordered, because one cation position in their structure can be occupied by atoms of two (or more) sorts [2]. However, the langasite family also involves crystals with an ordered structure [3]. These crystals are currently objects of intensive investigation.

2. The extreme members of this family are lead and barium gallium germanates ($Pb_3Ga_2Ge_4O_{14}$, $Ba_3Ga_2Ge_4O_{14}$), which have the largest sized cations and, hence, the largest unit cell parameters. According to extrapolation data, these crystals possess strong piezoelectric properties. However, upon melting, these compounds undergo decomposition and, therefore, cannot be prepared in the form of single crystals from a melt [1].

In this work, $Pb_3Ga_2Ge_4O_{14}$ isometric single crystals more than 1 cm^3 in volume were grown from both their own solution melts and solution melts diluted with lead fluoride [4].

3. The propagation of bulk acoustic waves in a $Pb_3Ga_2Ge_4O_{14}$ single crystal was studied using the pulsed ultrasonic method (30 MHz), which ensured an accuracy of better than $\pm 10^{-4}$ [5] in determining the velocity of bulk acoustic waves. As a rule, the determination of the electromechanical properties is based on measuring the velocities of bulk acoustic waves along particular directions. The velocity of bulk acoustic waves is related to the elastic moduli, piezoelectric constants, and dielectric constants (Table 1). The ultrasonic data were supplemented with the results of measuring the low-frequency permittivity $\varepsilon_{ij}^{\sigma}$ at a frequency of 1 kHz (the electric-bridge method). The measurements of the low-frequency permittivity $\varepsilon_{ij}^{\sigma}$ and the dielectric loss tangent $\tan\delta$ were carried out in the temperature range –100–150°C (Fig. 1). The piezoelectric activity

Table 1. Relationships between the velocities of bulk acoustic waves and piezoelectric-coupling constants for crystals of symmetry 32 and velocities of bulk acoustic waves in the $Pb_3Ga_2Ge_4O_{14}$ single crystal at 20°C

Mode no.	**N**	**U**	Wave type	Relationships for material constants	V_i, m/s
1	[001]	[001]	*L*	C_{33}	5128.1 ± 0.5
2	[001]		*S*	C_{44}	2743.5 ± 0.5
3	[100]	[100]	*L*	$C_{11} + \frac{e_{11}^2}{e_{11}^\eta}$	4618.0 ± 0.5
4	[100]		*SF*	$\frac{1}{2}(C_{44} + C_{66}) + \frac{1}{2}\sqrt{(C_{44} - C_{66})^2 + 4C_{14}^2}$	2932.9 ± 0.5
5	[100]		*SS*	$\frac{1}{2}(C_{44} + C_{66}) - \frac{1}{2}\sqrt{(C_{44} - C_{66})^2 + 4C_{14}^2}$	2257.3 ± 0.5
6	[010]	[100]	*S*	$C_{66} + \frac{e_{11}^2}{e_{11}^\eta}$	2413.4 ± 0.5
7	[010]		*QL*	$\frac{1}{2}(C_{44} + C_{11}) + \frac{1}{2}\sqrt{(C_{11} - C_{44})^2 + 4C_{14}^2}$	4630.3 ± 0.5
8	[010]		*QS*	$\frac{1}{2}(C_{44} + C_{11}) - \frac{1}{2}\sqrt{(C_{11} - C_{44})^2 + 4C_{14}^2}$	2713.1 ± 0.5
9	$\left[0\frac{1}{\sqrt{2}}\frac{1}{\sqrt{2}}\right]$	[100]	*S*	$\frac{1}{2}(C_{44} + C_{66} + 2C_{14}) + \frac{1}{2}\frac{(e_{11} + e_{14})^2}{e_{11}^\eta + e_{33}^\eta}$	2284.2 ± 0.5
10	$\left[0\frac{1}{\sqrt{2}}\frac{1}{\sqrt{2}}\right]$		*QL*	$\frac{1}{4}(C_{11} - 2C_{14} + 2C_{44} + C_{33}) + \frac{1}{4}\sqrt{(2C_{14} - C_{11} + C_{33})^2 + 4(C_{13} + C_{44} - C_{14})^2}$	5107.9 ± 0.5
11	$\left[0\frac{1}{\sqrt{2}}\frac{1}{\sqrt{2}}\right]$		*QS*	$\frac{1}{4}(C_{11} - 2C_{14} + 2C_{44} + C_{33}) - \frac{1}{4}\sqrt{(2C_{14} - C_{11} + C_{33})^2 + 4(C_{13} + C_{44} - C_{14})^2}$	2604.6 ± 0.5
12	$\left[0-\frac{1}{\sqrt{2}}\frac{1}{\sqrt{2}}\right]$	[100]	*S*	$\frac{1}{2}(C_{44} + C_{66} + 2C_{14}) + \frac{1}{2}\frac{(e_{11} - e_{14})^2}{e_{11}^\eta + e_{33}^\eta}$	2853.6 ± 0.5
13	$\left[0-\frac{1}{\sqrt{2}}\frac{1}{\sqrt{2}}\right]$		*QL*	$\frac{1}{4}(C_{11} + 2C_{14} + 2C_{44} + C_{33}) + \frac{1}{4}\sqrt{(2C_{14} + C_{11} - C_{33})^2 + 4(C_{13} + C_{44} + C_{14})^2}$	4830.5 ± 0.5
14	$\left[0-\frac{1}{\sqrt{2}}\frac{1}{\sqrt{2}}\right]$		*QS*	$\frac{1}{4}(C_{11} + 2C_{14} + 2C_{44} + C_{33}) - \frac{1}{4}\sqrt{(2C_{14} + C_{11} - C_{33})^2 + 4(C_{13} + C_{44} + C_{14})^2}$	2556.8 ± 0.5

Note: **N** and **U** are the unit vectors of propagation and polarization of the bulk acoustic waves.

was also determined by measuring the longitudinal piezoelectric effect with the use of a V7-30 electrostatic voltmeter. The structure of the samples used in our experiments had point symmetry 32. For example, the ultrasonic measurements were performed using samples with the following characteristics. The linear dimensions of the samples fell in the range 4–7 mm, the samples were oriented using an x-ray diffractometer

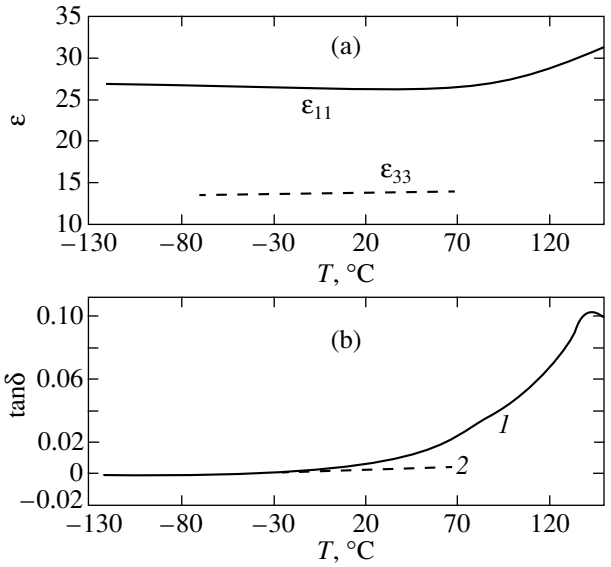

Fig. 1. Temperature dependences of (a) the low-frequency permittivity and (b) the dielectric loss tangent for the (*1*) *X* and (*2*) *Z* cuts of the $Pb_3Ga_2Ge_4O_{14}$ crystal.

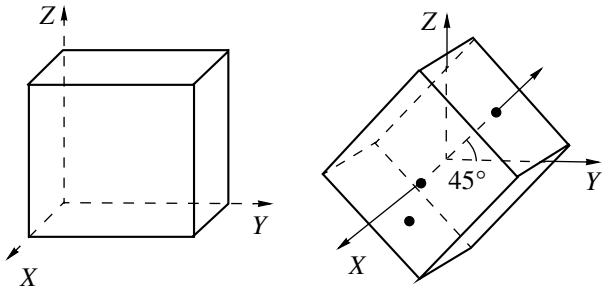

Fig. 2. Schematic representation of the orientation of samples used in ultrasonic investigations.

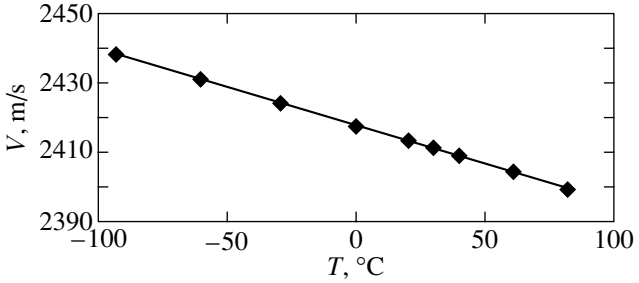

Fig. 3. Temperature dependence of the velocity of a pure shear wave propagating along the [010] direction (mode 6).

with an accuracy of better than ±3', and the deviations of the crystal facets from their plane-parallel orientation did not exceed ±1 μm/cm (Fig. 2). According to our earlier work [6], the $\left[0\ \frac{1}{\sqrt{2}}\ \frac{1}{\sqrt{2}}\right]$ and $\left[0\ -\frac{1}{\sqrt{2}}\ \frac{1}{\sqrt{2}}\right]$ directions in crystals of this symmetry differ in terms of their elastic properties; in particular, the condition for the elastic constant $C_{14} < 0$ is satisfied along the direction $\left[0\ \frac{1}{\sqrt{2}}\ \frac{1}{\sqrt{2}}\right]$.

The low-frequency permittivities $\varepsilon_{ij}^{\sigma}$ (the case of a mechanically free sample) and ε_{ij}^{η} (the case of a mechanically fixed sample) of crystals with symmetry 32 are governed by the following relationships:

$$\varepsilon_{11}^{\eta} = \varepsilon_{11}^{\sigma} - \frac{e_{11}^2}{\varepsilon_0 C_{11}^E}, \quad \varepsilon_{33}^{\eta} = \varepsilon_{33}^{\sigma}. \tag{1}$$

Here, e_{11} is the tensor component of the piezoelectric constants $e_{i\lambda}$, $\varepsilon_0 = 8.854 \times 10^{-12}$ F/m is the permittivity of free space, and C_{11}^E is the tensor component of the elastic moduli measured in a dc electric field. The parameters involved in relationships (1) were used to calculate the low-frequency permittivities ε_{ij}^{η}.

Table 2 presents the electromechanical characteristics of the $Pb_3Ga_2Ge_4O_{14}$ crystals in comparison with the data obtained for langasite crystals [5]. These characteristics are calculated from the data presented in Table 1 and the results of dielectric measurements.

Analysis of the data presented in Table 2 shows that, despite the predictions based on the extrapolation data, the $Pb_3Ga_2Ge_4O_{14}$ crystals possess weak piezoelectric properties, because the piezoelectric-coupling coefficients are less than 10%. The elastic moduli of the $Pb_3Ga_2Ge_4O_{14}$ crystals are less than those of the langasite crystals. This indicates that the $Pb_3Ga_2Ge_4O_{14}$ crystal has a smaller hardness as compared to the langasite crystal. The temperature dependence of the velocity of bulk acoustic waves (mode 6), which is determined by the elastic constant C_{66}, exhibits normal behavior (Fig. 3). This suggests that the $Pb_3Ga_2Ge_4O_{14}$ crystal has no temperature-compensated directions or cuts suitable for propagating bulk and surface acoustic waves. The quantitative comparative estimations demonstrated that the attenuation of elastic waves in $Pb_3Ga_2Ge_4O_{14}$ is insignificant.

It is worth noting that the temperature dependences of the dielectric parameters of $Pb_3Ga_2Ge_4O_{14}$ differ from those of the majority of crystals with a langasite structure, for which the permittivity, as a rule, obeys the relationship $\varepsilon_{33}^{\sigma} > \varepsilon_{11}^{\sigma}$. For example, the temperature dependence of the permittivity $\varepsilon_{33}^{\sigma}$ of langasite crystals has the form $\varepsilon_{33}^{\sigma}(T) \sim T^{-1}$, which corresponds to the contribution of the dipole polarization. It should also be noted that the slope of the temperature dependence $\varepsilon_{11}^{\sigma}$ for the $Pb_3Ga_2Ge_4O_{14}$ crystal changes at room temperature. This correlates with the increase observed in the

Table 2. Elastic, piezoelectric, and dielectric properties of $Pb_3Ga_2Ge_4O_{14}$ and $La_3Ga_5SiO_{14}$ crystals at 20°C

	$Pb_3Ga_2Ge_4O_{14}$	$La_3Ga_5SiO_{14}$
	Density ρ, kg/m^3 (calculation)	
	6884.8	5743
λμ	$C^E_{\lambda\mu}$, 10^{10} Pa	
11	14.65 ± 0.01	18.875
66	3.98 ± 0.01	4.2
33	18.12 ± 0.01	26.14
44	5.21 ± 0.01	5.35
14	–1.02 ± 0.01	–1.412
13	7.04 ± 0.01	9.59
*i*λ	$\lvert e_{i\lambda}\rvert$, C/m^2	
11	0.26 ± 0.03	0.44
14	0.09 ± 0.03	0.1
ij	$\varepsilon^{\sigma}_{ij}$	
11	26.2 ± 0.5	18.92
33	13.9 ± 0.5	50.7
ij	ε^{η}_{ij}	
11	26.1 ± 0.5	
33	13.9 ± 0.5	
	Piezoelectric-coupling coefficients, %	
The piezoactive longitudinal wave propagating along the *X* direction (mode 3)*	4.7	8
The piezoactive pure shear wave propagating along the *Y* direction and polarized along the *X* direction (mode 7)*	9	16

* The mode numbering is the same as in Table 1.

dielectric loss tangent in this range and can be explained by the relaxation ionic polarization due to hopping conduction.

ACKNOWLEDGMENTS

This work was supported by the Russian Federal program "Integration" (project no. 67).

REFERENCES

1. B. V. Mill and Yu. V. Pisarevsky, in *Proceedings of the 2000 IEEE/EIA International Frequency Control Symposium and Exhibition* (Kansas-City, USA, 2000), p. 133.
2. A. A. Kaminskiĭ, S. É. Sarkisov, B. V. Mill', and G. G. Khodzhabagyan, Izv. Akad. Nauk SSSR, Neorg. Mater. **18**, 1396 (1982).
3. B. H. T. Chai, A. N. P. Bustamante, and M. C. Chou, in *Proceedings of the 2000 IEEE/EIA International Frequency Control Symposium and Exhibition* (Kansas-City, USA, 2000), p. 163.
4. L. N. Bezmaternykh, A. D. Vasil'ev, I. A. Gudim, and V. L. Temerov, in *Abstracts of the X National Conference on Crystal Growth* (Moscow, 2002).
5. E. L. Belokoneva, S. Yu. Stefanovich, Yu. V. Pisarevskiĭ, and A. V. Mosunov, Zh. Neorg. Khim. **45** (11), 1786 (2000).
6. B. P. Sorokin, P. P. Turchin, and D. A. Glushkov, Fiz. Tverd. Tela (St. Petersburg) **36** (10), 2907 (1994) [Phys. Solid State **36**, 1545 (1994)].

Translated by I. Volkov

Physics of the Solid State, Vol. 46, No. 3, 2004, pp. 462–465. Translated from Fizika Tverdogo Tela, Vol. 46, No. 3, 2004, pp. 449–452.

SEMICONDUCTORS AND DIELECTRICS

Electrical Conductivity and Dielectric Properties of β-BaB_2O_4 Crystal in the Temperature Range 90–300 K

A. U. Sheleg and V. G. Gurtovoy

Institute of Solid-State and Semiconductor Physics, National Academy of Sciences of Belarus, ul. Brovki 17, Minsk, 220072 Belarus

e-mail: sheleg@ifttp.bas-net.by

Received July 24, 2003

Abstract—The electrical conductivity σ and dielectric properties (ε, tanδ) of β-BaB_2O_4 were studied in the temperature range 90–300 K. The quantities σ, ε, and tanδ were measured at frequencies of 0.1, 1, and 10 kHz and 1 MHz. The dielectric permittivity and electrical conductivity were found to grow with increasing temperature at all frequencies. The permittivity decreases and the electrical conductivity increases (by several orders of magnitude) with increasing frequency. Maxima were observed in the $\sigma = f(T)$ and $\tan\delta = f(T)$ curves for all frequencies; the maxima shift toward higher temperatures with increasing frequency. © *2004 MAIK "Nauka/Interperiodica".*

1. INTRODUCTION

Barium borate β-BaB_2O_4 crystals are a comparatively new and very promising nonlinear-optics material for use in laser technology for laser radiation conversion. β-BaB_2O_4 is a low-temperature modification of BaB_2O_4. This crystal has a trigonal structure (space group $R3c$) with unit cell parameters $a = 8.380$ Å and $\alpha = 96.65°$ (in the hexagonal axes, $a = b = 12.519$ Å, $c = 12.723$ Å) [1]. The absence of a center of symmetry accounts for the high nonlinearity in the optical properties of these crystals [2]. These crystals exhibit a high conversion efficiency and nonlinearity in their optical properties, as well as a considerable radiation resistance to breakdown, over a broad frequency region (extending from the UV to IR) [2–4]. Numerous publications can be found in the literature that deal with studies on the optical properties of these crystals and their application in laser technology. In order to make the use of these crystals still more efficient, however, one needs to know their thermal, dynamic, and dielectric characteristics, whose investigation has only recently been started. Studies of the heat capacity of β-BaB_2O_4 were reported in [5]. In [6], the temperature dependence of the unit cell parameters was measured and it was shown that these crystals exhibit a strong anisotropy in thermal expansion. The results of an investigation of the electrical conductivity and dielectric properties performed at a frequency of 1 kHz are presented in [7].

We report here on a study of the temperature dependence of the electrical conductivity and dielectric properties of β-BaB_2O_4 performed in the range 90–300 K in various crystallographic directions at measuring field frequencies of 0.1, 1, and 10 kHz and 1 MHz.

2. EXPERIMENTAL

The electrical conductivity σ, dielectric permittivity ε, and loss tangent tanδ of β-BaB_2O_4 crystals were measured with an E7-12 digital meter at 1 MHz and with an E7-14 instrument at frequencies of 0.1, 1, and 10 kHz. The temperature dependences of σ, ε, and tanδ were obtained under continuous quasi-stationary cooling, followed by continuous heating of the sample at a rate of ~0.5 K/min. The sample was fixed in a holder placed in liquid-nitrogen vapors. The samples were ~1- to 1.5-mm thick β-BaB_2O_4 single-crystal plates cut such that their major surfaces coincided with the (001) or (100) crystallographic plane. The sample surface was oriented with respect to the crystallographic planes to within 5′–10′ by using the x-ray diffraction technique. The sample temperature was measured with a chromel–copel thermocouple with its junction in contact with the sample surface. The temperature was varied by a controlled heater mounted in the sample holder. Silver paste was used to prepare the electrodes.

3. EXPERIMENTAL RESULTS AND DISCUSSION

Figure 1 presents temperature dependences of the dielectric permittivity of β-BaB_2O_4 measured in the [001] direction at various frequencies in the range 90–300 K. The values of ε are seen to grow with increasing temperature for all frequencies, the variation being nonlinear and stronger at higher frequencies. One can also see that the permittivity ε depends on the frequency of the measuring electric field. Figure 2 displays the dispersion curve of the permittivity at room temperature. As the frequency f increases from 0.1 kHz to 1 MHz, ε decreases from 10.73 to 8.45, which should

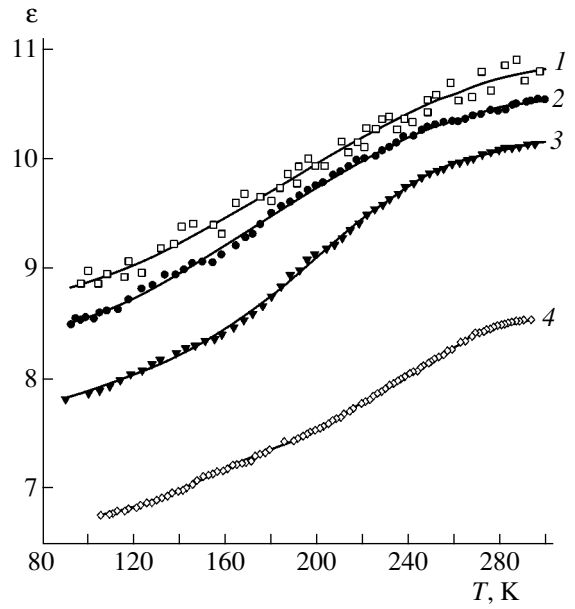

Fig. 1. Temperature dependences of the permittivity of β-BaB_2O_4 in the [001] direction measured in the range 90–300 K at frequencies of (*1*) 100 Hz, (*2*) 1 kHz, (*3*) 10 kHz, and (*4*) 1 MHz.

be assigned to the relaxation processes taking place in the higher frequency range.

The temperature dependences of tanδ of β-BaB_2O_4 measured at various frequencies in the [001] direction are shown graphically in Fig. 3. The values of tanδ at 1 MHz are seen to be substantially lower than those at frequencies of 10 and 1 kHz. It should be pointed out that the tanδ = *f*(*T*) curve passes through a maximum, which shifts toward higher temperatures as the frequency increases.

Figure 4 plots the electrical conductivity of β-BaB_2O_4 measured at various frequencies along the [001] direction as a function of temperature. The electrical conductivity is seen to increase with temperature. The σ = *f*(*T*) curves have maxima in the temperature interval 200–250 K at all frequencies (as is the case with tanδ). Note that the maxima shift with increasing frequency toward higher temperatures both for tanδ and for σ.

Figure 5 presents temperature dependences of the electrical conductivity of β-BaB_2O_4 measured in the [100] direction at various frequencies. The temperature and frequency dependences of the electrical conductivity measured in the [100] direction have the same pattern as those along [001]. However, the electrical conductivities in the two directions differ in magnitude; i.e., the electrical conductivity is anisotropic and smaller in the [001] than in the [100] direction.

Note that the magnitude of the electrical conductivity depends strongly on the frequency of the measuring electric field. The electrical conductivity grows rapidly with frequency. The magnitude of σ increases by several orders of magnitude with increasing frequency (Figs. 4, 5). This behavior of the electrical characteristics of β-BaB_2O_4, as well as the presence of maxima in the σ = *f*(*T*) and tanδ = *f*(*T*) curves, is apparently associated with specific features of the crystal structure and,

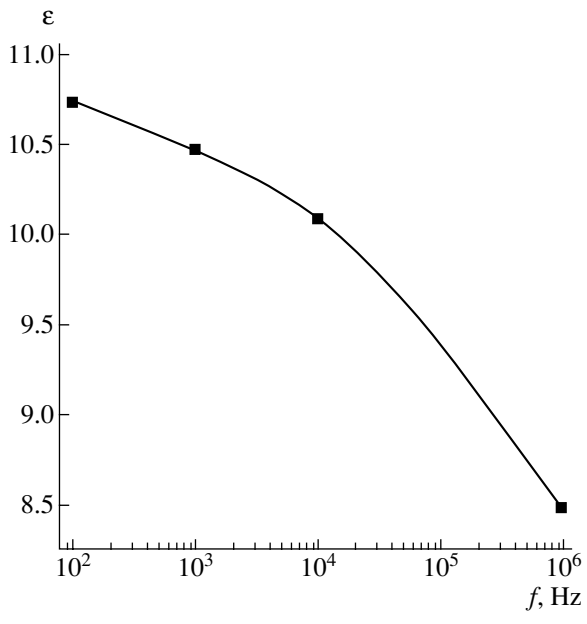

Fig. 2. Dispersion curve of the permittivity obtained for the [001] direction at *T* = 273 K.

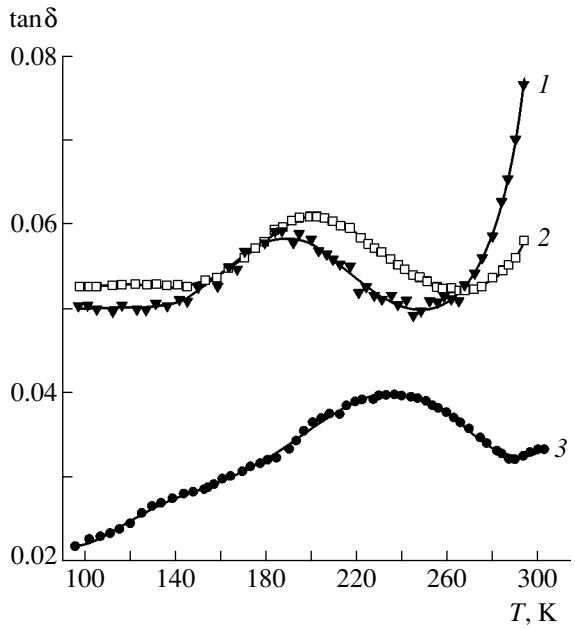

Fig. 3. Temperature dependences of tanδ of β-BaB_2O_4 in the [001] direction measured in the range 90–300 K at frequencies of (*1*) 1 kHz, (*2*) 10 kHz, and (*3*) 1 MHz.

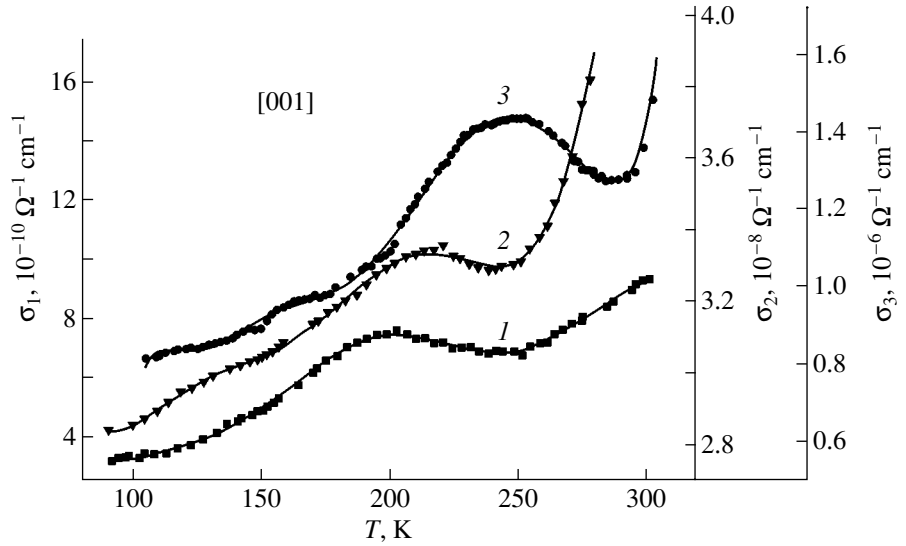

Fig. 4. Temperature dependences of the electrical conductivity of β-BaB_2O_4 in the [001] direction measured in the range 90–300 K at frequencies of (*1*) 1 kHz, (*2*) 10 kHz, and (*3*) 1 MHz.

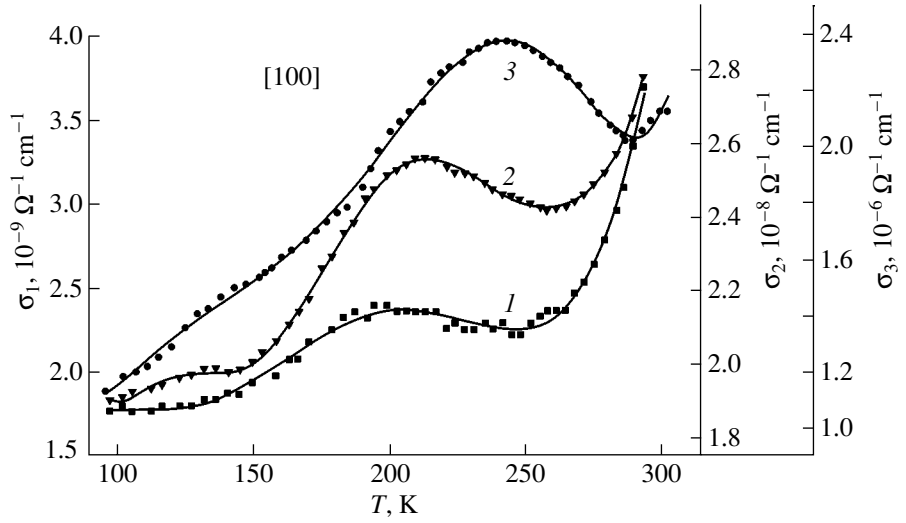

Fig. 5. Temperature dependences of the electrical conductivity of β-BaB_2O_4 in the [100] direction measured in the range 90–300 K at frequencies of (*1*) 1 kHz, (*2*) 10 kHz, and (*3*) 1 MHz.

as a consequence, with a complex charge transfer mechanism.

β-BaB_2O_4 crystallizes in a trigonal structure with six formula units in a cell. The unit cell of β-BaB_2O_4 consists of $(B_3O_6)^{3-}$ anion groups, which form nearly planar rings arranged perpendicular to the polar *c* axis. These rings are rigid and stable formations with strong interatomic coupling. The rings are linked with one another by weak ionic Ba–O bonds through the Ba^{2+} cation [4, 8]. Studies of the electronic structure of β-BaB_2O_4 and LiB_3O_5 [9] showed that the band gap is ΔE = 6.43 eV in β-BaB_2O_4 and 7.78 eV in LiB_3O_5. The reason the band gap ΔE of β-BaB_2O_4 is smaller than that of LiB_3O_5 is that the $(B_3O_6)^{3-}$ anion groups are practically isolated in the crystal lattice of β-BaB_2O_4, whereas in LiB_3O_5 the $(B_3O_7)^{5-}$ anion groups are fairly strongly bonded. Thus, Ba^{2+} ions can move freely in the (001) plane of the β-BaB_2O_4 crystal. This fact apparently accounts for the anisotropy in the electrical properties of β-BaB_2O_4.

The frequency dependence of the electrical conductivity of β-BaB_2O_4 obtained by us can be tentatively explained by assuming that, in addition to the ionic conduction, the hopping charge transfer mechanism

operates. This conjecture is corroborated by the data from [8], according to which the nonlinear optical properties of β-BaB_2O_4 are due to charge transfer from oxygen to boron in the $(B_3O_6)^{3-}$ metaborate anion.

Similar experimental results have been obtained for the frequency dependence of the electrical conductivity of $TlInS_2$, which also has a layered crystal structure [10]. An analysis of the dispersion curve of the electrical conductivity leads to the conclusion [10] that the charge transfer in $TlInS_2$ is affected through the hopping mechanism.

Hence, carrier transport in β-BaB_2O_4 crystals is realized by several different mechanisms, which accounts for the comparatively complex dependence of the electrical conductivity on temperature and on the frequency of the measuring electric field.

It should be pointed out that the values $\sigma = 7 \times 10^{-10}\ \Omega^{-1}\ cm^{-1}$ and $\varepsilon = 10.4$ obtained by us at room temperature along the [001] direction at a frequency of 1 kHz agree with the data presented in [7] for the same direction, namely, $\sigma \sim 10^{-10}\ \Omega^{-1}\ cm^{-1}$ and $\varepsilon \approx 10$.

REFERENCES

1. R. Frohlich, Z. Kristallogr. **168**, 109 (1984).
2. Chen Chuangtian, Wu Licheng, and Li Rikang, J. Cryst. Growth **99**, 790 (1990).
3. D. Eimerl, L. Davis, S. Velsko, *et al.*, J. Appl. Phys. **62** (5), 1968 (1987).
4. W. R. Bosenberg, L. K. Cheng, and C. L. Tang, Appl. Phys. Lett. **54**, 13 (1989).
5. A. U. Sheleg, N. P. Tekhanovich, T. I. Dekola, *et al.*, Neorg. Mater. **33** (11), 1366 (1997).
6. A. U. Sheleg, E. M. Zub, L. A. Stremoukhova, and A. M. Luginets, Fiz. Tverd. Tela (St. Petersburg) **39** (6), 1038 (1997) [Phys. Solid State **39**, 932 (1997)].
7. L. I. Ivleva, D. T. Kiselev, Yu. S. Kuz'minkov, and N. M. Polozkov, Neorg. Mater. **24** (7), 1153 (1988).
8. L. I. Ivleva, I. T. Gorgadze, Yu. S. Kuz'minkov, *et al.*, Neorg. Mater. **25** (5), 804 (1989).
9. R. H. French, J. W. Ling, F. S. Ohuchi, and C. T. Chen, Phys. Rev. B **44** (16), 8496 (1991).
10. S. N. Mustafaev, M. M. Asadov, and V. A. Ramazanzade, Fiz. Tverd. Tela (St. Petersburg) **38** (1), 14 (1996) [Phys. Solid State **38**, 7 (1996)].

Translated by G. Skrebtsov

Physics of the Solid State, Vol. 46, No. 3, 2004, pp. 466–469. Translated from Fizika Tverdogo Tela, Vol. 46, No. 3, 2004, pp. 453–456.

DEFECTS, DISLOCATIONS, AND PHYSICS OF STRENGTH

Effect of Gamma Irradiation on Internal Friction in Lithium Tetraborate

V. S. Bilanych*, N. D. Baĭsa, V. M. Rizak*, and I. M. Rizak*****

** Uzhgorod National University, Podgornaya ul. 46, Uzhgorod, 88000 Ukraine*

*** Kiev Institute of Management and Information Technologies, National Aviation University, Kiev, Ukraine*

**** Dnepropetrovsk National University, Nauchnyĭ pr. 13, Dnepropetrovsk, 49050 Ukraine*

Received June 20, 2003

Abstract—The effect of gamma irradiation on the mechanical properties of lithium tetraborate $Li_2B_4O_7$ in the single-crystal and vitreous states is investigated. It is found that, after irradiation of the $Li_2B_4O_7$ single crystal, the temperature range of the dissipative process initially occurring at 380–420 K becomes broader and the fine structure of the peak in the temperature dependence of the internal friction $Q^{-1}(T)$ undergoes a substantial transformation. After irradiation of the vitreous $Li_2B_4O_7$ sample, the increase in the internal friction, which is characteristic of the onset of the α relaxation in this material, is not observed in the dependence $Q^{-1}(T)$ up to a temperature of 570 K. It is shown that the mechanical properties of the irradiated samples are almost completely recovered after annealing at 570 K for 1 h. © *2004 MAIK "Nauka/Interperiodica".*

1. INTRODUCTION

Owing to its unique combination of physical properties, lithium tetraborate $Li_2B_4O_7$ has found wide application in acoustic devices, nonlinear optics, and dosimetry [1, 2]. Lithium tetraborate single crystals are resistant to gamma irradiation with an energy of 1.3 MeV and an irradiation dose $\Phi \le 10^6$ Gy [3]. To the best of our knowledge, the radiation stability of vitreous lithium tetraborate has not been investigated before. Earlier investigations into the infralow-frequency mechanical properties of lithium tetraborates in single-crystal [4] and vitreous [5] states have revealed that these materials undergo thermally activated dissipative processes due to the structural mobility in the cation subsystem.

According to the data available in the literature on the radiation resistance of lithium tetraborate single crystals [3], it is reasonable to assume that the formation of radiation-induced structural defects in lithium tetraborate should be accompanied by changes in the internal friction Q^{-1} and the shear modulus G.

It is known that lithium tetraborate can be obtained in the crystalline and vitreous states depending on the cooling conditions of the melt [6, 7]. By performing the measurements with crystalline and vitreous lithium tetraborate samples, which are identical in terms of their stoichiometry and background impurities, it is possible to correctly compare the obtained results and to investigate the influence of the degree of structural ordering of these compounds on the observed effects.

The purpose of this work was to investigate the effect of gamma irradiation on the infralow-frequency internal friction of lithium tetraborate in the vitreous and single-crystal states.

2. SAMPLE PREPARATION AND EXPERIMENTAL TECHNIQUE

Lithium tetraborate was synthesized in the single-crystal and vitreous states according to the procedures described in [6, 7]. Samples in the form of rectangular parallelepipeds $2 \times 2 \times 20$ mm in size were prepared from both single crystals oriented along the [001] direction and vitreous ingots. The vitreous and single-crystal states of the $Li_2B_4O_7$ compound were confirmed using x-ray powder diffraction, differential thermal analysis, and x-ray microanalysis.

The internal friction Q^{-1} and shear modulus G were measured on an automated experimental setup based on a torsion pendulum [8]. The dependences $Q^{-1}(T)$ and $G(T)$ were obtained during heating at a constant rate $v_h = 37.5$ K h^{-1} under continuous repeated deformation of the sample. The samples were irradiated on a radiation stand [9] of an M-30 microtron at the Institute of Electron Physics, National Academy of Sciences of Ukraine. The energy of bremsstrahlung gamma quanta was 15 MeV, and the absorbed radiation dose was 2.5×10^5 Gy. The dose was determined accurate to within 6%.

3. RESULTS AND DISCUSSION

Figures 1 and 2 show the dependences $Q^{-1}(T)$ and $G(T)$ for the initial, irradiated, and thermally cycled samples of the $Li_2B_4O_7$ compound in the single-crystal and vitreous states. It can be seen from Fig. 1 that the dependences $Q^{-1}(T)$ of the single-crystal samples exhibit a maximum in the temperature range 390–410 K. This maximum is characterized by the height

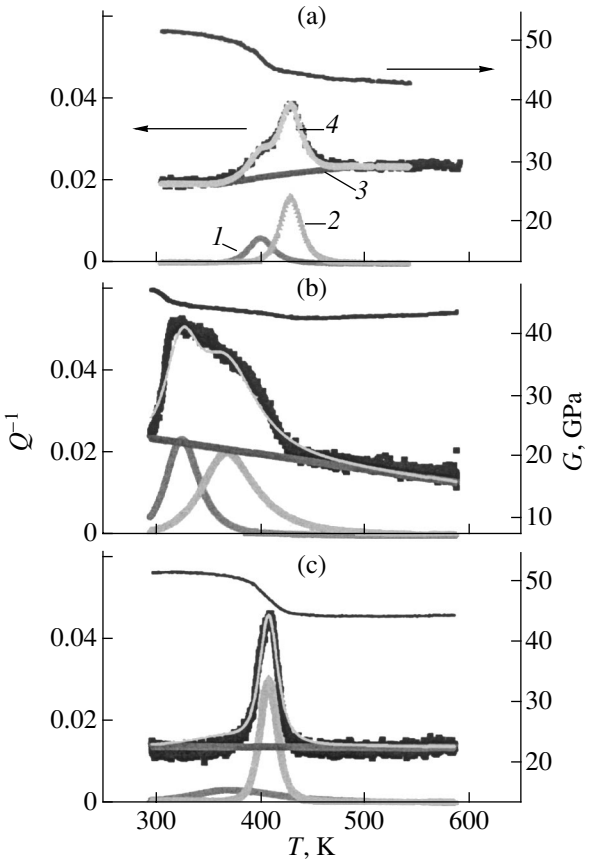

Fig. 1. Temperature dependences of the internal friction Q^{-1} and the shear modulus G of the $Li_2B_4O_7$ single crystal (along the [001] crystallographic direction) at a frequency of 80 mHz and a strain amplitude of 8×10^{-5}: (a) the initial sample, (b) the irradiated sample after the first heating, and (c) the irradiated sample after the second heating. (*1*, *2*) Approximated peaks of the internal friction, (*3*) the background of the internal friction, and (*4*) the resultant curve.

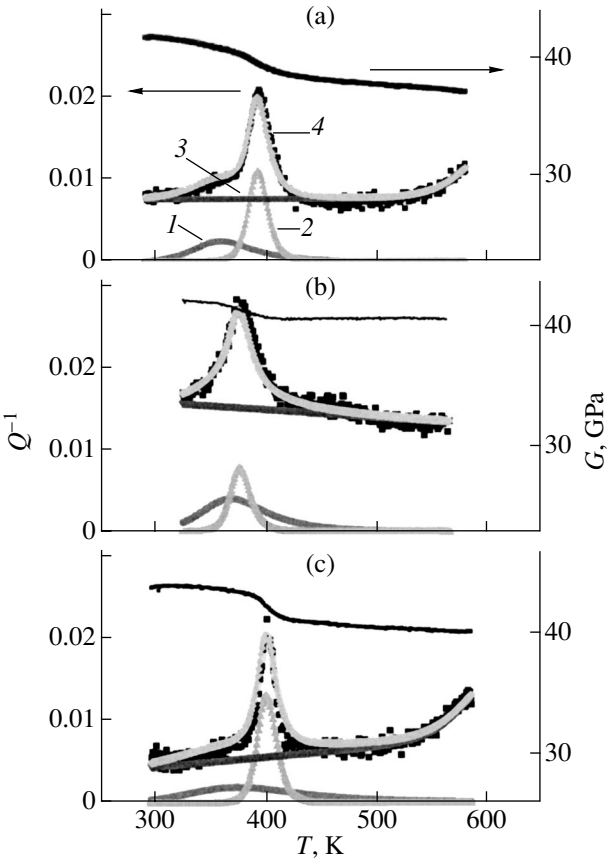

Fig. 2. Temperature dependences of the internal friction Q^{-1} and the shear modulus G of vitreous $Li_2B_4O_7$ at a frequency of 30 mHz and a strain amplitude of 8×10^{-5}: (a) the initial sample, (b) the irradiated sample after the first heating, and (c) the irradiated sample after the third heating. (*1*, *2*) Approximated peaks of the internal friction, (*3*) the background of the internal friction, and (*4*) the resultant curve.

Q_m^{-1}, temperature T_m, and the relative change in the shear modulus $\Delta G/G$. The irradiation of the samples substantially affects the shape and parameters of this anomaly. Upon irradiation, the position of the maximum of the internal friction, which is clearly pronounced for the initial sample, remains almost unchanged, whereas the weak shoulder observed in the curve $Q^{-1}(T)$ of the initial sample in the temperature range 360–380 K transforms into a clear maximum with height $Q_m^{-1} = 40 \times 10^{-3}$. The above changes in the dependence $Q^{-1}(T)$ indicate that the temperature range and intensity of the dissipative process increase significantly.

The variations in the mechanical properties of the samples exposed to irradiation also manifest themselves in the temperature dependences of the shear modulus. It can be seen from Fig. 1 that, after irradiation, the dependences $G(T)$ exhibit two jumps in the shear modulus at temperatures $T < 360$ K and $380 < T < 450$ K, whereas the curve $G(T)$ of the initial sample is characterized by only one jump. Judging from our results and the specific features in the manifestation of the dissipative processes in the curves of the internal friction in solids [10], the internal friction Q^{-1} of the irradiated $Li_2B_4O_7$ crystal in the temperature range 300–450 K has two maxima corresponding to the defects of the shear modulus $\Delta G/G$.

It can be seen from Fig. 2 that the irradiation also affects the mechanical properties of vitreous $Li_2B_4O_7$. The irradiated glass sample, like the initial sample, is characterized by a maximum in the internal friction. However, in the former case, the width of the maximum is two times greater and its position is somewhat shifted toward the low-temperature range. The dependences $G(T)$ exhibit only one jump in the temperature range $350 < T < 420$ K. It should be noted that no increase in the internal friction is observed in the curves $Q^{-1}(T)$ of

Parameters of the mathematical approximation of two peaks in the dependences $Q^{-1}(T)$ of irradiated lithium tetraborate samples

Parameters	Single-crystal $Li_2B_4O_7$		Vitreous $Li_2B_4O_7$	
	the first peak	the second peak	the first peak	the second peak
T_m, K	325	368	365	373
$Q_m^{-1} \times 10^3$	23	21	4	8
E, eV	0.48	0.64	0.41	1.45

the irradiated glass samples up to 600 K, whereas the internal friction Q^{-1} of the initial sample increases at temperatures $T > 520$ K (Fig. 2) due to the softening of the $Li_2B_4O_7$ glass [5].

It follows from the analysis of the experimental data that, upon irradiation of the $Li_2B_4O_7$ single crystal, the fine structure of the peak of the internal friction undergoes a substantial transformation and the temperature range of the dissipative process becomes broader. For the irradiated $L_2B_4O_7$ glass, the increase in the mechanical loss and compliance, which is characteristic of the softening of the initial unirradiated sample, does not occur in the temperature range 500–600 K.

In order to separate the maxima observed in the dependence $Q^{-1}(T)$ and to determine their parameters, we performed a mathematical treatment of the results obtained. As was shown in our previous works [5, 11], the shapes of the maximum in the internal friction and the attendant jump in the shear modulus in the temperature dependences of these parameters for the $Li_2B_4O_7$ compound characterize the changes in the mechanical properties during relaxation processes. The peaks observed in the dependence $Q^{-1}(T)$ were mathematically treated in the approximation of Debye relaxation [12].

For the purpose of approximating the peaks in the dependence $Q^{-1}(T)$, we used the relationship [13]

$$Q^{-1} = Q_m^{-1}\frac{2\omega\tau}{1+\omega^2\tau^2}, \quad (1)$$

where $\omega = 2\pi\nu$, ν is the frequency of deformation of the sample, Q^{-1} is the current value of the internal friction, Q_m^{-1} is the peak value of the internal friction, and τ is the relaxation time. The dependence $\tau(T)$ for the thermal activation of a kinetic particle is described by the relationship

$$\tau = \tau_0 \exp\left(\frac{E}{kT}\right), \quad (2)$$

where E is the activation energy, k is the Boltzmann constant, T is the temperature, and τ_0 is the preexponential factor. Taking into account relationship (2), we obtain the following expression for calculating the dependence $Q^{-1}(T)$ in the vicinity of the peak:

$$Q^{-1}(T) = Q_m^{-1}\frac{2\exp\frac{E}{k}\left(\frac{1}{T}-\frac{1}{T_m}\right)}{1+\exp\frac{2E}{k}\left(\frac{1}{T}-\frac{1}{T_m}\right)}. \quad (3)$$

The calculated maxima of the internal friction upon their extrapolation by two peaks of the dependence $Q^{-1}(T)$ were fitted using relationship (3). Then, we determined the parameters T_m, Q_m^{-1}, and E. For the mathematical treatment used in this case, the calculated dependences $Q^{-1}(T)$ agree well with the experimental data. From the mathematical approximation of the two peaks in the dependence $Q^{-1}(T)$ of irradiated samples and the background curve, we determined the parameters of the first and the second peaks (see table).

It can be seen that the peaks in the dependences $Q^{-1}(T)$ of the irradiated $Li_2B_4O_7$ single crystal are characterized by approximately equal heights but different activation energies and temperatures at the maxima. Since the height of the first peak appreciably increases upon irradiation of the sample, we can assume that gamma irradiation leads to an additional generation of sources of dissipation of the energy of an external mechanical field in the crystal. For the glass samples, the height of the first peak after irradiation remains small but the width of the peak in the dependence $Q^{-1}(T)$ increases significantly as the result of an increase in the number of kinetic particles responsible for the appearance of the peak in $Q^{-1}(T)$ for the unirradiated material.

An increase in the dissipation intensity and in the area under the peak in the curve $Q^{-1}(T)$ for the irradiated samples indicates that the concentration and (or) the amplitude of vibrations of kinetic particles (sources of absorption of the mechanical energy) increase under the action of a harmonically varying external mechanical field [10, 12].

In order to reveal the possibility of recovering the initial properties of this material after irradiation, we measured the dependences $Q^{-1}(T)$ and $G(T)$ for the irradiated samples during thermal cycling with holding at a temperature of 570 K for 1 h. It can be seen from Fig. 1 that, after the first cycle of heat treatment, the mechanical properties of the crystal are restored to a large extent. After the first heating, the low-temperature peak in the dependence $Q^{-1}(T)$ and the temperature range of the dissipative process decrease considerably and only one jump is observed in the dependence $G(T)$.

Upon annealing, the mechanical properties of the vitreous $Li_2B_4O_7$ sample are also restored. For example, after the first annealing cycle, the width of the peak in the dependence $Q^{-1}(T)$ decreases, whereas after the second annealing cycle, the internal friction in the

range $T > 520$ K increases again. This is associated with the onset of the α relaxation in this material.

4. CONCLUSIONS

Thus, the results obtained in this work are as follows.

The general regularities of the influence of gamma irradiation on the infralow-frequency mechanical properties of the $Li_2B_4O_7$ compound in the single-crystal and vitreous states were investigated.

It is found that gamma irradiation of the $Li_2B_4O_7$ single crystal leads to a substantial broadening of the temperature range of the dissipative process occurring at temperatures of 300–450 K. An increase in the temperature range and in the intensity of dissipation manifests itself as an abrupt increase in the height of the peak of the internal friction in the vicinity of 320 K. As a result, the intensity of absorption of the mechanical energy of the irradiated $Li_2B_4O_7$ crystal is redistributed. For vitreous $L_2B_4O_7$, the irradiation causes a broadening of the peak of the internal friction due to the activation of the mobility of lithium ions. After irradiation of the $Li_2B_4O_7$ glass, the increase in the internal friction, which is characteristic of the onset of the α elaxation in this material, is not observed in the dependence $Q^{-1}(T)$ in the temperature range 520–570 K. Heating of the irradiated samples from room temperature to 570 K and annealing at this temperature for 1 h lead to the recovery of the mechanical properties of the $Li_2B_4O_7$ compound in the single-crystal and vitreous states.

ACKNOWLEDGMENTS

We would like to thank V.M. Holovey and O.O. Parlag (Institute of Experimental Physics, National Academy of Sciences of Ukraine) for supplying the irradiated lithium tetraborate samples used in our measurements.

REFERENCES

1. J. Filipiak, A. Majchrowski, and T. Lukasiewicz, Arch. Acoust. **19** (1), 131 (1994).
2. R. Komatsu, T. Sugawara, and K. Sassa, Appl. Phys. Lett. **70** (26), 3492 (1997).
3. Ya. V. Burak, B. N. Kopko, I. T. Lyseĭko, *et al.*, Izv. Akad. Nauk SSSR, Neorg. Mater. **25** (7), 1226 (1989).
4. V. S. Bilanych, N. D. Baĭsa, V. M. Rizak, *et al.*, Fiz. Tverd. Tela (St. Petersburg) **45** (1), 80 (2003) [Phys. Solid State **45**, 82 (2003)].
5. V. S. Bilanych, N. D. Baĭsa, V. M. Rizak, *et al.*, Ukr. Fiz. Zh. **47** (4), 396 (2002).
6. I. I. Turok, V. M. Holovey, and P. P. Puga, Ukr. Patent No. 32242.
7. A. B. Kaplun and A. B. Meshalkin, Izv. Ross. Akad. Nauk, Neorg. Mater. **35** (11), 1349 (1999).
8. V. S. Bilanych, Candidate's Dissertation (Uzhgorod. Univ., Uzhgorod, 1993).
9. V. Masljuk, O. Parlag, and J. Gajnish, in *Proceedings of the Workshop 97 on Nuclear Engineering* (Prague, 1997), Vol. 4, p. 1463.
10. *Proceedings of the IV All-Union Scientific Conference on Relaxation Phenomena in Solids*, Ed. by V. S. Postnikov (Metallurgiya, Moscow, 1968).
11. V. M. Rizak, I. M. Rizak, N. D. Baisa, *et al.*, in *Proceedings of IFM-10* (Madrid, 2001), p. 219.
12. *Physical Acoustics: Principles and Methods*, Ed. by W. P. Mason (Academic, New York, 1966; Mir, Moscow, 1969), Vol. 3, Part A.
13. I. V. Andreev, Yu. S. Balashov, and V. A. Lomovskoĭ, Fiz. Khim. Stekla **10** (3), 296 (1984).

Translated by N. Korovin

Physics of the Solid State, Vol. 46, No. 3, 2004, pp. 470–473. Translated from Fizika Tverdogo Tela, Vol. 46, No. 3, 2004, pp. 457–460.

DEFECTS, DISLOCATIONS, AND PHYSICS OF STRENGTH

Stress Relaxation in an $Zr_{52.5}Ti_5Cu_{17.9}Ni_{14.6}Al_{10}$ Bulk Metallic Glass

O. P. Bobrov, S. N. Laptev, and V. A. Khonik

Voronezh State Pedagogical University, ul. Lenina 86, Voronezh, 394043 Russia

e-mail: khonik@vspu.ac.ru

Received August 5, 2003

Abstract—The isothermal relaxation of stresses in a bulk metallic glass is measured at temperatures below the glass transition point. The kinetic law of relaxation is determined. It is argued that the stress relaxation in the temperature range covered is due to the irreversible structural relaxation oriented by an external stress and characterized by a distribution of activation energies.

1. INTRODUCTION

Traditionally, metallic glasses in the form of ribbons up to 50 μm thick have been prepared by melt spinning at a quenching rate of the order of 10^6 K/s. In recent years, much progress toward an understanding of the physicochemical factors favorable for supercooling of melts and the development of methods for their purification have stimulated intensive research into so-called bulk metallic glasses produced by melt quenching in the form of plates (rods) up to several centimeters in thickness (diameter) [1, 2]. In this case, the quenching rate R depends on the preparation technique and falls in the range $10^{-1} < R < 10^3$ K/s. It can be assumed that such a large difference between the quenching rates of metallic glass ribbons and bulk metallic glasses should lead to a substantial difference in the kinetics of plastic deformation of these objects. However, this problem still remains to be investigated.

Unlike metallic glass ribbons, bulk metallic glasses, as a rule, are very stable against crystallization at temperatures above the glass transition point T_g. This manifests itself in a large difference $\Delta T = T_C - T_g$ (where T_C is the temperature of the onset of crystallization) and makes it possible to perform long-term experiments at temperatures higher than the glass transition point T_g. Most likely, that is the reason why particular interest has been expressed by researchers in the kinetics of atomic mobility in bulk metallic glasses under external stresses in this temperature range. However, there are only a few works dealing with the kinetics of plastic deformation of bulk metallic glasses at temperatures below the glass transition point T_g. In this respect, mention should be made of the recent work by Berlev *et al.* [3], who studied the nonisothermal creep of the $Zr_{52.5}Ti_5Cu_{17.9}Ni_{14.6}Al_{10}$ bulk metallic glass. It is evident that these investigations are necessary for elucidating both the mechanism of plastic deformation of bulk metallic glasses and the role of the quenching rate as a factor affecting the kinetics of formation of a noncrystalline structure.

It is generally agreed that, at $T > T_g$, glasses are in a metastable equilibrium state and no spontaneous irreversible structural relaxation occurs. In the temperature range 400 K $< T < T_g$, metallic glass ribbons undergo intensive irreversible structural relaxation. It is this process that is responsible for the occurrence of the so-called homogeneous plastic flow at these temperatures. The main regularities of the homogeneous plastic flow for metallic glass ribbons have been reliably established and can be summarized as follows: (i) the shear viscosity η linearly increases with an increase in the duration of the isothermal test [4–6]; (ii) the rate of increase in the viscosity $\partial\eta/\partial t$ decreases with an increase in the temperature [4, 5]; and (iii) the strain rate rapidly decreases with an increase in the duration of annealing preceding the onset of the test [7]. These (and other) regularities in the homogeneous plastic flow under conditions of different mechanical tests are described within a unified model of directional structural relaxation. According to this model, the homogeneous plastic flow is a result of irreversible structural relaxation oriented by an external stress (see [8–10] and references therein).

The lack of reliable information on the kinetics of homogeneous flow of bulk metallic glasses at $T < T_g$ and the necessity of assessing the applicability of the above model of directional structural relaxation for the interpretation of the mechanism of deformation of these materials determined the main objectives of the present work. In our experimental investigations, we used the stress relaxation method, which was successfully applied earlier to the study of the kinetics of plastic deformation of various materials.

1063-7834/04/4603-0470$26.00

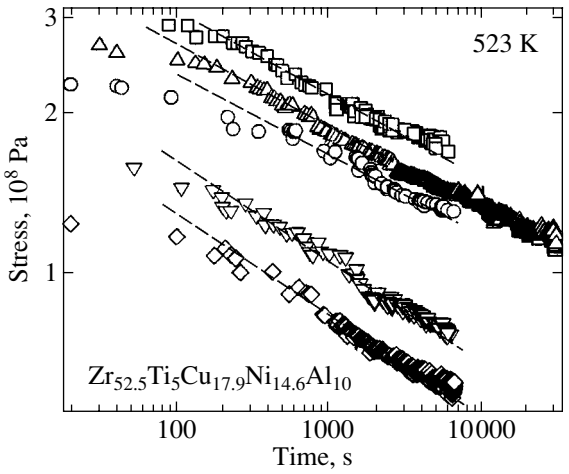

Fig. 1. Stress relaxation curves in the logarithmic coordinates at T = 523 K for different initial stresses. Dashed straight lines are drawn with the same slope.

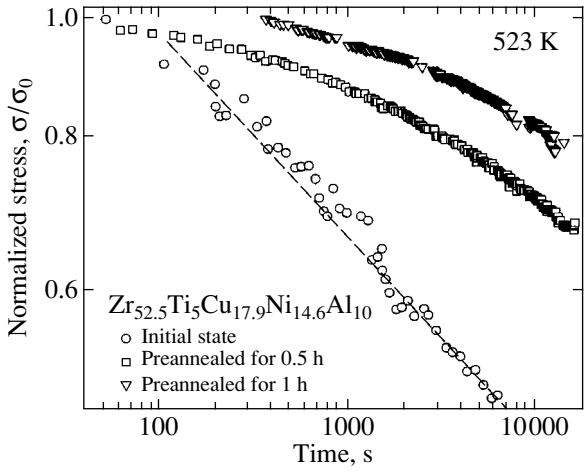

Fig. 2. Effect of preliminary annealing for 0.5 and 1 h on the kinetics of stress relaxation at T = 523 K.

2. SAMPLE PREPARATION AND EXPERIMENTAL TECHNIQUE

An initial alloy of composition $Zr_{52.5}Ti_5Cu_{17.9}Ni_{14.6}Al_{10}$ (at. %) was prepared by induction levitation melting under vacuum at a residual pressure of $\approx 10^{-2}$ Pa. A glass sample was produced by quenching the melt from a silica tube into a copper mold under vacuum at a residual pressure of $\approx 5 \times 10^{-3}$ Pa. The ingots thus prepared were $2 \times 5 \times 60$ mm in size. The quenching rate of melts was directly measured using a thermocouple placed in a quenching cavity. Since the glass transition temperature could not be determined experimentally during quenching of the melt, the quenching rate R in the glass transition range was estimated from the inequality $80 < R < 800$ K/s. According to these estimates, the quenching rate was at least three orders of magnitude less than that used in preparing metallic glass ribbons through melt spinning. The absence of crystalline phases in the ingots was carefully checked using x-ray diffraction analysis.

The tensile testing with stress relaxation was performed with samples prepared in the form of strips (thickness, 100–150 μm; width, ≈0.8 mm; length ≈30 mm) cut from the ingots with the use of a diamond disk. The stress relaxation in the samples was measured on a string-type tensile-testing machine. In these measurements, the samples were electrostatically excited at a fundamental resonant frequency f in the course of extension. The applied stress σ was calculated from the formula $\sigma = 4\rho f^2 l^2$, where l is the sample length (as a rule, it is approximately equal to 20 mm) and $\rho = (6.69 \pm 0.03) \times 10^3$ kg/m^3 is the material density determined by hydrostatic weighing. The rigidity in the tension of the testing machine was considerably greater than that of the samples. The testing procedure involved heating of the sample to the test temperature at a rate of 30 K/min (at a temperature 15–20 K below the test temperature, the heating rate was decreased to 3–5 K/min in order to attain an isotherm without overheating), isothermal treatment for 20 s, loading of the sample to a required stress for approximately 10 s, and measurement of the stress relaxation with the use of a computer for 8×10^3–3×10^4 s. The measurements were carried out at temperatures of 523, 548, 573, 598, and 623 K. According to differential scanning calorimetry, the glass transition temperature of the metallic glass sample at a heating rate of 4 K/min was approximately equal to 640 K.

3. RESULTS AND DISCUSSION

Figure 1 shows typical stress relaxation curves in logarithmic coordinates on both axes for five different initial stresses at T = 523 K. Examination of the stress relaxation curves revealed the following features in the relaxation kinetics: (i) in the time range $t > 200$–400 s, the logarithm of the stress linearly decreases with an increase in the logarithm of the time, whereas at shorter times $t < 200$–400 s, the stress relaxation curve deviates from linearity and $\ln\sigma$ decreases more slowly with the increase in $\ln t$ as compared to that at longer times, and (ii) the slope of the $\ln t$–$\ln\sigma$ straight lines at long times does not depend on the initial stress and remains constant at the given temperature. Similar results were obtained for other test temperatures. Moreover, it was found that the slope of the straight lines increases with an increase in the temperature T.

Since the relaxation kinetics of metallic glass ribbons under quasi-static loading is uniquely determined by the kinetics of irreversible structural relaxation [10], it is expedient to evaluate the effect of preliminary heat treatment on the kinetics of stress relaxation in the bulk glass. Figure 2 depicts the relaxation curves of the normalized stress σ/σ_0 (where σ_0 is the initial relaxation stress) at T = 523 K for the initial sample and the sam-

ples subjected to annealing for 0.5 and 1 h prior to loading. It can be seen from Fig. 2 that, first, the preliminary annealing leads to a drastic decrease in the relaxation depth. This decrease indicates that the irreversible structural relaxation affects the kinetics of stress relaxation. Second, the dependences $\ln\sigma$–$\ln t$ become nonlinear at long times t, so that the derivative $\partial\ln\sigma/\partial\ln t$ increases with an increase in the time t. Similar data were obtained for other test temperatures.

Taking into account that the kinetics of stress relaxation in metallic glass ribbons can be adequately described within the model of directional structural relaxation [10–12] and that the preliminary annealing has a profound effect on the relaxation kinetics (Fig. 2), we attempted to apply this model for analyzing the results of our investigations. In the framework of the aforementioned model of directional structural relaxation [9, 10], the isothermal stress relaxation at $t \gg \tau$ (where τ is the effective time of annealing prior to loading) can be described by the relationship

$$\partial\ln\sigma/\partial\ln t = -kTMN_0\Omega C, \quad (1)$$

where k is the Boltzmann constant, M is the effective Young modulus for the sample–machine system, N_0 is the volume density of irreversible structural relaxation centers per unit range of activation energies, Ω is the volume in which an elementary relaxation act occurs, and C is a constant accounting for the orienting effect of the external stress on the kinetics of accumulation of macroscopic deformation. The effective time of preliminary annealing can be estimated as $\tau = \tau_h + \tau_T$, where τ_h is the effective time specified by a finite rate of heating to the test temperature and τ_T is the time of annealing at the test temperature prior to loading. As was shown by Fursova and Khonik [13], the first term τ_h can be estimated from the expression

$$\tau_h = \nu^{-1}\exp(A/k), \quad (2)$$

where ν is the frequency of attempts to overcome the activation barrier and A is a constant dependent on the frequency ν and the heating rate $\dot{T}$. According to the numerical calculations performed in [14], these parameters have the following values: $A = 2.98\times10^{-3}$ eV/K at $\nu = 10^{13}$ s^{-1} and $\dot{T} = 30$ K/min [14]. After substituting these parameters into expression (2), we obtain $\tau_h = 98$ s and $\tau = 118$ s.

Hence, it follows from relationship (1) that, in the logarithmic coordinates at times $t \gg 118$ s, the kinetic curves of stress relaxation should straighten and the slope of the straight lines should increase with an increase in the temperature. As was noted above, the relaxation curves become straight lines at time $t > 200$–400 s (which is in reasonable agreement with the estimates obtained for the effective time τ) and their slope actually increases with an increase in the temperature T. It should be remembered that relationship (1) was deduced under the assumption that relaxation centers in the structure are activated only once and disappear as a result of activation. Since this relationship adequately describes the experimental results, we can assume that the processes responsible for stress relaxation in the bulk metallic glass are irreversible in character. This assumption is confirmed by the drastic decrease in the rate of stress relaxation after preliminary annealing (Fig. 2). Note also that the condition $t \gg \tau$ for linearity of the $\ln t$–$\ln\sigma$ curves is not satisfied at $\tau = 0.5$ and 1 h; in this case, the stress relaxation curves actually deviate from linearity (Fig. 2).

Let us now dwell on another important circumstance. We introduce the shear viscosity $\eta = \sigma/3\dot{\varepsilon}$ and take into account that, in the case of stress relaxation tests, the strain rate can be written in the form $\dot{\varepsilon} = -\dot{\sigma}/M$. Then, from relationship (1), it is easy to obtain the expression

$$\eta = t/3kTN_0\Omega C. \quad (3)$$

From analyzing expression (3), it follows that, first, the linear behavior of the dependences $\ln\sigma(\ln t)$ corresponds to a linear increase in the shear viscosity with an increase in the duration of the isothermal experiment and, second, the rate of increase in the viscosity $\partial\eta/\partial t$ is inversely proportional to the test temperature, because the product $N_0\Omega C$ increases with an increase in the temperature T. As was already mentioned, these two regularities have been reliably established for metallic glass ribbons.

The results obtained allow us to evaluate the apparent energy spectrum of the irreversible relaxation processes responsible for stress relaxation and to compare it with the spectrum reconstructed from the experimental data (taken from [3]) on the nonisothermal creep of the same metallic glass. Relationship (1) was derived under the assumption that the activation energies are characterized by a flat-spectrum. Within this approximation, it is assumed that, since the isothermal experiment corresponds to a relatively narrow range of activation energies, the volume density of relaxation centers satisfies the condition $N_0 \approx \text{const} \neq f(E)$. The lower ($E_{\min}$) and upper ($E_{\max}$) limits of this range of activation energies can be estimated from the following expressions [9, 10]:

$$\begin{aligned} E_{\min} &= kT\ln\nu\tau, \\ E_{\max} &= kT\ln\nu(\tau + t_{\max}), \end{aligned} \quad (4)$$

where $t_{\max}$ is the duration of the isothermal experiment. By assuming that the quantities Ω and C do not depend on the activation energy, the sought spectrum of activation energies can be represented up to a constant by the product $N_0\Omega C$ as a function of the activation energy. This product can be calculated from relationship (1) and the experimental slopes $\partial\ln\sigma/\partial\ln t$ at long times t. Setting again $\nu = 10^{13}$ s^{-1}, we reconstruct the energy spectrum in the form of five horizontal segments (cor-

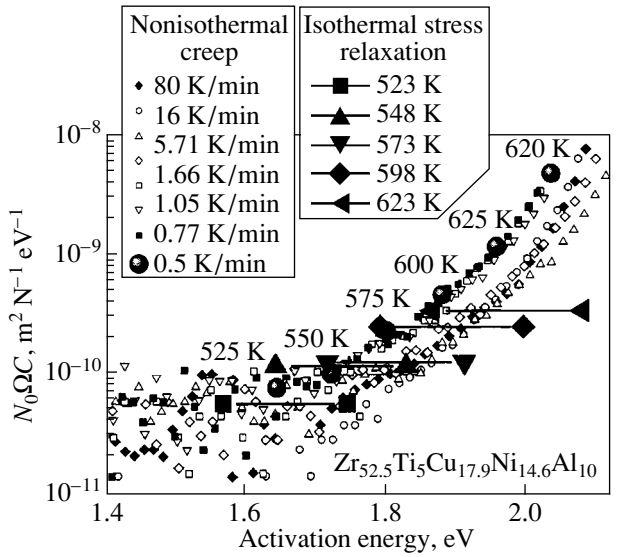

Fig. 3. Graphs illustrating the reconstruction of the apparent energy spectra of irreversible structural relaxation from experimental data on the isothermal stress relaxation (horizontal segments) and in the framework of the directional structural relaxation model from experimental data on the nonisothermal creep according to two independent methods [3].

responding to five test temperatures), as is shown in Fig. 3. Figure 3 also presents the energy spectra reconstructed in the framework of the directional structural relaxation model from experimental data on the nonisothermal creep according to two independent methods. One method is based on the processing of kinetic data on the strain rate at a constant heating rate, and the other method involves an analysis of the isothermal dependences of the shear viscosity on the heating rate [3]. As can be seen from Fig. 3, all three independent methods of reconstructing the energy spectra offer results that are in good agreement with each other. This suggests that, first, the irreversible structural relaxation is responsible for plastic deformation in the temperature range 400 K < T < T_g and, second, the laws of plastic deformation derived in the framework of the directional structural relaxation model are also consistent. It is worth noting that both the energy spectrum and the magnitudes of the product $N_0\Omega C$ for bulk metallic glasses are very similar to those for metallic glass ribbons [3]. This circumstance allows us to assume that even a very large change (by a factor of no less than one thousand) in the quenching rate has only a slight effect on the volume density of relaxation centers frozen in the structure upon quenching of the melt. Further investigations in this direction seem to be promising for the elucidation of the microscopic nature of relaxation centers.

4. CONCLUSIONS

Thus, in this work, the isothermal stress relaxation in a bulk glass was measured for the first time. It was revealed that, after a short transient period, the logarithm of the stress linearly decreases with an increase in the logarithm of the time, which corresponds to a linear increase in the shear viscosity with an increase in the duration of the isothermal experiment. The rate of increase in the viscosity decreases with an increase in the temperature, and the stress relaxation depth drastically decreases with an increase in the time of annealing prior to loading. These regularities are identical to those observed for metallic glass ribbons and can be explained in the framework of the directional structural relaxation model as a result of irreversible structural relaxation with distributed activation energies.

ACKNOWLEDGMENTS

This work was supported in part by the US Civilian Research and Development Foundation for the Independent States of the Former Soviet Union (CRDF), grant no. RP1-2320-VO-02.

REFERENCES

1. W. L. Johnson, MRS Bull. **24** (10), 42 (1999).
2. A. Inoue, *Bulk Amorphous Alloys: Practical Characteristics and Applications* (Transtech., Uetikon–Zuerich, 1999), Materials Science Foundation, Vol. 6.
3. A. E. Berlev, O. P. Bobrov, K. Csach, *et al.*, J. Appl. Phys. **92** (10), 5898 (2002).
4. A. I. Taub and F. Spaepen, Acta Metall. **28** (12), 1781 (1980).
5. A. I. Taub and F. E. Luborsky, Acta Metall. **29** (12), 1939 (1981).
6. A. Hernando, O. V. Nielsen, and V. Madurga, J. Mater. Sci. **20**, 6 (1985).
7. A. I. Taub and F. Spaepen, Scr. Metall. **13** (3), 195 (1979).
8. V. A. Khonik, A. T. Kosilov, V. A. Mikhailov, and V. V. Sviridov, Acta Mater. **46** (10), 3399 (1998).
9. V. A. Khonik, Phys. Status Solidi A **177** (1), 173 (2000).
10. V. A. Khonik, J. Non-Cryst. Solids **296** (3), 47 (2001).
11. O. P. Bobrov, A. T. Kosilov, and V. A. Khonik, Fiz. Tverd. Tela (St. Petersburg) **38** (4), 1086 (1996) [Phys. Solid State **38**, 601 (1996)].
12. O. P. Bobrov, V. A. Khonik, and V. S. Zhelezny, J. Non-Cryst. Solids **223** (3), 241 (1998).
13. Yu. V. Fursova and V. A. Khonik, Philos. Mag. Lett. **82** (10), 567 (2002).
14. V. A. Khonik, K. Kitagawa, and H. Morii, J. Appl. Phys. **87** (12), 8440 (2000).

Translated by O. Borovik-Romanova

Physics of the Solid State, Vol. 46, No. 3, 2004, pp. 474–478. Translated from Fizika Tverdogo Tela, Vol. 46, No. 3, 2004, pp. 461–465.

MAGNETISM AND FERROELECTRICITY

Influence of an In-Plane Magnetic Field on Pulsed Magnetization Reversal of Single-Crystal $(Bi,Lu)_3(Fe,Ga)_5O_{12}$ Films with (210) Orientation

V. V. Randoshkin*, A. M. Saletsky*, N. N. Usmanov*, and D. B. Chopornyak**

**Moscow State University, Vorob'evy gory, Moscow, 119992 Russia*

e-mail: sam@rector.msu.ru

***Research Institute of Nuclear Physics, Moscow State University, Vorob'evy gory, Moscow, 119992 Russia*

Received June 20, 2003

Abstract—Photoresponse was used to study the influence of an in-plane magnetic field on pulsed magnetization reversal and relaxation in single-crystal $(Bi,Lu)_3(Fe,Ga)_5O_{12}$ films with (210) orientation. Dynamic domain structures were observed using high-speed photography. *© 2004 MAIK "Nauka/Interperiodica".*

The response time of magnetooptical devices can be shortened using single-crystal, bismuth-containing garnet-ferrite (GF) films with rhombic magnetic anisotropy [1]. In particular, domain walls moving at a high velocity (≥300 m/s) were observed in $(Bi,Lu)_3(Fe,Ga)_5O_{12}$ films grown on $Gd_3Ga_5O_{12}$ substrates with (210) orientation [2].

In this work, we study the influence of pulsed (H_p) and in-plane (H_{in}) magnetic fields on pulsed magnetization reversal and relaxation in single-crystal (210)-oriented $(Bi,Lu)_3(Fe,Ga)_5O_{12}$ films.

The studies were carried out on a magnetooptical setup in which photoresponse is used to detect magnetization reversal [3]. A He–Ne laser beam was focused on the sample surface onto a spot 1 mm in diameter. The angle between the polarizer and analyzer transmission axes was such that amplitude contrast of the domain structure was observed. A FÉU-51 photomultiplier was used as a photodetector. The photomultiplier signal was fed to the inputs of an analog-to-digital converter and a two-channel oscilloscope.

The dynamic domain structures formed during pulsed magnetization reversal have also been observed using high-speed laser photography [4]. For illumination, a pulsed laser (wavelength $\lambda = 510$ nm) was used with a pulse duration of 10 ns.

A dc (bias) magnetic field H_b, directed normally to the film, was produced by a coil, inside which the sample for study was placed. The pulsed magnetic field (PMF) that caused magnetization reversal of the sample was applied in the opposite direction. This field was produced by a six-turn pancake coil 2 mm in diameter. The rise and fall times of a magnetic field pulse were 7 and 40 ns, respectively. Pulses of the magnetization-reversing field were synchronized with a laser firing pulse using a G5-67 pulser.

The magnetization was reversed through the motion of the so-called magnetic-moment flip wave [5–10] or of the end domain wall (EDW) [11] at large and small H_p amplitudes, respectively. The experiments were carried out under conditions corresponding to the latter mechanism. We note that, due to PMF inhomogeneity, the EDW was dome-shaped rather than planar as in [12]; moreover, its curvature increased with the magnetic field.

The in-plane magnetic field H_{in}, which was applied perpendicular to the projection of the easy magnetization axis (EMA) onto the film plane, was induced by a pair of Helmholtz coils between which the sample was placed.

We consider the data obtained on a sample (previously studied in [3, 11]) with the following parameters: film thickness $h = 11$ μm, EMA tilt angle $\theta = 46°$, saturation magnetization $4\pi M_s = 43$ G, dimensionless Gilbert damping parameter $\alpha \approx 0.01$, and constant of uniaxial magnetic anisotropy $K_u = 1050$ erg/cm^3.

In the initial state, the field $H_b = 23$ Oe was applied to the sample; this field exceeded the film saturation field $H_s = 17$ Oe and was not changed during the experiments.

The dimensionless damping parameter was determined from the ferromagnetic resonance (FMR) linewidth. The FMR signal contained two strong lines (which indicates the layered structure of the Bi-containing GF film), as well as a number of modes of the spin wave resonance. The strongest line was associated with the basic film volume. We note that the value of α indicated above can be overestimated because of the film inhomogeneity. The value of $H_K - 4\pi M_s$ was also determined from the FMR data, more specifically, from the resonant fields corresponding to the external magnetic fields oriented perpendicular and parallel to the

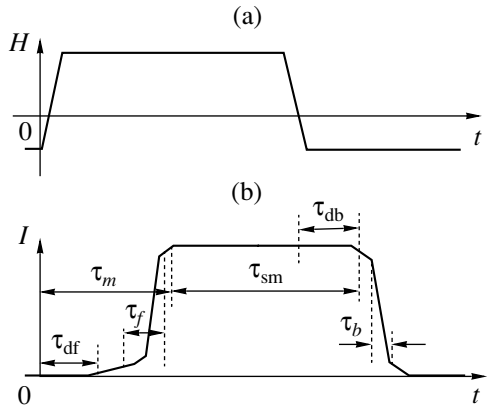

Fig. 1. Schematic diagrams of (a) a magnetization-reversal pulse and (b) the photoresponse signal; τ_{df} is the delay time of magnetization reversal, τ_f is the rise time of the photoresponse signal, τ_m is the magnetization reversal time, τ_{db} is the delay time of the drop in the photoresponse signal, τ_{sm} is the sample residence time in the remagnetized (single-domain) state, and τ_b is the fall time of the photoresponse signal.

film plane. The value of $4\pi M_s$ was calculated from the bubble domain collapse field (the effect of the EMA tilt was neglected).

Figure 1 schematically shows the magnetization-reversal pulse and the photoresponse signal. The photoresponse signal was characterized by the following parameters: the delay time of magnetization reversal τ_{df} the rise time τ_f of the photoresponse signal, the magnetization reversal time τ_m, the delay time τ_{db} of the photoresponse signal drop, the sample residence time τ_{sm} in the remagnetized (single-domain) state, and the fall time τ_b of the photoresponse signal. These parameters were determined at the levels of 0.05 (τ_{df}), 0.1–0.9 (τ_f, τ_b), and 0.95 (τ_m, τ_{sm}, τ_{db}) of the amplitude value.

Figure 2 shows the dependences of the delay time of the photoresponse signal drop on the in-plane magnetic field for a fixed amplitude H_p = 78 Oe and various values of the pulse duration τ_p. We can see that the $\tau_{db}(H_{in})$ dependences are asymmetric with respect to the vertical axis and have local maxima. The deepest minimum is observed at τ_p = 1.10 μs (curve *1* in Fig. 2); the minimum delay time increases with the duration of a magnetic field pulse to ~1.2 μs (curve *4*). The maximum delay time ($\tau_{db} \approx 2.0$ μs) remains practically unchanged as the pulse duration is varied from 1.10 μs (curve *1* in Fig. 2) to 30.0 μs (curve *4*).

To understand the physical nature of the maxima in the $\tau_{db}(H_{in})$ curves (Fig. 2) and their asymmetry, it needs to be determined whether the EDW collapses completely when it reaches the opposite film surface during a magnetic field pulse or EDW fragments survive near this surface after the pulse. In the former case, it is highly probable that the mechanism of magnetization reversal is the same after a magnetic field pulse and during it. The only difference is that the effective magnetic field is $-H_b$ rather than $H_p - H_b$. In the case where EDW fragments survive, the delay of the backward

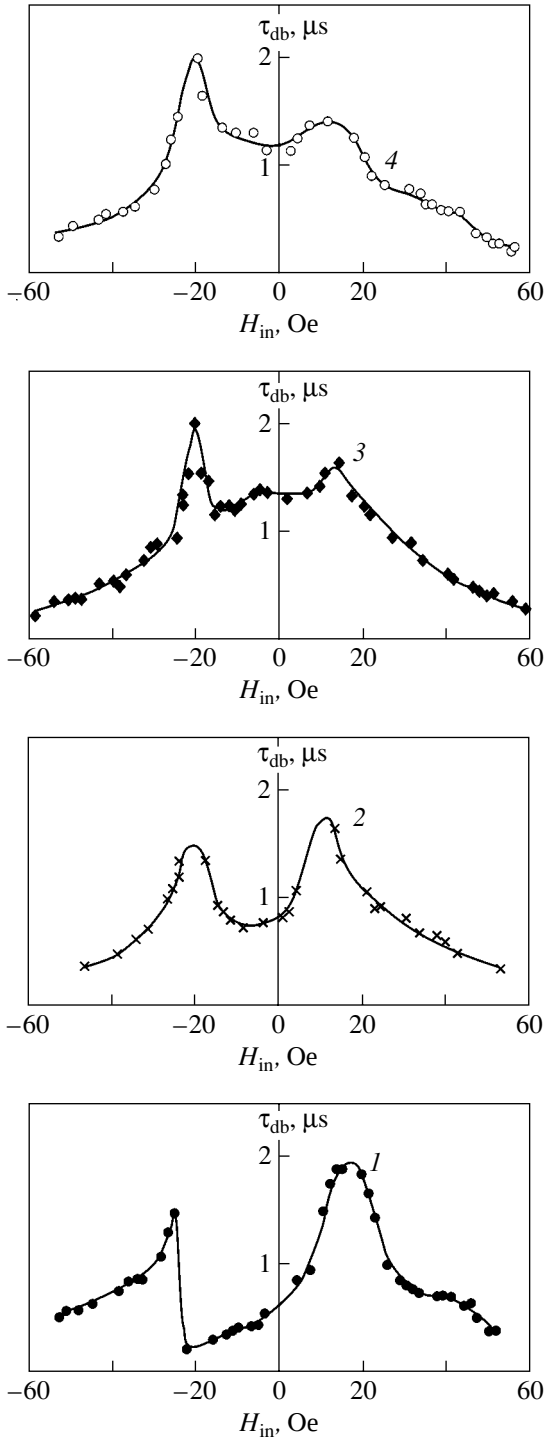

Fig. 2. Dependences of the delay time of the drop in the photoresponse signal on the in-plane magnetic field for PMF amplitude H_p = 78 Oe and various durations of the field pulse: (*1*) τ_p = 1.10, (*2*) 1.35, (*3*) 1.45, and (*4*) 30.0 μs.

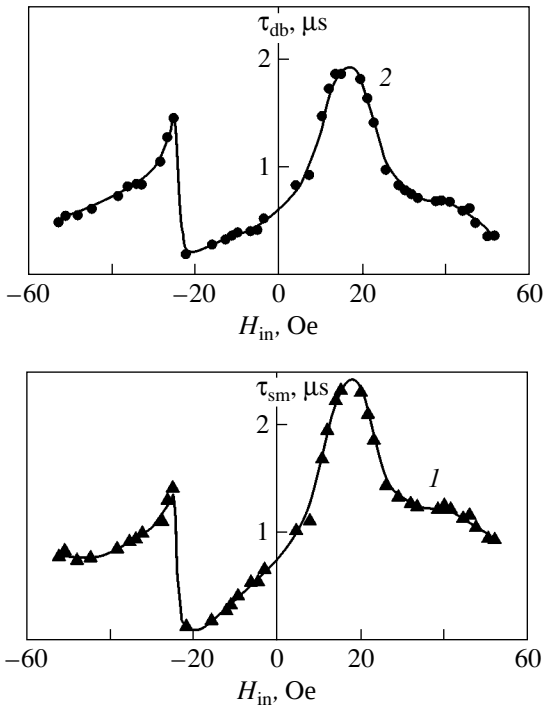

Fig. 3. Dependences of (*1*) the sample residence time τ_{sm} in the magnetized single-domain state and (*2*) the delay time of the drop in the photoresponse signal τ_{db} on the in-plane magnetic field for PMF amplitude H_p = 78 Oe and field pulse duration τ_p = 1.10 μs.

motion of the EDW can be associated with the mechanisms discussed in [13–18].

The asymmetry in the $\tau_{db}(H_{in})$ curves (Fig. 2) is not unexpected; asymmetric curves have also been observed for other effects [19–22] and can be explained by the fact that the effective internal magnetic field has a nonzero in-plane component [23].

Figure 3 shows the delay time of the photoresponse signal drop and the sample residence time in the remagnetized single-domain state as a function of the in-plane magnetic field H_{in} for a fixed amplitude and the minimum pulse duration of the magnetic field used in the experiment. We can see that the curves are similar in shape and have maxima for both directions of the in-plane magnetic field and that the delay time of magnetization reversal makes up a major fraction of the sample residence time in the remagnetized single-domain state.

Figure 4 shows the dependences of the delay time of magnetization reversal, the rise time of the photoresponse signal, the magnetization reversal time, and the fall time of the photoresponse signal on the in-plane magnetic field H_{in} for a magnetic field pulse of the same amplitude as that in Fig. 3 and of the maximum duration used in the experiment (τ_p = 30.0 μs).

A comparison between curve *1* in Fig. 4 and curve *4* in Fig. 2, as well as between curves *2* and *4* in Fig. 4,

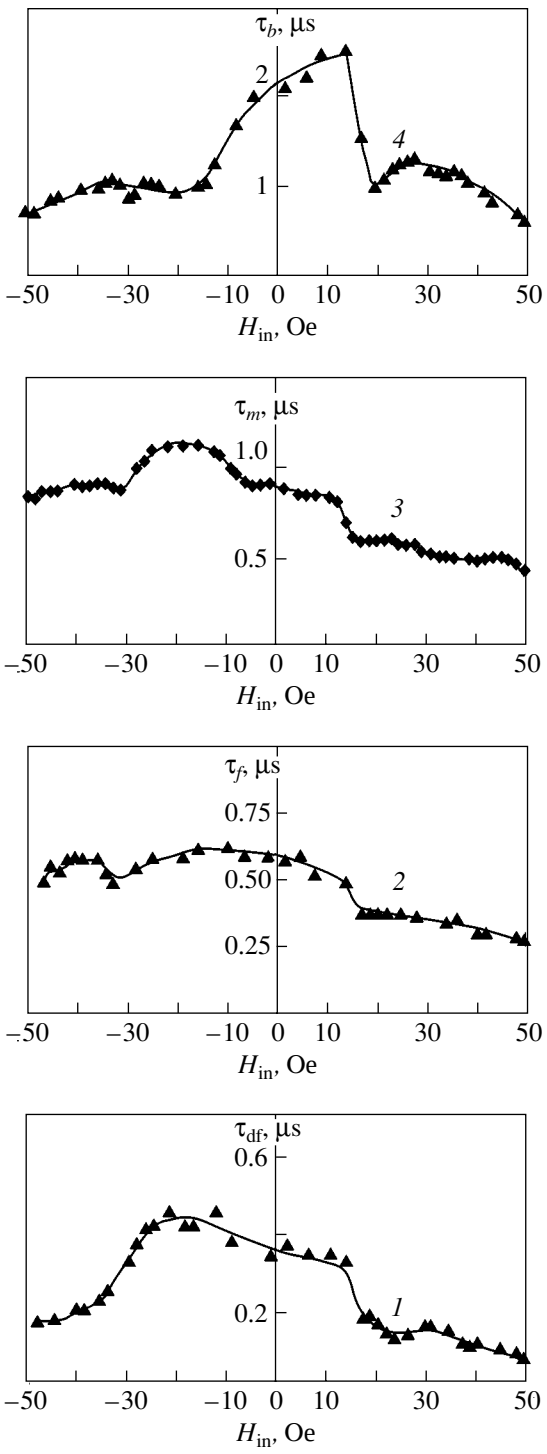

Fig. 4. Dependences of (*1*) the delay time of magnetization reversal τ_{df}, (*2*) the rise time of the photoresponse signal τ_f, (*3*) the magnetization reversal time τ_m, and (*4*) the fall time of the photoresponse signal τ_b on the in-plane magnetic field for PMF amplitude H_p = 78 Oe and field pulse durations τ_p = 30 μs.

permits the conclusion that the processes that proceed during the rise time and fall time of the magnetization-reversal pulse are most likely similar. The fact that the

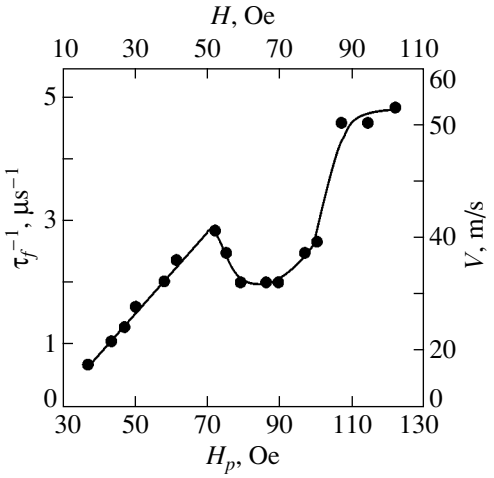

Fig. 5. Dependence of the inverse rise time τ_f^{-1} of the photoresponse signal on the magnetic field pulse amplitude H_p and the effective field H.

local maxima in curve *1* in Fig. 4 and curve *4* in Fig. 2 are more pronounced than those in curves *2* and *4* in Fig. 4 can be explained by the difference in the magnitude of the effective magnetic fields (23 and 55 Oe in the former and latter cases, respectively). We can see from Fig. 4 that the in-plane magnetic fields at which the local maxima are observed in the $\tau_{db}(H_{in})$, $\tau_f(H_{in})$, and $\tau_m(H_{in})$ curves and in the $\tau_b(H_{in})$ curve are opposite in direction.

Figure 5 shows the dependence of the inverse rise time of the photoresponse signal on the magnetic field pulse amplitude H_p and on the effective magnetic field $H = H_p - H_b$. Assuming that the rise time is controlled by the time of EDW motion through the film thickness, we can estimate the average EDW velocity as

$$V \approx h/\tau_f.$$

The values of V are shown in Fig. 5. At first glance, the shape of the initial portion of the $V(H)$ curve in Fig. 5 seems typical of uniaxial magnets with damping parameter $\alpha < 1$ [24]; namely, the initial portion near the origin is linear and there is a nonlinear portion with negative differential mobility. The value of H_p corresponding to the end of the initial linear portion of the $V(H)$ curve (where the motion of the domain wall becomes unsteady) is very high for Bi-containing GF films, in which there are no fast-relaxing ions. This fact can be explained by an increase in α in the presence of an external or an internal effective magnetic field in the film plane [22, 25–29]. The fact that the nonlinear portion of the $V(H)$ curve is followed by a portion with a differential mobility exceeding the initial one, as well as by a saturation portion, is explained by the domain wall motion being accompanied by the emission of spin waves, which initiate local rotation of the magnetization in front of the moving wall [22, 30, 31].

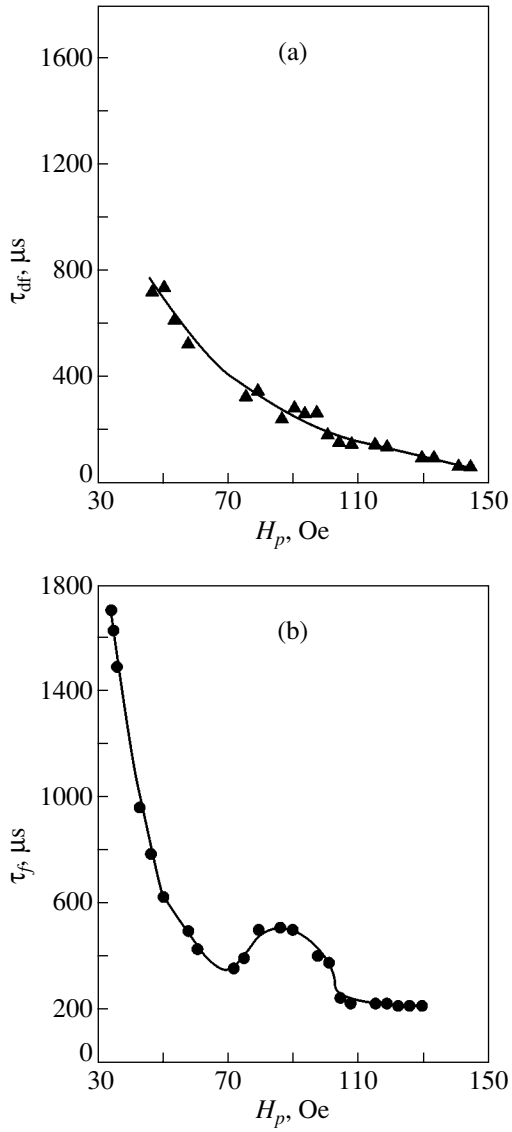

Fig. 6. Dependences of (a) the delay time of magnetization reversal τ_{df} and (b) the rise time τ_f of the photoresponse signal on the PMF amplitude H_p.

The fact that the average EDW velocity (Fig. 5) is approximately three times lower than the velocity of the EDW passing through the film center [11] can be explained as resulting from irregular EDW motion.

Figure 6 shows the dependences of the delay time of magnetization reversal and the rise time of the photoresponse signal on the PMF amplitude. We can see that τ_{df} decreases monotonically as H_p increases (Fig. 6a), while the $\tau_f(H_p)$ curve (Fig. 6b) is inverse with respect to the curve shown in Fig. 5.

Thus, the data obtained in this study of (210)-oriented single-crystal $(Bi,Lu)_3(Fe,Ga)_5O_{12}$ films subjected to pulsed magnetization reversal allow the following conclusions.

(i) The film magnetization reversal at the leading and trailing edges of the magnetic field pulse is realized via the same mechanism.

(ii) The delay time of magnetization reversal decreases monotonically as the effective magnetic field increases.

(iii) In the range of effective magnetic fields where $H/4\pi M_s \approx 2$, the film magnetization reversal is realized via EDW nucleation and motion.

(iv) The dependences of the delay time of the drop in the photoresponse signal after the end of the magnetic-field pulse and of the sample residence time in the remagnetized single-domain state on the in-plane magnetic field have maxima for both directions of the field.

(v) The EDW velocity vs. effective magnetic field curve consists of an initial linear portion corresponding to EDW steady motion, a nonlinear portion corresponding to EDW unsteady motion, a portion with increased differential mobility, and a saturation portion corresponding to EDW motion with the emission of spin waves.

REFERENCES

1. V. V. Randoshkin and A. Ya. Chervonenkis, *Applied Magnetooptics* (Énergoatomizdat, Moscow, 1990).
2. A. M. Balbashov, A. S. Logginov, and E. P. Shabanov, Zh. Tekh. Fiz. **61** (6), 159 (1991) [Sov. Phys. Tech. Phys. **36**, 680 (1991)].
3. V. V. Randoshkin, A. M. Saletsky, and N. N. Usmanov, Fiz. Tverd. Tela (St. Petersburg) **44** (4), 717 (2002) [Phys. Solid State **44**, 744 (2002)].
4. N. N. Usmanov, E. N. Il'icheva, and A. G. Shishkov, Vestn. Mosk. Univ., Ser. 3: Fiz., Astron. **36**, 74 (1995).
5. A. S. Logginov and G. S. Nepokoĭchitskiĭ, Pis'ma Zh. Éksp. Teor. Fiz. **35** (1), 22 (1982) [JETP Lett. **35**, 27 (1982)].
6. L. P. Ivanov, A. S. Logginov, and G. S. Nepokoĭchitskiĭ, Zh. Éksp. Teor. Fiz. **84** (3), 1006 (1983) [Sov. Phys. JETP **57**, 583 (1983)].
7. L. P. Ivanov, F. V. Lisovskiĭ, A. S. Logginov, and G. S. Nepokoĭchitskiĭ, Fiz. Mnogochast. Sist., No. 6, 75 (1984).
8. N. N. Kudel'kin, A. M. Prokhorov, V. V. Randoshkin, *et al.*, Dokl. Akad. Nauk SSSR **281** (4), 848 (1985) [Sov. Phys. Dokl. **30**, 307 (1985)].
9. M. V. Logunov, V. V. Randoshkin, and V. B. Sigachev, Fiz. Tverd. Tela (Leningrad) **29** (8), 2247 (1987) [Sov. Phys. Solid State **29**, 1296 (1987)].
10. M. V. Logunov and V. V. Randoshkin, Fiz. Tverd. Tela (Leningrad) **30** (2), 378 (1988) [Sov. Phys. Solid State **30**, 215 (1988)].
11. V. V. Randoshkin, A. M. Saletsky, N. N. Usmanov, and D. B. Chopornyak, Fiz. Tverd. Tela (St. Petersburg) **44** (5), 862 (2002) [Phys. Solid State **44**, 899 (2002)].
12. A. P. Gubarev, V. V. Randoshkin, V. B. Sigachev, and A. Ya. Chervonenkis, Zh. Tekh. Fiz. **55** (7), 1393 (1985) [Sov. Phys. Tech. Phys. **30**, 803 (1985)].
13. R. V. Telesnin, A. M. Balbashov, A. F. Martynov, *et al.*, Pis'ma Zh. Éksp. Teor. Fiz. **7** (16), 1001 (1981) [JETP Lett. **7**, 10 (1981)].
14. S. Uba, A. Maziewski, and J. J. Simsova, J. Phys. C: Solid State Phys. **16** (12), L383 (1983).
15. V. V. Osiko, V. V. Randoshkin, V. B. Sigachev, and M. I. Timoshechkin, Zh. Tekh. Fiz. **54** (12), 2423 (1984) [Sov. Phys. Tech. Phys. **29**, 1433 (1984)].
16. A. Maziewski, M. Tekiela, and P. Gornert, Acta Phys. Pol. **68** (1), 15 (1985).
17. M. Kisielewski, A. Maziewski, and P. Gornert, J. Phys. D: Appl. Phys. **20** (2), 222 (1987).
18. V. V. Randoshkin, A. F. Martynov, and A. Ya. Chervonenkis, Fiz. Tverd. Tela (St. Petersburg) **38** (5), 1592 (1996) [Phys. Solid State **38**, 875 (1996)].
19. M. V. Logunov and V. V. Randoshkin, Pis'ma Zh. Tekh. Fiz. **12** (1), 28 (1986) [Sov. Tech. Phys. Lett. **12**, 12 (1986)].
20. F. V. Lisovskiĭ, A. S. Logginov, G. S. Nepokoĭchitskiĭ, and T. V. Rozanova, Pis'ma Zh. Éksp. Teor. Fiz. **45** (7), 339 (1987) [JETP Lett. **45**, 430 (1987)].
21. V. V. Randoshkin and Yu. N. Sazhin, Zh. Tekh. Fiz. **66** (8), 83 (1996) [Tech. Phys. **41**, 790 (1996)].
22. V. V. Randoshkin, Fiz. Tverd. Tela (St. Petersburg) **39** (8), 1421 (1997) [Phys. Solid State **39**, 1260 (1997)].
23. V. V. Randoshkin, V. A. Polezhaev, Yu. N. Sazhin, *et al.*, Pis'ma Zh. Tekh. Fiz. **28** (14), 38 (2002) [Tech. Phys. Lett. **28**, 595 (2002)].
24. V. V. Randoshkin, Fiz. Tverd. Tela (St. Petersburg) **37** (3), 652 (1995) [Phys. Solid State **37**, 355 (1995)].
25. V. V. Randoshkin, V. B. Sigachev, V. I. Chani, and A. Ya. Chervonenkis, Fiz. Tverd. Tela (Leningrad) **31** (7), 70 (1989) [Sov. Phys. Solid State **31**, 1138 (1989)].
26. M. V. Logunov, V. V. Randoshkin, and Yu. N. Sazhin, Fiz. Tverd. Tela (Leningrad) **32** (5), 1456 (1990) [Sov. Phys. Solid State **32**, 849 (1990)].
27. V. V. Randoshkin and M. V. Logunov, Fiz. Tverd. Tela (St. Petersburg) **36** (12), 3498 (1994) [Phys. Solid State **36**, 1858 (1994)].
28. V. V. Randoshkin, Pis'ma Zh. Tekh. Fiz. **21** (23), 64 (1995) [Tech. Phys. Lett. **21**, 979 (1995)].
29. V. V. Randoshkin, A. M. Galkin, Yu. A. Durasova, *et al.*, Vestn. Mosk. Univ., Ser. 3: Fiz., Astron., No. 5, 62 (2002).
30. V. V. Randoshkin, Fiz. Tverd. Tela (St. Petersburg) **37** (10), 3056 (1995) [Phys. Solid State **37**, 1684 (1995)].
31. V. V. Randoshkin, Izv. Vyssh. Uchebn. Zaved., Fiz. **7**, 9 (1997).

Translated by A. Kazantsev

Physics of the Solid State, Vol. 46, No. 3, 2004, pp. 479–483. Translated from Fizika Tverdogo Tela, Vol. 46, No. 3, 2004, pp. 466–470.

MAGNETISM AND FERROELECTRICITY

Effect of Internal Stray Fields on the High-Frequency Properties of Magnetic Thin Films

N. G. Chechenin

Skobeltsin Research Institute of Nuclear Physics, Moscow State University, Vorob'evy gory, Moscow, 119899 Russia

Received April 10, 2003; in final form, July 3, 2003

Abstract—The effect of internal stray fields generated in nanocrystalline ultrasoft films with inducted uniaxial magnetic anisotropy (due to an arbitrary orientation of the crystallites) on the high-frequency magnetic susceptibility is considered. It is demonstrated that internal stray fields comparable to the field of magnetic anisotropy can lead to a substantial broadening and a bimodal form of the magnetic resonance. The effect of the internal stray fields should be taken into account in the analysis of the dispersion properties limiting the range of working frequencies of ferromagnetic films. © *2004 MAIK "Nauka/Interperiodica".*

1. INTRODUCTION

The development of the technology of magnetic carriers with a high density of elements (>100 Gbit/cm^2) requires high rates of recording and reading. This can be achieved in circuits based on magnetic films with a saturation induction $B_s > 2.0$ T and a high susceptibility in the frequency range $f > 1$ GHz [1–3]. Similar requirements have been imposed on magnetic inductors and transformer cores in integrated circuits of high-frequency devices used in microelectronics [4]. Although permalloy is widely used in microelectronic devices, it is not suited for these purposes because of the relatively low induction ($B_s < 1.6$ T for $Ni_{45}Fe_{55}$). Nanocrystalline thin films of the type Fe–*X*–N [5, 6] (where *X* = Ta, Cr, Zr, and other elements of the alloy) or Co–Ge–Ni [7–9], prepared by sputtering or electrochemical deposition, are promising materials capable of meeting strict design requirements.

The range of working frequencies of these films is limited by the frequency and width of the ferromagnetic resonance. In practice (see, for example, [10]), the width of ferromagnetic resonance is related to the damping parameter in the Landau–Lifshitz phenomenological equation [11]. The results obtained in the present work demonstrate that, apart from the contribution of dissipative sources (characteristic of crystalline and polycrystalline ferromagnets) to the width of ferromagnetic resonance, nanocrystalline ferromagnets are characterized by a contribution due to the local angular dispersion of the magnetization vector (the so-called micromagnetic ripple). Hoffmann [12] proved that the parameters of the micromagnetic ripple are determined by the exchange interaction, induced magnetic anisotropy, crystallite sizes, and averaging of the orientation of crystallites in the film.

These variations in the local magnetization lead to a specific variation in the contrast (ripple contrast) of the out-of-focus image of the Lorentz transmission electron microscopy in the Fresnel mode [13, 14]. The period and magnitude of the contrast can be analytically related in a sufficiently rough approximation to the period λ and the amplitude of the angular dispersion β_0 of the magnetization vector [15, 16]. In our previous works [16, 17], we showed that, depending on the microstructure of the soft magnetic films, the period λ can vary from one hundred nanometers to several microns and the amplitude of angular oscillations β_0 changes from tenths to several degrees.

In this work, the parameters of the micromagnetic ripple were related to the electromagnetic response of a thin ferromagnetic film in the range of ferromagnetic resonance and the contribution of this factor to the width and the shape of the ferromagnetic resonance was estimated.

2. THE STRAY FIELD

The angular dispersion of the magnetization vector in nanocrystalline ferromagnets is caused by an inferior averaging of the crystalline magnetic anisotropy, which leads to a local deviation of the easy magnetization axis from the mean direction. As has been shown by Hoffmann [12], this leads to the generation of an internal stray field. It is assumed that the mean direction of the easy magnetization axis in a film located in the *xy* plane is parallel to the *x* axis. For simplicity, we assume that the deviation of the local easy magnetization axis from the mean direction is governed by a harmonic law; i.e., the local magnetization has the form

$$\begin{aligned} Mx &= M\cos\beta, \quad My = M\sin\beta, \\ \beta &= \beta_0\sin(2\pi x/\lambda). \end{aligned} \tag{1}$$

For a thin film, the *z* component of the magnetization is completely compensated for by the demagnetizing field. In expression (1), we took into account only the longitudinal oscillations of the magnetization vector,

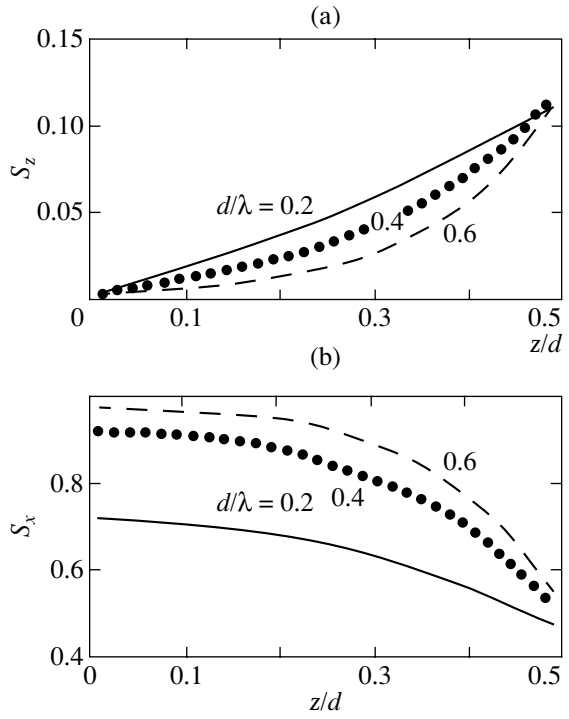

Fig. 1. Variation in the S factors calculated from relationships (a) (7) and (b) (9) and characterizing the variation in the stray field along the film thickness.

because the transversal oscillations are energetically unfavorable because of the large contribution from the exchange interaction [13]. Moreover, we assume that the variations in M are homogeneous throughout the film thickness. Hence, we can write the following relationship for the inducted magnetic charge:

$$\rho(\mathbf{r}) = -\mathrm{div}\,\mathbf{M} = M\sin\beta(\partial\beta/\partial x) - M\cos\beta(\partial\beta/\partial y) = (\pi M\beta_0^2/\lambda)\sin(4\pi x/\lambda). \quad (2)$$

This implies that the inducted magnetic charges change only along the x axis. For the magnetic potential, we have

$$U = \int \rho(\mathbf{r}')/|\mathbf{r}' - \mathbf{r}_0|\,dV'. \quad (3)$$

The internal stray field can be represented in the form

$$\mathbf{H}_{\mathrm{str}}(\mathbf{r}_0) = -\nabla U. \quad (4)$$

According to relationships (3) and (4), the y component of the internal stray field in a film that has a thickness d and is infinite in the xy plane can be written in the form

$$H_{\mathrm{str},y} = -\partial U/\partial y = -\int_{-\infty}^{\infty}\rho(x')dx'\int_{-d/2}^{d/2}dz' \times \int_{-\infty}^{\infty}dy'\frac{\partial}{\partial y}\left\{\frac{1}{[(x'-x)^2 + (y'-y)^2 + (z'-z)^2]^{1/2}}\right\} = 0 \quad (5)$$

(after differentiation, we obtain an integral of the odd function in symmetric limits).

Since the thickness of the film is finite, no complete compensation of the internal stray field of magnetic charges along the z axis occurs. For the z component of the internal stray field, we have

$$H_{\mathrm{str},z} = -\partial U/\partial z = -\pi M_0\beta_0^2\sin(4\pi x/\lambda) \times \int_{-\infty}^{\infty}\cos(4\pi\chi)d\chi\int_{-\infty}^{\infty}d\xi\int_{d-2z/2\lambda}^{d+2z/2\lambda}\frac{\zeta d\zeta}{[\chi^2+\xi^2+\zeta^2]^{3/2}}, \quad (6)$$

where $\zeta = (z' - z)/\lambda$, $\xi = (y' - y)/\lambda$, and $\chi = (x' - x)/\lambda$. After performing the true integration in formula (6), we obtain the following result:

$$H_{\mathrm{str},z} = -\pi M_0\beta_0^2\sin(4\pi x/\lambda)S_z, \quad (7)$$

$$S_z = (1/4)\exp(-2\pi d/\lambda)\sinh(4\pi z/\lambda). \quad (8)$$

The dependence $S_z(d)$ for different parameters d/λ is shown in Fig. 1a. The values $z = 0$ and 0.5 correspond to the center and the surface of the film. It can be seen that the z component of the internal stray field $H_{\mathrm{str},z}$ vanishes only at the center of the film. In the case when the thickness d exceeds 0.6λ, the z component of the internal stray field becomes negligible.

Similarly, for the x component of the internal stray field, we obtain

$$H_{\mathrm{str},x} = -\pi M_0\beta_0^2\cos(4\pi x/\lambda)S_x(z), \quad (9)$$

where

$$S_x(z) = 2\int_{-\infty}^{\infty}\chi\sin(4\pi\chi)d\chi\int_{-(d+2z)/2\lambda}^{d-2z/2\lambda}d\zeta \times \int_{-\infty}^{\infty}\frac{d\xi}{[\chi^2+\xi^2+\zeta^2]^{3/2}} = \exp[-\pi(d-2z)/\lambda]\sinh[\pi(d-2z)/\lambda] + \exp[-\pi(d+2z)/\lambda]\sinh[\pi(d+2z)/\lambda]. \quad (10)$$

Analysis of the factor $S_x(z)$ (Fig. 1b) shows that the x component of the internal stray field in the surface layer is suppressed. This effect of suppression is small when the film has a thickness $d > 0.6\lambda$.

3. EFFECT OF THE INTERNAL STRAY FIELD ON THE HIGH-FREQUENCY PROPERTIES

Let us assume that a dc magnetic field H_{dc} is applied parallel to the easy magnetization axis and a radio-frequency field H_{rf} is directed perpendicular to the easy magnetization axis in the plane of the film (Fig. 2). The film is located in the xy plane, and the local easy magnetization axis deviates from the x axis through an angle β. The magnetization $\mathbf{M}$ deviates from the x axis

through an angle ϕ, from the z axis through an angle θ, and from the surface of the film through an angle $\psi = 90° - \theta$. In what follows, we will assume that the thickness of the film is considerably less than the skin layer; therefore, the contribution of the losses due to the eddy currents can be disregarded.

The Landau–Lifshitz equation for precession of the magnetic moment can be written in the form

$$d\mathbf{M}/dt = \gamma\mathbf{T} - (\alpha\gamma/M)\mathbf{M}\times\mathbf{T}. \quad (11)$$

Here, the angular momentum is given by the formula

$$\mathbf{T} = \mathbf{M}\times\mathbf{F} = -\mathbf{M}\times\nabla\mathbf{E} \quad (12)$$

and $\mathbf{F} = -\nabla E$ is the generalized force. The free energy can be represented in the form

$$\begin{aligned} E &= K\sin^2(\phi-\beta) - H_{dc}M\cos\psi\cos\phi \\ &- H_{str,x}M\cos\psi\cos\phi - H_{str,z}M\sin\psi \\ &+ H_{rf}M\cos\psi\sin\phi + (1/2)N_zM^2\sin^2\psi. \end{aligned} \quad (13)$$

Here, $\gamma = eg/m_ec = g\mu_B$ is the gyromagnetic factor, e is the electron charge, m_e is the electron mass, c is the velocity of light, $g = 2.023$ is the factor of spectroscopic splitting, α is the damping parameter, K is the anisotropy constant, and $N_z = 4\pi$ is the demagnetizing factor of the film along the z axis. In expression (13), the term related to the exchange energy is absent, because, for longitudinal oscillations of the magnetization with a period greater than the length of the exchange interaction $L_{ex} = 30$–40 nm [18], this contribution, as was mentioned above, is small and leads to only a slight decrease in the amplitude of the angular dispersion [19].

Next, we rewrite the Landau–Lifshitz equation in the spherical coordinates $\{M, \theta, \phi\}$ and obtain the system of differential equations

$$(d\phi/dt)M\cos\psi = \gamma\partial E/\partial\psi - (\alpha\gamma/\cos\psi)\partial E/\partial\phi, \quad (14)$$

$$-(d\psi/dt)M = (\gamma/\cos\psi)\partial E/\partial\phi + \alpha\gamma\partial E/\partial\psi. \quad (15)$$

Then, we assume that $\alpha, \phi, \beta, \psi \ll 1$, H_{str}, H_{dc}, $H_k = 2K/M \ll M$, and $H_{rf} \ll H_{str}$, H_{dc}, H_k. Differentiating expression (14) and using relationship (15), we obtain the following linear differential equation:

$$\begin{aligned} &d^2\phi/dt^2 + \alpha\gamma N_zM(d\phi/dt) + \omega_0^2\phi - \gamma^2\beta N_zMH_k \\ &\quad - \gamma^2N_zMH_{rf} - i\alpha(\partial H_{rf}/\partial t) = 0, \end{aligned} \quad (16)$$

where

$$\omega_0^2 = \gamma^2N_zM(H_{eff} + H_{str,x}), \quad H_{eff} = H_k + H_{dc}. \quad (17)$$

Note that the z component of the stray field $H_{str,z}$ does not enter into relationship (16) and, consequently, does not affect the solution to this equation in the small-angle approximation. Equation (16) has a nontrivial solution under the condition

$$H_{eff} + H_{str,x} > 0. \quad (18)$$

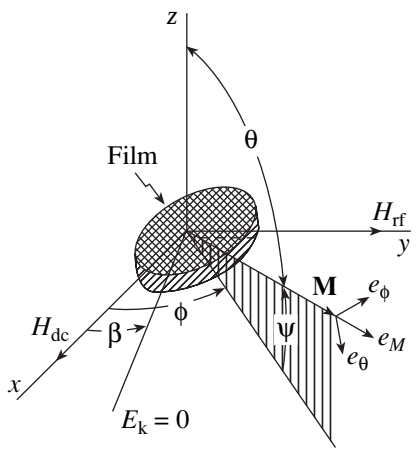

Fig. 2. Geometry of the experiments on high-frequency response in an ac magnetic field oriented perpendicularly to the easy magnetization axis.

If the radio-frequency field obeys the law $H_{rf} = h_{rf}\exp(i\omega t)$, we seek the solution in the form

$$\phi(t) = \phi_0 + \phi_1\exp(i\omega t + i\delta). \quad (19)$$

Substituting $\phi(t)$ into expression (16), we derive the following relationships:

$$\begin{aligned} \phi_0 &= -\beta H_k/(H_{eff} + H_{str,x}), \\ \phi_1 &= \gamma^2h_{rf}N_zM/[(\omega_0^2 - \omega^2)^2 + (\alpha\gamma\omega N_zM)^2]^{1/2}, \\ \tan\delta &= \alpha\gamma\omega N_zM/(\omega_0^2 - \omega^2). \end{aligned} \quad (20)$$

The internal stray field $H_{str,x}$ is a periodic function of x. According to relationship (17), this means that adjacent regions of the film are characterized by different natural frequencies ω_0 and, in the case when the angular dispersion of the magnetization is sufficiently large and $|H_{str,x}| > H_{eff}$, some regions of the film do not exhibit an electromagnetic response.

Similar treatment can be performed for a transverse dc magnetic field under the assumption that H_{dc} is directed normally to the easy magnetization axis and H_{rf} is aligned parallel to the easy magnetization axis. This case can be simply described when $H_{dc} \gg Hk$ and the angle ϕ is close to $\pi/2$, so that $\eta = \pi/2 - \phi \ll 1$. Differential equations (14)–(16) hold if we set $H_{eff} = H_{dc} - H_k$ in relationship (17). Generalizing, we obtain

$$\omega_0^2 = \gamma^2N_zM(H_{dc} \pm H_k + H_{str,x}), \quad (21)$$

where the "plus" and "minus" signs refer to the longitudinal and transverse H_{dc} magnetic fields, respectively. If the amplitude of local variations in the stray fields does not exceed the sum $H_{dc} \pm H_k$, the broadening of the ferromagnetic resonance can be roughly estimated as

$$\langle\Delta\omega_0^2\rangle = \gamma^2N_zM\langle H_{str,x}^2\rangle^{1/2} = (2)^{1/2}\pi\gamma^2N_zM^2\beta_0^2. \quad (22)$$

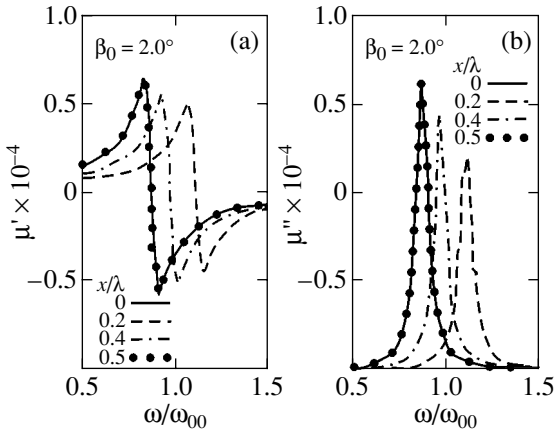

Fig. 3. Frequency dependences of the (a) real and (b) imaginary components of the magnetic permeability at different points of the film within the limits of the oscillation period.

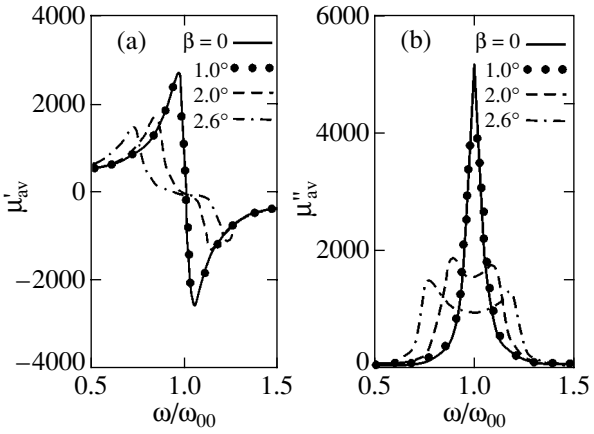

Fig. 4. Frequency dependences of the (a) real and (b) imaginary x-averaged components of the magnetic permeability for different amplitudes of the angular dispersion of magnetization.

Equation (22) can be used only for crude estimations. For the magnetic permeability, we can write

$$\begin{aligned}\mu &= 4\pi M(\phi - \phi_0)/H_{rf} + 1 \\ &= 4\pi M\phi_1 \exp(i\delta)/h_{rf} + 1.\end{aligned} \tag{23}$$

Hence, for the real and imaginary parts of the permeability, we have

$$\mu' = \frac{4\pi\dfrac{M}{H_{dc} \pm H_k}\left[1 + \dfrac{H_{str,x}}{H_{dc} \pm H_k} - \left(\dfrac{\omega}{\omega_{00}}\right)^2\right]}{\left[1 + \dfrac{H_{str,x}}{H_{dc} \pm H_k} - \left(\dfrac{\omega}{\omega_{00}}\right)^2\right]^2 + 2\alpha^2\left(\dfrac{\omega}{\omega_{00}}\right)^2\dfrac{N_z M}{H_{dc} \pm H_k}}, \tag{24}$$

$$\mu'' = \frac{4\pi\alpha\left(\dfrac{\omega}{\omega_{00}}\right)(2N_z)^{1/2}\left(\dfrac{M}{H_{dc} \pm H_k}\right)^{3/2}}{\left[1 + \dfrac{H_{str,x}}{H_{dc} \pm H_k} - \left(\dfrac{\omega}{\omega_{00}}\right)^2\right]^2 + 2\alpha^2\left(\dfrac{\omega}{\omega_{00}}\right)^2\dfrac{N_z M}{H_{dc} \pm H_k}}, \tag{25}$$

where $\omega_{00} = \gamma[2N_z M(H_{dc} \pm H_k)]^{1/2}$ is the resonance frequency at which the stray field is absent and S_{str} is varied according to relationships (7) and (8). As an example, Fig. 3 shows the dependences $\mu'(\omega/\omega_0)$ and $\mu''(\omega/\omega_0)$ for several points within the limits of the period λ. These dependences were calculated for reasonable values of the parameters: $H_k = 20$ Oe, $H_{dc} = 0$, $\beta_0 = 2.0°$, $4\pi M = 1.7 \times 10^4$ G, and $\alpha = 0.01$, which are characteristic of ultrasoft magnetic thin films [16, 17].

For comparison with experimental data on the frequency dependence of the magnetic permeability, relationships (24) and (25) should be integrated over the whole volume of the film:

$$\mu_{av}(\omega) = \int_0^{d/2} dz \int_0^{x_{max}} \mu(\omega, x, z)dx, \tag{26}$$

$$x_{max} = \begin{cases} 0.25\lambda, & \pi M_0 \beta_0^2 S_x(z) < 1 \\ \dfrac{\lambda}{4\pi}\arccos\left(-\dfrac{H_{eff}}{\pi M_0 \beta_0^2 S_x(z)}\right), & \pi M_0 \beta_0^2 S_x(z) > 1. \end{cases} \tag{27}$$

Figure 4 presents the real and imaginary components of the magnetic permeability, which were integrated with respect to the x coordinate within the limits of the oscillation period of the magnetization vector for different amplitudes of the angular dispersion. Beginning from certain values of β_0 (in our case, $\beta_0 = 2°$), the width of the resonance of the imaginary component of the magnetic permeability sharply increases and the spectrum takes the bimodal form, which is frequently observed in the spectra of thin nanocrystalline (or amorphous) magnetic films. The nature of this bimodality either is altogether not discussed in the literature or is explained in terms of local inhomogeneity of the magnetic anisotropy H_k [20, 21]. It is evident that the existence of several modes with different amplitudes or periods of the magnetization oscillations should lead to a smoothing of the bimodal distribution, even though the contribution of the internal stray field to the width of the ferromagnetic resonance can remain predominant.

4. CONCLUSIONS

The above consideration demonstrated that the angular dispersion of the local magnetization vector brings about the generation of an internal stray field

which spatially oscillates in magnitude and orientation. The spatial oscillation of the internal stray field leads to local variations in the natural frequencies of the magnetic film material and, correspondingly, to a broadening of the ferromagnetic resonance line in the frequency spectrum of the imaginary part of the magnetic susceptibility and to the disappearance of the high-frequency edge of the real part of the magnetic susceptibility of the nanocrystalline magnetic film. Thus, not only the damping parameter of the electromagnetic oscillations but also the internal stray field can lead to a broadening of the ferromagnetic resonance. The proposed model allows the prediction that the internal stray field can lead to the bimodal dependence of the magnetic susceptibility on frequency that is sometimes observed in the high-frequency spectra of nanocrystalline magnetic thin films.

ACKNOWLEDGMENTS

This work was supported by the Dutch Technology Foundation (STW), Netherlands (grant no. GWN.4561), and in part by the Grants Council of the President of the Russian Federation (project no. NSh-1619.2003.2).

REFERENCES

1. E. D. Daniel, C. D. Mee, and M. H. Clark, in *The First 100 Years* (IEEE Press, New York, 1998).
2. E. Grochowski and D. A. Thompson, IEEE Trans. Magn. **30** (6), 3797 (1994).
3. E. Grochowski and R. Hoyt, IEEE Trans. Magn. **32** (3), 1850 (1996).
4. N. X. Sun, A. M. Crawford, and S. X. Wang, Mater. Res. Soc. Symp. Proc. **721**, 249 (2002).
5. A. R. Chezan, C. B. Craus, N. G. Chechenin, *et al.*, Phys. Status Solidi A **189** (3), 833 (2002).
6. A. Chezan, C. B. Craus, N. G. Chechenin, *et al.*, IEEE Trans. Magn. **38** (5), 3144 (2002).
7. T. M. Harris, G. M. Whitney, and I. M. Croll, J. Electrochem. Soc. **142** (4), 1031 (1995).
8. T. Osaka, Electrochim. Acta **45** (20), 3311 (2000).
9. X. Liu, G. Zangari, and L. Shen, J. Appl. Phys. **87** (9), 5410 (2000).
10. E. van de Riet and F. Roosenboom, J. Appl. Phys. **81** (1), 350 (1997).
11. L. Landau and E. Lifshitz, Phys. Z. Sowjetunion **8**, 153 (1935).
12. H. Hoffmann, Thin Solid Films **58** (2), 223 (1979).
13. H. W. Fuller and M. E. Hale, J. Appl. Phys. **31** (2), 238 (1960).
14. N. G. Chechenin, C. B. Craus, A. R. Chezan, *et al.*, Mater. Res. Soc. Symp. Proc. **720**, 103 (2002).
15. D. Wohlleben, J. Appl. Phys. **38** (8), 3341 (1967).
16. N. G. Chechenin, A. R. Chezan, C. B. Craus, *et al.*, J. Magn. Magn. Mater. **242–245** (1), 180 (2002).
17. N. G. Chechenin, C. B. Craus, A. R. Chezan, *et al.*, IEEE Trans. Magn. **38** (5), 3027 (2002).
18. G. Herzer, J. Magn. Magn. Mater. **157–158**, 133 (1996).
19. S. Middelhoek, *Ferromagnetic Domains in Thin Ni–Fe Films* (Academisch Proefschrift, Amsterdam, 1961).
20. D. Spenato, A. Fessant, J. Gieraltowski, *et al.*, J. Phys. D: Appl. Phys. **26** (10), 1736 (1993).
21. G. Alexander, Jr., J. Rantschler, T. J. Silva, and P. Kabos, J. Appl. Phys. **87** (9), 6633 (2000).

Translated by O. Moskalev

Physics of the Solid State, Vol. 46, No. 3, 2004, pp. 484–490. Translated from Fizika Tverdogo Tela, Vol. 46, No. 3, 2004, pp. 471–477.

MAGNETISM AND FERROELECTRICITY

Magnetic Phase Transitions in the Iron-Doped $Pr_{0.7}Ca_{0.3}Mn_{1-y}Fe_yO_3$ Manganites at High Pressures

D. P. Kozlenko*, V. I. Voronin, V. P. Glazkov***, I. V. Medvedeva**, and B. N. Savenko***

**Joint Institute for Nuclear Research, Dubna, Moscow oblast, 141980 Russia*
e-mail: denk@nf.jinr.ru
***Institute of Metal Physics, Ural Division, Russian Academy of Sciences, ul. S. Kovalevskoĭ 18, Yekaterinburg, 620219 Russia*
**** Russian Research Centre Kurchatov Institute, pl. Kurchatova 1, Moscow, 123182 Russia*

Received July 9, 2003

Abstract—The atomic and magnetic structures of the iron-doped $Pr_{0.7}Ca_{0.3}Mn_{1-y}Fe_yO_3$ manganites (y = 0, 0.1) have been studied at high pressures of up to 4 GPa in the temperature range 16–300 K. At normal pressure, $Pr_{0.7}Ca_{0.3}MnO_3$ undergoes a phase transition from the paramagnetic to an antiferromagnetic (AFM) state of the pseudo-CE type and $Pr_{0.7}Ca_{0.3}Mn_{0.9}Fe_{0.1}O_3$ undergoes a phase transition from the paramagnetic to the ferromagnetic state at low temperatures. Partial substitution of Mn atoms by Fe brings about a noticeable decrease in the average magnetic moment per atom. A new *A*-type AFM state was observed to form in $Pr_{0.7}Ca_{0.3}MnO_3$ at a pressure $P \approx 2.2$ GPa and in $Pr_{0.7}Ca_{0.3}Mn_{0.9}Fe_{0.1}O_3$ at 2.7 GPa. This phenomenon may originate from the anisotropy in the compressibility, which causes uniaxial contraction of the oxygen octahedra MnO_6 in the structure and provides favorable conditions for the formation of an *A*-type AFM state. The structural parameters obtained were used to calculate the pressure dependence of bandwidth in the compounds under study. © *2004 MAIK "Nauka/Interperiodica".*

1. INTRODUCTION

The $A_{1-x}A'_xMnO_3$ perovskite-like manganites (*A* is a rare earth and *A*' is an alkaline earth element) exhibit a variety of magnetic and electronic properties depending on the atomic number of the *A*' element and its content. The interest in these compounds was stirred by the discovery of colossal magnetoresistance (CMR), which originates from the magnetic, electronic, and transport properties of the manganites being strongly correlated [1].

Interestingly, chemical pressure, i.e., contraction of the average radius of the *A*/*A*' cation $\langle r_A \rangle$ at a fixed concentration *x*, and high external pressure affect the magnetic and transport properties of the manganites differently. Although the unit cell decreases in volume in both cases, the chemical pressure brings about a decrease in the insulator–metal transition temperature T_{I-M} and in the Curie temperature T_C [2], whereas external pressure increases both T_{I-M} and T_C [3]. It is believed [3] that this phenomenon is due to the chemical and external pressures acting differently on the bandwidth *W*, which determines, in the double-exchange model [4–6], the values of T_{I-M} and T_C, namely, $T_{I-M} \approx T_C \propto W$. The bandwidth *W* is determined by the Mn–O bond lengths and Mn–O–Mn valence angles in the MnO_6 oxygen octahedra [3]. Chemical pressure reduces *W* through reduction of the Mn–O–Mn valence angle, whereas external pressure is expected to increase the Mn–O–Mn valence angle.

The $Pr_{0.7}Ca_{0.3}Mn_{1-y}Fe_yO_3$ compounds are promising objects for investigating the relation between the changes in the crystal and magnetic structures and in the transport and magnetic properties induced by a high external pressure. In normal conditions, the original composition $Pr_{0.7}Ca_{0.3}MnO_3$ [7, 8] has orthorhombic structure (space group *Pnma*) and is a paramagnetic insulator. As the temperature is lowered, this compound undergoes an electronic phase transition at $T_{CO} \approx 200$ K associated with charge ordering of the Mn^{3+}/Mn^{4+} ions in the structure. At $T_N \approx 140$ K, $Pr_{0.7}Ca_{0.3}MnO_3$ transfers to a pseudo-CE type antiferromagnetic (AFM) phase, which has two magnetic sublattices with wave vectors q_1 = (0 0 1/2) and q_2 = (1/2 0 1/2) formed by the Mn^{3+} and Mn^{4+} ions [1]. As the temperature is lowered still further, one observes a complex magnetic state, which includes a pseudo-CE type AFM and a ferromagnetic (FM) component [8, 9]. According to [9], the formation of this magnetic state in $Pr_{0.7}Ca_{0.3}MnO_3$ is caused by phase separation at low temperatures, which gives rise to the coexistence of the AFM and FM phases. This conjecture, however, has not received final confirmation. For instance, in [10], no phase separation was observed in $Pr_{0.7}Ca_{0.3}MnO_3$ and it was established that the magnetic structure of this compound is a canted antiferromagnet having AFM and FM components.

It was reported in [11] that a high external pressure $P > 0.5$ GPa initiates an insulator–metal phase transition in $Pr_{0.7}Ca_{0.3}MnO_3$ and that $T_{I–M}$ increases markedly with increasing pressure. A neutron diffraction study of $Pr_{0.7}Ca_{0.3}MnO_3$ single crystals performed in [12] at pressures of up to 2 GPa revealed suppression of the AFM component and an increase in the FM component at low temperatures [12].

The Ca concentration $x \approx 0.3$ in $Pr_{1-x}Ca_xMnO_3$ is close to the phase boundary separating the AFM and FM states, so that small variations in the chemical composition can change the magnetic state of the system. For instance, a study of the $Pr_{0.7}Ca_{0.3}Mn_{1-y}Fe_yO_3$ systems established that substitution of part of the Mn atoms by Fe atoms brings about a breakdown of the Mn^{3+}/Mn^{4+} charge ordering and the appearance of an FM metallic state in the low-temperature region for $y > 0.02$ [13]. While suppression of the Mn^{3+}/Mn^{4+} charge ordering by iron doping was also observed to occur in the $Pr_{0.5}Ca_{0.5}Mn_{1-y}Fe_yO_3$ systems [14, 15], they remain insulators at low temperatures and the transition to the metallic state takes place only under application of an external magnetic field [15].

We report here on a neutron-diffraction study of the effect of external high pressure on the atomic and magnetic structure of iron-doped $Pr_{0.7}Ca_{0.3}Mn_{1-y}Fe_yO_3$ manganites ($y = 0$, 0.1) in the low-temperature region and of the relation between the observed structural changes and the variation in the magnetic and transport properties.

2. EXPERIMENTAL

Polycrystalline $Pr_{0.7}Ca_{0.3}Mn_{1-y}Fe_yO_3$ samples ($y = 0$, 0.1) were prepared using the standard solid-phase reaction. Stoichiometric mixtures of Pr_6O_{11}, $CaCO_3$, MnO_2, and Fe_2O_3 powders were calcined in air at a temperature of 1173 K for 24 h. The synthesis was performed at 1473 K for 96 h with intermediate grinding and pelletizing.

Measurements were conducted with a DN-12 spectrometer [16] on a pulsed high-flux IBR-2 reactor (Frank NPL, JINR, Dubna) with the use of high-pressure sapphire-anvil chambers [17] at pressures of up to 4 GPa. Samples were $V \approx 2$ mm^3 in volume. Diffraction spectra were measured at scattering angles $2\theta = 92°$ and 45.9°. The resolution of the spectrometer at wavelength $\lambda = 2$ Å for these scattering angles was $\Delta d/d = 0.02$ and 0.025, respectively. The time needed to obtain one spectrum was typically ~20 h. The pressure in the chamber was derived from the shift of the ruby luminescence line to within 0.05 GPa. For the pressure applied to the sample, we accepted its value averaged over measurements made at several points on the sample surface. The pressure variation over the sample surface did not exceed 10%. Measurements in the high-pressure chamber at low temperatures down to 16 K were made with the use of a special closed-cycle helium cryostat. The diffraction data were Rietveld-refined with codes MRIA [18] (atomic structure) and FULLPROF [19] (atomic and magnetic structure) by invoking well-known structural models [8, 9].

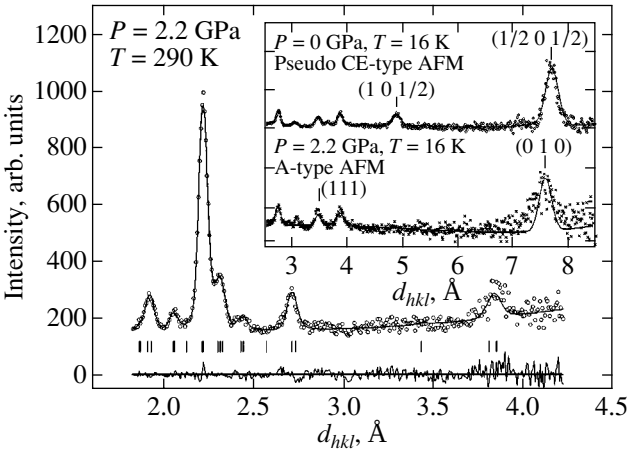

Fig. 1. Diffraction spectra of $Pr_{0.7}Ca_{0.3}MnO_3$ measured for $P = 2.2$ GPa at $T = 290$ K (scattering angle $2\theta = 92°$) and for $P = 0$ and 2.2 GPa at $T = 16$ K (scattering angle $2\theta = 45.9°$; see inset) and subjected to the Rietveld refinement procedure. Also shown are the experimental points, calculated peak profile, and difference curve (for $P = 2.2$ GPa, $T = 290$ K). The Miller indices are given for the strongest AFM reflections.

3. RESULTS

Figure 1 displays parts of the $Pr_{0.7}Ca_{0.3}MnO_3$ diffraction spectra obtained at various pressures and temperatures. The atomic structure of this compound was found to retain the original orthorhombic symmetry throughout the pressure range covered, up to 4 GPa. The structural parameters of $Pr_{0.7}Ca_{0.3}MnO_3$ under normal conditions derived from the diffraction data (see table) are in good agreement with the previous measurements made on this compound [8, 9]. The spectrum measured at normal pressure and $T = 16$ K can be identified with the pseudo-CE AFM state, which is indicated by the presence of the superstructural magnetic peaks indexed (1/2 0 1/2) and (1 0 1/2) (see inset to Fig. 1). An analysis of the diffraction data showed the magnetic moments of Mn ions to be aligned with the *b* crystallographic axis and to be approximately the same for both sublattices, $\mu_{q1} \approx \mu_{q2} = 2.6(1)\mu_B$. These figures agree with the total magnetic moment of $Pr_{0.7}Ca_{0.3}MnO_3$ obtained in [10], $\mu = 2.53(7)\ \mu_B$.

Our study did not reveal an FM component in $Pr_{0.7}Ca_{0.3}MnO_3$ in the temperature region $T < 100$ K. The oxygen content refined from diffraction data showed it to differ slightly from 3.0 and that $Pr_{0.7}Ca_{0.3}MnO_{2.98}$ is the correct chemical formula of the compound. The oxygen off-stoichiometry probably

Room-temperature structural parameters of $Pr_{0.7}Ca_{0.3}MnO_3$ and $Pr_{0.7}Ca_{0.3}Mn_{0.9}Fe_{0.1}O_3$ for various pressures

Parameter	$Pr_{0.7}Ca_{0.3}MnO_3$			$Pr_{0.7}Ca_{0.3}Mn_{0.9}Fe_{0.1}O_3$		
P, GPa	0	2.2	4	0	2.7	3.7
a, Å	5.468(5)	5.468(5)	5.468(5)	5.461(5)	5.461(5)	5.461(5)
b, Å	7.677(8)	7.63(1)	7.56(1)	7.685(8)	7.61(1)	7.59(1)
c, Å	5.435(5)	5.435(5)	5.435(5)	5.431(5)	5.431(5)	5.431(5)
Pr/Ca: *x*	0.036(3)	0.038(5)	0.036(5)	0.041(3)	0.046(5)	−0.051(5)
z	−0.013(4)	−0.030(6)	−0.026(6)	−0.008(4)	−0.032(6)	−0.027(4)
O1: *x*	0.486(4)	0.489(5)	0.477(5)	0.486(4)	0.483(5)	0.484(5)
z	0.070(3)	0.068(5)	0.064(5)	0.070(3)	0.066(5)	0.066(5)
O2: *x*	0.286(2)	0.287(3)	0.287(3)	0.288(2)	0.290(3)	0.290(3)
y	0.039(2)	0.035(4)	0.034(4)	0.039(2)	0.039(4)	0.038(4)
z	0.714(2)	0.713(3)	0.713(3)	0.712(2)	0.710(3)	0.710(3)
μ_{AFM}, μ_B	2.6(1)	1.6(1)	2.1(1)	–		1.5(1)
μ_{FM}, μ_B	–	–	–	1.4(1)		0.8(1)
Mn/Fe–O1, Å	1.958(8)	1.94(1)	1.93(1)	1.961(8)	1.94(1)	1.93(1)
Mn/Fe–O2, Å	1.972(8)	1.968(12)	1.967(12)	1.971(8)	1.973(12)	1.972(12)
	1.969(8)	1.965(12)	1.963(12)	1.968(8)	1.970(12)	1.969(12)
Mn/Fe–O1–Mn/Fe	157.2(1)°	157.2(2)°	157.6(2)°	157.1(1)°	157.9(2)°	158.0(2)°
Mn/Fe–O2–Mn/Fe	156.1(1)°	157.9(2)°	157.9(2)°	155.5(1)°	155.1(2)°	155.4(2)°
R_p, %	2.81	7.62	10.33	5.54	8.11	8.68
R_{wp}, %	2.90	6.36	8.15	3.39	6.77	6.16

Note: Mn/Fe atoms occupy positions 4(b) (0, 0, 0.5), Pr/Ca and O1 atoms are in positions 4(*c*) (*x*, 1/4, *z*), and O2 atoms are in positions 8(d) (*x*, *y*, *z*) of the *Pnma* space group. Also given are the average magnetic moments of the Mn/Fe atoms for $T = 16$ K, Mn/Fe–O1 and Mn/Fe–O2 valence bonds, and Mn/Fe–O1–Mn/Fe and Mn/Fe–O2–Mn/Fe valence angles.

accounts for the absence of the FM component in our sample, because it can markedly affect the properties of the manganites [20].

At pressure $P = 2.2$ GPa, new magnetic peaks were detected in $Pr_{0.7}Ca_{0.3}MnO_3$ at temperatures $T \le 150$ K (Fig. 1); their positions are at odds with the original pseudo-CE type AFM structure. An analysis of the diffraction data showed these peaks to correspond to a new AFM state with an *A*-type structure [1] and a wave vector $q = (0\ 1\ 0)$. According to [11], this state is metallic. The magnetic moments of the Mn ions in the *A*-type AFM structure lie in the (*ac*) crystallographic plane and are $\mu_{AFM} = 1.6(1)\mu_B$ at $P = 2.2$ GPa and $T = 16$ K. The structural parameters of $Pr_{0.7}Ca_{0.3}MnO_3$ obtained at various pressures are listed in the table.

Interestingly, a neutron diffraction study of $Pr_{0.7}Ca_{0.3}MnO_3$ single crystals carried out in [12] at pressures of up to 2 GPa likewise revealed suppression of the pseudo-CE AFM magnetic-structure component. In that experiment, however, the reciprocal space was scanned only in the vicinity of some of the strongest magnetic reflections originating from the pseudo-CE AFM and FM magnetic-structure components and no transition to the *A*-type AFM state was revealed.

Figure 2 presents parts of the diffraction spectra of $Pr_{0.7}Ca_{0.3}Mn_{0.9}Fe_{0.1}O_3$ obtained at various pressures and temperatures. Studied at normal pressure under decreasing temperature, this compound revealed an increase in the integrated intensity of the (101)/(020) and (200)/(002)/(121) diffraction peaks for $T < 100$ K, which indicated formation of the FM state. An analysis of the diffraction data showed the magnetic moments of the Mn/Fe ions to lie in the (*ac*) plane and to have an average magnitude $\mu_{FM} = 1.4(1)\mu_B$ at $T = 16$ K. By analogy with the $Pr_{0.6}Ca_{0.4}Mn_{1-y}Fe_yO_3$ compounds, which are close in terms of their chemical composition and magnetic properties [13], it can be suggested that the FM state mentioned above is also metallic. Substitution of Fe for 10 at. % of the Mn atoms brings about a noticeable decrease in the average magnetic moment of the Mn/Fe ions, which was 2.6 μ_B in the original $Pr_{0.7}Ca_{0.3}MnO_3$ compound. A similar phenomenon was also observed in $La_{0.7}Ca_{0.3}Mn_{1-y}Fe_yO_3$ in [21]. Iron ions in these compounds substituting for part of the Mn^{3+} ions are in the Fe^{3+} state ($t_{2g}^3 e_g^2$) with $2e_g$ electrons. This substitution weakens the double-exchange interaction responsible for the formation of the FM state in manganites [1] and gives rise to magnetic inhomogeneities [14]. These factors act jointly to reduce the

average magnetic moment of the Mn/Fe ions and the magnetization [14, 21]. As the pressure was increased, new magnetic diffraction peaks were also observed in $Pr_{0.7}Ca_{0.3}Mn_{0.9}Fe_{0.1}O_3$ at $P = 2.7$ GPa and $T \approx 40$ K; these peaks corresponded to the *A*-type AFM state, which coexisted with the original FM state down to 16 K (Fig. 2). The average magnetic moments of the Mn/Fe ions at $P = 3.7$ GPa and $T = 16$ K were calculated to be $\mu_{AFM} = 1.5(1)\ \mu_B$ in the AFM phase and $\mu_{FM} = 0.8(1)\ \mu_B$ in the FM phase. The structural parameters of $Pr_{0.7}Ca_{0.3}Mn_{0.9}Fe_{0.1}O_3$ are listed in the table for various pressures.

Both compounds reveal a noticeable anisotropy in the compressibility. The coefficient of linear compressibility $k_i = (1/a_{i0})(da_i/dP)_T$ for the unit cell parameter b was calculated to be $k_b = 0.004$ GPa^{-1} for $Pr_{0.7}Ca_{0.3}MnO_3$ and 0.003 GPa^{-1} for $Pr_{0.7}Ca_{0.3}Mn_{0.9}Fe_{0.1}O_3$ at room temperature, whereas the corresponding values for the other cell parameters are k_a, $k_c < 0.0015$ GPa^{-1} for both compounds. The diffraction-peak broadening at high pressures, which is a consequence of a pressure distribution gradient over the volume of the sample under study, precluded accurate determination of the variation in the unit cell parameters a and c; therefore, the values of k_a and k_c should be considered as estimates only.

The anisotropy in the compressibility of the various lattice cell parameters brings about uniaxial contraction of the MnO_6 oxygen octahedra along the b crystallographic axis. The lengths of the two Mn–O2 valence bonds in the (ac) plane practically do not change with pressure, and their average value is $\langle l_{Mn-O2}\rangle \approx 1.97(1)$ Å, whereas the length of the Mn–O1 valence bond oriented along the b crystallographic axis decreases from $l_{Mn-O1} \approx 1.96$ to 1.93 Å in both compounds (Fig. 3). The linear compressibility coefficient of the bond length $\langle$Mn–O$\rangle$ averaged over the oxygen octahedron $k_{\langle Mn-O\rangle} = (1/l_{\langle Mn-O\rangle 0})(dl_{\langle Mn-O\rangle}/dP)_T$ is $k_{\langle Mn-O\rangle} = 0.0018$ GPa^{-1} for $Pr_{0.7}Ca_{0.3}MnO_3$ and 0.0011 GPa^{-1} for $Pr_{0.7}Ca_{0.3}Mn_{0.9}Fe_{0.1}O_3$. The calculated value of $k_{\langle Mn-O\rangle}$ for $Pr_{0.7}Ca_{0.3}MnO_3$ is in agreement with $k_{\langle Mn-O\rangle} = 0.00232$ GPa^{-1} obtained within a narrower pressure region up to 0.6 GPa [8]. In $Pr_{0.7}Ca_{0.3}MnO_3$, as the pressure is increased from 0 to 4 GPa, the valence angles in the MnO_6 oxygen octahedra increase, with the Mn–O2–Mn angle increasing from 156.1° to 157.6° and the Mn–O1–Mn angle, from 157.2° to 157.9°. In $Pr_{0.7}Ca_{0.3}Mn_{0.9}Fe_{0.1}O_3$, with an increase in pressure to 3.7 GPa, the Mn–O2–Mn angle changes only slightly, $\alpha_{Mn-O2-Mn} \approx 155.42°$, while the Mn–O1–Mn angle increases from 157.2° to 158°.

4. RESULTS AND DISCUSSION

The formation of the *A*-type AFM metallic state in $Pr_{0.7}Ca_{0.3}MnO_3$ and $Pr_{0.7}Ca_{0.3}Mn_{0.9}Fe_{0.1}O_3$ is probably caused by the anisotropy in the compressibility of these compounds, which results in a noticeable uniaxial contraction of the MnO_6 oxygen octahedra along the b crystallographic axis. Recent theoretical [22] and experimental [23] studies revealed that the magnetic properties of the manganites exhibiting the colossal magnetoresistance effect depend substantially on the tetragonal distortion c_p/a_p of the parameters of the pseudocubic unit cell in the perovskite structure. The orthorhombic cell parameters (a, b, c) of perovskite-

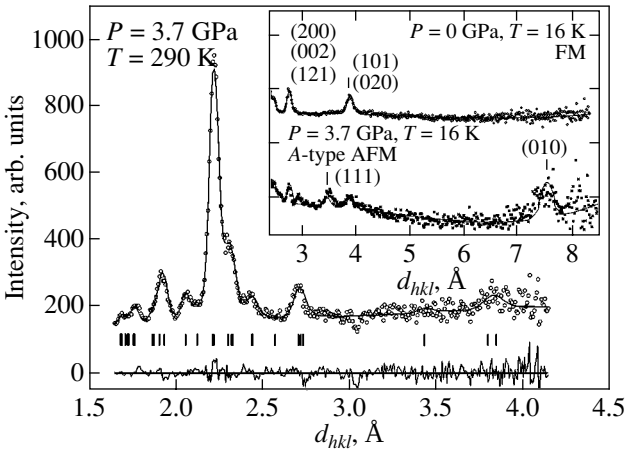

Fig. 2. Diffraction spectra of $Pr_{0.7}Ca_{0.3}Mn_{0.9}Fe_{0.1}O_3$ measured for $P = 3.7$ GPa at $T = 290$ K (scattering angle $2\theta = 92°$) and for $P = 0$ and 3.7 GPa at $T = 16$ K (scattering angle $2\theta = 45.9°$, inset) and subjected to the Rietveld refinement procedure. Also shown are the experimental points, calculated peak profile, and difference curve (for $P = 3.7$ GPa, $T = 290$ K). The Miller indices are indicated for the strongest structural reflections having an FM contribution (at $P = 0$) and for AFM reflections (at $P = 3.7$ GPa).

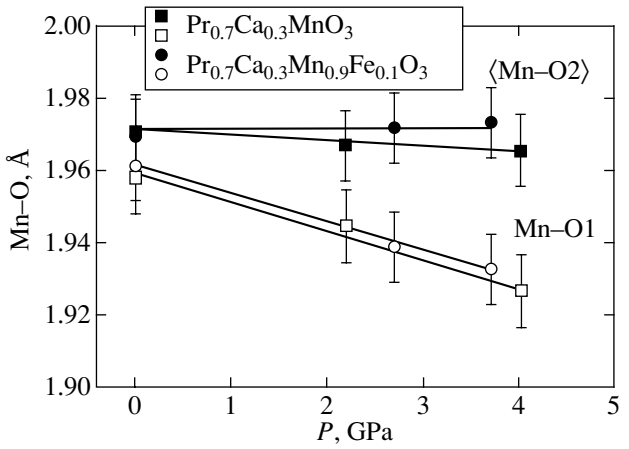

Fig. 3. Pressure dependences of the Mn–O1 bond length and average ⟨Mn–O2⟩ bond length in $Pr_{0.7}Ca_{0.3}MnO_3$ and $Pr_{0.7}Ca_{0.3}Mn_{0.9}Fe_{0.1}O_3$ and their linear interpolation (solid lines).

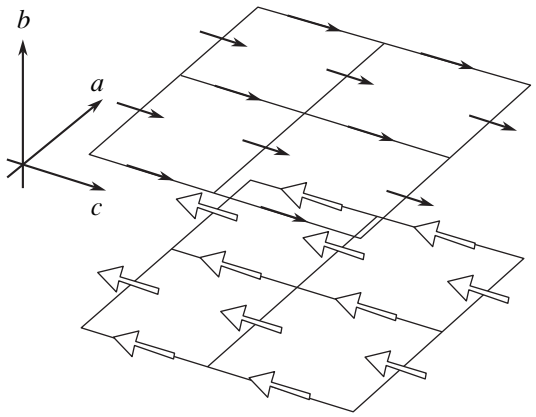

Fig. 4. Magnetic-moment orientation of the Mn/Fe ions in the *A*-type magnetic structure for $Pr_{0.7}Ca_{0.3}MnO_3$ and $Pr_{0.7}Ca_{0.3}Mn_{0.9}Fe_{0.1}O_3$ at high pressures (schematic).

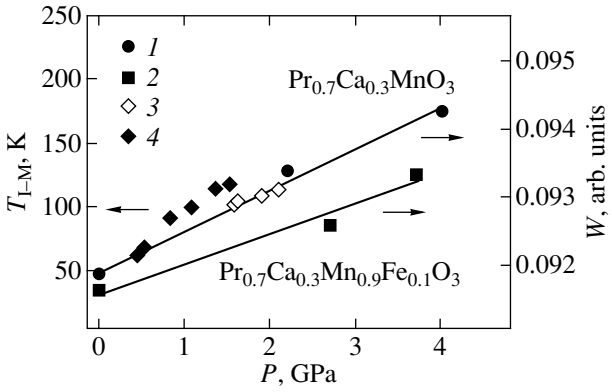

Fig. 5. Pressure dependences of bandwidth *W* calculated for (*1*) $Pr_{0.7}Ca_{0.3}MnO_3$ and (*2*) $Pr_{0.7}Ca_{0.3}Mn_{0.9}Fe_{0.1}O_3$ and their linear interpolation (solid lines). Also shown are (*3*) the pressure dependence of the insulator–metal transition temperature $T_{I–M}$ obtained for the $Pr_{0.7}Ca_{0.3}MnO_3$ sample under study and (*4*) the corresponding data taken from [10].

like manganites (space group *Pnma*) and the parameters c_p and a_p are related through $a \approx c \approx a_p\sqrt{2}$ and $b \approx 2c_p$. Neglecting the difference between the parameters *a* and *c* of the $Pr_{0.7}Ca_{0.3}MnO_3$ and $Pr_{0.7}Ca_{0.3}Mn_{0.9}Fe_{0.1}O_3$ orthorhombic structure (which does not exceed 1%), the magnitude of the tetragonal distortions in these compounds can be readily estimated as $c_p/a_p \approx l_{Mn–O1}/l_{\langle Mn–O2\rangle}$. The values thus obtained are $c_p/a_p = 0.986$ for $Pr_{0.7}Ca_{0.3}MnO_3$ at $P = 2.2$ GPa and 0.984 for $Pr_{0.7}Ca_{0.3}Mn_{0.9}Fe_{0.1}O_3$ at $P = 2.7$ GPa and decrease with a further increase in pressure or decrease in temperature. According to [22, 24], for tetragonal distortions $c_p/a_p < 1$, the Mn $d(x^2 - y^2)$ orbitals are preferentially occupied (and an orbitally ordered state forms) and the exchange integral J_1 between the nearest neighbors along the direction of uniaxial contraction decreases. These factors are conducive to the formation of the *A*-type AFM state, which is characterized by an alternation (along the *b* axis of the orthorhombic structure) of the (*ac*) ferromagnetic planes with oppositely directed magnetic moments of the Mn/Fe ions (Fig. 4).

The occurrence of an *A*-type metallic antiferromagnetic state was also observed in some manganites under normal pressure at low temperatures, namely, in $Pr_{1-x}Sr_xMnO_3$ for $0.48 < x < 0.58$ [25], $Nd_{1-x}Sr_xMnO_3$ for $0.48 < x < 0.58$ [26], and $(Nd_{1-z}La_z)_{0.5}Sr_{0.5}MnO_3$ for $0.4 < z < 0.6$ [11]. The transition to the *A*-type AFM state in this case was also accompanied by a considerable uniaxial contraction of the MnO_6 oxygen octahedra, which was caused by a noticeable decrease in the parameter *b* and a slight increase in the unit cell parameters *a* and *c*.

Ordering of the Mn $d(x^2 - y^2)$ orbitals in the (*ac*) planes favors the formation of a pseudo-two-dimensional conduction band, whose width *W* can depend substantially on the interatomic distances and angles. Considered in terms of the double-exchange model [5–7], the variation in the insulator–metal transition temperature $T_{I–M}$ and in the Curie temperature T_C under variation of the chemical composition or application of an external pressure is determined by the variation in the bandwidth *W*, namely, $T_{I–M}$ (T_C) $\propto W$. The dependence of *W* on the structural parameters in ABO_3 perovskite materials can be written as [27, 28]

$$W \propto \frac{\cos\omega}{l_{B–O}^{3.5}}. \qquad (1)$$

Here, ω is the average tilt angle of the BO_6 octahedra in the valence bond plane, $\omega = (1/2)(\pi - \langle B–O–B\rangle)$, and $l_{B–O}$ is the average *B*–O bond length.

The decrease in the average bond length ⟨Mn–O⟩ and the increase in the average interatomic angle ⟨Mn/Fe–O–Mn/Fe⟩ (the increase in cosω) cause a nearly linear increase in *W* (Fig. 5) in the $Pr_{0.7}Ca_{0.3}Mn_{1-y}Fe_yO_3$ compounds with increasing pressure. Figure 5 also shows the pressure dependence of the insulator–metal transition temperature $T_{I–M}(P)$ measured for the $Pr_{0.7}Ca_{0.3}MnO_3$ sample under study in the pressure region 1.5–2.1 GPa at the Institute of Metal Physics (Ural Division, RAS) and analogous data for $Pr_{0.7}Ca_{0.3}MnO_3$ obtained earlier in the interval 0.5–1.5-GPa [11]. As seen from Fig. 5, $Pr_{0.7}Ca_{0.3}MnO_3$ exhibits a noticeable correlation between the $T_{I–M}(P)$ and $W(P)$ dependences. The discrepancy between the values of $T_{I–M}(P)$ for the $Pr_{0.7}Ca_{0.3}MnO_3$ sample studied by us and the data quoted in [11] can be accounted for apparently by a small deviation of the oxygen content (2.98) from the ideal value (3.0).

The earlier studies of the $A_{0.7}A'_{0.3}MnO_3$ manganites [2] with various average radii $\langle r_A\rangle$ of the *A*/*A*' cation

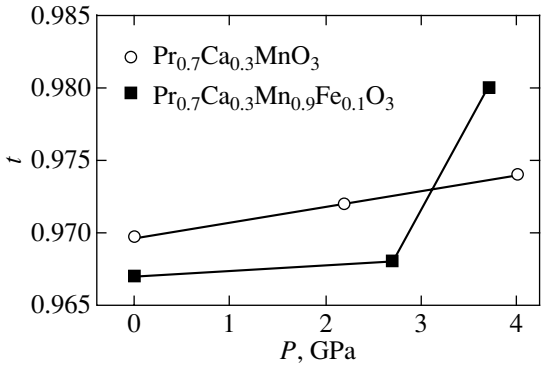

Fig. 6. Pressure dependences of tolerance factor t for $Pr_{0.7}Ca_{0.3}MnO_3$ and $Pr_{0.7}Ca_{0.3}Mn_{0.9}Fe_{0.1}O_3$.

revealed a close relation between the insulator–metal transition temperature and the so-called tolerance factor, which characterizes the geometric distortion of the crystal structure as compared to the ideal perovskite cubic structure:

$$t = l_{A\text{–}O}/\sqrt{2}l_{Mn\text{–}O}, \quad (2)$$

where $\langle l_{A\text{–}O}\rangle$ is the distance between the A/A' cations and the oxygen atoms and $\langle l_{Mn\text{–}O}\rangle$ is the Mn–O valence bond length. For the ideal cubic perovskite structure, we have $t = 1$. The tolerance factor for the $Pr_{0.7}Ca_{0.3}MnO_3$ compound lies near the insulator–metal transition boundary [2]. Calculations with tabulated standard ionic radii of the A/A' cation corresponding to a coordination number $N = 12$ of the oxygen atoms linking this cation yielded $t \approx 0.96$ for $Pr_{0.7}Ca_{0.3}MnO_3$ [29]. As t increased, first a growth in $T_{I\text{–}M}$ was observed (up to $t \approx 0.98$) and then a slight decrease in $T_{I\text{–}M}$.

The anisotropy in the lattice contraction at high pressures results in inequivalent variations in various interatomic distances. In this case, t can be calculated using the interatomic distances averaged over the first coordination sphere $\langle l_{A\text{–}O}\rangle$ and $\langle l_{Mn\text{–}O}\rangle$, $t = \langle l_{A\text{–}O}\rangle/\sqrt{2}\langle l_{Mn\text{–}O}\rangle$. The value $t = 0.97$ calculated in this way for $Pr_{0.7}Ca_{0.3}MnO_3$ for $P = 0$ agrees well with the data quoted in [29]. As the pressure is increased to $P = 4$ GPa, t increases from 0.97 to 0.974 in $Pr_{0.7}Ca_{0.3}MnO_3$ and from 0.967 to 0.98 in $Pr_{0.7}Ca_{0.3}Mn_{0.9}Fe_{0.1}O_3$ (Fig. 6). Assuming the behavior of $T_{I\text{–}M}$ as a function of t to be qualitatively similar for the cases where external (P) or chemical pressure (decrease in $\langle r_A\rangle$) is applied, an increase in $T_{I\text{–}M}$ to $T_{I\text{–}M} \sim 140$ K can be expected for $Pr_{0.7}Ca_{0.3}MnO_3$ as t increases by 0.41%, which corresponds to an increase in pressure to 4 GPa. It was shown in [11] that the insulator–metal transition temperature in $Pr_{0.7}Ca_{0.3}MnO_3$ increases from $T_{I\text{–}M} = 66$ to 118 K in the interval 0.5–1.5 GPa, with the growth rate of $T_{I\text{–}M}$ decreasing with increasing pressure.

The tolerance factor is apparently a universal characteristic: it qualitatively characterizes the variations in the properties of manganites both under application of an external pressure and under a variation in $\langle r_A\rangle$.

5. CONCLUSIONS

The results obtained in this study show that the application of a high external pressure gives rise to the formation of an A-type AFM state in the manganites under investigation; this state is metallic in $Pr_{0.7}Ca_{0.3}MnO_3$ and apparently metallic in $Pr_{0.7}Ca_{0.3}Mn_{0.9}Fe_{0.1}O_3$. This phenomenon can possibly be caused by the anisotropy in the compressibility of these compounds, which brings about uniaxial contraction of the MnO_6 oxygen octahedra and a preferential occupation of the Mn $d(x^2 - y^2)$ orbitals.

The calculations based on the structural data thus obtained have shown that pressure initiates an increase in the bandwidth W. Interpreted in terms of the double-exchange model, this result correlates qualitatively with the experimentally observed increase in the insulator–metal transition temperature $T_{I\text{–}M}$ in the compounds under study.

ACKNOWLEDGMENTS

The authors are indebted to G.H. Rao for providing the samples used in the experiments.

This study was supported by the Russian Foundation for Basic Research (project no. 03-02-16879) and the Ministry of Industry, Science, and Technology (project no. 40.012.1.1.1148).

REFERENCES

1. M. B. Salamon and M. Jaime, Rev. Mod. Phys. **73**, 583 (2001).
2. H. Y. Hwang, S.-W. Cheong, P. G. Radaelli, *et al.*, Phys. Rev. Lett. **75**, 914 (1995).
3. H. Y. Hwang, T. T. M. Palstra, S.-W. Cheong, and B. Batlogg, Phys. Rev. B **52**, 15046 (1995).
4. C. Zener, Phys. Rev. **81**, 440 (1951); Phys. Rev. **82**, 403 (1951).
5. P. W. Anderson and H. Hasegawa, Phys. Rev. **100**, 675 (1955).
6. P.-G. de Gennes, Phys. Rev. B **118**, 141 (1960).
7. Z. Jirak, S. Krupicka, Z. Simsa, *et al.*, J. Magn. Magn. Mater. **53**, 153 (1985).
8. P. G. Radaelli, G. Iannone, M. Marezio, *et al.*, Phys. Rev. B **56**, 8265 (1997).
9. P. G. Radaelli, R. M. Ibberson, D. N. Argyriou, *et al.*, Phys. Rev. B **63**, 172419 (2001).
10. A. M. Balagurov, V. Yu. Pomjakushin, D. V. Sheptyakov, *et al.*, Phys. Rev. B **64**, 024420 (2001).
11. Y. Moritomo, H. Kuwahara, Y. Tomioka, and Y. Tokura, Phys. Rev. B **55**, 7549 (1997).

12. H. Yoshizawa, R. Kajitomo, H. Kawano, *et al.*, Phys. Rev. B **55**, 2729 (1997).
13. F. Damay, A. Maignan, C. Martin, and B. Raveau, J. Appl. Phys. **82**, 1485 (1997).
14. S. Hebert, A. Maignan, C. Martin, and B. Raveau, Solid State Commun. **121**, 229 (2002).
15. F. Damay, C. Martin, A. Maignan, and B. Raveau, J. Magn. Magn. Mater. **183**, 143 (1998).
16. V. L. Aksenov, A. M. Balagurov, V. P. Glazkov, *et al.*, Physica B (Amsterdam) **265**, 258 (1999).
17. V. P. Glazkov and I. N. Goncharenko, Fiz. Tekh. Vys. Davleniĭ **1**, 56 (1991).
18. V. B. Zlokazov and V. V. Chernyshev, J. Appl. Crystallogr. **25**, 447 (1992).
19. J. Rodriguez-Carvajal, Physica B (Amsterdam) **192**, 55 (1993).
20. S. V. Trukhanov, I. O. Troyanchuk, F. P. Korshunov, *et al.*, Fiz. Nizk. Temp. **27**, 385 (2001) [Low Temp. Phys. **27**, 283 (2001)].
21. G. H. Rao, J. R. Sun, A. Kattwinkel, *et al.*, Physica B (Amsterdam) **269**, 379 (1999).
22. Z. Fang, I. V. Solovyev, and K. Terakura, Phys. Rev. Lett. **84**, 3169 (2000).
23. Y. Konishi, Z. Fang, M. Isumi, *et al.*, J. Phys. Soc. Jpn. **68**, 3790 (1999).
24. S. Krupicka, *Physik der Ferrite und der Verwandten Magnetischen Oxide* (Academia, Praha, 1973; Mir, Moscow, 1976), Vol. 1.
25. E. Pollert, Z. Jirák, J. Hejtmánek, *et al.*, J. Magn. Magn. Mater. **246**, 290 (2002).
26. R. Kajimoto, H. Yoshizawa, H. Kawano, *et al.*, Phys. Rev. B **60**, 9506 (1999).
27. W. A. Harrison, *The Electronic Structure and Properties of Solids* (Freeman, San Francisco, 1980), p. 430.
28. M. Medarde, J. Mesot, P. Lacorre, *et al.*, Phys. Rev. B **52**, 9248 (1995).
29. W. Archibald, J.-S. Zhou, and J. B. Goodenough, Phys. Rev. B **53**, 14 445 (1996).

Translated by G. Skrebtsov

Physics of the Solid State, Vol. 46, No. 3, 2004, pp. 491–497. Translated from Fizika Tverdogo Tela, Vol. 46, No. 3, 2004, pp. 478–483.

MAGNETISM AND FERROELECTRICITY

Magnetic Properties of Copper Metaborate: Two-Parameter Phenomenological Model

M. A. Popov*, G. A. Petrakovskiĭ, and V. I. Zinenko****

** Krasnoyarsk State University, Krasnoyarsk, 660041 Russia*

*** Kirensky Institute of Physics, Siberian Division, Russian Academy of Sciences, Akademgorodok, Krasnoyarsk, 660036 Russia*

e-mail: rsa@iph.krasn.ru

Received July 21, 2003

Abstract—Symmetry analysis is performed for the magnetic subsystem of copper metaborate, and a phenomenological model is proposed with two two-component order parameters that correspond to ferromagnetism and antiferromagnetism vectors lying in the tetragonal plane of this crystal. Owing to the $I\bar{4}2d$ space group of symmetry of this crystal, the thermodynamic potential contains the Lifshitz invariant having the form of an antisymmetric product of the order parameters and their spatial derivatives. Analysis of this model shows that the temperatures of ordering in the magnetic subsystem and of the formation of a spiral structure in it can be different. This fact allows numerical calculation of the temperature dependences of the spiral wave vector, magnetization, and intensities of first- and third-order magnetic satellites in the incommensurate phase that arise in neutron elastic scattering, as well as the field dependence of the magnetization. The experimental data, including a magnetic-field–temperature phase diagram, are satisfactorily described. The parameters of the phenomenological thermodynamic potential of the magnetic subsystem of copper metaborate are estimated. © *2004 MAIK "Nauka/Interperiodica".*

1. INTRODUCTION

Copper oxide compounds exhibit a wide variety of types of magnetic ordering and magnetic properties. Such compounds include not only various collinear ferromagnets but also weak ferromagnets, spin glasses, singlet magnets, ferrimagnets, and incommensurate magnetic structures. Interest in the magnetic properties of these materials has quickened due to the discovery of high-temperature superconductors, in which magnetic correlations are likely to play an important role in the formation of a superconducting state.

As shown in [1–5], copper metaborate CuB_2O_4 has especially interesting magnetic properties. According to the neutron diffraction data and magnetic measurements, the magnetic subsystem of this crystal transforms from a paramagnetic state into an easy-plane weak ferromagnet at $T_N = 20$ K. However, the temperature dependences of the specific heat and magnetic susceptibility in the tetragonal plane of the crystal exhibit specific features not only at T_N but also at $T_i = 10$ K. The magnetic peaks observed in neutron diffraction patterns in the temperature range from T_N to T_i coincide with the lattice peaks, which reflects the coincidence of the magnetic unit cell and the crystal unit cell [3]. Therefore, the phase transition at T_N corresponds to a wave vector at the center of the Brillouin zone, $\mathbf{q} = 0$.

The special high-resolution neutron diffraction study reported in [3] showed that the crystal did not undergo any structural phase transitions down to a temperature of 1.5 K. However, as the temperature decreases below T_i, magnetic satellites appear in the neutron diffraction patterns in symmetrical positions with respect to the reciprocal-lattice points of the commensurate phase. These satellites were attributed to a periodic magnetic structure that is incommensurate to the lattice structure along the tetragonal axis of the crystal and represents a spin-density phase-modulated wave [3]. The presence of higher order magnetic satellites generated by the incommensurate phase in neutron diffraction patterns near T_i indicates the formation of a magnetic soliton lattice.

Studies of elastic neutron scattering in strong magnetic fields have shown that the incommensurate magnetic structure in copper metaborate undergoes a first-order transition into a commensurate phase when the magnetic field reaches a certain critical value that is dependent on temperature [4, 5].

To the best of our knowledge, there is only one case (described in [6] for the $NiBr_2$ crystal) where the transition from a commensurate to an incommensurate phase also occurs with decreasing temperature. Since the symmetry of $NiBr_2$ prohibits any Lifshitz invariants, the mechanism of the appearance of the incommensurate phase in the crystal is related to a possible temperature dependence of competing exchange interactions [6]. As will be shown below, the symmetry of copper metaborate allows a small relativistic Lifshitz invariant having an unconventional form. This invariant

allows one to phenomenologically describe the unusual sequence of phase transitions observed in copper metaborate and a number of its magnetic properties.

2. INCOMPLETE THERMODYNAMIC POTENTIAL OF COPPER METABORATE

The x-ray diffraction and neutron diffraction studies performed in [3] at room temperature showed that copper metaborate belongs to the space group $I\bar{4}2d$ and its lattice parameters are $a = 11.528$ Å and $c = 5.607$ Å. The unit cell contains twelve formula units. The Cu^{2+} ions occupy two nonequivalent positions; namely, Cu(*b*) is in the 4*b* position with point symmetry S_4 (0,0,1/2) and Cu(*d*) is in the 8*d* position with point symmetry C_2 (0.0815, 1/4,1/8). The Cu(*b*) ion is at the center of the square formed by four oxygen ions, and the Cu(*d*) ion is surrounded by six oxygen ions localized at the vertices of a distorted octahedron.

The point group $\bar{4}2m$ of the crystal contains eight symmetry elements [7]:

$$1, \bar{4}_3^1, 4_3^2, \bar{4}_3^3, 4_1^2, 4_2^2, m_4, m_5.$$

This group has five irreducible representations. Four of them (Γ_1, Γ_2, Γ_3, Γ_4) are one-dimensional, and one (Γ_5) is two-dimensional. The reductions of the magnetic representations for the two nonequivalent copper sublattices in copper metaborate have the form

$$\Gamma_{4b} = \Gamma_1 + \Gamma_2 + 2\Gamma_5,$$
$$\Gamma_{8d} = \Gamma_1 + 2\Gamma_2 + 2\Gamma_3 + \Gamma_4 + 3\Gamma_5.$$

The magnetic modes that transform according to irreducible representations of the group $\bar{4}2m$ in the Cu(*b*) copper ion sublattice are

$$\Gamma_1: S_{b1z} - S_{b2z},$$
$$\Gamma_2: S_{b1z} + S_{b2z},$$
$$\Gamma_5: (S_{b1x} + S_{b2x}, -S_{b1y} - S_{b2y}), \quad (1)$$
$$\Gamma_5: (S_{b1y} - S_{b2y}, S_{b1x} - S_{b2x}). \quad (2)$$

The modes corresponding to the representations Γ_1 and Γ_2 of the 4*b* position describe antiferromagnetic and ferromagnetic ordering along the tetragonal **c** axis, respectively, while the modes related to the representation Γ_5 describe a noncollinear magnetic structure in the tetragonal plane. For the Cu(*d*) copper ion sublattice, the magnetic modes transform as follows:

$$\Gamma_1: S_{d1x} + S_{d2y} - S_{d3x} - S_{d4y},$$
$$\Gamma_2: S_{d1y} - S_{d2x} - S_{d3y} + S_{d4x},$$
$$\Gamma_2: S_{d1z} + S_{d2z} + S_{d3z} + S_{d4z},$$
$$\Gamma_3: S_{d1y} + S_{d2x} - S_{d3y} - S_{d4x},$$
$$\Gamma_3: S_{d1z} - S_{d2z} + S_{d3z} - S_{d4z},$$
$$\Gamma_4: S_{d1x} - S_{d2y} - S_{d3x} + S_{d4y},$$
$$\Gamma_5: (S_{d1x} + S_{d2x} + S_{d3x} + S_{d4x}, -S_{d1y} - S_{d2y} - S_{d3y} - S_{d4y}), \quad (3)$$
$$\Gamma_5: (S_{d1x} - S_{d2x} + S_{d3x} - S_{d4x}, S_{d1y} - S_{d2y} + S_{d3y} - S_{d4y}), \quad (4)$$
$$\Gamma_5: (S_{d2z} - S_{d4z}, S_{d1z} - S_{d3z}).$$

The numeration of ions for this sublattice corresponds to the sequential application of the $\bar{4}_3^1$ symmetry operation.

An incommensurate inhomogeneous phase should be described by inhomogeneous magnetic modes. The modes that are linear in the spatial derivative along the **c** axis are

$$\Gamma_3: (S_{b1z} - S_{b2z})',$$
$$\Gamma_4: (S_{b1z} + S_{b2z})',$$
$$\Gamma_5: (-S_{b1y} - S_{b2y}, S_{b1x} + S_{b2x})',$$
$$\Gamma_5: (S_{b1x} - S_{b2x}, S_{b1y} - S_{b2y})',$$

for the 4*b* position and

$$\Gamma_1: (S_{d1y} + S_{d2x} - S_{d3y} - S_{d4x})',$$
$$\Gamma_1: (S_{d1z} - S_{d2z} + S_{d3z} - S_{d4z})',$$
$$\Gamma_2: (S_{d1x} - S_{d2y} - S_{d3x} + S_{d4y})',$$
$$\Gamma_3: (S_{d1x} + S_{d2y} - S_{d3x} - S_{d4y})',$$
$$\Gamma_4: (S_{d1y} - S_{d2x} - S_{d3y} + S_{d4x})',$$
$$\Gamma_4: (S_{d1z} + S_{d2z} + S_{d3z} + S_{d4z})',$$
$$\Gamma_5: (-S_{d1y} - S_{d2y} - S_{d3y} - S_{d4y}, S_{d1x} + S_{d2x} + S_{d3x} + S_{d4x})',$$
$$\Gamma_5: (S_{d1y} - S_{d2y} + S_{d3y} - S_{d4y}, S_{d1x} - S_{d2x} + S_{d3x} - S_{d4x})',$$
$$\Gamma_5: (S_{d1z} - S_{d3z}, S_{d2z} - S_{d4z})',$$

for the 8*d* position, where $f' \equiv df/dz$.

Analysis of the neutron diffraction pattern [3] consisting of 25 purely magnetic peaks showed that the spins of both the Cu(*b*) and Cu(*d*) sublattices of copper metaborate form a noncollinear magnetic structure in the commensurate phase ($T_i < T < T_N$). In the Cu(*b*) sublattice, the antiferromagnetism vector in the tetragonal plane is dominant, while the ferromagnetism vector

that is perpendicular to this vector and also lies in the tetragonal plane, as well as the antiferromagnetism vector along the **c** axis, is relatively small. In the Cu(*d*) sublattice, the antiferromagnetism vector along the **c** axis is likely to be dominant, while the orthogonal antiferromagnetism vector in the tetragonal plane is relatively small. A ferromagnetism vector in this sublattice has not been detected within the limits of experimental error. In the commensurate phase, the magnetic moment of a copper ion in the 8*d* position is far less than that of a copper ion in the 4*b* position. All vectors indicated above correspond to the magnetic modes found in the symmetry analysis.

In the incommensurate phase ($T < T_i$), the magnetic structure is ordered in the tetragonal plane in the form of a spiral along the **c** axis. For theoretical analysis of the magnetic properties of copper metaborate in terms of the phenomenological thermodynamic potential, it is essential that its symmetry group not contain inversion center $\bar{1}$. This operation enters only in combination with 90° rotation about the **c** axis, namely, $\bar{4}_3^1$ and $\bar{4}_3^3$. Therefore, the thermodynamic potential can contain a Lifshitz-type invariant that should be bilinear in the two-component order parameters and their spatial derivatives and be responsible for the appearance of an incommensurate phase.

Taking into account all eight single-component and five two-component homogeneous magnetic modes in the framework of the phenomenological approach results in an extremely cumbersome expression for the thermodynamic potential of the system. Therefore, it is necessary to separate modes that allow one to describe the basic experimental properties of copper metaborate. Since ordering in the tetragonal plane is dominant, we first consider the corresponding two-component modes. The following circumstance should be taken into account in this case. If we represent an arbitrary *i*th homogeneous mode in the Γ_5 representation in the form $\eta_i = (\eta_{i1}, \eta_{i2})$, then the corresponding inhomogeneous mode in this representation is $\eta_i' = (\eta_{i2}, \eta_{i1})'$. The invariant $\eta_i \cdot \eta_i' = \eta_{i1}\eta_{i2}' + \eta_{i1}'\eta_{i2}$ turns out to be the complete derivative with respect to *z*, and it is impossible to construct a Lifshitz invariant for a single mode. In terms of the theory of representations, this feature is due to the fact that the antisymmetric square $\{\Gamma_5^2\}$ transforms according to the representation Γ_2, the vector component parallel to the tetragonal axis transforms according to the representation Γ_3, and the perpendicular component transforms according to the representation Γ_5 [8].

Let us represent the incomplete thermodynamic potential as a functional of two two-component order parameters, $\eta_1 = (\eta_{11}, \eta_{12})$ and $\eta_2 = (\eta_{21}, \eta_{22})$:

$$\Phi\{\eta\} = \int\Bigg\{\frac{A_{11}}{2}\eta_1\cdot\eta_1 + \frac{A_{22}}{2}\eta_2\cdot\eta_2 + A_{12}\eta_1\cdot\eta_2 + \frac{B_{22}}{4}(\eta_2\cdot\eta_2)^2 + C_{12}(\eta_1\cdot\eta_2' - \eta_1'\cdot\eta_2) + \frac{D_{11}}{2}\nabla\eta_1\cdot\nabla\eta_1 + \frac{D_{22}}{2}\nabla\eta_2\cdot\nabla\eta_2 + D_{12}\nabla\eta_1\cdot\nabla\eta_2 - \eta_1\cdot H_1\Bigg\}dV, \quad (5)$$

where integration is performed over the entire volume of the crystal, $A_{11} = a_{11}(T - T_1)$, $A_{22} = a_{22}(T - T_2)$, $a_{11} > 0$, $a_{22} > 0$, $B_{22} > 0$, $D_{11} > 0$, $D_{11}D_{22} > D_{12}^2$, $\nabla\eta_\alpha = (\nabla\eta_{\alpha2}, \nabla\eta_{\alpha1})$, and H_1 is the field conjugate to the parameter η_1. The order parameters are assumed to be dependent on spatial coordinates.

The parameters η_1 and η_2 are different linear combinations of the magnetic modes transforming according to the representation Γ_5. The fact that the magnetic subsystem of copper metaborate below T_N is an easy-plane weak ferromagnet spiraling below T_i allows one to compose the parameter η_1 from ferromagnetic modes described by Eqs. (1) and (3) and the parameter η_2 from antiferromagnetic modes given by Eqs. (2) and (4). Correspondingly, $H_1 = (H_{11}, H_{12}) = (H_x, -H_y)$. However, a weak ferromagnet is characterized by $T_1 \lesssim 0$ and $T_2 \approx T_N$. It should be noted that, unlike in [3], the order parameter responsible for the transition at T_i is not chosen in a explicit form in the thermodynamic potential (5).

The invariant with coefficient C_{12} is the known Lifshitz invariant [8] generalized to the case of two two-component order parameters; namely, this invariant is the antisymmetric product of different order parameters and their spatial derivatives rather than the antisymmetric product of the components of a single order parameter and their spatial derivatives.

Out of the invariants of the fourth order, only the invariant related to the temperature dependence of the antiferromagnetic parameter is retained in Eq. (5). The invariants that are quadratic in the spatial derivatives of the order parameters are taken in the simplest isotropic form. The presence of the other order parameters in Eq. (5), as will be shown below, is not a decisive factor for describing the evolution of the structure of copper metaborate with decreasing temperature from the paramagnetic phase above 20 K to the incommensurate phase below 10 K.

3. EQUILIBRIUM STATE IN THE MODEL

In the absence of the Lifshitz invariant, the equilibrium state in the model described by phenomenological potential (5) is homogeneous because of the positive definiteness of the other inhomogeneous terms of the potential. The Lifshitz invariant disturbs the stability of this state along the tetragonal axis. To find a new equilibrium state, we use the fact that higher order magnetic satellites in neutron diffraction patterns in the absence of an applied dc magnetic field were detected only in the vicinity of the transition to the incommensurate phase [2, 3].

Therefore, we represent the equilibrium state in a zero applied field in the form

$$\begin{aligned}\eta_1 &= (p_{11}\cos(qz+\varphi_{11}),\ p_{12}\cos(qz+\varphi_{12})),\\ \eta_2 &= (p_{21}\cos(qz+\varphi_{21}),\ p_{22}\cos(qz+\varphi_{22})),\end{aligned} \tag{6}$$

where the amplitudes $p_{\alpha\beta}$ and the phases $\varphi_{\alpha\beta}$ of a spatial wave are independent of z. Putting $\varphi_{11} = 0$ in Eq. (6), we set a reference point along the tetragonal axis without loss of generality. The set of necessary conditions for an extremum that is obtained from Eq. (5) by variation with respect to the parameters given in Eq. (6) is rather awkward. We give only its solution:

$$\begin{aligned}p_{11} &= -(A_{12q}p_{21} - C_{12q}p_{22})/A_{11q},\\ p_{12} &= -(A_{12q}p_{21} + C_{12q}p_{22})/A_{11q},\end{aligned} \tag{7}$$

$$\begin{aligned}p_{21} &= p_{22}\\ &= \mathrm{Re}\{[(A_{12q}^2 + C_{12q}^2 - A_{11q}A_{22q})/A_{11q}B_{22}]^{1/2}\},\end{aligned} \tag{8}$$

$$q = \mathrm{Re}\left\{\left[\frac{\left(\dfrac{4A_{11}D_{11}C_{12}^2 - (A_{11}D_{12} - A_{12}D_{11})^2}{D_{11}D_{22} - D_{12}^2}\right)^{1/2} - A_{11}}{D_{11}}\right]^{1/2}\right\}, \tag{9}$$

$$\varphi_{11} = \varphi_{21} = 0, \quad \varphi_{12} = \varphi_{22} = \pi/2, \tag{10}$$

where $A_{\alpha\beta q} = A_{\alpha\beta} + D_{\alpha\beta}q^2$ and $C_{12q} = 2C_{12}q$.

Unlike the relationships in [9] considered for a one-parameter potential, these relationships feature a possible difference between the temperature of ordering in the magnetic system ($p_{21} \neq 0$) and the temperature of formation of a spiral structure in it ($q \neq 0$). For example, a spiral magnetic structure exists in the temperature range (T_{q1}, T_{q2}) with

$$T_{q1} = T_{q0} - \Delta T_q, \quad T_{q2} = T_{q0} + \Delta T_q, \tag{11}$$

where

$$T_{q0} = T_1 + (A_{12}D_{12} + 2C_{12}^2)/(a_{11}D_{22}),$$

$$\Delta T_q = [(A_{12}D_{12} + 2C_{12}^2)^2 - A_{12}^2 D_{11}D_{22}]^{1/2}/(a_{11}D_{22}).$$

Ordering occurs at the temperature

$$\begin{aligned}T_p &= T_{p0} + \Delta T_p,\\ T_{p0} &= [T_1 + T_2 - (D_{11}/a_{11} + D_{22}/a_{22})q^2]/2,\\ \Delta T_p &= \{[T_1 - T_2 - (D_{11}/a_{11} - D_{22}/a_{22})q^2]^2\\ &\quad + 4(A_{12q}^2 + C_{12q}^2)/(a_{11}a_{22})\}^{1/2}/2.\end{aligned} \tag{12}$$

Note that, in the incommensurate phase, according to Eqs. (7), (8), and (10), the order parameter η_1 forms an elliptical spiral along the tetragonal axis and the order parameter η_2, a circular spiral. The ellipticity of the spiral means that the magnetic moments deviate from the tetragonal plane to form a wave of their components that are parallel to the tetragonal axis.

We describe the state of the crystal in an external magnetic field applied along the tetragonal plane with the equations

$$\begin{aligned}\eta_1 &= (p_{11q}\cos(qz+\varphi_{11q}) + p_{11k}\cos(kz+\varphi_{11k}),\\ &\quad p_{12q}\cos(qz+\varphi_{12q}) + p_{12k}\cos(kz+\varphi_{12k})),\\ \eta_2 &= (p_{21q}\cos(qz+\varphi_{21q}) + p_{21k}\cos(kz+\varphi_{21k}),\\ &\quad p_{22q}\cos(qz+\varphi_{22q}) + p_{22k}\cos(kz+\varphi_{22k})),\\ H_1 &= (H\cos(kz), -H\sin(kz)).\end{aligned} \tag{13}$$

The passage to the case of a homogeneous applied field ($k = +0$) in $\Phi\{\eta\}$ should be performed only after integrating over the volume of the crystal.

The variational equations permit two solutions characterized by the following common relations:

$$\begin{aligned}p_{11q} &= -(A_{12q}p_{21q} - C_{12q}p_{22q})/A_{11q},\\ p_{12q} &= -(A_{12q}p_{21q} + C_{12q}p_{22q})/A_{11q},\\ p_{11k} &= (H - A_{12}p_{21k})/A_{11},\\ p_{12k} &= (H - A_{12}p_{22k})/A_{11},\\ \varphi_{11q} &= \varphi_{21q} = \varphi_{11k} = \varphi_{21k} = 0,\\ \varphi_{12q} &= \varphi_{22q} = \varphi_{12k} = \varphi_{22k} = \pi/2.\end{aligned} \tag{14}$$

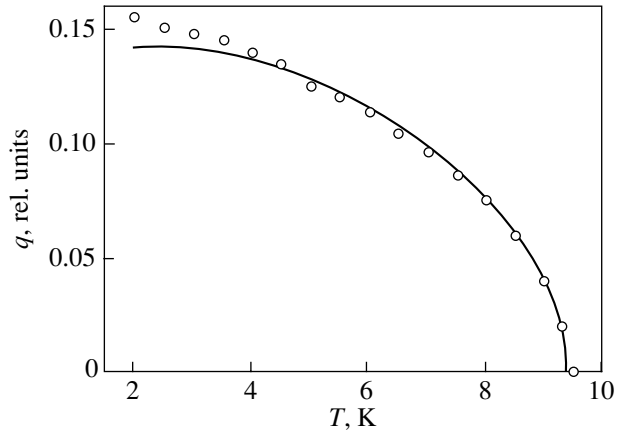

Fig. 1. Temperature dependence of the wave vector of the magnetic structure in copper metaborate at a zero applied field. Points are experimental data and the solid line is calculation.

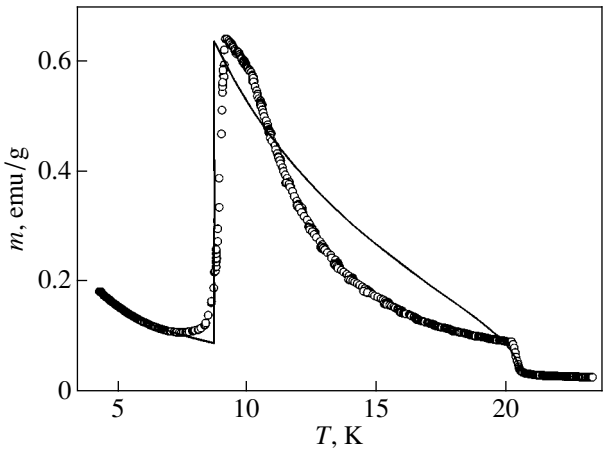

Fig. 2. Temperature dependence of the magnetization of single-crystalline copper metaborate in an applied filed of 0.25 kOe in the tetragonal plane.

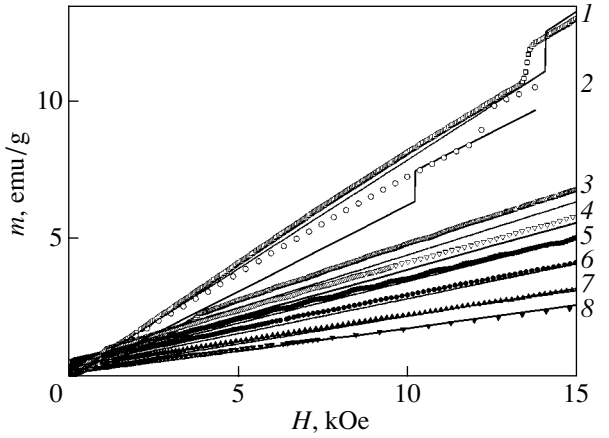

Fig. 3. Field dependence of the magnetization of single-crystalline copper metaborate in the tetragonal plane at various temperatures: (*1*) $T = 4.2$, (*2*) 5, (*3*) 8, (*4*) 9, (*5*) 10, (*6*) 12, (*7*) 15, and (*8*) 18 K.

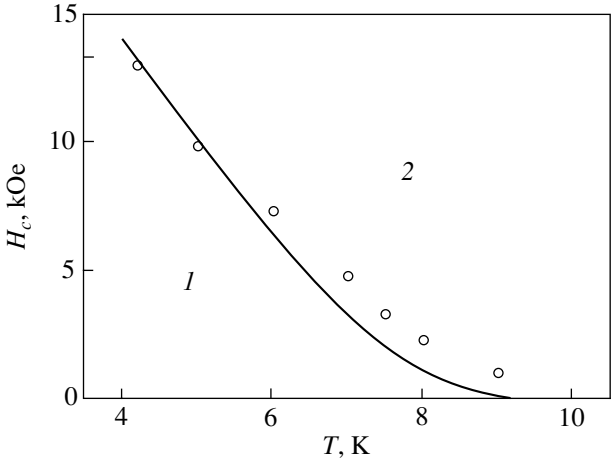

Fig. 4. Temperature–field phase diagram of copper metaborate: (*1*) incommensurate phase and (*2*) easy-plane weak-ferromagnetic phase.

One solution corresponds to a homogeneous state of the magnetic system,

$$p_{21q} = p_{22q} = 0, \quad p_{21k} = p_{22k} = p_{2k}, \qquad (15)$$

where p_{2k} satisfies the equation

$$A_{11}B_{22}p_{2k}^3 + (A_{11}A_{22} - A_{12}^2)p_{2k} + A_{12}H = 0.$$

The other solution describes an inhomogeneous state,

$$p_{21q} = p_{22q} = p_{2q}, \quad p_{21k} = p_{22k} = p_{2k}, \qquad (16)$$

where p_{2q} and p_{2k} are determined from the set of equations

$$A_{11q}B_{22}p_{2q}^2 + A_{11q}(A_{22q} + 2B_{22}p_{2k}^2) = A_{12q}^2 + C_{12q}^2,$$

$$3A_{11}A_{11q}B_{22}p_{2k}^3 + [2A_{11}A_{11q}A_{22q} + A_{11q}A_{12}^2 - A_{11}A_{11q}A_{22} - 2A_{11}(A_{12q}^2 + C_{12q}^2)]p_{2k} = A_{11q}A_{12}H.$$

The wave vector **q** is equal to zero or determined by Eq. (9) depending on the stability of the corresponding solutions (15) or (16). The stability of a solution depends on the relation between the parameters of thermodynamic potential (5) and the value of the magnetic field.

4. DISCUSSION OF THE RESULTS

The case where the temperatures of ordering in the magnetic subsystem and of the formation of a spiral

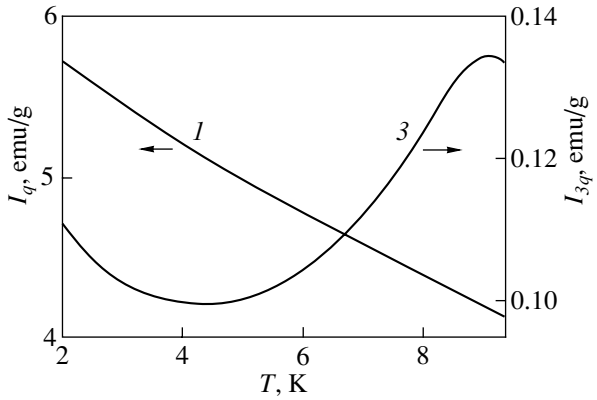

Fig. 5. Calculated temperature dependences of the intensities of (*1*) the fundamental (I_q) and (*3*) the third (I_{3q}) harmonics of the antiferromagnetism vector in copper metaborate at a zero applied field.

structure in it are different [and are given by Eqs. (11) and (12)] corresponds to the properties of copper metaborate described in Introduction. Indeed, for certain relations between the parameters of thermodynamic potential (5), we can obtain $T_p > T_{q2}$ and a stable homogeneous state ($\mathbf{q} = 0$) at intermediate temperatures. In this case, the temperature T_N for copper metaborate can be related to T_p given by Eq. (12) and T_i can be related to T_{q2} given by Eq. (11). Let us compare the relations derived for the temperature and field dependences of the wave vector and of the order parameters with the experimental data.

Figures 1–5 show the results of numerical calculation by Eqs. (6)–(16) using the following coefficients of the incomplete thermodynamic potential (5):

$$a_{11} = a_{22} = 3.3 \times 10^2 \frac{\mathrm{G}^2\,\mathrm{g}^2}{\mathrm{erg\ cm}^3\,\mathrm{K}},$$

$$T_1 = 0.19\ \mathrm{K}, \quad T_2 = 20.4\ \mathrm{K},$$

$$B_{22} = 5.2 \times 10^1 \frac{\mathrm{G}^4\,\mathrm{g}^4}{\mathrm{erg}^3\,\mathrm{cm}^3},$$

$$A_{12} = -1.8 \times 10^2 \frac{\mathrm{G}^2\,\mathrm{g}^2}{\mathrm{erg\ cm}^3},$$

$$C_{12}\left(\frac{2\pi}{c}\right) = -5.3 \times 10^3 \frac{\mathrm{G}^2\,\mathrm{g}^2}{\mathrm{erg\ cm}^3},$$

$$D_{11}\left(\frac{2\pi}{c}\right)^2 = 3.7 \times 10^4 \frac{\mathrm{G}^2\,\mathrm{g}^2}{\mathrm{erg\ cm}^3},$$

$$D_{22} = D_{11}, \quad D_{12} = 0.$$

As seen from Figs. 1–5, we failed to achieve excellent agreement between the calculated and experimental data; however, the calculated temperature and field dependences of the parameters of the magnetic subsystem of copper metaborate are in satisfactory agreement with the experiment.

In the incommensurate phase, the spontaneous contribution to the magnetization of the whole crystal disappears because of the spiral structure and only the magnetization induced by an applied field is nonzero (Fig. 2) [1, 2]. As the applied field increases, a first-order transition to the easy-plane weak-ferromagnetic phase occurs; namely, the component of the antiferromagnetism vector with $\mathbf{q} \neq 0$ vanishes in a jump at the field $H_c(T)$, whereas the component with a zero wave vector increases in a jump [4, 5]. This behavior of the magnetic subsystem also manifests itself in the magnetization (Fig. 3), which is related to the antiferromagnetism vector through the Dzyaloshinskiĭ invariant (with coefficient A_{12}). The presence of this invariant corresponds to nonzero values of magnetization in a zero field when its field dependence is linearly approximated in fields above $H_c(T)$ [1, 2]. Figure 4 shows the experimental [2] and calculated temperature–field phase diagrams in the temperature range 4–10 K.

The presence of higher harmonics in the spiral of the incommensurate phase is characteristic of the temperature range where the Lifshitz invariant is comparable to the anisotropy invariant [9]. For magnetic systems described by a one-parameter thermodynamic potential, the wave vector $\mathbf{q}$ differs from zero even at the ordering temperature ($T_i = T_p$) and the anisotropy invariant (which is proportional to $|\eta|^4$ for a tetragonal crystal) becomes comparable to the Lifshitz invariant (which is proportional to $q|\eta|^2$) substantially below T_i, near the transition to the low-temperature commensurate phase. In copper metaborate, however, q increases sharply from zero at $T_i < T_p$ (Fig. 1) [3] and the invariants can become comparable only in a narrow vicinity of T_i or in the range where q varies smoothly. According to the experimental data in [3], only the former possibility is realized.

Figure 5 shows the calculated temperature dependences of the intensities of the fundamental and third harmonics of the antiferromagnetism vector at a zero applied field. To describe them, we added the anisotropy invariant

$$\frac{E_{22}}{2}\int \eta_{21}^2 \eta_{22}^2 dV$$

to thermodynamic potential (5). The intensity of the fundamental harmonic is higher than that of the third harmonic by a factor of approximately 30 (as observed in [3] at $T = 9.35$ K) for $E_{22} = 7\ (\mathrm{G\ g})^4/(\mathrm{erg\ cm})^3$. As seen from Fig. 5, this difference increases as the temperature decreases, which hampers the possible observation of the higher harmonic.

The sharp decrease in the intensity of magnetic peaks $(3, 3, \pm q)$ at $T = 1.8$ K and the fact that thereafter q does not vary with decreasing temperature [4, 5] can be related to a lock-in transition to the commensurate

phase. This transition is accompanied by the sudden appearance of a gap in the energy spectrum of excitations that are transverse with respect to the order parameter and by the corresponding decrease in the correlation functions.

ACKNOWLEDGMENTS

We thank S.N. Martynov for helpful discussions.

This work was supported by the Ministry of Education of the Russian Federation (project no. E02-3.4-227) and the Russian Foundation for Basic Research (project no. 03-02-16701).

REFERENCES

1. G. Petrakovskii, D. Velikanov, A. Vorotinov, *et al.*, J. Magn. Magn. Mater. **205** (1), 105 (1999).
2. G. A. Petrakovskiĭ, A. D. Balaev, and A. M. Vorotynov, Fiz. Tverd. Tela (St. Petersburg) **42** (2), 313 (2000) [Phys. Solid State **42**, 321 (2000)].
3. R. Roessli, J. Schefer, G. A. Petrakovskii, *et al.*, Phys. Rev. Lett. **86** (9), 1885 (2001).
4. J. Schefer, M. Boehm, B. Roessli, *et al.*, Appl. Phys. A **74** (Suppl. 1), S1740 (2002).
5. M. Boehm, B. Roessli, J. Schefer, *et al.*, Physica B (Amsterdam) **318** (4), 277 (2002).
6. Yu. A. Izyumov, *Neutron Diffraction by Long-Period Structures* (Énergoatomizdat, Moscow, 1987).
7. O. V. Kovalev, *Representations of the Crystallographic Space Groups: Irreducible Representations, Induced Representations, and Corepresentations* (Nauka, Moscow, 1986; Gordon and Breach, Yverdon, Switzerland, 1993).
8. L. D. Landau and E. M. Lifshitz, *Course of Theoretical Physics*, Vol. 5: *Statistical Physics*, 3rd ed. (Nauka, Moscow, 1976; Pergamon, Oxford, 1980), Part 1.
9. I. E. Dzyaloshinskiĭ, Zh. Éksp. Teor. Fiz. **47** (3), 992 (1964) [Sov. Phys. JETP **20**, 573 (1964)].

Translated by K. Shakhlevich

Physics of the Solid State, Vol. 46, No. 3, 2004, pp. 498–501. Translated from Fizika Tverdogo Tela, Vol. 46, No. 3, 2004, pp. 484–487.

MAGNETISM AND FERROELECTRICITY

Magnetorefractive Effect in Nanocomposites: Dependence on the Angle of Incidence and on Light Polarization

A. B. Granovsky[1], M. Inoue[2, 3], J. P. Clerc[4], and A. N. Yurasov[1]

[1]*Moscow State University, Vorob'evy gory, Moscow, 119992 Russia*
e-mail: granov@magn.ru
[2]*Toyohashi University of Technology, Toyohashi, 441-8580 Japan*
[3]*CREST, Japan Science and Technology Corporation, Kawaguchi, 332-0012 Japan*
[4]*École Polytechnique, Université de Marseille, Technopole de Chateau Gombert, Marseille, 13453 France*

Received July 21, 2003

Abstract—The polarization and angular dependences of the magnetorefractive effect (MRE) in metal–insulator nanocomposites in reflection and transmission geometries have been calculated in terms of the high-frequency, spin-dependent tunneling mechanism. The MRE exhibits a weak polarization and angular response at small angles of incidence. The MRE in reflection and transmission starts to grow strongly with increasing angle of incidence. The MRE in reflection in nanocomposites with metal contents corresponding to the insulating phase near the percolation threshold reaches the largest values with *p*-polarized light at an angle of incidence close to the Brewster angle. The results of the calculation are in a qualitative agreement with experimental data.

1. INTRODUCTION

The magnetorefractive effect (MRE), is a new even-parity magnetooptic (MO) phenomenon observed in magnets with a sufficiently high magnetoresistance (MR) and consists in a change in their optical properties under magnetization (see [1, 2] and references therein). The MRE is observed in metal multilayers and granular alloys with a giant MR. In magnetic nanocomposites with tunneling MR, the change in the reflection coefficient under magnetization can be as high as 1.3%, which exceeds the conventional MO effects by two orders of magnitude [1, 2]. The theory of the MRE in reflection in metal–insulator magnetic nanocomposites was developed in [1] for the case of normal light incidence. This theory is based on describing the tunneling contact between grains as a tunneling resistor and a capacitor connected in parallel. We use this approach to consider the dependence of the MRE in nanocomposites on the angle of incidence and on the polarization of light in reflection geometry, as well as the MRE in transmission.

2. THEORY

For definiteness, we first consider the case of a *p*-polarized light wave traveling in a transparent nonmagnetic insulator (medium *1* with a real refraction coefficient n_1) and impinging in the *xy* plane on a magnetic sample (medium *2* with a complex refraction coefficient $\eta_2 = n_2 - ik_2$) at an angle of incidence ϕ_0. In calculating the MRE in reflection, we disregard the reflection from the substrate (medium *3*) and the possible related interference effects; in other words, the magnetic sample is considered to be sufficiently thick. Then, the reflection coefficient R for a sample magnetized in the z direction can be written as [3]

$$R = \left|r_{12}^p\right|^2,$$
$$r_{12}^p = \frac{g_1\eta_2^2 - g_2 n_1^2}{g_1\eta_2^2 + g_2 n_1^2} - \frac{g_1\eta_2^2\varepsilon_{xy}}{g_2 n_1^2(g_1\eta_2^2 + g_2 n_1^2)^2}, \quad (1)$$

$$g_1 = \sqrt{n_1^2 - n_1^2\sin^2\phi_0}, \quad g_2 = \sqrt{\eta_2^2 - n_1^2\sin^2\phi_0}. \quad (2)$$

By definition, $\varepsilon_2^d = \eta_2^2 = (n_2 - ik_2)^2$ is a diagonal elements of the permittivity tensor of the magnet containing the term quadratic in the magnetization M [1]:

$$\varepsilon = \varepsilon_2^d = \varepsilon_0(1 + bM^2), \quad b = b_a + b_{\mathrm{MRE}}. \quad (3)$$

Here, b_a relates to the contribution due to the magnetization-induced anisotropy of the magnet [4], b_{MRE} is the MRE contribution, and ε_0 is the dielectric permittivity of the magnet in the demagnetized state. The off-diagonal element ε_{xy} of the dielectric permittivity tensor in Eq. (1) is responsible for the linear (in magnetization) Kerr and Faraday MO effects. As seen from Eq. (1), the even (in magnetization) orientational MO effect [5, 6] is associated to both with the term $\varepsilon_0 b_a M^2$ in diagonal element (3) and with the off-diagonal element. The off-diagonal element ε_{xy} is expressed, as a rule, through the experimentally measurable MO parameter Q as $\varepsilon_{xy} = -i\varepsilon_0 Q$; the parameter Q is a frequency-dependent complex quantity and is linear in spin-orbital coupling and,

hence, in magnetization. The term $\varepsilon_0 b_a M^2$ in Eq. (3) is of order $\varepsilon_0 Q^2$. Because $b_a M^2 \sim Q^2$, and $b_{\mathrm{MRE}} M^2 \sim \Delta\rho/\rho$ [1, 2] (where $\Delta\rho/\rho$ is the MR), and because Q does not exceed 0.02 in the visible spectral region and decreases in the IR region, one can obviously neglect the contribution from the conventional even MO effect to the MRE for any magnet exhibiting noticeable MR. The results of the calculation based on Eq. (1) and plotted in Fig. 1 support the above statement. Therefore, in what follows, we set $b_a = Q = 0$, which leaves only the MRE for consideration. We denote the magnetization-induced changes in the refraction and extinction coefficients as

$$\frac{n_2 - n_2^0}{n_2^0} = cM^2, \quad \frac{k^2 - k_2^0}{k_2^0} = dM^2 \tag{4}$$

and assume them to be small parameters of the problem. In this case, we can obtain a general expression for the MRE in reflection, i.e., for the magnetization-induced change in the reflection coefficient R of a sample:

$$\frac{\Delta R}{R} = \frac{R(M=0) - R(M)}{R(M=0)} \tag{5}$$

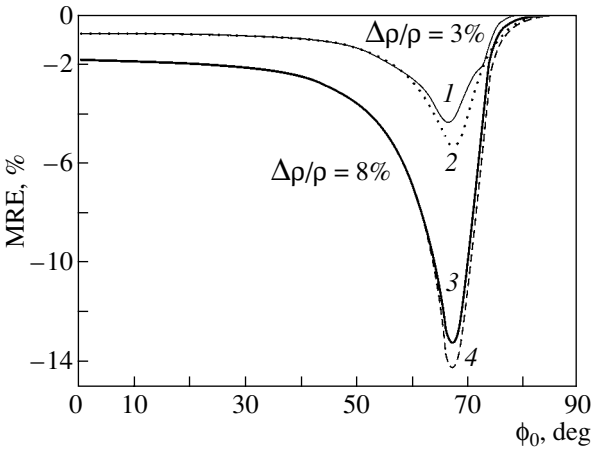

Fig. 1. Dependence of the MRE of a nanocomposite on the angle of incidence of *p*-polarized light obtained (*1*, *3*) with inclusion of and (*2*, *4*) neglecting the even-parity orientational magnetooptical effect for (*1*, *2*) $\Delta\rho/\rho = 3\%$ (*1*, *2*) and (*3*, *4*) 8%; $n = 2.5$, $k = 0.5$, $Q = -0.034 + 0.003i$, and $\lambda = 9$ μm.

can be represented in the following general form based on Eqs. (1)–(5):

$$\begin{aligned}\frac{\Delta R}{R} = {} & \frac{4M^2}{[(a_1\cos\phi_0 - g_1)^2 + (a_2\cos\phi_0 - g_2)^2][(a_1\cos\phi_0 + g_1)^2 + (a_2\cos\phi_0 + g_2)^2]} \\ & \times [(a_1^2\cos^2\phi_0 - g_1^2)(b_1 g_1\cos\phi_0 - a_1\cos\phi_0\,\mathrm{Re}(b/2g)) \\ & + (a_2^2\cos^2\phi_0 - g_2^2)(b_2 g_2\cos\phi_0 - a_2\cos\phi_0\,\mathrm{Im}(b/2g)) \\ & + 2b_1\cos\phi_0(2a_1a_2g_2\cos^2\phi_0 - g_1g_2^2 - g_1a_2^2\cos^2\phi_0) \\ & + 2b_2\cos\phi_0(2a_1a_2g_1\cos^2\phi_0 - g_2g_1^2 - g_2a_1^2\cos^2\phi_0) \\ & - 2\,\mathrm{Re}(b/2g)(a_1a_2^2\cos^3\phi_0 + a_1g_2^2\cos\phi_0 - 2g_1a_2g_2\cos\phi_0) \\ & - 2\,\mathrm{Im}(b/2g)(a_2a_1^2\cos^3\phi_0 + a_2g_1^2\cos\phi_0 - 2g_1a_1g_2\cos\phi_0)],\end{aligned} \tag{6}$$

where

$$\begin{gathered}a = a_1 - ia_2, \quad a_1 = n^2 - k^2, \quad a_2 = 2nk, \\ b = b_1 - ib_2, \quad b_1 = 2cn^2 - 2dk^2, \\ b_2 = 2nk(c+d),\end{gathered} \tag{7}$$

$$g = g_1 - ig_2 = \sqrt{(a_1 - ia_2)^2 - \sin^2\varphi_0}. \tag{8}$$

In a similar way, one can calculate the transmission coefficient T of *p*-polarized light for an infinitely thin film

$$T = \left|t_{12}^p\right|^2, \quad t_{12}^p = \frac{2g_1\eta_2}{g_1\eta_2^2 + g_2n_1^2}, \tag{9}$$

the MRE in transmission $\Delta T/T$, and the same quantities for the case of *s* polarization.

If medium *1* is a vacuum ($n_1 = 1$) and light is incident at a close-to-normal angle ($\varphi_0 = 0$), then all the above expressions become considerably simplified and we have

$$R = \frac{(1-n_2)^2 + k_2^2}{(1+n_2)^2 + k_2^2}, \tag{10}$$

$$\begin{aligned}\frac{\Delta R}{R} = {} & (1-R)M^2 \\ & \times\left[c\frac{1 - (n_2^0)^2 + (k_2^0)^2}{(1-n_2^0)^2 + (k_2^0)^2} - 2d\frac{(k_2^0)^2}{(1-n_2^0)^2 + (k_2^0)^2}\right],\end{aligned} \tag{11}$$

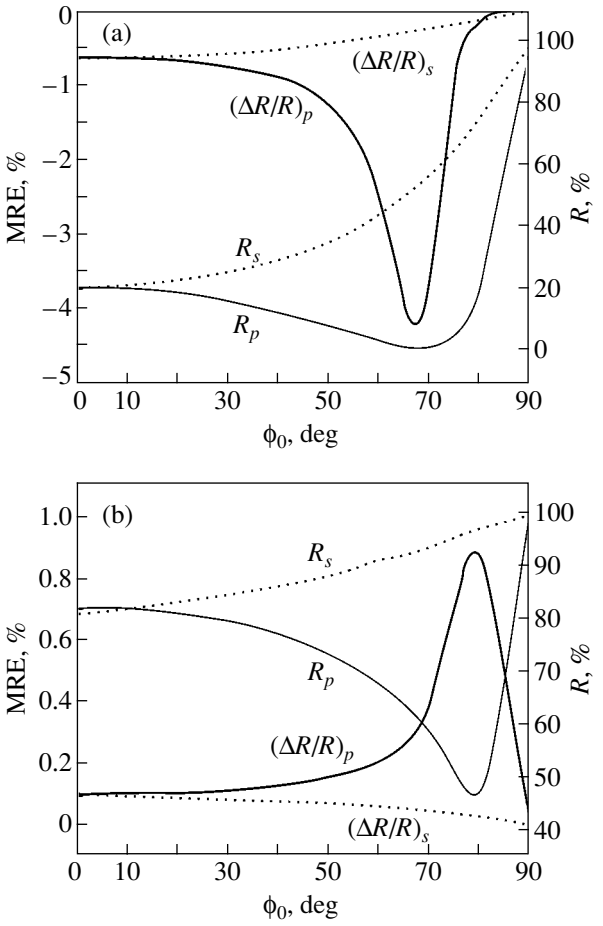

Fig. 2. Angular dependences of the MRE and of the reflection coefficient for the *p* (solid line) and *s* (dotted line) polarization calculated (a) for an insulating nanocomposite (below the percolation threshold) for $\Delta\rho/\rho = 3\%$, $n = 2.5$, and $k = 0.5$ and (b) for $\Delta\rho/\rho = 3\%$, $n = 4$, and $k = 8$.

$$\frac{\Delta T}{T} = \frac{1}{2}M^2T[cn_2^0(n_2^0+1) + d(k_2^0)^2]. \quad (12)$$

These expressions are general in nature, because they relate the MRE of an arbitrary system with its optical parameters, as well as with the microscopic parameters *c* and *d*. The latter parameters depend on the mechanism of the MRE. For nanocomposites with tunneling MR

$$\frac{\Delta\rho(H)}{\rho} = \frac{\rho(0)-\rho(H)}{\rho(0)}, \quad (13)$$

if the tunneling contact between grains is represented by an equivalent capacitor and a tunneling resistor connected in parallel [1, 2], we obtain

$$dM^2 = \frac{\Delta\rho}{\rho}\frac{1}{1+(k/n)^2}, \quad cM^2 = \frac{\Delta\rho}{\rho}\frac{(k/n)^2}{1+(k/n)^2}. \quad (14)$$

In Eq. (14), we dropped both index 2 specifying the magnetic medium and superscript 0 denoting the demagnetized state. In the particular case of normal incidence of light from vacuum, Eqs. (10)–(14) yield the following relations:

$$\frac{\Delta R}{R} = -(1-R)\frac{\Delta\rho}{\rho}k^2\left[\frac{3n^2-k^2-1}{(n^2+k^2)[(1-n)^2+k^2]}\right], \quad (15)$$

$$\frac{\Delta T}{T} = \frac{1}{2}\frac{\Delta\rho}{\rho}Tk^2\frac{2n^2+n}{n^2+k^2}. \quad (16)$$

In the case of an arbitrary angle of incidence of *p*-polarized light, Eqs. (6)–(8) should be used in combination with the relations (14); the expressions derived for the case of *s* polarization are analogous to those written above.

3. RESULTS AND DISCUSSION

Figure 1 presents the angular dependence of the MRE for *p*-polarized light calculated for two values of MR. The optical parameters *n* and *k* chosen are typical of composites near the percolation threshold [7] in the IR spectral region ($\lambda = 9$ μm), and the MO parameter *Q* corresponds to Fe in the visible region. Unfortunately, the value of the MO parameter in the near IR region of the spectrum is unknown, however, it is certain to be smaller than that in the visible region. As already mentioned, the results of the calculation suggest that the conventional even-parity MO effect is insignificant under arbitrary angles of incidence, except in the immediate vicinity of the Brewster angle, i.e., in the region where MRE measurements in reflection are impossible. With the exception of this angular interval, the contribution from the orientational effect is less than 0.01%, as should be expected from the smallness of the spin–orbit coupling.

Figure 2 displays calculated angular dependences of the MRE for the *p* and *s* polarizations, as well as those of the reflection coefficient. Data are presented for compositions on both sides of the percolation threshold; namely, Fig. 2a corresponds to the insulator composition, where the Brewster phenomenon is most clearly pronounced, and Fig. 2b, to the metallic composition, where this phenomenon plays an insignificant role. A correlation between the MRE and the reflection coefficient for each polarization is clearly seen, although it is not linear. At small incidence angles, the MRE is practically independent of the polarization. This is in accord with the experimental results quoted for a Fe–SiO_2 nanocomposite in [1]. In the case of insulator compositions, the MRE increases considerably with the angle of incidence for the *p*-polarized light while decreasing only slightly for the *s* polarization. For the metallic composition, the dependence of the MRE on the polarization of light is fairly weak up to 70°–80°, i.e., to the angles corresponding to the principal angle of incidence for the metal. These findings offer an explanation for the experimental data obtained for the polarization dependences of the MRE in the

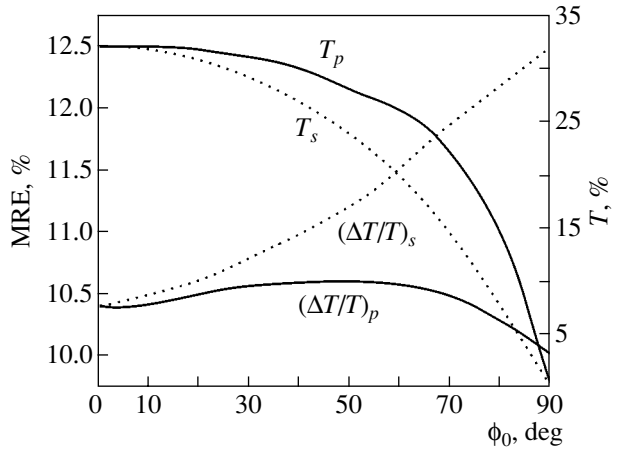

Fig. 3. Angular dependences of the MRE and of the transmission coefficient of a nanocomposite obtained for the *p* (solid line) and *s* (dotted line) polarization; $\Delta\rho/\rho = 8\%$, $n = 2.5$, and $k = 0.5$.

$CoFe–Al_2O_3$ nanocomposites [8]. Furthermore, this result suggests a way of increasing the MRE substantially by properly choosing the nanocomposite composition. It should be pointed out that the MRE for nanocomposites in the metallic phase is positive, which is likewise in agreement with the results reported in [8].

Figure 3 plots the data for the MRE in transmission obtained for the air–nanocomposite film (2 μm thick)–silicon substrate system [1]. In contrast to Eq. (9), the possible effect of reflection from the substrate was included here [3]. As is evident from Fig. 3, the polarization dependences of the MRE in transmission differ strongly from those measured in reflection; indeed, the MRE in transmission depends only weakly on the angle of incidence for *p*-polarized light, whereas in the case of *s* polarization the dependence is strong.

As follows from the calculations, the angular and polarization responses of the MRE should behave similarly for various wavelengths. For the CoFe–MgF system, however, an increase in the MRE with increasing angle of incidence, as shown in [1], is observed to occur in the interval 2–5 μm but is not seen in the 10-μm region, which indicates the possible existence of an additional MRE mechanism.

4. CONCLUSIONS

The MRE in nanocomposites with tunneling MR is connected in a complex manner with optical parameters, with the correlation between the MRE and the reflection coefficient not being linear. At large angles of incidence, the MRE exhibits a strong polarization dependence and is considerably larger for the *p* component in reflection and for the *s* component in transmission. The calculations showed that the MRE should be pronounced most clearly in the spectral regions of strong absorption and that it can be both negative (in the insulator phase of the nanocomposite) and positive (in the metallic phase), which accounts for some experimental data.

ACKNOWLEDGMENTS

The authors are indebted to E.A. Gan'shina, I.V. Bykov, V.S. Gushchin, and A.A. Kozlov for helpful discussions.

This study was supported by the Russian Foundation for Basic Research (project no. 03-02-16127) and the "Universities of Russia" program.

REFERENCES

1. A. B. Granovskiĭ, I. V. Bykov, E. A. Gan'shina, *et al.*, Zh. Éksp. Teor. Fiz. **123** (6), 1256 (2003) [JETP **96**, 1104 (2003)].
2. A. Granovsky and M. Inoue, J. Magn. Soc. Korea **8** (2), 45 (2002).
3. V. M. Maevskiĭ, Fiz. Met. Metalloved. **59** (2), 213 (1985).
4. G. S. Krinchik and M. V. Chetkin, Zh. Éksp. Teor. Fiz. **36** (6), 1924 (1959) [Sov. Phys. JETP **9**, 1368 (1959)].
5. G. S. Krinchik and V. S. Gushchin, Pis'ma Zh. Éksp. Teor. Fiz. **10** (6), 1969 (1969).
6. G. A. Bolotin, Fiz. Met. Metalloved. **39** (4), 731 (1975).
7. G. A. Niklasson and C. G. Granqvist, J. Appl. Phys. **55** (9), 3382 (1984).
8. D. Bozec, V. G. Kravets, J. A. D. Matthew, *et al.*, J. Appl. Phys. **91** (10), 8795 (2002).

Translated by G. Skrebtsov

Physics of the Solid State, Vol. 46, No. 3, 2004, pp. 502–509. Translated from Fizika Tverdogo Tela, Vol. 46, No. 3, 2004, pp. 488–494.

MAGNETISM AND FERROELECTRICITY

Reciprocal and Nonreciprocal Magnetic Linear Birefringence in the γ-Dy_2S_3 Sesquisulfide

B. B. Krichevtsov* and H.-J. Weber**

**Ioffe Physicotechnical Institute, Russian Academy of Sciences, Politekhnicheskaya ul. 26, St. Petersburg, 194021 Russia*

***Dortmund University, Dortmund, 44221 Germany*

Received July 29, 2003

Abstract—A study has been made of the spectral dependence of the Cotton–Mouton effect (CME) quadratic in magnetic field, nonreciprocal birefringence (NB) linear in magnetic field, and the Faraday effect (FE) in the cubic magnetic semiconductor γ-Dy_2S_3. Unlike the FE, the CME and the NB in this crystal are anisotropic, with the pattern of the anisotropy being dependent on the photon energy. The dependence of the CME and NB dispersion on the direction of the magnetic field **B** indicates contribution from a variety of electronic transitions and mechanisms to these phenomena. It is shown that the resonant contributions to the CME and NB in the transparency region originate from electronic transitions near $E \cong 3.4$ eV (beyond the band edge $E_g = 2.8$ eV), which are likely transitions from the localized ground state of the Dy^{3+} ion to states derived from mixing of the band and $4f^{N-1}5d$ states of the dysprosium ion. The character of the CME anisotropy in the transparency region and near the local electronic transition ${}^6H_{15/2} \longrightarrow {}^6F_{3/2}$ connecting states of the unfilled 4*f* shell of the Dy^{3+} ion suggests the presence of a strong axial component of the crystal field acting on the rare earth ion. © *2004 MAIK "Nauka/Interperiodica".*

1. INTRODUCTION

The rare earth sesquisulfides γ-Ln_2S_3, where Ln^{3+} is a trivalent rare earth ion, crystallize in a cubic noncentrosymmetric lattice described by point symmetry group T_d and are magnetic semiconductors with a band gap $E_g \approx 3$ eV. The presence of a rare earth ion Ln^{3+} with an unfilled 4*f* shell accounts for the paramagnetism of these compounds, which manifests itself strongly in γ-Dy_2S_3 because of the Dy^{3+} ion having a large magnetic moment ($m = 10.6\mu_B$). The interest in the sesquisulfides is due, on the one hand, to the presence in their electronic structure of band states derived from the 3*p* states of sulfur (the valence band), as well as from the *Ln* 5*d* and 6*s* states (the conduction band), and localized electronic states of the $4f^N$ shell of the Ln^{3+} ion, which are responsible for the magnetic properties of these crystals, and on the other hand, to the specific features of their crystal structure. The Ln^{3+} vacancies are an inherent structural component of the sesquisulfides. The vacancies (*V*) are randomly distributed over the lattice, so that only $10\frac{2}{3}$ out of the 12 possible positions in the unit cell are occupied; therefore, the chemical formula of the sesquisulfides should actually be written as $Ln_{3-x}V_xS_4$ ($x = 1/3$). The presence of vacancies is a necessary condition for the existence of a broad band gap in γ-Ln_2S_3, because filling of all positions by Ln^{3+} ions confers metallic character on the conduction.

The electronic structure and magnetic, optical, and electrical properties of the sesquisulfides and of γ-Dy_2S_3 in particular were subjects of the studies covered in reviews [1, 2]. Optical methods were used to investigate the absorption and reflectance spectra in this crystal, as well as the spectral response of the linear electrooptical effect (EOE), photoconductivity (PC), and photovoltaic effect (PVE) [3–8]. The magnetooptical (MO) properties of γ-Dy_2S_3 were studied in [9–14]. A large Faraday effect (FE), ~500 deg/cm T, is observed in the transparency region of this crystal, and its dispersion is described by an effective oscillator with a resonance energy $E_{\text{eff}} \approx 3.8$ eV, which is noticeably in excess of the band gap width $E_g = 2.8$ eV. Studies of the polar Kerr effect (KE) near the fundamental absorption edge of γ-Dy_2S_3 revealed the presence of two paramagnetic-type bands with energies $E_{\text{eff}} \approx 3.4$ and 3.8 eV and a diamagnetic band of energy $E_{\text{eff}} \approx 6.2$ eV [12, 13]. An analysis of the effective oscillator energies in various sesquisulfides, as well as in insulator crystals and glasses containing rare earths, led to the conclusion [10–13] that the FE in γ-Ln_2S_3 is associated with optical transitions from the ground state of the Ln^{3+} ion to the excited states resulting from the mixing of the $4f^{N-1}5d$ states of the Ln^{3+} ion with the electronic states of the conduction band. As far as we know, this conjecture has not been experimentally confirmed yet. Nevertheless, it might be expected that the second-order magnetooptical effects due to such transitions, for instance, the

1063-7834/04/4603-0502$26.00 © 2004 MAIK "Nauka/Interperiodica"

effects quadratic in magnetic field or bilinear in magnetic field and in the wave vector of light, would exhibit features characteristic of both local and nonlocal (interband) optical transitions.

Investigation of the optical properties of the sesquisulfides has been limited, until recently, to the phenomena described by tensors of the second rank (absorption and reflection of light, PC) and third rank (FE, KE, EOE, PVE), which are characterized by a single independent parameter in crystals of T_d symmetry. It has recently been shown that sesquisulfides, in particular, γ-Dy_2S_3, exhibit magnetic linear birefringence (MLB) at the wavelength $\lambda = 633$ nm; this effect represents a linear combination of two contributions, namely, the reciprocal Cotton–Mouton effect (CME), which is quadratic in magnetic field, and nonreciprocal birefringence (NB), which is linear in magnetic field and is due to the spatial dispersion induced by a magnetic field [15]. These phenomena are described by fourth-rank tensors (polar for the CME and axial for the NB), which have two independent parameters in crystals belonging to group T_d. In cubic crystals, the CME and NB are anisotropic; i.e., their magnitude depends on the orientation of the magnetic field **B** and of the light wave vector **k** with respect to the crystallographic axes.

The anisotropic magnetooptical phenomena in crystals containing rare earth elements have been studied, until recently, primarily in paramagnetic and magnetically ordered dielectrics [16–18]. Investigation of these phenomena in rare-earth–based semiconductors can yield new information on the electronic structure of these crystals. Our work was aimed at studying the angular, field, and spectral dependences of the CME and NB in γ-Dy_2S_3. It also appeared of interest to compare the spectral behavior of these phenomena with that observed in magnetic conductors of the $Cd_{1-x}Mn_xTe$ family containing $3d$ Mn^{2+} ions distributed randomly over the lattice. The structure of these materials also belongs to the T_d point group, and the magnetooptical phenomena in the transparency region are related to interband optical transitions [19, 20].

2. EXPERIMENTAL TECHNIQUES

The MLB was studied using the technique described in [19, 20]. We measured the rotation φ of the plane of polarization of light passing through a crystal placed in a magnetic field **B** (up to 0.5 T) oriented perpendicular to the light propagation direction **k** and through a tunable quarter-wavelength plate. After passing through the $\lambda/4$ plate, the azimuth of the light polarization vector was modulated by a Faraday modulator. As the light source, we employed a tunable Ti-sapphire laser operating in the wavelength range $\lambda = 700$–900 nm, an argon laser with $\lambda = 488$ nm, a helium–neon laser with $\lambda = 633$ nm, and a laser diode operating at $\lambda = 670$ nm. The measurements were conducted in the **E** || **B** and **E**45**B** geometries, which made it possible to determine the difference Δn between the light refraction coefficients for the normal modes oriented at an angle of $\pm 45°$ relative to the magnetic field direction, as well as parallel and perpendicular to **B**. To exclude the influence of the photochromic effect, the laser beam intensity was attenuated with filters. The rotation of the plane of polarization was found to be independent of the light intensity. The sensitivity of measuring the polarization rotation was about 10´´. To measure the angular response of the MLB, the crystal was rotated about an axis parallel to the **k** direction through an angle in the range $\Theta = 0°$–$360°$ to within $\approx 2°$. The MLB components quadratic and linear in magnetic field were separated by measuring, at each value of the azimuth Θ of the sample, the angle of rotation of the polarization plane φ in magnetic fields **B** = 0 and ± 0.5 T. The NB α [deg/cm T] linear in magnetic field was found from the expression $\alpha = [\varphi(+B) - \varphi(-B)]/2Bd$, where d is the sample thickness. The quadratic-in-field CME β [deg/cm T^2] was calculated from the formula $\beta = \{[\varphi(+B) + \varphi(-B)]/2 - \varphi(0)\}/B^2d$. In measuring the FE, the magnetic field was oriented along the direction of light propagation, **B** || **k**.

The γ-Dy_2S_3 single crystals, cut in the (110)-type plane, were plates with a thickness of 0.5–1 mm and face area of 2×3 mm. The crystals were oriented using Laue x-ray diffraction patterns. The deviation of the sample surface plane from the (110) plane was less than 3°. To avoid possible effects of crystalline aggregates and mosaic blocks, the Laue patterns were obtained from various parts of the samples. The samples were polished using diamond powders with a minimum grit size of about 0.5 μm.

3. RESULTS

Figure 1 presents the dependences of the CME $\beta(\Theta)$ on the angle Θ between the direction of the magnetic field and the [001] axis in γ-Dy_2S_3 obtained in the **E**45**B** geometry at various wavelengths. The CME is seen to exhibit a strong anisotropy throughout the spectral range covered, with the effect reversing its sign as the magnetic field direction is switched from **B** || [001] to **B** || [111]. The $\beta(\Theta)$ dependences can be fitted by combinations of the zeroth, second, and fourth harmonics in the Θ angle.

The CME is well known to be described by a fourth-rank polar tensor $\rho_{\{ij\}\{kl\}}$, which is symmetric in the two pairs of indices and relates the variation of the optical indicatrix ΔB_{ij} to the magnetic field, $\Delta B_{ij} = \rho_{ijkl}B_kB_l$. In cubic crystals of T_d symmetry, the CME can be charac-

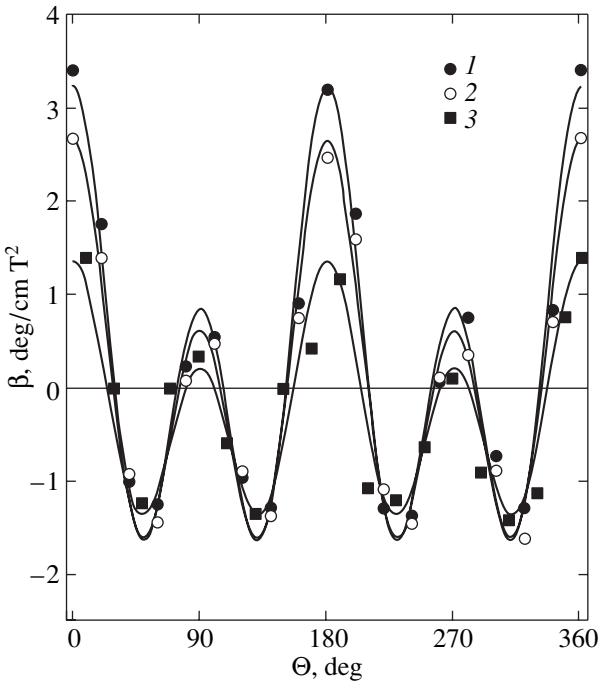

Fig. 1. Angular dependences of the CME in γ-Dy_2S_3 measured in the **E**45**B** geometry for **k** ∥ [1$\bar{1}$0] at various photon energies *E*: (*1*) 2.54, (*2*) 2.41, and (*3*) 1.85 eV.

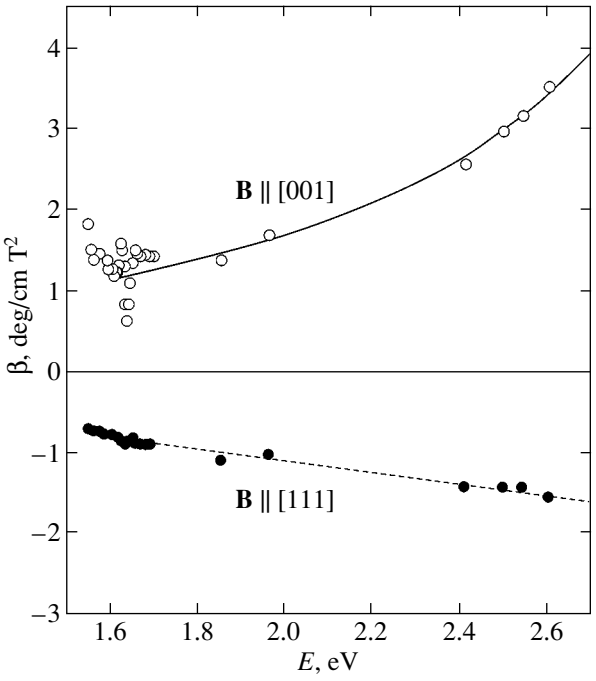

Fig. 2. Spectral dependences of the CME in γ-Dy_2S_3 measured for **k** ∥ [1$\bar{1}$0]. The solid line plots calculations made within the one-oscillator model with E_{eff} = 3.4 eV, and the dashed line is a linear approximation.

terized by the components $(\rho_{11} - \rho_{12})$ and ρ_{44} [16, 21]. For a magnetic field directed in the (110) plane along [001] (β_{001}, Θ = 0) or along [111] (β_{111}, Θ = 55°) and for light propagating in the direction perpendicular to this plane, the quantity β can be written as

$$\beta_{001} = -\pi(1/2)n^3(\rho_{11} - \rho_{12})/\lambda, \quad (1)$$

$$\beta_{111} = -\pi n^3 \rho_{44}/\lambda. \quad (2)$$

In a [110]-oriented magnetic field, the CME is equal to the half-sum of β_{001} and β_{111} (this rule holds for even effects). As seen from Fig. 1, the β(Θ) dependences satisfy this requirement, which means that the presence of a large number of vacancies does not destroy the cubic symmetry of the crystal. The parameters $(\rho_{11} - \rho_{12})$ and ρ_{44} in γ-Dy_2S_3 are opposite in sign and, therefore, depend differently on the wavelength of light.

Figure 2 displays the spectral responses of β_{001} and β_{111} in γ-Dy_2S_3. Even though β_{001} and β_{111} increase in absolute value with increasing photon energy *E*, the dispersions of these quantities are essentially different. The magnitude of β_{111} grows linearly with *E*, which implies that the birefringence Δn_{111} is independent of photon energy (because $\beta \sim E\Delta n$). By contrast, β_{001} increases resonantly with *E*. At $E \cong 1.6$ eV, the spectral response of β_{001} exhibits a feature in the region of a relatively narrow absorption band associated with the intra-configurational optical $^6H_{15/2} \longrightarrow {}^6F_{3/2}$ transition in the Dy^{3+} ion [4] (Fig. 3). The CME dispersion in the region of the transition is described by the second derivative of the absorption band profile. In the spectral response of β_{011}, this feature is weaker and is almost entirely absent from the β_{111} dependence.

Figure 4 displays the NB angular dependences, α(Θ), obtained in the **E** ∥ **B** and **E**45**B** geometries. The NB is described by a fourth-rank axial tensor $\gamma_{\{ij\}kl}$ symmetric in one pair of indices [22, 23]. The γ_{ijkl} tensor defines the contribution from the terms that are bilinear in the magnetic field **B** and in the light wave vector **k** to the permittivity tensor $\varepsilon_{ij}(\omega, \mathbf{B}, \mathbf{k}) = \gamma_{ijkl}B_k k_l$ and describes the optical phenomena associated with magnetically induced spatial dispersion. In crystals with T_d symmetry, the tensor γ_{ijkl} has two independent parameters, *A* and *g*. In accordance with a phenomenological consideration [19, 20], the α(Θ) relations in the $(1\bar{1}0)$ plane are described by a combination of first- and third-order harmonics. As seen from Fig. 4, the angular dependences of α(Θ) are well fitted by the combination $A_1\cos\Theta + B_1\cos 3\Theta$ in the **E** ∥ **B** geometry and by the combination $A_2\sin\Theta + B_2\sin 3\Theta$ in the **E**45**B** geometry at various wavelengths.

Figure 5 presents spectral responses of the NB measured in the **E**45**B** geometry at Θ = 90° (**B** ∥ [011]) – α_{011}, and in the **E** ∥ **B** geometry at Θ = 0° (**B** ∥ [001]) – α_{001}. In the former case, the magnitude of the NB is determined by a combination of parameters *A* and *g*,

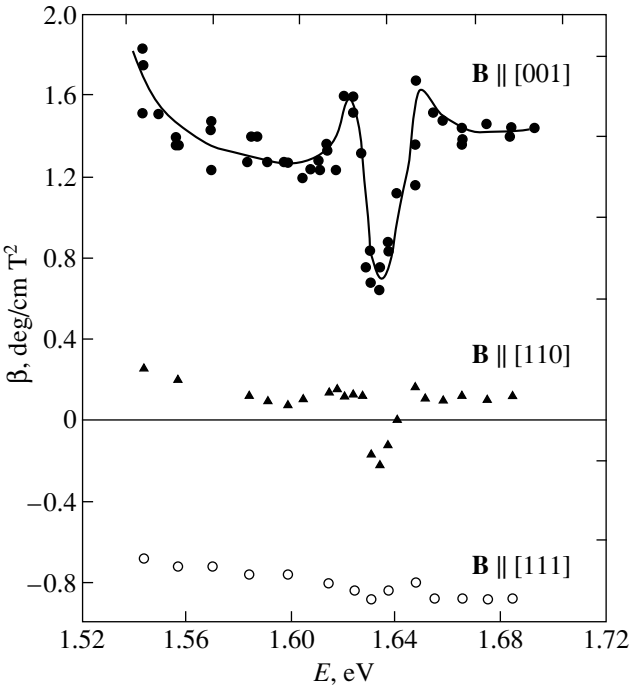

Fig. 3. Spectral dependences of the CME for **k** || [1$\bar{1}$0] measured at various magnetic field orientations in the region of the $^6H_{15/2} \longrightarrow {}^6F_{3/2}$ transition in the Dy^{3+} ion.

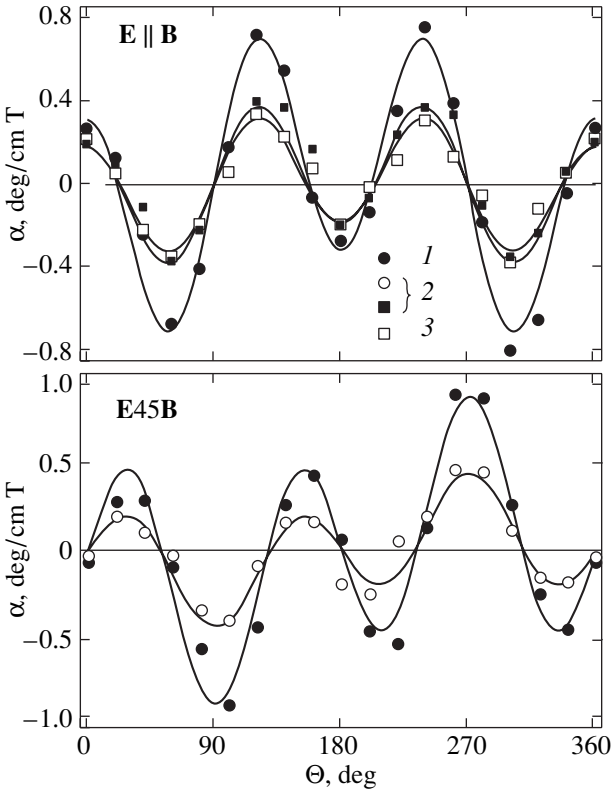

Fig. 4. Angular dependences of the NB in γ-Dy_2S_3 measured in the **E**45**B** and **E** || **B** geometries for various photon energies *E*: (*1*) 2.54, (*2*) 1.85, and (*3*) 1.7 eV.

$$\alpha_{011} = \pi(3A + 2g)k/4n\lambda, \quad (3)$$

and in the latter case, by the parameter *g* only,

$$\alpha_{001} = \pi gk/n\lambda. \quad (4)$$

As is evident from Fig. 5, the quantity α_{001} and, hence, the parameter *g* depend only weakly on photon energy in the range *E* = (1.4–2.6) eV. By contrast, α_{011} increases in a resonant manner with increasing *E*, thus indicating a strong dispersion of the parameter *A*.

The magnitude and dispersion of the FE measured on our γ-Dy_2S_3 samples are in agreement with the results reported in [9–14].

4. DISCUSSION OF THE RESULTS

The Cotton–Mouton effect in γ-Dy_2S_3 is highly anisotropic throughout the spectral range covered (Figs. 1, 2). This manifests itself in the parameters $(\rho_{11} - \rho_{22})$ and ρ_{44} being similar in magnitude but opposite in sign. Moreover, the spectral responses of these parameters differ substantially. The resonant enhancement of $(\rho_{11} - \rho_{22})$ with increasing *E* and the absence of any sign of such an increase in the parameter ρ_{44} indicate either that electronic transitions differing in energy contribute to the CME or that two radically different CME mechanisms operate. Similar to the case of the FE [9–14], the dispersion of β_{001} and β_{111} is not described by the relation $\beta \sim E(E_g - E)^{-\tau}$ [24] (this relation is standard for semiconductors and exhibits a fast growth of the CME as one approaches the band edge, E_g = 2.8 eV). This fact shows that CME in the γ-Dy_2S_3 magnetic semiconductor is not directly related to interband transitions. The one-oscillator model provides a satisfactory description of the β_{001} dispersion:

$$\beta_{001} = RE/(E_{\text{eff}}^2 - E^2) \quad (5)$$

with E_{eff} = 3.4 eV (*R* is a parameter that is independent of photon energy). The error in determining E_{eff} with this approximation is as small as 5%. The results of calculation are shown in Fig. 2 by a solid line. Thus, the electronic transition at *E* = 3.4 eV revealing itself in the KE spectra [12, 13], as well as in the reflectance spectrum of γ-Dy_2S_3 [5, 6], is responsible for the part of the CME that is observed in the transparency region and is described by the parameter $(\rho_{11} - \rho_{22})$. If this transition had contributed to the parameter ρ_{44}, the dispersion of the latter parameter would also have a resonant character, which is not observed experimentally. The weak dispersion of β_{111} and, accordingly, of the parameter ρ_{44} is obviously associated with the manifestation of higher energy transitions, whose energy E_{eff} is much larger

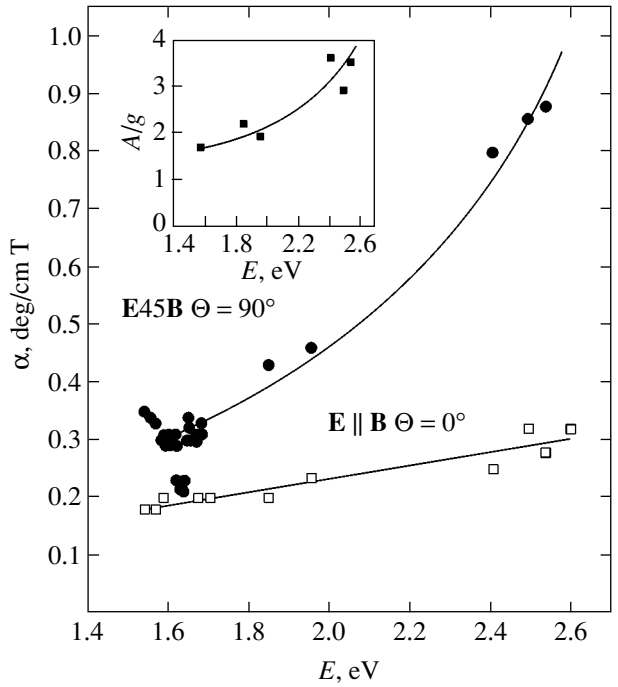

Fig. 5. Spectral dependences of the NB in γ-Dy_2S_3 measured in the **E**45**B** geometry with **B** ∥ [011] and in the **E** ∥ **B** geometry for **B** ∥ [001]. Inset shows the spectral response of the *A*/*g* parameter ratio.

than E = 3.4 eV. As seen from Eq. (5), for $E_{\text{eff}} \gg E$, the quantity Δn should depend only weakly on photon energy E; hence, the magnitude of β decreases linearly with decreasing E.

Consider the anisotropy of CME in γ-Dy_2S_3 in terms of the phenomenological "axial model" treated in [25]. This model assumes that the interaction energy δW_i between light and a paramagnetic ion occupying position i in the crystal contains the terms

$$\delta W_i = \xi(\mathbf{E}\mathbf{u}_i)^2(\mathbf{B}\mathbf{u}_i)^2, \quad (6)$$

where **E** is the light polarization and $\mathbf{u}_i$ is a unit vector characterizing the direction of the axial crystal-field component at the local position i. The contribution of terms (6) to the interaction energy of light and the crystal can be dominant only in the case of strongly polarized optical transitions (where the dipole moments of the transitions are parallel to $\mathbf{u}_i$ or lie in a plane perpendicular to it) and of a strong dependence of the ground and excited state splitting of the paramagnetic ion on the mutual orientation of the magnetic field **B** and the vector $\mathbf{u}_i$. Note that such an Ising-type behavior is typical of the Dy^{3+} ion occupying low-symmetry positions. This property manifests itself in a strong anisotropy of the g factor of the ground and excited states [26] and indicates the presence of a strong axial crystal-field component at the positions occupied by the Dy^{3+} ion.

After summing δW_i over all positions i of the cubic unit cell, the axial model predicts a strictly specified anisotropy of quadratic magnetooptical phenomena relative to the chosen direction of vector $\mathbf{u}_i$. For $\mathbf{u}_i \parallel \{001\}$, the CME is described by the parameter $(\rho_{11} - \rho_{12})$ alone, while for $\mathbf{u}_i \parallel \{111\}$, it is described by ρ_{44} only. The anisotropy of CME originating from the transition at E = 3.4 eV corresponds in this model to direction $\mathbf{u}_i$ in the local positions of the Dy^{3+} ion along the fourfold crystallographic axes. Experiment showed that the CME due to the ${}^6H_{15/2} \longrightarrow {}^6F_{3/2}$ local electronic transition has the same anisotropy ($\beta_{001} \neq 0$, $\beta_{111} = 0$; Fig. 3). In the sesquisulfide Th_3P_4-type lattice, the Ln^{3+} ions occupy positions inside eight-vertex polyhedra formed by sulfur ions with S_4 point group symmetry [27]. The axial crystal-field component in various positions of the paramagnetic ion in this lattice coincides in direction with the fourfold (S_4) crystallographic axes, which agrees with the predictions from the axial model.

By contrast, the CME observed for **B** ∥ [111] (characterized by β_{111}) is related, according to the axial model, to axial distortions $\mathbf{u}_i$ directed along the [111]-type axes. Such distortions are possible if the structure possesses a large number of vacancies, i.e., empty eight-vertex polyhedra, which can distort the crystal field in the neighboring positions occupied by the rare earth ion. However, the presence of Dy^{3+} ions in the positions distorted along the [111] direction should also have resulted in a contribution to the CME caused by transitions with an energy E_{eff} = 3.4 eV, i.e., in a resonant behavior of the component β_{111}, which is not observed in experiment. It may thus be concluded that the component β_{111} originates from transitions to states lying substantially higher than E = 3.4 eV, to which the conclusions drawn from the axial model are inapplicable.

One of the reasons for the appearance of the component β_{111} could be the existence of a secondary mechanism involving a combination of the quadratic magnetoelectric (ME) and linear EOE effect. The component r_{123} of the third-rank polar tensor r_{ijk} describing these phenomena is nonzero in noncentrosymmetric crystals belonging to the group T_d. In these crystals, a magnetic field can induce an electric polarization $P_i = r_{ijk}^{ME} B_j B_k$, which is quadratic in magnetic field (the ME effect of the B^2E type). Application of an external electric field **E** gives rise to deformations of the optical indicatrix $\Delta B_{ij} = r_{ijk}^{\text{EO}} E_k$, which are linear in **E** (EOE). These deformations can be expressed in terms of the polarization **P** induced by the electric field; namely, $\Delta B_{ij} = \tau_{ijk}^{\text{EO}} P_k = r_{ijk}^{\text{EO}} P_k / \varepsilon_0(\varepsilon - 1)$, where ε is the dielectric constant of the crystal [28]. Therefore, the contribution to the CME is

$$\Delta B_{ij} = \tau_{ijk}^{\text{EO}} r_{klm}^{\text{ME}} B_l B_m. \quad (7)$$

The product of the tensors τ_{ijk}^{EO} and r_{ijk}^{ME}, each of which is characterized by a single parameter, contributes only to the component ρ_{44} of the tensor ρ_{ijkl}, i.e., to β_{111}. The electrooptical coefficient r_{ijk}^{EO} in γ-Dy_2S_3 was shown in [7] to exhibit a weak dispersion in the transparency region, so that the spectral response of the EOE is governed primarily by the dispersion of the refractive index $n(E)$. Estimation of the ME parameter r_{123}^{ME}, which is necessary to explain the experimentally observed CME (β_{111}), was made using the values $n^3 r_{123}^{EO} = 5.6 \times 10^{-12}$ m/V [7], $\lambda = 633$ nm, and $\varepsilon = 23$ [1] and yielded $r_{123}^{ME} \cong 2 \times 10^{-17}$ s/A. This estimate is about an order of magnitude larger than the quadratic ME parameter observed in other dysprosium compounds crystallizing in a noncentrosymmetric structure [29]. There are currently no experimental data on the magnitude of the parameter r_{123}^{ME} in γ-Dy_2S_3; the contribution due to this CME mechanism can be expected to be less than 10% of the experimentally observed value. It should be pointed out, however, that the expression used to reduce the electrooptical parameters describing the relation of birefringence to external electric field $\mathbf{E}(r_{ijk}^{EO})$ and polarization (τ_{ijk}^{EO}), $\tau_{ijk}^{EO} = r_{ijk}^{EO}/\varepsilon_0(\varepsilon - 1)$, is fairly rough as applied to the magnetoelectric effect, because the contributions to polarization **P** (i.e., the ion displacements, electron shell deformations) induced by an electric field in a crystal may differ substantially from those induced by a magnetic field **B**. Thus, the CME component β_{111} in γ-Dy_2S_3 can, in principle, be assigned to the combined CME mechanism.

The dispersion of the NB in γ-Dy_2S_3, as well as that of the CME, depends on the magnetic field orientation with respect to the crystallographic axes. The quantity $\alpha_{001} \sim gE/n$ (measured in the $\mathbf{E} \parallel \mathbf{B}$ geometry) grows linearly with **E** in the range **E** = 1.6–2.6 eV. By contrast, $\alpha_{011} \sim (3A + 2g)E/4n$ (measured in the **E**45**B** geometry) increases resonantly in this range. The spectral dependence of $\alpha_{011}(E)$ is well described by the one-oscillator model: $\alpha_{011}(E) = CE/(E_{eff}^2 - E^2)$, with energy $E_{eff} = (3.4 \pm 0.1)$ eV (Fig. 5). Thus, just as in the case of the CME, the NB dispersion in γ-Dy_2S_3 is determined by transitions in the region of energy $E \cong 3.4$ eV.

Consider the possible mechanisms of NB in γ-Dy_2S_3. As shown in [15], the ratio of the parameters A and g of tensor γ_{ijkl} at the wavelength $\lambda = 633$ nm is close to 2, which is characteristic of second-order magnetoelectric susceptibility in the optical range [30]. As the photon energy increases to $E \sim 2.6$ eV, the A/g ratio increases ($A/g \sim 3.5$; see inset to Fig. 5), which implies that other mechanisms are operative in this region. Note that the ratio $A/g \cong 3.5$ was also observed at $\lambda = 633$ nm in γ-Pr_2S_3 [15]. Considered from the standpoint of the local-transition model, the deviation of the A/g ratio from 2 suggests a manifestation of the quadrupole mechanism of NB [30]. In this case, however, the validity of the local-transition model may be questioned, because the transition energy lies considerably above the band edge E_g and the excited states may be assumed to actually represent a mixture of band and ionic $4f^{N-1}5d$ states.

It appears to be of interest in this connection to compare the spectral behavior and the anisotropy of magnetooptical phenomena observed in magnetic semiconductors of the $Cd_{1-x}Mn_xTe$ and $Zn_{1-x}Mn_xTe$ family and in the rare earth semiconductor γ-Dy_2S_3. In the former compounds, the pronounced MO phenomena in the transparency region are connected with the *sp–d* exchange splitting of the band states, which originates from wave-function overlap between the band electrons and the 3*d* electrons of the Mn^{2+} ions. Here, interband transitions provide the dominant contribution to the linear and quadratic MO phenomena [31–33]. Unlike Mn^{2+}, the wave functions of the ground $4f^N$ state of the Ln^{3+} rare earth ions are more compact and overlap the wave functions of the band states only weakly. As a result, the contribution from interband transitions to the FE in γ-Ln_2S_3 is relatively small [12, 13] and the FE in the γ-Ln_2S_3 sesquisulfides is an order of magnitude smaller than that in the $Cd_{1-x}Mn_xTe$ crystals.

The dispersion of the MO phenomena in $Cd_{1-x}Mn_xTe$ in the transparency region is described by dependences of the type $(E - E_g)^{-\tau}$, which have a singularity at $E = E_g$ characteristic of interband optical transitions [19, 20]. By contrast, in γ-Dy_2S_3, the major contribution to the NB and CME, as well as to the FE, comes from transitions above the band edge. In the FE, as shown in [10] and supported by our measurements, the effective oscillator energy is $E_{eff} \approx 3.8$ eV. In the case of the CME and NB, the components β_{001} and α_{011} are related to transitions occurring at $E \approx 3.4$ eV, whereas β_{111} is determined by higher energy transitions.

The CME anisotropy in $Cd_{1-x}Mn_xTe$ differs radically from that in γ-Dy_2S_3. While the former crystals exhibit isotropic CME [19, 20], this phenomenon in γ-Dy_2S_3 is characterized by a strong anisotropy, which reflects the crystal field symmetry in the local positions of the paramagnetic ion. Note that the anisotropic behavior of the CME at $T = 294$ K was also observed in the insulating crystals DyAlG and DyGaG [15], in which the MO phenomena are associated with the $4f^N \longrightarrow 4f^{N-1}5d$ local transitions.

However, the spectral behavior and anisotropy of the NB in γ-Dy_2S_3 have features in common with those observed in the magnetic semiconductors $Cd_{1-x}Mn_xTe$ and $Zn_{1-x}Mn_xTe$. In the transparency region of all these

crystals, a very weak dispersion of the parameter g and a strong increase in the parameter A with increasing E are observed. As shown in [19, 20], when interband transitions are included, this behavior of the parameter A as $E \longrightarrow E_g$ in $Cd_{1-x}Mn_xTe$ is accounted for by the presence of terms linear and cubic in the wave vector $\mathbf{q}$ in the dispersion $E_{r,s}(\mathbf{q})$ of the valence band r and the conduction band s and by the wave-vector $\mathbf{k}$ dependence (characterized by the Kane parameter) of the matrix elements of the current operator $\mathbf{J}(\mathbf{k})$. These mechanisms could also be expected to become manifest in γ-Dy_2S_3 if the excited states for the transitions at $E \approx 3.4$ eV that are responsible for the NB are a mixture of the electronic band states and the $4f^{N-1}5d$ states of the Dy^{3+} ion. As the photon energy is lowered to a region far from the resonances, these crystals exhibit NB, which depends weakly on E and whose anisotropy is described by the parameter ratio $A/g \cong 2$ characteristic of second-order magnetoelectric susceptibility in the optical range [34].

5. CONCLUSIONS

Thus, we can conclude that the spectral dependence of the linear and quadratic MO phenomena in the transparency region of γ-Dy_2S_3 is due to electronic transitions from the ground state of the unfilled $4f^0$ shell of the Dy^{3+} ion to states in the energy region $E \approx 3.4$ eV. The anisotropy of the CME caused by these transitions, as well as by local transitions occurring between states of the $4f^N$ shell of the Dy^{3+} ion, attests to the presence of a strong axial crystal-field component directed along the S_4 axes in the local positions occupied by the paramagnetic ion and indicates the "Ising" behavior of this ion in the sesquisulfide lattice. At the same time, the anisotropy and spectral response of the NB in γ-Dy_2S_3 demonstrates features characteristic of the interband mechanism of magnetically induced spatial dispersion, which suggests that the excited states for the transitions occurring at $E \approx 3.4$ eV are actually a mixture of the band and $4f^{N-1}5d$ states of the Dy^{3+} ion.

ACKNOWLEDGMENTS

The authors are indebted to N.F. Kartenko for x-ray-diffraction-assisted orientation of the samples, to V.A. Yankovskaya for crystal preparation, and to A.Yu. Zyuzin for helpful discussions.

This study was supported by the Russian Foundation for Basic Research and DFG, project no. 02-02-04003.

REFERENCES

1. V. P. Zhuze and A. I. Shelykh, Fiz. Tekh. Poluprovodn. (Leningrad) **23**, 393 (1989) [Sov. Phys. Semicond. **23**, 245 (1989)].
2. S. Methfessel and D. C. Hattis, in *Handbuch der Physic*, Vol. 18, Part 1: *Magnetism*, Ed. by H. P. J. Wijn (Springer, New York, 1968; Mir, Moscow, 1972).
3. J. R. Henderson, M. Muramoto, and E. Loh, J. Chem. Phys. **47**, 3347 (1967).
4. J. R. Henderson, M. Muramoto, J. B. Gruber, and R. Menzel, J. Chem. Phys. **52**, 2311 (1970).
5. V. P. Zhuze, A. A. Kamarzin, M. G. Karin, *et al.*, Fiz. Tverd. Tela (Leningrad) **21**, 3410 (1979) [Sov. Phys. Solid State **21**, 1968 (1979)].
6. V. P. Zhuze, M. G. Karin, K. K. Sidorin, *et al.*, Fiz. Tverd. Tela (Leningrad) **27**, 3662 (1985) [Sov. Phys. Solid State **27**, 2205 (1985)].
7. T. I. Volkonskaya, A. I. Shelykh, V. V. Sokolov, and I. A. Smirnov, Fiz. Tverd. Tela (Leningrad) **27**, 1132 (1985) [Sov. Phys. Solid State **27**, 684 (1985)].
8. T. M. Batirov, K. A. Verkhovskaya, A. A. Kamarzin, *et al.*, Fiz. Tverd. Tela (Leningrad) **24**, 1313 (1982) [Sov. Phys. Solid State **24**, 746 (1982)].
9. A. I. Shelykh, Pis'ma Zh. Tekh. Fiz. **13**, 1351 (1987) [Sov. Tech. Phys. Lett. **13**, 564 (1987)].
10. R. Dagys, G. Babonas, and G. Pukinskas, Litov. Fiz. Sb. **28**, 559 (1988).
11. Yu.-G. Babonas, R. Dagys, and G. Pukinskas, Opt. Spektrosk. **68**, 824 (1990) [Opt. Spectrosc. **68**, 481 (1990)].
12. G. Babonas, R. Dagys, and G. Pukinskas, Fiz. Tverd. Tela (Leningrad) **30**, 3460 (1988) [Sov. Phys. Solid State **30**, 1985 (1988)].
13. G. Babonas, R. Dagys, and G. Pukinskas, Phys. Status Solidi B **153**, 741 (1989).
14. A. V. Prokofiev, A. I. Shelykh, A. V. Golubkov, and I. A. Smirnov, J. Alloys Compd. **219**, 172 (1995).
15. B. B. Krichevtsov, Zh. Éksp. Teor. Fiz. **119**, 954 (2001) [JETP **92**, 830 (2001)].
16. R. V. Pisarev, in *Physics of Magnetic Dielectrics* (Nauka, Leningrad, 1974).
17. A. K. Zvezdin and V. A. Kotov, *Modern Magnetooptics and Magnetooptical Materials* (Inst. of Physics, Bristol and Philadelphia, 1997).
18. A. K. Zvezdin, A. I. Popov, and Kh. I. Turkmenov, Fiz. Tverd. Tela (Leningrad) **28**, 1760 (1986) [Sov. Phys. Solid State **28**, 974 (1986)].
19. B. B. Krichevtsov, R. V. Pisarev, A. A. Rzhevsky, *et al.*, Phys. Rev. B **57**, 14611 (1998).
20. B. B. Krichevtsov, R. V. Pisarev, A. A. Rzhevskiĭ, *et al.*, Zh. Éksp. Teor. Fiz. **114** (3), 1018 (1998) [JETP **87**, 553 (1998)].
21. R. V. Pisarev, Fiz. Tverd. Tela (Leningrad) **17**, 1396 (1975) [Sov. Phys. Solid State **17**, 898 (1975)].
22. D. L. Portigal and E. Burstein, J. Phys. Chem. Solids **32**, 603 (1971).
23. V. M. Agranovich and V. L. Ginzburg, *Crystal Optics with Spatial Dispersion and Excitons*, 2nd ed. (Nauka, Moscow, 1979; Springer, New York, 1984).

24. F. F. Sizov and Yu. I. Ukhanov, *Faraday and Voigt Magnetooptical Effects in Semiconductors* (Naukova Dumka, Kiev, 1979).

25. B. B. Krichevtsov and R. V. Pisarev, Zh. Éksp. Teor. Fiz. **84**, 865 (1983) [Sov. Phys. JETP **57**, 501 (1983)].

26. A. K. Zvezdin, V. M. Matveev, A. A. Mukhin, and A. I. Popov, *Rare-Earth Ions in Magnetically Ordered Crystals* (Nauka, Moscow, 1985).

27. P. P. Kripyakevich, Kristallografiya **7**, 686 (1962) [Sov. Phys. Crystallogr. **7**, 556 (1962)].

28. T. S. Narasimhamurty, *Photoelastic and Electro-Optic Properties of Crystals* (Plenum, New York, 1981; Mir, Moscow, 1984).

29. B. K. Ponomarev, Ferroelectrics **280**, 95 (2002).

30. B. B. Krichevtsov, A. A. Rzhevskii, and H.-J. Weber, Phys. Rev. B **61**, 10084 (2000).

31. J. K. Furdyna, J. Appl. Phys. **64**, R29 (1988).

32. A. I. Savchuk and P. I. Nikitin, Usp. Fiz. Nauk **160**, 167 (1990) [Sov. Phys. Usp. **33**, 491 (1990)].

33. B. B. Krichevtsov, R. V. Pisarev, A. A. Rzhevskiĭ, *et al.*, Pis'ma Zh. Éksp. Teor. Fiz. **67**, 569 (1998) [JETP Lett. **67**, 602 (1998)].

34. V. N. Gridnev, Fiz. Tverd. Tela (St. Petersburg) **43**, 656 (2001) [Phys. Solid State **43**, 682 (2001)].

Translated by G. Skrebtsov

Physics of the Solid State, Vol. 46, No. 3, 2004, pp. 510–514. Translated from Fizika Tverdogo Tela, Vol. 46, No. 3, 2004, pp. 495–499.

MAGNETISM AND FERROELECTRICITY

Equilibrium Magnetic and Orbital States of the Manganites with Four Manganese Atoms in the Unit Cell

S. M. Dunaevsky and V. V. Deriglazov

Konstantinov St. Petersburg Nuclear Physics Institute, Russian Academy of Sciences, Gatchina, Leningrad oblast, 188300 Russia

e-mail: dunaevsk@mail.pnpi.spb.ru

Received September 1, 2003

Abstract—The carrier energy spectrum and the total energy of various magnetic and orbital crystal-structure configurations of the manganites $R_{1-x}A_xMnO_3$ (R = La, Pr, Nd, Sm, etc.; A = Ca, Sr, Ba) with four manganese atoms in the unit cell have been calculated for the electron doping region $x > 0.5$. The equilibrium magnetic and orbital configurations of the model are determined by minimizing the total energy of the system with respect to the angles θ_i^S, φ_i, and θ_i^O, which define the directions of the local manganese magnetic moments and the type of orbital mixing of the e_g electrons in the manganites. Assuming the parameters of the Heisenberg exchange interaction to be $0.018t < J_{AFM} < 0.022t$, the Hund exchange interaction to be $J_H = 2.5t$, and the Jahn–Teller splitting to be $\Delta = 1.5ty$, the model with four manganese atoms in the unit cell predicts the experimentally observed magnetic phase alternation sequence *G–C–A* with increasing doping level $y = 1 - x$. For the values $J_{AFM} < 0.018t$ and $y < 0.28$, this model allows the existence of a collinear phase *H* not observed earlier. © *2004 MAIK "Nauka/Interperiodica".*

1. The present communication reports on the first calculation of phase diagrams of the $R_{1-x}A_xMnO_3$ manganites (R = La, Pr, Nd, Sm, etc.; A = Ca, Sr, Ba) for a crystal structure with four manganese atoms in the unit cell. The phase diagrams of the manganites are constructed only for the electron doping region where the concentration of divalent atoms in the compound exceeds the value $x = 0.5$. In this region, the mobile carriers are d electrons and, as their concentration $y = 1 - x$ increases, they fill the degenerate e_g band of the manganites to less than one eighth its capacity. The small number of carriers in the conduction band permits us to disregard, in a first approximation, the inter- and intra-atomic Coulomb repulsion, which somewhat simplifies the form of the Hamiltonian of the compounds under study.

For the effective Hamiltonian describing the manganite properties in the electron doping region, we use the Hamiltonian of the degenerate DE model [1–3], which in the local atomic basis can be written as

$$H = H_{DE} + H_H + H_{JT},$$

$$H_{DE} = \sum_{i\alpha\sigma} \varepsilon_{i\alpha} d^\dagger_{i\alpha\sigma} d_{i\alpha\sigma} - J_H S \sum_{i\alpha\sigma} \boldsymbol{\sigma} d^\dagger_{i\alpha\sigma} d_{i\alpha\sigma}$$

$$+ \sum_{ij\alpha\beta\sigma'\sigma} t^{\sigma\sigma'}_{ij\alpha\beta} d^\dagger_{i\alpha\sigma} d_{j\beta\sigma'},$$

$$H_H = \sum J_{AFM} \mathbf{S}_i \mathbf{S}_j,$$

$$t^{\sigma\sigma'}_{ij\alpha\beta} = \begin{cases} t_{ij\alpha\beta} \cos\dfrac{\theta_{ij}}{2} & (\sigma = \sigma') \\ \pm t_{ij\alpha\beta} \sin\dfrac{\theta_{ij}}{2} & (\sigma \neq \sigma'), \end{cases} \quad (1)$$

$$H_{JT} = \sum_{i\sigma} \Delta_i (d^\dagger_{i\alpha\sigma} d^\dagger_{i\beta\sigma}) \begin{pmatrix} \cos\theta_i^O & \sin\theta_i^O \\ \sin\theta_i^O & -\cos\theta_i^O \end{pmatrix} \begin{pmatrix} d_{i\alpha\sigma} \\ d_{i\beta\sigma} \end{pmatrix}.$$

This Hamiltonian describes only the manganese sublattice of the real crystal structure of the manganites. It consists of the double-exchange Hamiltonian H_{DE} for the degenerate e_g manganese level and for a finite value of the intra-atomic (Hund) parameter J_H, the Heisenberg Hamiltonian H_H of the localized t_{2g} electrons, and the Hamiltonian H_{JT} describing the Jahn–Teller splitting of the e_g level. A detailed derivation of this model Hamiltonian is given in [4] for the case of infinitely large J_H. The Hamiltonian includes strong intra-atomic Coulomb interaction between the e_g and t_{2g} electrons, which obeys Hund's rule. All the other interelectron Coulomb interactions are neglected here, which is justified, in a first approximation, for a small number of e_g electrons in the conduction band.

In Eq. (1), the indices α and β label the degenerate atomic e_g orbitals $|1\rangle = |z^2\rangle$ and $|2\rangle = |x^2 - y^2\rangle$ and the

indices i and j enumerate the atoms. Operators $d^{\dagger}_{i\alpha\sigma}$ and $d_{j\beta\sigma'}$ are the creation and annihilation operators of electrons at the ith site with the spin oriented either along or opposite to that of the localized t_{2g} electrons $\mathbf{S}_i$ ($\sigma = \uparrow, \downarrow$). Also in Eq. (1), $\varepsilon_{i\alpha}$ is the energy of an atomic orbital of type α, J_H is the intra-atomic Hund integral, J_{AFM} is the exchange integral of the Heisenberg model for localized t_{2g} electrons, Δ_i is a parameter describing the splitting of the e_g level of atom i, and $t_{ij\alpha\beta}$ are the effective hopping integrals between the local spinor-state components of the nearest neighbor manganese ions. The hopping of e_g electrons in the double-exchange model does not entail spin flip; therefore, the hopping integral $t_{ij\alpha\beta}$ depends on the mutual orientation (angle θ_{ij}) of the nearest neighbor spins $\mathbf{S}_i$ and $\mathbf{S}_j$. The role of the oxygen ions, which are located between the manganese ions in the perovskite structure, results in the effective hopping integral $t_{ij\alpha\beta}$ being expressed through the hopping integral t between the e_g manganese orbital and the p orbital of the nearest neighbor oxygen ion (the Koster–Slater parameter $V_{pd\sigma}$) in the second-order perturbation theory. The hopping integral $t_{ij\alpha\beta}$ is anisotropic in real space [2, 3].

The phase diagram of the manganites was calculated in terms of the degenerate DE model for the first time in [1], where a modified dispersion relation for the ferromagnetic (FM) state of the manganite crystal structure with one manganese atom in the unit cell [5] was used for $\varepsilon(\mathbf{k})$. The modification consisted in introducing into the expressions for $\varepsilon(\mathbf{k})$ two hopping integrals, $t_{xy} = t\cos(\theta_{xy}/2)$ and $t_z = t\cos(\theta_z/2)$, depending on the angles between adjacent spins, which are confined either in the same (001) plane (θ_{xy}) or in adjacent planes (θ_z). The approach developed in [1] stirred considerable interest and stimulated a series of theoretical studies of the phase diagrams of electron-doped manganites [6, 7].

Considered from the theoretical point of view, the introduction of two different angles between adjacent spins is possible only if there are at least four inequivalent atoms in the manganite unit cell. In this case, the carrier spectrum $\varepsilon(\mathbf{k})$ should be directly calculated, rather than modified, based on the corresponding Hamiltonian matrix.

A two-sublattice model of the manganites was considered in [8, 9], where the equilibrium types of the magnetic and orbital structures were found by minimizing the total energy in the angle between the neighboring spins θ_{ij} and two orbital intra-atomic mixing angles θ_i^o. This communication reports on the first application of this approach to the model of the manganite crystal structure containing four manganese atoms in the unit cell, without making any assumptions regarding the type of the spin and orbital ordering.

2. It is known that doped manganites $R_{1-x}A_xMnO_3$ crystallize most frequently in the orthorhombic and rhombohedral structures (the R phase). Figure 1 shows

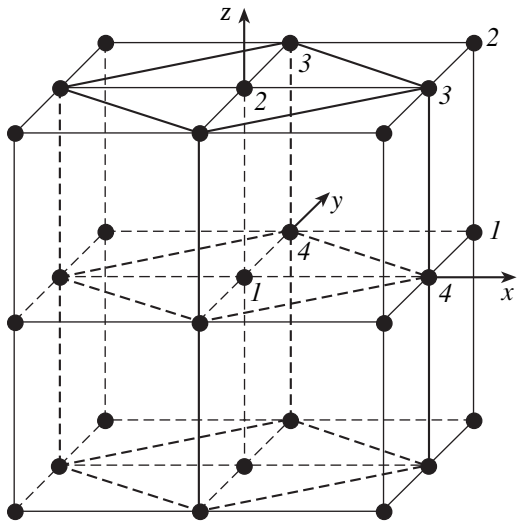

Fig. 1. *Pnma* unit cell of Mn ions nested in the cubic lattice.

a manganese sublattice of orthorhombic symmetry nested in the starting cubic perovskite structure ABO_3. The unit cell of the manganese sublattice contains four translationally inequivalent atoms, which are numbered in Fig. 1 and in this particular case are related through symmetry transformations of the crystallographic space group *Pnma*. If the magnetic and crystallographic symmetries coincide, the four manganese atoms are equivalent. This imposes certain constraints on possible magnetic structures. The *Pnma* magnetic structures usually observed in experiments are of the following main types: (1) structure F with ferromagnetic ordering of all local manganese magnetic moments along one of the axes x, y, or z (F_x, F_y, or F_z); (2) a type-A antiferromagnetic (AFM) structure with AFM alternation of the (001)-type FM planes; (3) a type-C AFM structure with an AFM arrangement of FM spin chains along one of the axes x, y, or z; and (4) a type-G AFM structure with conventional AFM ordering of the magnetic moments of the nearest neighbors.

In addition to these "pure" magnetic structures, the orthorhombic symmetry allows the observation of more complex magnetic structures (of the types C_xA_z, $C_zA_yF_x$, etc.), which belong to one of the irreducible representations of a Heisenberg-type Hamiltonian. For the *Pnma* group, there are only four such irreducible representations for the magnetic moments of manganese and eight representations for the magnetic moments of rare earth ions. For instance, the noncoplanar structure $G_zA_yF_x$ corresponds to the FM arrangement of the S_x component of the spin magnetic moment of manganese ions, to type-A ordering of S_y, and to type-G ordering of S_z. The magnetic structures of rare earth ions can have only pair combinations (for example, C_xA_y). All possible types of magnetic ordering are presented in [10] for both the manganese atoms and the rare earth ions in the *Pnma* orthorhombic structure (or *Pbnm* for the other choice of the reference frame).

When confronting the general problem of finding the ground state, all initial constraints on the possible types of magnetic and orbital ordering have to be lifted. Hamiltonian (1) is not of the Heisenberg type; therefore, the magnetic structures derived from it may differ from those described above and their symmetry may turn out to be lower than that of the crystal lattice. In this case, interaction of the electronic and spin degrees of freedom with the lattice may bring about distortions of the lattice and lower its symmetry to one of the subgroups characterizing the magnetic symmetry. However, our model, assuming a rigid lattice, does not allow such back action, a factor that somewhat degrades the self-consistency of the problem.

3. A self-consistent calculation of the carrier kinetic energy made in the tight-binding approximation for manganites with four manganese atoms in the unit cell requires consideration of Hamiltonian matrices with dimensions not less than 16×16 in **k** space.

In this case, the Hamiltonian matrix of the system can be specified in the form

$$H(\mathbf{k}) = \begin{pmatrix} H_{11}(\mathbf{k}) & H_{12}(\mathbf{k}) & 0 & H_{14}(\mathbf{k}) \\ H_{21}(\mathbf{k}) & H_{22}(\mathbf{k}) & H_{23}(\mathbf{k}) & 0 \\ 0 & H_{32}(\mathbf{k}) & H_{33}(\mathbf{k}) & H_{34}(\mathbf{k}) \\ H_{41}(\mathbf{k}) & 0 & H_{43}(\mathbf{k}) & H_{44}(\mathbf{k}) \end{pmatrix}, \quad (2)$$

where the matrices H_{ij} describe the interaction between the nearest neighbor Mn ions in the lattice shown in Fig. 1.

If from the outset we do not impose any constraints on possible types of magnetic and orbital structures, we will have to specify three angles θ_i^s, φ_i, and θ_i^o for each manganese atom in the unit cell; these angles define the local spin direction and the type of orbital mixing. The local atomic basis of the ith atom should involve the spinors $|\alpha\rangle$ and $|\beta\rangle$ connected with the atomic orbitals through the well-known transformation

$$\begin{pmatrix} |\gamma\rangle'_{i\uparrow} \\ |\gamma\rangle'_{i\downarrow} \end{pmatrix} = \begin{pmatrix} \cos\frac{\theta_i^s}{2} & i\sin\frac{\theta_i^s}{2}\exp(-i\varphi_i) \\ -i\sin\frac{\theta_i^s}{2}\exp(i\varphi_i) & \cos\frac{\theta_i^s}{2} \end{pmatrix} \times \begin{pmatrix} |\gamma\rangle_{i\uparrow} \\ |\gamma\rangle_{i\downarrow} \end{pmatrix}. \quad (3)$$

In Eq. (3), the primes denote the spinor components in the local reference frame, the arrows identify the electron spin projections onto an arbitrarily chosen axis, and $|\gamma\rangle_i$ is the orbital state of an e_g electron, which, in turn, is a linear combination of the e_g orbitals

$$|\gamma\rangle_i \equiv \begin{pmatrix} |\alpha\rangle_i \\ |\beta\rangle_i \end{pmatrix} = \begin{pmatrix} \cos\frac{\theta_i^o}{2} & \sin\frac{\theta_i^o}{2} \\ -\sin\frac{\theta_i^o}{2} & \cos\frac{\theta_i^o}{2} \end{pmatrix} \begin{pmatrix} |3z^2 - r^2\rangle_i \\ |x^2 - y^2\rangle_i \end{pmatrix}. \quad (4)$$

In spinor (4), the state $|\alpha\rangle_i$ is occupied and the state $|\beta\rangle_i$ is empty. If the e_g level is degenerate, both states have the same energy and thereby there should be no orbital order (OO), which is at odds with numerous experiments. The Jahn–Teller-type splitting of the e_g level in the DE model lifts its orbital degeneracy [8, 9]. This gives one grounds to assume that $\varepsilon_{i\alpha} = -\Delta$ and $\varepsilon_{i\beta} = \Delta$, where $\Delta \sim y$.

Written in the local basis, the hopping integral between identical orbitals of the nearest neighbor manganese atoms has the form

$$t_{ij\alpha\alpha}^{\uparrow\uparrow} = \langle \alpha_i^{\uparrow} | \alpha_j^{\uparrow} \rangle = t_{ij\alpha\alpha}\left[\cos\frac{\theta_i}{2}\cos\frac{\theta_i}{2} + \sin\frac{\theta_i}{2}\sin\frac{\theta_j}{2}e^{i(\varphi_i - \varphi_j)}\right]. \quad (5)$$

In the same way, one can readily obtain all the other hopping integrals and specify Hamiltonian matrix (2) in explicit form for an arbitrary spin and orbital structure of the four manganese sublattices of the manganites. The technique used to calculate the carrier spectrum and the total energy of arbitrary spin and orbital configurations of the manganites with four manganese atoms in the unit cell can be found in [11].

The Hamiltonian matrices for two sublattices were constructed earlier with the use of expressions similar to Eq. (5), where all the azimuthal angles were considered equal and the magnetic structures could be only collinear or coplanar-canted.

The spectrum of the carriers and their kinetic energy depend in this approach on 12 variables determining the ground state of the system. In the absence of magnetic anisotropy, the spin structure is not fixed relative to the crystallographic axes. By arbitrarily choosing the spin direction of one of the four manganese atoms and the direction from which the azimuthal angle φ is reckoned relative to this atom, one reduces the number of variable angles to nine.

The matrix of the general form of (2) obviously includes, as a particular case, the two-sublattice model, where the types of possible magnetic and orbital structures coincide or one of them (or both simultaneously) is ferromagnetic. This constraint is removed in the model considered in this paper. Instead of being speci-

fied, the OO type is determined by minimizing the total energy. In contrast to the two-sublattice model, such an approach allows the existence of a broader variety of canting types of the manganese sublattice magnetic moments, not limited by a specific parameterization.

4. Figure 2 shows a phase diagram of the model with four manganese atoms in the unit cell. Despite the presence of a large number of local minima close in energy, we succeeded in determining the absolute energy minima for all magnetic phases; these minima turned out to be nondegenerate. The diagram obtained resembles, in general outline, the phase diagram of the two-sublattice model. All the equilibrium magnetic phases in the four-sublattice model are also found to be either collinear or coplanar.

The total energies were calculated separately for the particular case of magnetic structures compatible with the *Pnma* symmetry group. These calculations also showed that it is the collinear or coplanar magnetic structures of this space group that possess minimum energy. All noncoplanar magnetic structures of *Pnma* symmetry turned out to be energetically unfavorable.

Phases *A* and *C* are the well-known AFM structures with FM ordering of the $|x^2 - y^2\rangle$ and $|3z^2 - r^2\rangle$ type, respectively. The small central region *A'* is actually the same *A* structure with ferromagnetic OO but with a small intersublattice canting. Phase *F* (as before) is the FM structure with triply degenerate ferromagnetic OO of the $|3z^2 - r^2\rangle$ type, and *Fa* is the FM structure with the *A*-type antiferromagnetic OO $(\pi/2, -\pi/2)$. The other phases in the diagram are new. Phase *C*' is the magnetic *C* structure with ferromagnetic OO of the $|3z^2 - r^2\rangle$ type but with intrasublattice spin canting. Phases *G'a* and *G'c* are coplanar, spin-canted *G* structures with AFM orbital order of the *A* and *C* types, $|3z^2 - r^2\rangle$ and $|x^2 - y^2\rangle$, respectively (left-hand inset to Fig. 3). The spin canting in these phases can be described by two angles, $\gamma = \theta_{14}$ (or θ_{12}) and $\eta = \theta_{13} = \theta_{24}$, which are the angles of the inter- and intrasublattice canting, respectively, with respect to the *G* structure. Such a spin configuration cannot be described by the two angles θ_{xy} and θ_z, which parameterize the *G* phase canting only of types *A* ($\gamma = \theta_z$, $\eta = \theta_{xy}$) and *C* ($\eta = \theta_z$, $\gamma = \theta_{xy}$), where $\theta_z = \theta_{12} = \theta_{34}$, $\theta_{xy} = \theta_{14} = \theta_{23}$. If the magnetic moment in the *G'a* phase is directed along a diagonal of one of the cubic cell faces, the magnetic and orbital structures will be described by the monoclinic space group $P2_1/b$, which is a subgroup of *Pnma*.

Orbital ordering in both phases (*G'a*, *G'c*) is almost degenerate, first, because of the specific feature of the *G* structure (double exchange is hampered as a result of the AFM ordering of all neighboring spins) and, second, because of the small doping level *y*. Variation of the orbital mixing angles changes the total energy only within about 1 K. As a result, the orbital states are dynamically averaged even at low temperatures, which manifests itself in the corresponding experiments as the absence of OO in the *G* phase (see [8, 9] and references therein).

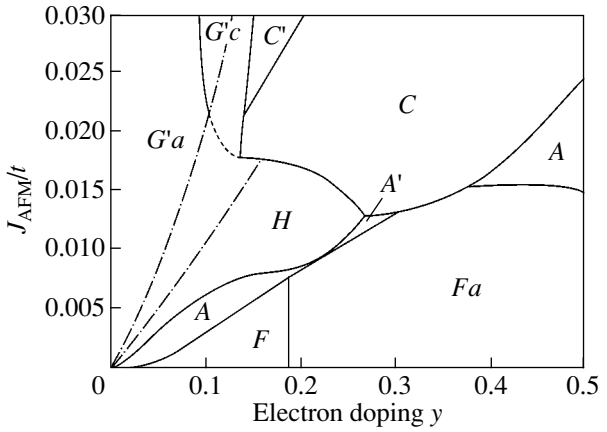

Fig. 2. Phase diagram of the four-sublattice model in the electron doping region calculated for the parameters $J_H = 2.5t$ and $\Delta = 1.5ty$. The phases are described in the text and the table.

An increase in the electron concentration in phase *G'a* gives rise to triclinic distortions, which result in a smooth transition of this phase to a new collinear ferrimagnetic phase *H* (right-hand inset to Fig. 3) in which one of the spins is directed opposite to the other three. In this case, each of the manganese atoms has collinear surroundings characteristic of one of the neighboring phases, namely, *G* for atom *1*, *A* for atom *2*, *F* for atom *3*, and *C* for atom *4*. As a result, the unit cell–averaged Heisenberg exchange energy in Eq. (1) is zero. The OO in phase *H* is also well defined and correlates with its magnetic structure. A description of all the phases obtained is given in the table.

Equilibrium magnetic and orbital structures of the four-sublattice manganite model

Phase	Magnetic structure	Orbital structure
A	Collinear AFM with FM planes	FM $\|x^2 - y^2\rangle$
C	Collinear AFM with FM chains	FM $\|3z^2 - r^2\rangle$
A'	AFM with FM planes and interplanar canting	FM $\|x^2 - y^2\rangle$
C'	AFM with FM chains and canting inside chains	FM $\|3z^2 - r^2\rangle$
G'a	Doubly canted *G* with a magnetic moment	AFM-*A* $\|3z^2 - r^2\rangle/\|x^2 - y^2\rangle$
G'c	"	AFM-*C* $\|3z^2 - r^2\rangle/\|x^2 - y^2\rangle$
F	Collinear FM	FM $\|3z^2 - r^2\rangle$
Fa	"	AFM-*A* $(-\pi/2, \pi/2)$
H	Collinear ferrimagnetic *A* + *C* + *G* + *F*	$\|3z^2 - r^2\rangle(1, 3, 4)/\|x^2 - y^2\rangle$ (2)

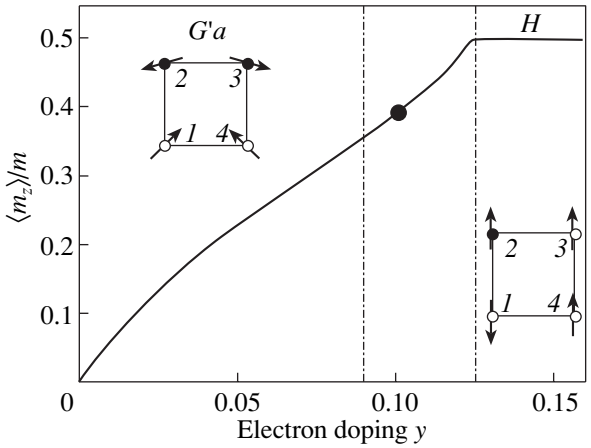

Fig. 3. Average magnetization per Mn ion normalized to the Mn magnetic moment and calculated for the parameters $J_{AFM} = 0.015t$, $J_H = 2.5t$, and $\Delta = 1.5ty$. The left-hand inset shows the coplanar spin structure of the *G'a* phase, and the right-hand inset shows the collinear spin structure of phase *H*. These two phases are separated by the region of triclinic distortions. The filled circles denote the $|x^2 - y^2\rangle$ orbital state, and the open circles denote the $|3z^2 - r^2\rangle$ state. The point in the graph at $y = 0.1$ is the experimental value of the magnetization of $Ho_{0.1}Ca_{0.9}MnO_3$ [13].

Figure 3 shows the doping-level dependence of the cell-averaged local ferromagnetic moment $\langle m_z\rangle/m$ for the values $J_{AFM} = 0.015t$, $J_H = 2.5t$, and $\Delta = 1.5ty$. This magnetic moment per Mn^{4+} ion reaches the maximum value $0.5m_{Mn^{4+}} = 1.5\mu_B$ in the *H* phase, to vanish altogether for $y > 0.25$. A similar behavior of spontaneous magnetization was also observed in the experiment in [12], where the magnetization first increased with increasing *y*, to vanish near $y = 0.2$. Remarkably, the theoretical value of $\langle m_z\rangle/m$ at $y = 0.1$ coincides with the experimental value of the FM component in $Ho_{0.1}Ca_{0.9}MnO_3$ [13], despite the fact that the magnetic structure of this compound was determined by the diffraction of unpolarized neutrons to be noncoplanar. Comparison of the theoretical curve with magnetization data obtained for the samarium and praseodymium manganites is complicated by the fact that the ground state of these compounds is heterogeneous at low electron concentrations.

5. Thus, the double-exchange model for the e_g electrons, combined with the Heisenberg model for localized t_{2g} electrons, when applied to the crystal structure of manganites with four manganese atoms in the unit cell in the parameter region $0.018t < J_{AFM} < 0.022t$, $J_H = 2.5t$, and $\Delta = 1.5ty$, correctly predicts the experimentally observed *G–C–A* magnetic phase alternation with increasing doping level *y*. For the values $J_{AFM} < 0.018t$ and $y < 0.28$, this model allows the existence of a collinear phase *H* not observed earlier.

ACKNOWLEDGMENTS

This study was supported by the Russia–Belarus project (no. 02-02-81012 Bel2002-a) of the Russian Foundation for Basic Research.

REFERENCES

1. J. van den Brink and D. I. Khomskii, Phys. Rev. Lett. **82**, 1016 (1999).
2. S. M. Dunaevskiĭ, Fiz. Tverd. Tela (St. Petersburg) **43**, 2161 (2001) [Phys. Solid State **43**, 2257 (2001)].
3. T. Ohsawa and J. Inoue, Phys. Rev. B **65**, 134442 (2002).
4. Yu. A. Izyumov and Yu. N. Skryabin, Usp. Fiz. Nauk **171** (2), 121 (2001) [Phys. Usp. **44**, 109 (2001)].
5. H. Shiba, R. Shina, and A. Takahashi, J. Phys. Soc. Jpn. **66**, 941 (1997).
6. G. Venketeswara Pai, Phys. Rev. B **63**, 064431 (2001).
7. I. V. Solovyev and K. Terakura, Phys. Rev. B **63**, 174425 (2001).
8. S. M. Dunaevskiĭ and V. V. Deriglazov, Fiz. Tverd. Tela (St. Petersburg) **45**, 681 (2003) [Phys. Solid State **45**, 714 (2003)].
9. S. M. Dunaevsky and V. V. Deriglazov, Phys. Rev. B **67**, 014409 (2003).
10. E. F. Bertaut, in *Magnetism*, Ed. by G. T. Rado and H. Suhl (Academic, New York, 1963), Vol. 3, Chap. 4.
11. S. M. Dunaevsky and V. V. Deriglazov, Preprint No. 2522, PNPI (St. Petersburg Inst. of Nuclear Physics, Russian Academy of Sciences, 2003).
12. J. J. Neumeier and J. L. Cohn, Phys. Rev. B **61**, 14319 (2000).
13. K. Hagdorn, D. Hohlwein, J. Ihringer, *et al.*, Eur. Phys. J. B **11**, 243 (1999).

Translated by G. Skrebtsov

Physics of the Solid State, Vol. 46, No. 3, 2004, pp. 515–520. Translated from Fizika Tverdogo Tela, Vol. 46, No. 3, 2004, pp. 500–504.

MAGNETISM AND FERROELECTRICITY

Optical Investigations of the Effect of Gradual Substitution $NH_4 \longrightarrow Cs$ on the Ferroelastic Phase Transition in a $CsLiSO_4$ Crystal

S. V. Mel'nikova and V. A. Grankina

Kirensky Institute of Physics, Siberian Division, Russian Academy of Sciences, Akademgorodok, Krasnoyarsk, 660036 Russia
e-mail: msv@iph.krasn.ru

Received July 1, 2003

Abstract—Crystals of $Cs_x(NH_4)_{1-x}LiSO_4$ ($0.39 \le x \le 1.0$) solid solutions are grown and investigated using polarized light microscopy and measurements of the birefringence in the temperature range 100–530 K. The (x–T) phase diagram of the $Cs_x(NH_4)_{1-x}LiSO_4$ solid solutions is constructed. It is demonstrated that, upon substitution of ammonium for cesium in the $CsLiSO_4$ crystal, the phase transition temperature gradually increases to such a degree that the ferroelastic phase can exist at room temperature. The triple point of intersection of the *Pmcn*, $P2_1cn$, and $P112_1/n$ phase boundaries is determined. It is established that the introduction of ammonium in small amounts has an unusually strong effect on the refractive properties and character of the ferroelastic phase transition in the $CsLiSO_4$ crystal. © *2004 MAIK "Nauka/Interperiodica".*

1. INTRODUCTION

Crystals of the $ALiSO_4$ (A = K, NH_4, Rb, Cs) family contain LiO_4 and SO_4 tetrahedral groups that are linked into a framework structure of the tridymite type (cations A occupy large-sized holes). These crystals are convenient model objects for investigating phase transitions owing to the great diversity of phases and sequences of changes in the symmetry upon phase transitions. Moreover, structural transformations occurring in these materials are primarily associated with step-by-step orientational ordering of structural groups [1].

For crystals with a large-sized Cs^+ cation, namely, crystals of cesium lithium sulfate $CsLiSO_4$, the initial structure with symmetry *Pmcn* ($c = c_0$) is most stable in the crystal family under investigation and is retained up to a temperature $T_{01} \approx 202$ K, at which the $CsLiSO_4$ crystal undergoes only one ferroelastic phase transition from the initial phase to the phase with monoclinic symmetry $P112_1/n$ ($c = c_0$) [2]. The unit cell parameters of this crystal at room temperature (293 K) are as follows: $a = 5.456$ Å, $b = 9.456$ Å, and $c = 8.820$ Å [2].

For crystals with a small-sized A^+ cation, namely, crystals of ammonium lithium sulfate NH_4LiSO_4 in the β modification [3], the initial phase becomes unstable at higher temperatures. During cooling, this compound undergoes the following sequence of phase transitions with a change in the initial symmetry:

$$Pmcn(c = c_0) \rightleftharpoons P2_1cn(c = c_0)$$

$$\rightleftharpoons P2_1/c11(c = 2c_0) \rightleftharpoons C1c1(c = 2c_0)$$

at temperatures $T_1 = 460$ K, $T_2 = 284$ K, and $T_3 = 27$ K, respectively [4–6]. The phase is ferroelectric with considerable spontaneous polarization at room temperature ($a = 5.28$ Å, $b = 9.14$ Å, $c = 8.786$ Å) [5] and ferroelastic below ~284 K.

Earlier [7], we showed that, in the concentration range $0 \le x \le 0.35$, $Cs_x(NH_4)_{1-x}LiSO_4$ crystals form a continuous series of solid solutions. An increase in the cesium content x leads to a gradual decrease in the phase transition temperatures T_1 and T_2. However, the character of the high-temperature phase transition does not change [the critical exponent, which corresponds to the temperature dependence of the birefringence $(n_a - n_b)(T)$, remains constant and equal to $2\beta = 0.24 \pm 0.01$ for all compositions], even though the magnitudes of the birefringence and enthalpy anomalies decrease with an increase in the cesium content x in the crystal. As the cesium content increases, the low-temperature transition at $T = T_2$ becomes more similar to a first-order transition: the birefringence jump δn increases, and the temperature hysteresis ΔT becomes more pronounced. Moreover, according to the (x–T) phase diagram [7], the region of existence of the ferroelectric phase is more extended at low contents x and the ferroelastic phase with symmetry $P2_1/c11$ disappears at $x > 0.22$. In this respect, it is important to determine the boundaries of the regions of the initial, ferroelectric, and ferroelastic phases with symmetries *Pmcn*, $P2_1cn$, and $P112_1/n$, respectively.

In the present work, we continued our investigations of $Cs_x(NH_4)_{1-x}LiSO_4$ solid solutions in the concentration range $0.35 \le x \le 1.0$. For this purpose, we used polarized light microscopy and measurements of the birefringence of the crystals under investigation.

1063-7834/04/4603-0515$26.00

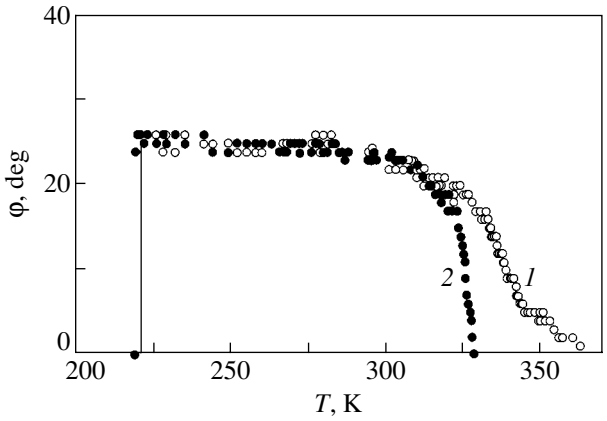

Fig. 1. Graph illustrating the influence of annealing on the temperature and character of the phase transition in a $Cs_x(NH_4)_{1-x}LiSO_4$ ($x = 0.5$) solid solution according to the results of measurements of the rotation angle of the optical indicatrix $\varphi(T)$ with respect to the [001] direction: (*1*) prior to annealing and (*2*) after annealing.

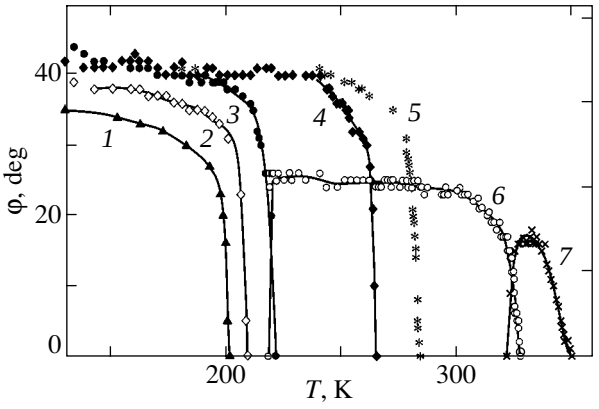

Fig. 2. Temperature dependences of the rotation angle of the optical indicatrix with respect to the [001] direction in $Cs_x(NH_4)_{1-x}LiSO_4$ crystals at cesium contents x = (*1*) 1.00, (*2*) 0.95, (*3*) 0.90, (*4*) 0.80, (*5*) 0.71, (*6*) 0.5, and (*7*) 0.39.

2. SAMPLE PREPARATION AND EXPERIMENTAL TECHNIQUE

Single crystals suitable for our experiments were prepared using two procedures described earlier in [7]. The quantitative composition of these crystals was determined by atomic absorption analysis. Crystals with a cesium content in the range $x = 0.35$–0.6 were grown from a mixture of NH_4LiSO_4 and $CsLiSO_4$ solutions in caustic ammonia taken in required proportion. Compounds with a cesium content in the range $x = 0.6$–1.0 were prepared through slow evaporation of the appropriate mixtures of NH_4LiSO_4 and $CsLiSO_4$ aqueous solutions at $T \approx 310$ K. For optical investigations, samples in the form of plates with different orientations and thicknesses were oriented using a URS-1 x-ray instrument. For the reasons given in [7], prior to optical and thermal investigations, the samples were necessarily annealed at a temperature of approximately 470 K for 2 h. The necessity of performing this annealing is illustrated in Fig. 1, which presents the results of measurements of the rotation angle of the optical indicatrix $\varphi(T)$ with respect to the [001] direction for a solid solution with $x = 0.5$ prior to and after annealing. For the sample not subjected to annealing, the phase transition temperature increases and inhomogeneous stresses arising in the crystal lead to a smearing of the observed anomaly, because, as was shown by Chekmasova *et al.* [8], the hydrostatic pressure substantially affects the phase transition temperature of the NH_4LiSO_4 crystal ($dT_1/dp = 90$ K/GPa). Upon annealing, the stresses are relieved and the dependence $\varphi(T)$ acquires a more perfect shape.

The crystal plates prepared were used in optical investigations and measurements of the birefringence from the (001) and (100) sections in the temperature range from 77 to ~500 K. The birefringence was measured on a Berec compensator with an accuracy of $\cong 10^{-5}$ and a Senarmont compensator with a sensitivity of no less than $\cong 10^{-7}$. The former compensator made it possible to examine small-sized samples and to determine the birefringence magnitude. The rotation angle of the optical indicatrix was measured using a polarizing microscope with an accuracy of ±0.5°.

3. EXPERIMENTAL RESULTS

Observations of the single-crystal plates in polarized light revealed that crystals of all the studied compositions (in the corresponding temperature ranges) are characterized by a twin structure typical of the $CsLiSO_4$ ferroelastic phase. At temperatures below T_{01}, crystal plates of the (001) section have a streaky structure. The structural components differ in the extinction positions by an angle 2φ. The temperature dependences of the rotation angle of the optical indicatrix $\varphi(T)$ with respect to the [001] direction of a single twin are depicted in Fig. 2. Curve *1* represents the experimental data for pure cesium lithium sulfate $CsLiSO_4$. A comparison of curves *1*–*5* shows that an increase in the ammonium content in the solid solution leads to a gradual displacement of the phase transition toward the high-temperature range. This is accompanied by an increase in the rotation angle of the optical indicatrix, but the phase transition, as before, proceeds in a gradual manner. For these compositions, the phase with monoclinic symmetry $P112_1/n$ is retained up to the liquid-nitrogen temperature. In the case of a solid solution with $x = 0.5$, i.e., when the ammonium content is equal to the cesium content (Fig. 2, curve *6*), the phase transition temperature increases to such a degree that the monoclinic phase can exist already at room temperature; however, the stability region of the monoclinic phase becomes substantially narrower. Upon cooling in the tempera-

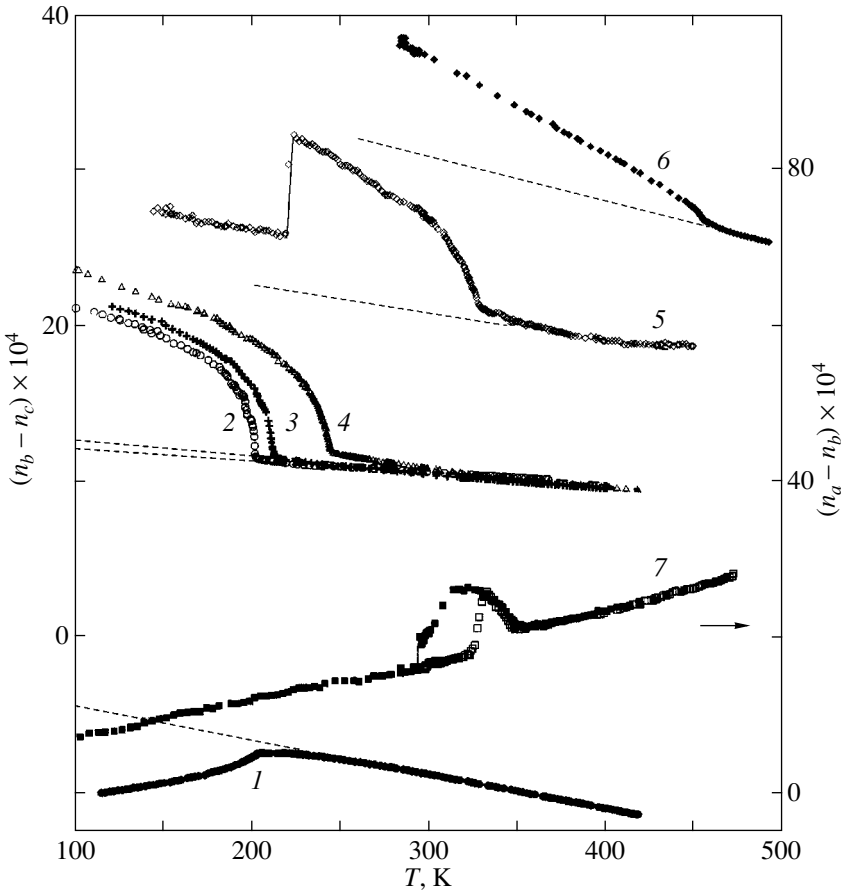

Fig. 3. Temperature dependences of the birefringence $(n_b - n_c)(T)$ for $Cs_x(NH_4)_{1-x}LiSO_4$ solid solutions at cesium contents x = (*1*) 1.00, (*2*) 0.99, (*3*) 0.95, (*4*) 0.80, (*5*) 0.5, and (*6*) 0. (*7*) Temperature dependence of the birefringence $(n_a - n_b)(T)$ for the sample at x = 0.39 upon heating and cooling.

ture range close to the phase transition point $T_{02} \approx 220$ K, the magnitude of the rotation angle of the optical indicatrix drastically decreases to zero and the crystal again transforms into the orthorhombic phase. For the sample at a cesium content x = 0.39 (Fig. 2, curve *7*), the phase with monoclinic symmetry $P112_1/n$ is observed only in a narrow temperature range (~25 K). The thermal investigations of the second optical harmonic in samples at cesium contents x = 0.5 and 0.39 revealed that the crystal has a center of symmetry (the second optical harmonics is absent) at temperatures above $T = T_{02}$ and is characterized by the 2ω generation below this temperature. As a result, the crystal loses the center of symmetry and transforms into the phase with an orthorhombic polar group.

The results of investigations into the temperature dependences of the birefringence $\Delta n_a = (n_b - n_c)$ for $Cs_x(NH_4)_{1-x}LiSO_4$ solid solutions with different cesium contents x are presented in Fig. 3. These data also indicate a gradual displacement of the phase transition toward the high-temperature range with an increase in the ammonium content in the material. Moreover, it is found that the substitution $NH_4 \longrightarrow Cs$ strongly affects the refractive properties of the $CsLiSO_4$ crystal. The introduction of small amounts of ammonium into the $CsLiSO_4$ compound radically changes the optical indicatrix. As a result, the birefringence Δn_a reverses sign. It is known that the refractive indices of the initial crystals are in the following proportions: $n_c > n_b$ for the $CsLiSO_4$ crystal [9] and $n_b > n_c$ for the NH_4LiSO_4 crystal [10]. Indeed, as can be seen from Fig. 3, the birefringence $\Delta n_a = (n_b - n_c)$ is negative for pure $CsLiSO_4$ (curve *1*) and positive for pure NH_4LiSO_4 (curve *6*). The introduction of 1 mol % NH_4^+ into the $CsLiSO_4$ compound leads to a change in the sign of the birefringence Δn_a and affects the temperature dependence of Δn_a (Fig. 3, curve *2*). A further increase in the ammonium content in the crystal affects only the phase transition temperature (Fig. 3, curves *3*–*5*). For a cesium content x = 0.5 (Fig. 3, curve *5*), the crystal undergoes the second phase transition at a temperature $T_{02} \approx 220$ K, which is attended by a jump in the birefringence. For comparison, curve *6* in Fig. 3 shows the temperature dependence of the birefringence Δn_a for

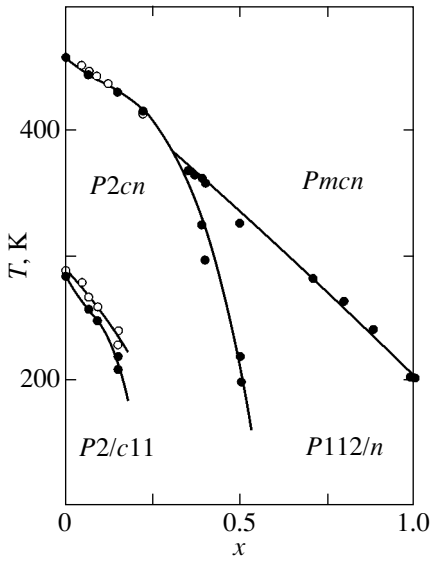

Fig. 4. Phase (x–T) diagram of the $Cs_x(NH_4)_{1-x}LiSO_4$ solid solutions according to the DSC data obtained upon heating [7] (open circles) and the results of optical investigations upon cooling (closed circles).

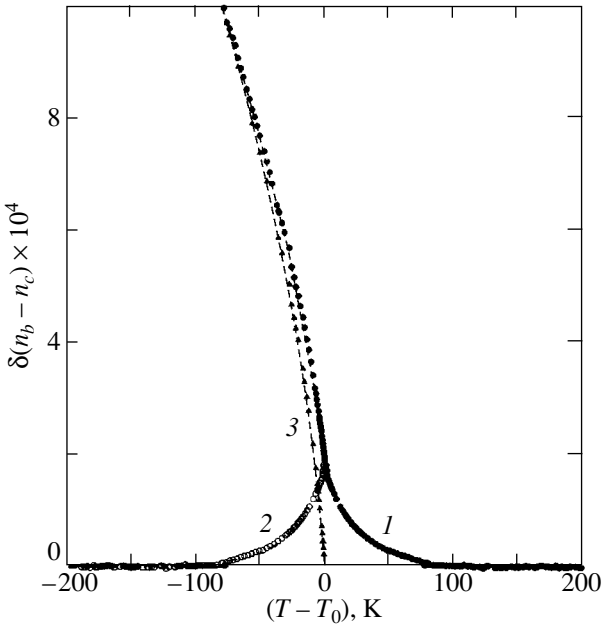

Fig. 5. (*1*) Anomaly of the birefringence of the $CsLiSO_4$ crystal and the decomposition of this anomaly into (*2*) the fluctuation component and (*3*) the component associated with the parameter of the phase transition.

pure NH_4LiSO_4 upon the phase transition $Pmcn \rightleftharpoons P2_1cn$.

Solid solutions with a cesium content $x = 0.39$ were examined using a crystal plate of the (001) section (Fig. 3, curve *7*). The temperature dependence $(n_a - n_b)(T)$, like the dependence $\varphi(T)$, is characterized by two special points that correspond to two phase transitions. The high-temperature transformation observed at a temperature T_{01} exhibit features specific to second-order phase transitions. The birefringence jump and pronounced temperature hysteresis ($\Delta T \approx 30$ K) observed at a temperature T_{02} indicate that this transformation is a first-order phase transition.

4. DISCUSSION

The phase diagram of the $Cs_x(NH_4)_{1-x}LiSO_4$ solid solutions (Fig. 4) was constructed according to the results of optical investigations performed in this work and data obtained earlier in [7]. As can be seen from Fig. 4, the dependence of the instability temperature of the initial phase on the cesium content in the solid solution exhibits a nearly linear behavior. The end points of this dependence correspond to the $CsLiSO_4$ and NH_4LiSO_4 compounds. The compositions with cesium contents $x \approx 0.4$ are characterized by a triple point at which the $Pmcn$, $P2_1cn$, and $P112_1/n$ phases coexist. The quantity dT_{02}/dx for the $P112_1/n$–$P2_1cn$ phase boundary is considerably larger than that for the other phase boundaries.

The temperature dependence of the anomalous component of the birefringence of the $CsLiSO_4$ crystal in the range below the phase transition temperature T_{01} is plotted in Fig. 5. This dependence was obtained by subtracting the linear dependence of the birefringence (extrapolated from the initial phase) from the dependences depicted in Fig. 3. As can be seen, the pretransition effects are observed over a wide temperature range (≈100 K) above the phase transition temperature. Similar effects were revealed earlier in the temperature dependences of the lattice parameters and in the heat capacity curve [11]. At temperatures close to T_{01}, the anomalous component of the birefringence governed by the pretransition phenomena reaches 20% of the total anomaly. For this reason, the phase transition temperature and the birefringence anomaly associated with the parameter of the phase transition below T_{01} cannot be determined from the temperature dependence of the birefringence Δn_a. The fluctuation contribution of the transition parameter to the birefringence can be excluded, by analogy with [12], under the assumption that the temperature dependence of the fluctuation component of the birefringence anomaly above and below the phase transition temperature is symmetric with respect to the T_{01} temperature. The decomposition of the birefringence anomaly near T_{01} into the fluctuation component and the component associated with the transition parameter (δn_a) for the $CsLiSO_4$ crystal is illustrated in Fig. 5. The temperature dependence of the latter component on a logarithmic scale makes it possible to determine the critical index of the temperature behavior of the transition parameter. Making allowance for the fact that the anomalous component of the birefringence measured in the orthorhombic setting is proportional to the transition parameter squared, i.e.,

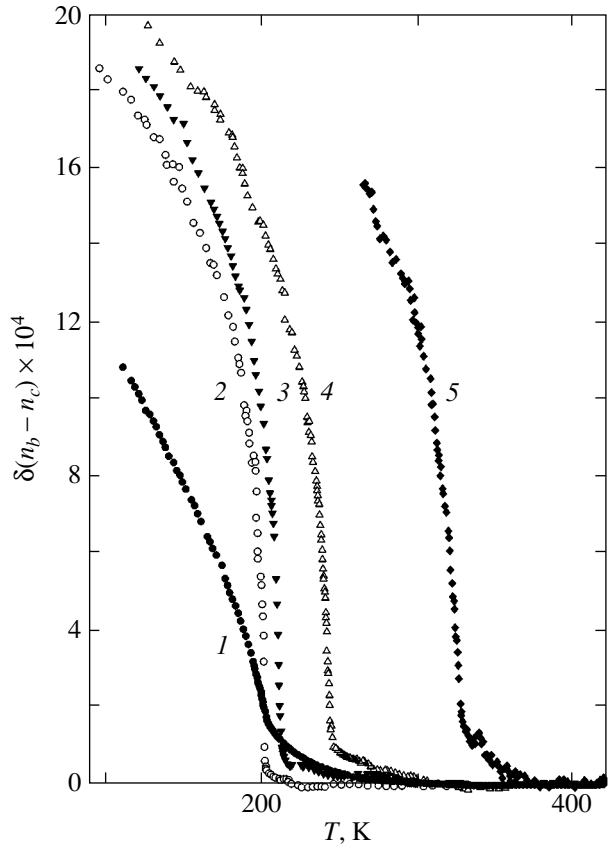

Fig. 6. Temperature behavior of the anomalous component of the birefringence in the ferroelastic phase of $Cs_x(NH_4)_{1-x}LiSO_4$ crystals at cesium contents x = (*1*) 1.00, (*2*) 0.99, (*3*) 0.95, (*4*) 0.80, and (*5*) 0.5.

$\delta n_a(T) \sim \eta^2 \sim (T_0 - T)^{2\beta}$, we determine the "nonclassical" critical index $\beta = 0.38 \pm 0.01$. The nonclassical magnitude of the critical index can be explained by the closeness of the phase transition to the Landau tricritical point. In this case, the term with η^6 must be taken into account in the expansion of the thermodynamic potential because of the smallness of the coefficient of η^4. In actual fact, the results of calculations performed according to the procedure described in [13] demonstrated that all experimental points of the curve $\delta n_a(T)$ fall on a linear curve $\Delta T/\delta n \sim \delta n$. The phase transition point is found to be close to the tricritical point (second-order phase transitions), and the quantity $(T_c - T_0)$ is the measure of closeness to the point T_c (in our case, this difference is equal to 1.1 K).

The introduction of small amounts of ammonium (1 mol %) into the initial compound $CsLiSO_4$ brings about a drastic decrease in the pretransition effects and a change in the shape and magnitude of the birefringence anomaly (Fig. 6). With a further increase in the content x, the birefringence "tail" associated with the pretransition phenomena increases progressively but the shape and magnitude of the birefringence anomaly in the distorted phase remain unchanged. The critical index β was determined from the dependence $\delta n_a(T)$ plotted on a logarithmic scale. For all compositions with $x \neq 1$, the critical index proved to be equal to $\beta = 0.25 \pm 0.01$. Moreover, the linear relationship $(\delta n_a)^2 \sim \eta^4 \sim T - T_{01}$ is satisfied within a temperature range 60 K below the phase transition point. This indicates that, in the solid solutions under investigation, the phase transition corresponds to the Landau tricritical point and that the coefficient of the term with η^4 in the expansion of the thermodynamic potential is equal to zero.

5. CONCLUSIONS

Thus, the results of the above investigations demonstrated that the substitution of even small amounts of ammonium for cesium in the cesium lithium sulfate compound substantially affects the optical characteristics of the material and the character of the phase transition; however, the ferroelastic nature of the phase transition remains unchanged. The assumption was made that the observed change in the optical properties is most likely associated with the specific features of the molecular ion NH_4^+ introduced into the initial compound. It should also be noted that our earlier investigations [14], in which the atomic cation Rb^+ was substituted for the Cs^+ ion, did not reveal radical changes in either the optical properties of the crystal or the character of the phase transition.

ACKNOWLEDGMENTS

This work was supported by the Ministry of Industry and Science of the Russian Federation, project no. NSh-930.2003.2.

REFERENCES

1. K. S. Aleksandrov and B. V. Beznosikov, *Structural Phase Transitions in Crystals (The Potassium Sulfate Family)* (Nauka, Novosibirsk, 1993).
2. A. I. Kruglik, M. A. Simonov, and E. P. Zhelezin, Dokl. Akad. Nauk SSSR **247** (7), 1384 (1979) [Sov. Phys. Dokl. **24**, 596 (1979)].
3. S. V. Mel'nikova, A. V. Kartashev, V. A. Grankina, and I. N. Flerov, Fiz. Tverd. Tela (St. Petersburg) **45** (8), 1497 (2003) [Phys. Solid State **45**, 1572 (2003)].
4. A. I. Kruglik, M. A. Simonov, and K. S. Aleksandrov, Kristallografiya **23**, 494 (1978) [Sov. Phys. Crystallogr. **23**, 274 (1978)].
5. K. Itoh, H. Ishikuta, and E. Nakamura, Acta Crystallogr. B **37**, 664 (1981).
6. A. Dollase, Acta Crystallogr. B **25**, 2298 (1969).
7. S. V. Mel'nikova, V. A. Grankina, and A. V. Kartashev, Fiz. Tverd. Tela (St. Petersburg) **44** (2), 365 (2002) [Phys. Solid State **44**, 379 (2002)].
8. T. I. Chekmasova, I. S. Kabanov, and V. I. Yusvak, Phys. Status Solidi A **44**, K155 (1977).

9. A. T. Anistratov, A. V. Zamkov, L. A. Kot, *et al.*, Fiz. Tverd. Tela (Leningrad) **24** (9), 2763 (1982) [Sov. Phys. Solid State **24**, 1565 (1982)].

10. A. T. Anistratov and S. V. Mel'nikova, Izv. Akad. Nauk SSSR, Ser. Fiz. **39** (4), 808 (1975).

11. K. S. Aleksandrov, L. I. Zherebtsova, I. M. Iskornev, *et al.*, Fiz. Tverd. Tela (Leningrad) **22**, 3673 (1980) [Sov. Phys. Solid State **22**, 2150 (1980)].

12. F. J. Schäfer and W. Kleeman, J. Appl. Phys. **57**, 2606 (1985).

13. S. V. Mel'nikova, I. N. Flerov, and A. T. Anistratov, Fiz. Tverd. Tela (Leningrad) **23** (12), 3570 (1981) [Sov. Phys. Solid State **23**, 2074 (1981)].

14. S. V. Melnikova, A. D. Vasiliev, V. A. Grankina, *et al.*, Ferroelectrics **170**, 139 (1995).

Translated by O. Borovik-Romanova

Physics of the Solid State, Vol. 46, No. 3, 2004, pp. 521–525. Translated from Fizika Tverdogo Tela, Vol. 46, No. 3, 2004, pp. 505–509.

MAGNETISM AND FERROELECTRICITY

Heat Capacity of the $PbFe_{1/2}Ta_{1/2}O_3$ Perovskite-Like Compound

M. V. Gorev*, I. N. Flerov*, V. S. Bondarev*, Ph. Sciau, and A. G. Lehmann*****

**Kirensky Institute of Physics, Siberian Division, Russian Academy of Sciences, Akademgorodok, Krasnoyarsk, 660036 Russia*

e-mail: gorev@iph.krasn.ru

***CEMES-CNRS, 29 Rue Jeanne Marvig, Toulouse, 31055 France*

****Instituto Nazionale di Fisica della Materia (INFM) e Dipartimento di Fisica, Monserrato (Cagliari), 090124 Italy*

Received July 8, 2003

Abstract—The heat capacity $C_p(T)$ of the complex perovskite $PbFe_{1/2}Ta_{1/2}O_3$ has been studied using adiabatic calorimetry in the temperature range 150–370 K. Three diffuse anomalies in $C_p(T)$ are found to exist at temperatures $T_d \approx 350$ K, $T_m \approx 250$–300 K, and $T_c \approx 205$ K. The anomalous and the lattice contribution to the heat capacity are separated, and the change in the entropy is determined. The results of the study are discussed jointly with the data on the structure and physical properties of the compound. © *2004 MAIK "Nauka/Interperiodica".*

1. INTRODUCTION

Double perovskites of type 1 : 1, with the general formula $Pb B^{3+}_{1/2} B^{5+}_{1/2} O_3$, are classical model objects for the investigation of ferroelectrics–relaxors. Their properties can vary considerably without changing the chemical composition as a result of a variation in the ordering of the B^{3+} and B^{5+} ions over equivalent positions in the lattice [1, 2]. Highly ordered perovskites undergo ferroelectric or antiferroelectric phase transitions, whereas in the disordered state they exhibit properties characteristic of relaxors [2], namely, an anomaly in the dielectric permittivity ε broadened over a wide temperature interval and pronounced dependences of the temperature of its maximum (T_m) and of the magnitude of the maximum (ε_m) on the measuring field frequency.

The $PbFe_{1/2}Ta_{1/2}O_3$ compound (PFT) was first synthesized in the form of a ceramic and studied in [3]. It was found that the PFT has cubic symmetry *Pm3m* at room temperature and that the Fe^{3+} and Ta^{5+} ions are distributed randomly over the *B* positions of the perovskite lattice. The cubic symmetry of the compound at room temperature was confirmed in subsequent x-ray measurements performed on single crystals [4].

The change in the PFT symmetry over a broad temperature range was studied by x-ray diffraction on single crystals [5–7]. Two phase transitions, at 270 and 220 K, were identified. The high-temperature phase, which is stable for $T > 270$ K, is paraelectric and optically uniaxial, despite its (pseudo)cubic symmetry. At 350 K, the symmetry of the compound was refined in space group *Pm3m*. The compound is characterized by a strong anisotropy in the oxygen thermal vibration parameters and by positional disorder or a strong anharmonicity in the thermal motion of the lead ions [6]. The intermediate phase ($270 > T > 220$ K) was identified as tetragonal (*P4mm*). Within the interval $220 > T > 200$ K, the tetragonal phase coexists with the monoclinic phase. Below 200 K, only the monoclinic phase (*Cm*) is stable. The isostructural compound $PbFe_{1/2}Nb_{1/2}O_3$ (PFN) was also observed to undergo the cubic ⟶ tetragonal ⟶ monoclinic phase sequence [8].

The two low-temperature distorted phases were refined by the Rietveld method with the use of neutron and synchrotron experiments [5]. The distortions of the cubic phase are fairly small and were detected only as line broadenings in the diffraction pattern obtained with the angular resolution achievable with synchrotron radiation.

The low-temperature monoclinic phase *Cm* reveals large lead ion displacements along the [111] pseudocubic axis, so that the main lattice distortion, despite the monoclinic symmetry, is rhombohedral. The role of the monoclinic *Cm* phase, which couples the tetragonal and rhombohedral phases in complex lead-containing perovskites, is currently a subject of intense debate [9–11].

Small structural distortions in PFT and the difficulties encountered in establishing its symmetry were also pointed out in [12], where elastic neutron scattering studies were performed. These studies did not reveal any symmetry change within the temperature interval from 300 to 10 K. The data obtained by Rietveld refinement were interpreted in terms of the *R3m* rhombohedral space group, which provided slightly better convergence as compared to the *Pm3m* cubic lattice with positionally disordered lead ions [12].

There are numerous publications on the investigation of the dielectric properties of PFT [1, 13–15]. In addition to the diffuse, frequency-dependent maximum in $\varepsilon(T)$ at $T_m \approx 243$ K, which is typical of relaxors, a small feature was observed in the behavior of $\varepsilon(T)$ at a

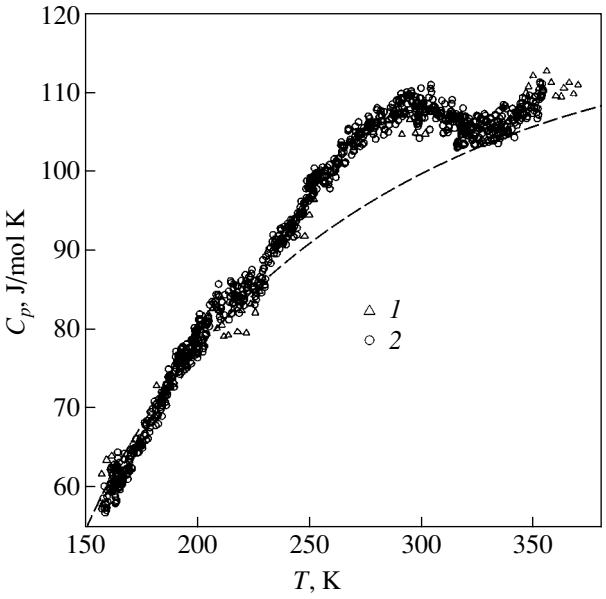

Fig. 1. Temperature dependence of the specific heat of $PbFe_{1/2}Ta_{1/2}O_3$ obtained by (*1*) discrete heating and (*2*) continuous heating. Dashed line plots the lattice specific heat.

temperature T_{ip} [15], which is 30–40 K lower than T_m. Below this temperature, the frequency dispersion of ε is considerably weaker than that seen at higher temperatures [15]. This behavior is similar to that observed in $PbSc_{1/2}Ta_{1/2}O_3$ and $PbSc_{1/2}Nb_{1/2}O_3$ at the spontaneous transition from the relaxor to normal ferroelectric state [16].

To the best of our knowledge, spontaneous polarization in PFT was studied only in [14] along the [100] direction in electric fields of up to 8 kV/cm. The spontaneous polarization exists even above 300 K and reaches 28 μC/cm^2 at liquid-nitrogen temperature.

Birefringence Δn was observed in PFT in the range from 20 K up to the first-order phase transition temperature of 210 K [17]. Above 210 K, Δn is small and attains levels characteristic of growth defects as the temperature is increased [17].

As seen from this brief overview, the results obtained in various studies of PFT and their interpretations are more often than not at odds with one another. Despite the large number of diverse studies performed, many features in the behavior of PFT remain unclear.

Here, we report on a study of the heat capacity and thermodynamic parameters of PFT in order to obtain additional information on the changes in the energy characteristics that can take place in the elastic and electrical subsystems of PFT.

2. SAMPLE AND MEASUREMENT TECHNIQUES

The calorimetric measurements were performed on a sample studied earlier by neutron diffraction [5].

The PFT crystals were grown from a solution of the starting oxides in a PbO melt using the technique proposed in [18]. The remainder of the PbO melt was removed by rinsing the crystals in 30 wt % nitric acid. The grown crystals, having the pyrochlore structure, were sorted by hand in polarized light under a microscope. The PFT crystals selected in this way were ground. To reduce the strains created by grinding, the powders thus obtained were annealed for several hours at a temperature of about 850 K. After the annealing, the material was subjected to x-ray diffraction analysis, which showed the sample to be free of foreign phases and to produce clear and narrow Bragg reflections.

The heat capacity was studied in the temperature interval 100–370 K using adiabatic calorimetry, which made it possible to obtain absolute values of the heat capacity with a high accuracy. The sample ground to powder was placed in an indium container made airtight in a helium environment. Helium was employed as a heat-exchange gas to equalize the temperature over the sample. The mass of the sample was ~1 g, and the mass of the container was 9.8 g. Measurements were performed using the traditional technique of discrete heating and also in an automated regime under continuous heating with a variation in temperature at a rate $dT/dt \approx (2–3) \times 10^{-1}$ K min^{-1}. The experiment yielded the total heat capacity of the sample and the container. The heat capacity of the container was measured in a separate experiment. The accuracy with which the total heat capacity could be determined depends on the actual heating technique employed and is (0.1–0.5)%.

3. RESULTS OF THE STUDIES

Figure 1 displays the temperature dependences of the PFT specific heat obtained using the methods of discrete and continuous heating. The scatter of experimental points about the smoothing curve does not exceed 2%. The fact that this error is slightly larger than usual should be attributed to the heat capacity of the sample making up only a small fraction (about 10%) of the total heat capacity of the container plus sample system.

The analysis of the heat capacity should take into account the anharmonic contributions resulting in a difference between the isobaric (C_p) and isochoric (C_V) specific heats. The volume expansion coefficient estimated for the temperature range from 300 to 700 K from data on the temperature dependence of the cubic cell parameter varies from 9×10^{-6} to 35×10^{-6} K^{-1}. To the best of our knowledge, there are no data on the compressibility of PFT. We used data from [19] obtained in a study of the effect of pressure on the unit cell parameters of $PbZr_{1/2}Ti_{1/2}O_3$, which is related to PFT; its modulus of volume compressibility was measured to be 2.3×10^{-11} Pa^{-1}. Using these data, the anharmonic contribution to the specific heat was found to be ≤1 J/mol K below 700 K. Because this small quantity is within the experimental error, we disregarded the difference between C_p and C_V in the subsequent analysis. The

smallness of the anharmonic contribution is due to the comparatively small thermal expansion coefficient.

The lattice heat capacity C_L can be derived from the general relation

$$C_L = (\partial E/\partial T) = \frac{\partial}{\partial T}(\int d\omega G(\omega) n(\omega) \hbar\omega), \quad (1)$$

where E is the internal energy of the system, $n(\omega)$ is the Bose–Einstein distribution function, and $G(\omega)$ is the density of vibrational states. The density-of-states function $G(\omega)$ over the whole frequency range is, as a rule, unknown for fairly complex crystals. For this reason, the temperature dependence of heat capacity is calculated using a simplified approach. In most cases, in order to analyze the temperature dependence of the heat capacity and to separate the lattice and anomalous contributions, a simple model is used in which the lattice heat capacity of a compound is approximated by a combination of the Debye and Einstein functions. It is this approach that we used in the case with PFT. In the temperature range of interest to us, the heat capacity is only weakly sensitive to fine details in the vibration spectrum, which validates our separation of the lattice contribution.

The anomalous component of the specific heat $\Delta C_p = C_p - C_L$ is shown in Fig. 2. The maximum value of ΔC_p is 11 J/mol K, or ~10% of the lattice specific heat. The $\Delta C_p(T)$ relation clearly exhibits three regions of anomalous behavior, namely, near $T_1 \approx 350$ K, $T_2 \approx$ 250–300 K, and $T_3 \approx 205$ K.

The change in specific entropy associated with the anomalous behavior of the heat capacity can be calculated as $\Delta S(T) = \int_{100}^{T} \frac{\Delta C_p}{T} dT$; this quantity is plotted in Fig. 3 and constitutes 3.7 J/mol K.

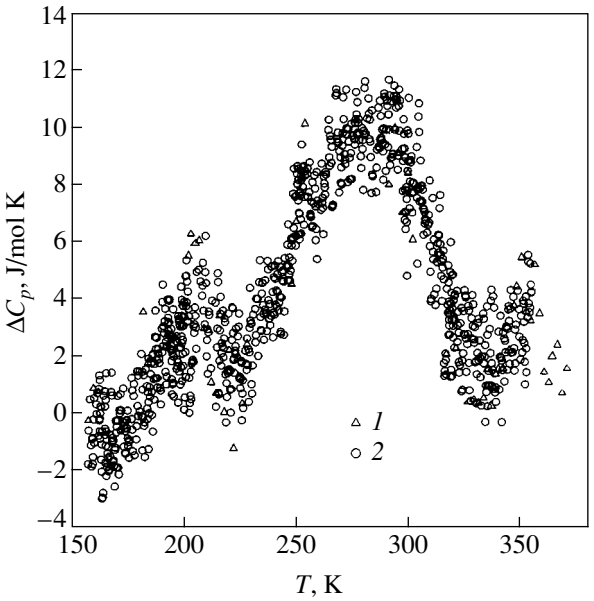

Fig. 2. Temperature dependence of the anomalous component of the specific heat of $PbFe_{1/2}Ta_{1/2}O_3$ obtained by (*1*) discrete heating and (*2*) continuous heating.

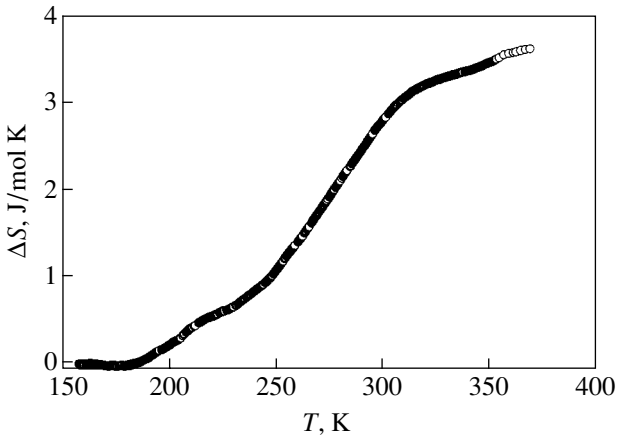

Fig. 3. Temperature dependence of the anomalous contribution to the specific entropy of $PbFe_{1/2}Ta_{1/2}O_3$.

4. DISCUSSION AND CONCLUSIONS

The heat capacity anomalies coincide in temperature with the anomalous behavior of the structural, magnetic, optical, and dielectric properties.

In the temperature region near 350 K, earlier studies revealed deviations of the lattice parameters from their regular course [4] and of the $\varepsilon(T)$ behavior from the Curie–Weiss law [13, 15]. The anomalous behavior of the heat capacity over the temperature range 250–300 K correlates with that of the dielectric permittivity [13, 15] and of the interplanar distance d_{222} [7]. Near T_3, jumps in the birefringence [17] and in d_{222} [7] and specific features in the $\varepsilon(T)$ behavior [13, 15] were observed. The fairly large scatter of experimental points in the interval 160–170 K can probably be assigned to the transition of PFT to the antiferromagnetic state [14].

On the one hand, our calorimetric results agree to a certain extent with the data reported in [4–7]. The PFT can be expected to undergo the following sequence of structural transformations with decreasing temperature: cubic paraelectric (*Pm3m*, $T > 350$ K) $\longrightarrow$ tetragonal antiferroelectric ($350 < T < 270$ K) $\longrightarrow$ tetragonal ferroelectric (*P4mm*, $270 > T > 205$ K) $\longrightarrow$ monoclinic ferroelectric (*Cm*, $205 > T > 160$ K) $\longrightarrow$ antiferromagnetic phase ($T < 160$ K).

On the other hand, the diffuseness of the heat capacity anomalies, the noticeable dispersion of ε, and its clearly pronounced relaxor behavior [13, 15] may signal a certain structural inhomogeneity of this compound and permit interpretation of our data from other standpoints as well.

In double perovskites of the $AB'_{1/2}B''_{1/2}O_3$ composition, the *B*' and *B*'' cations can either occupy positions

at the centers of octahedra in a random manner or alternate in adjacent octahedra. Such compositional ordering gives rise to unit cell doubling and the formation of a superstructure. The degree of compositional ordering is quantified by a parameter s, which is unity in the completely ordered state and zero in the state of disorder. Compositional ordering occurs under cooling as a result of a phase transition and consists in a diffusive redistribution of the ions [20]. The temperature of transition to the compositionally ordered state is determined by the difference in size and valency between the B' and B'' ions. For low transition temperatures, the disordered or partially ordered state can also persist at fairly low temperatures, where diffusion is practically impossible.

Present-day relaxor models attach a significant role to the existence of compositionally ordered regions randomly distributed in a disordered crystal matrix. Such nanoscale regions have been revealed using various methods in the model relaxors $PbMg_{1/3}Nb_{2/3}O_3$ and $PbSc_{1/2}Ta_{1/2}O_3$. The existence of such regions in PFT could be experimentally verified by detecting weak superstructural reflections in x-ray diffraction studies of the crystals [13] and by investigating antiferromagnetic ordering [14, 21]. In the latter case, the Néel temperatures (T_N is 143 K for the ceramics studied in [21] and 180 K for the crystal [14]) lie between the values calculated for the completely ordered and totally disordered states, which is interpreted as an argument for partial compositional ordering of the ions, because T_N depends strongly on the number of magnetically active ions in adjacent cells [22]. The degree of ordering substantially depends on the method of preparation and thermal history of a sample. It is also pointed out that the ordering process is most likely to be of a local nature; i.e., the crystal contains mesoscopic regions with various degrees of order. The x-ray superstructural reflections are very weak because of the scattering powers of ordering ions being similar and because of the smallness of the ordered regions, which diffuses the reflections.

The existence of ordered and disordered regions and the variation in their symmetry with temperature could make interpretation of structural data difficult.

Compositional nonuniformity of a material generates random local electric fields and mechanical strains, which play a significant role in the formation of polar nanoregions and the relaxor properties of perovskites [2, 23]. The correlation length of polar clusters is fairly small, such that no macroscopic polarization appears in the sample. In PFT, these polar regions possibly appear at the Burns temperature $T_d \approx 350$ K. At this temperature, the dielectric permittivity begins to deviate from the Curie–Weiss law and anomalies are observed in the behavior of the unit cell parameter $a(T)$ and of the heat capacity. Note that the anomalous behavior of $a(T)$ in this temperature region is associated with the formation of polar regions and the deviation of the rms polarization from zero [24].

The entropy change in PFT is $\sim 0.4R$, which indicates that an important role is played in the formation of polar nanoregions by order–disorder-type processes, which are related, as in other lead-containing perovskites, with positional ordering of lead ions in interoctahedral cavities below the Burns temperature. In ordered regions with Fe^{3+} and Ta^{5+} ions alternating along the cubic cell edges and with $Fm\bar{3}m$ symmetry for $T > T_d$, lead can turn out to be distributed over four positions displaced from the center of the cavity along the $[111]_c$-type directions. Lead ion ordering should bring about a change in the entropy $\Delta S = R\ln(4)$ if the whole crystal has undergone the transition. The experimental value of ΔS is only 3.7 J/mol K, or ~30% of the maximum possible value, which is close to the volume fraction of ordered regions derived from structural [13] and magnetic [14] studies.

To describe the behavior of relaxors containing interacting polar nanoregions at temperatures $T < T_d$, a spherical random-bond–random-field model was proposed in [25]. The model considers a system of coupled, randomly reorienting nanoclusters in the presence of random electric fields. It is assumed that both random interactions (or bonds) and random electric fields have Gaussian distributions [25].

In the absence of an external field ($E = 0$), there are two sets of solutions. One of them, $P = 0$, $q \neq 0$, corresponds to a phase without long-range order (spherical glass). The other solution, $P \neq 0$, $q \neq 0$, describes a phase with long-range order (ferroelectric phase).

For $J_0 < \sqrt{J^2 + \Delta}$ (J_0 is the average interaction, J is the standard deviation of the interaction, and Δ is the variance of the field; the mean field is equal to zero), long-range order does not arise and the system resides in the spherical glass (SG) state down to 0 K. If $\Delta = 0$, as is the case with magnetic spin glasses, a transition from the paraelectric to the SG phase occurs at $T_f = J/k$. For $\Delta \neq 0$ and $\Delta \ll J^2$, there is no longer a clearly defined phase transition, but the dielectric permittivity [25] and the heat capacity [26] pass through a maximum at $T_m = T_f \approx (\sqrt{J^2 + \Delta})/k$. For $J_0 > \sqrt{J^2 + \Delta}$, long-range order can arise and a phase transition to a nonuniform ferroelectric phase can take place at $T_c = J_0(1 - \Delta/(J_0^2 - J^2))/k < T_m$.

Thus, the temperatures of the three heat capacity anomalies observed in PFT can, in our opinion, be identified with the temperatures T_d (the temperature of formation of polar regions), T_m (the temperature of the maximum permittivity), and T_c (the temperature of the spontaneous transition to the ferroelectric state).

ACKNOWLEDGMENTS

This study was supported in part by the Ministry of Industry, Science, and Technology of the Russian Federation (project no. NSh-939.2003.2) and the DPS RAS (project no. 2.2.6.1).

REFERENCES

1. I. P. Raevskiĭ, V. V. Eremkin, V. G. Smotrakov, *et al.*, in *Proceedings of International Seminar on Order, Disorder, and Properties of Oxides* (Sochi, 2001), p. 246.
2. E. L. Cross, Ferroelectrics **151**, 305 (1994).
3. G. A. Smolenskiĭ, A. I. Agranovskaya, and V. A. Isupov, Fiz. Tverd. Tela (Leningrad) **1** (6), 990 (1959) [Sov. Phys. Solid State **1**, 907 (1959)].
4. Yu. Venevtsev, N. E. Skorohodov, and V. V. Chechkin, Ferroelectrics **137** (1), 57 (1992).
5. N. Lampis, Ph. Sciau, and A. G. Lehmann, J. Phys.: Condens. Matter **12** (11), 2367 (2000).
6. A. G. Lehmann, F. Kubel, and H. Schmid, J. Phys.: Condens. Matter **9** (39), 8201 (1997).
7. A. G. Lehmann and Ph. Sciau, J. Phys.: Condens. Matter **11** (5), 1235 (1999).
8. W. Bonny, M. Bonin, Ph. Sciau, *et al.*, Solid State Commun. **102**, 347 (1997).
9. R. Guo, E. L. Cross, S. E. Park, *et al.*, Phys. Rev. Lett. **84** (23), 5423 (2000).
10. B. Noheda, J. A. Gonzalo, E. L. Cross, *et al.*, Phys. Rev. B **61** (13), 8687 (2000).
11. B. Noheda, D. E. Cox, G. Shirane, *et al.*, Phys. Rev. B **63**, 014103 (2001).
12. S. A. Ivanov, S. Eriksson, N. W. Thomas, *et al.*, J. Phys.: Condens. Matter **13** (1), 25 (2001).
13. I. P. Raevskiĭ, V. V. Eremkin, V. G. Smotrakov, *et al.*, Kristallografiya **47** (6), 1076 (2002) [Crystallogr. Rep. **47**, 1007 (2002)].
14. S. Nomura, H. Takabayashi, and T. Nakagawa, Jpn. J. Appl. Phys. **7** (6), 600 (1968).
15. I. P. Raevski, S. A. Prosandeev, U. Waghmare, *et al.*, cond-mat/0208116 (2002).
16. F. Chu, I. M. Reaney, and N. Setter, Ferroelectrics **151**, 343 (1994).
17. W. Brixel, J. P. Rivera, and H. Schmid, Ferroelectrics **55**, 181 (1984).
18. W. Brixel, R. Boutellier, and H. Schmid, J. Cryst. Growth **82**, 396 (1987).
19. J. Roquette, J. Haines, V. Bornand, *et al.*, Phys. Rev. B **65** (21), 214102 (2002).
20. A. A. Bokov and I. P. Raevski, Ferroelectrics **144**, 147 (1993).
21. M. V. Plotnikov, K. P. Mitrofanov, V. S. Shpinel', and Yu. N. Venevtsev, *Barium Titanate* (Nauka, Moscow, 1973), p. 156.
22. Yu. N. Venevtsev, V. V. Gagulin, and V. N. Lyubimov, *Ferroelectrics* (Nauka, Moscow, 1982).
23. H. Qian and A. Bursill, Int. J. Mod. Phys. B **10**, 2007 (1996).
24. G. A. Samara, J. Phys.: Condens. Matter **15**, 367 (2003).
25. R. Pirc and R. Blinc, Phys. Rev. B **60** (19), 13470 (1999).
26. M. V. Gorev, I. N. Flerov, V. S. Bondarev, and Ph. Sciau, Zh. Éksp. Teor. Fiz. **123** (3), 599 (2003) [JETP **96**, 531 (2003)].

Translated by G. Skrebtsov

Physics of the Solid State, Vol. 46, No. 3, 2004, pp. 526–531. Translated from Fizika Tverdogo Tela, Vol. 46, No. 3, 2004, pp. 510–514.

LATTICE DYNAMICS AND PHASE TRANSITIONS

Atomic Dynamics of an $Al_{0.62}Cu_{0.255}Fe_{0.125}$ Icosahedral Quasicrystal

P. P. Parshin*, M. G. Zemlyanov*, A. V. Mashkov*, R. A. Brand, A.-J. Dianoux***, and Y. Calvayrac******

** Russian Research Centre Kurchatov Institute, pl. Kurchatova 1, Moscow, 123182 Russia*
e-mail: zeml@isssph.kiae.ru
*** Gerhard-Mercator-Universität Duisburg, Duisburg, D-47048 Germany*
**** Institut Laue–Langevin, BP 156, Grenoble Cedex-9, F-38042 France*
***** CECM/CNRS, 15, rue G. Urbain, Vitry Cedex, F-94407 France*
Received July 16, 2003

Abstract—The atomic dynamics of an $Al_{0.62}Cu_{0.255}Fe_{0.125}$ icosahedral quasicrystal is investigated using inelastic neutron scattering (the isotopic contrast method). The partial vibrational spectra of copper, iron, and aluminum atoms in the icosahedral quasicrystal and the total spectrum of thermal vibrations of the compound are directly reconstructed from the experimental data for the first time. It is found that the vibrational energies of copper and iron atoms fall in relatively narrow ranges near 16 and 30 meV, respectively, whereas the vibrational energies of aluminum atoms lie in a wide range (up to 60 meV). © *2004 MAIK "Nauka/Interperiodica"*.

1. INTRODUCTION

A quasicrystalline state of solids can be regarded as intermediate between crystalline and amorphous states. Quasicrystalline materials, unlike crystals, have no translational symmetry but, unlike amorphous systems, are characterized by a long-range order in spatial atomic arrangement. Such an unusual structure can be associated with specific features in the interatomic interaction, which manifest themselves in the spectra of thermal vibrations. In this respect, detailed information on the spectra of atomic thermal vibrations can provide the basis for an adequate description of interatomic force interactions and, consequently, better understanding of the conditions necessary for the formation and stability of a quasicrystalline structure and many physical properties of quasicrystals.

Modern techniques of synthesizing quasicrystals, in particular, compounds in the Al–Cu–Fe ternary system, make it possible to prepare sufficiently homogeneous single-phase samples weighing a few grams. This has opened up fresh opportunities for neutron scattering study of the structure and dynamic properties of quasicrystals. These investigations have been performed by different research groups [1, 2] over a period of several years. However, reliable information on the spectrum of thermal vibrations in a standard experiment on inelastic neutron scattering in powder samples of quasicrystals can be obtained only in the form of the so-called neutron-weighted vibrational spectrum $G(E)$. The function $G(E)$ is the sum of the atomic partial spectra of different chemical elements. The partial spectra, as a rule, are taken with specific "neutron" weighting factors (equal to the ratio between the cross section for neutron scattering by the nucleus of a particular element and the nuclear mass). The neutron-weighted vibrational spectrum qualitatively reflects the main features of the energy distribution of atomic thermal vibrations but cannot be used to describe this distribution quantitatively. Moreover, information on atomic thermal vibrations of different chemical elements, which is particularly important for elucidating the specific features of interatomic force interactions, cannot be extracted from the spectrum $G(E)$. Consequently, the currently available data on the atomic dynamics of quasicrystals are very scarce and further investigation of this problem calls for new approaches. In the present work, we experimentally investigated the partial vibrational spectra of aluminum, copper, and iron atoms in an $Al_{0.62}Cu_{0.255}Fe_{0.125}$ icosahedral quasicrystal.

2. EXPERIMENTAL TECHNIQUE

The atomic dynamics of an $Al_{0.62}Cu_{0.255}Fe_{0.125}$ icosahedral quasicrystal was examined using the method of isotopic contrast in inelastic neutron scattering [3]. With this method, the partial vibrational spectra of atoms of different chemical elements entering into the composition of a polyatomic compound can be directly obtained from the experimental data without model assumptions. It is known that, for isotopes of the same chemical element, the neutron scattering cross sections can differ significantly [4]. Therefore, the use of samples with different isotopic compositions with respect to a particular chemical element makes it possible to determine the contribution of this element to the experimentally measured spectrum $G(E)$ and, thus, to obtain

the partial spectrum of atomic thermal vibrations for the given chemical element [5].

Among the three chemical elements in the composition of the $Al_{0.62}Cu_{0.255}Fe_{0.125}$ quasicrystal, only copper and iron have isotopes whose neutron scattering cross sections differ substantially: ^{nat}Cu (σ = 8.2 barn), ^{65}Cu (σ = 14.5 barn), ^{nat}Fe (σ = 11.62 barn), and ^{57}Fe (σ = 1.0 barn) [4]. For this reason, the experiments were carried out with three quasicrystalline samples of different isotopic compositions, namely, a sample with a natural isotopic mixture of all three elements (sample **A**), a sample synthesized with the use of a ^{65}Cu isotope (sample **B**), and a sample synthesized with a ^{57}Fe isotope (sample **C**). Inelastic neutron scattering was measured at room temperature on an IN6 time-of-flight spectrometer (Institut Laue–Langevin, Grenoble, France). The experimental procedure was described in detail in [6].

As is known [7], information on the spectrum of lattice vibrations can be extracted from the results of measuring single-phonon inelastic incoherent neutron scattering in a polycrystalline sample. In the case when the studied compound is monoatomic and its nuclei incoherently scatter neutrons (for example, vanadium), the phonon spectrum can be directly reconstructed from the inelastic neutron scattering spectrum. For a polyatomic incoherently scattering compound, it is possible to reconstruct the generalized (neutron-weighted) spectrum $G(E)$ of lattice vibrations. Note that the problem regarding the contribution of multiphonon neutron scattering to the function $G(E)$ calls for separate consideration.

For compounds consisting of atoms whose nuclei are characterized by a high coherent scattering intensity (including the quasicrystal under investigation), the function $G(E)$ can be determined from the inelastic neutron scattering spectra of a polycrystalline sample only by averaging the data over a large phase-space volume (incoherent approximation) [8]. In this case, the larger the phase-space volume V covered in the experiment (as compared to the volume of the Brillouin zone V_{BZ}), the more accurate the averaging and the closer the agreement between the measured spectrum and the spectrum $G(E)$. The volume of the Brillouin pseudozone in the *i*-AlCuFe quasicrystal was estimated as $V_{BPZ} \sim 4.5$ Å^{-3}. On the other hand, the phase-space volume over which the averaging was performed in the experiments with quasicrystals was determined to be $V = 70$ Å^{-3} for elastically scattered neutrons and $V = 750$ Å^{-3} for neutrons with an energy of 60 meV (near the edge of the vibrational spectrum). Therefore, the use of the incoherent approximation is fairly justified over the entire spectral range measured, even though the accuracy in reconstructing the spectrum in the low-energy range is less than that in the high-energy range.

The inelastic neutron scattering spectra were processed within the incoherent approximation. The Debye–Waller factor and the contribution of multiphonon scattering processes were included with the iterative procedure. In the first iteration, it was assumed that multiphonon scattering makes a negligible contribution. As a result, the function $G(E)$ derived from the experimental data can be written in the form

$$G(E) = \sum_i \frac{c_i\sigma_i}{M_i} g_i(E)\exp(-2W_i). \quad (1)$$

Here, c_i is the atomic concentration, σ_i is the total neutron scattering cross section, M_i is the atomic mass, $g_i(E)$ is the partial spectrum of thermal vibrations, $2W_i = \langle u_i^2 \rangle Q^2$ is the partial Debye–Waller temperature factor, $\langle u_i^2 \rangle$ is the mean-square thermal displacements of atoms of the *i*th chemical element, and Q^2 is the square of the momentum transferred in a scattering event. The spectrum of thermal vibrations of the compound (phonon spectrum) can be represented as $g(E) = \sum c_i g_i(E)$. It follows from relationship (1) that, unlike the function $g(E)$, the function $G(E)$ involves the partial vibrational spectra with a specific neutron factor σ_i/M_i. It is this factor in relationship (1) that makes it possible to apply the isotopic contrast method for determining the partial vibrational spectra.

The function $g_i(E)$ is defined in such a way that the integral of this function is equal to unity [7]. Moreover, as a first approximation, we can assume that the partial temperature factors are small and do not depend on the temperature. In this case, we obtain $\exp(-2W_i) \sim 1$ and

$$\int G(E)dE = \sum_i \frac{c_i\sigma_i}{M_i}. \quad (2)$$

Relationship (2) determines the condition for mutual normalization of the functions $G(E)$ obtained from the experimental data on inelastic neutron scattering in samples of different isotopic compositions. This normalization, which can be defined as the scattering power of the formula unit of the compound in an inelastic process, was used at the first stage of the data processing.

To a first approximation, the partial vibrational spectra of copper and iron atoms were calculated as the difference between the functions $G(E)$ measured in the experiment with samples of different isotopic compositions: $g_{Cu}(E) \sim G_{\mathbf{B}}(E) - G_{\mathbf{A}}(E)$ and $g_{Fe}(E) \sim G_{\mathbf{A}}(E) - G_{\mathbf{C}}(E)$. After the appropriate normalization of the spectra $g_{Cu}(E)$ and $g_{Fe}(E)$, the partial vibrational spectrum of aluminum atoms was determined as the difference

$$g_{Al}(E) \sim G_{\mathbf{A}}(E) - \frac{c_{Cu}\sigma_{Cu}}{M_{Cu}} g_{Cu}(E) - \frac{c_{Fe}\sigma_{Fe}}{M_{Fe}} g_{Fe}(E). \quad (3)$$

It was assumed that the partial vibrational spectra $g_i(E)$ do not depend on the isotopic composition of the samples. This assumption is justified because the

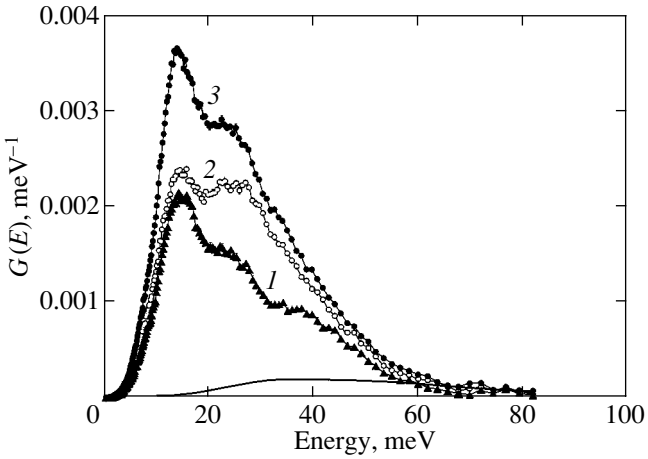

Fig. 1. Single-phonon neutron-weighted vibrational spectra of $Al_{0.62}Cu_{0.255}Fe_{0.125}$ icosahedral quasicrystals containing (*1*) the ^{57}Fe isotope, (*2*) a natural isotopic mixture of all chemical elements, and (*3*) the ^{65}Cu isotope. The solid line represents the contribution of multiphonon neutron scattering to spectrum *2*.

masses of the isotopes used differ by no more than a few percent.

The partial vibrational spectra $g_i(E)$ obtained as a first approximation were used in the iterative procedure for calculating the mean-square thermal displacements $\langle u_i^2 \rangle \sim \int g_i(E) \coth(E/2kT)/E dE$, the partial temperature factors W_i, and the partial contributions of multiphonon neutron scattering to the function $G(E)$. In our calculation, only the contributions of the two- and three-phonon processes were taken into account, because the contribution of the four-phonon processes at room temperature is considerably smaller than the statistical error in measurement. These contributions were calculated using the algorithm described in [7], according to which the contributions of the two-phonon and three-phonon scattering by atoms of the *i*th chemical element are determined by the convolutions

$$f_{2,i}(E) = \int f_{1,i}(E) f_{1,i}(E - E') dE', \quad (4)$$

$$f_{3,i}(E) = \int f_{2,i}(E) f_{1,i}(E - E') dE', \quad (5)$$

where

$$f_{1,i}(E) = \frac{g_i(E)}{E(1 - \exp(E/kT))}. \quad (6)$$

The partial contributions of the multiphonon neutron scattering by aluminum, copper, and iron atoms were calculated from expressions (4)–(6) with the functions $g_i(E)$, which were obtained experimentally as a first approximation, and with due regard for the isotopic composition of the samples. Then, the calculated contributions were subtracted from the experimental data. As a result, we obtained the first approximation of the single-phonon function $G(E)$. Thereafter, we carried out the second and third iterations beginning with the normalization of the functions $G(E)$. The sole difference lay in the fact that, since the partial vibrational spectra $g_i(E)$ and the partial temperature factors W_i for atoms of all chemical elements were determined in the first iteration, the mutual normalization of the functions $G(E)$ was performed not with formula (2) but with the more correct expression

$$\int G(E) dE = \sum_i \frac{c_i \sigma_i}{M_i} \int g_i(E) \exp(-2W_i) dE. \quad (7)$$

The multiphonon scattering contributions obtained after the second and third iterations differ by no more than 10%. For this reason, the calculations of the single-phonon functions $G(E)$ were limited to three iterations. The above processing made it possible to reconstruct the single-phonon neutron-weighted vibrational spectrum $G(E)$ for each of the three samples (Fig. 1). The calculated contribution of the two- and three-phonon neutron scattering processes for the sample of natural isotopic composition is also presented in Fig. 1.

3. RESULTS

The spectra $G(E)$ shown in Fig. 1 substantially differ from each other, even though they reflect the atomic dynamics of the same compound, namely, the $Al_{0.62}Cu_{0.255}Fe_{0.125}$ icosahedral quasicrystal. The differences observed in the spectra stem from the differences in the isotopic composition of the samples and can be considered a manifestation of the isotopic contrast in inelastic neutron scattering. Indeed, the contribution from thermal vibrations of copper atoms to the spectrum of sample **B** (with the ^{65}Cu isotope) is more pronounced than that of sample **A** (with the natural isotopic composition). In turn, the contribution from thermal vibrations of iron atoms to the spectrum of sample **A** is larger than that of sample **C** (with the ^{57}Fe isotope). Recall that the spectra shown in Fig. 1 are normalized according to expression (7).

The partial vibrational spectra of copper, iron, and aluminum atoms (Fig. 2) were obtained using the above procedure as the differences between the corresponding single-phonon functions $G(E)$ and were normalized to the atomic concentration of each chemical element in the quasicrystal. The spectrum $g(E)$ of thermal vibrations of the quasicrystal (phonon spectrum) (Fig. 3) was calculated as the sum of the partial contributions from thermal vibrations of copper, iron, and aluminum atoms. The area under the spectrum is equal to unity.

The partial vibrational spectra of copper, iron, and aluminum atoms were used to calculate the integrated dynamic characteristics of these atoms in the *i*-AlCuFe quasicrystal (Table 1).

An analysis of the experimental neutron scattering spectra measured for the quasicrystalline samples with

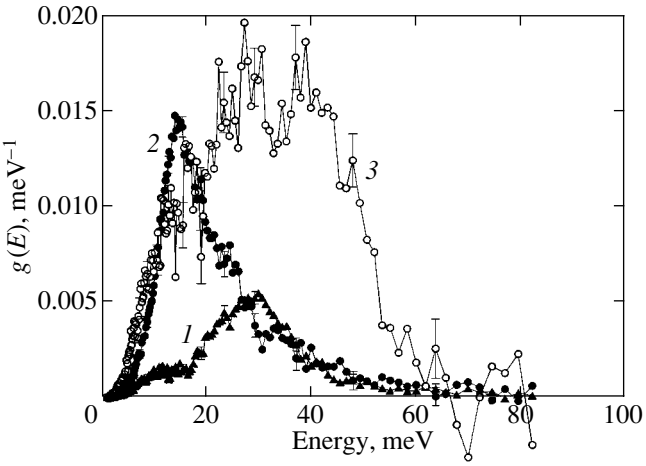

Fig. 2. Partial spectra of thermal vibrations of (*1*) iron, (*2*) copper, and (*3*) aluminum atoms in the *i*-AlCuFe quasicrystal.

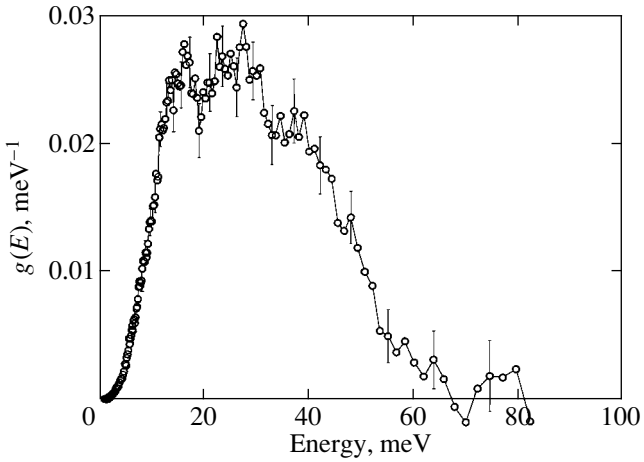

Fig. 3. Spectrum of thermal vibrations of the *i*-AlCuFe quasicrystal.

different isotopic compositions over a wide range of angles (10°–113°) with a step of 1°–2° (wavelength of neutron scattering by the sample, 4.12 Å) can provide additional information on the structure of the quasicrystal under investigation. For this purpose, the spectral regions corresponding to elastic neutron scattering were separated from the total time-of-flight spectrum for each scattering angle (after all the appropriate normalizations and subtraction of the contribution from the scattering background associated with the sample holder). Then, we constructed the dependence of the integrated intensity for these regions on the wave vector of scattering. Actually, for each sample, we obtained the diffraction pattern corresponding to elastic coherent neutron scattering by the quasicrystal (Fig. 4). These diffraction patterns differ from conventional neutron diffraction patterns measured on a diffractometer in that, first, they were obtained with a larger angular step and, second, they did not contain the contribution of the inelastic neutron scattering background.

4. DISCUSSION

A comparison of the partial vibrational spectra depicted in Fig. 2 shows that the vibrational energies of copper and iron atoms fall in relatively narrow ranges near 16 and 30 meV, respectively, whereas the vibrational energies of aluminum atoms lie in a wide range (up to 60 meV). Therefore, as a first approximation, the vibrations of copper and iron atoms can be treated as quasi-local modes in a strongly modified aluminum matrix. It is worth noting that the partial vibrational spectra of copper and iron atoms differ significantly: the vibrational spectrum of copper is considerably softer than that of iron. This difference in the spectra cannot be explained only by the difference in the atomic masses, because they differ by 10%, whereas the energies averaged over the vibrational spectrum differ by 40% (Table 1). Consequently, bonds of copper atoms in the quasicrystal are, on average, weaker than those of iron atoms. This is confirmed by the estimate of the mean force constant, which for copper atoms appears to be smaller than that for iron atoms. Furthermore, as can be seen from Table 1, the mean-square amplitude of thermal vibrations of copper atoms is appreciably larger than that of iron atoms, which also suggests that the weaker bonds are formed by copper atoms. The difference in the vibrational spectra of copper and iron atoms indicates that, in the structure of the quasicrystal, at least part of these atoms regularly occupy positions with substantially differing bonds and, most likely, with different nearest environments.

Cornier-Quiquandon *et al.* [9] performed the neutron diffraction investigation into the structure of an *i*-AlCuFe single quasicrystal and proposed a model of atom decoration. Within this model, the structure considered in a six-dimensional space contains not only a surface occupied by aluminum atoms and a surface filled with atoms of all chemical elements but also a surface occupied only by copper atoms. According to the proposed model, we can assume that copper atoms located in the positions corresponding to the projection of the last surface onto the physical space form weaker

Table 1. Integrated thermodynamic characteristics of the *i*-AlCuFe quasicrystal

Atom	$\langle u^2 \rangle$, 10^{-3} Å^2	$\langle E \rangle$, meV	$\langle B \rangle$, N/m
Al	10.9 ± 0.4	32.1 ± 1.7	127 ± 12
Cu	7.06 ± 0.15	23.8 ± 0.9	187 ± 14
Fe	5.6 ± 0.2	31.0 ± 1.0	248 ± 16

Designations: $\langle u^2 \rangle$ is the mean-square atomic thermal displacement at T = 300 K, $\langle E \rangle$ is the spectrum-averaged vibrational energy, and $\langle B \rangle$ is the mean force constant.

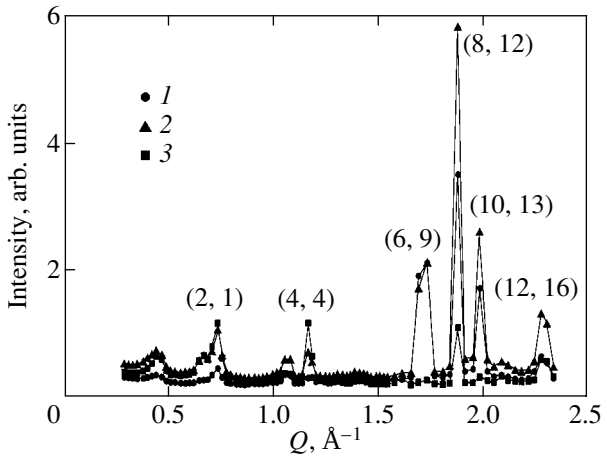

Fig. 4. Neutron diffraction patterns of $Al_{0.62}Cu_{0.255}Fe_{0.125}$ icosahedral quasicrystals containing (*1*) a natural isotopic mixture of all chemical elements, (*2*) the ^{65}Cu isotope, and (*3*) the ^{57}Fe isotope.

bonds with the nearest environment. In any case, our results are consistent with the concept that, in the structure of the quasicrystal, there exist positions that are characterized by a specific geometry and specific atomic composition of the nearest environment and can be occupied only by copper atoms.

The partial vibrational spectrum of aluminum atoms in the quasicrystal (Fig. 2) considerably differs from that of face-centered cubic aluminum. Specifically, the limiting energy of the vibrational spectrum of aluminum atoms in the quasicrystal ($E_l \approx 60$ meV) substantially exceeds the limiting energy of the spectrum of metallic aluminum ($E_l = 40$ meV). The results obtained demonstrate that the bonds formed by aluminum atoms in the quasicrystal are stronger than those in crystalline aluminum.

The most intense reflections in the neutron diffraction patterns shown in Fig. 4 can be indexed with the six-dimensional cubic parameter $a = 6.45$ Å according to the scheme proposed by Cahn *et al.* [10]. The relevant indices (N, M) are presented in Fig. 4. It can be seen that the intensities of reflections strongly depend on the isotopic composition of the samples (Table 2); i.e., the neutron diffraction patterns exhibit a pronounced isotopic contrast. In particular, the analysis of the neutron diffraction pattern of sample **C** (containing the weakly scattering iron isotope) revealed that the (6, 9) and (10, 13) reflections virtually disappear, the intensity of the (8, 12) reflection considerably decreases, and the intensity of the (4, 4) reflection increases as compared to those in the neutron diffraction pattern of sample **A** (with the natural isotopic composition). On the other hand, in the neutron diffraction pattern of sample **B** (with the strongly scattering copper isotope), the intensities of the (2, 1), (8, 12), (10, 13), and (12, 16) reflections are substantially higher than those in the neutron diffraction pattern of sample **A**.

Table 2. Amplitudes b of incoherent neutron scattering

Isotope	b, fm
^{nat}Cu	7.718
^{65}Cu	10.61
^{nat}Fe	9.45
^{57}Fe	2.3
^{nat}Al	3.449

Unfortunately, the large discreteness in obtaining the experimental data, the limited range of momenta attainable in the experiment, and the possible error in determining the scattering angle make any reliable quantitative estimations of the atom decoration impossible. However, the mere fact that the neutron diffraction patterns exhibit an isotopic contrast indicates an ordered arrangement of copper, iron, and aluminum atoms, which occupy specific positions in the structure of the icosahedral quasicrystal under investigation. In the immediate future, we intend to perform neutron diffraction experiments with isotopically enriched samples in the *i*-AlCuFe system.

5. CONCLUSIONS

Thus, the partial spectra of thermal vibrations of aluminum, copper, and iron atoms in an $Al_{0.62}Cu_{0.255}Fe_{0.125}$ icosahedral quasicrystal and the total spectrum of thermal vibrations of the compound were reconstructed for the first time without model assumptions. The results obtained in this work demonstrated that, as a first approximation, the vibrations of heavier atoms of copper and iron can be considered quasi-local modes in a strongly modified aluminum matrix. In turn, the bonds formed by aluminum atoms in quasicrystals are stronger than those in a pure metal. The large difference between the partial vibrational spectra of copper and iron atoms in the *i*-AlCuFe compound and the small difference in their masses indicate that, in the structure of the quasicrystal, at least part of these atoms regularly occupy positions with different nearest environments and substantially differing bonds.

ACKNOWLEDGMENTS

We would like to thank A.V. Irodova for her participation in discussions of the structural aspects of our investigation.

This work was supported by the Russian Foundation for Basic Research (project no. 01-02-16092), the State Program of Support for Leading Scientific Schools of the Russian Federation (project no. 00-15-96712), the Russian State Scientific and Technical Program "Topical Directions in the Physics of Condensed Matter: Neutron Investigations of Condensed Matter" (State Contract no. 40.012.1.1.1148), and the DFG Focus Program "Quasikristalle: Struktur und physikalische Eigenschaften."

REFERENCES

1. T. Klein, G. Pares, J.-B. Suck, *et al.*, J. Non-Cryst. Solids **153–154**, 562 (1993).
2. J.-B. Suck, J. Non-Cryst. Solids **153–154**, 573 (1993).
3. P. P. Parshin, M. G. Zemlyanov, and P. I. Soldatov, Zh. Éksp. Teor. Fiz. **101** (2), 750 (1992) [Sov. Phys. JETP **74**, 400 (1992)].
4. V. F. Sears, Neutron News **3** (3), 26 (1992).
5. Yu. Kagan, Zh. Éksp. Teor. Fiz. **42** (5), 1375 (1962) [Sov. Phys. JETP **15**, 954 (1962)].
6. R. A. Brand, A.-J. Dianoux, and Y. Calvayrac, Phys. Rev. B **62** (13), 8849 (2000).
7. V. F. Turchin, *Slow Neutrons* (Atomizdat, Moscow, 1963; Israel Program for Scientific Translations, Jerusalem, 1965).
8. V. S. Oskotskiĭ, Fiz. Tverd. Tela (Leningrad) **9** (2), 550 (1967) [Sov. Phys. Solid State **9**, 420 (1967)].
9. M. Cornier-Quiquandon, A. Quivy, S. Lefebre, *et al.*, Phys. Rev. B **44** (5), 2071 (1991).
10. J. W. Cahn, D. Shechtman, and D. Gratias, J. Mater. Res. **1** (1), 13 (1986).

Translated by O. Borovik-Romanova

Physics of the Solid State, Vol. 46, No. 3, 2004, pp. 532–536. Translated from Fizika Tverdogo Tela, Vol. 46, No. 3, 2004, pp. 515–519.

LATTICE DYNAMICS AND PHASE TRANSITIONS

Effect of Synthesis Conditions on the Metal–Semiconductor Phase Transition in Vanadium Dioxide Thin Films

R. A. Aliev* and V. A. Klimov**

**Amirkhanov Institute of Physics, Dagestan Scientific Center, Russian Academy of Sciences, ul. 26 Bakinskikh Komissarov 94, Makhachkala, 367003 Russia*

***Ioffe Physicotechnical Institute, Russian Academy of Sciences, Politekhnicheskaya ul. 26, St. Petersburg, 194021 Russia*

e-mail: V.Klimov@mail.ioffe.ru

Received July 1, 2003

Abstract—The effect of the conditions of synthesis and of the substrate material on the metal–semiconductor phase transition in thin vanadium dioxide films prepared using laser ablation has been studied. The broadening of the hysteresis loop is shown to be due to a decrease in the size of the crystal grains making up the film. Conjectures are put forward to explain the formation of asymmetric hysteresis loops. *© 2004 MAIK "Nauka/Interperiodica".*

1. INTRODUCTION

The phase transition in vanadium dioxide (VO_2) is observed to occur at 340 K and is accompanied by a sharp change in the optical properties and electrical conductivity. The latter quantity changes by five orders of magnitude. When cooled to below 340 K, tetragonal VO_2 is believed to undergo a martensitic transition to a lower symmetry monoclinic phase, which exhibits semiconducting properties (band-gap width ~0.7 eV) [1]. The phase transition generates noticeable elastic stresses, which result in the destruction of single crystals because of the low plasticity of the transition. For this reason, it is thin films of vanadium dioxide (capable of withstanding unlimited cycling near the phase equilibrium temperature) that are dealt with in an appreciable part of the research on this topic and in most practical applications.

Hysteresis is a characteristic feature of the phase transition in vanadium dioxide. The magnitude of the jump in the physical parameters, as well as the width and shape of the hysteresis loop, depends substantially on the size of the crystal grains making up a film and on the deviation of its composition from stoichiometry. An approach was proposed in [2, 3] based on the assumption that the crystal grain distributions in terms of size and the deviation from stoichiometry are of importance in a film. The former distribution is responsible for the distribution in the width of the so-called elementary hysteresis loops (i.e., loops corresponding to a single grain), whereas the latter accounts for the distribution of grains in phase equilibrium temperatures. By specifying or determining these distributions, one can construct the main (i.e., relating to the whole film) hysteresis loop through straightforward summation of the elementary loops, which are considered to be square in shape. It is this approach that underlies the analysis of the experimental results obtained in this study.

2. EXPERIMENTAL RESULTS AND DISCUSSION

Vanadium dioxide films were prepared using laser ablation. The target was metallic vanadium (99.9%), and the synthesis was conducted under monitoring of the substrate temperature and of the oxygen pressure in the working chamber. The films prepared under optimum conditions exhibit a jump in conductivity that is four orders of magnitude or larger in the phase transition. The width of the main hysteresis loop is 4–6 K, and above 340 K, the conductivity practically coincides in temperature behavior with that characteristic of single crystals [4, 5].

There were also films with slimmer hysteresis loops. Figure 1 presents the behavior of the relative fraction of the metallic phase in such a VO_2 film under heating and cooling. The loop width is seen to be about 1 K; i.e., the width is comparable to that typical of vanadium dioxide single crystals, where it usually does not exceed 2 K. However, in most practical applications, for instance, for reversible recording of optical information, films that exhibit a broad loop approaching a square shape are required.

To obtain a broad main hysteresis loop, one has to increase the width of elementary loops [2, 3]. Because the latter is proportional to the grain cross-sectional size, it is desirable to prepare as fine-grained films as possible. The size of the grains forming in the course of film preparation is governed by the actual conditions of nucleation and growth of vanadium dioxide on the substrate surface. The surface diffusion coefficient of vanadium, which limits these processes, increases with decreasing oxygen partial pressure and with increasing

1063-7834/04/4603-0532$26.00

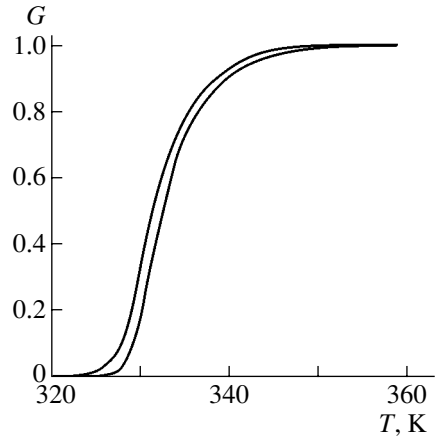

Fig. 1. Temperature dependence of the fraction of the metallic phase in a vanadium dioxide film grown on a sapphire substrate. Film thickness ~500 Å. Here and in Figs. 2 and 4, the graphs were constructed by processing hysteresis loops of the film reflectance at a wavelength of 1.54 μm.

substrate temperature [6]. In general, this coefficient also depends on the substrate material. It is well known that films grown on various substrates have different hysteresis loop widths. Films with the narrowest (~1 K) loops can be prepared on substrates of single-crystal Al_2O_3 (Fig. 1). The smallest loop width of the films prepared on other substrates increases in the order TiO_2, ZrO_2, Si, and fused SiO_2. This behavior can be related to the decrease in the surface diffusion coefficient of vanadium in this series. One cannot, however, rule out the effect of surface tension of the substrate–film interface, which may play an important part in the deviation ΔT from the phase equilibrium temperature necessary for the phase transformation to set in (in a first approximation, the width of an elementary loop is $2\Delta T$). The important role of surface tension is corroborated by the results of [7, 8], where optical-transmission hysteresis loops of composites prepared by ion implantation of VO_2 into Al_2O_3 and SiO_2 matrices were studied. While it was shown in [7, 8] that the hysteresis loop width increases with decreasing VO_2 grain size, the loop in Al_2O_3 is narrower than that in SiO_2 for the same grain size.

Figure 2 displays the effect of oxygen pressure in the working chamber on the shape and width of hysteresis loops of vanadium dioxide films synthesized using laser ablation on Si(001) and Al_2O_3(0001) substrates. An increase in oxygen pressure (with the other synthesis conditions maintained constant) brings about loop broadening, which we assign, in accordance with [6], to a decrease in the average size of the grains in the films. The width and shape of the hysteresis loops measured on films prepared on silicon at an elevated oxygen pressure are acceptable for reversible recording of optical information.

It should be pointed out that, by varying only the oxygen pressure in the working chamber, we depart

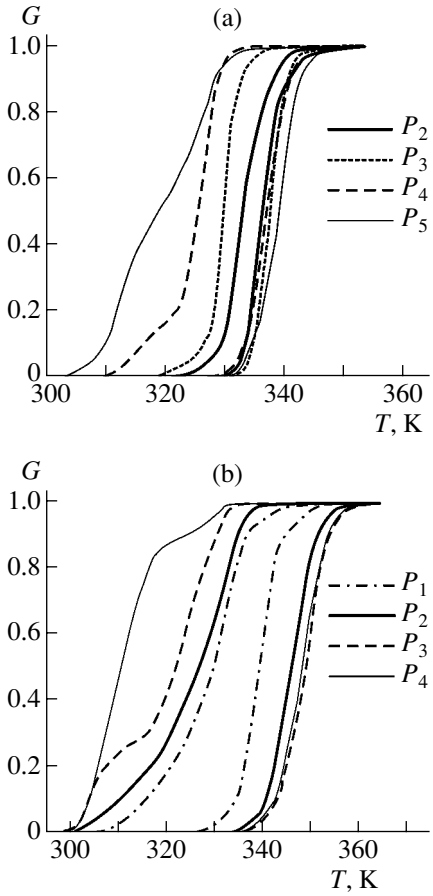

Fig. 2. Effect of the pressure in the working chamber on the shape of hysteresis loops of vanadium dioxide films prepared using laser ablation on substrates of (a) Si and (b) Al_2O_3. Film thickness ~800 Å. The oxygen pressure was varied from 10 to 100 mTorr, with $P_5 > P_4 > P_3 > P_2 > P_1$. Substrate temperature ~850 K.

from the optimum vanadium dioxide growth conditions. Therefore, the loop broadening observed in Fig. 2 is accompanied by decreased jumps in the electrical conductivity and reflectance. At pressure P_5, the phase transition disappears in films grown on silicon, and at still higher pressures, it likewise does not occur in films prepared on sapphire. Actually, this means that the vanadium dioxide films grown by us at elevated oxygen pressures are no longer single phase. As is evident from Fig. 2, the hysteresis loop width is larger in films grown on silicon substrates. The maximum loop width for these films is also noticeably larger than that for the films prepared on sapphire. With this in mind, one may expect films grown on fused quartz to exhibit still broader loops.

From Fig. 2, which illustrates loop transformation with increasing oxygen pressure, it is seen that, as the loop width increases, a step appears in the branch depicting the vanadium dioxide transition from the metallic to the semiconducting phase. Such steps have been observed earlier for films obtained by various

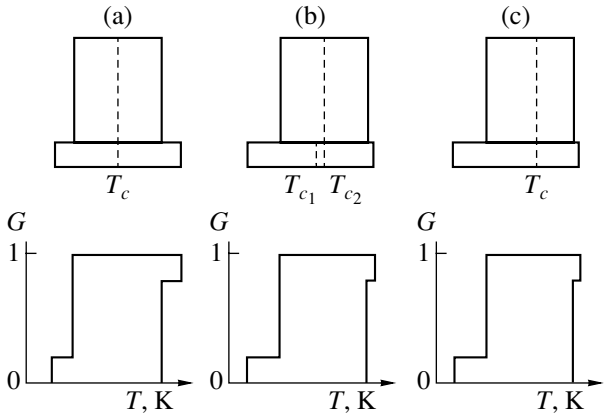

Fig. 3. Construction of the main hysteresis loop for the hypothetical case of a vanadium dioxide film consisting of the same number of grains differing in cross-sectional size by a factor two. According to [3], the width of the elementary loops should differ by a factor of $\sqrt{2}$. The fraction of the film material in the form of larger grains is four times that of smaller grains. Thus, a rectangular loop representing the sum of narrow elementary loops is four times higher and $\sqrt{2}$ times narrower than a loop representing the sum of the remaining elementary loops associated with small grains. The sum total of all loops, which is shown in the bottom line of the figure, depends on the temperature position of the loops and their symmetry: (a) elementary loops are symmetric, and the phase equilibrium temperature T_c is the same for all grains; (b) the loops are symmetric, and T_{c_1} and T_{c_2} are the phase equilibrium temperatures for small and large grains, respectively; and (c) the phase equilibrium temperatures are the same in all grains, but the elementary loops are asymmetric.

methods [9, 10]. Considering this in terms of the approach proposed in [2, 3], the simplest explanation of this behavior consists in assuming the existence of two maxima in the film grain distribution in size and, hence, width of the elementary loops adding up to form the main loop. Assuming that the phase equilibrium temperature in all the grains is the same and that the elementary loops are symmetric with respect to this temperature, summation of the elementary loops would produce steps in both branches of the main hysteresis loop. This is illustrated in Fig. 3a, which gives a schematic representation of the formation of the main loop for the simplest hypothetical case of a film consisting of equal numbers of grains differing in cross-sectional size by a factor two. The appearance of a step in only one branch of the main loop can be assigned either to the phase equilibrium temperature being dependent on grain size (Fig. 3b) or to an asymmetry in the elementary loops, which is likewise correlated with grain size (Fig. 3c). In real films, the grains are naturally distributed within certain intervals of both size and phase equilibrium temperature; this is what brings about smoothening of the steps or just the appearance of knees in hysteresis loop branches in place of them.

Grain distributions in size with two maxima could be associated with two types of vanadium dioxide nucleation on the substrate surface, namely, heterogeneous and homogeneous nucleation. In the first case, the nuclei (microislands of a film) form primarily on substrate defects, such as scratches, roughness, and (in the case of single-crystal substrates) small-angle boundaries or sites of dislocation emergence. Because nucleation on defects is energetically favorable, grains form on them earlier and grow to larger sizes than in the case of homogeneous nucleation, i.e., on defect-free parts of the substrate. As the oxygen pressure is increased, the fraction of small particles in the film increases because of the decreasing surface diffusion coefficient; this is manifested in a gradual upward displacement of the step in Fig. 2.

Consider the physical reasons that can account for the displacement of broader elementary loops toward lower temperatures. The position of an elementary loop (i.e., the phase equilibrium temperature in a given grain) is determined to a large extent by the stoichiometric composition of the grain and, in the case where a coherent boundary is formed between the substrate and the film, by the mutual orientation of the interfacing structures [11, 12]. The schematic pattern in Fig. 3b may be the result either of the grain size being dependent on the lattice matching conditions or of the grain off-stoichiometry being dependent on the grain size. Following the Laplace law, the equilibrium vapor pressure above a growing particle is inversely proportional to its size. This may bring about a larger oxygen deficiency in a smaller grain and, as a consequence, a lower phase equilibrium temperature. It is unlikely, however, that such an explanation is applicable to our case of relatively thick films (without islands).

The difference in composition between small and large grains, needed to account for the observed results, can also appear for purely kinetic reasons. The fact is that oxygen diffuses into a film and outwards most efficiently along grain boundaries. As a result, the composition of smaller grains should respond more quickly to pressure changes in the working chamber. If, in the course of film cooling from the growth temperature, the oxygen pressure is less than the equilibrium value, the oxygen deficiency can become more pronounced in smaller grains in the case of a comparatively fast cooling, which likewise would correspond to Fig. 3b.

Figure 3c illustrates the situation where the elementary loops are asymmetric, with the deviation of the phase transition temperature from the phase equilibrium point in each grain being larger under cooling than under heating. In our opinion, the most probable reason for this asymmetry is associated with stresses at the substrate–film interface. The stresses occur and increase under cooling from the growth temperature because of the difference in thermal expansion coefficients between the substrate and the film. As the phase transition temperature is reached, the stresses change

dramatically; therefore, the additional energy expended in generating elastic stresses in the substrate and the film can contribute substantially to ΔT. When heated, this stored energy will favor the onset of the reverse transition and the value of ΔT will decrease. The size effect consists essentially in that the probability of partial stress relaxation through the formation of misfit dislocations or microcracks increases with increasing stresses, which are directly proportional to grain volume.

If the phase equilibrium temperature is the same for all grains, one can say that the wider the elementary hysteresis loop, i.e., the smaller a given crystal grain, the lower the temperature at which the grain will undergo a martensitic transformation into the semiconducting phase. The phase transition in smaller grains will be elastically affected through grain boundaries by larger grains in which this transition has already terminated. We may recall that it is such an elastic interaction among individual regions of a microcrystal that brings about destruction of the crystal in the phase transition. It appears only natural to assume that elastic stresses in films are also capable of contributing to the asymmetry of both the elementary and main loop. The structure of the grain boundaries, in turn, depends on the extent to which a film is textured or epitaxial; therefore, this structure is determined to a considerable extent by the actual conditions of synthesis, the substrate type, and the film thickness. In this case, the width of an elementary loop and its asymmetry should obviously be determined not only by the grain size but also by the shape of the grain distribution function in size and by the part of this distribution to which the given grain belongs.

The shape alone of the hysteresis loops displayed in Fig. 2 does not allow us to make an unambiguous decision regarding a concrete mechanism of step formation. We readily see, however, that after the oxygen pressure has reached the optimum level, the loop broadening is determined primarily by the displacement of the branch on which the step is located toward lower temperatures. This displacement is markedly larger than the displacement (toward higher temperatures) of the branch associated with the reverse transformation in vanadium dioxide. The loop transformation is observed against the background of the formation of higher vanadium oxides (most probably, V_2O_5) in the film. This is indicated both by the decrease in the conductivity jump at the phase transition and by the substantial decrease, by several orders of magnitude, in the conductivity itself. Therefore, one could hardly expect the phase equilibrium temperature in small grains to decrease in the case where the conditions of preparation practically exclude oxygen deficiency in a film. We are inclined to believe that the asymmetry of the main loop in our case arises most likely in accordance with the scheme shown in Fig. 3c, i.e., that it originates from the asymmetry of the elementary hysteresis loops.

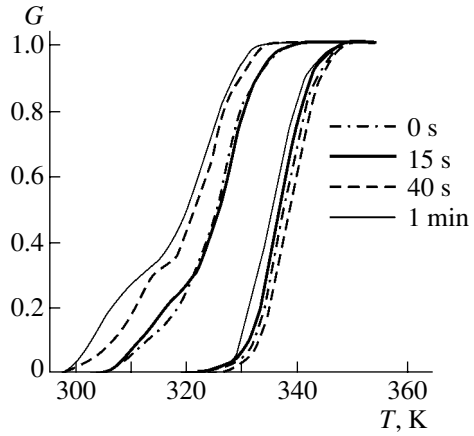

Fig. 4. Effect of annealing time at 730 K on hysteresis loop shape. The thickness of the vanadium dioxide film deposited on the silicon substrate is ~800 Å.

The vanadium dioxide grain size can be reduced by directly acting on the already prepared film. One possibility consists in additional oxidation of the film by heating it rapidly to a high temperature at atmospheric pressure, then holding it for a short time at this temperature, and cooling it rapidly thereafter. Figure 4 shows the sequence of loop hysteresis variations with increasing annealing time at 730 K. This thermal treatment eventually transforms all of the film material into V_2O_5, the highest vanadium oxide. As the film undergoes oxidation, the regions occupied by vanadium dioxide in the grains contract and we observe a broadening of the main hysteresis loop, which is caused, to a considerable extent, by the size effect. One also cannot with certain rule out the influence of defects, which form when a sample is quenched from the annealing temperature. It is appropriate to note here that the elastic interaction of these defects with dislocations born in the transformation determines the phase transition diffuseness (i.e., the hysteresis loop shape) at the microscopic level in terms of the model developed in [13].

Additional oxidation, as seen from Fig. 4, also reveals the existence of a double-humped grain distribution in size in the original film. As the regions with vanadium dioxide in the grains decrease in size, the step discussed earlier appears in the loop. It should be noted that the position of the step on the vertical axis does not depend, in a first approximation, on annealing time. This means that the ratio of the volume fractions of large and small grains remains unchanged in the course of annealing, which is possible only if the film is fairly smooth (under the assumption that the oxidation front is parallel to the film surface). We note that, in speaking about the size effect, we have to understand here not the cross-sectional size of grains, which does not vary in this situation, but rather the thickness of the layer occupied by vanadium dioxide. A similar effect of the vanadium dioxide film thickness on the width of the hysteresis loop was pointed out in [14]. In general, we believe

that one should take into account not only the cross-sectional grain size but also the film thickness. Assuming the crystal grain to have the shape of a rectangular parallelepiped, it appears more reasonable to take for the size of such a grain the diagonal of the parallelepiped rather than one of its edges, as should be done in accordance with [3].

3. CONCLUSIONS

We have demonstrated the effect of crystal grain size on the width and shape of the metal–semiconductor phase transition hysteresis loop in vanadium dioxide films. It was shown that films can be obtained with hysteresis loops varying from 1 to 40 K in width, depending on the actual conditions of film preparation and the substrate material. The assumption that there are two types of nucleation was used to explain the origin of a step in the hysteresis loop branch corresponding to the phase transition from the metallic to the semiconducting state.

ACKNOWLEDGMENTS

This study was supported by the Department of Physical Sciences, Russian Academy of Sciences.

REFERENCES

1. A. A. Bugaev, B. P. Zakharchenya, and F. A. Chudnovskiĭ, *Metal–Semiconductor Phase Transition and Its Applications* (Nauka, Leningrad, 1979).
2. T. G. Lanskaya, I. A. Merkulov, and F. A. Chudnovskiĭ, Fiz. Tverd. Tela (Leningrad) **20**, 336 (1978) [Sov. Phys. Solid State **20**, 193 (1978)].
3. I. A. Khakhaev, F. A. Chudnovskiĭ, and E. B. Shadrin, Fiz. Tverd. Tela (St. Petersburg) **36** (6), 1643 (1994) [Phys. Solid State **36**, 898 (1994)].
4. V. N. Andreev, M. A. Gurvich, V. A. Klimov, *et al.*, Pis'ma Zh. Tekh. Fiz. **19** (9), 63 (1993) [Tech. Phys. Lett. **19**, 283 (1993)].
5. V. N. Andreev, V. A. Klimov, and F. A. Chudnovskiĭ, Pis'ma Zh. Éksp. Teor. Fiz. **60** (9), 637 (1994) [JETP Lett. **60**, 647 (1994)].
6. M. Nagashima and H. Wada, J. Cryst. Growth **179**, 539 (1997).
7. R. Lopez, L. A. Boahter, and T. E. Haynes, J. Appl. Phys. **92** (7), 4031 (2002).
8. R. Lopez, L. A. Boahter, and T. E. Haynes, Phys. Rev. B **65**, 224113 (2002).
9. F. Guinneton, L. Sauques, and J. C. Valmalette, J. Phys. Chem. Solids **62**, 1229 (2001).
10. J. Livage, Coord. Chem. Rev. **190–192**, 391 (1999).
11. Y. Muraoka and Z. Hiroi, Appl. Phys. Lett. **80** (4), 583 (2002).
12. Y. Muraoka, Y. Ueda, and Z. Hiroi, J. Phys. Chem. Solids **63**, 965 (2002).
13. G. A. Malygin, Usp. Fiz. Nauk **171** (2), 187 (2001) [Phys. Usp. **44**, 173 (2001)].
14. Yu. A. Aleksandrov, Yu. Yu. Baryshnikov, I. L. Makin, and M. Yu. Terman, Izv. Akad. Nauk SSSR, Neorg. Mater. **23** (9), 1572 (1987).

Translated by G. Skrebtsov

Physics of the Solid State, Vol. 46, No. 3, 2004, pp. 537–542. Translated from Fizika Tverdogo Tela, Vol. 46, No. 3, 2004, pp. 520–525.

LOW-DIMENSIONAL SYSTEMS AND SURFACE PHYSICS

Fluctuation Theory of Photoluminescence of Porous Silicon

V. N. Bondarev, P. V. Pikhitsa, and S. V. Zelenin

Research Institute of Physics, Mechnikov National University, Odessa, 65026 Ukraine

e-mail: bondvic@mail.ru, pvp@dtp.odessa.ua

Received June 10, 2003

Abstract—A theory of photoluminescence (PL) kinetics of porous silicon (PS) is developed. In this theory, the approach suggested by the authors earlier is extended to the case of finite temperatures. The theory is based on the concept of electron–hole recombination, which occurs in structural units of PS both through the tunneling mechanism (playing a role even for $T = 0$ K) and through thermally activated diffusion of photoexcited carriers. The PL kinetics is analyzed in terms of two models considered in the literature, in which PS is treated as a random ensemble of spherical nanocrystallites or quantum wires. The results are applied to interpret experimental data on the kinetics and instantaneous PL spectra of PS. Although both models basically provide an adequate quantitative description of the experimental data at both low and room temperatures, the model of spherical nanocrystallites seems preferable. © *2004 MAIK "Nauka/Interperiodica".*

1. INTRODUCTION

Porous silicon (PS) still attracts considerable attention as a promising material for practical applications (e.g., in optical devices) and is also interesting from the point of view of fundamental physics [1]. This interest is related to the fact that PS exhibits properties typical of any disordered system; namely, the photoluminescence (PL) kinetics of PS differs essentially from the Debye type [1–3] and the temperature dependence of PL relaxation times has a non-Arrhenius form [4].

The theory of the low-temperature PL of PS was developed by us in [5] using the concept of the tunneling mechanism of radiative recombination of photoexcited electrons and holes in silicon nanocrystallites embedded in SiO_2 layers, where the nanocrystallites were modeled by spheres (quantum dots, QDs) with random (Gaussian) radius distribution. To the best of our knowledge, to date, there has been no consistent theoretical analysis of numerous experimental data on the kinetics and spectral characteristics of PL at finite temperatures *T.* Such an analysis seems necessary, since even now some ill-justified assumptions [6] are made in interpreting experimental data on PS photoluminescence (e.g., when processing the temperature dependence of kinetic characteristics [1]). For example, in [6] and in subsequent papers (see, e.g., [1, 3]), an ad hoc concept of the two-level structure of exciton excitations in PS was used and practically no model was suggested in [6] for the experimentally observed nonexponential decay of PL (of the type of Kohlrausch's stretched exponential). Moreover, the formula used in those papers for the temperature dependence of the characteristic decay time of PL cannot be reconciled with the clearly pronounced non-Arrhenius temperature dependence of the characteristic decay time $\tau(T)$ obtained in experiments on the PL kinetics of PS [4].

Such a non-Arrhenius $\tau(T)$ dependence implies that, at finite temperatures, in addition to tunneling recombination of electron–hole pairs in QDs, effects related to the diffusive transport of photoexcited carriers to their place of recombination in QDs are of importance and this diffusion should reflect the random character of the PS structure. In this case, the observed PL of PS is determined by the total recombination probability in the tunneling and in the diffusion channel (e.g., according to Mott's diffusion mechanism in a random landscape [7]) inside each of the QDs (here, we do not discuss the photoexcited carriers that leave to the SiO_2 matrix and possible nonradiative effects [8], which are important in the temperature region of PL quenching). In this approach, only two more parameters (in addition to those introduced in [5]) appear in the theory. These parameters characterize Mott's diffusion and can, in principle, be determined from independent experiments (see, e.g., [7]).

In this work, we use both the QD model and the quantum wire (QW) model to analyze the PL kinetics of PS. We note that PS was considered as a system of QWs, e.g., in [9] (see also [1]), although the QD model [1, 9] is more common. We will show that basically both models (with appropriate choice of the parameters) can be used to quantitatively interpret published experimental data on the kinetics and instantaneous spectra of PS photoluminescence up to room temperature. However, it is important that the computational procedure for the QW model appears to be more intricate than that for the QD model (see below). Furthermore, the latter model adequately describes the kinetics and spectra of PS photoluminescence [1, 2] for values of the parameters that seem closer to those determined from independent measurements. On the other hand, it is possible that, in the experimental situation considered in [10], the QW model would be more adequate for

interpreting PS photoluminescence. However, since there are no published experimental data on the PL kinetics (on time scales of milliseconds or shorter) for PS samples prepared by the method applied in [10], we cannot discuss the problem of the proper choice of the model for such samples.

2. PHOTOLUMINESCENCE KINETICS IN MODELS OF POROUS SILICON OF DIFFERENT GEOMETRIES

2.1. Quantum Dot Model

In considering the PS structure in terms of the model used in our earlier paper [5] (see also Introduction), we assume that the photogeneration of electron–hole pairs and the subsequent PL take place inside each of the QDs. According to this model, for $T \neq 0$, photoexcited electrons and holes captured by traps of the donor and acceptor types, respectively, located at the QD/matrix interface can recombine (emitting PL photons) through both the tunneling mechanism and Mott's mechanism of thermally stimulated transport (specifically, we assume that only one type of carrier, e.g., electrons, takes part in transport). For the latter mechanism, we can assume that the transport of a photoexcited electron to the place of recombination in the specified QD proceeds through a system of random energy levels at the QD/SiO_2 interface. One can reasonably assume[1] that the two-dimensional diffusion coefficient for such an interface must obey Mott's law:

$$D = D_0 \exp\left[-\left(\frac{T_0}{T}\right)^{1/3}\right], \qquad (1)$$

where D_0 and T_0 are characteristic constants.

Passing to the kinetics of PS photoluminescence, we note that it is determined by recombination in each of the QDs. If an electron–hole pair is photoexcited in a QD and the distance between this electron and hole (localized at the surface of the QD) is r, then the contribution from this pair to the PL kinetics is described by the function [5]

$$I_r(t) = -\frac{d}{dt}e^{-W(r)t}, \qquad (2)$$

where $W(r)$ is the recombination probability rate. From the above discussion, it follows that this recombination rate (as for $T = 0$ K [5]) contains the term $W_1(r) = W_{\max}\exp(-2r/R_0)$ describing the tunneling recombination (R_0 is the characteristic localization radius of the particles of the pair, $W_{\max}$ is a constant). In addition, $W(r)$ also contains a diffusion term, whose structure can be established using the well-known Einstein formula (see, e.g., [7]) that relates the average particle displacement and the elapsed time. Assuming that r^2 is the average electron displacement squared and that diffusion is two-dimensional, we can represent the diffusion term in $W(r)$ in the form $W_2(r) = 4D/r^2$, where D is given by Eq. (1).

Before writing out an expression for the function $I_E(t)$ that defines the PS photoluminescence kinetics for a given radiation energy E, we note the following. We might expect that, due to Coulomb interaction between the photoexcited electron and hole, they will be localized in the QD at the nearest neighbor traps of the donor and acceptor types. Setting r to be the distance from a given donor trap to the nearest neighbor acceptor trap, we take into account that, generally, the probabilities of different values of r are not equal; i.e., in calculations, we take account of the distribution in r (for simplicity, the distribution function was taken to be constant in [5]). To be more specific, we assume that the donor trap density is lower than the acceptor trap density. Then, the distribution function of r will be similar to that used in [11] for recombination in a bulk compensated semiconductor. We extend the assumption made in [11] concerning the exponential form of the distribution function to the case of a spherical surface and introduce the polar angle ϑ [such that $r = L\sin(\vartheta/2)$] and the azimuth angle φ specifying the position of the acceptor trap with respect to the nearest neighbor donor trap (which is assumed to be located at $\vartheta = 0$). It can be seen that the probability density (normalized over the range of angles ϑ, φ) of finding the nearest neighbor donor and acceptor traps at a given angular distance ϑ on a QD surface of diameter L is

$$p^{(\mathrm{QD})}(\vartheta) = \frac{n_h L^2}{4}\frac{\exp[-\pi n_h L^2 \sin^2(\vartheta/2)]}{1 - \exp(-\pi n_h L^2)}. \qquad (3)$$

Here, we assumed that the probability density does not depend explicitly on φ; n_h is the surface density of acceptor traps.

As is usually done (see, e.g., [9]), we choose the distribution function in L in the form of a lognormal distribution (in contrast to [5], where we used a Gaussian distribution). As earlier [5], we take into account that the members of a pair separated by a distance r in a QD of diameter L recombine to emit a photon of energy $E_g + c_1/L + c_2/L^2 + e^2/(\varepsilon r)$, where the terms containing L describe the size dependence of the band gap of the QD (E_g is the band gap for macroscopic Si, c_1 and c_2 are constants [1]) and the last term describes Coulomb interaction between the charged donor and acceptor [12] (e is the elementary charge, ε is the effective permittivity of the medium).

The function $I_E(t)$ describing the PL decay can be obtained by averaging Eq. (2) over the QD diameters L

[1] See the comment in [7] on measuring the Si/SiO_2 interface conductivity.

and over the distances r limited by the QD size. The result for the function $I_E^{(\mathrm{QD})}(t)$ is

$$I_E^{(\mathrm{QD})}(t) = \frac{2\pi}{\sqrt{\pi}\sigma}\int_0^\infty \frac{dL}{L}\exp\left[-\frac{1}{\sigma^2}\ln^2\left(\frac{L}{L_0}\right)\right]$$
$$\times\int_0^\pi d\vartheta\sin\vartheta W\left[L\sin\left(\frac{\vartheta}{2}\right)\right]\exp\left\{-W\left[L\sin\left(\frac{\vartheta}{2}\right)\right]t\right\} \quad (4)$$
$$\times p^{(\mathrm{QD})}(\vartheta)\delta\left\{E - E_g - \frac{c_1}{L} - \frac{c_2}{L^2} - \frac{e^2}{\varepsilon L\sin(\vartheta/2)}\right\},$$

where $W(r) = W_1(r) + W_2(r)$, L_0 and σ are the parameters of the normalized lognormal distribution and the δ function accounts for energy conservation in the recombination process.

Integrating over ϑ in Eq. (3), we obtain

$$I_E^{(\mathrm{QD})}(t) = \frac{4\gamma}{\sqrt{\pi}\sigma E_0}\int_{\min}^\infty \exp\left[-\frac{1}{\sigma^2}\ln^2\left(\frac{\xi}{\xi_0}\right)\right]$$
$$\times\left\{W_{\max}\exp[-2\xi x(\xi)] + \frac{4D}{\xi^2 x^2(\xi)R_0^2}\right\}$$
$$\times\left\{-W_{\max}t\exp[-2\xi x(\xi)] - \frac{4Dt}{\xi^2 x^2(\xi)R_0^2}\right\} \quad (5)$$
$$\times\frac{\exp[\gamma\xi^2 x^2(\xi)]}{\exp(\gamma\xi^2) - 1}\xi^2 x^2(\xi)d\xi,$$

where

$$\xi_0 = L_0/R_0, \quad x(\xi) = E_0\xi/(\tilde{E}\xi^2 - E_1\xi - E_2),$$
$$\xi_{\min} = (E_1 + E_0 + \sqrt{(E_1 + E_0)^2 + 4\tilde{E}E_2})/(2\tilde{E}),$$
$$\tilde{E} = E - E_g, \quad E_1 = c_1/R_0, \quad E_2 = c_2/R_0^2, \quad (6)$$
$$E_0 = e^2/(\varepsilon R_0), \quad \gamma = \pi n_h R_0^2.$$

Expression (5) allows us to analyze the kinetics of PS photoluminescence for arbitrary radiation energies up to temperatures at which nonradiative effects become important. Naturally, due to the presence of the diffusion term, the PL rate at finite temperatures becomes greater as compared to the case with $T = 0$ K. It can be seen from Eq. (5) that, for a high enough temperature T, the recombination through the diffusion mechanism can become dominant, but the PL decay remains nonexponential. The decay is of the type of that given by the empirical Kohlrausch's formula, which is commonly used to describe experimental data on PS photoluminescence [1].

2.2. Quantum Wire Model

It is worthwhile to construct an analog of Eq. (5) for the case of cylindrical geometry, since, in addition to the QD model, a model considering PS as a system of QWs is discussed in the literature (see, e.g., [1, 10]). In this case, the distribution function in distances r between the nearest neighbor donor and acceptor traps plays the key role in describing the PL kinetics in the QW model, since the cylinder length is assumed to be infinite. Actually, this role amounts to effective exclusion of the pairs with large r from the recombination process. In our case, $r = \sqrt{z^2 + L^2\sin^2(\varphi/2)}$, where z and φ are the cylindrical coordinates of the acceptor impurity measured with respect to the donor impurity (we place the donor impurity at the point $z = 0$, $\varphi = 0$ on the cylindrical surface). If r is much greater than the cylinder diameter L, we again assume that the distribution function in this quasi-one-dimensional geometry is exponential [11] and write this function in the form $\sim\exp(-n_1 r) \approx \exp(-n_1|z|)$, where n_1 is the linear trap density (per unit length of the quasi-one-dimensional system considered) related to the above density n_h and to the QW diameter L by the formula $n_1 = \pi L n_h$. Taking this simplest distribution function (independent of φ) for any z, we obtain the following expression for the probability density (normalized over the range of z, φ) of finding the nearest neighbor donor and acceptor impurities at a distance z:

$$p^{(\mathrm{QW})}(z) = \frac{n_1}{4\pi}\exp(-n_1|z|). \quad (7)$$

In this case, the function $I_E^{(\mathrm{QW})}(t)$ describing the kinetics of PS photoluminescence for the radiation energy E in the QW model can be written as

$$I_E^{(\mathrm{QW})}(t) = \frac{1}{\sqrt{\pi}\sigma}\int_0^\infty \frac{dL}{L}\exp\left[-\frac{1}{\sigma^2}\ln^2\left(\frac{L}{L_0}\right)\right]$$
$$\times\int_0^{2\pi} d\varphi\int_{-\infty}^\infty dz W\left[\sqrt{z^2 + L^2\sin^2\left(\frac{\varphi}{2}\right)}\right]$$
$$\times\exp\left\{-W\left[\sqrt{z^2 + L^2\sin^2\left(\frac{\varphi}{2}\right)}\right]t\right\}p^{(\mathrm{QW})}(z) \quad (8)$$
$$\times\delta\left\{E - E_g - \frac{c_1}{L} - \frac{c_2}{L^2} - \frac{e^2}{\varepsilon\sqrt{z^2 + L^2\sin^2\left(\frac{\varphi}{2}\right)}}\right\}.$$

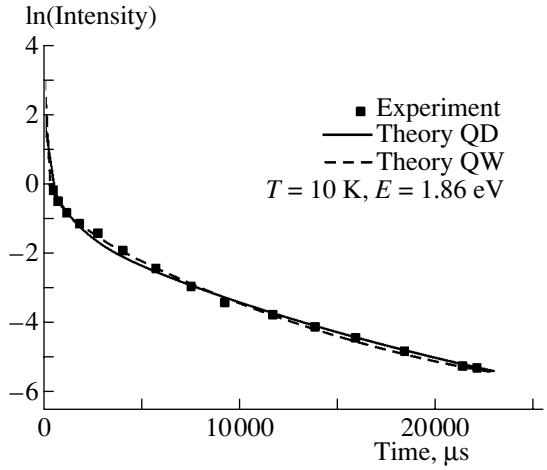

Fig. 1. Experimental data [2] (solid squares) and calculations based on Eq. (5) (solid curve) and Eq. (9) (dashed curve) for PL decay in PS at $T = 10$ K. The values of the parameters are indicated in the text.

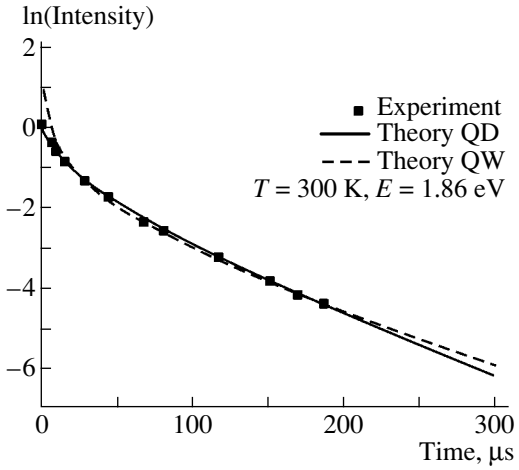

Fig. 2. Experimental data [2] (solid squares) and calculations based on Eq. (5) (solid curve) and Eq. (9) (dashed curve) for PL decay in PS at $T = 300$ K. The values of the parameters are indicated in the text.

The presence of the δ function removes one integration (in z), and we obtain

$$I_E^{(\mathrm{QW})}(t) = \frac{2\gamma}{\pi^{3/2}\sigma E_0}\left(\int_{\xi_{\min}}^{\infty} \exp\left[-\frac{1}{\sigma^2}\ln^2\left(\frac{\xi}{\xi_0}\right)\right]\right.$$

$$\times\left\{W_{\max}\exp[-2\xi x(\xi)] + \frac{4D}{\xi^2 x^2(\xi)R_0^2}\right\}$$

$$\times\exp\left\{-W_{\max}t\exp[-2\xi x(\xi)] - \frac{4Dt}{\xi^2 x^2(\xi)R_0^2}\right\}$$

$$\times x^3(\xi)g_1(\gamma, x(\xi))\xi d\xi + \int_{\xi'_{\min}}^{\xi_{\min}} \exp\left[-\frac{1}{\sigma^2}\ln^2\left(\frac{\xi}{\xi_0}\right)\right] \quad (9)$$

$$\times\left\{W_{\max}\exp[-2\xi x(\xi)] + \frac{4D}{\xi^2 x^2(\xi)R_0^2}\right\}$$

$$\times\exp\left\{-W_{\max}t\exp[-2\xi x(\xi)] - \frac{4Dt}{\xi^2 x^2(\xi)R_0^2}\right\}$$

$$\left.\times x^2(\xi)g_2(\gamma, x(\xi))\xi d\xi\right),$$

where, in addition to the functions $\xi_{\min}$, $x(\xi)$, and γ defined above, we introduced the functions

$$g_1(\gamma, x(\xi)) = \int_0^1 \frac{d\nu}{\sqrt{1-\nu^2}}\frac{\exp(-\gamma\xi^2 x(\xi)\sqrt{1-\nu^2})}{\sqrt{1-\nu^2 x^2(\xi)}}, \quad (10)$$

$$g_2(\gamma, x(\xi)) = \int_0^1 \frac{d\nu}{\sqrt{1-\nu^2}}\frac{\exp(-\gamma\xi^2 x(\xi)\sqrt{1-\nu^2/x^2(\xi)})}{\sqrt{1-\nu^2/x^2(\xi)}}, \quad (11)$$

$$\xi'_{\min} = (E_1 + \sqrt{E_1^2 + 4\tilde{E}E_2})/(2\tilde{E}). \quad (12)$$

Unfortunately, the resulting expression (9) cannot be further simplified and calculating $I_E^{(\mathrm{QW})}(t)$ requires evaluation of double integrals.

3. PROCESSING OF EXPERIMENTAL PHOTOLUMINESCENCE DATA FOR POROUS SILICON

Equation (5), based on the model representing a disordered medium as a random ensemble of QDs, admits a quantitative interpretation of numerous experimental data on the kinetics and instantaneous spectra of PS luminescence (in the range from helium to room temperature) [1–3]. Analysis of PL experiments for the same PS samples in such a wide temperature range makes it possible not only to show the self-consistency of the theory but also to obtain sufficiently full information on the parameters characterizing the physical properties of the material. In what follows, we also analyze

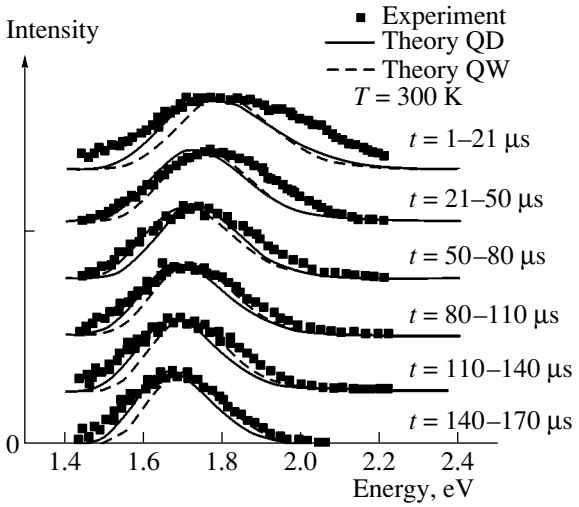

Fig. 3. Instantaneous PL spectra at $T = 300$ K. Solid squares correspond to experimental data from [2], and solid and dashed curves are calculated using Eqs. (5) and (9), respectively, for the values of the parameters corresponding to the curves in Fig. 2.

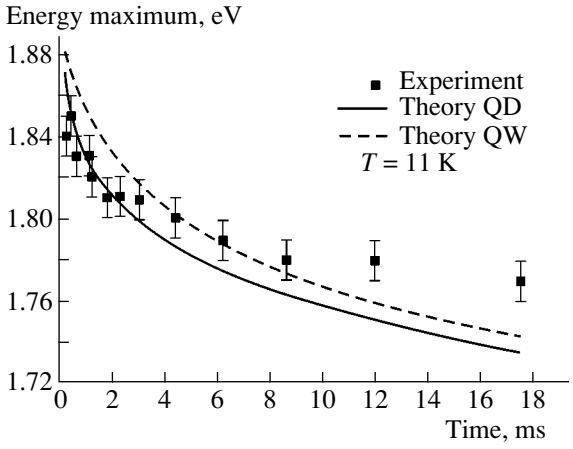

Fig. 4. Time evolution of the position of the maximum in the instantaneous PL spectra at $T = 11$ K. Solid squares correspond to the experimental data from [2], the solid curve to calculations by Eq. (5), and the dashed curve to calculations by Eq. (9); the values of the parameters correspond to the curves in Fig. 1.

the experimental data on PS photoluminescence in the QW model.

As above (as in [5]), we use the values $c_1 = 18.4$ eVÅ and $c_2 = 202$ eVÅ^2 [1]. We also note that the quantity E_g is, in general, temperature-dependent (see, e.g., [13]). We estimate T_0 by using arguments similar to those described in [7] and obtain $T_0^{1/3} \sim 10$ K$^{1/3}$. The values of the other parameters in Eq. (5) are chosen so as to ensure the best agreement between the theory and experimental data [2] on both the kinetics and instantaneous spectra of PS photoluminescence at temperatures close to absolute zero and at room temperature.

In Figs. 1 and 2, we show the experimental data [2] on the PL kinetics (for $E = 1.86$ eV) of a PS sample with a porosity of 65% at T = 300 and 10 K, respectively, and the theoretical curves corresponding to the QD model (solid lines) and QW model (dashed lines). The parameters used for plotting the theoretical curves are listed in the table.

We note that the cited values of E_g reflect (even quantitatively) the trend of the crystalline silicon band gap narrowing with increasing temperature [13].

The same values of the parameters were used to calculate theoretical PL spectra by Eqs. (5) and (9) at different times. In Fig. 3, we show the experimentally measured instantaneous PL spectra of the same PS sample at $T = 300$ K [2] together with the results of our calculations (solid lines correspond to the QD model; dashed lines. To the QW model). In Figs. 4 and 5, we plot the experimentally measured [2] and theoretical time dependence (solid lines correspond to Eq. (5); dashed lines, to Eq. (9)) of the positions of the maxima of the instantaneous PL spectra of PS at $T = 10$ and 300 K, respectively.

It is seen from Figs. 1–3 that Eqs. (5) and (9) based on the alternative models of PS structure reproduce the experimental PL data reasonably well. It is important that, in the framework of the QW model, quantitative agreement with experimental data is reached due to the introduction of the function $p^{(QW)}(z)$ [the QD model is much less sensitive to variations in function $p^{(QD)}(\vartheta)$]. Therefore, from the experimental data on PL kinetics, one can hardly unambiguously establish which of the models discussed describes the real PS structure more adequately. However, the above analysis shows that, in order to reach agreement between the experimental data and the QW model, we have to choose a substantially greater value of T_0 than that for the QD model ($T_0^{1/3} \approx 20$ K$^{1/3}$ is closer to the estimate made in [7]).

Parameters in Eqs. (5) and (9)

Parameter	QD model	QW model
L_0, Å	47	46
σ	0.24	0.22
ε	3.6	3.6
R_0, Å	8.3	9
W_{max}, 10^6 s^{-1}	1.9	4.6
D_0, 10^9 cm^2 s^{-1}	8.5	1
$T_0^{1/3}$, K$^{1/3}$	20	35
$E_g(T = 10$ K), eV	1.21	1.24
$E_g(T = 300$ K), eV	1.13	1.12
γ	0.05	0.2

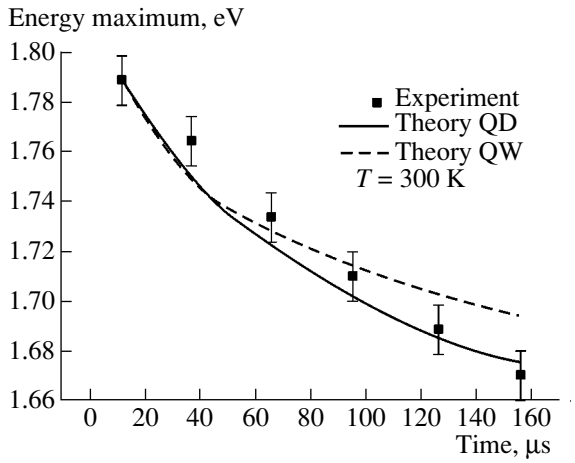

Fig. 5. Time evolution of the position of the maximum in the spectra shown in Fig. 3. Solid squares correspond to the experimental data from [2], the solid curve to calculations by Eq. (5), and the dashed curve to calculations by Eq. (9); the values of the parameters correspond to the curves in Fig. 3.

Moreover, the electron microscopy data [9] seem to favor the QD model.

We note that certain information on the trap density in PS can be obtained by measuring the ac conductivity $\sigma(\omega)$, since this conductivity occurs by hopping and is determined to a considerable degree by the trap density. As in any disordered system, the electric response of PS is essentially of non-Debye type; indeed, there exists a wide frequency range in which $\sigma(\omega)$ increases as a power-law function with a fractional exponent [1]. Joint analysis of the experimental data on PL and ac conductivity would allow us to obtain information about various physical parameters of PS.

4. CONCLUSIONS

Starting from the concept of PS as a random system of structural building blocks (spheres or cylinders of various radii), we have developed a theory of PL kinetics that takes into account both tunneling recombination of electron–hole pairs captured in traps and thermally activated diffusion. The function describing the PL kinetics has been obtained by averaging over the size distribution of building blocks and over the relative positions of an electron and a hole in each pair. The theory provided a good quantitative description of the PL kinetic curves in the temperature range from helium to room temperature and of the temperature variation of instantaneous PL spectra. It was shown that both models can be applied to interpret experimental data on PS photoluminescence, although there are good reasons to prefer the QD model.

Finally, we note that, in principle, our theory of PL, with necessary modifications, can be adapted to study the functional features of PS-based optical devices used in practice (multilayer structures, optical resonators, etc.) [1].

REFERENCES

1. O. Bisi, S. Ossicini, and L. Pavesi, Surf. Sci. Rep. **38** (1), 1 (2000).
2. L. Pavesi, J. Appl. Phys. **80** (1), 216 (1996).
3. L. Pavesi and M. Ceschini, Phys. Rev. B **48** (23), 17625 (1993).
4. V. F. Agekyan, V. V. Emtsev, A. A. Lebedev, *et al.*, Fiz. Tekh. Poluprovodn. (St. Petersburg) **33** (12), 1462 (1999) [Semiconductors **33**, 1315 (1999)].
5. V. N. Bondarev and P. V. Pikhitsa, Fiz. Tverd. Tela (St. Petersburg) **43** (12), 2142 (2001) [Phys. Solid State **43**, 2237 (2001)].
6. P. D. J. Colcott, K. J. Nash, L. T. Canham, *et al.*, J. Phys.: Condens. Matter **5**, L91 (1993).
7. N. F. Mott and E. A. Davis, *Electron Processes in Non-Crystalline Materials*, 2nd ed. (Clarendon, Oxford, 1979; Mir, Moscow, 1982).
8. J. C. Vial, A. Bsiesi, F. Gaspard, *et al.*, Phys. Rev. B **45** (24), 14171 (1992).
9. Y. Kanemitsu, T. Ogawa, K. Shiraishi, and T. Takeda, Phys. Rev. B **48** (7), 4883 (1993).
10. M. E. Kompman, E. G. Kuz'minov, V. B. Kulik, *et al.*, Pis'ma Zh. Éksp. Teor. Fiz. **64** (10), 695 (1996) [JETP Lett. **64**, 748 (1996)].
11. D. J. Dunstan, Phys. Rev. B **32** (10), 6910 (1985).
12. D. G. Tomas, J. J. Hopfield, and W. M. Augustyniak, Phys. Rev. **140** (11), A202 (1965).
13. M. K. Seeger, *Semiconductor Physics* (Springer, Wien, 1973; Mir, Moscow, 1977).
14. W. Wang and H. Fritzsche, in *Amorphous Silicon and Related Materials*, Ed. by H. Fritzsche (World Sci., Singapore, 1989; Mir, Moscow, 1991).

Translated by I. Zvyagin

Physics of the Solid State, Vol. 46, No. 3, 2004, pp. 543–551. Translated from Fizika Tverdogo Tela, Vol. 46, No. 3, 2004, pp. 526–533.

LOW-DIMENSIONAL SYSTEMS AND SURFACE PHYSICS

Analytical Model of Oscillating Size Dependence of Energy and Force Characteristics of Subatomic Metal Films

V. P. Kurbatsky and V. V. Pogosov

Zaporozh'e National Technical University, Zaporozh'e, 69063 Ukraine

e-mail: vpogosov@zstu.edu.ua

Received May 6, 2003

Abstract—For a wide thin film of thickness L, the expansion of energy characteristics in powers of $1/L$ is constructed using the free-electron approximation and a model of a potential well of finite depth. The errors in each order of the expansion are analyzed. Using the exact formulas, the thickness dependences of the work function and of the electronic contribution to the elastic force for Al, Au, Ag, and Na films are calculated. It is concluded that the work function of a low-dimensional metal structure is always smaller than that of the corresponding semi-infinite metal. © *2004 MAIK "Nauka/Interperiodica".*

1. INTRODUCTION

Analytical approaches to the determination of the density of states and the Fermi energy for metal films were proposed in [1, 2] on the basis of the free-electron model. Analytical calculations using the Euler–Maclaurin summation rule have only been possible for infinitely high surface barriers. Using the same ideas, in [3] it was noted that the contact potential difference for a film can be quantized and in [4–6] the jumps of the elastic force for a point contact observed experimentally in [7, 8] were explained. However, the work function cannot be determined in this simple model.

Existing detailed calculations (among them *ab initio* calculations) do not determine the thickness dependence of the work function of isolated films and wires unambiguously, and the oscillations obtained are too large to be realistic [9–14]. The work function of Ag layers (varying in thickness from one to twelve monolayers) on Fe(100) substrates was recently measured in [15].

Point contacts of gold samples were studied experimentally in [7] by elongating the contacts to the rupture point. It was shown that oscillations in the values of the elastic constants appear simultaneously with an abrupt variation in conductance. The dimensionality of a contact must vary when the circuit is interrupted. Indeed, at the moment of formation of a contact, the contact region can be represented as a layer, whereas at the moment of its rupture the contact region becomes a wire. Thus, in such experiments, a transition occurs from a two-dimensional (or zero-dimensional) to a one-dimensional open electron system.

In this paper, we develop analytical theory for thickness-dependent energy and force characteristics of metal films by using an elementary one-particle approach not involving the Euler–Maclaurin summation formula. A simple model makes it possible to improve or correct the previous theories and calculate the oscillating thickness dependence of the work function and the elastic force. Under the assumption of ideal plastic strain, the volume of the film remains constant during stretching; this allows comparison with the experimental results reported in [7]. Thermal effects are not taken into account.

2. STATEMENT OF THE PROBLEM

We consider a thin metal film whose thickness L_z is of the order of the Fermi wavelength λ_F^0 and is much smaller than its other dimensions, $L_x \gg L_z$ and $L_y \gg L_z$; thus, the discreteness of the electron momentum components p_x and p_y can be ignored. For typical values of the electron density in metals, we have $\lambda_F^0 \simeq 0.5$ nm.

To the first approximation, the electron potential-energy profile in the film can be represented as a rectangular potential well of constant depth U_0 with dimensions L_x, L_y, and L_z. A solution to the Schrödinger equation for such a potential is characterized by a set of electron wave numbers $k_{xj} = 2\pi j/L_x$, $k_{ys} = 2\pi s/L_y$ ($j, s = 0, \pm 1, \pm 2, \pm 3, \ldots$), and k_{zi} ($i = 1, 2, 3, \ldots$), which are roots of the equation

$$k_{zi}L_z = -2\arcsin(k_{zi}/k_0) + \pi i, \qquad (1)$$

where $\hbar k_0 = \sqrt{2mU_0}$ and m is the electron mass.

A set of wave numbers determines the electron energy:

$$E_{ijs} = \frac{\hbar^2}{2m}(k_{xj}^2 + k_{ys}^2 + k_{zi}^2).$$

Since $E_{ijs} < U_0$, the number of possible electron states is finite.

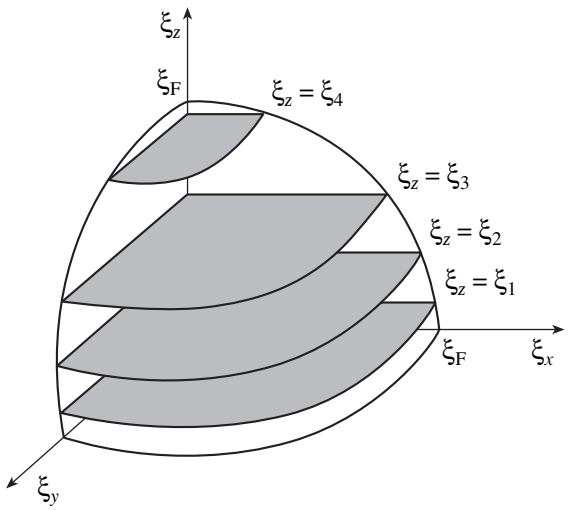

Fig. 1. Geometrical diagram of electron-state filling in ξ space.

It is convenient to pass to dimensionless variables by choosing U_0 as a unit of energy and k_0^{-1} as a unit of length. We introduce the following notation:

$$\xi_i = k_{zi}/k_0, \quad \xi_{xj} = k_{xj}/k_0, \quad \xi_{ys} = k_{ys}/k_0,$$

$$l = k_0 L_z/\pi, \quad l_x = k_0 L_x/2\pi, \quad l_y = k_0 L_y/2\pi.$$

With these units, the energy can be interpreted as the square of the state vector in the ξ space, $\xi_{ijs}^2 = \xi_{xj}^2 + \xi_{ys}^2 + \xi_i^2$, with $\xi_{ijs} \le 1$.

Equation (1) assumes the form

$$l\xi_i = -\frac{2}{\pi}\arcsin\xi_i + i. \tag{2}$$

Note that not only solutions of Eq. (2) but also the number of levels in the potential well are fully determined by the film thickness l; namely, $i_{\max} = [l] + 1$, where $[a]$ stands for the integer part of a. Let us now discuss the distribution of electron states.

3. DISTRIBUTION OF STATES IN ξ SPACE AND DENSITY OF STATES

Let us estimate the interval $\Delta\xi$ between neighboring values of ξ_z. Since the distances between two consecutive values of ξ_x and ξ_y are small, namely, $\Delta\xi_x = \xi_{xj+1} - \xi_{xj} = 1/l_x$ and $\Delta\xi_y = 1/l_y$, it follows from Eq. (2) that, for sufficiently large values of l,

$$\Delta\xi \approx l^{-1}. \tag{3}$$

For the relative values of the film dimensions assumed by us, it follows from Eq. (3) that $\Delta\xi \gg \Delta\xi_x, \Delta\xi_y$. We see that the possible electron states $\{\xi_{xj}, \xi_{ys}, \xi_i\}$ form a system of parallel planes $\xi_z = \xi_i$ in ξ space and that the density of states on all these planes is the same and is equal to

$$\sigma = 2/(\Delta\xi_x\Delta\xi_y) = 2l_x l_y. \tag{4}$$

The factor 2 takes into account the two possible values of the electron spin projection.

The states are filled by electrons, beginning at the point $\{0, 0, \xi_1\}$, in ascending order of ξ, i.e., of the state energy. Therefore, it appears that all occupied states lie in the ξ-space domain bounded by the plane $\xi_z = \xi_1$ and the hemisphere of radius $\xi_F = \sqrt{E_F/U_0}$, where E_F is the Fermi energy equal to the maximum energy of occupied states.

The occupied states are distributed with density σ over the disks bounded by the intersections of the Fermi hemisphere with the planes $\xi_z = \xi_i$, with $i = 1, 2, \ldots, i_F$ (Fig. 1). The area of each disk is $S_i = \pi(\xi_F^2 - \xi_i^2)$. The number of occupied states coincides with the number of valence electrons in the film and is equal to

$$N = \sigma\sum_{i=1}^{i_F} S_i = 2l_x l_y \sum_{i=1}^{i_F} \pi(\xi_F^2 - \xi_i^2), \tag{5}$$

where i_F is the number of occupied levels in the potential well.

The number of occupied states per unit volume is

$$\nu \equiv \frac{N}{l_x l_y l} = \frac{2\pi}{l}\left(i_F\varepsilon_F - \sum_{i=1}^{i_F}\xi_i^2\right), \tag{6}$$

where we used the notation $\varepsilon_F \equiv E_F/U_0 = \xi_F^2$ for the Fermi energy.

By definition, the density of states $\rho(E)$ is the number of states per unit energy interval near the energy E and per unit volume of the metal. In order to find this quantity, we write Eq. (6) in the form

$$\nu = \frac{2\pi}{l}\left(i_\varepsilon\varepsilon - \sum_{i=1}^{i_c}\xi_i^2\right) \tag{7}$$

and interpret ν as the number of states (per unit volume) whose energies do not exceed ε. In Eq. (7), i_ε is the index of the greatest of the roots of Eq. (2) satisfying the condition $\xi_i^2 \le \varepsilon$. The function $i_\varepsilon(\varepsilon)$ is assumed to be constant inside each interval (ξ_i^2, ξ_{i+1}^2), $i = 1, 2, \ldots, [l]$ and to change by 1 at the boundaries of these intervals.

We find from Eq. (2) that

$$i = l\xi_i + \frac{2}{\pi}\arcsin\xi_i.$$

Substituting here the values of ξ_i in ascending order of i, we obtain the sequence of natural numbers. We let ξ

take any value in the limits from ξ_1 to 1 and form an integer-valued increasing function such that at the points $\xi = \xi_i$ the value of the function is increased by one and in the intervals between these points the function does not change. Substituting $\xi = \sqrt{\varepsilon}$, we obtain

$$i_\varepsilon = \left[l\sqrt{\varepsilon} + \frac{2}{\pi}\arcsin\sqrt{\varepsilon} \right], \quad \xi_1^2 \le \varepsilon \le 1. \tag{8}$$

By differentiating Eq. (7) under the condition $i_\varepsilon = \text{const}$, we find $\rho(\varepsilon) = d\nu/d\varepsilon$. Using Eq. (8) and working backward through the normalizations, we obtain

$$\begin{aligned} \rho(E) &= \frac{1}{V}\frac{dN}{dE} \\ &= \frac{m}{\pi\hbar^2 L_z}\left[\frac{L_z\sqrt{2mE}}{\pi\hbar} + \frac{2}{\pi}\arcsin\sqrt{\frac{E}{U_0}} \right], \end{aligned} \tag{9}$$

where $V = L_x L_y L_z$.

4. GENERAL SIZE DEPENDENCE OF THE FERMI ENERGY

From Eq. (6), we obtain

$$\varepsilon_F = \frac{1}{i_F}\left(\frac{\nu l}{2\pi} + \sum_{i=1}^{i_F} \xi_i^2 \right). \tag{10}$$

Using Eq. (8), we find that the number of occupied levels is

$$i_F = \left[l\sqrt{\varepsilon_F} + \frac{2}{\pi}\arcsin\sqrt{\varepsilon_F} \right]. \tag{11}$$

In what follows, we assume that the electron density in the film does not depend on its size and is

$$\frac{N}{V} = \frac{k_0^3}{4\pi^3}\nu = \bar{n}. \tag{12}$$

If the depth of the well is fixed, then Eq. (12) implies that $\nu = \text{const}$.

Turning back to Eq. (2), we readily see that its roots ξ_i are determined by l alone. Therefore, in Eqs. (10) and (11), the dependence on the potential well depth appears only in the parameter ν. Thus, only this parameter determines both the valence electron density and the well depth. The thickness dependence of the Fermi energy $\varepsilon_F(l)$ can be found by solving the set of equations (10) and (11) under the additional condition $\nu = \text{const}$.

All terms in Eq. (10) admit a simple geometrical interpretation in ξ space. It follows from the definition $\nu \equiv N/l_x l_y l$ and from Eq. (5) that $S = 1/2\nu l$, where $S = \sum_{i=1}^{i_F} S_i$ is the total area occupied by the valence electrons (i.e., the sum of the areas of the disks in Fig. 1). Then, $\nu l/2\pi = \sum_{i=1}^{i_F} \rho_i^2$, where ρ_i is the radius of the ith disk. Therefore, Eq. (10) is obtained by summing the obvious equality $\xi_F^2 = \rho_i^2 + \xi_i^2$.

Substituting the expression $\bar{n} \equiv (k_F^0)^3/3\pi^2$ into Eq. (12) (k_F^0 is the electron Fermi momentum for the infinite metal), we find

$$\nu = \frac{4}{3}\pi(\xi_F^0)^3, \tag{13}$$

where $\xi_F^0 \equiv k_F^0/k_0$; i.e., ν is equal to the double of the volume of the Fermi hemisphere in ξ space in the limiting case $l \longrightarrow \infty$.

Setting $i_F = \text{const}$, from Eq. (10) we obtain

$$\frac{d\varepsilon_F}{dl} = \frac{1}{i_F}\left(\frac{\nu}{2\pi} + \frac{d}{dl}\sum_{i=1}^{i_F} \xi_i^2 \right). \tag{14}$$

In order to see how the roots of Eq. (2) change with varying l, we differentiate both parts of this equation and find that

$$\frac{d}{dl}\xi_i^2 = -\frac{2\xi_i^2}{l + \dfrac{2}{\pi\sqrt{1-\xi_i^2}}} \le 0. \tag{15}$$

Here, the equality takes place only in the limit $l \longrightarrow \infty$, i.e., as $\xi_i \longrightarrow 0$ for all i.

The disks in Fig. 1 are lowered with increasing l. The lowering rate gradually decreases, so that the lower disks move more slowly than the higher ones. Accordingly, the distance between the disks decreases and their number i_F grows. It is seen from Eq. (11) that this number increases by 1 each time the equality $\varepsilon_F = \xi_{i_F+1}^2$ is satisfied. The process of disk lowering is accompanied by the "pulsation" of the Fermi hemisphere. Its radius $\xi_F = \sqrt{\varepsilon_F}$ alternately increases (as $d\varepsilon_F/dl > 0$) and decreases (as $d\varepsilon_F/dl < 0$), having the average tendency to decrease.

Now, let us study the behavior of the function $\varepsilon_F(l)$ at the points where the number of occupied levels increases, $i_F \longrightarrow i_F + 1$. We denote the corresponding value of l by l_{i_F+1}. Let ε_F^- be the limit of the function $\varepsilon_F(l)$ as $l \longrightarrow l_{i_F+1}$ from the left and let ε_F^+ be the limit of this function as $l \longrightarrow l_{i_F+1}$ from the right. The difference between these limits is

$$\varepsilon_F^+ - \varepsilon_F^- = \frac{\xi_{i_F+1}^2 - \varepsilon_F^-}{i_F + 1}.$$

At the point $l = l_{i_F+1}$, as noted above, we have $\xi^2_{i_F+1} = \varepsilon_F^-$ and, therefore, $\varepsilon_F^- = \varepsilon_F^+$; this means that the function $\varepsilon_F(l)$ is continuous. For its derivative, the situation is different.

We introduce the notation $d\varepsilon_F^{\pm}/dl = \lim_{l \to l_{i_F+1} \pm 0} d\varepsilon_F/dl$. The difference between these derivatives is

$$\frac{1}{i_F+1}\frac{d}{dl}(\xi^2_{i_F+1} - \varepsilon_F^-) \le 0.$$

At the points $l = l_{i_F+1}$ the derivative $d\varepsilon_F/dl$ is discontinuous; the value of the jump decreases with increasing l, since the number of occupied levels i_F grows with l.

Let us find the limit of $\varepsilon_F(l)$ as $l \longrightarrow \infty$. It follows from Eq. (2) that $\xi_i \longrightarrow 0$ as $\xi_i = i/l$; therefore, the first term on the right-hand side of Eq. (2) can be neglected compared to i and we obtain $\xi_i = i/l$. The sum in Eq. (10) is easily calculated to give

$$\varepsilon_F = \frac{\nu}{2\pi}\frac{l}{i_F} + \frac{1}{6l^2}(2i_F^2 + 3i_F + 1).$$

From Eq. (11) for large l, we obtain

$$i_F \approx l\sqrt{\varepsilon_F}, \tag{16}$$

i.e., i_F and l are of the same order of magnitude. Using Eqs. (16) and (13), we obtain $\varepsilon_F = \varepsilon_F^0$ in the approximation chosen. In what follows, we determine the asymptotic form of the function $\varepsilon_F(l)$ for large l by using the series expansion in powers of $1/l$.

5. SIZE DEPENDENCE OF THE WORK FUNCTION

As noted above, the minimum value of L_z corresponds to approximately one monolayer. Let us estimate the minimum value of l. To this end, we use the relations $l = L_z\sqrt{2mU_0}/\pi\hbar$, where $L_z = 0.5$ nm, and

$$U_0 = E_F^0 + W_0, \quad E_F^0 = \frac{\hbar^2}{2m}(3\pi^2\bar{n})^{2/3}, \tag{17}$$

with $U_0 = 3.50$ and 15.94 eV for Cs and Al, respectively. We obtain $1.6 < l_{\min} < 3.5$. In what follows, we assume that $1/l$ is small and use a power expansion in $1/l$ in calculating the Fermi energy.

Now, we introduce the notation $\alpha \equiv 1/l$. The $\xi_i(\alpha)$ dependence is implicitly determined by Eq. (2), which can be written as

$$\frac{\xi_i}{\alpha} = -\frac{2}{\pi}\arcsin\xi_i + i. \tag{18}$$

We look for the roots ξ_i in the form of the expansion

$$\xi_i = \xi_i|_{\alpha=0} + \xi_i'|_{\alpha=0}\alpha + \frac{1}{2}\xi_i''|_{\alpha=0}\alpha^2 + \frac{1}{6}\xi_i'''|_{\alpha=0}\alpha^3 + \ldots. \tag{19}$$

Keeping the terms to the order α^3, we obtain the Fermi energy to the order α^2. It is seen from Eq. (18) that

$$\xi_i|_{\alpha=0} = 0, \quad \xi_i/\alpha|_{\alpha=0} = i. \tag{20}$$

Differentiating both sides of Eq. (18) with respect to α and multiplying the result by α gives

$$\xi_i' - \frac{\xi_i}{\alpha} = -\frac{2}{\pi}\frac{1}{\sqrt{1-\xi_i^2}}\alpha\xi_i'. \tag{21}$$

Setting $\alpha = 0$, we find

$$\xi_i'|_{\alpha=0} = i. \tag{22}$$

In a similar way, we obtain

$$\xi_i''|_{\alpha=0} = -\frac{4i}{\pi}, \quad \xi_i'''|_{\alpha=0} = -\frac{24i}{\pi^2}.$$

Substituting the obtained expressions into Eq. (19), we find

$$\xi_i = i\alpha - \frac{2i}{\pi}\alpha^2 + \frac{4i}{\pi^2}\alpha^3 + O(\alpha^4). \tag{23}$$

First, we evaluate the Fermi energy to first order in α. For this purpose, it suffices to keep the first two terms in Eq. (23) when substituting it into Eq. (10). Indeed, the order of magnitude of the error $\delta\xi_i$ does not exceed $i_F\alpha^3$ in this case. The error of ξ_i^2 is $2\xi_i\delta\xi_i$, and its order of magnitude also does not exceed $i_F\alpha^3$, since $\xi_i \le 1$. The error of the sum $\sum_{i=1}^{i_F}\xi_i^2$ is smaller than $i_F^2\alpha^3$, and the order of magnitude of the error of the whole expression (10) does not exceed $i_F\alpha^3$. Since $i_F \simeq \sqrt{\varepsilon_F}/\alpha$, as follows from Eq. (16), this estimate of the Fermi energy is correct to first order in α.

After the above-mentioned substitution into Eq. (10), we have

$$\varepsilon_F = \frac{\nu}{2\pi}\frac{1}{i_F\alpha} + \left(\frac{i_F^2}{3} + \frac{i_F}{2}\right)\alpha^2 - \frac{4i_F^2}{3\pi}\alpha^3 + O(\alpha^2). \tag{24}$$

We divide the range of variation of α into intervals (α_{i+1}, α_i), $i = 2, 3, \ldots$, where $\alpha_i \equiv 1/l_i$; inside these intervals, we have $i_F = i$. The values $\alpha > 0.3$, which correspond to $l < l_{\min}$, are nonphysical. Let us find the boundaries of the intervals.

As shown above, for $\alpha = \alpha_i$, we have $\varepsilon_F = \xi_{i+1}^2$. In zeroth approximation, we can write

$$\varepsilon_F = \frac{\nu}{2\pi}\frac{1}{i\alpha_{i+1}} + \frac{i^2}{3}\alpha_{i+1}^2, \quad \xi_{i+1}^2 = i^2\alpha_{i+1}^2. \qquad (25)$$

Using Eqs. (25) and (13), we find

$$\alpha_{i+1} = \frac{1}{i}\sqrt{\varepsilon_F^0}. \qquad (26)$$

From Eqs. (23) and (24), we can obtain an exact equation for α_{i+1}:

$$\frac{8i^3}{3\pi}\alpha_{i+1}^4 - \left(\frac{2i^3}{3} + \frac{3i^2}{2}\right)\alpha_{i+1}^3 + \frac{\nu}{2\pi} = 0. \qquad (27)$$

According to Descartes's rule of signs, Eq. (27) has two real positive roots. In zeroth approximation, one of them is $\sim\sqrt{\varepsilon_F^0}/i$ and the other is of a higher order of smallness. We are interested in the first root of Eq. (27), because this root determines the boundaries of the intervals (α_{i+1}, α_i) with constant i_F,

$$\alpha_p = \frac{1}{i}\sqrt{\varepsilon_F^0} + \frac{1}{2i^2}\sqrt{\varepsilon_F^0}\left(\frac{4}{\pi}\sqrt{\varepsilon_F^0} \mp 1\right). \qquad (28)$$

The minus sign corresponds to $p = i + 1$, and the plus sign to $p = i$. Thus, the width of the interval (α_{i+1}, α_i) decreases as $1/i^2$ with increasing i (or l), since $\alpha_i - \alpha_{i+1} = \sqrt{\varepsilon_F^0}/i^2$.

Unexpectedly, the examination of function $\varepsilon_F(l)$ indicates the insufficiency of its approximation by step function (24), corresponding to the most trivial representation of the size effect. In order to take the terms of order $\sim\alpha^2$ on the right-hand side of Eq. (24) into account, we must include the following terms, which were earlier neglected:

$$\frac{1}{6}\alpha^2 - \frac{2i_F}{\pi}\alpha^3 + \frac{4i_F^2}{\pi^2}\alpha^4. \qquad (29)$$

In this case, the $\varepsilon_F(l)$ dependence is represented by a concave curve in each interval (l_i, l_{i+1}), $i = 2, 3, \ldots$. Note that straightforward numerical calculation of ε_F by using Eq. (24) produces error, which arises due to taking the terms $\sim\alpha^2$ into account incorrectly and leads to an artificial oscillating dependence on l.

At the points where changes occur in the number of occupied levels $l = l_i$, the derivative $d\varepsilon_F/dl$ is discontinuous and the jump is $-2\varepsilon_F^{0\,3/2}/i^2$. To the left of the jump, the function grows, and to the right of it, the function decreases. The jump in the derivative results in the appearance of kinks in the plot. The sharpness of the kinks decreases with increasing i.

5.1. The Asymptotic Form of $\varepsilon_F(l)$

For large values of l, Eq. (11) can be written as

$$i_F = \frac{\sqrt{\varepsilon_F^0}}{\alpha} + O(\alpha^0). \qquad (30)$$

Indeed, if we omit the operation of taking the integer part of a number, then we make an error whose value is smaller than unity. The omitted term in Eq. (11) likewise does not exceed unity.

Substituting Eq. (30) into Eq. (24) and using conventional units, we obtain

$$E_F = E_F^0 + \frac{\pi\hbar}{2}\sqrt{\frac{E_F^0}{2m}}\left(1 - \frac{8}{3\pi}\sqrt{\frac{E_F^0}{U_0}}\right)\frac{1}{L_z}. \qquad (31)$$

The expression in parentheses is positive; i.e., asymptotically, we always have $E_F > E_F^0$.

The dimensional work function is trivially defined by

$$W = U_0 - E_F. \qquad (32)$$

By this definition, W is the energy separation between the highest occupied level of the quasi-continuous spectrum and the electron energy level in vacuum. The value of W differs from that of W_0 (for a semi-infinite metal) and $W < W_0$. The role of the size dependence of the bottom of the potential well $U(L_z)$ is discussed in Section 8.

6. ELECTRON KINETIC ENERGY AND THE OSCILLATING PART OF THE ELASTIC FORCE

In order to calculate force characteristics, we must find the confined electron kinetic energy. We denote the total kinetic energy of the electron liquid by $\varepsilon \equiv K/U_0$.

As noted above, the one-electron kinetic energy ε_{ijk} is numerically equal to the square of the position vector of the point in ξ space representing the electron state. The contribution from the corresponding element dS of the disk to the total kinetic energy is $d\varepsilon = \varepsilon_{ijk}\sigma dS$, where the density of states σ is defined by Eq. (4). Next, we must integrate over the disk area and sum the contributions from all disks.

We introduce the notation $\rho \equiv (\xi_{xj}^2 + \xi_{ys}^2)^{1/2}$. The maximum value of ρ in the ith disk is equal to the disk radius $\rho_i = (\varepsilon_F - \xi_i^2)^{1/2}$. We have

$$\begin{aligned}\varepsilon &= 4\pi l_x l_y \sum_{i=1}^{i_F}\int_0^{\rho_i} d\rho\rho(\xi_i^2 + \rho^2) \\ &= \pi l_x l_y\left(i_F\varepsilon_F^2 - \sum_{i=1}^{i_F}\xi_i^4\right).\end{aligned} \qquad (33)$$

Performing the summation with the required accuracy, we find

$$\varepsilon = \pi l_x l_y \left[\left(\frac{\nu^2}{4\pi^2} \frac{1}{i_F \alpha^2} + \frac{\nu}{3\pi} i_F^2 \alpha - \frac{4}{45} i_F^5 \alpha^4 \right) + \left(\frac{\nu}{2\pi} i_F \alpha - \frac{4\nu}{3\pi^2} i_F^2 \alpha^2 - \frac{1}{6} i_F^4 \alpha^4 + \frac{32}{45\pi} i_F^5 \alpha^5 \right) \right]. \quad (34)$$

The asymptotic form of this expression in conventional units is

$$K = \frac{3}{5} N E_F^0 + \frac{3\pi\hbar}{8} N \sqrt{\frac{E_F^0}{2m}} \left(1 - \frac{32}{15\pi} \sqrt{\frac{E_F^0}{U_0}} \right) \frac{1}{L_z}, \quad (35)$$

where N is the number of valence electrons in the film. Let us discuss the origin of the different terms in Eq. (35).

The first term in Eq. (35) is the kinetic energy in the case where the film thickness L_z is comparable to the other system dimensions. The distance between the disks in ξ space is so small in this case that the summation in Eq. (33) can be replaced by integration.

The dependence of the kinetic energy on the film surface area $L_x L_y$ is included in the density of states σ from the outset (note that no term in Eq. (35) has any relation to the surface energy, which cannot be defined in this model). In contrast to the second term, the first term in Eq. (35) depends on L_z as well; therefore, this term is proportional to the volume or (for a constant electron density) to the number of electrons.

The second term in parentheses in Eq. (35) is the correction for a finite well depth. This correction is rather important and makes a contribution of about 50%. In contrast to the case of an infinite well, electron localization in a well of finite depth is not strict; therefore, the kinetic energy in the latter case is smaller.

Now, we discuss the electron gas pressure on the walls. By reducing the film dimensions, we perform work against the pressure; as a result, for a fixed well depth, the electron gas kinetic energy increases. In the expression for the energy differential

$$d\varepsilon = \frac{\partial \varepsilon}{\partial l_x} dl_x + \frac{\partial \varepsilon}{\partial l_y} dl_y + \frac{\partial \varepsilon}{\partial l_z} dl_z$$

the negative of a partial derivative is the corresponding component of the dimensionless force. For example, the force acting in the direction of the z axis is

$$f_z = -(\partial \varepsilon / \partial l_z)_{l_x, l_y}.$$

A real film is an electron–ion system; consequently, the total force arising when the film is deformed cannot be calculated in the one-particle formulation of the problem.

In order to compare the results of our model calculation with the experimental data from [7, 8], we find the oscillating electronic contribution to the elastic force under the conditions of ideal plastic strains, i.e., in the case where the total film volume is conserved:

$$f_z = -(\partial \varepsilon / \partial l_z)_V.$$

This part of the force is in no way related to the phases of stretching that are accompanied by a change in volume; rather, it determines the variation in film elastic properties as the film thickness is varied. This force depends on the number of particles in the film; therefore, it is convenient to consider the force normalized by N,

$$\frac{F_z}{N} = \frac{\hbar^2}{2m} \left(-\frac{\pi \bar{n}}{i} + \frac{2\pi^2}{3} \frac{i^2}{L_z^3} - \frac{\pi^3}{9\bar{n}} \frac{i^5}{L_z^6} + \pi^2 \frac{i}{L_z^3} - \frac{4\pi^2}{k_0} \frac{i^2}{L_z^4} + \frac{5\pi^3}{24\bar{n}} \frac{i^4}{L_z^6} + \frac{16\pi^3}{15\bar{n} k_0} \frac{i^5}{L_z^7} \right). \quad (36)$$

7. POINT CONTACT

When the film is brought into contact with the shores, the electron chemical potentials are equalized and the electronic system should be considered as an open system with $W(L_z) = W_0$. The electrical neutrality of the cluster (film) is broken, and a part δN of the electron liquid passes out to the bath. As a result, the contact potential difference $\delta\varphi$ appears.

In order to determine the contact potential difference, we consider energy cycles in which the electron charge is transferred first to infinity and then to the shores (electrodes). By analogy with a spherical cluster [16], we express the ionization potential of the film having charge $+e\delta N$ as

$$\mathrm{IP} = E_{N-\delta N-\Delta} - E_{N-\delta N} = W\Delta + \frac{e^2}{2C}[(\delta N - \Delta)^2 - \delta N^2],$$

and write the energy of adsorption of the charge $-e\Delta$ by the bath as $\mathrm{EA} = W_0\Delta$; equating these two quantities, we obtain

$$(W_0 - W) + \frac{e^2}{2C}(-2\delta N + \Delta) = 0, \quad (37)$$

where C is the sample capacitance.

We note that Δ can be infinitesimal, since the "last" electron can pass through the contact only partially (i.e., it can be detected on both sides of the geometrical contact with a nonzero probability). This situation is typical for one-electron devices [17]. Therefore, δN can be considered as a smoothly varying quantity.

We also assume that C corresponds to the total capacitance C_c of both contacts. The validity of this assumption depends on the cluster geometry. Near the ends of the parallelepiped, the surface distribution of an

excess positive charge should be similar to that for real ionization due to the presence of faces. This is not true for a ball-shaped cluster in direct contact with electrodes, but it is valid for a cubic cluster or a film. Setting $C_c = e\delta N/\delta\varphi$, $\delta N \ll N$, and $\Delta \longrightarrow 0$, we obtain from Eq. (37)

$$\delta\varphi = (W_0 - W)/e. \quad (38)$$

Now, we have to find the energy spectrum of the $N_1 = N - \delta N$ electrons that remain in the film for a rectangular potential well of a different depth $U_1 = U_0 - e\delta\varphi$. In this approach, the Fermi energies for an isolated cluster E_F and for a cluster in the contact E_{F1} coincide. The total kinetic energy K_1 of the remaining electrons can be determined in the same way as for an isolated film but with a different energy spectrum and a different number of electrons. For the oscillating part of the elastic force, we have $F_{z1} = -(\partial\Omega/\partial L_z)_V$, where $\Omega = K_1 + W_0N_1$ is the thermodynamic potential.

8. RESULTS

Calculations are performed for films of trivalent Al and monovalent Au, Ag, and Na with electron density $\bar{n} = 3/4\pi r_s^3$, where r_s = 2.07, 3.01, 3.02, and 3.99 a_0, respectively; the work functions for semi-infinite metals are taken to be W_0 = 4.25, 4.3, 4.3, and 2.7 eV, respectively.

Figure 2 shows the results of calculating the work function for isolated films of different thicknesses. The inequality $W < W_0$ is satisfied for the whole thickness range. This variation of W is in general agreement with the experimental data from [15] and with the results of self-consistent calculations using the Kohn–Sham method for infinitely long cylindrical nanowires [12,14,18] and for films [13]; however, there is disagreement with the results from the calculations performed in [9–11]. The amplitudes of the largest oscillations of the work function ~0.1–0.2 eV are even more acceptable than those obtained in the cited theoretical papers, since the observed oscillations are small. Comparing the work function variation for various metals, it is easily seen that all differences are determined by the values of r_s. For aluminum (with the smallest r_s), the amplitude of oscillations of the work function $1 - W/W_0$ is the largest, the period ΔL is the smallest, and the positions of the kinks are displaced to the left. These features are well described by the approximate relations $1 - W/W_0 \sim 1/r_sL$, $\Delta L \sim r_s$, and $L_i \sim ir_s$, which follow from Eqs. (28) and (31).

We note that it is the ionization potential

$$\mathrm{IP} = W + e^2/2C \quad (39)$$

that is always measured experimentally.

For wide films or long wires, we have $C \longrightarrow \infty$ and the work function coincides with the ionization potential. In the opposite case, the quantity W is useful only from the methodical point of view but it is not directly measured. To calculate the ionization potential IP, the film capacity can be estimated as the capacity of the equivalent disk of the same thickness (e.g., of volume 3 nm^3). Since the spectrum is quasi-continuous, we can consider only the first two oscillation periods. It appeared that in this size interval we have IP > W_0. The condition IP < W_0 can only be satisfied for wires [19].

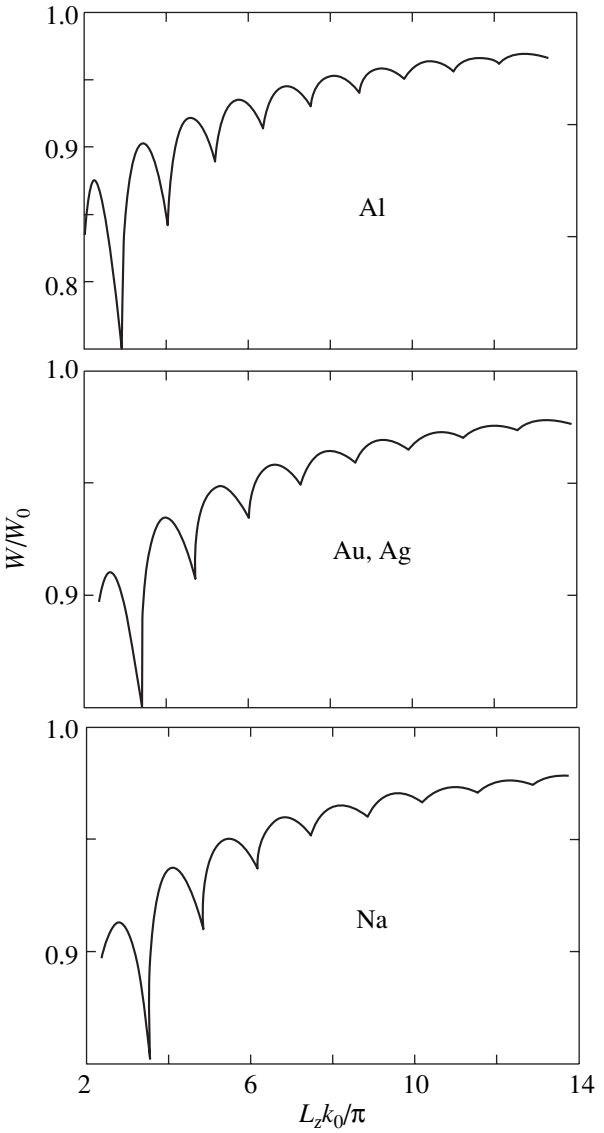

Fig. 2. Thickness dependence of the work function for films of different metals.

In order to clarify the role of the thickness dependence of the bottom of the well, we consider the data presented in Fig. 3. These data are extracted from the results of the self-consistent calculations performed in [20]. In that work, the electron energy spectrum was calculated for a self-consistent spherical potential whose form was far from being rectangular. In our equivalent energy diagram, the position of the lowest

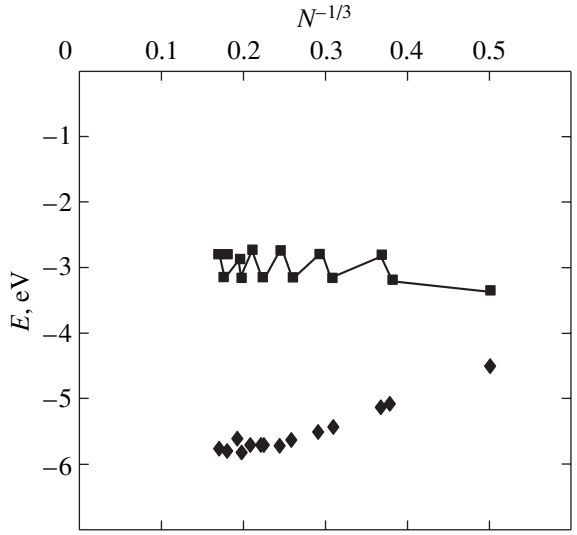

Fig. 3. Calculated positions of the lowest and highest occupied levels in spherical clusters Na_N [20].

occupied level varies with respect to the flat bottom of the potential well and, as the well width is increased (i.e., as $N \longrightarrow \infty$), this level is lowered to the bottom. Hence, we can obtain reliable information on the size dependence of the depth of the rectangular well by determining the confinement behavior of the lowest level in the potential profile corresponding to the spherical cluster [20] (lower points in Fig. 3).

This dependence is close to monotonic and is asymptotically weak. Moreover, it is weaker than the thickness dependence of the Fermi energy in Eq. (32) and gives a minor contribution to Eq. (31). Accounting for the $U(L_z)$ dependence strengthens the inequality $W < W_0$.

Using the data from Fig. 2, we can also determine the contact potential difference $\delta\varphi$. This potential difference (which is much smaller than that predicted in [3]) produces a negative shift of the well depth (for the thinnest film, it attains 0.5 – 1 eV); in turn, this leads to a displacement of the density of states to values corresponding to greater thicknesses. Regarding the contact, the stretched sample acts as an "electron pump" with respect to the shores, alternately ejecting electronic liquid and drawing it back.

In Fig. 4, we show the part of the elastic force related to quantum confinement. It can be seen that the amplitude of force oscillations in magnitude shown in this figure reveals a strong dependence on r_s. For sodium, the oscillation amplitude is 8 times smaller than that for aluminum. The character of this dependence can be determined from Eq. (36) to be $(F_z/N)_i \sim ir_s^3$.

The first maximum of the oscillating part of the force F_z/N for Au (corresponding to a film thickness of one monolayer) is 0.2 nN; i.e., it is much smaller than the experimental value for a wire equal to 1.5 nN [3].

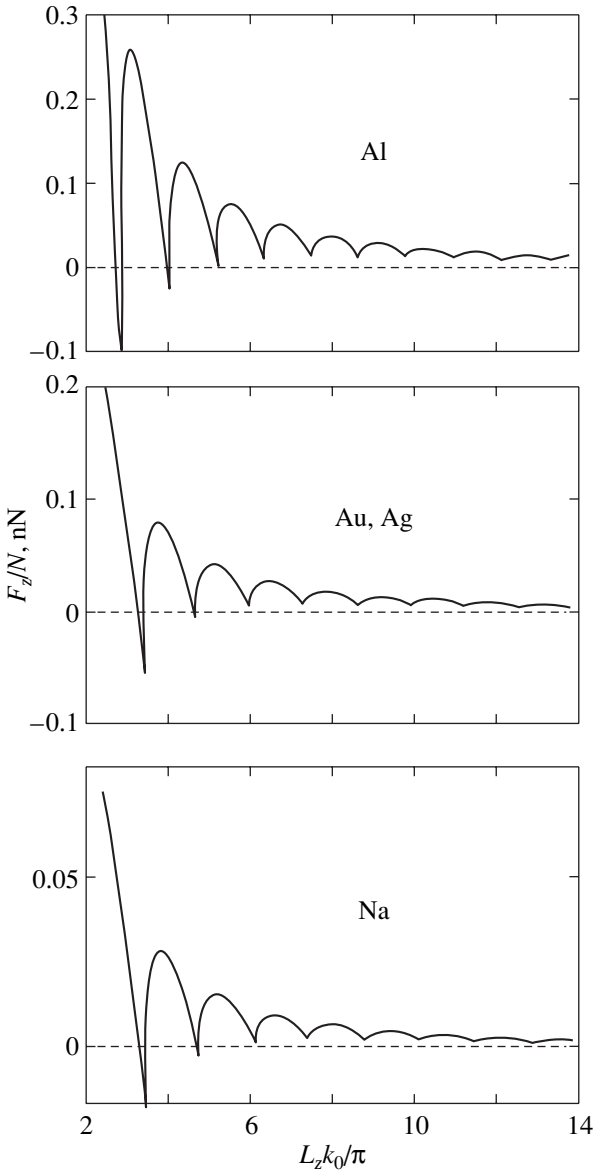

Fig. 4. Component of the elastic force F_z/N oscillating with film thickness.

This difference can be explained by both the difference in the dimensionality of the electron gas in a wire and in a film and the effect of current flowing through a contact estimated in [21]. There are no experimental data for films.

Our estimations showed that, in the case of films in a contact, force oscillations will be analogous in shape and amplitude. Kinks on the curves are possible due to the difference in the density of states of an isolated film and the film in a contact.

ACKNOWLEDGMENTS

This study was supported by the Ministry of Education and Science of Ukraine, project no. 06113.

REFERENCES

1. J. P. Rogers III, P. H. Cutler, T. E. Feuchtwang, and A. A. Lucas, Surf. Sci. **181**, 436 (1987).
2. É. L. Nagaev, Usp. Fiz. Nauk **162** (9), 49 (1992) [Sov. Phys. Usp. **35**, 747 (1992)].
3. M. V. Moskalets, Pis'ma Zh. Éksp. Teor. Fiz. **62** (9), 702 (1995) [JETP Lett. **62**, 719 (1995)].
4. J. M. van Ruitenbeek, M. H. Devoret, D. Esteve, and C. Urbina, Phys. Rev. B **56** (19), 12566 (1997).
5. C. A. Stafford, D. Baeriswyl, and J. Bürki, Phys. Rev. Lett. **79** (15), 2863 (1997).
6. S. Blom, H. Olin, J. L. Costa-Kramer, *et al.*, Phys. Rev. B **57** (16), 8830 (1998).
7. C. Untiedt, G. Rubio, S. Vieira, and N. Agraït, Phys. Rev. B **56** (4), 2154 (1997).
8. G. Rubio-Bollinger, S. R. Bahn, N. Agraït, *et al.*, Phys. Rev. Lett. **87** (2), 026101 (2001).
9. P. J. Feibelman and D. R. Hamann, Phys. Rev. B **29** (12), 6463 (1984).
10. J. C. Boettger, Phys. Rev. B **53** (19), 13133 (1996).
11. A. Kiejna, J. Peisert, and P. Scharoch, Surf. Sci. **54**, 432 (1999).
12. N. Zabala, M. J. Puska, and R. M. Nieminen, Phys. Rev. B **59** (15), 12652 (1999).
13. I. Sarria, C. Henriques, C. Fiolhais, and J. M. Pitarke, Phys. Rev. B **62** (3), 1699 (2000).
14. E. Ogano, N. Zabala, and M. J. Puska, Nanotechnology **13** (3), 363 (2002).
15. J. J. Paggel, C. M. Wei, M. Y. Chou, *et al.*, Phys. Rev. B **66** (23), 233403 (2002).
16. I. T. Iakubov, A. G. Khrapak, L. I. Podlubny, and V. V. Pogosov, Solid State Commun. **53** (4), 427 (1985).
17. K. K. Likharev, Proc. IEEE **87**, 606 (1999).
18. A. N. Smogunov, L. I. Kurkina, and O. V. Farberovich, Fiz. Tverd. Tela (St. Petersburg) **42** (10), 1848 (2000) [Phys. Solid State **42**, 1898 (2000)].
19. V. V. Pogosov, D. P. Kotlyarov, A. Kiejna, and K. F. Wojciechowski, Surf. Sci. **472**, 172 (2001).
20. W. Ekardt, Phys. Rev. B **29** (4), 1558 (1984).
21. M. Brandbyge, J.-L. Mozos, P. Ordejon, *et al.*, Phys. Rev. B **65** (16), 165401 (2002).

Translated by I. Zvyagin

Physics of the Solid State, Vol. 46, No. 3, 2004, pp. 552–556. Translated from Fizika Tverdogo Tela, Vol. 46, No. 3, 2004, pp. 534–537.

LOW-DIMENSIONAL SYSTEMS AND SURFACE PHYSICS

Nanocrystalline Nature of High-Symmetry Ce^{4+}–Eu^{3+} Centers in Silica Gel Glasses

G. E. Malashkevich*, V. N. Sigaev, G. I. Semkova*, and B. Champagnon*****

** Institute of Molecular and Atomic Physics, National Academy of Sciences of Belarus, pr. F. Skoriny 70, Minsk, 220072 Belarus*

e-mail: malash@imaph.bas-net.by

*** Mendeleev University of Chemical Technology, Miusskaya pl. 9, Moscow, 125190 Russia*

**** University of Lyon-1, Villeurbanne Cedex Lyon, 69622 France*

Received April 10, 2003; in final form, July 24, 2003

Abstract—The spectral–luminescent properties of silica gel glasses coactivated by Ce^{4+} and Eu^{3+} ions are investigated. The structure of the glasses is studied using x-ray powder diffraction and small-angle neutron scattering. The inference is drawn that Ce^{4+}–Eu^{3+} centers with high-symmetry Eu(III) oxo complexes, which are formed in the glasses, have nanocrystalline nature. These centers are characterized by a weak vibronic interaction of Eu^{3+} ions with the matrix. The size of nanocrystallites formed under the synthesis conditions and at coactivator concentrations used is approximately equal to 10 nm. © *2004 MAIK "Nauka/Interperiodica".*

1. INTRODUCTION

It is known [1–3] that coactivation of Ln^{3+}-containing silica gel glasses by Ce^{4+} ions can be accompanied by the formation of two types of Ce^{4+}–Ln^{3+} optical centers involving Ln(III) oxo complexes with high or low symmetry. The luminescence spectra of high-symmetry oxo complexes, as a rule, are characteristic of crystalline matrices rather than of vitreous matrices, even though no crystalline phases have been revealed in lightly doped samples. Making allowance for the observed weakening of cross-relaxation quenching of the Nd^{3+} luminescence for high-symmetry Ce^{4+}–Nd^{3+} centers [3], this circumstance gives grounds to assume that such centers are oxide nanoparticles in which Ln^{3+} ions are surrounded by Ce(IV) oxo complexes. However, the mechanism of formation of these centers is poorly understood. Moreover, the presence of nanoinhomogeneities in the glasses under investigation has not been confirmed by direct structural methods. The purpose of the present work was to fill this gap.

2. SAMPLE PREPARATION AND EXPERIMENTAL TECHNIQUE

Samples were prepared using the direct sol–gel–glass transition according to the procedure described in [4]. The glasses were activated by impregnating porous xerogels with cerium and europium chloride solutions at different contents *C*. The xerogels were sintered until the formation of transparent glasses in air at $T = 1250°C$ under identical temperature–time conditions. All reactants used in the synthesis were of special-purity grade.

The luminescence spectra and luminescence excitation spectra were recorded on an SDL-2 spectrofluorimeter and were then corrected for the spectral sensitivity of the recording system and spectral density of exciting radiation, respectively. The spectra were normalized to unity at the maximum of the intensity and were represented in the form of the dependence of the number of photons per unit range of wavelengths $dn/d\lambda$ on the wavelength λ. The complex spectral bands were decomposed into individual components, and their barycenters were determined according to the standard methods of computer processing.

The presence of crystalline phases in glasses was controlled on a DRON-2.0 x-ray diffractometer (λ = 1.54184 nm). The submicrostructure of the glasses was investigated using small-angle neutron scattering (SANS). The dependence of the scattering intensity *I* on the scattering vector $q = 4\pi\sin\theta/\lambda$ [5] was examined in the range $0.01 < q < 0.3$ Å^{-1} on a D11 diffractometer installed on a high-flux nuclear reactor (Institut Laue–Langevin, Grenoble, France). The inhomogeneity sizes were estimated in the Guinier approximation [6] (from the slope of the straight-line portion of the SANS curve in the q^2–$\ln I$ coordinates in the range of small scattering vectors *q* under the assumption that there is a statistically uniform distribution of spherical particles in the homogeneous matrix). The samples were prepared in the form of disks approximately 15 mm in diameter and 10 mm thick.

3. RESULTS

Figure 1 depicts the luminescence spectra (Fig. 1a) and luminescence excitation spectra (Fig. 1b) of low-symmetry (curves *1*, *3*) and high-symmetry (curves *2*, *4*) Ce^{4+}–Eu^{3+} centers in the range of the $^5D_0 \longrightarrow {}^7F_j$

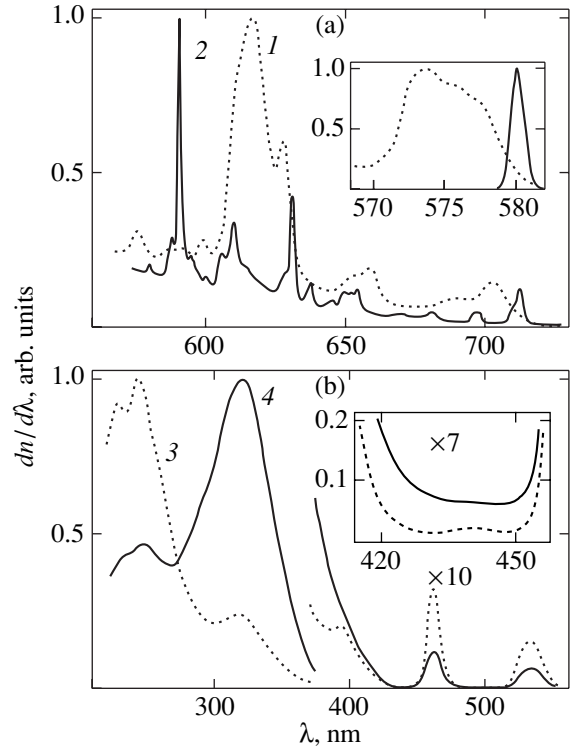

Fig. 1. (a) Luminescence spectra and (b) luminescence excitation spectra of Ce^{4+}–Eu^{3+} centers in silica glasses at coactivator contents C_{CeCl_3} = 2 wt % and C_{EuCl_3} = 1 wt %. λ_{exc} = (*1*) 395 and (*2*) 320 nm. λ_{rec} = (*3*) 615 and (*4*) 591 nm. $\Delta\lambda_{exc}$ = 1 (inset a) and 3 nm (total spectra, inset b). $\Delta\lambda_{rec}$ = 0.3 (inset a) and 1 nm (total spectra, inset b). T = 77 (inset a) and 298 K (total spectra, inset b).

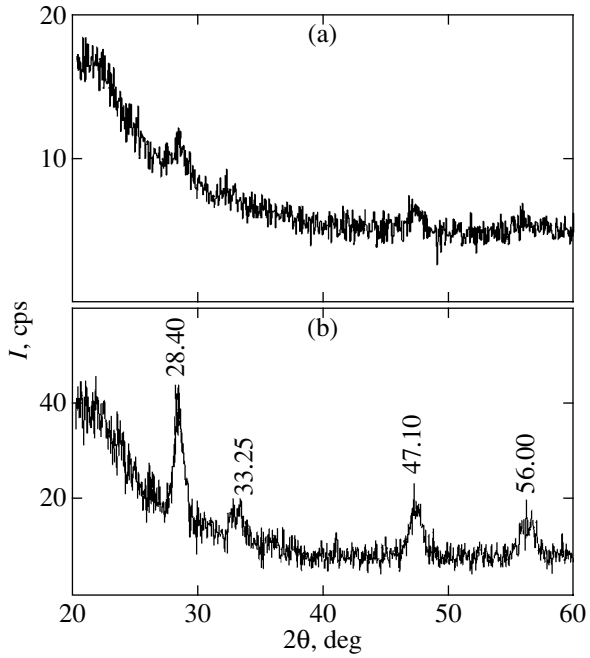

Fig. 2. X-ray diffraction patterns of silica gel glasses containing cerium and europium: (a) C_{CeCl_3} = 2 wt %, C_{EuCl_3} = 1 wt % and (b) C_{CeCl_3} = 6 wt %, C_{EuCl_3} = 0.6 wt %.

transitions in silica glasses at coactivator contents C_{CeCl_3} = 2 wt % and C_{EuCl_3} = 1 wt %. The half-widths of the excitation ($\Delta\lambda_{exc}$) and recording ($\Delta\lambda_{rec}$) bands in the total spectra at T = 298 K are equal to 3 and 1.0 nm, respectively. The inset to Fig. 1a shows the luminescence spectra of the optical centers in the range of the nonsplit $^5D_0 \longrightarrow {}^7F_0$ band at 77 K. The spectra were measured with a high resolution ($\Delta\lambda_{exc}$ = 1 nm, $\Delta\lambda_{rec}$ = 0.3 nm) and were then normalized to unity at the maximum of the intensity. The inset to Fig. 1b shows the luminescence excitation spectra of the optical centers in the range of the vibronic component of the $^7F_0 \longrightarrow {}^5D_2$ transition at 298 K. These spectra were recorded on an enlarged scale ($\Delta\lambda_{exc}$ = 3 nm, $\Delta\lambda_{rec}$ = 1 nm). It can be seen from Fig. 1 that, compared to the low-symmetry centers excited into the *f*–*f* bands of Eu^{3+} ions (curve *1*, λ_{exc} = 395 nm), the high-symmetry centers excited through a sensitizer (curve *2*, λ_{exc} = 320 nm) are characterized not only by a considerably smaller luminescence branching ratio for the electric dipole transitions but also by a multiple narrowing of the $^5D_0 \longrightarrow {}^7F_0$ band. In the case where the luminescence is recorded at the wavelength λ_{rec} = 617 nm, i.e., in the range of the maximum ratio of the luminescence intensity of the low-symmetry centers to the luminescence intensity of the high-symmetry centers, the luminescence excitation spectrum contains a sufficiently intense vibronic component at $\lambda \sim 440$ nm (curve *3*; see inset). However, this component is not observed when the luminescence excitation spectra are recorded in the range of the maximum luminescence intensity of the high-symmetry centers (λ_{rec} = 591 nm, curve *4*).

Figure 2 presents the x-ray diffraction patterns of silica gel glasses containing cerium and europium at coactivator contents C_{CeCl_3} = 2 wt % and C_{EuCl_3} = 1 wt % (Fig. 2a) and C_{CeCl_3} = 6 wt % and C_{EuCl_3} = 0.6 wt % (Fig. 2b). As can be seen from Fig. 2, the x-ray diffraction pattern of the glass at a low coactivator content exhibits smeared but sufficiently clear peaks at the angles $2\theta \approx 28°$, 47°, and 56° and also indications of a peak at $2\theta \approx 33°$. In the diffraction pattern of the glass at a high coactivator content, the intensities of these peaks are considerably higher, their widths are smaller, and there appear weak peaks (whose intensities are several times lower) at the angles $2\theta \approx 59.0°$, 69.2°, 76.5°, 78.9°, 88.2°, and 95.2° (not shown in Fig. 2). The x-ray

diffraction patterns of nonactivated glasses do not exhibit any indications of crystalline phases.

Figure 3 shows the SANS curves for the nonactivated silica gel glass (curve *1*) and the glass containing cerium and europium at coactivator contents C_{CeCl_3} = 2 wt % and C_{EuCl_3} = 1 wt % (curve *2*). It can be seen that the SANS intensity for the nonactivated glass does not depend on the scattering vector q (the glass is homogeneous on a nanometer scale), whereas the coactivated glass contains nanoinhomogeneities. The SANS curves similar to curve *2* are also observed for the glass doped only with cerium. It should be noted that variations in the temperature–time conditions of synthesis, the doping procedure, and the activator concentration lead to appreciable changes in the slope of the linear portion of the SANS curve in the q^2–ln$I$ coordinates.

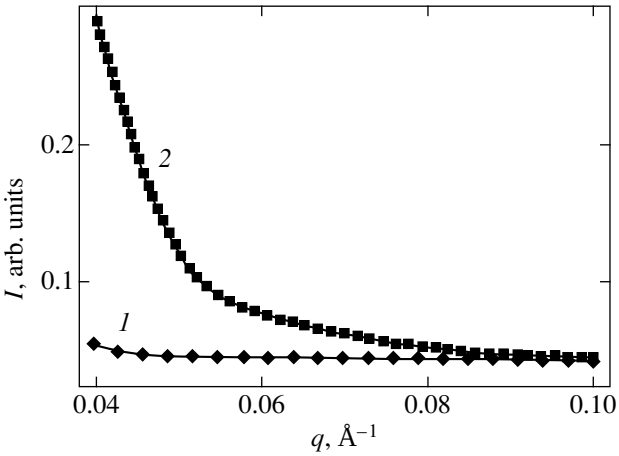

Fig. 3. Dependences of the small-angle neutron scattering intensity on the scattering vector for (*1*) nonactivated silica gel glass and (*2*) glass containing cerium and europium (C_{CeCl_3} = 2 wt %, C_{EuCl_3} = 1 wt %).

4. DISCUSSION

One of the keys to solving the posed problem regarding the elucidation of the nature of high-symmetry Ce^{4+}–Eu^{3+} centers lies in analyzing the luminescence spectra and luminescence excitation spectra shown in the insets to Fig. 1. First and foremost, it is worth noting that, compared to the luminescence spectrum of low-symmetry centers, the luminescence spectrum of high-symmetry centers is characterized by a multiple narrowing of the $^5D_0 \longrightarrow {}^7F_0$ band of Eu^{3+} ions. The half-width $\Delta\lambda$ of this band for high-symmetry centers is equal to 1.0 nm ($\Delta\tilde{\nu} \sim 30$ cm^{-1}). This value is close to the half-width of the analogous band for oxides (~30 cm^{-1} for the dominant type of centers at T = 298 K) [7] and is three times less than the half-width characteristic of europium-containing silica gel glasses upon selective laser excitation at T = 77 K [8]. These findings can be a weighty argument in support of the nanocrystalline nature of the high-symmetry centers, especially as the fraction of surface ions in these nanocrystallites and, correspondingly, the inhomogeneous broadening should be considerably larger than those for oxide powders. Moreover, the actual half-width of the $^5D_0 \longrightarrow {}^7F_0$ band for high-symmetry centers can be substantially narrower than that observed in our experiment, because the very low intensity of this band due to the decrease in the efficiency of excitation of the above centers with a decrease in the temperature T[1] made the use of a higher spectral resolution impossible. The second argument in support of the nanocrystalline nature of the high-symmetry centers is the absence of a pronounced vibronic component of the $^7F_0 \longrightarrow {}^5D_2$ transition in their luminescence excitation spectrum (cf. curves *3*, *4*). The calculated energy spacing between the barycenters of the corresponding bands in curve *3* is found to be $\tilde{\nu} \approx 1080$ cm^{-1}, which is close to the wave number of the stretching vibrations of Si–O–Si bridges [9]. The disappearance of the vibronic component in the spectra of high-symmetry centers as compared to the spectra of complex centers with low-symmetry Eu(III) oxo complexes indicates that the structural units of the matrix are displaced from the high-symmetry centers. In this case, the low symmetry of the latter centers that are not transformed into oxide nanoparticles can be associated with the disturbing effect of single Ce^{4+} ions incorporated into the first cation shell of isolated Eu^{3+} ions. As was noted in [2], the Ce^{4+} ions can play the role of buffer units that facilitate the incorporation of highly coordinated Ln^{3+} ions into the silicon–oxygen network. This assumption is confirmed by the fact that the luminescence excitation spectra of low-symmetry Ce^{4+}–Eu^{3+} centers do not exhibit a pronounced vibronic component, which corresponds to vibrations of the Si–O^- bonds ($\tilde{\nu} \approx 910$ cm^{-1}) and is characteristic of the Eu–O chemical clusters formed in silica gel glass containing europium [8, 10]. Therefore, the formation of isolated low-symmetry Ce^{4+}–Eu^{3+} centers seems to be quite reasonable.

According to [11], cerium dioxide has a cubic lattice with space group of symmetry O_h^5–$Fm3m$, in which the coordination number of the cations is 8. In [2], it was demonstrated that, in high-symmetry complex centers, Eu^{3+} ions also form [EuO_8] polyhedra with cubic symmetry. Therefore, it can be assumed that these centers are formed upon replacement of cerium ions by triply charged europium ions in CeO_2 nanoparticles. Since the radius of Eu^{3+} ions is 18% larger than the radius of Ce^{4+} ions [12], the Eu(III) oxo complex upon this

[1] The origin of this effect will be analyzed in a separate work.

replacement is compressed by the structural framework of the nanoparticle, which should result in an increase in the degree of covalence of the Eu–O bond. Most likely, it is this circumstance that is responsible for the considerable shift (by approximately 4 nm or 120 cm^{-1}) of the barycenter of the $^5D_0 \longrightarrow {}^7F_0$ band ($\bar{\lambda} \sim 580$ nm) toward the long-wavelength range in the luminescence spectrum of the high-symmetry centers as compared to that of the low-symmetry centers (Fig. 1a). Moreover, since the studied glasses contain no alkali and alkaline-earth elements, the Ce^{4+} ion can be replaced by the Eu^{3+} ion without local charge compensation. This is supported by the fact that the symmetry of the ligand field in a rigid silicon–oxygen matrix is retained with a change in the valence of the rare-earth activator, and the total charge compensation can be provided by defects in the matrix [13].

The analysis of the x-ray diffraction patterns of the glasses containing cerium and europium (Fig. 2) revealed the presence of the crystalline phase in both the lightly and heavily doped samples. According to the data available in the JCPDS-1998 Powder Diffraction File, the Bragg reflections at the angles $2\theta = 28.55°$, 33.10°, 47.48°, 56.34°, 59.09°, 62.42°, 76.70°, 79.08°, 88.43°, and 95.41° with relative intensities of 1.0, 0.27, 0.46, 0.34, 0.06, 0.06, 0.12, 0.07, 0.10, and 0.09 correspond to the CeO_2 cubic lattice with space group $Fm3m$. These data are in good agreement with the locations and intensities of the narrow peaks in the x-ray diffraction patterns shown in Fig. 2. From general considerations, we can draw the conclusion that the content of the crystalline phase even in the lightly doped sample is no less than 5%. Judging from the width of the diffraction peaks in Fig. 2a and the absence of opalescence in the samples, the crystallite sizes are substantially less than 1 μm. These results support the assumption that the high-symmetry Ce^{4+}–Eu^{3+} centers are formed through the replacement of cerium by europium in CeO_2 nanoparticles; more precisely, they confirm the existence of the necessary prerequisite for the above replacement, i.e., the presence of the CeO_2 nanoparticles in the glass samples.

The presence of nanoinhomogeneities in the glasses containing cerium and europium is directly confirmed by the dependence of the SANS intensity on the scattering vector q (Fig. 3, curve *2*). The diameter of these inhomogeneities was determined in the Guinier approximation [6] with the use of curve *2* and the formula $D = R_g\sqrt{20/3}$, where $R_g = \sqrt{-3\Delta \ln I/\Delta q^2}$ is the gyration radius of inhomogeneities and the ratio $\Delta \ln I/\Delta q^2$ is calculated from the linear portion of the dependence $\ln I(q^2)$ in the range of small scattering vectors q. The calculated diameter of inhomogeneities was approximately equal to 10 nm. Since the SANS intensity I for the nonactivated glass is almost completely independent of the scattering vector q, we can assert that the observed inhomogeneities are not inherent in the initial matrix and arise upon activation of the glasses by rare-earth ions.

The change in the slope of the linear portion of the SANS curve in the q^2–$\ln I$ coordinates with variations in the doping procedure and the temperature–time conditions of synthesis is explained by the change in the size of the nanoparticles.

5. CONCLUSIONS

Thus, the experimental results obtained in this work can be summarized as follows.

(1) The half-width of the $^5D_0 \longrightarrow {}^7F_0$ band of Eu^{3+} ions in the luminescence spectra of high-symmetry complex Ce^{4+}–Eu^{3+} centers in the silica gel glasses containing cerium and europium is characteristic of oxides.

(2) The vibronic component of the $^7F_0 \longrightarrow {}^5D_2$ transition, which is associated with the vibrations of structural units of the matrix, is not observed in the luminescence excitation spectrum of high-symmetry Ce^{4+}–Eu^{3+} centers.

(3) The x-ray diffraction patterns of the silica gel glasses containing cerium and europium exhibit maxima attributed to the CeO_2 lattice. The structure of this lattice is identical to that of Eu(III) oxo complexes in high-symmetry complex centers.

(4) The glass under investigation contains nanoinhomogeneities ~10 nm in size. This confirms the assertion that the high-symmetry Ce^{4+}–Eu^{3+} centers are oxide nanoparticles in which Eu^{3+} ions are surrounded by Ce(IV) oxo complexes.

ACKNOWLEDGMENTS

We are grateful to V.I. Akimov for his assistance in performing the x-ray diffraction powder analysis.

This work was supported by the Belarussian Foundation for Basic Research (project no. F02R-003), the Russian Foundation for Basic Research (project no. 02-03-81002), and the "Science for Peace" NATO program (grant no. SfP 977980).

REFERENCES

1. G. E. Malashkevich, E. N. Poddenezhnyĭ, I. M. Mel'nichenko, and A. V. Semchenko, Fiz. Tverd. Tela (St. Petersburg) **40** (3), 458 (1998) [Phys. Solid State **40**, 420 (1998)].
2. G. E. Malashkevich, A. G. Makhanek, A. V. Semchenko, *et al.*, Fiz. Tverd. Tela (St. Petersburg) **41** (2), 229 (1999) [Phys. Solid State **41**, 202 (1999)].
3. G. E. Malashkevich, G. I. Semkova, V. E. Gaĭshun, and A. V. Mudryĭ, Pis'ma Zh. Éksp. Teor. Fiz. **74** (7), 426 (2001) [JETP Lett. **74**, 388 (2001)].
4. G. E. Malashkevich, E. N. Poddenezhny, I. M. Melnichenko, and A. A. Boiko, J. Non-Cryst. Solids **188**, 107 (1995).

5. K. Ibel, J. Appl. Crystallogr. **9** (4), 296 (1976).
6. A. Guinier and G. Fournet, *Small-Angle Scattering of X-rays* (Wiley, New York, 1955).
7. G. E. Malashkevich, V. A. Lapina, G. I. Semkova, *et al.*, Pis'ma Zh. Éksp. Teor. Fiz. **77** (6), 341 (2003) [JETP Lett. **77**, 291 (2003)].
8. T. Hayakawa and M. Nogami, J. Appl. Phys. **90** (5), 2200 (2001).
9. A. R. Silin' and A. N. Trukhin, *Point Defects and Elementary Excitations in Crystalline and Vitreous SiO_2* (Zinatne, Riga, 1985).
10. M. Nogami and Y. Abe, J. Non-Cryst. Solids **197**, 73 (1996).
11. N. S. Poluéktov, N. P. Efryushina, and S. A. Gava, *Determination of Microquantities of Lanthanides from Luminescence of Phosphor Crystals* (Naukova Dumka, Kiev, 1976).
12. *Chemistry and Periodic Table*, Ed. by K. Saito (Iwarami Shoten, Tokyo, 1979; Mir, Moscow, 1982).
13. G. O. Karapetyan, D. M. Yudin, and D. G. Galimov, Izv. Akad. Nauk SSSR, Ser. Fiz. **31** (5), 809 (1967).

Translated by O. Borovik-Romanova

Physics of the Solid State, Vol. 46, No. 3, 2004, pp. 557–562. Translated from Fizika Tverdogo Tela, Vol. 46, No. 3, 2004, pp. 538–543.

LOW-DIMENSIONAL SYSTEMS AND SURFACE PHYSICS

Low-Energy Electron Bremsstrahlung from Metal Clusters

L. I. Kurkina

Kutateladze Institute of Thermal Physics, Siberian Division, Russian Academy of Sciences, pr. Akademika Lavrent'eva 1, Novosibirsk, 630090 Russia

e-mail: kurkina@itp.nsc.ru

Received July 29, 2003

Abstract—Expressions are derived allowing numerical calculation of the matrix element of the dipole moment between states that belong to a continuous spectrum for the case where a charged particle in an arbitrary orbital state is scattered by a spherically symmetric short-range potential. The calculation scheme is based on expanding a diverging matrix element into a sum of converging integrals. The method is used to study static bremsstrahlung of a slow electron scattered by sodium clusters. The bremsstrahlung cross section is shown to be resonant. The resonances arise at certain energies (depending on a cluster) of an electron having emitted a photon and are due to electron capture on quasi-steady-state levels. © *2004 MAIK "Nauka/Interperiodica".*

1. INTRODUCTION

Bremsstrahlung that is emitted when a charged particle is scattered by a target characterized by an intrinsic electronic structure (atom, cluster, solid) consists of two components, "ordinary" (static) and polarization (dynamic) bremsstrahlung [1, 2]. In the former case, an incident charged particle emits radiation when being decelerated in the target static field. In the latter case, an incident particle virtually excites target electrons, which emit photons in passing to the initial state. The polarization component of bremsstrahlung is closely related to the target polarizability and exhibits resonances at the same photon energies as the dynamic polarizability. Judging from the conventional models, the static-bremsstrahlung cross section of a charged particle scattered by an atom varies monotonically as the photon energy increases. The peaks observed in the bremsstrahlung spectra of charged particles colliding with atoms are associated with the polarization component and lie near the ionization thresholds of the atomic electron shells or near the energies of dipole transitions between discrete energy levels. Although the dynamic-polarizability spectra of metal clusters exhibit features caused by one-electron transitions, the resonance associated with excitation of dipole surface plasma oscillations is dominant in them [3–6]. Calculations of fast-electron bremsstrahlung in scattering by metal clusters [7–9] showed that, near the surface-plasmon energy, the polarization component should be three to four orders of magnitude more intense than the ordinary bremsstrahlung. However, the latter component becomes prevalent below the surface-plasmon energy. Since the Born approximation is inapplicable to slow-electron scattering and the bremsstrahlung cross section cannot be expressed in terms of the form factor (as was done, e.g., in [7–9]), the problem of calculating the radial matrix elements of radiative transitions between states belonging to the continuous spectrum needs to be solved. The point is that these matrix elements involve diverging integrals taken from zero to infinity. Earlier studies of electron–atom collisions were restricted to the case of *s*-electron scattering [10, 11]. Later on, the approach based on the following procedure became popular. Within a certain range $0 < r \le r_0$, the matrix element is constructed in terms of wave functions that were found by numerically solving the corresponding radial Schrödinger equation and numerical integration is carried out using numerical methods. At $r \ge r_0$, asymptotic expressions are used for the wave functions and the corresponding integrals are calculated analytically [12–18]. However, the approximations indicated above are invalid in the case of slow-electron scattering on metal clusters, because states with large orbital angular momenta (orbital numbers) make a significant contribution to the cross section of electron–metal-cluster static bremsstrahlung. Calculations of the electron phase shifts in scattering by various metal clusters have shown that, e.g., for an Na_{20} cluster target, states with orbital numbers ranging from zero to at least three should be included in the static-bremsstrahlung calculation even for an initial electron energy of ~0.1 eV. As the cluster size and the electron energy increase, the number of orbital states that must be included increases rapidly. If the incident electron energy is low and the orbital angular momentum is large, then the radial wave function reaches its asymptotic value to an acceptable accuracy at so large a value of r_0 that numerical calculation of the diverging oscillating integral over the range from zero to r_0 cannot be performed to a reasonable accuracy and yields meaningless results. We also note that the value of the integral in this case oscillates with increasing r_0.

In this paper, we develop a numerical technique for calculating the matrix element of the dipole moment in

the case of electron scattering by a spherical short-range potential. In this technique, the diverging integral is expanded into a sum of converging integrals, which makes it possible to include the states of an incident electron with any orbital angular momentum. The technique is applied to study electron–sodium-cluster static bremsstrahlung, and it is shown that the static-bremsstrahlung cross section is resonant in the case of slow-electron scattering by metal clusters.

2. FORMALISM

We describe clusters in terms of the "jellium" model, in which valence electrons are assumed to move in the field of a homogeneous positively charged background of uniformly spread cluster ions. This model describes the electronic properties of clusters with weakly bound valence electrons well [3, 4, 6], such as alkali-metal clusters. In the jellium model, spheres with closed electron shells correspond to the most stable clusters (with a "magic" number of valence electrons). The potential of a jellium sphere rapidly tends to zero outside the positive background and can be closely approximated by a spherically symmetric square potential well with a rounded edge.

In the nonrelativistic dipole approximation, the static-bremsstrahlung cross section of a charged particle moving in an external force field can be expressed in terms of the dipole moment matrix element between states belonging to the continuous spectrum [19]. In the case of electron scattering from a spherically symmetric potential $V(r)$, by expanding the wave function of the incident particle in partial waves, the bremsstrahlung cross section σ can be reduced to the following form [20] (in the system of units where $\hbar = 2m = 1$, $e^2 = 2$, energies are measured in rydbergs and lengths in units of the Bohr radius a_0)

$$\omega\left(\frac{d\sigma}{d\omega}\right) = \frac{16\omega^4}{3c^3k_1^3k_2}\sum_{l_1l_2} l_> \left|D_{l_2l_1}\right|^2, \quad (1)$$

where

$$D_{l_2l_1} = \int_0^\infty u_{l_2}(k_2, r) r u_{l_1}(k_1, r) dr, \quad (2)$$

$u_l(k, r)$ is the solution to the radial Schrödinger equation for an electron in the field $V(r)$, ω is the photon energy, c is the speed of light, and k_1 and l_1 (k_2, l_2) are the momentum and orbital quantum number of the incident (scattered) electron, respectively; for dipole radiation, we have $l_2 = l_1 \pm 1$ and $l_> = \max\{l_1, l_2\}$.

In terms of the theory of the electron density functional [21], the potential of the spherical jellium cluster is given by

$$V(r) = \frac{1}{4\pi}\int V(\mathbf{r}) d\Omega,$$
$$V(\mathbf{r}) = 2\int \frac{\rho(\mathbf{r}') - \rho^+(\mathbf{r}')}{|\mathbf{r} - \mathbf{r}'|} d\mathbf{r}' + V_{xc}(\mathbf{r}), \quad (3)$$

where

$$\rho(\mathbf{r}) = \sum_i^{occ} |\psi_i(\mathbf{r})|^2$$

is the cluster electron density (occ indicates that summation is performed over all occupied states), the one-electron wave functions $\psi_i(\mathbf{r})$ are self-consistent solutions to the time-independent Schrödinger equation with the potential given by Eq. (3) (the Kohn–Sham equation)

$$[-\nabla^2 + V(\mathbf{r})]\psi_i(\mathbf{r}) = E_i\psi_i(\mathbf{r}),$$

$\rho^+(r) = 3\Theta(R - r)/4\pi r_s^3$ is the density of the positive jellium background (which is equal in magnitude to the average density of valence electrons in the corresponding bulk metal), $\Theta(R - r)$ is the Heaviside step function, $R = r_s N^{1/3}$ is the radius of the positive background of the jellium sphere (the cluster radius), N is the number of cluster atoms (which is equal to the number of valence electrons in the cluster for alkali metals), r_s is the Wigner–Seitz radius, and $V_{xc}(\mathbf{r})$ is the local exchange-correlation potential (in this study, we employ the parametrization used by Vosko *et al.* [22]).

Let d be the potential $V(r)$ range (radius). In the range $0 < r \le d$, numerical calculation of the matrix element $D_{l_2l_1}$ does not present any difficulties. In this range, the electron wave functions $u_l(k, r)$ before and after scattering on a cluster can be readily obtained by numerically integrating (e.g., using Milne's method [23]) the radial Schrödinger equation with the potential $V(r)$ for the energy $E = k^2$.

The major problem consists in correctly calculating Eq. (2) in the range $d \le r < \infty$, since the integral diverges as r increases. Since the jellium sphere potential $V(r)$ decreases rapidly to zero in the range $R < r < d$, the wave function $u_l(k, r)$ at $r \ge d$ can be written as a combination of regular and irregular (at zero) solutions to the Schrödinger equation for a free electron (the spherical Bessel $j_l(kr)$, and Neumann functions $n_l(kr)$)

$$u_l(k, r) = kr\cos\delta_l[j_l(kr) - \tan\delta_l n_l(kr)], \quad (4)$$

where δ_l is the phase shift of an electron with momentum k and orbital quantum number l scattered by the potential $V(r)$ (this phase shift is determined from the continuity condition of the wave function $u_l(k, r)$ and its first derivative at the point $r = d$). Substitution of Eq. (4) into

Eq. (2) at $r \geq d$ yields a sum of diverging integrals of the products of Bessel and Neumann functions and r^3:

$$\int_d^\infty u_{l_2}(k_2, r) r u_{l_1}(k_1, r) dr = k_1 k_2 \cos\delta_{l_1} \cos\delta_{l_2} \times [I_1 - \tan\delta_{l_1} I_2 - \tan\delta_{l_2} I_3 + \tan\delta_{l_1} \tan\delta_{l_2} I_4],$$

where

$$I_1 = \int_d^\infty j_{l_2}(k_2 r) j_{l_1}(k_1 r) r^3 dr,$$

$$I_2 = \int_d^\infty j_{l_2}(k_2 r) n_{l_1}(k_1 r) r^3 dr,$$

$$I_3 = \int_d^\infty n_{l_2}(k_2 r) j_{l_1}(k_1 r) r^3 dr,$$

$$I_4 = \int_d^\infty n_{l_2}(k_2 r) n_{l_1}(k_1 r) r^3 dr.$$

Using the recurrent relation for the Bessel and Neumann functions (see [23])

$$z_{l+1}(kr) = \frac{2l+1}{kr} z_l(kr) - z_{l-1}(kr), \quad (5)$$

where $z_l(kr)$ stands for $j_l(kr)$ or $n_l(kr)$, the integrals I_i ($i = 1, 2, 3, 4$) can be written as

$$\int_d^\infty x_{l_2}(k_2 r) y_{l_1}(k_1 r) r^3 dr = (-1)^{t+s} \int_d^\infty x_g(k_2 r) y_t(k_1 r) r^3 dr + \sum_{p=s}^{l_1-1} (-1)^{p+s} \frac{2(l_1-p)+1}{K} \int_d^\infty x_{l_1-p}(k_2 r) y_{l_1-p}(k_1 r) r^2 dr. \quad (6)$$

Here, $x_l(kr)$ stands for $j_l(kr)$ or $n_l(kr)$; $y_l(kr)$ stands for $j_l(kr)$ or $n_l(kr)$; $g = 0$ and $t = 1$ for odd values of l_1; $g = 1$ and $t = 0$ for even values of l_1; $s = 0$ for $l_2 = l_1 + 1$ ($l_1 \geq 1$); $s = 1$ for $l_2 = l_1 - 1$ ($l_1 \geq 2$); $K = k_1$ for odd p; and $K = k_2$ for even p.

For the integrals under the summation sign in Eq. (6), further expansion can be carried out using recurrent relation (5):

$$\int_d^\infty x_l(k_2 r) y_l(k_1 r) r^2 dr = \int_d^\infty x_s(k_2 r) y_s(k_1 r) r^2 dr + \frac{1}{k_1 k_2} \sum_{\substack{p=2 \\ (\Delta p = 2)}}^{l-1} (2(l-p)+1)^2 C_{l-p} - \left[\frac{1}{k_1^2} + \frac{1}{k_2^2}\right] \times \sum_{\substack{p=2 \\ (\Delta p = 2)}}^{l-1} (2(l-p)+1) C_{l-p} \sum_{\substack{q=1 \\ (\Delta q = 2)}}^{p-1} (2(l-q)+1) + \frac{2}{k_1 k_2} \sum_{\substack{p=3 \\ (\Delta p = 2)}}^{l-1} (2(l-p)+1) C_{l-p} \sum_{\substack{q=1 \\ (\Delta q = 2)}}^{p-2} (2(l-q)+1) + (-1)^{l+1} \left[\frac{1}{Q_1} \int_d^\infty x_1(k_2 r) y_0(k_1 r) r dr + \frac{1}{Q_2} \int_d^\infty x_0(k_2 r) y_1(k_1 r) r dr\right] \sum_{\substack{p=1 \\ (\Delta p = 2)}}^{l-1} (2(l-p)+1), \quad (7)$$

where $s = 1$, $Q_1 = k_1$, and $Q_2 = k_2$ for odd l; $s = 0$, $Q_1 = k_2$, and $Q_2 = k_1$ for even l; and

$$C_{l-p} = \int_d^\infty x_{l-p}(k_2 r) y_{l-p}(k_1 r) dr.$$

2.1. Calculation of I_1

Let us write I_1 and the corresponding integrals entering Eq. (6) in the form $\int_d^\infty = \int_0^\infty - \int_0^d$. Similarly to Eq. (6), we obtain

$$\int_0^\infty j_{l_2}(k_2 r) j_{l_1}(k_1 r) r^3 dr = (-1)^{t+s} \int_0^\infty j_g(k_2 r) j_t(k_1 r) r^3 dr + \sum_{p=s}^{l_1-1} (-1)^{p+s} \frac{2(l_1-p)+1}{K} \int_0^\infty j_{l_1-p}(k_2 r) j_{l_1-p}(k_1 r) r^2 dr, \quad (8)$$

where g and t take on values 0 or 1 [see comments to Eq. (6)].

Using the explicit expressions [23]

$$j_0(kr) = \frac{\sin kr}{kr},$$

$$j_1(kr) = \frac{\sin kr}{(kr)^2} - \frac{\cos kr}{kr},$$

it can be readily shown that

$$\int_0^\infty j_1(k_2 r) j_0(k_1 r) r^3 dr = 0.$$

for any k_1 and k_2.

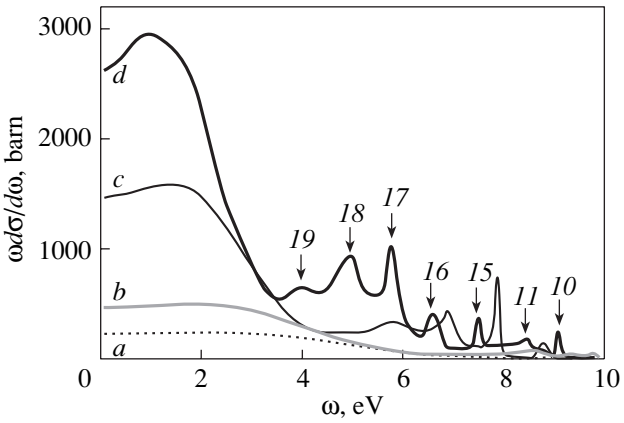

Fig. 1. Spectral dependences of the static-bremsstrahlung cross section of an electron with initial energy E_1 = 10 eV scattered by sodium clusters containing (a) 8, (b) 20, (c) 92, and (d) 196 atoms. The step is $\Delta\omega$ = 0.1 eV. For cluster Na_{196}, arrows indicate the resonances; numerals above the arrows are the orbital quantum numbers l_2 (after the emission of a photon) of electrons subject to resonant scattering.

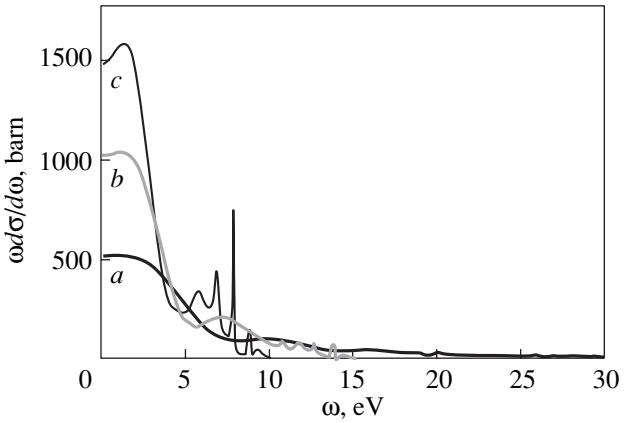

Fig. 2. Spectral dependences of the static-bremsstrahlung cross section of an electron with initial energy (a) E_1 = 30, (b) 15, and (c) 10 eV scattered by a Na_{92} cluster. The step is $\Delta\omega$ = 0.1 eV.

According to the relation [24]

$$\int_0^\infty j_l(k_2r)j_l(k_1r)r^2dr = \frac{\pi}{2k_1^2}\delta(k_1-k_2),$$

we have

$$\int_0^\infty j_l(k_2r)j_l(k_1r)r^2dr = 0$$

for any l and $k_1 \neq k_2$.

Thus, the right-hand side of expression (8) is zero and I_1 reduces to the integral

$$I_1 = -\int_0^d j_{l_2}(k_2r)j_{l_1}(k_1r)r^3dr,$$

which can be easily calculated numerically.

2.2. Calculation of I_2, I_3, and I_4

To calculate I_2, I_3, and I_4, expressions (6) and (7) should be used. All integrals entering these formulas converge and can be derived using conventional numerical and analytical techniques [23, 25].

3. RESULTS

This approach is applied to calculate the bremsstrahlung cross section for electrons scattered by Na clusters ($r_s = 3.98a_0$) with a magic number of atoms. Although this study is aimed at analyzing the bremsstrahlung cross section for electron energies lower than the excitation energy of surface plasmons (for sodium clusters, this energy range is below 3 eV), it is expedient to consider a wider range of energies of incident electrons and emitted photons. Figure 1 shows the spectral dependences of the static-bremsstrahlung cross section of an electron with an initial energy of 10 eV for various sizes of target Na_N clusters (N = 8, 20, 92, 196). The calculation was carried out with the step $\Delta\omega$ = 0.1 eV. As expected, an increase in the cluster size in general causes an increase in the bremsstrahlung cross section. As ω increases, the cross section initially varies slightly, then abruptly decreases, and oscillations arise, whose number increases with the cluster size. The relatively large bremsstrahlung cross section at low energies of emitted photons is associated with strong overlapping of the electron wave functions before and after photon emission. As ω increases, the difference between the electron wave functions before and after emission increases, the overlap between them decreases, and matrix element (2) and cross section (1) also decrease.

Figure 2 shows the dependences of the static bremsstrahlung spectra on the incident electron energy. The bremsstrahlung cross sections are given for an electron with initial energy E_1 = 10, 15, and 30 eV scattered by a Na_{92} cluster. We can see that, as the incident electron energy increases, oscillations in the spectral dependence are smoothed and almost disappear even at E_1 = 30 eV. This means that the spectral dependence of the static-bremsstrahlung cross section should be smooth for fast electrons. However, for slow electrons, oscillations should be pronounced. As calculations showed, the resonances in the bremsstrahlung cross section arise at certain electron energies after the emission of a photon. Figure 3 shows the bremsstrahlung cross section for an electron with initial energy E_1 =

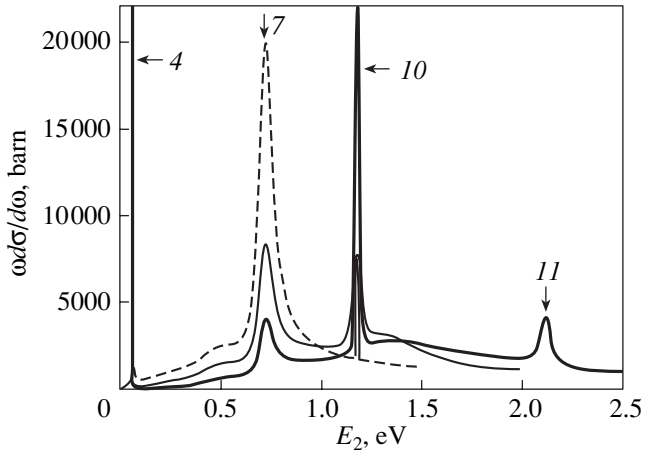

Fig. 3. Static-bremsstrahlung cross section of an electron with initial energy $E_1 = 1.5$ eV (dashed curve), 2.0 eV (thin solid curve), and 2.5 eV (bold solid curve) in the case of scattering by a Na_{92} cluster in relation to the electron energy E_2 after the emission of a photon. The step is $\Delta E_2 = 0.001$ eV. Arrows indicate the resonances; numerals near arrows are the orbital quantum numbers l_2 (after the emission of a photon) for electrons subject to resonant scattering.

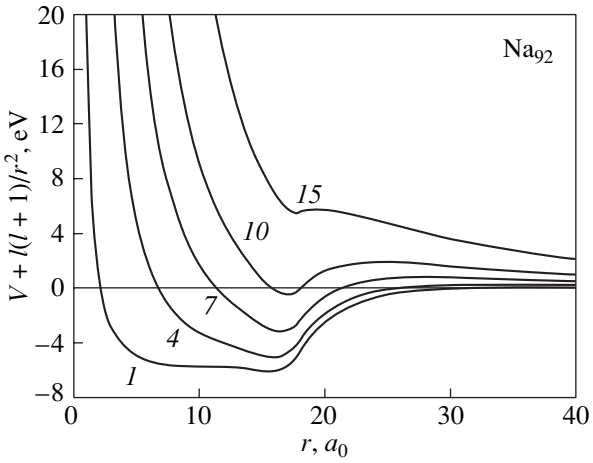

Fig. 4. One-electron potential of the Na_{92} jellium cluster including the centrifugal term for certain orbital quantum numbers l. Numerals near curves indicate the corresponding values of l. The cluster radius is $R = 17.97a_0$.

1.5, 2.0, and 2.5 eV, scattered by a Na_{92} cluster, in relation to the electron energy $E_2 = E_1 - \omega$ after the emission of a photon (the step is $\Delta E_2 = 0.001$ eV). The peak positions coincide in all the curves. An analysis of the results showed that the spectral peaks are caused by the transition of the electron phase shifts δ_{l_2} through $\pi/2$. According to scattering theory, the transition of the electron phase shift through $\pi/2$ means that an electron with a given energy and a given orbital angular momentum can form a quasi-steady state with the target. Thus, after electron deceleration accompanied by the emission of radiation, the electron can be captured on a quasi-steady level, which causes a resonance in the bremsstrahlung cross section. It is clear that a metal cluster has a specific spectrum of possible quasi-steady states. For this reason, the resonances in the bremsstrahlung cross sections are observed only at certain electron energies E_2. For the Na_{196} cluster in Fig. 1 and the Na_{92} cluster in Fig. 3, arrows indicate the bremsstrahlung spectral peaks; the orbital quantum numbers of electrons (after the emission of a photon), whose phase shifts pass through $\pi/2$ at given resonant energies E_2, are indicated by the numerals near the arrows. The contribution from matrix elements (2) for these electrons to cross section (1) near the peaks exceeds the total contribution from all other electronic states. Figures 1 and 3 show that the orbital quantum numbers of the states exhibiting resonant scattering increase with E_2 and have certain upper and lower bounds for every target cluster. Figure 4 shows the potential $V(r) + l(l+1)/r^2$ at various values of l for the Na_{92} cluster. As l increases, the potential well becomes shallower and, hence, the energy of possible quasi-steady states increases. The existence of the minimum value $l_2^{\min}$ for which resonant scattering is still possible is due to a very low height of the barrier or its absence in the system potential at $l_2 < l_2^{\min}$, where there are no allowed states with a positive energy in the potential well. At $l_2 > l_2^{\max}$, the potential well is so shallow (or altogether absent) that it cannot have any states.

For the Na_{92} cluster, it can be seen from Fig. 3 that the resonances at various E_2 have different half-widths Γ; however, Γ is independent of E_1 for each specific resonant value of E_2 (although the peak height changes). From the half-width Γ, we can estimate the lifetime of the quasi-steady state of the "cluster plus electron" system by using the uncertainty relation $\tau = \hbar/\Gamma$. For example (see Fig. 3), for the resonances at $E_2 \approx 0.73$ eV ($l_2 = 7$) and $E_2 \approx 2.12$ eV ($l_2 = 11$), we have $\Gamma \sim 0.1$ eV, which corresponds to the lifetime $\tau \sim 10^{-14}$ s. This lifetime is comparable to the time of flight of an electron with an energy of 1 eV through the cluster field range. The lifetime of quasi-steady states corresponding to the resonances at $E_2 \approx 0.065$ and 1.185 eV ($l_2 = 4$ and 10, respectively) is two orders of magnitude longer.

4. CONCLUSIONS

In summary, we note that the technique developed here for numerically calculating the static-bremsstrahlung cross section in a short-range spherically symmetric potential makes it possible to correctly include the contributions from all orbital states of an incident electron. In studying the bremsstrahlung of slow electrons scattered by metal clusters, this is an important factor, since the bremsstrahlung cross sections exhibit peaks due to resonant electron scattering in states with large

orbital quantum numbers. The resonances arise at electron energies (after the emission of a photon) that are specific for a cluster and caused by electron capture on quasi-steady levels. The resonance width (the lifetime of quasi-steady states) is independent of the energy E_1 of the incident electron. However, the strength of resonant peaks decreases as E_1 increases; therefore, the static-bremsstrahlung cross section for fast electrons should be smooth.

ACKNOWLEDGMENTS

This study was supported by the Russian Foundation for Basic Research (project no. 03-03-32055) and the federal program "Fundamental Problems in the Physics and Chemistry of Nanometer Systems and Nanomaterials" (project no. 8.5).

REFERENCES

1. *Polarized Bremsstrahlung from Particles and Atoms*, Ed. by V. N. Tsytovich and I. M. Oĭringel' (Nauka, Moscow, 1987).
2. V. A. Astapenko, L. A. Bureeva, and V. S. Lisitsa, Usp. Fiz. Nauk **172** (2), 155 (2002) [Phys. Usp. **45**, 149 (2002)].
3. W. Ekardt, Phys. Rev. B **31** (10), 6360 (1985).
4. D. E. Beck, Phys. Rev. B **35** (14), 7325 (1987).
5. K. Selby, V. Kresin, J. Masui, *et al.*, Phys. Rev. B **43** (6), 4565 (1991).
6. L. I. Kurkina and O. V. Farberovich, Phys. Rev. B **54** (20), 14791 (1996).
7. J. P. Connerade and A. V. Solov'yov, J. Phys. B **29** (15), 3529 (1996).
8. A. V. Korol and A. V. Solov'yov, J. Phys. B **30** (5), 1105 (1997).
9. L. G. Gerchikov, A. N. Ipatov, and A. V. Solov'yov, J. Phys. B **31** (10), 2331 (1998).
10. O. B. Firsov and M. I. Chibisov, Zh. Éksp. Teor. Fiz. **39** (6), 1770 (1960) [Sov. Phys. JETP **12**, 1235 (1960)].
11. T. Ohmura and H. Ohmura, Phys. Rev. **121** (2), 513 (1961).
12. J. L. Stilley and J. Callaway, Astrophys. J. **160** (4), 245 (1970).
13. H. K. Tseng and R. H. Pratt, Phys. Rev. A **3** (1), 100 (1971).
14. M. S. Pindzola and H. P. Kelly, Phys. Rev. A **14** (1), 204 (1976).
15. M. Aymar and M. Crance, J. Phys. B **13** (9), L287 (1980).
16. J. Vackář, A. Šimůnek, and O. Šipr, Comput. Phys. Commun. **66** (2–3), 259 (1991).
17. A. V. Korol, A. G. Lyalin, and A. V. Solov'yov, J. Phys. B **28** (22), 4947 (1995).
18. C. D. Shaffer, R. H. Pratt, and S. D. Oh, Phys. Rev. A **57** (1), 227 (1998).
19. V. B. Berestetskiĭ, E. M. Lifshitz, and L. P. Pitaevskiĭ, *Quantum Electrodynamics*, 3rd ed. (Nauka, Moscow, 1989; Pergamon, Oxford, 1982).
20. V. P. Kraĭnov and B. M. Smirnov, *Emission Processes in Atomic Physics* (Vysshaya Shkola, Moscow, 1983).
21. *Theory of the Inhomogeneous Electron Gas*, Ed. by S. Lundqwist and N. H. March (Plenum, New York 1983; Mir, Moscow, 1987).
22. S. H. Vosko, L. Wilk, and M. Nusair, Can. J. Phys. **58** (8), 1200 (1980).
23. *Handbook of Mathematical Functions with Formulas, Graphs and Mathematical Tables*, Ed. by M. Abramowitz and I. A. Stegun (National Bureau of Standards, Washington, 1964; Nauka, Moscow, 1979).
24. I. P. Grant and H. M. Quiney, J. Phys. A **26** (24), 7547 (1993).
25. I. S. Gradshteyn and I. M. Ryzhik, *Table of Integrals, Series, and Products*, 4th ed. (Nauka, Moscow, 1971; Academic, New York, 1980).

Translated by A. Kazantsev

Physics of the Solid State, Vol. 46, No. 3, 2004, pp. 563–568. Translated from Fizika Tverdogo Tela, Vol. 46, No. 3, 2004, pp. 544–548.

LOW-DIMENSIONAL SYSTEMS AND SURFACE PHYSICS

Growth of an Eu–Si(111) Thin Film Structure: The Stage of Silicide Formation

T. V. Krachino, M. V. Kuz'min, M. V. Loginov, and M. A. Mittsev

Ioffe Physicotechnical Institute, Russian Academy of Sciences, Politekhnicheskaya ul. 26, St. Petersburg, 194021 Russia

Received July 31, 2003

Abstract—Silicide formation in thin films produced by depositing Eu atoms on the Si(111) surface is studied using LEED, Auger electron spectroscopy, contact potential difference, and isothermal thermal-desorption spectroscopy. It is shown that if Eu is deposited on a substrate at room temperature, the growing film is disordered and consists of almost pure Eu. At high temperatures ($T \geq 500$ K), the Eu–Si(111) system forms through the Stranski–Krastanow mechanism; namely, first a two-dimensional transition layer (reconstruction) with the (2×1) structure forms and then three-dimensional silicide crystallites grow on it. A specific feature of this system is a low rate of diffusion of Si atoms in the europium silicides. This feature accounts for the concentration gradient of Si atoms across the silicide film thickness and, as a consequence, the multiphase film composition.

1. INTRODUCTION

Investigation of the interfaces between rare earth (RE) metals and silicon is of interest both for obtaining information on the interaction of RE metals with silicon and because thin RE silicide films that form on the surface of silicon are promising candidates for use in integrated microelectronics [1–3]. Their successful application requires, as a prerequisite, good knowledge of the growth mechanisms and morphology of films forming for various conditions under which RE metals are deposited on the silicon surface.

The interaction of Eu atoms with the Si(111) surface was studied in [4–6]. The Eu was deposited on a substrate maintained at room temperature, and then the Eu–Si(111) structure thus formed was annealed at a certain temperature. By contrast, in our studies [7, 8], Eu atoms were deposited on a heated substrate. The results obtained in those experiments related primarily to the submonolayer coverage range. According to those studies, a film structure forms in two steps, namely, in an adsorption stage, in which an adsorbed transition layer (reconstruction) grows on the surface, and in a silicide formation stage. Our previous studies [7, 8] dealt primarily with the adsorption stage. The present communication discusses the results obtained in the stage of silicide formation.

2. EXPERIMENTAL

The studies were conducted on a setup based on an USU-4 ultrahigh-vacuum chamber described in detail in [9]. The base pressure in the vacuum chamber was 6×10^{-11} Torr, and the pressure during deposition of the RE metal on silicon did not exceed 1×10^{-9} Torr.

Substrates were $40 \times 2 \times 0.3$-mm, (111)-oriented silicon strips cut from an *n*-type phosphorus-doped silicon plate with an electrical resistivity of ~10 Ω cm. Prior to being placed in the chamber, the strips were treated using the Shiraki method [10].

We used isothermal thermal-desorption spectroscopy (ITDS), Auger electron spectroscopy (AES), low-energy electron diffraction (LEED), and the contact potential difference (CPD) method.

Eu was deposited on a silicon surface at a substrate temperature T_s ranging from room temperature to 1000 K. Measurements were conducted with substrates maintained at room temperature. The ITDS experiments were described in considerable detail in [11].

The temperature of a substrate was monitored by measuring the electric current passing through it. For the range $T > 1000$ K, the temperature was calibrated by means of a Piro optical pyrometer, and for $T < 1000$ K, with an IRCON infrared optical pyrometer.

The Eu was deposited from tantalum cells using indirect radiation heating. The calibration of the RE flux intensity directed from the cells onto a silicon surface was described in [11]. One-monolayer (ML) coating ($\theta = 1$) is defined as that at which there is one RE metal atom for each surface atom of the unreconstructed Si(111)-(1×1) face. To one monolayer corresponds a surface concentration of Eu atoms of 7.84×10^{14} cm^{-2}. In all experiments, the rate of europium deposition on the silicon surface was ~0.01 ML/s.

3. EXPERIMENTAL RESULTS

3.1. Low-Energy Electron Diffraction

The structural studies performed by LEED showed that, when Eu is deposited on a substrate maintained at

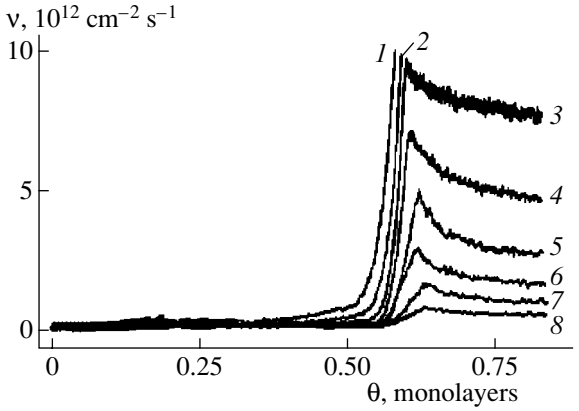

Fig. 1. Concentration dependences of the ITDS data at various Eu deposition temperatures T_s on the substrate: (*1*) 1135, (*2*) 1110, (*3*) 1080, (*4*) 1045, (*5*) 1025, (*6*) 1005, (*7*) 985, and (*8*) 965 K.

300 K, the diffraction pattern of the (7 × 7) structure disappeared gradually (as in [7, 8]) to be replaced by reflections of the (1 × 1) structure, which persisted up to coverages of 0.75–0.80. At higher coverages, only a diffuse background was observed. This behavior indicates that at room temperature a disordered Eu film grows on the silicon surface; the observed (1 × 1) diffraction pattern may be caused by electrons diffracted from a part of the surface not occupied by Eu atoms.

When europium is deposited on a substrate heated to a temperature $T \geq 750$ K or higher, a series of superstructures form within the region of submonolayer coverage; these superstructures replace one another as the surface coverage by Eu atoms increases. Rather than dwelling here on the totality of the superstructures whose nature and properties were discussed earlier in [7, 8], we mention the following observation. The (2 × 1) structure corresponding to the densest (substrate-matched) adsorbed layer of europium atoms appears at surface coverages $\theta \sim 0.5$–0.6. The upper limit of the coverages θ_c at which the diffraction pattern of this structure is still observed depends on the Eu deposition temperature. For instance, for $T_s = 800$ K, we have $\theta_c = 10$; for $T_s = 900$ K, $\theta_c = 30$; and for $T_s = 1000$ K, the (2 × 1) pattern was observed even for $\theta = 65$. For $\theta > \theta_c$, only a diffuse background was observed. These results imply that, after the (2 × 1) two-dimensional reconstruction has formed, three-dimensional islands begin to grow and that the coverage starting from which these islands coalesce depends on the surface temperature.

3.2. Isothermal Thermal-Desorption Spectroscopy

Figure 1 displays a family of isotherms obtained by ITDS in the course of Eu deposition on an originally clean Si(111) surface. Curves *1* and *2* relate to the adsorption stage of the Eu–Si(111) structure formation. In this stage, the flux of Eu atoms evaporating from the surface increases with increasing surface coverage, to become equal to the flux incident on the surface at a certain value of θ dependent on the substrate temperature. At this instant, the film growth stops and adsorption equilibrium is established on the substrate surface.

As the substrate temperature is lowered (curves *3–8* in Fig. 1), adsorption equilibrium on the surface is not reached and the film continues to grow indefinitely. At $\theta_{max} \cong 0.6$, a pronounced maximum appears in the curves. According to the theory of heterogeneous nucleation [12], the presence of this maximum indicates an island-type film growth and the existence of a noticeable activation barrier to island formation. An analysis of the Eu evaporation rates at coverages in excess of θ_{max} provides an answer to the question of whether the clusters growing in these conditions consist of pure metallic europium or of silicide. Straightforward calculation shows that, at temperatures at which the ITDS relations are obtained, clusters of pure metallic europium could not exist because of its extremely high rate of evaporation, which is five to six orders of magnitude higher than that observed in the experiments. Hence, what grows on the surface is 3D clusters of the europium silicide.

The ITDS studies also provide an answer to another question, namely, how the silicide evaporates. When a silicide film is heated, only Eu atoms evaporate into vacuum. No silicide molecules or Si atoms escape from the surface. This means that the silicide breaks down during evaporation, with the Eu atoms desorbing and the Si atoms remaining on the surface.

3.3. Auger Electron Spectroscopy

Figure 2 displays concentration dependences of the Auger signals of europium and silicon obtained at various temperatures of europium deposition on the surface. Consider their main features. We see that, when Eu atoms are deposited on the substrate surface at room temperature, the Auger signal of silicon falls off monotonically without exhibiting any features and then vanishes at $\theta \cong 8$. This dependence differs radically from the corresponding relations measured on the Yb–Si(111) [11] and Sm–Si(111) [13] systems. The concentration dependences obtained for the latter two systems have steps, which indicate considerable mixing of Si atoms with the rare earth metal deposited on the silicon surface. Therefore, the absence of steps in curve *1* of Fig. 2a shows that there is no appreciable mixing of the Si and Eu atoms in the Eu–Si(111) system. To support this suggestion, we calculated the concentration dependence of the Auger signal of silicon coated by a nearly uniform-in-thickness, impurity-free, amorphous europium film. We used the relation $I = I_0 e^{-d\theta/\lambda}$ [14], where d is the geometric thickness of the europium monolayer, for which we took the covalent diameter of the Eu atom [15]. For the effective escape depth of Auger electrons, we accepted the value $\lambda = 5$ Å derived from the universal relation $\lambda = f(E)$ [16] (E is the electron energy) for $E = 92$ eV. Figure 3 plots this calculated

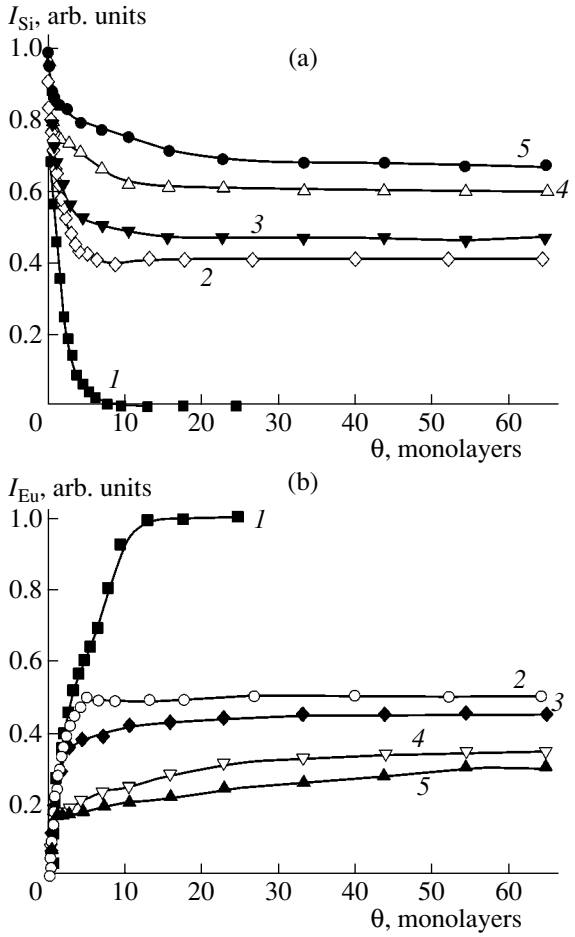

Fig. 2. Concentration dependences of the amplitudes of the Auger peaks (a) $N_{4,5}O_{2,3}N_{6,7}$ (104 eV) of europium and (b) $L_{2,3}VV$ (92 eV) of silicon. Eu was deposited on the Si surface at various temperatures T_s: (*1*) 300, (*2*) 500, (*3*) 800, (*4*) 900, and (*5*) 1000 K.

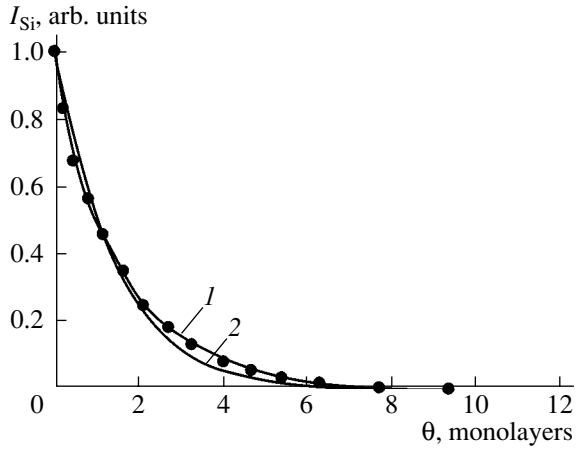

Fig. 3. Concentration dependences of the silicon Auger peak amplitude obtained under Eu deposition on the silicon surface. The deposition was carried out at room temperature. (*1*) Experiment and (*2*) calculation performed assuming the film to be uniform over the thickness (see text).

relation and experimental data. The curves are seen to be very close to each other. This implies that deposition of Eu atoms on the Si(111)-(7 × 7) surface at 300 K produces a metallic europium film which does not contain a noticeable amount of Si atoms.

The dependence of the europium Auger signal amplitude on the thickness of the deposited film (curve *1* in Fig. 2a) has a more complex shape than that for the silicon signal. Furthermore, the europium signal assumes a constant value (independent of coverage) at $\theta \cong 13$. The latter value considerably exceeds the coverage at which the silicon signal becomes zero. One possible explanation for such a large difference in the limiting coverages assumes that the electronic state of europium atoms (on which the yield of Auger electrons depends) is a function of the film thickness. Because we are planning to verify this conjecture in the future, we do not dwell on it here further.

Increasing the deposition temperature from room temperature to $T = 500$ K is accompanied by a decrease in magnitude of the Eu signal and an increase in the silicon signal. This suggests noticeable mixing of the deposited atoms with the substrate material at this temperature. As the temperature is increased even further, the variation in the Auger signals grows and the coverages at which the concentration dependences level off vary. The latter observation becomes particularly revealing in the behavior of the Eu Auger signal. Indeed, for $T_s = 500$ K, the plateau is reached at $\theta = 5$–6; for $T_s = 800$ K, this occurs at $\theta = 20$–30; for $T_s = 900$ K, at $\theta = 30$–40; and for $T_s = 1000$ K, no saturation is observed to occur at coverages $\theta \leq 65$.

3.4. Contact Potential Difference

Figure 4 shows the concentration dependences of the variation of the surface work function $\Delta\varphi = f(\theta)$ obtained under various conditions of Eu deposition on silicon; $\Delta\varphi = \varphi - \varphi_{Si}$, where φ is the work function of the Si(111) surface coated by a film of either europium or silicide and $\varphi_{Si} = 4.6$ eV is the work function of the clean Si(111) surface [17]. We see that varying the temperature exerts a substantial and ambiguous influence on the surface work function for any coverage. Since the small-coverage region was considered in [7, 8], we dwell here on the region of large coverages θ only.

First, it has to be pointed out that, unlike the systems Yb–Si(111) [18] and Sm–Si(111) [17], the dependence of the work function on θ for $T_s \geq 800$ K persists to the largest coverages studied. Second, an increase in the substrate temperature brings about, in the beginning, a decrease in the work function (temperature interval 300–500 K) and, afterwards, an increase (over the range $500 < T < 1000$ K). The latter may be caused by an increase in silicon concentration on the film surface, which is in agreement with the Auger spectroscopy data (Fig. 2). The effect of substrate temperature on the con-

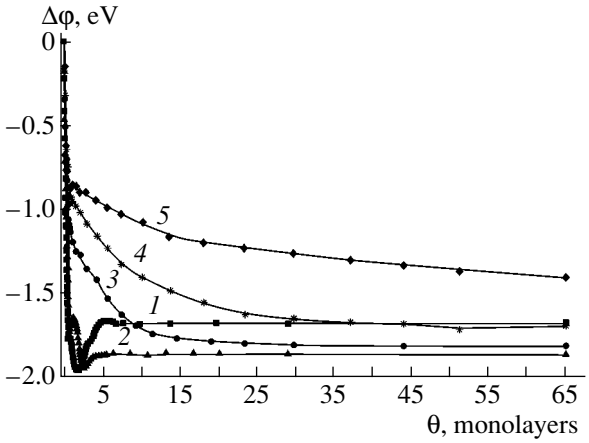

Fig. 4. Concentration dependences of Δφ obtained at various temperatures T_s of Eu deposition on the silicon surface: (*1*) 300, (*2*) 500, (*3*) 800, (*4*) 900, and (*5*) 1000 K.

centration dependences of both Auger signals and the work function of the surface manifests itself substantially earlier, according to LEED measurements, than the deposited Eu film undergoes ordering.

4. RESULTS AND DISCUSSION

The results presented in the preceding section suggest the general conclusion that the growth mechanism of the films, their morphology, and chemical composition depend on temperature. We consider this point in more detail.

At room temperature, as follows from the LEED and AES measurements, a disordered metallic europium film that is uniform in thickness forms on the silicon surface. The concentration of the Si atoms dissolved in this film is low.

At high temperatures, the Eu–Si(111) system forms through the Stranski–Krastanow mechanism; namely, the densest Si(111)-matched two-dimensional (2×1) reconstruction stops growing at $\theta = 0.5$–0.6, after which three-dimensional silicide clusters begin to grow on it.

As follows from LEED measurements, the coalescence of crystallites occurs at coverages whose value increases with temperature. It would seem that AES data suggest the same conclusion. Indeed, as pointed out in the preceding section (Fig. 2), the silicon and europium Auger signals cease to depend on the amount of deposited europium at coverages whose magnitude grows dramatically with temperature. According to our analysis [13], this growth may indicate that the coalescence occurs at coverages that increase with temperature. However, a comparative analysis of all the results obtained in this study shows that the pattern of the concentration dependences of Auger signals in the Eu–Si(111) system is determined not only by the silicide film structure. The CPD measurements (Fig. 4) show that variations in temperature and in the amount of deposited europium affect the elemental composition of the upper layers in silicide films. For instance, an increase in temperature in the interval 500–1000 K is accompanied by an increase in the work function. This may mean that, as the temperature increases, the concentration of Si atoms in the upper layer(s) of the film also increases. At the same time, an increase in the amount of deposited europium for $\theta > 5$ entails a decrease in the work function. This means that the concentration of Eu atoms in the upper layer of the film increases with θ. The region of coverages within which this growth takes place depends on temperature. As the temperature is increased, this region broadens and, at the highest temperature (1000 K), exceeds the θ interval studied.

The increase in the Eu atom concentration in the upper layer(s) with increasing θ should obviously be accompanied by a broadening of the coverage region within which the silicon and europium Auger signals vary. Therefore, in the Eu–Si(111) system, the value of θ_c cannot be derived from the concentration dependence of Auger signals alone. The LEED method offers a more reliable determination.

A comparison of the results obtained for the Eu–Si(111) and the Sm–Si(111) system mentioned earlier stresses a general similarity between the concentration dependences of the Auger signals and a qualitative difference between the other results. The difference consists, first, in that the values of the work function for the Sm–Si(111) system obtained at different temperatures (900, 1140 K) differ from one another only for $\theta < 2$. For $\theta > 2$, these values coincide to within a few hundredths of an electronvolt. Second, for $\theta > 2$, the work function no longer depends on the coverage. Third, the samarium silicide films have the (1×1) structure, whereas no structure was revealed in europium silicide films.

The interpretation of the differences between the properties of the two systems is fairly obvious. In the case of the Sm–Si(111) system, an ordered silicide film, which is homogeneous in elemental composition, forms on the silicon surface. The stoichiometry of the film depends neither on its thickness nor on temperature. The temperature affects only the value of coverage at which the silicide crystallites coalesce. This dependence may be due to a variation in either the concentration of the nuclei or in their shape, or both. The conclusion that a variation in the concentration of nuclei can affect the magnitude of θ_c can be readily supported by straightforward calculations, from which it follows that, if, for instance, the crystallites have the shape of hemispheres or spherical segments, a decrease in their

concentration should bring about coalescence at higher coverages. In the second case, where the crystallite shape changes, the coverage θ_c will increase with temperature if the ratio of the height of the crystallites to their base area increases. The third case is intermediate.

Thus, the above comparison of the experimental data obtained for the Eu–Si(111) and Sm–Si(111) systems reveals a substantial difference between them. This difference is most likely due to the low Si diffusion rate both in metallic europium and in the europium silicides. In particular, the low diffusion rate in silicides at all temperatures brings about a low concentration of Si atoms in films, which accounts for their work function being noticeably lower (at $\theta = 65$, it varies within the interval 2.75–3.2 eV) than that of samarium silicide films (4.1 eV [19]). Furthermore, due to the low Si diffusion rate in silicide films, a concentration gradient of Si atoms arises along the direction perpendicular to the sample surface. This gradient causes the work function to decrease with increasing silicide film thickness. This decrease is observed even at the highest temperature studied here (1000 K), above which europium starts to evaporate from the surface.

An increase in temperature is accompanied by an increase in the Si diffusion rate. This brings about an increase in the work function in the interval 500–1000 K, a growth of the silicon Auger signals, and a decrease in the europium Auger signals.

The limiting role of the Si diffusion rate in the formation of RE silicide films has thus far been observed only in the Ce–Si(111) system. It was shown in [20] that deposition of cerium films on a silicon surface at room temperature followed by heating gives rise to the formation of a variety of $CeSi_x$ phases (differing in structure and elemental composition), which can coexist. The films become more uniform in phase composition with increasing film-heating temperature.

In view of the fact that Si atom diffusion is of importance in both the Ce–Si(111) and Eu–Si(111) systems, it can be conjectured that europium silicide films, as well as cerium silicide films, are multiphase. The phases lying nearer the interface with the substrate should have a higher silicon content, and the phases that are closer to the surface should be enriched in Eu atoms. The europium silicide films having complex structure is supported by the fact that our studies of the diffraction pattern, rather than revealing any reflections due to thick silicide films, recorded only a diffuse background.

5. CONCLUSIONS

The mechanisms of formation and the properties of thin-film structures that form when europium is deposited on the (111) face of silicon at various temperatures have been studied using a number of experimental techniques. At room temperature, disordered metallic films grow that possess a low concentration of dissolved silicon. At high temperatures ($T \geq 500$ K), the Eu–Si(111) system forms through the Stranski–Krastanow mechanism; namely, first a two-dimensional transition layer (reconstruction) with the (2×1) structure forms and then three-dimensional crystallites of silicides grow on it. The distinctive feature of the system studied is shown to be a low rate of Si atom diffusion in the europium silicides. This feature accounts for the gradient of Si concentration over the thickness of the silicide films and, as a consequence, for their multiphase composition.

ACKNOWLEDGMENTS

This study was supported by the Ministry of Industry, Science, and Technology of the Russian Federation, state program “Surface Atomic Structures” (project no. 2.5.99).

REFERENCES

1. J. E. Baglin, F. M. d’Heurle, and C. S. Peterson, Appl. Phys. Lett. **36** (7), 294 (1980).
2. F. P. Netzer, J. Phys.: Condens. Matter **7**, 991 (1995).
3. K. N. Tu, R. D. Thompson, and B. Y. Tsaur, Appl. Phys. Lett. **38** (8), 626 (1981).
4. W. A. Henle, M. G. Ramsey, F. P. Netzer, and K. Norn, Surf. Sci. **254**, 182 (1991).
5. A. Yu. Grigor’ev, A. M. Shikin, G. V. Prudnikova, *et al.*, Fiz. Tverd. Tela (St. Petersburg) **40** (3), 562 (1998) [Phys. Solid State **40**, 519 (1998)].
6. L. Ming, L. Grill, M. G. Ramsey, *et al.*, Surf. Sci. **375**, 24 (1997).
7. T. V. Krachino, M. V. Kuz’min, M. V. Loginov, and M. A. Mittsev, Fiz. Tverd. Tela (St. Petersburg) **42** (3), 553 (2000) [Phys. Solid State **42**, 566 (2000)].
8. T. V. Krachino, M. V. Kuz’min, M. V. Loginov, and M. A. Mittsev, Appl. Surf. Sci. **182**, 115 (2001).
9. M. V. Kuz’min, M. V. Loginov, M. A. Mittsev, and T. V. Krachino, Fiz. Tverd. Tela (St. Petersburg) **37** (4), 1030 (1995) [Phys. Solid State **37**, 559 (1995)].
10. A. Ishizaka and Y. Shiraki, J. Electrochem. Soc. **133** (4), 666 (1986).
11. T. V. Krachino, M. V. Kuz’min, M. V. Loginov, and M. A. Mittsev, Fiz. Tverd. Tela (St. Petersburg) **39** (2), 256 (1997) [Phys. Solid State **39**, 224 (1997)].
12. J. P. Hirth and K. L. Moased, in *Physics of Thin Films: Advances in Research and Development*, Ed. by G. Haas and R. Toon (Mir, Moscow, 1970; Academic, New York, 1975), Vol. 4.
13. T. V. Krachino, M. V. Kuz’min, M. V. Loginov, and M. A. Mittsev, Fiz. Tverd. Tela (St. Petersburg) **40** (2), 371 (1998) [Phys. Solid State **40**, 341 (1998)].

14. R. Kern, G. Le Lay, and J. J. Metois, Curr. Top. Mater. Sci. **3** (3), 179 (1979).

15. *Properties of Elements*, Part 1: *Physical Properties*, Ed. by G. V. Samsonov (Metallurgiya, Moscow, 1976).

16. L. Feldman and J. Mayer, *Fundamentals of Surface and Thin Film Analysis* (North-Holland, New York, 1986; Mir, Moscow, 1989).

17. W. Mönch, *Semiconductor Surfaces and Interfaces* (Springer, Berlin, 1993).

18. T. V. Krachino, M. V. Kuz'min, M. V. Loginov, and M. A. Mittsev, Fiz. Tverd. Tela (St. Petersburg) **39** (9), 1672 (1997) [Phys. Solid State **39**, 1493 (1997)].

19. T. V. Krachino, M. V. Kuz'min, M. V. Loginov, and M. A. Mittsev, Fiz. Tverd. Tela (Leningrad) **40** (10), 1937 (1998) [Phys. Solid State **40**, 1758 (1998)].

20. I. Manke, H. J. Wen, A. Hohr, *et al.*, J. Vac. Sci. Technol. B **13** (4), 1657 (1995).

Translated by G. Skrebtsov

Physics of the Solid State, Vol. 46, No. 3, 2004, pp. 569–573. Translated from Fizika Tverdogo Tela, Vol. 46, No. 3, 2004, pp. 549–553.

POLYMERS AND LIQUID CRYSTALS

Photoinduced Birefringence in Comblike Poly-*n*-(fluoroalkyl methacrylates) and Their Hydrocarbon Analogs with Nonlinear Optical Chromophores in Side Chains

G. K. Lebedeva*, V. N. Ivanova*, S. A. Ivanov, V. A. Lukoshkin***, N. N. Smirnov*, I. M. Sokolova****, L. V. Khokhlova*, and V. V. Kudryavtsev***

** Institute of Macromolecular Compounds, Russian Academy of Sciences, Bol'shoĭ pr. 31, St. Petersburg, 199004 Russia*
e-mail: kudryav@hq.macro.ru
*** Moscow State University, Vorob'evy gory, Moscow, 119992 Russia*
**** Ioffe Physicotechnical Institute, Russian Academy of Sciences, Politekhnicheskaya ul. 26, St. Petersburg, 194021 Russia*
e-mail: V.Lukosh@mail.ioffe.ru
***** St. Petersburg State University of Electrical Engineering, ul. Professora Popova 5, St. Petersburg, 197022 Russia*
Received May 28, 2003; in final form, July 7, 2003

Abstract—Comblike polymers (copolymers) of methacrylates with nonlinear optical photochromic chromophores in the side chains are synthesized. An increase in the induced birefringence under laser radiation is studied in poly-*n*-(fluoroalkyl methacrylates) and their hydrocarbon analogs. It is demonstrated that the chemical structure and composition of polymers (copolymers) affect the rise and decay of the photoinduced birefringence and the stability of the second-harmonic generation signal. *© 2004 MAIK "Nauka/Interperiodica".*

1. INTRODUCTION

Recent progress in photonic technologies, which are most efficient in optical information processing, has stimulated a continuously increasing interest in polymer materials whose properties can be controlled by light. The most popular chromophores in photosensitive polymers are azo and azomethine dyes with an extended system of delocalized π electrons and polar donor–acceptor substituents. As a rule, these dyes possess a high nonresonant nonlinear optical susceptibility and can undergo a reversible *trans–cis* photoisomerization, which leads to a substantial change in the physical and chemical properties of polymers [1]. The high speed of response renders these chromophores promising for the creation of quick data-processing systems.

The efficiency and stability of induced processes in polymers depend on the chemical nature of the chromophore and the polymer, as well as on the method of introducing the chromophore into the polymer (for example, the chromophore can be introduced (i) in the form of a composite or a covalently bonded group, (ii) into the main or side chain of the polymer, and (iii) through a flexible spacer or in a rigid manner) [2].

This work is a continuation of our systematic investigations into the orientation of nonlinear optical chromophores in external fields [3] and the relaxation processes in polymers (copolymers) of methacrylates with chromophore groups in the side chains [4, 5]. In the present work, we studied the kinetics of photo-orientation of chromophore groups under exposure to laser radiation.

For our investigations, we synthesized a series of comblike polymers (copolymers) of methacrylates. The chemical structures and designations of the polymers synthesized are given in the table.

The polymers differ in the structure of the second comonomer. The second comonomer contains either the alkyl side chain (copolymers CP3, CP6) or the fluoroalkyl side chain (copolymers CP2, CP4, CP5). The third comonomer (which increases the free volume) is introduced into copolymers CP4–CP6. The nonlinear optical chromophores in the polymers also have different structures. The conjugated chain in the chromophores includes the azo group in copolymers CP5 and CP6, the azomethine group in homopolymer P1 and copolymers CP2–CP4, and the benzothiazole fragment in copolymer CP6. Moreover, the polymers differ in the structure of the spacer attaching the chromophore group to the macromolecular backbone. The side chain involves either a sequence of $–CH_2–$ groups in copolymers CP2–CP6 or a sequence of $–CF_2–$ groups in homopolymer P1. The study of this series of compounds makes it possible to reveal a correlation between the kinetics of photoinduced processes and the chemical structure of polymers (copolymers). Note that the influence of fluorine-containing methylene groups in the polymer structure and heterocyclic fragments in the chromophore structure on the photoinduced birefringence has never been considered in the literature.

1063-7834/04/4603-0569$26.00 © 2004 MAIK "Nauka/Interperiodica"

Structures of the polymers under investigation

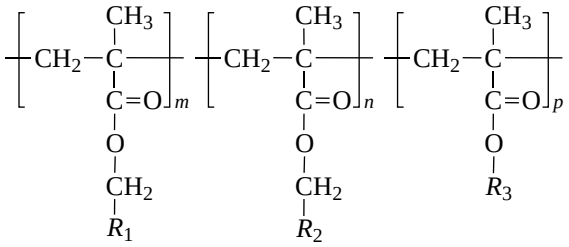

Polymer	*m*	*n*	*p*	R_1	R_2	R_3
P1	100	0	0	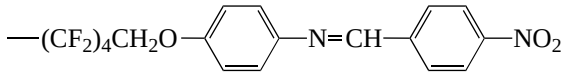	–	–
CP2	20	80	0	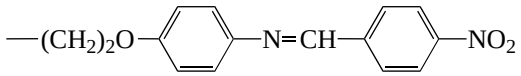	$-(CF_2)_4H$	–
CP3	20	80	0	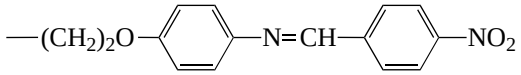	$-(CH_2)_4H$	–
CP4	25	35	40	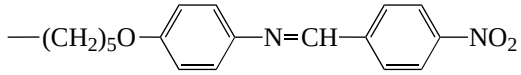	$-(CF_2)_4H$	–H
CP5	5	90	5	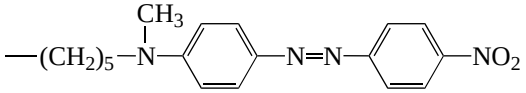	$-(CF_2)_4H$	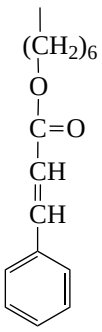
CP6	20	45	35	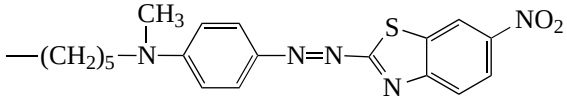	$-(CH_2)_4H$	–H
p2MAN [11]	100	0	0	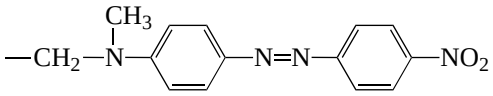	–	–

2. SAMPLE PREPARATION AND EXPERIMENTAL TECHNIQUE

Homopolymer P1 was prepared by thermal polymerization. The separation, purification, and physical properties of this homopolymer were described in our earlier work [3]. Copolymers CP2–CP6 were synthesized through the radical polymerization of the corresponding monomers in an *N*,*N*-dimethylacetamide solution (30 wt %) with dinitrilazodiizobutyric acid (1 wt %) as an initiating agent at a temperature of 60°C. The characteristics of copolymers CP2 and CP3 are given in [5], and the parameters of copolymer CP5 are presented in [6]. The structure and composition of the synthesized polymers were identified by ^{1}H NMR and UV spectroscopy. The ^{1}H NMR spectra were recorded on a Bruker AC-200 spectrometer (200.1 MHz) with respect to the signals from the solvent. Deuterated acetone $(CD_3)_2CO$ and dimethyl sulfoxide (*DMSO-d6*) were used as solvents.

The absorption electronic spectra were measured on a Specord M-400 spectrophotometer. The percentage ratio (*n* : *m* : *p*) of the repetitive units in copolymers was estimated from the ratio of the signals from protons of particular groups in the ^{1}H NMR spectra. The UV

absorption spectra of polymer films exhibit absorption bands characteristic of chromophores in the range 328–344 nm (homopolymer P1, copolymers CP2–CP4) and at 540 nm (copolymer CP6).

Chromophores, namely, 4'-(4-nitrobenzylideneamino)phenol derivatives, were synthesized according to the procedure similar to that described in [7]. 2-[4'-(*N*-Methyl-*N*-6-hydroxyhexyl)aminophenylazo]-6-nitrobenzothiazole was prepared using the procedure described in [8]. Chromophore-containing methacrylates were synthesized by the procedure described in [7]. The phase (aggregate) state was examined using differential scanning calorimetry (DSC) on a DSM-2M scanning calorimeter (scanning rate, 16 K/min; weighing portion, 20 mg; threshold sensitivity, 10^{-4} W) for homopolymer P1 and copolymers CP4–CP6 and dielectric spectrometry (dielectric loss measurements) on a TP-9701 instrument in the temperature range from –160 to 150°C for copolymers CP2 and CP3 [5].

The softening temperatures T_g are as follows: 80°C for homopolymer P1 and copolymer CP4, 280°C for copolymer CP5, 135°C for copolymer CP6 (DSC data), and 60–70°C for copolymers CP2 and CP3 (dielectric data). The photoinduced birefringence, the orientation of chromophore groups upon electrification in a corona discharge, and the second-harmonic generation were investigated with the use of samples prepared by centrifugation in the form of 2-μm-thick polymer films on 180-μm-thick cover glasses. The samples were heat treated at a temperature of 100°C for 3 h and at 50°C for 100 h under vacuum.

The kinetics of photoinduced birefringence was examined on a photo-optical setup described in [9, 10]. The vertically polarized writing beam of an argon laser (λ = 488 nm, intensity P = 0.18 W/cm^2) was directed toward the chosen region of the polymer film. In order to measure photoinduced changes in the polymer film, the reading beam of an He–Ne laser (λ = 633 nm) was directed toward the same region of the sample. The angle between the planes of polarization of the writing and reading beams was equal to 45°. The intensity of the reading beam passing through the sample and the analyzer was measured with a photodiode and a special recording system. The results of these measurements were used to determine the phase shift $\varphi(t)$ in the reading beam components with parallel and perpendicular polarizations relative to the polarization of the writing beam.

The samples were electrified in a dc corona discharge (the current strength did not exceed 5 μA) with the use of a three-electrode circuit according to the technique described in [3].

The second-harmonic generation was investigated on a setup described in [3]. The second harmonic was generated by a pulsed YAG : Nd^{3+} laser operating in a Q-switching mode (radiation wavelength, 1.064 μm; pulse width, 15 ns).

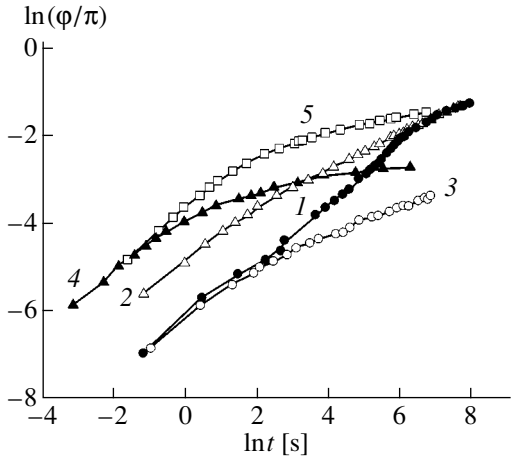

Fig. 1. Dependences of the phase shift φ/π on the exposure time for polymers (*1*) CP2, (*2*) CP3, (*3*) CP4, (*4*) CP5, and (*5*) p2MAN.

3. RESULTS AND DISCUSSION

In polymers containing photochromic fragments (for example, azo derivatives) that can undergo *trans–cis* isomerization, the photochromic azo dye molecules and adjacent side groups are oriented under exposure to linearly polarized laser radiation [2, 9, 10]. In this case, the molecules are predominantly arranged in such a way that their long axes are perpendicular to the electric field vector E of the light wave, which gives rise to birefringence. Initially, the optically isotropic polymer film acquires optical properties similar to those of a uniaxial crystal whose optic axis is parallel to the vector E.

In the general case, the photo-orientation is a complex process involving several stages, such as *trans–cis–trans* … isomerization, photoselection, orientation of dye molecules and mesogenic groups, motion of the main chain, etc. [2, 10]. This manifests itself in the kinetics of rise and decay of photoinduced birefringence.

The kinetics curves of photoinduced birefringence for copolymers CP2–CP5 and homopolymer p2MAN [11] are depicted in Fig. 1.

Polymers P1 and CP2–CP4 contain the same azomethine dye and (except for copolymer CP3) identical chains of $–CF_2$ groups. These groups are characterized by strong intermolecular interaction, spatial ordering [12], and a tendency toward the formation of hydrogen bonds with the participation of protons of the $–CF_2H$ terminal group [13]. As can be seen from Fig. 1, the replacement of hydrogen atoms by fluorine atoms in the side radical leads to a considerable decrease in the rate of rise of the birefringence. This effect is most pronounced at short exposure times (t < 20 s), when the short-range order is formed. The decisive role in this process is played by the dye molecules whose long axis is parallel to the vector E of writing radiation (these molecules have the highest rate of *trans–cis* isomeriza-

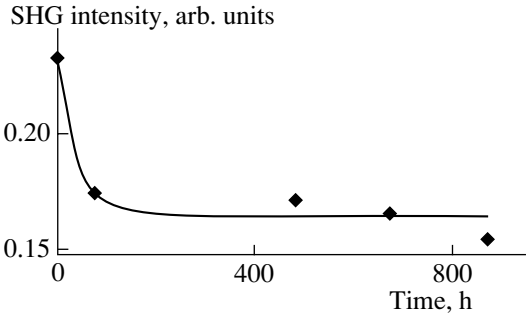

Fig. 2. Decay kinetics of the intensity of the second-harmonic generation signal in a CP6 copolymer film ~2 μm thick at 20°C after electrification at T_e = 100°C.

tion). At this stage, the mobility of the main chain is of little importance. Indeed, the initial portions of the kinetic curves for polymers CP2 and CP4 (Fig. 1) differ only slightly, even though the final birefringence of copolymer CP4 is appreciably less than that of copolymer CP2. Such a behavior of the birefringence can be explained by the fact that the photo-orientation is substantially affected by both the mobility of dye molecules (the initial portion of the kinetic curve) and the mobility of the main chain (at long exposure times). The spacer in copolymer CP4 is longer than that in copolymer CP2, which could provide a higher mobility of photochromic fragments [2]. However, the presence of the third comonomer in copolymer CP4 brings about the formation of numerous hydrogen bonds, which increase the rigidity of the system (matrix) and decrease the degree of photo-orientation. The structures of copolymers CP2 and CP3 differ only in the chemical nature of the side chain of the second comonomer (see table). As was noted above, the fluorine-containing chains significantly affect the photochromic properties of the polymer, most likely, due to the strong interaction of fluoromethylene fragments of methacrylate molecules [13, 14]. At long exposure times (t > 400 s), the kinetics of photoinduced birefringence in copolymers CP2 and CP3 is almost identical (Fig. 1; curves *1*, *2*). This circumstance can be associated with the large distance between the main chain and the proton of the $–CF_2H$ terminal group (the proton is prone to the formation of hydrogen bonds). Consequently, the $–CF_2H$ group, whose effect is pronounced at the early stages of photo-orientation, only slightly affects the mobility of the main chain.

At long exposure times, the kinetics of rise of the birefringence is governed primarily by the specific features in the formation (or reorientation) of microdomains [2]. For copolymer CP2, this process apparently occurs at exposure times t > 400 s. It should be noted that, at the early stage, the photo-orientation is hindered by the strong intermolecular interaction of the $–CF_2$ groups [12]. By contrast, at the next stage (the initial arrangement of azomethine dye molecules is disturbed, but microdomains are not formed), this interaction can promote photo-orientation (Fig. 1; curve *1*, exposure times t = 20–400 s).

The most pronounced effect of fluoromethylene chain fragments on the birefringence kinetics is observed in homopolymer P1. The introduction of these fragments into the composition of the spacer results in the suppression of photo-orientation (the birefringence is not observed). Possibly, this is caused by the fact that the free volume in homopolymer P1 is absent (or the free volume in homopolymer P1 is smaller than that in copolymers CP2–CP4).

A comparison of the results obtained in [3] and in the present work shows that polymers with a rigid structure (homopolymer P1), which hinders the isomerization and reorientation, are characterized by the maximum degree of orientation of chromophore groups and the highest intensity and stability of the second-harmonic generation signal.

It was revealed that, under laser radiation, copolymers CP5 and CP6 with different structures of photochromic groups exhibit different photoinduced effects.

In copolymer CP6, no birefringence is observed, even though the copolymer has a sufficiently loose structure [the copolymer contains the third comonomer, is free of fluorine-containing side substituents, and involves the long spacer attaching the chromophore group (see table)]. It is known [15] that the replacement of a phenyl ring by a naphthalene ring leads to a drastic decrease in the rate of photoinduced processes. In our case, the conjugation of the benzene ring with the thiazole ring (see table), which has a planar structure and contains two heteroatoms [16], most likely also results in suppression of the *trans–cis* isomerization.

The time dependences of the photoinduced birefringence for copolymer CP5 containing 5% nitrogen-substituted 4-nitroazobenzene (classical photochrome) and homopolymer p2MAN with the same photochromic group exhibit identical behavior (Fig. 1; curves *4*, *5*). At the initial stage, the exposure of copolymer CP5 to laser radiation is attended by a rapid increase in the birefringence, which is comparable to the birefringence of homopolymer p2MAN. With further exposure, the birefringence of copolymer CP5 increases more slowly and reaches a nearly steady-state value. This behavior can be explained by the fact that, at the early stage, the long spacer attaching the photochromic group in copolymer CP5 facilitates the photoinduced processes. However, as the exposure time increases, the specific properties of fluorine-containing side chains manifest themselves [17], which leads to a decrease in the mobility of photochromic fragments and to stabilization of the process.

It should be noted that the exposure of copolymer CP6 and homopolymer P1 to an external electric field induced by the corona discharge is also accompanied by an efficient orientation of chromophore groups in the polymer film and the appearance of a stable second-harmonic generation signal. Figure 2 shows the time

dependence of the intensity of the second-harmonic generation signal for copolymer CP6. It can be seen from Fig. 2 that the signal intensity decreases by approximately 20% in the first three days and remains nearly constant over the next month.

4. CONCLUSIONS

Thus, the results obtained in this work demonstrated that the specific features of the structure and chemical nature of polymer matrices and photochromic groups are the factors responsible for the appearance, magnitude, and kinetic parameters of the photoinduced birefringence in polymers. The replacement of hydrogen atoms by fluorine atoms in side alkyl substituents of acrylates (methacrylates) results in a decrease in the photoinduced birefringence due to an increase in the rigidity of the structure. The modification of the structure of the azo dye through the introduction of the thiazole ring with two heteroatoms into the conjugated chain leads to complete suppression of the birefringence. This can be associated with the planar structure of the benzothiazole fragment and the ability of heteroatoms to form hydrogen bonds [16]. It was found that there is a correlation between the photoinduced birefringence and the stability of the nonlinear optical properties of the polymers. The second-harmonic generation signal is most stable in polymers in which the photoinduced birefringence is absent and appears to be unstable in polymers with a considerable birefringence [3]. Therefore, the assumption can be made that polymers in which the photoinduced processes of *trans–cis* isomerization and reorientation are hindered hold promise for nonlinear optics.

ACKNOWLEDGMENTS

We would like to thank S.G. Kostromin for supplying the p2MAN polymer samples.

REFERENCES

1. J. A. Delaire and K. Nakatani, Chem. Rev. **100**, 1817 (2000).
2. A. Natansohn and P. Rochon, Chem. Rev. **102** (11), 4139 (2001).
3. G. K. Lebedeva, I. M. Sokolova, V. N. Ivanova, *et al.*, Fiz. Tverd. Tela (St. Petersburg) **43** (4), 750 (2001) [Phys. Solid State **43**, 783 (2001)].
4. N. V. Afanas'eva, T. I. Borisova, G. K. Lebedeva, *et al.*, Vysokomol. Soedin., Ser. B **40** (12), 2083 (1998).
5. N. V. Afanas'eva, T. I. Borisova, V. N. Ivanova, *et al.*, Fiz. Tverd. Tela (St. Petersburg) **45** (5), 936 (2003) [Phys. Solid State **45**, 983 (2003)].
6. G. K. Lebedeva, N. L. Loretsyan, V. N. Ivanova, *et al.*, Fiz. Tverd. Tela (St. Petersburg) **44** (2), 379 (2002) [Phys. Solid State **44**, 395 (2002)].
7. B. K. Mandal, T. Takahashi, M. Maeda, *et al.*, Macromol. Chem. Phys. **192**, 1009 (1991).
8. H.-Q. Xie, Z.-H. Liu, and J. Sh. Guo, Polymer **39** (12), 2393 (1998).
9. V. P. Shibaev, S. G. Kostromin, and S. A. Ivanov, *Polymers as Electrooptical Active Media*, Ed. by V. P. Shibaev (Springer, Berlin, 1996).
10. V. P. Shibaev, S. G. Kostromin, and S. A. Ivanov, Vysokomol. Soedin., Ser. A **39** (1), 43 (1997).
11. S. Freiberg, F. Lagugne-Labarthet, P. Rochon, and A. Natansohn, Macromolecules (2003) (in press).
12. L. D. Budovskaya, V. N. Ivanova, L. N. Oskar, *et al.*, Zh. Fiz. Khim. **63** (5), 1231 (1989).
13. L. D. Budovskaya, Yu. M. Boyarchuk, V. M. Denisov, *et al.*, Vysokomol. Soedin., Ser. A **34** (7), 98 (1992).
14. L. D. Budovskaya, V. N. Ivanova, L. N. Oskar, *et al.*, Vysokomol. Soedin., Ser. A **32** (3), 561 (1990).
15. M. S. Ho, A. Natansohn, and P. Rochon, Macromolecules **28**, 6124 (1995).
16. B. I. Stepanov, *Introduction to Chemistry and Technology of Organic Dyes* (Khimiya, Moscow, 1971).
17. T. P. Stepanova, L. L. Burshteĭn, L. D. Baklagina, *et al.*, Zh. Fiz. Khim. **58** (8), 1949 (1984).

Translated by O. Borovik-Romanova

Physics of the Solid State, Vol. 46, No. 3, 2004, pp. 574–578. Translated from Fizika Tverdogo Tela, Vol. 46, No. 3, 2004, pp. 554–558.

POLYMERS AND LIQUID CRYSTALS

Dielectric Properties of Liquid Crystals of the Cyano Derivative Compounds with Different Fragments in the Molecular Core

B. A. Belyaev, N. A. Drokin, V. F. Shabanov, and V. A. Baranova

Kirensky Institute of Physics, Siberian Division, Russian Academy of Sciences, Akademgorodok, Krasnoyarsk, 660036 Russia

e-mail: belyaev@iph.krasn.ru

Received July 15, 2003

Abstract—This paper reports on the results of investigations into the influence of variations in the chemical composition of the aromatic core of cyano-containing molecules of liquid crystals on their dielectric properties in the frequency range 1–2000 MHz. It is shown that the dispersion of the longitudinal permittivity is adequately described by the sum of two Debye processes with different weighting factors and relaxation times. The frequency dependence of the transverse permittivity is well approximated by the Debye process with a continuous distribution of relaxation times in a specified range. It is established that the replacement of one benzene ring in the biphenyl core of the 5CB liquid-crystal molecule by a cyclohexane (or bicyclooctane) fragment leads to a considerable decrease in both relaxation times for the longitudinal permittivity, a change in the low-frequency limit of the relaxation time range for the transverse permittivity, and the evolution of the frequency dependence of the dielectric anisotropy. © *2004 MAIK "Nauka/Interperiodica".*

1. INTRODUCTION

Investigation into the influence of the chemical composition and structure of molecules of liquid crystals belonging to a homologous series on the dispersion of the permittivity makes it possible to elucidate the nature of relaxation processes, to explain the origin of specific features observed in the dielectric spectra, and to reveal a correlation between the physical characteristics and microscopic parameters. For example, in our earlier works [1–3], the dispersion of the longitudinal and transverse high-frequency permittivities of liquid crystals of the alkylcyanobiphenyl group *n*CB was studied as a function of the length of the alkyl tail (n = 5–8). The results of those investigations enabled us to separate the contributions of the motions of rigid and flexible molecular fragments and to assign them to the specific features observed in the dielectric spectra. In particular, it was demonstrated that, apart from the conventional Debye relaxation of molecules, the dielectric spectra of liquid crystals in the high-frequency range are characterized by the resonance dispersion regions associated with intramolecular motions of the alkyl fragments. Liquid crystals of the homologous series of alkylcyanobiphenyls *n*CB, alkyloxycyanobiphenyls *n*OCB, and cyclohexane derivatives were examined using dielectric methods in [4, 5]. Dunmur and Tomes [4] and Urban *et al.* [5] investigated how the chemical composition of the rigid core of molecules affects the dipole moment, order parameter, activation enthalpy, Debye relaxation time, and the retardation factors of molecular motion introduced in the framework of the Mayer–Meyer theory of dielectric relaxation. A number of authors (see, for example, [6, 7]) analyzed the changes in the molecular packing coefficients and rheological parameters of cyano-containing liquid crystals due to the replacement of one benzene fragment in the rigid core of the liquid-crystal molecules by other fragments.

The aim of the present work was to measure the frequency dependences of the permittivity of cyano-containing liquid crystals, to approximate these dependences numerically, and to compare the temperature dependences of the permittivities and refractive indices. For this purpose, we used the following nematic liquid crystals: 4-*n*-pentyl-4-cyanobiphenyl (5CB), *trans*-4-pentyl-(4-cyanophenyl)-cyclohexane (5PCH), and 4-(4'-pentyl-bicyclo[2.2.2]octane)-phenyl (5BCO). The structural formulas of the liquid-crystal molecules under investigation and the temperatures T_c of phase transitions of the liquid crystals from a nematic liquid-crystal state to an isotropic liquid state are presented in Fig. 1. These molecules differ from each other only in the chemical composition of the aromatic core. Specifically, one benzene fragment in the aromatic core of the 5PCH and 5BCO molecules is replaced by the cyclohexane and bicyclooctane fragments, respectively. However, the lengths of the alkyl tails are identical in all the molecules studied. It should be noted that, in this work, the dielectric spectra were measured for the first time over a wide frequency range (f = 1– 2000 MHz), including the poorly studied high-frequency range of dielectric relaxation.

2. EXPERIMENTAL TECHNIQUE

The permittivities of the liquid-crystal samples in the frequency range 1–30 MHz were measured on a Tesla BM-560 standard Q-meter with the use of a mea-

1063-7834/04/4603-0574$26.00 © 2004 MAIK "Nauka/Interperiodica"

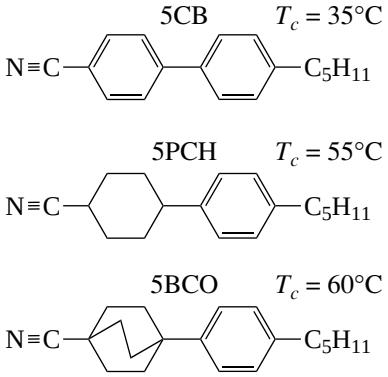

Fig. 1. Structural formulas of the liquid-crystal compound and temperatures T_c of the transition from the nematic phase to the isotropic liquid phase.

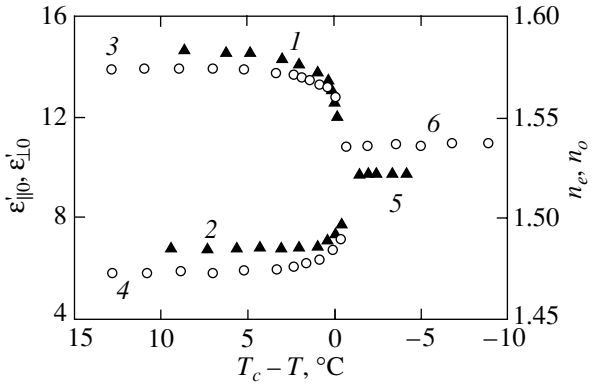

Fig. 2. Temperature dependences of the optical n_e and n_o (closed symbols) and dielectric $\varepsilon'_{\parallel 0}$ and $\varepsilon'_{\perp 0}$ (open symbols) parameters for the 5PCH liquid crystal in the temperature range of the transition from the nematic phase to the isotropic liquid phase (for explanation of the curves, see text).

suring cell in the form of a parallel-plate capacitor. In the meter and decimeter wavelength ranges, the dielectric measurements were performed with specially devised highly sensitive frequency-tuned sensors based on ring-type microstrip resonators [2].

The real permittivities ε' were determined according to a standard technique, i.e., by measuring the difference in the resonance frequencies of the sensors with and without the sample. The imaginary permittivities ε'' were calculated from the change in the loaded Q-factor of the resonator after relaxation of the liquid-crystal sample placed in it. The amplitude–frequency characteristics of the microstrip sensors were recorded on R4-37 and R4-38 automated meters intended for measuring complex transmission gain factors. The absolute errors in determining the dielectric characteristics were no larger than $\delta\varepsilon' \sim 0.05$ and $\delta\varepsilon'' \sim 0.1$. The orientation of the long axes of molecules in the studied samples with respect to the polarization of a microwave electric pump field was provided by a static magnetic field H = 2500 Oe. The measurements were performed in a thermostat in the temperature range 0–95°C. The temperature was maintained accurate to ±0.5°C.

The numerical approximation of the dielectric spectra required knowledge of the ordinary (n_o) and extraordinary (n_e) refractive indices. These data for the 5CB and 5BCO liquid crystals were taken from [8, 9]. The ordinary and extraordinary refractive indices for the 5PCH liquid crystal were measured at the wavelength λ = 0.589 μm with the use of an IRF-454B standard refractometer with a homeotropic orientation of the director in the measuring cell.

3. RESULTS AND DISCUSSION

The experimental temperature dependences of the extraordinary n_e (closed symbols *1*) and ordinary n_o (closed symbols *2*) refractive indices of the 5PCH liquid crystal are depicted in Fig. 2. This figure also shows the temperature dependences of the real parts of the longitudinal $\varepsilon'_{\parallel}$ (open symbols *3*) and transverse $\varepsilon'_{\perp}$ (open symbols *4*) permittivities, which were measured in parallel and perpendicular orientations of the liquid-crystal director with respect to the polarization of the ac electric field. The temperature dependences of the refractive index and the permittivity of the 5PCH liquid crystal in the isotropic phase are shown by symbols *5* and *6*, respectively. The heating rate of the studied sample was approximately equal to 5 K/h. In this experiment, the permittivities were measured at a pump frequency f = 1 MHz, at which the frequency dispersion does not manifest itself. Consequently, the dielectric characteristics thus obtained are close to the static permittivities $\varepsilon'_{\parallel 0}$ and $\varepsilon'_{\perp 0}$. It can be seen from Fig. 2 that, except for the phase transition range, the measured parameters only slightly depend on the temperature in both the nematic ($T < T_c$) and isotropic ($T > T_c$) phases of the liquid-crystal compound.

All the dielectric spectra of the liquid crystals studied were measured in the nematic phase at a temperature $T = T_c - 5$°C. Figure 3 shows the frequency dependences of the real parts of the longitudinal $\varepsilon'_{\parallel}(f)$ and transverse $\varepsilon'_{\perp}(f)$ permittivities and the frequency dependences of the imaginary parts of $\varepsilon''_{\parallel}(f)$ and $\varepsilon''_{\perp}(f)$ for three liquid crystals. In this figure, solid lines represent the results of the numerical approximation of the experimental dependences of the real parts of the longitudinal and transverse permittivities.

The frequency dependences of the longitudinal permittivity were approximated as follows. In our previous work [2], we showed that the frequency dependence of the longitudinal permittivity $\varepsilon'_{\parallel}(f)$ over a wide range of frequencies can be correctly approximated using the

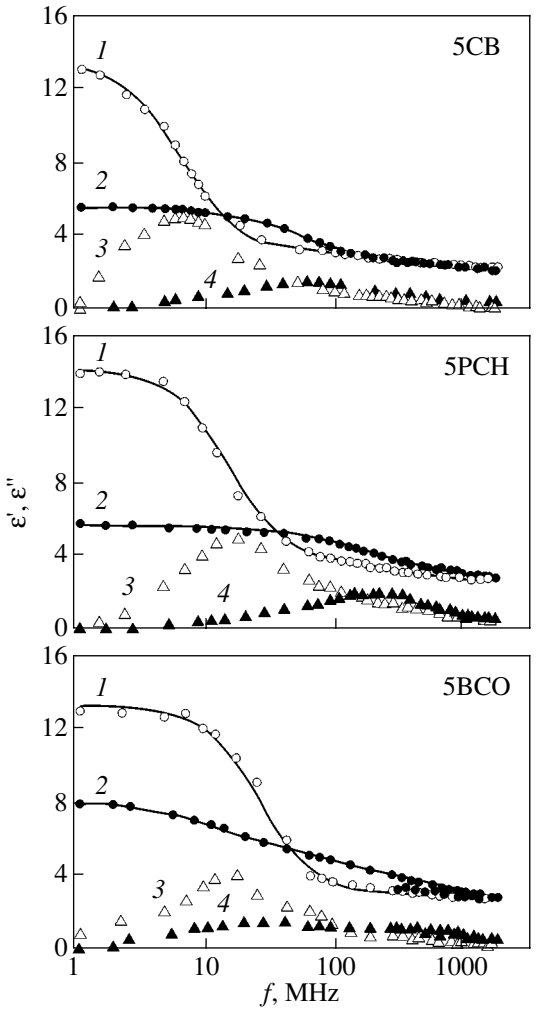

Fig. 3. Frequency dependences of the (*1*, *2*) real and (*3*, *4*) imaginary parts of the (*1*, *3*) longitudinal and (*2*, *4*) transverse permittivities of the liquid crystals. Solid lines correspond to the Debye approximations.

sum of two Debye processes with different relaxation times; that is,

$$\varepsilon'_{\parallel}(f) - n_e^2 = \frac{(\varepsilon'_{\parallel 0} - n_e^2)g_1}{1 + \omega\tau_{\parallel 1}^2} + \frac{(\varepsilon'_{\parallel 0} - n_e^2)g_2}{1 + \omega^2\tau_{\parallel 2}^2}. \qquad (1)$$

Table 1. Main characteristics of the liquid crystals under investigation for parallel orientations of the liquid-crystal director with respect to the microwave electric pump field

Liquid crystal	$\tau_{\parallel 1}$, 10^{-9} s	$\tau_{\parallel 2}$, 10^{-10} s	ΔH, kJ/mol	$\varepsilon'_{\parallel 0}$	$\varepsilon'_{\parallel\infty}$	n_e^2
5CB	24–25	6–7	66.7	16.4	3.13	3.13
5PCH	9–9.5	3–4	71.5	14.0	2.69	2.53
5BCO	6–6.5	0.9–1.0	92	13.2	2.49	2.49

Here, n_e is the extraordinary refractive index, $\varepsilon'_{\parallel 0}$ is the static permittivity, $\omega = 2\pi f$, $\tau_{\parallel 1}$ and $\tau_{\parallel 2}$ are the relaxation times of the two Debye processes, and g_1 and g_2 are the weighting factors corresponding to these processes ($g_1 + g_2 = 1$). It should be noted that, for all the studied samples, the best agreement between the results of the numerical approximation and the experimental points was achieved with weighting factors $g_1 \approx 0.92$ and $g_2 \approx 0.08$. Table 1 presents the relaxation times $\tau_{\parallel 1}$ and $\tau_{\parallel 2}$, which characterize the dipole relaxation upon rotation of the liquid-crystal molecules about the short and long molecular axes, respectively. This table also lists the molar activation enthalpies ΔH obtained by numerical processing of the dielectric spectra measured at three different temperatures: $T_1 = T_c - 5$°C, $T_2 = T_c - 10$°C, and $T_3 = T_c - 15$°C. The activation enthalpy ΔH was determined from the temperature-dependent relaxation time $\tau_{\parallel 1}$ according to the Bauer equation [10]:

$$\tau_{\parallel 1} = \left(\frac{2\pi I}{k_B T}\right)^{1/2} \exp\left(\frac{-\Delta S}{R}\right)\exp\left(\frac{\Delta H}{RT}\right), \qquad (2)$$

where ΔS and ΔH are the molar activation entropy and the molar activation enthalpy of the dipole reorientation, respectively; I is the moment of inertia of the molecule; R is the gas constant; k_B is the Boltzmann constant; and T is the absolute temperature. The exact value of the moment of inertia I for the liquid crystals studied is unknown. However, according to estimates [10, 11], we have $I \sim (1–3) \times 10^{-43}$ kg m^2 and $\Delta S \sim 100–135$ kJ/mol.

It can be seen from Table 1 that the activation enthalpy ΔH characterizing the reorientation of molecules about the short axis monotonically increases in the series 5CB–5PCH–5BCO. Our results are in good agreement with the data obtained by Urban *et al.* [5] for 5CB and 5PCH liquid crystals. The observed increase in the activation enthalpy ΔH can be explained by the increase in the molecular packing coefficient due to an increase in the size of the molecular core [11].

An analysis demonstrated that the shorter time of longitudinal relaxation $\tau_{\parallel 2}$ is virtually temperature-independent in the temperature range under investigation and proves to be shortest for the 5BCO liquid crystal (Table 1). As can be seen from Table 1, the quantities n_e^2 and $\varepsilon'_{\parallel\infty}$ determined from the frequency dependences of the permittivities are in excellent agreement.

Thus, the approximation approach proposed in our earlier work [2] offers reasonable agreement between the calculated frequency dependence of the longitudinal permittivity and the experimental data for all the liquid-crystal samples over the entire frequency range covered.

As was shown in [2], the transverse permittivity $\varepsilon'_{\perp}(f)$ should be approximated using a dispersion relation with a continuous distribution of relaxation times in a specified range. In the general case, when the relax-

ator times are distributed in the range from 0 to ∞, the Debye dispersion relation has the form

$$\varepsilon'_\perp(f) - n_o^2 = (\varepsilon'_{\perp 0} - n_o^2)\int_0^\infty \frac{G(\tau)}{1 + (2\pi f\tau)^2} d\tau, \qquad (3)$$

where n_o is the ordinary refractive index and $G(\tau)$ is the distribution function of relaxation times. The function $G(\tau)$ describes the motion of large- and small-sized molecular aggregates and individual molecules and also small-scale intramolecular motions associated, for example, with vibrations of mobile molecular fragments of the alkyl tails.

The necessity of applying the above approach to the approximation of the transverse permittivity $\varepsilon'_\perp(f)$ stems from the fact that, for all the liquid crystals under investigation, the frequency dependences of the transverse permittivity differ from the Debye behavior. As a consequence, the approximation of the dispersion of the transverse permittivity by the sum of two or even three Debye processes with different relaxation times, as a rule, leads to poor agreement with the experimental data. To put it differently, unlike parallel pumping, perpendicular pumping (perpendicular orientation of the polarization of the microwave electric field with respect to the director of molecules) ensures efficient excitation of various intramolecular motions with a continuous distribution of relaxation times in a specified range from $\tau_{\perp L}$ to $\tau_{\perp R}$.

For liquid crystals, the distribution function $G(\tau)$ and the range of its definition are unknown. In this work, the frequency dependence of the transverse permittivity $\varepsilon'_\perp(f)$ was approximated using two different functions $G(\tau)$. The first function $G(\tau)$ is a symmetric function describing the uniform distribution of relaxators in the range $\tau_{\perp L}$–$\tau_{\perp R}$. Upon substitution of this function into relation (3), we obtain the analytical expression [12]

$$\varepsilon'(\omega) = \frac{\varepsilon_0 - \varepsilon_\infty}{2\ln a}\ln\frac{a^2 + k^2}{1 + k^2}, \qquad (4)$$

where $a = \tau_{\perp L}/\tau_{\perp R}$ and $k = \omega\tau_{\perp L}$. By applying the numerical method for expression (4), it is easy to determine the limits $\tau_{\perp L}$ and $\tau_{\perp R}$ of the relaxation time range for each liquid crystal that provide the best agreement between the results of the chosen approximation and the experimental data over the entire frequency range. An analysis of the dependences $\varepsilon'_\perp(f)$ thus obtained (see Fig. 3, curves *2*) demonstrates that this approach offers an adequate description of the relaxation processes in the studied liquid crystals for perpendicular orientations of the director of liquid-crystal molecules with respect to the polarization of the electric pump field. It should be noted that intramolecular motions can substantially affect the permittivity $\varepsilon'_\perp(f)$, starting from the orientational dispersion region up to frequencies in the infrared region. Hence, it is reasonable to assume that relaxators can make different contributions to the permittivity over such a wide range of frequencies. In this respect, it is of interest to compare the results of the above approximation with the data obtained for the following asymmetric distribution function of relaxation times [13]:

$$G(\tau) = \frac{1}{A}\left(\frac{1}{\tau^{1-p}}\right), \quad \tau_{\perp R} \le \tau \le \tau_{\perp L},$$
$$G(\tau) = 0, \quad \tau_{\perp R} > \tau > \tau_{\perp L}, \qquad (5)$$

where p is the asymmetry parameter ($0 \le p < 1$) and A is a numerically determined coefficient. The calculations demonstrate that the frequency dependences of the permittivity thus approximated almost coincide with those obtained for the symmetric uniform distribution function of relaxation times in the range $\tau_{\perp L}$–$\tau_{\perp R}$. Moreover, even the limits of the relaxation time range, i.e., $\tau_{\perp L}$ and $\tau_{\perp R}$, which are calculated within the above approximations also nearly coincide with each other. The numerical values of these limits for the liquid crystals under investigation are given in Table 2. This table also presents the relaxation times $\tau_{\perp\varepsilon''}$ corresponding to the transverse permittivity $\varepsilon''_\perp$ at the maximum, the asymmetry parameters p of distribution function (5), the optical anisotropies $\Delta n = n_e - n_o$, and the ordinary refractive indices squared n_o^2.

Table 2. Main characteristics of the liquid crystals for perpendicular orientations of the liquid-crystal director with respect to the microwave electric pump field

Liquid crystal	$\tau_{\perp L}$ 10^{-9} s	$\tau_{\perp R}$ 10^{-11} s	$\tau_{\perp\varepsilon''}$ 10^{-10} s	p	Δn	n_o^2
5CB	9–10	2–6	3.5	0.4–0.45	0.245	2.325
5PCH	6–8	1–4	4.5	0.2–0.25	0.1	2.22
5BCO	25–30	4–9	6.4	0.05–0.1	0.08	2.25

It follows from Table 2 that, in the series 5CB–5PCH–5BCO, the limits of the relaxation time range vary insignificantly, except in the lower relaxation limit for the 5BCO liquid crystal. It is quite possible that, owing to the large molecular packing coefficient of the 5BCO liquid crystal, the rotation of molecules about the long axis is retarded as the result of stronger intermolecular interactions associated either with the aromatic cores or with the alkyl tails.

The distinctive feature of the dielectric spectrum of the 5CB liquid crystal is that the frequency dependence of the transverse permittivity in the high-frequency range significantly deviates from the Debye behavior. The dependence $\varepsilon'_\perp(f)$ for this liquid crystal can be satisfactorily approximated using the asymmetric distribution function (5) with a sufficiently large asymmetry parameter (p = 0.40–0.45). The dispersion of the trans-

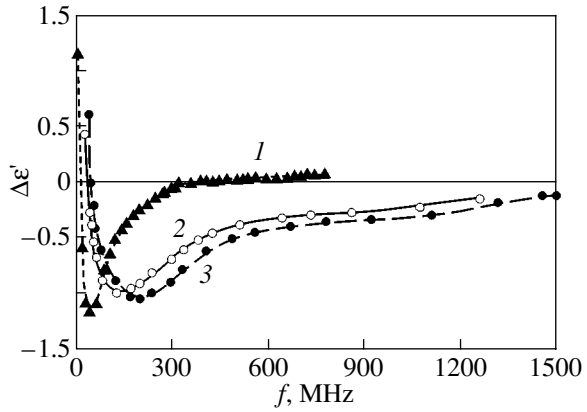

Fig. 4. Frequency dependences of the dielectric anisotropy for (*1*) 5CB, (*2*) 5PCH, and (*3*) 5BCO liquid crystals.

verse permittivity of the 5CB liquid crystal leads to double inversion of the sign of the dielectric anisotropy $\Delta\varepsilon' = \varepsilon'_{\parallel} - \varepsilon'_{\perp}$ in the frequency range ~350–450 MHz. The dependences $\Delta\varepsilon'(f)$ in the high-frequency relaxation region for all the liquid crystals studied are plotted in Fig. 4. As can be seen, the frequency range of negative dielectric anisotropies for the 5CB liquid crystal is considerably narrower than that for the cyclohexane and bicyclooctane homologs. As the frequency increases, the dielectric anisotropy of the 5PCH and 5BCO liquid crystals monotonically tends to zero. For these samples, zero dielectric anisotropy should be observed in the high-frequency range $f > 2000$ MHz. This behavior can be explained by the appreciable decrease in the optical anisotropy (Table 2), which the dielectric anisotropy approaches.

4. CONCLUSIONS

Thus, the permittivities of liquid crystals of the cyano derivative compounds based on alkylcyanobiphenyl (5CB), in which one benzene ring in the biphenyl core of the molecule is replaced by a cyclohexane or bicyclooctane fragment, were measured over a wide range of frequencies. It was demonstrated that the frequency dependence of the longitudinal permittivity $\varepsilon'_{\parallel}(f)$ for liquid crystals in the nematic phase is well approximated by the sum of two Debye processes with different relaxation times. It was found that the activation energy determined from the temperature dependence of the longitudinal relaxation time $\tau_{\parallel 1}$ increases in the series 5CB–5PCH–5BCO. The assumption was made that the observed increase in the activation energy is associated with the increase in the molecular packing coefficient. In the above series, this coefficient is maximum for the 5BCO compound.

It was established that the frequency dependence of the transverse permittivity $\varepsilon'_{\perp}(f)$ for liquid crystals in the nematic phase can be well approximated by the Debye dispersion relation with either a symmetric function or an asymmetric function of the continuous distribution of relaxation times in a specified range. It was revealed that the behavior of the dielectric anisotropy of the 5CB liquid crystal in the relaxation region differs from that of the other two compounds under investigation.

ACKNOWLEDGMENTS

This work was supported by the Russian Foundation for Basic Research, project no. 03-03-32470.

REFERENCES

1. B. A. Belyaev, N. A. Drokin, V. F. Shabanov, and V. N. Shepov, Fiz. Tverd. Tela (St. Petersburg) **42** (5), 956 (2000) [Phys. Solid State **42**, 987 (2000)].
2. B. A. Belyaev, N. A. Drokin, V. F. Shabanov, and V. N. Shepov, Zh. Tekh. Fiz. **72** (4), 99 (2002) [Tech. Phys. **47**, 470 (2002)].
3. B. A. Belyaev, N. A. Drokin, V. F. Shabanov, and V. N. Shepov, Fiz. Tverd. Tela (St. Petersburg) **45** (3), 567 (2003) [Phys. Solid State **45**, 598 (2003)].
4. D. A. Dunmur and A. E. Tomes, Mol. Cryst. Liq. Cryst. **97** (1), 241 (1983).
5. B. Urban, B. Gestblom, and A. Würflinger, Mol. Cryst. Liq. Cryst. **331**, 113 (1999).
6. V. V. Belyaev, M. F. Grebenkin, and V. F. Petrov, Zh. Fiz. Khim. **64** (4), 958 (1990).
7. V. V. Belyaev and V. B. Nemtsov, Zh. Fiz. Khim. **66** (10), 2763 (1992).
8. D. A. Dunmur, M. R. Manterfield, W. H. Miller, and J. K. Dunleavy, Mol. Cryst. Liq. Cryst. **45**, 127 (1978).
9. E. M. Aver'yanov, P. V. Adomenas, V. A. Zhuĭkov, *et al.*, Zh. Éksp. Teor. Fiz. **87** (5), 1686 (1984) [Sov. Phys. JETP **60**, 984 (1984)].
10. K. Toriyama, S. Sugimori, K. Moriya, *et al.*, J. Phys. Chem. **100** (1), 307 (1996).
11. V. V. Belyaev, Izv. Akad. Nauk, Ser. Fiz. **60** (4), 12 (1996).
12. M. A. Leshchenko and Yu. M. Poplavko, Ukr. Fiz. Zh. **37** (6), 898 (1992).
13. A. A. Potapov and M. S. Mitsek, *Dielectric Polarization* (Irkut. Gos. Univ., Irkutsk, 1986).

Translated by O. Borovik-Romanova

Physics of the Solid State, Vol. 46, No. 3, 2004, pp. 579–583. Translated from Fizika Tverdogo Tela, Vol. 46, No. 3, 2004, pp. 559–562.

POLYMERS AND LIQUID CRYSTALS

Dielectric Relaxation of *trans*-4-Propyl-(4-Cyanophenyl)-Cyclohexane Liquid Crystals

B. A. Belyaev, N. A. Drokin, and V. F. Shabanov

Kirensky Institute of Physics, Siberian Division, Russian Academy of Sciences, Akademgorodok, Krasnoyarsk, 660036 Russia
e-mail: belyaev@iph.krasn.ru

Received July 28, 2003

Abstract—The frequency dependences of the permittivity of a *trans*-4-propyl-(4-cyanophenyl)-cyclohexane (3PCH) liquid crystal in the nematic phase are measured in the frequency range 1–2000 MHz for different orientations of the director of liquid-crystal molecules with respect to the polarization of an ac electric field. The temperature dependences of the dielectric and optical characteristics are compared in the range of the transition from the nematic phase to the isotropic liquid phase. The dielectric spectra are approximated numerically, and the times of dipole relaxation upon rotation of the molecules about the short and long axes are determined. It is demonstrated that intramolecular motions make a significant contribution to the relaxation. The activation enthalpies are calculated. © *2004 MAIK "Nauka/Interperiodica".*

1. INTRODUCTION

It is known that the difference between static permittivities of nematic liquid crystals with parallel $\varepsilon_{\parallel 0}$ and perpendicular ($\varepsilon_{\perp 0}$) orientations of the director of liquid-crystal molecules with respect to the electric pump field is associated with rotations of the molecules about the short and long molecular axes [1]. As a rule, the frequency dependences of the longitudinal (parallel) $\varepsilon_\parallel(f)$ and transverse (perpendicular) $\varepsilon_\perp(f)$ permittivities are adequately described by the Debye equations with relaxation times $\tau_\parallel$ and $\tau_\perp$, which can differ from each other by several orders of magnitude. It is worth noting that the Debye relaxation time for molecules of many liquid crystals in an isotropic state approximately coincides with the relaxation time $\tau_\perp$. The frequency dependence of the longitudinal permittivity $\varepsilon_\parallel(f)$ of liquid crystals in the nematic phase is considerably shifted to the low-frequency range due to the interaction of liquid-crystal molecules, which is responsible for the formation of the potential barrier to rotations of the molecules about the short axis [1, 2].

However, the experimental dielectric spectra of liquid crystals measured over a wide range of frequencies are often characterized by noticeable deviations from the Debye behavior due to the contributions from additional relaxation mechanisms associated, for example, with intramolecular motions. In particular, this is characteristic of the dielectric spectra of liquid crystals belonging to the alkylcyanobiphenyl group *n*CB ($n = 5$–9). Molecules of these compounds contain a rigid aromatic core and an alkyl tail consisting of conformationally mobile methylene fragments. It should be noted that the dielectric spectra of the aforementioned liquid crystals significantly deviate from the Debye behavior in high- and ultrahigh-frequency ranges for perpendicular orientations of the director of molecules with respect to the polarization of the electric pump field [3–6]. The observed deviations are associated with the induced polarizability of the alkyl chains due to a change in their conformational equilibrium in microwave electric fields. The greater the number of methylene groups in liquid-crystal molecules, the more widely the frequency dependence of the real part of the transverse permittivity $\varepsilon'_\perp(f)$ deviates from the Debye behavior, because the number of overlapping ranges of natural frequencies of characteristic conformational vibrations increases and, correspondingly, their frequency range becomes wider.

Earlier [7], we showed that the frequency dependence of the real part of the transverse permittivity $\varepsilon'_\perp(f)$ for *n*CB liquid crystals ($n \geq 5$) can be numerically approximated to a high accuracy by the Debye dispersion relation with a continuous distribution of relaxation times in a specified range. This distribution is adequately described by an asymmetric function. However, within the proposed approach, it is impossible to separate and identify the contributions from different molecular motions to the relaxation processes and to determine the relaxation times associated with the motion of the aromatic core and the flexible terminal fragments of the molecules. With a decrease in the number of methylene groups to $n = 3$ in the alkyl tail, for example, for a 5-propyl-2-(*p*-cyanophenyl)-pyridine liquid crystal, the dielectric spectrum $\varepsilon'_\perp(f)$ can be well approximated using the Debye dispersion relation with a symmetric continuous distribution function of relaxation times in a relatively narrow range (23.9–1.85) $\times 10^{-9}$ s [8]. In this case, fluctuations of chain bending due to internal rotations of fragments in the

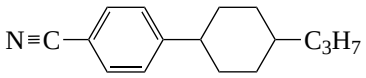

Fig. 1. Structural formula of the *trans*-4-propyl-(4-cyanophenyl)-cyclohexane liquid-crystal compound.

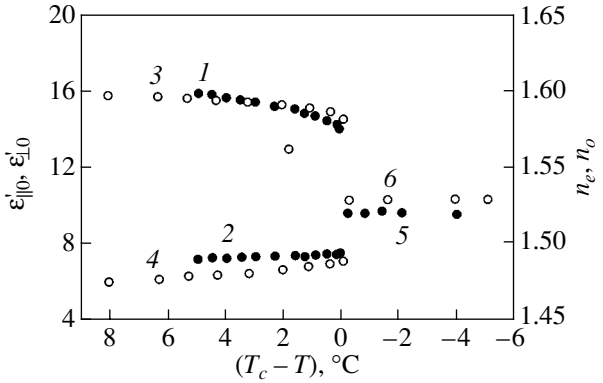

Fig. 2. Temperature dependences of the optical n_e and n_o (closed symbols) and dielectric $\varepsilon'_{\parallel 0}$ and $\varepsilon'_{\perp 0}$ (open symbols) parameters for the 3PCH liquid crystal in the temperature range of the transition from the nematic phase to the isotropic liquid phase (for explanation of the curves, see text).

alkyl tail can be considered to be statistically independent [9], because the distribution functions of their natural frequencies virtually do not overlap with each other.

In the present work, we measured and analyzed the dielectric spectra of a monotropic liquid crystal, namely, *trans*-4-propyl-(4-cyanophenyl)-cyclohexane (3PCH), with a short alkyl tail (n = 3). The structural formula of the *trans*-4-propyl-(4-cyanophenyl)-cyclohexane liquid-crystal compound is presented in Fig. 1. The monotropic properties of the 3PCH liquid crystal manifest themselves in the fact that this compound undergoes a transition to the liquid-crystal phase at a temperature T_c = 46°C only from the isotropic phase formed upon preliminary heating of the compound to temperatures $T > T_c$. The crystallization temperature of the 3PCH compound ($T \le 36$°C) depends on the cooling rate. The purpose of this work was to separate the contributions from different rotational (reorientational) molecular and intramolecular motions to the frequency dependences of the permittivities of the 3PCH liquid crystal. The dielectric spectra were measured over a wide frequency range (f = 1–2000 MHz) at several fixed angles φ between the director of liquid-crystal molecules and the polarization of the microwave pump field. The experimental temperature dependences of the permittivities and refractive indices were obtained in the temperature range of the phase transition from the nematic liquid crystal to the isotropic liquid.

Investigation into the optical and dielectric properties of the 3PCH nematic liquid crystal is of particular interest, because this compound is similar in molecular structure to the well-known and thoroughly studied liquid crystals of the alkylcyanobiphenyl group *n*CB (n = 5–9) [3–7]. The only difference between them lies in the fact that, in the rigid core of the 3PCH molecule, one benzene ring is replaced by a cyclohexane fragment. Moreover, the number of methylene fragments (n = 3) in the alkyl tail of the 3PCH molecule is rather small for liquid crystals and equal to that for a 5-propyl-2-(*p*-cyanophenyl)-pyridine liquid crystal [8]. However, unlike the pyridine-containing liquid-crystal compound, the 3PCH nematic liquid crystal is characterized by a permanent dipole moment associated with the presence of the –C≡N group and directed along the long molecular axis.

2. EXPERIMENTAL TECHNIQUE

The permittivities of the 3PCH nematic liquid crystal were measured with the use of capacitive and special microstrip sensors. The sensor design, equipment, and technique of measurements were thoroughly described in our previous works [10, 11]. The absolute errors in determining the dielectric characteristics were no larger than $\delta\varepsilon' \sim 0.05$ and $\delta\varepsilon'' \sim 0.1$. The required angle φ between the long axes of molecules in the 3PCH sample and the polarization of the microwave electric field in the measuring cell was specified by the appropriate direction of the static magnetic field H = 2500 Oe. The dielectric spectra were recorded at a temperature $T = T_c - 5$°C. In order to calculate the activation enthalpies upon longitudinal and transverse pumping of the sample, the dielectric spectra were measured at a temperature $T = T_c - 10$°C. The measurements of the static permittivities were performed at temperatures of 30–60°C and a frequency of 1 MHz, at which the dispersion is virtually absent. The temperature was maintained accurate to ±0.5°C.

The temperature dependences of the ordinary (n_o) and extraordinary (n_e) refractive indices were measured at the wavelength λ = 0.589 μm with the use of an IRF-454B refractometer with a homeotropic orientation of the director in the measuring cell. These data were required for the numerical approximation of the dielectric spectra.

3. RESULTS AND DISCUSSION

The experimental temperature dependences of the extraordinary n_e (closed symbols *1*) and ordinary n_o (closed symbols *2*) refractive indices for the nematic phase and the temperature dependence of the refractive index for the isotropic phase (closed symbols *5*) are depicted in Fig. 2. This figure also shows the temperature dependences of the real parts of the longitudinal $\varepsilon'_{\parallel}$ (open symbols *3*) and transverse $\varepsilon'_{\perp}$ (open symbols *4*)

permittivities of the 3PCH nematic liquid crystal, which were measured in parallel and perpendicular orientations of the director of liquid-crystal molecules with respect to the electric pump field. The temperature dependence of the permittivity for the isotropic phase is represented by open symbols *6*. In this case, the cooling rate of the sample was approximately equal to 4 K/h. It can be seen from Fig. 2 that the measured parameters only slightly depend on the temperature in both the nematic (curves *1–4*) and isotropic (curves *5*, *6*) phases. It is worth noting that the optical anisotropy is relatively small: $\Delta n = n_e - n_o \approx 0.11$.

The frequency dependences of the real and imaginary parts of the permittivity of the 3PCH liquid crystal in the nematic phase were measured for the following angles between the director of liquid-crystal molecules and the polarization of the electric pump field: $\varphi = 0°$, 10°, 20°, 45°, 70°, 80°, and 90°. The dielectric spectra $\varepsilon'_\varphi(f)$ were numerically approximated by the sum of three Debye processes with different relaxation times τ_1, τ_2, and τ_3; that is,

$$\frac{\varepsilon'(f) - n_\varphi^2}{(\varepsilon'_{0\varphi} - n_\varphi^2)} = \sum_{i=1}^{3} \frac{g_i}{1 + 4\pi^2 f^2 \tau_i^2}, \qquad (1)$$

where $n_\varphi = n_e\cos^2\varphi + n_o\sin^2\varphi$, $\varepsilon'_{0\varphi}$ is the static permittivity at a given angle φ, and g_i are the weighting factors ($g_1 + g_2 + g_3 = 1$). It is assumed that the first two terms in expression (1) characterize the rotation (reorientation) of molecules about the short and long axes, respectively, and the third term describes the conformational motion of methylene groups in the alkyl tail. It is evident that, within this approach, the quantity τ_3 is the mean (or most probable) relaxation time for all conformational motions in the alkyl tail.

Figure 3 shows the frequency dependences of the normalized real permittivity $\varepsilon'(f)$ (open symbols) and the magnitude of the imaginary permittivity $\varepsilon''(f)$ (closed symbols) measured at angles $\varphi = 0°$, 45°, and 90°. In this figure, solid lines represent the results of the numerical Debye approximation of these dependences according to expression (1) and dashed lines *1–3* correspond to individual contributions from the three aforementioned relaxation processes to the total dispersion of the permittivity. It should be noted that the frequency dependence of the permittivity calculated within the proposed approximation is in good agreement with the experimental data obtained for all the director orientations over the entire frequency range covered.

As could be expected, at $\varphi = 0°$, the dielectric spectrum $\varepsilon'(f) = \varepsilon'_\parallel(f)$ in the low-frequency dispersion region is predominantly determined by the rotation of molecules about the short molecular axis ($g_1 = 0.95$, $\tau_1 = 9$ ns). The activation enthalpy $\Delta H_1 = 72 \pm 4$ kJ/mol was calculated from the temperature dependence of the relaxation time $\tau_1(T)$. This value is characteristic of the reorientation of liquid-crystal molecules about the short axis in the nematic phase. Moreover, the dielectric spectrum in the high-frequency dispersion region is characterized by a small contribution from the conformational motions of the alkyl tail ($g_3 = 0.05$, $\tau_3 = 0.2$ ns). However, for this director orientation, the rotation of molecules about the long axis does not contribute to the dispersion of the longitudinal permittivity $\varepsilon'_\parallel(f)$ ($g_2 = 0$).

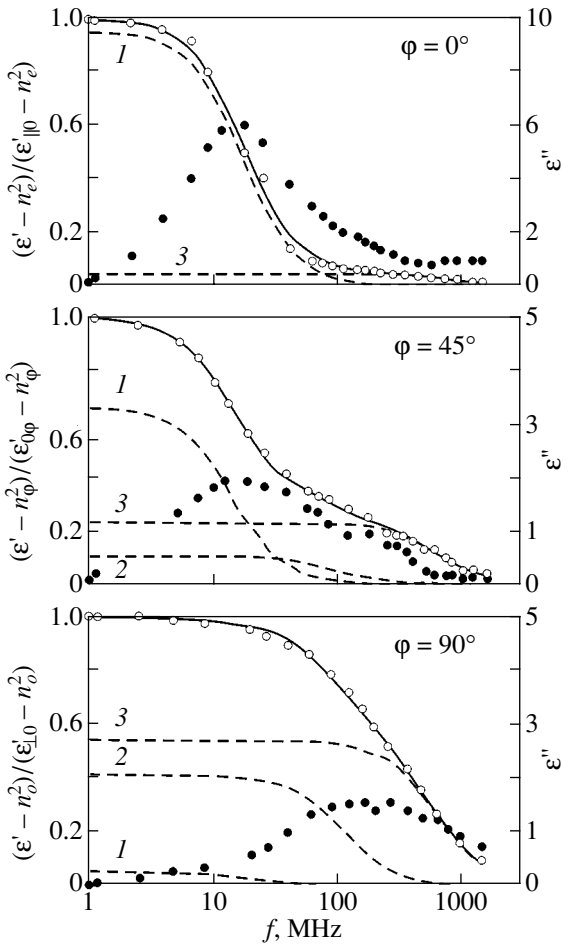

Fig. 3. Frequency dependences of the real (open symbols) and imaginary (closed symbols) permittivities of the 3PCH liquid crystal for different orientations of the director of the liquid-crystal molecules. Solid lines correspond to the Debye approximations. Dashed lines *1–3* indicate the contributions from three relaxation mechanisms (for explanation of the curves, see text).

It can be seen from Fig. 3 that, at $\varphi = 45°$, the dielectric dispersion contains contributions from all three relaxation processes under consideration. The weighting factors of these processes are of the same order of magnitude ($g_1 = 0.66$, $g_2 = 0.11$, $g_3 = 0.23$). Note that the contribution from the rotation of molecules about the long axis (relaxation time $\tau_2 = 1.4$ ns) is maximum, whereas the contribution from the rotation of molecules about the short axis is minimum. At $\varphi = 90°$, the dielectric spectrum $\varepsilon'(f) = \varepsilon'_\perp(f)$ should also be approxi-

Main characteristics of the liquid crystal for different orientations of the polarization of a microwave electric field with respect to the director of molecules

φ, deg	τ_1, ns	τ_2, ns	τ_3, ns	g_1	g_2	g_3	n	ε_0
0	9	–	0.20	0.95	0	0.05	1.600	15.69
10	8	–	0.25	0.90	0	0.10	1.597	13.70
20	8	–	0.25	0.90	0	0.10	1.596	12.50
45	11	1.56	0.23	0.66	0.11	0.23	1.545	9.57
70	13	1.40	0.25	0.35	0.30	0.35	1.503	7.55
80	10	1.41	0.24	0.10	0.44	0.46	1.493	6.10
90	8	1.40	0.25	0.05	0.41	0.54	1.490	6.05

mated with allowance made for all three relaxation processes. In this case, the contribution from the reorientation of molecules about the short axis decreases significantly ($g_1 = 0.05$). Although the contributions from the other two mechanisms are comparable in magnitude ($g_2 = 0.41$, $g_3 = 0.54$), the contribution from the conformational motion of the alkyl tail appears to be dominant. This is a rather unexpected result; nonetheless, it accounts for the fact that the dielectric spectra $\varepsilon'_\perp(f)$ noticeably deviate from the Debye behavior in the high-frequency range.

It should be noted that, like the time of longitudinal relaxation τ_1, the time of transverse relaxation τ_2 is a function of the temperature. However, the activation enthalpy calculated from the temperature dependence $\tau_2(T)$ proves to be substantially less: $\Delta H_2 = 9 \pm 2$ kJ/mol. For the nematic liquid-crystal phase, the relaxation time τ_3 does not depend on the temperature in the range studied.

The table presents the relaxation times, weighting factors, refractive indices, and static permittivities of the liquid crystal under investigation for different orientations of the director of liquid-crystal molecules with respect to the polarization of the electric pump field. It can be seen from the table that the relaxation times only weakly depend on the angle φ. However, the relaxation time τ_1 reaches a maximum at $\varphi \approx 70°$, whereas the maximum value of τ_2 is observed at $\varphi \approx 45°$. This suggests that weak relaxation processes manifest themselves at particular angles φ and hinder the reorientation of molecules about the long and short axes. The relaxation time τ_3 can be considered to be virtually independent of the angle φ.

4. CONCLUSIONS

Thus, the permittivities of the *trans*-4-propyl-(4-cyanophenyl)-cyclohexane liquid-crystal compound were measured over a wide frequency range for different orientations of the director of liquid-crystal molecules with respect to the polarization of the electric field. The dielectric spectra were numerically approximated using the sum of three Debye processes with different relaxation times. The proposed approximation of the dielectric spectra $\varepsilon'(f)$ made it possible to reveal important features in the dependence of the ratio of the contributions from three dominant mechanisms of relaxation in the liquid crystal (rotations of molecules about the short and long molecular axes and intramolecular conformational motions of the alkyl tail of the 3PCH molecule) on the angle φ between the polarization of the electric pump field and the director of the liquid-crystal molecules. However, the approximation approach used in our consideration offers an adequate description only for molecules with a small number n of methylene fragments in the alkyl tail in the case where the real distributions of relaxation times do not overlap in the vicinity of τ_1, τ_2, and τ_3. As the number of methylene groups in the alkyl tail of liquid-crystal molecules increases ($n > 3$), the range of relaxation times corresponding to intramolecular motions becomes wider and, therefore, the parameter τ_3 as an effective relaxation time loses its meaning. In this case, the dielectric spectra can be well approximated by the Debye dispersion relation with an asymmetric continuous distribution function of relaxation times in a specified range.

The above investigations demonstrated that the intramolecular motions in liquid crystals slightly affect the dispersion of the longitudinal permittivity $\varepsilon'_\parallel(f)$, even though it is determined primarily by rotations of molecules about the short axis. At the same time, rotations of the molecules about the long axis do not contribute to the dispersion of the longitudinal permittivity. It was also established that the dispersion of the transverse permittivity $\varepsilon'_\perp(f)$ is governed by the contributions from all three relaxation mechanisms; however, the greatest contribution in this case is made by intramolecular motions.

ACKNOWLEDGMENTS

This work was supported by the Russian Foundation for Basic Research, project no. 03-03-32470.

REFERENCES

1. L. M. Blinov, *Electro-Optical and Magneto-Optical Properties of Liquid Crystals* (Nauka, Moscow, 1978; Wiley, New York, 1983).

2. A. A. Potapov and M. S. Mitsek, *Dielectric Polarization* (Irkut. Gos. Univ., Irkutsk, 1986).
3. D. A. Dunmur, M. R. Manterfield, W. H. Miller, and J. K. Dunleavy, Mol. Cryst. Liq. Cryst. **45**, 127 (1978).
4. P. G. Gummins, D. A. Dunmur, and D. A. Laidler, Mol. Cryst. Liq. Cryst. **30**, 109 (1975).
5. B. R. Ratna and R. Shashidar, Mol. Cryst. Liq. Cryst. **42**, 185 (1977).
6. J. M. Wacrenier, C. Druon, and D. Lippens, Mol. Phys. **43**, 97 (1981).
7. B. A. Belyaev, N. A. Drokin, V. F. Shabanov, and V. N. Shepov, Fiz. Tverd. Tela (St. Petersburg) **45** (3), 567 (2003) [Phys. Solid State **45**, 598 (2003)].
8. B. A. Belyaev, N. A. Drokin, and V. F. Shabanov, Fiz. Tverd. Tela (St. Petersburg) **45** (4), 756 (2003) [Phys. Solid State **45**, 797 (2003)].
9. E. M. Aver'yanov, *Local Field Effects in Optics of Liquid Crystals* (Nauka, Novosibirsk, 1999).
10. B. A. Belyaev, N. A. Drokin, and V. N. Shepov, Zh. Tekh. Fiz. **65** (2), 189 (1995) [Tech. Phys. **40**, 216 (1995)].
11. B. A. Belyaev, N. A. Drokin, V. F. Shabanov, and V. N. Shepov, Zh. Tekh. Fiz. **72** (4), 99 (2002) [Tech. Phys. **47**, 470 (2002)].

Translated by O. Borovik-Romanova

Physics of the Solid State, Vol. 46, No. 3, 2004, pp. 584–589. Translated from Fizika Tverdogo Tela, Vol. 46, No. 3, 2004, pp. 563–568.

FULLERENES AND ATOMIC CLUSTERS

Density and Thermodynamics of Hydrogen Adsorbed Inside Narrow Carbon Nanotubes

A. S. Fedorov[1] and S. G. Ovchinnikov[1, 2]

[1]*Kirensky Institute of Physics, Siberian Division, Russian Academy of Sciences, Akademgorodok, Krasnoyarsk, 660036 Russia*

e-mail: alex99@akadem.ru

[2]*UNESCO Faculty "New Materials and Technologies," Krasnoyarsk State Technical University, Krasnoyarsk, 660074 Russia*

Received July 8, 2003

Abstract—A model is proposed for calculating the thermodynamic functions and the equilibrium density of a one-dimensional chain of molecules (atoms) adsorbed inside a narrow nanotube. The model considers both the interaction between introduced atoms (molecules) and their interaction with the nanotube walls. The quantum-mechanical effects resulting in discrete energy levels of a particle and in its smeared position between neighbors are taken into account. In calculating the free energy at a nonzero temperature, the phonon contribution and the particle transitions to excited levels are considered. The model is applied to calculate the thermodynamic parameters of adsorbed hydrogen molecules inside extremely narrow single-wall carbon nanotubes of the (3,3) and (6,0) type. It is shown that external pressure gives rise to a sequence of first-order phase transitions, which change the density of adsorbed hydrogen molecules. © *2004 MAIK "Nauka/Interperiodica".*

1. INTRODUCTION

The experimental detection of carbon nanotubes in 1991 [1] has offered new opportunities for both technology and fundamental physics. The nanometer scale and one-dimensionality inherent to such structures have led to discoveries of interesting mechanical, chemical, and electrical properties in them [2]. One of the remarkable properties of carbon nanotubes (CNTs) is their ability to adsorb various atoms or molecules. The huge specific area of the CNT surface (as large as several hundred square meters per gram) allows adsorption of large amounts of inert gases, hydrogen, metals, water, etc. For example, it was experimentally shown in [3] that CNTs can absorb more than 3.5 wt % of hydrogen, which makes them promising hydrogen accumulators. It was also shown in [3] that this application of CNT can be economically advantageous in the motor industry even in the case of a hydrogen content of ≅6.5%.

One-dimensional chain systems in which particles cannot jump over one another (single-file systems) have been studied in a large number of papers [4–6]. Recently, such systems with an extremely small channel diameter (4–5 Å) have been successfully produced by annealing zeolite $AlPO_4$–5 whose channels contained hydrocarbons [7, 8]. A quantum theory of molecular separation was developed in [9, 10]. This theory predicts that isotopes (especially those of hydrogen) can be efficiently separated inside extremely narrow channels at low temperatures, because isotopes differ in the quantized energy levels of their transverse motion. In other theoretical papers, dedicated to the diffusion of particles during their longitudinal motion in these systems, it was shown that diffusion is characterized by extraordinary properties under these conditions. For example, the mean square of particle displacements $\langle z^2 \rangle$ is proportional to the square root of the observation time $t^{1/2}$ rather than to the time t, as is usually the case. This extraordinary property was convincingly proved experimentally in [11]. Theoretical analysis of chain systems is significantly complicated by the fact that the positions of adsorbed particles strictly correlate with the positions of all other particles in the system. For this reason, analytical results are scarce or are obtained using various approximations. The conventional approximate techniques applied in such studies are the Monte Carlo methods [diffusion Monte Carlo (DMC) or canonical methods], the one-dimensional lattice gas model, and the molecular-dynamics (MD) method. The DMC method [12] allows one to perform quantum-mechanical calculations of the thermodynamic parameters, correlation functions, and the equilibrium particle density in terms of the wave function of the system. However, since calculations are complicated, the temperature effects are usually ignored in the DMC method. The canonical Monte Carlo method [13] makes it possible to include the temperature effects. However, this method is based on the classical-mechanical dynamics equations and interparticle interaction potentials; hence, the quantum-mechanical effects are ignored. Furthermore, any Monte Carlo computation involves a large number (~10^6) of different configurations, which complicates such calculations. The lattice

1063-7834/04/4603-0584$26.00 © 2004 MAIK "Nauka/Interperiodica"

gas model [6] is also based on classical interaction potentials and disregards the quantum-mechanical effects. Moreover, in this model, particles are positioned discretely at N equidistant sites separated by potential barriers of height E_b. In this case, the frequency of hopping to a neighboring site is calculated as $P = P_0\exp(-E_b/k_BT)$, where the pre-exponential factor P_0 is dictated by the activation mechanism. Unfortunately, this model is statistical and ignores actual motion of adsorbate molecules inside the nanotube. Moreover, the parameter P_0 cannot be calculated within the model and is fitted. The molecular dynamics methods [14, 15] (both the non-empirical one and that based on empirical interaction potentials of atoms or molecules) allow calculations of the dynamics of atoms in terms of the forces acting on the atoms. A fundamental constraint of any MD calculation is the fact that atoms are assumed to obey the classical Newtonian equations of motion rather than the quantum-mechanical laws. This method disregards the zero-point oscillations of atoms, energy quantization, and tunneling effect. Therefore, any MD calculation cannot adequately predict even qualitative results for particle motion at a low temperature when the particle kinetic energy is lower than the potential barrier height, $E_{kin} < E_b$. We also note that certain recent studies partially include the quantum effects in the MD calculation scheme for simple systems [16, 17].

2. MODEL

This paper is devoted to a theoretical study of the equilibrium properties of a one-dimensional chain of atoms (molecules) interacting with one another via a pair potential $V(r)$ and with the tube walls via a potential $V_{tube}(r)$. The study is based on a model that allows calculation of the thermodynamic properties of such a system at various temperatures and includes the quantum effects. The interaction potentials are determined using *ab initio* calculations. The behavior of hydrogen molecules inside ultrathin single-wall carbon nanotubes of the (3,3) and (6,0) type [18] with a diameter of 4.07 and 4.70 Å, respectively, is studied. To verify the assumption of strictly one-dimensional motion of adsorbate molecules along the axis of each of these nanotubes, molecular-dynamic calculations are carried out for the hydrogen molecule dynamics inside the nanotubes at various temperatures. It is established that the maximum value of the angle α between the moving molecule and the nanotube axis is small ($\alpha \cong 5°$ for the (3,3) tube at $T = 200$ K); hence, the motion of adsorbed particles can be considered one-dimensional.

The model is based on the solution of the one-dimensional Schrödinger equation for a particle (hydrogen molecule) moving along the nanotube axis in the potential that is the sum of the potentials $V(r - R_r)$ and $V(r - R_l)$ produced by the right-hand and left-hand neighbors (identical molecules) of the particle, respectively, and of the potential produced by the nanotube atoms:

$$\left(-\frac{\nabla^2}{2m} + V(r)\right)\Psi_i(r) = \varepsilon^i\Psi_i(r), \quad (1)$$

$$V(r) = V(r - R_l) + V(r - R_r) + V_{tube}(r), \quad (2)$$

where ε^i is the particle energy in state i. Both neighbors of the particle are assumed to be fixed. This case corresponds to the mean-field approximation, in which the positions of the neighbor particles inducing the potential are replaced with their averages. The position of the particle itself is described by the probability density $|\Psi_i(r)|^2$. In the case of $T \neq 0$, where the particle can transfer to the excited energy levels ε^i, the average energy of the particle is calculated using the Gibbs distribution

$$\langle U\rangle = \frac{1}{Z}\sum_i \varepsilon^i \exp\left(-\frac{\varepsilon^i}{k_BT}\right), \quad Z = \sum_i \exp\left(-\frac{\varepsilon^i}{k_BT}\right), \quad (3)$$

where Z is the partition function.

The interaction potential $V_{tube}(r)$ between the molecule and the nanotube walls is defined as the change ΔE_{tot} in the total energy of the system consisting of the nanotube and the hydrogen molecules at its axis (with a sufficiently large distance between hydrogen molecules to remove their interaction) as the molecule position along the tube axis is varied. The maximum values (in kelvins) of the potential $V_{tube}(r)$ for the (6,0) and (3,3) nanotubes are $V_{max} \cong 2300$ and 211 K, respectively. Such a significant difference is explained as follows. In the (6,0) nanotube, atoms on its sides are opposite to each other and their influences on the hydrogen molecule are in phase. In the (3,3) nanotube, atoms on opposite sides alternate and their influences on the hydrogen molecule are in antiphase, which decreases the potential $V_{tube}(r)$ amplitude by an order of magnitude. The period of the potential $V_{tube}(r)$ for the (6,0) tube is longer than that of the (3,3) tube by a factor of $\sqrt{3}$. Similarly, the interaction potential $V(r - R)$ between the hydrogen molecules is defined as the change in the total energy of the system (consisting of the nanotube and the hydrogen molecules at its axis) as the distance between the molecules is varied.

The total energy E_{tot} of the system is determined from *ab initio* calculations using the VASP software package [19, 20], based on an expansion in terms of plane waves and on the Vanderbilt pseudopotentials [21], within the density functional formalism. The use of the plane-wave basis is appropriate for studying periodic one-dimensional systems such as CNTs. The use of the Vanderbilt pseudopotentials allows one to significantly decrease the number of plane waves necessary for the calculation. In the calculations we carried out, the maximum kinetic energy E_{cut} defined by the carbon pseudopotential was 286 eV.

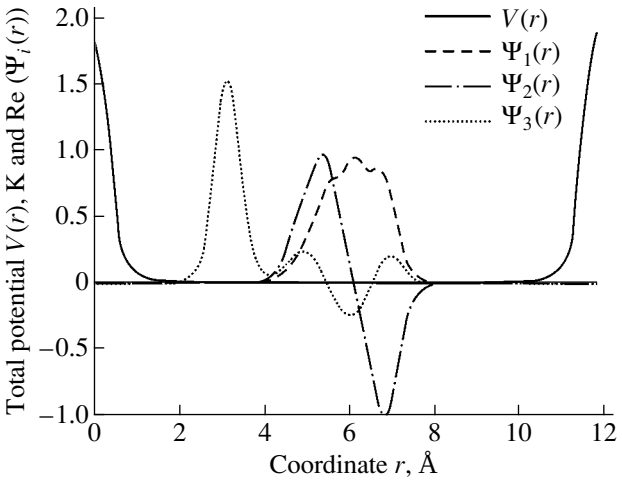

Fig. 1. Potential $V(r)$ (in kelvins) and the wave functions $\Psi_i(r)$ for the lowest states $i = \{1, 2, 3\}$ of an H_2 molecule in the (3,3) CNT.

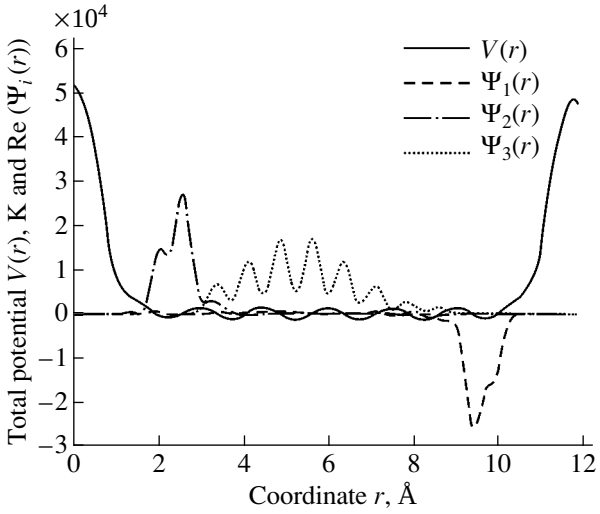

Fig. 2. Same as in Fig. 1 but for the (6,0) CNT.

The Schrödinger equation for the adsorbate molecule was solved by expanding the wave function with respect to plane waves:

$$\Psi_i(r) = \sum_{\mathbf{G}} C_k^i \exp(i\mathbf{G}\mathbf{r}). \quad (4)$$

In the calculations, we used the reciprocal lattice vectors **G** with the maximum magnitude $G \le G_{max} = 50$ (measured in units of $2\pi/a$, where $a = 2d$; d is the distance between the adsorbed particles).

Figures 1 and 2 show the total potentials acting on the hydrogen molecule inside the (3,3) and (6,0) nanotubes, respectively; the distance between the particles is equal to 6 Å. The potentials consist of two parts. One of them is defined by the interaction potential between the particle and its left-hand and right-hand neighbors (described by the steeply rising portions of the curve of the total potential near the ends). The other part is defined by the interaction potential between the particle and the nanotube atoms and is responsible for oscillations of the potential with a relatively small amplitude. Figures 1 and 2 also show the corresponding wave functions $\Psi_{1,2,3}(r)$ of the three lowest levels of the hydrogen molecule. We can see the difference in the molecule localization, which is due to the difference in the amplitude of the potential exerted on the particle by the nanotube atoms. Inside the (3,3) tube, this potential is weak and the particle is weakly localized and does not correlate with the positions of the minima of the potential. Inside the (6,0) nanotube, oscillations of the potential are ten times larger and the particle is mostly localized at the minima of the potential. These differences cause the average distances between hydrogen molecules inside the (6,0) tube to be more sensitive to external pressure than inside the (3,3) tube. External pressure causes molecules to jump from one local minimum to another.

We studied the dependence of the equilibrium distance between particles on external parameters, namely, the pressure p and temperature T. The equilibrium of the system at $\{p, T\} \neq 0$ corresponds to a minimum of the Gibbs thermodynamic potential $\Phi = \langle U\rangle - TS + PV = G + PV$ (where G is the free energy, S is the entropy, P is the external pressure, V is the volume of the system). Therefore, in addition to the internal energy $\langle U\rangle$, we should take into account the contributions from the entropy S and the volume energy PV. In the free energy G (per adsorbate molecule), we included two contributions. One of them is the free energy G_1 related to the average energy $\langle\varepsilon\rangle$ of the particles (determined at fixed positions of both neighbor adsorbate molecules) and to the entropy S_1 of their distribution over the energy levels; the other contribution, G_{ph}, is associated with deviations of the neighbors from their equilibrium positions. These deviations cause a change in the energy levels of the central molecule and, hence, a change in the total energy of the system. This change, in turn, gives rise to a restoring force acting on the neighbor molecules and produces the contribution G_{ph} to the free energy associated with phonon vibrations (with frequencies ω_i) of the chain of adsorbed molecules. Thus, we have

$$G = G_1 + G_{ph}, \quad G_1 = \langle U\rangle - TS_1, \quad (5)$$

$$S_1 = -k_B \sum_i P_i \ln P_i, \quad P_i = \frac{1}{Z}\exp\left(-\frac{\varepsilon^i}{k_B T}\right), \quad (6)$$

$$G_{ph} = \langle U\rangle_{ph} - TS_{ph} \quad (7)$$

$$= \sum_i \left[\frac{\hbar\omega_i}{2} + k_B T \ln\left(1 - \exp\left(-\frac{\hbar\omega_i}{k_B T}\right)\right)\right]. \quad (8)$$

Since the adsorbed molecules in the model interact via pair potentials, half the particle potential energy $[(1/2)\langle U_{pot}\rangle = (1/2)\langle E - E_{kin}\rangle]$ should be subtracted from the total internal and free energies ($\langle U\rangle$, G_1) in order to avoid counting the pairs twice. The particle kinetic energy in state i is calculated as $E_{kin}^i = \langle\Psi_i^*(r)|-\frac{\nabla^2}{2m}|\Psi_i(r)\rangle$.

The phonon frequencies $\omega_i(r, T)$ are calculated from the dispersion relation for phonons in a one-dimensional chain of particles of mass m mutually spaced at a distance d and interacting via the forces characterized by elastic constants $f(r, T)$. The result is

$$\omega_i(r, T) = 2\left(\frac{f(r, T)}{m}\right)^{1/2}\left|\sin\left(\frac{1}{2}q_i d\right)\right|, \quad (9)$$

$$f(r, T) = \frac{\partial^2\langle U_{pot}\rangle(r, T)}{\partial r^2}. \quad (10)$$

The elastic constants $f(d, T)$ are calculated for various temperatures, and the intermolecular distances d, by considering the displacement Δ of a particle positioned between two neighbors. The energy levels ε^i of the neighbors and, therefore, their average energies $\langle U(r \pm \Delta)\rangle$ and the total energy of the system vary in the second order with respect to Δ, giving rise to phonon vibrations. It should be noted that, although the model is based on the mean-field approximation, in which the positions of both neighbors of the particle are assumed to be fixed, the inclusion of the phonon contribution G_{ph} in the free energy partially eliminates the disadvantages of this approximation. In this case, perturbations in the positions of the neighboring particles with respect to their average positions are taken into account in the harmonic approximation.

The energy levels ε^i of a particle and, hence, the free energy per adsorbed particle depend on the phase r_{phase} of the periodic potential $V_{tube}(r - r_{phase})$ exerted on the particle by the nanotube atoms, $\varepsilon^i = \varepsilon^i(r_{phase})$. Therefore, we should perform Gibbs averaging of ε^i over various phases r_{phase}. Since the phases r_{phase} of the potential $V_{tube}(r - r_{phase})$ acting on neighboring particles are mutually correlated, this correlation should be correctly taken into account in the averaging. To this end, for each value of the average interparticle distance d, a cluster (chain of neighbors) of N particles is selected so that the phases of the potential $V_{tube}(r - r_{phase})$ acting on the first and last particles in the cluster are identical (the accuracy was 1/20 of the interatomic distance in the nanotube). Generally, this required setting approximately ten particles in the cluster. Then, positions i of interior particles in the cluster are varied to minimize

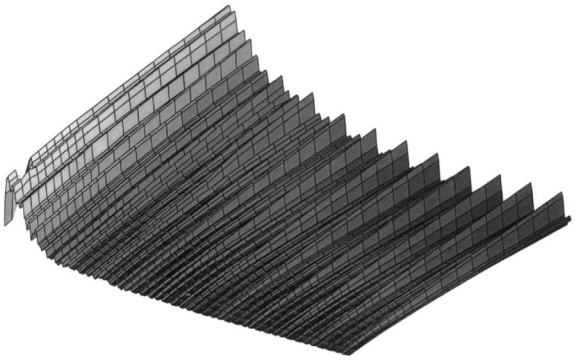

Fig. 3. Dependence of the average Gibbs free energy $\langle G(d, T)\rangle$ of a H_2 molecule on temperature T and interparticle distance d in the (3,3) CNT.

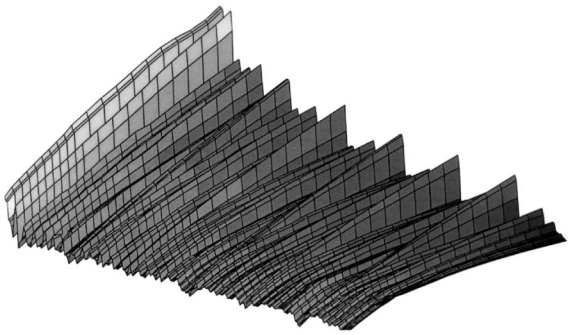

Fig. 4. Same as in Fig. 3 but for the (6,0) CNT.

the total free energy G_{cl} of the cluster and to calculate the average free energy of a particle:

$$\langle G(d, T)\rangle = 1/N\langle G_{cl}(T)\rangle, \quad (11)$$

$$G_{cl}(T, r_{phase}) = \min_{r_{phase\,i}}\left\{\sum_{i=2}^{N-1} G_i(T, r_{phase\,i})\right\}, \quad (12)$$

$$\langle G_{cl}(T)\rangle = \frac{1}{\tilde{Z}}\sum_{r_{phase}} G_{cl}(T, r_{phase})\exp\left(-\frac{G_{cl}(T, r_{phase})}{k_B T}\right), \quad (13)$$

$$\tilde{Z} = \sum_{r_{phase}}\exp\left(-\frac{G_{cl}(T, r_{phase})}{k_B T}\right). \quad (14)$$

These energies $\langle G(d, T)\rangle$ for hydrogen molecules inside both nanotubes are shown in Figs. 3 and 4. We note that the contribution of phonons to the free energy vanishes at certain interparticle distances l for which the force constants $f(l, T)$ are negative, which gives rise to the free-energy oscillations in Figs. 3 and 4.

By calculating the internal and free energies of particles and the Gibbs thermodynamic potential $\Phi = \Phi(P, T)$ at various temperatures and average intermolecular

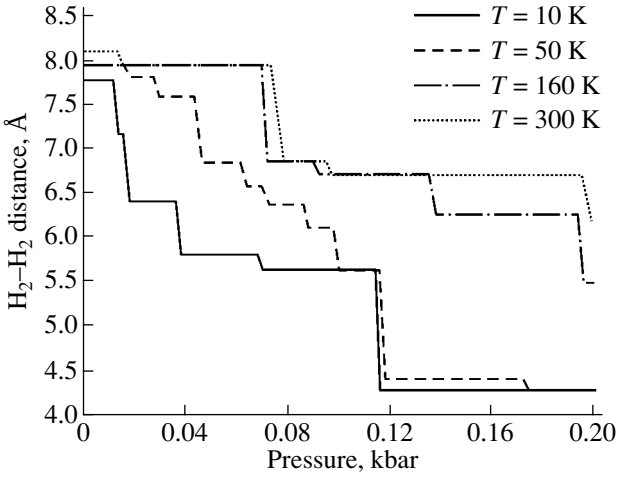

Fig. 5. Dependence of the equilibrium intermolecular H_2–H_2 distance $\langle d(P, T)\rangle$ in the (3,3) CNT on temperature T and external pressure P.

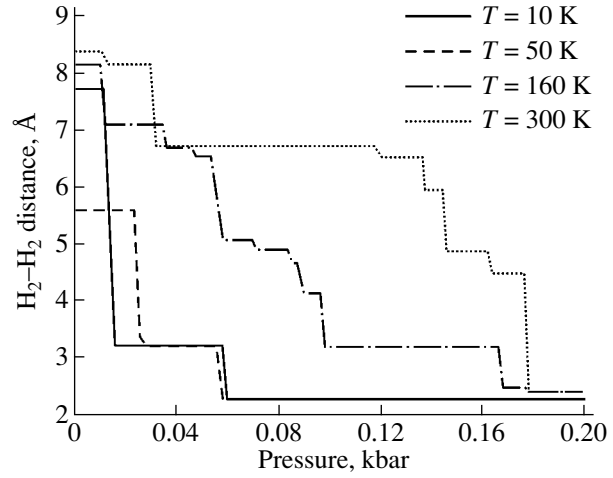

Fig. 6. Same as in Fig. 5 but for the (6,0) CNT.

distances d and by minimizing $\Phi(P, T)$ at each value of external pressure P, we found the equilibrium intermolecular distances $\langle d\rangle = \langle d(P, T)\rangle$ for both nanotubes (Figs. 5, 6). We can see that the density of adsorbed hydrogen molecules undergoes a series of phase transitions at all temperatures (not exceeding the upper limit T_{max} = 300 K of the temperature range covered in this study) as the external pressure increases (up to 0.2 kbar). The transitions are caused by the fact that, as the pressure increases, the hydrogen molecules begin to jump from deeper to less deep minima, since the change $\Delta(PV)$ in the contribution from the volume energy to Φ in this case becomes larger than the change in the free energy in the local minima. We can see from Figs. 3 and 4 that the number of local minima in the (6,0) nanotube is larger than that in the (3,3) tube. A particle jumps into these minima as the external pressure increases, which results in a larger compressibility of hydrogen inside the (6,0) nanotube in comparison with that for the (3,3) nanotube.

These results qualitatively agree with the experimental data from [3] (although CNTs of a significantly larger diameter were used in [3]). For example, the density of adsorbed hydrogen in [3] was ≃0.3 wt % at T = 290 K and P = 0.1 kbar. In our model, the calculated density of adsorbed hydrogen at this pressure and temperature is 0.42 wt %. In [3], the density of adsorbed hydrogen increased essentially nonlinearly with pressure, as was the case in our model.

3. CONCLUSIONS

A method for calculating the thermodynamic functions and the equilibrium density of a one-dimensional chain of molecules adsorbed inside a nanotube has been proposed. The model takes into account the interactions of incorporated molecules with one another (within the mean-field approximation) and with the nanotube walls. Data obtained in *ab initio* calculations using the pseudopotential method in the framework of the density functional formalism were used to calculate all the interactions. The model is quantum-mechanical and, hence, correctly includes the quantization of the energy levels of a particle and transitions of the particle to excited levels. The contribution from phonons is taken into account in calculating the free energy at nonzero temperature. This contribution improves the mean-field approximation and partly takes into account the contribution from vibrations of particles with respect to their average positions in the harmonic approximation. The method can be readily generalized to the case of adsorption in more complex systems (on two- and quasi-two-dimensional surfaces). The method has been applied to calculate hydrogen molecule adsorption in (3,3)- and (6,0)-type CNTs. It was shown that under pressure a sequence of first-order phase transitions occurs in which the density of adsorbed hydrogen changes in a jump.

ACKNOWLEDGMENTS

This study was supported by the federal program "Integration," project no. B0017.

REFERENCES

1. S. Ijima, Nature **354**, 56 (1991).
2. P. M. Ajayan and T. W. Ebbesen, Rep. Prog. Phys. **60**, 1025 (1997).
3. H. Zhu, A. Cao, X. Li, *et al.*, Appl. Surf. Sci. **178**, 50 (2001).
4. C. Rödenbeck, J. Kärger, and K. Hahn, Phys. Rev. E **55** (5), 5697 (1997).
5. A. J. Ramirez-Pastor, T. P. Eggarter, V. D. Pereyra, and J. L. Riccardo, Phys. Rev. B **59** (16), 11027 (1999).
6. M. Hodak and L. A. Girifalco, Phys. Rev. B **64**, 035407 (2001).

7. N. Wang, Z. K. Tang, C. D. Li, and J. S. Chen, Nature **408**, 50 (2000).
8. L. M. Peng, Z. L. Zhang, Z. Q. Xue, *et al.*, Phys. Rev. Lett. **85** (15), 3249 (2000).
9. J. J. M. Beenakker, V. D. Borman, and S. Yu. Krylov, Chem. Phys. Lett. **232** (4), 379 (1995).
10. Q. Wang, S. R. Challa, D. S. Sholl, and J. K. Johnson, Phys. Rev. Lett. **82** (5), 956 (1999).
11. K. Hahn, J. Karger, and V. Kukla, Phys. Rev. Lett. **76** (15), 2762 (1996).
12. M. C. Cordillo, J. Boronat, and J. Casulleras, Phys. Rev. B **65**, 014503 (2002).
13. K. A. Williams and P. C. Eklund, Chem. Phys. Lett. **320** (3), 352 (2000).
14. R. Car and M. Parrinello, Phys. Rev. Lett. **55** (22), 2471 (1985).
15. G. Kresse and J. Hafner, Phys. Rev. B **49** (20), 14251 (1994).
16. S. Hammes-Schiffer and J. C. Tully, J. Chem. Phys. **101** (6), 4657 (1994).
17. J. C. Tully, J. Chem. Phys. **93** (2), 1061 (1990).
18. C. T. White, D. H. Robertson, and J. W. Mintmire, Phys. Rev. B **47** (9), 5485 (1993).
19. G. Kresse and J. Hafner, Phys. Rev. B **47** (1), 558 (1993); Phys. Rev. B **49** (20), 14251 (1994).
20. G. Kresse and J. Furthmüller, Phys. Rev. B **54** (16), 11169 (1996).
21. D. Vanderbilt, Phys. Rev. B **41** (11), 7892 (1990).

Translated by A. Kazantsev

Physics of the Solid State, Vol. 46, No. 3, 2004, pp. 590–593. Translated from Fizika Tverdogo Tela, Vol. 46, No. 3, 2004, pp. 569–572.

FULLERENES AND ATOMIC CLUSTERS

Sign Inversion of the Radiation-Induced Plastic Effect in C_{60} Single Crystals upon the SC–FCC Phase Transition

Yu. I. Golovin*, A. A. Dmitrievskiĭ*, I. A. Pushnin*, M. V. Pavlov*, and R. K. Nikolaev**

** Tambov State University, Internatsional'naya ul. 33, Tambov, 392622 Russia*

e-mail: golovin@tsu.tmb.ru

*** Institute of Solid-State Physics, Russian Academy of Sciences, Chernogolovka, Moscow oblast, 142432 Russia*

Received June 2, 2003

Abstract—A reversible variation in the microhardness of C_{60} single crystals induced by low-dose β irradiation is found to change sign in the vicinity of the phase transition at T_c = 250–260 K. Radiation hardening is observed at $T < T_c$ and radiation softening, at $T > T_c$. The kinetic characteristics of the β-induced variation in the microhardness of C_{60} and its recovery to the initial value are studied in the temperature range 170–350 K. Both processes are found to be thermally activated. The activation energies are determined and are shown to be different for sc and fcc lattices. © *2004 MAIK "Nauka/Interperiodica".*

1. INTRODUCTION

In [1], we revealed the effect of reversible softening of C_{60} single crystals induced by low-dose ($D < 1$ cGy) β radiation at room temperature. The mechanism of the changes in the microhardness of fullerites caused by low doses is unknown.

The orientational sc–fcc phase transition observed to occur in C_{60} at T_c = 250–260 K is known to be accompanied by changes in various physical properties. In this temperature range, anomalous peaks were observed in the temperature dependences of the specific heat [2], velocity of sound [3], and internal friction [4]. The volume [5], Young's modulus [6], and microhardness [7] were also found to change sharply in the vicinity of the phase transition temperature. Moreover, Osip'yan *et al.* [8] revealed sign inversion in the magnetoplastic effect in C_{60} single crystals during the sc–fcc phase transition. It was assumed in [8] that the lattice structure changes under the action of a pulsed magnetic field with a pulse duration of ~100 μs and an amplitude of ~25 T. Earlier [9], we found that the effect of β-stimulated softening of C_{60} single crystals is sensitive to preliminary exposure of the crystals to a pulsed magnetic field; therefore, we may expect the temperature dependence of the radiation-plastic effect to also exhibit sharp changes when passing through T_c. The purpose of this work is to study the effect of low-dose β radiation on the microhardness of a single-crystalline fullerite in a wide temperature range, including the sc–fcc phase transition range.

2. EXPERIMENTAL

We studied pure vapor-deposited 3- to 5-mm C_{60} single crystals having facets typical of fcc crystals. The single crystals were glued on a LiF substrate with salinigrin such that their working surface was parallel to the stage of a PMT-3 microhardness tester, which was used to measure the microhardness H.

For β irradiation, we used a $^{90}Sr + {}^{90}Y$-based material with activity A = 14.5 MBq and an average energy of emitted electrons E = 0.536 MeV.

To study low-temperature β-stimulated processes and the subsequent recovery of the C_{60} microhardness to the initial value, the samples were sealed in bags of thin polyethylene and placed in a container cooled with liquid nitrogen. To study the radiation-induced plastic effect at elevated temperatures, the samples were placed in a furnace. The temperature of the samples during β irradiation was controlled with a thermocouple and varied from 170 to 350 K. The microhardness was always measured at room temperature, T_0 = 293 K. In other words, we actually determined the residual change in the microhardness after β irradiation performed at various temperatures.

It is known that, during natural aging in air, the microhardness of C_{60} single crystals changes due to photoinduced oxidation and polymerization of the surface [10, 11]. To inhibit photoinduced aging of the samples, all procedures except microhardness measurements were performed in darkness. Indentation diagonals were measured in weak red light. Check experiments carried out under these conditions (in the absence of external factors) showed that the microhardness of the C_{60} samples remained unchanged for at least 10 days after removal from an evacuated capsule.

The samples were loaded for 10 s at a load of 0.2 N. All experimental points were obtained by averaging 15–20 measurements. The effect was characterized by the variation in the microhardness $\Delta H = H_\beta - H_0$ (rather than by the absolute value of microhardness H), where H_0 and H_β were the values of microhardness of a sample before and after ionizing irradiation, respectively.

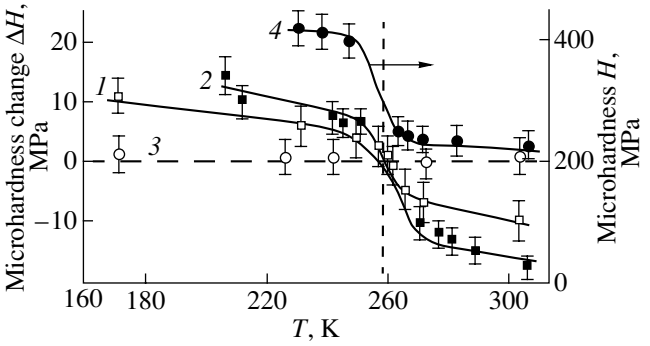

Fig. 1. Temperature dependences of changes in the microhardness ΔH: (*1*) residual ΔH measured after cooling to a temperature T and subsequent β irradiation and heating to room temperature T_0; (*2*) the same but for exposure to a pulsed magnetic field (B = 25 T, t = 100 μs) at a temperature T [8];and (*3*) check cooling–heating experiments without external factors. (*4*) Temperature dependence of the microhardness H [7].

3. RESULTS AND DISCUSSION

We found that, unlike the β-induced softening of fullerites at room temperature [1], the β irradiation of single-crystalline C_{60} at temperature $T < T_c$ leads to an increase rather than to a decrease in its microhardness as compared to the initial value. Thus, at a temperature near the phase transition temperature, the radiation-induced plastic effect changes sign (Fig. 1).

In the temperature range under study (as well as at room temperature [1]), the dependence of the β-induced change in the microhardness of C_{60} on the irradiation time, $\Delta H(t)$, is saturated. The irradiation time t_{sat} it takes for the $\Delta H(t)$ dependence to be saturated is found to depend on the β-irradiation temperature. In the temperature range under study, t_{sat} varied from 2.5 h at T = 350 K to 7.5 h at T = 170 K.

The increase in the microhardness of C_{60} induced by β irradiation at temperatures below the phase transition temperature, as well as the β-induced softening of the fullerite at $T > T_c$, can be reproduced many times after recovery of the initial microhardness of a sample, which occurs in a time τ_r. The relaxation time τ_r is also temperature-dependent and varies from 8 h at T = 350 K to 150 h at T = 170 K. The dependences of the variation in the fullerite microhardness on the irradiation time t and on the subsequent rest time τ at various temperatures become linear in the semilogarithmic coordinates $\ln H_r = f(t)$ and $\ln H_r = f(\tau)$ with a correlation coefficient close to unity. Here, $H_r = (\Delta H_{max} - \Delta H)/\Delta H_{max}$, where ΔH is the current change in microhardness at the instant of time t or τ and ΔH_{max} is the maximum β-induced change in microhardness at $t = t_{sat}$ and $\tau = 0$ (Fig. 2). A comparison of the slopes characterizing the rates of varying H at various temperatures (Fig. 2) shows that both t_{sat} and τ_r decrease with increasing temperature. These results indicate that the β-induced variation in H

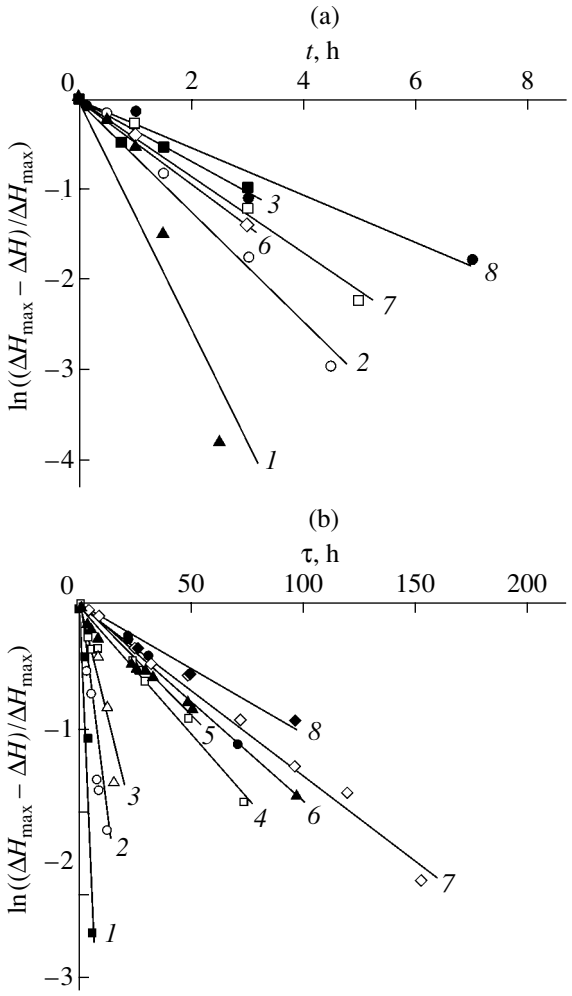

Fig. 2. Dependences of the residual change in microhardness ΔH of C_{60} single crystals on (a) the β irradiation time and (b) the subsequent relaxation time τ in the semilogarithmic coordinates at temperatures (*1*) T = 350, (*2*) 325, (*3*) 300, (*4*) 273, (*5*) 263, (*6*) 257, (*7*) 243, and (*8*) 200 K.

and the subsequent relaxation to the initial state occur via first-order reactions and are thermally activated.

In the semilogarithmic coordinates, the slope of the dependence of the rate of varying the microhardness on the reciprocal temperature is the activation energy for the process (if Arrhenius's law is obeyed). The temperature dependences of the rates of changes in H in the course of β-induced hardening/softening (Fig. 3a) and the subsequent relaxation (Fig. 3b) can be approximated by two intersecting straight lines. The region of intersection of the lines includes the phase transition point T_c; in this region, the fullerite consists of two phases. We believe that this circumstance causes the N-like break of the $\ln(dH_r/dt) = f(1/T)$ curve (Fig. 3a). The activation energies for the processes of β-induced variation in the microhardness and its relaxation thus estimated are different for the sc and fcc phases and are

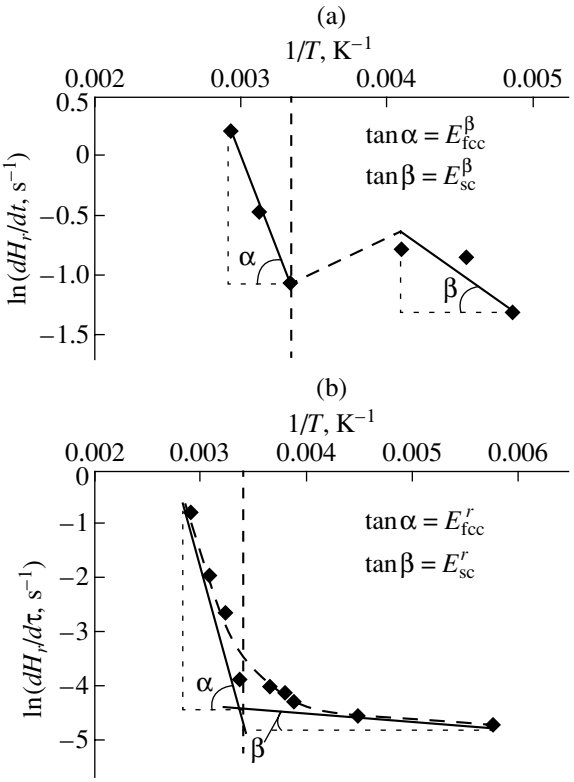

Fig. 3. Dependences of the rate of variation in the microhardness of the single-crystalline C_{60} on the reciprocal temperature of β irradiation (a) before and (b) during subsequent relaxation.

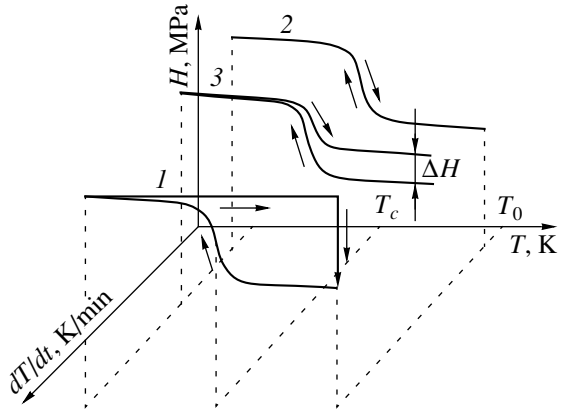

Fig. 4. Schematic diagram for the temperature dependences of the microhardness of C_{60} for three values of the heating rate dT/dt of samples: (*1*) above a certain critical value, (*2*) less than 5 K/min, and (*3*) an intermediate value.

equal to $E^{\beta}_{sc} = 0.06 \pm 0.02$, $E^{\beta}_{fcc} = 0.28 \pm 0.02$, $E^{r}_{sc} = 0.05 \pm 0.02$ eV, and $E^{r}_{fcc} = 0.58 \pm 0.02$ eV. Hence, the lattice type plays an important role in the radiation-induced plastic effect and the mechanisms of the effect of β irradiation on the plastic properties of the fullerite are different for the sc and fcc phases. According to the data from [8], the activation energy for the relaxation of H in the state induced by a pulsed magnetic field is $E^r = 0.18 \pm 0.02$ eV. This value was compared with the potential barrier between the *p* and *h* molecule configurations $E = 0.245$ and 0.3 eV for rotations about the twofold and threefold axes, respectively [12]. This comparison allowed the authors of [8] to assume that the magnetic field can affect the population of the *h* and *p* states in C_{60} molecules. Although the temperature dependences of the magnetoplastic and radiation-induced plastic effects are similar (Fig. 1), we cannot draw an analogous conclusion based on the activation energies that were determined in our case. However, it should be noted that the radiation-induced plastic effect is sensitive to a pulsed magnetic field [9]. This fact indicates that both low-dose β irradiation and a pulsed magnetic field affect the same objects in C_{60} single crystals, although the mechanisms of their influence are obviously different. In the case of the radiation-induced plastic effect, two different mechanisms are likely to exist, one for the sc phase and one for the fcc phase.

Kobelev *et al.* [6] showed that the fcc–sc phase transition in the C_{60} fullerite is accompanied by a significant (~10%) increase in all elastic moduli. The microhardness H is the measure of the resistance of a sample to the elastoplastic penetration of a harder body and, therefore, depends on the elastic moduli and increases with them. The reversible changes in H measured in [7] during the fcc–sc phase transition are qualitatively similar to the residual changes ΔH found in this work after β irradiation at the corresponding temperatures. A certain quantitative discrepancy can be explained by the following.

Unlike in [7], where H was measured directly in the sc and fcc phases, we measured the residual change in microhardness ΔH. In principle, because of a hysteresis characteristic of phase transitions in the solid state, the sc lattice can survive at $T = 300$ K if the heating rate dT/dt is higher than a certain critical value. In this case, the residual change in microhardness ΔH (measured at T_0) should coincide with the results obtained in [7] (Fig. 4, curve *1*). However, to avoid the so-called quenching-induced defects [13–15], dT/dt has to be smaller than 5 K/min. Our special experiments showed that "freezing–unfreezing" of the samples at $dT/dt = 5$ K/min without irradiation does not cause considerable changes in the microhardness of C_{60} single crystals (Fig. 1); i.e., the residual change in microhardness ΔH was equal to zero (Fig. 4, curve *2*). Obviously, intermediate states can also exist when the rate dT/dt is such that the crystal lattice transforms incompletely (Fig. 4, curve *3*).

Thus, sign inversion in the radiation-induced plastic effect can be due to the fact that β irradiation of C_{60} single crystals at $T < T_c$ results in fixation of the sc phase or decreases the rate of reconstruction of the sc lattice to the fcc lattice upon heating. In this case, the residual changes in microhardness ΔH detected even at $dT/dt <$

5 K/min can be identified with ΔH (Fig. 4, curve *3*) that can be obtained at certain heating rates ($dT/dt > 5$ K/min) on nonirradiated samples.

However, the fixation of the sc phase does not explain the β-induced softening of C_{60} single crystals at $T > T_c$. The sign inversion in the magnetoplastic effect observed at T_c suggests that β irradiation at $T > T_c$ stimulates processes that cannot occur at temperatures below the phase transition point. The authors of [16, 17] showed that one of the conditions for the dimerization of a fullerite exposed to an electron beam is the capability of C_{60} molecules to rotate, which occurs only at $T > T_c$. The dissociation of dimers is a first-order reaction and, as follows from [18], a thermally activated process with an activation energy of 1.75 ± 0.05 eV (for dimers produced under pressure). Although this value differs significantly from the activation energies determined in this work, we can assume that dimerization of the fullerite takes place under the action of low doses of β irradiation in a certain temperature range.

ACKNOWLEDGMENTS

This work was supported by the program "Fullerenes and Atomic Clusters" (project no. 541-02), the Russian Foundation for Basic Research (project no. 02-02-17571), the program "Russian Universities" (project no. UR.01.01.013), and the federal program "Integration" (project no. 30475/1558).

REFERENCES

1. Yu. A. Golovin, A. A. Dmitrievskiĭ, R. K. Nikolaev, and I. A. Pushnin, Dokl. Akad. Nauk **385** (1), 1 (2002) [Dokl. Phys. **47**, 485 (2002)].
2. P. A. Heiney, J. E. Fisher, A. R. McGhie, *et al.*, Phys. Rev. Lett. **66** (22), 2911 (1991).
3. X. D. Shi, A. R. Cortan, J. M. Williams, *et al.*, Phys. Rev. Lett. **68**, 827 (1992).
4. S. Hoen, N. G. Chorpa, X.-D. Xiang, *et al.*, Phys. Rev. B **46** (19), 12737 (1992).
5. I. O. Bashkin, V. I. Rashchupkin, A. F. Gurov, *et al.*, J. Phys.: Condens. Matter **6**, 7491 (1994).
6. N. P. Kobelev, A. P. Moravskiĭ, Ya. M. Soĭfer, *et al.*, Fiz. Tverd. Tela (St. Petersburg) **36** (9), 2732 (1994) [Phys. Solid State **36**, 1491 (1994)].
7. M. Tachibana, M. Michiyama, K. Kikuchi, *et al.*, Phys. Rev. B **49** (21), 14945 (1994).
8. Yu. A. Osip'yan, Yu. I. Golovin, R. B. Morgunov, *et al.*, Fiz. Tverd. Tela (St. Petersburg) **43** (7), 1333 (2001) [Phys. Solid State **43**, 1389 (2001)].
9. Yu. I. Golovin, A. A. Dmitrievskiĭ, R. K. Nikolaev, and I. A. Pushnin, Fiz. Tverd. Tela (St. Petersburg) **45** (1), 187 (2003) [Phys. Solid State **45**, 197 (2003)].
10. V. I. Orlov, V. I. Nikitenko, R. K. Nikolaev, *et al.*, Pis'ma Zh. Éksp. Teor. Fiz. **59** (10), 667 (1994) [JETP Lett. **59**, 704 (1994)].
11. I. Manika and J. Maniks, Fullerene Sci. Technol. **5** (1), 149 (1997).
12. V. D. Natsik, S. L. Lubenets, and L. S. Fomenko, Fiz. Nizk. Temp. **22** (3), 337 (1996) [Low Temp. Phys. **22**, 264 (1996)].
13. V. M. Egorov, B. I. Smirnov, V. V. Shpeĭzman, and R. K. Nikolaev, Fiz. Tverd. Tela (St. Petersburg) **38** (7), 2214 (1996) [Phys. Solid State **38**, 1219 (1996)].
14. V. V. Shpeĭzman, N. N. Peschanskaya, V. M. Egorov, *et al.*, Fiz. Tverd. Tela (St. Petersburg) **42** (9), 1721 (2000) [Phys. Solid State **42**, 1771 (2000)].
15. V. M. Egorov, R. K. Nikolaev, B. I. Smirnov, and V. V. Shpeĭzman, Fiz. Tverd. Tela (St. Petersburg) **42** (9), 1716 (2000) [Phys. Solid State **42**, 1766 (2000)].
16. T. L. Makarova, Fiz. Tekh. Poluprovodn. (St. Petersburg) **35** (3), 257 (2001) [Semiconductors **35**, 243 (2001)].
17. Y. B. Zhao, D. M. Poirier, R. J. Pechman, and J. H. Weaver, Appl. Phys. Lett. **64**, 577 (1994).
18. S. Lebedkin, A. Gromov, S. Giesa, *et al.*, Chem. Phys. Lett. **285**, 210 (1998).

Translated by K. Shakhlevich